OPTIMIZATION OF AUTOMOTIVE LIGHT DISTRIBUTIONS FOR DIFFERENT REAL LIFE TRAFFIC SITUATIONS

DISSERTATION VON
JONAS KOBBERT

TECHNISCHE
UNIVERSITÄT
DARMSTADT

Vom Fachbereich Elektro- und Informationstechnik
der Technischen Universität Darmstadt

zur Erlangung des akademischen Grades
eines Doktors der Ingenieurwissenschaften
(Dr.-Ing.)

von Jonas Kobbert, M.Sc.
geboren in Heidelberg

1. Prüfer: Prof. Dr.-Ing. habil. Tran Quoc Khanh
2. Prüfer: Prof. Dr. rer. nat. Cornelius Neumann

Tag der Einreichung: 23.08.2018
Tag der mündlichen Prüfung: 07.12.2018

Darmstadt 2019
D17

Jonas Kobbert: *Optimization of Automotive Light Distributions for Different Real Life Traffic Situations*

Darmstadt, Technische Universität Darmstadt
Jahr der Veröffentlichung der Dissertation auf TUprints: 2019
Tag der mündlichen Prüfung: 07.12.2018

ABSTRACT

The major goal of this thesis is to find a way to optimize current automotive headlamps in order to provide safer nighttime driving. While this has already been done in the past with the works by Damasky and Huhn, the current approach combines methods previously not used in one single study. In the first steps, the influence of different headlamp parameters on viewing distance of the driver is evaluated in field tests. In the second step, the current German traffic space is analysed before in the third step, the gaze behaviour of drivers is recorded and investigated for different situations. The combination of these studies is then used to propose new light distributions.

In the first part, field tests are conducted in order to investigate detection distances with different lighting conditions. The gained data is used to provide recommended luminous intensity values for certain detection distances. Furthermore, the data is used to extract luminous intensity recommendations for different angular positions relative to the hot spot. These investigations show, that the current limits set by the ECE for high beam headlamps are sufficient to provide safe detection distances for nearly all situations. However, the data also shows, that low beam should be disregarded for any situation and only be used if high beam cannot be used at all.

The traffic space analysis in the second part of this thesis shows, that there are significant differences between different road categories in terms of object location and frequency. For these situations, optimized segment distributions are proposed, leading to significant benefits over the conventional high beam setup. The difference between the proposed segment partitioning and the standard setup is, that the segments are not set equal in size. The segments at the centre of the distribution are set to be smaller in order to better mask out traffic that is further away. Furthermore, it is shown, that the benefit of additional segments is limited at around 280 segments, where a performance identical to a 10000 pixel headlamp is achieved.

In the last section, regarding the gaze analysis a large driving test, including 54 test subjects is performed. Here the findings by Diem, Damasky, Brückmann and Weber are confirmed. New approaches regarding the correlation between the driver's gaze and objects in the traffic space are tested. On a general level, no correlation between the object distribution and the gaze is found. However, a large databank containing object positions as well as driver's gaze, speed, lighting condition and position in the world is set up for further, more detailed information. The data from all presented studies is then used to propose new, optimized light distributions.

ZUSAMMENFASSUNG

Das Hauptziel dieser Arbeit ist es, einen Weg zu finden, aktuelle Kfz-Scheinwerfer zu optimieren, um eine sicherere Nachtfahrt zu ermöglichen. Während dies bereits in der Vergangenheit durch Arbeiten von z.B. Damasky und Huhn geschehen ist, kombiniert der vorgestellte Ansatz Methoden, die bisher nicht in einer einzigen Studie verwendet wurden. In den ersten Schritten wird der Einfluss verschiedener Scheinwerferparameter auf die Sichtweite des Fahrers in Feldtests bewertet. Im zweiten Schritt wird der deutsche Verkehrsraum analysiert, bevor im dritten Schritt das Blickverhalten der Fahrer erfasst und für verschiedene Situationen untersucht wird. Die Kombination dieser Studien wird abschließend genutzt, um neue, optimierte Lichtverteilungen zu generieren.

Im ersten Teil der Arbeit werden Feldtest durchgeführt, die Detektionsabstände bei unterschiedlichen Lichtverhältnissen analysieren. Aus den gewonnenen Daten werden empfohlene Lichtstärkewerte für bestimmte Sichtbarkeitsweiten abgeleitet. Darüber hinaus werden die Daten verwendet, um Lichtstärkeempfehlungen für verschiedene Winkelpositionen relativ zum Fahrer zu extrahieren. Diese Untersuchungen zeigen, dass die von der ECE für Fernlichtscheinwerfer festgelegten Lichtstärkegrenzen ausreichen, um sichere Detektionsabstände für fast alle Situationen zu gewährleisten. Die Daten zeigen aber auch, dass das Abblendlicht nur dann eingesetzt werden sollte, wenn das Fernlicht überhaupt nicht genutzt werden kann, da die Sichtbarkeitsweiten deutlich niedriger sind als für eine sichere Fahrt notwendig.

Die Verkehrsraumanalyse im zweiten Teil der Arbeit zeigt, dass es signifikante Unterschiede zwischen verschiedenen Straßenkategorien in Bezug auf Lage und Häufigkeit von Objekten gibt. Für diese Situationen werden optimierte Segmentverteilungen vorgeschlagen, die zu signifikanten Vorteilen gegenüber dem konventionellen Aufbau von blendfreiem Fernlicht führen. Der Vorteil wird dadurch generiert, dass die Segmente in ihrer Größe variabel angeordnet werden. Segmente in der Mitte der Verteilung sind kleiner eingestellt, um weiter entfernten Verkehr besser abzudecken zu können. Außerdem wird gezeigt, dass der Nutzen zusätzlicher Segmente auf etwa 280-Segmente begrenzt ist, wo eine identische Fahrbahnausleuchtung wie mit einem 10000-Segment-Scheinwerfer erzielt wird.

Im letzten Abschnitt wird bezüglich des Blickverhaltens von Autofahrern ein Fahrversuch mit 54 Testpersonen durchgeführt. Hier werden die Ergebnisse von Diem, Damasky, Brückmann und Weber bestätigt. Neue Ansätze zur Korrelation zwischen dem Blick des Fahrers und Objekten im Verkehrsraum werden erprobt. Auf einer allgemeinen Ebene wird keine Korrelation zwischen der Objektverteilung und dem Blick gefunden. Eine große Datenbank mit Objektpositionen sowie Blickwinkel, Geschwindigkeit und Lichtverhältnisse relativ zum Autofahrer ist jedoch für weitere, detailliertere Informationen eingerichtet. Die Daten, die in allen Teilen der Thesis erarbeitet wurden werden im letzten Abschnitt zu einer neuen, beispielhaften Lichtverteilung kombiniert und diese wird mit herkömmlichen Lichtverteilungen verglichen und Hauptunterschiede zwischen diesen Lichtverteilungen werden herausgearbeitet.

ACKNOWLEDGEMENTS

The studies and the results shown in this thesis were carried out from 2015 to 2018 at the Laboratory of Lighting Technology in Darmstadt, with the goal to acquire a Doctoral degree in Electrical Engineering and Information Technology from the Technische Universität Darmstadt. With this acknowledgement section, I intend to explicitly thank the ones who made this thesis possible by supporting me over the last years.

First of all, I owe my deepest gratitude to my supervisor Prof. Dr.-Ing. habil. Tran Quoc Khanh, with whom I had the chance to create the steps needed to full-fill the goals of this thesis. His help in terms of automotive lighting, physiological and psychological evaluation of photometric parameters has been fundamental for the success of this thesis.

Furthermore, I am deeply grateful to Prof. Dr. rer. nat. Cornelius Neumann for his agreement to be the second referee during the doctoral examination phase following the thesis' submission.

Special thanks goes to Kyriakos Kosmas for his valuable support in all the presented studies. Moreover, I am indebted to many of my colleagues from the Laboratory of Lighting Technology, Darmstadt who always provided fruitful and very inspiring discussions on miscellaneous topics leading to a further broadening of my horizons beyond the scope of my own research.

Last but not least, this thesis would not have been possible without the backing and the support by Ann-Kathrin Seifert, my parents, Kornelia Wojtalla-Kobbert and Hans Kobbert, as well as my friends over the last years. They have not only supported me mentally throughout this time, but many have been participating in long nights of pre-test sessions that needed to be done before the actual testing phase could start.

CONTENTS

LIST OF FIGURES

LIST OF TABLES

ACRONYMS

ADB Advanced Driving Beam

AFS Advanced Frontlighting System

API Application Programming Interface

BCD Borderline between Comfort and Discomfort

CCT Correlated Colour Temperature

CDF Cumulated Distribution Function

CIE Commission Internationale de l'Éclairage

DLP Digital Light Processing

eCDF empirical Cumulated Distribution Function

ECE Economic Commission for Europe

EEG Electroencephalography

EOG Electro-OculoGraphy

FMVSS Federal Motor Vehicle Safety Standards

FWHM Full Width at Half Maximum

gfHB glare free High Beam

GPS General Positioning System

HID High Intensity Discharge

IoU Intersection of Union

ipRGC intrinsically photosensitive Retinal Ganglion Cells

LASER Light Amplification by Stimulated Emission of Radiation

LCD Liquid Cristal Display

LED Light Emitting Diode

MSE Mean Square Error

OSM OpenStreetMap

POG Photo-Oculo Graphy

PR Purkinje Reflection

PWM Pulse Width Modulation

ROI Region of Interest

SAE Society of Automotive Engineers

TFT Thin-Film Transistor

UNECE United Nations Economic Commission

UTM Universal Transverse Mercator

VOG Video-Oculo Graphy

SYMBOL DIRECTORY

Symbol	**SI Unit**	**Meaning**
λ	nm	Wavelength
V(λ)		Human Spectral Sensitivity During the Day
V′(λ)		Human Spectral Sensitivity During the Night
ϕ	lm	Luminous Flux
I	cd	Luminous Intensity
E	lx	Illuminance
E_0	lx	Base Illuminance
L	cd/m^2	Luminance
Ω		Solid Angle
A	m^2	Area
r	m	Distance
L_a	cd/m^2	Adaptation Luminance
L_O	cd/m^2	Object Luminance
α	deg	Viewing Angle
t	s	Time
σ		Standard Deviation
μ		Mean
d	m	Distance
w		Psychological Glare
H	lx·s	Exposure
H_0	lx·s	Base Exposure
P	mm	Pupil Diameter
P_0	mm	Base Pupil Diameter
T_0	s	Base Pulse Duration

Part I

INTRODUCTION

"Progress lies not in enhancing what is, but in advancing toward what will be."

– Khalil Gibran

1

INTRODUCTION

The presented thesis investigates possibilities to optimize existing and future light distributions for automotive headlamps. Over the last decades, new headlamps have been based on research conducted by Damasky, Huhn, Kleinkes or Diem [1–4]. Since technology, for both headlamps as well as for the technology available to evaluate light distributions has evolved over the last decades with the introduction of new and more powerful computational power, this thesis will present updated approaches to these works. For this, field tests are conducted in order to evaluate current performance of state-of-the-art headlamps. The gained results are used to deduct necessary intensities for optimal detection under different angles. Furthermore, the new or updated approaches include new and precise gaze tracking to estimate where drivers look at during day- and nighttime driving, while simultaneously measuring the traffic space and objects within the driver's field of view. For this, an experimental vehicle is setup with current eye tracking equipment and the most recent object recognition hard- and software. Object recognition algorithms are trained and the data is analysed. The complete data from all performed studies are then used to deduct optimized light distributions for maximum detection distances, German traffic space and driver's gaze behaviour. With the proposed light distribution, this thesis aims at improving safety for nighttime driving as well as increasing the comfort for drivers.

1.1 MOTIVATION

Over the last couple of years, the overall traffic density steadily increased, while the total amount of vehicles on the road has stayed the same. This is due to an increase in the overall driven distance per year per vehicle by 10 %. [5, 6]
With more and more vehicles being on the road simultaneously, one of the key challenges for vehicle manufacturers is to create a safer environment for the road users. In fact, traffic accident statistics reveal, that while the overall traffic is significantly reduced during night, the probability of being involved in an accident is significantly increased, as shown in figure 1.1, where the ratio of accidents relative to the traffic volume is shown over different day times. The data is split into fatal accidents (dashed line) and accidents resulting in injuries (solid line). The accident data shown is set in relation to the accident ratio between 10:00 - 11:00 and shows, that the minimal accident probability is found between around 07:00 to 21:00 with a slight local maximum at around 17:00. This shows, that with the exception of the evening rush hour, where the traffic density is at its peak, the highest probability for crashes is found during night time. [6, 7]

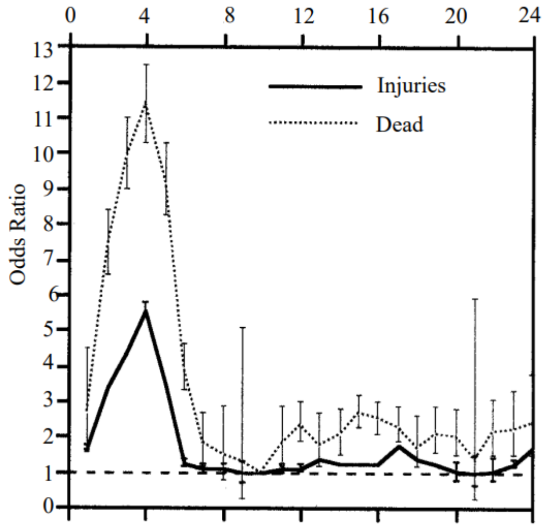

Figure 1.1 – Probability of being involved an accident over different day times relative to driving between 10:00 - 11:00. The relative probability for being in an accident with fatal outcome is shown in the dashed line and the relative probability to be involved in any accident is shown in the solid line. [7]

While the overall number of fatal accidents during night has been decreasing, a significant amount of deaths remains, e.g. around 1000 fatal night time accidents per year in Germany alone. The numbers of fatal injuries over the last decade on German roads are shown in figure 1.2 where the overall accidents are shown in red and the data for night time fatalities are shown in blue. [6]

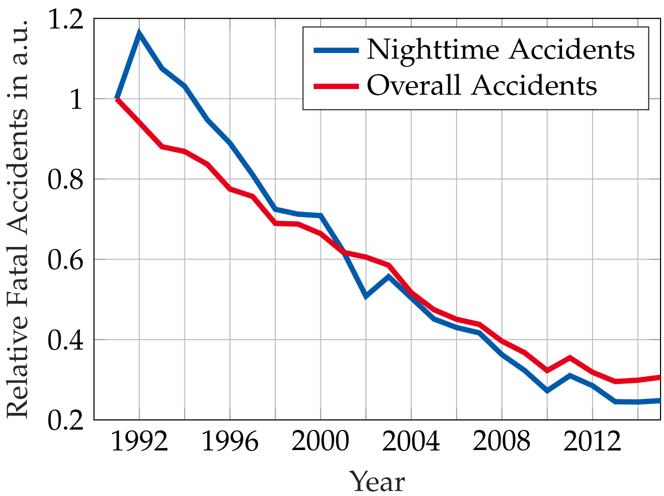

Figure 1.2 – Ratio of accidents with fatal outcome since 1991 relative to the accident numbers of 1991 according to the ADAC [6].

The data is normalized to the number of accidents and fatal accidents from 1991. The data shows, that both accident types decline very similar. This indicates, that the major reason for the reduction of fatal accidents is found in development and improvement of technology, that helps reducing the impact of accidents for both day and night at the same time. This is not to say, that the introduction of new headlamp technology is not helpful in reducing the impact of night time crashes. However the distribution of high end headlamp systems is rather limited and has only been rising over the last couple of years with High Intensity Discharge (HID) headlamps having a market share of only 5 % and Light Emitting Diodes (LEDs)

being at 10 %. However, the market share of LED headlamps has been steadily rising since the introduction of the first full LED headlamp. [8]
Combining these two findings shows, that there is still a large possibility for the reduction in nighttime accidents, with the goal of getting the accident probability at night down to similar levels as for daytime driving. Since the main difference between daytime driving and driving at night is the level of illumination and knowing, that the main information by the driver is obtained visually [9], the obvious choice has to be the improvement of the driver's visibility by improving current headlamps and headlamp technology. This is already one of the main issues for headlamp and car manufacturers as evident when reviewing the current development of newly introduced technology and functionality in this area as shown in the following sections.

1.2 THESIS AIMS AND OUTLINE

While new headlamps and new intelligent lighting functions have been introduced, the general light distributions have stayed the same with the exception of sharper cut-off lines and the introduction of vertical cut-off lines for glare free High Beam (gfHB). For this reason, the goal of this thesis is the analysis of different factors to optimize current and new headlamp technologies in terms of visibility. In order to do so, a series of studies is devised and set up. These studies split the presented thesis into four parts.
The basic foundations needed to understand the work presented a general introduction into the perception of light, where the general setup of human eyes and the perception and measurement of light is explained in chapter 2. This chapter includes an excursion into eye tracking, explaining the foundations needed to understand how the tracking of human vision works and where the limitations are set.
The next chapter, chapter 3, is dedicated to the most recent development of automotive front lighting. Here a short summary of the historic development of automotive front lighting system is given. The major part of this chapter is however dedicated to state-of-the-art headlamp technology and estimated future development for headlamps. The last part of this chapter summarized the current regulations for headlamps than confine the possibilities for different light distributions.
Chapter 4 analyses an excerpt of previous research that is relevant to the work presented in this thesis. This starts with research regarding detection and glare in automotive use. For a more complete overview over the different influencing factors, laboratory and field studies are included. Where available, studies conducted within a driving simulator, are reviewed as well. Further more, the analysis of gaze behaviour and the optimization of light distributions presented in the last years is reviewd.
The main part of this thesis, chapter 5, is then split into four sections according to the main investigations presented here. In the first section, section 5.1, three field tests are presented. These field tests investigate the influence of the luminous intensity on detection in terms of low and high beam. Furthermore, the influence of different object locations in the field of view is analysed.
The second section, 5.2, shows the analysis of German traffic space. This analysis is done in two steps. The first step represents a basic traffic simulation for German country roads. In this simulation, traffic is mapped into a traffic density distribution. Based on this distribution, gfHB segments are optimized for highest possible road illumination. This theoretical traffic density distribution is then obtained via a field test with over 6000 km of driving, in which

the traffic of urban roads, country roads and motorways are analysed. The same optimization that was done using the simulation is repeated with the real life traffic data to obtain a more realistic data set.

Section 5.3 focuses on the correlation between short illuminance pulses registered in real life driving and the glare perception. For this, two laboratory experiments are devised. The first study investigates the correlation between the pupil diameter, photometric values and the glare perception for rectangle light pulses. In the second study, the influence of the pulse form on the glare perception is further analysed. The last section, 5.4 shows the analysis of the driver's gaze and fixation behaviour in different traffic situations. In this section, not only the general gaze is analysed, but the influence of different traffic situations on the gaze behaviour is analysed. These situations include situations known from previous work, like the gaze behaviour in different road categories or while driving through a corner, but expand to new situations like traffic density and object positions as well.

The obtained data from all studies is then used to propose exemplary new light distributions for different purposes. This thesis is then concluded with a summary and a critical review of the obtained data.

Part II

FUNDAMENTALS OF VISUAL PERCEPTION

"Facts matter not at all. Perception is everything. It's certainty."

– Stephen Colbert

2 FUNDAMENTALS OF VISUAL PERCEPTION

The main part of this thesis is set upon the investigation of pupil contraction in different light situations, both in an isolated laboratory environment, and in real life traffic situations, and on the analysis of human gaze and fixation behaviour in different traffic situations. In order to understand the principle of the physiological response of human eyes, the following sections introduce the basic foundations of human light perception. This starts with the physiological setup and the basic movement of the human eye. This knowledge is then used to introduce methods on eye or gaze tracking as well as the measurement of the pupil diameter. In the next part, the relevant lighting parameters for this thesis are introduced and both glare and detection in a general context are introduced.

2.1 THE HUMAN EYE

The main part of this thesis focuses on human gaze behaviour during driving tasks in different traffic situations. To understand what a driver is looking at, and espeacially why a driver is looking at something and even more importantly, what the driver perceives while looking at something, it is crucial to understand the basic concept of visual perception. Visual perception of the environment is considered to be one of the most complex tasks humans perform [10] and as such, it can be divided into multiple tasks such as perception of colour and/or luminance differences, identification of object form and movement as well as combinations of these parameters [11]. To fully understand the following chapters a deeper knowledge of the human eye is necessary. This section will therefore focus on the physiology of the human eye and its movement before discussing different ways to monitor its movement.

2.1.1 PHYSIOLOGY OF THE HUMAN EYE

The human eye is not a perfect sphere but rather elliptically shaped with an average size of about 24.2 mm · 23.8 mm · 24.5 mm transversal, sagittal and axial if measured from sclera, the white, protective outer layer of the eye, to sclera. While the exact reported size and shape of the human eye varies from person to person [12], the overall structure of the eye remains identical for most humans, with some exceptions, due to different diseases, that will not be discussed further. Figure 2.1 shows a cut through the human eye and its most important parts in order to visualize the basic setup and the most important parts of the human eye.

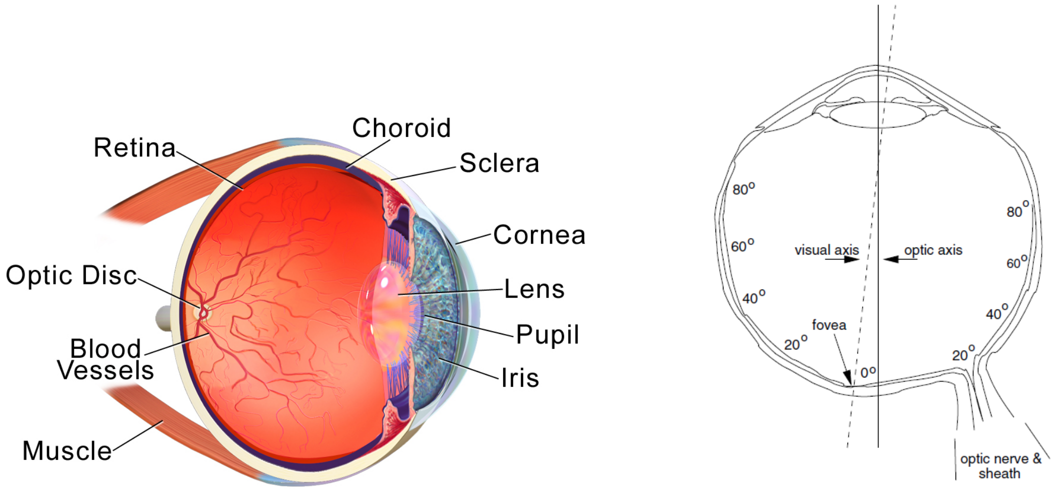

(a) (b)

Figure 2.1 – Anatomy of the human eye with regard to optical and visual axis. The optic disk or optic nerve is seen in both images. Figure (a) shows the schematic anatomy of the human eye. Light falls onto the retina by passing through the cornea, the pupil and the lens. (b) Shows the important difference between optical axis, which is setup through the pupil and the centre of the eyeball, and the visual axis, going from pupil to fovea.

Following figure 2.1a from right to left: the transparent cornea, covering the iris and the pupil and accounts for approximately 4/5 of the eyes optical refraction [13]; the iris, which forms the pupil; the lens, focusing objects onto the retina [14]; the sclera, the white of the eye, protecting the eye; muscles to move the eye; the optical disc where nerve endings exit the eye and connect to the brain [15] and of course the retina, consisting of photoreceptor cells, rods and cones, to detect light and therefore enabling humans to see. In total, there are four different types of cones of which only three are relevant for this work. The distribution of rods and cones on the retina is shown in figure 2.2. Cones are concentrated in the middle of the retina, the fovea, the only area on the retina where humans can actually see objects sharply. And while it might appear, as if the middle of the pupil, the middle of the eyeball itself and the fovea align, this is not the case. The optical axis of the human eye is tilted by a few degrees away from the centre of the eyeball, as shown in figure 2.1b. This misalignment varies similarly to the variation of the eye ball size from person to person.
The rods are located more to the outside. The part of the fovea, where the optical nerve moves through the retina and towards the brain is called blind-spot. Due to the special layering of the human retina, the optical nerve blocks any kind of photoreceptor cell. Therefore, the eye cannot perceive any information on this particular spot.

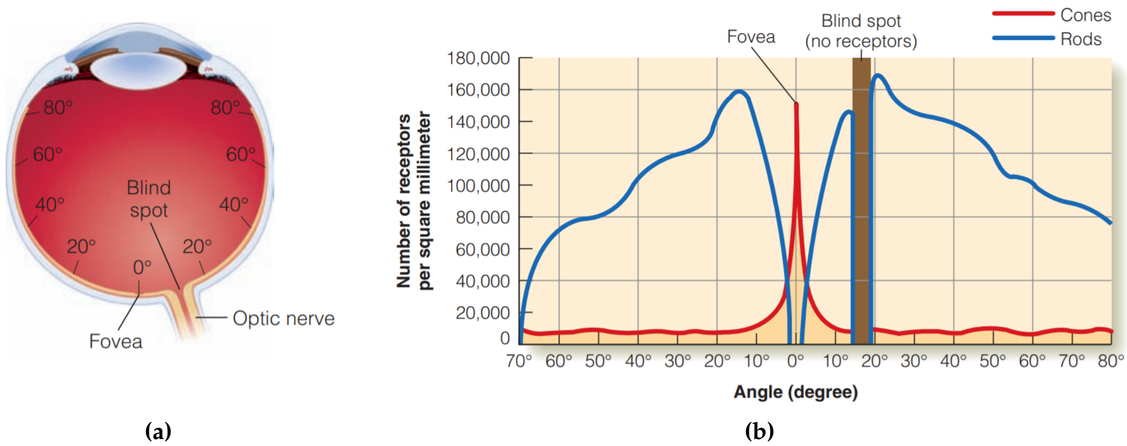

Figure 2.2 – The distribution of rods and cones on the human retina. (a) sets up a coordinate system in degrees relative to the fovea. These coordinates are repeated along the bottom of (b). The vertical brown bar near 20 degrees indicates the optical disc, the blind spot.[13]

As mentioned above, cones can be split into four more categories. Three of them are responsible for the perception of colour (S-, M-, L-Cones). Their wavelength sensitivity is shown in figure 2.3.S-, M- and L-cones absorb light of short, medium and long wavelength, respectively. As shown, they have their absorption maximum at about 420 nm, 534 nm and at 564 nm. Rods are sensitive from 400 nm to 600 nm and have their maximum absorption at 498 nm, compared to colour information delivered by cones, rods only supply information on brightness. The fourth cone type, the intrinsically photosensitive Retinal Ganglion Cells (ipRGC), will not be discussed here since their function to suppress melatonin is not relevant for this thesis. [16]

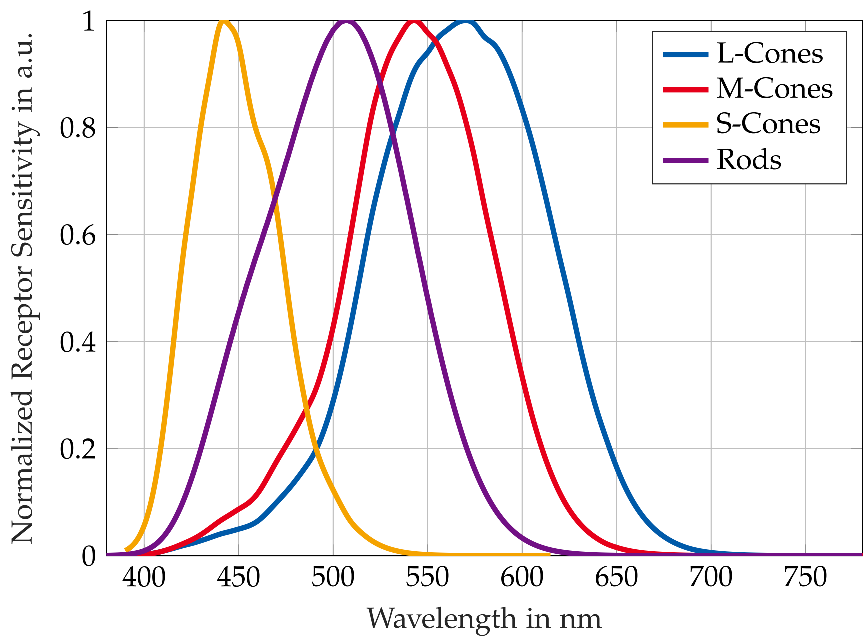

Figure 2.3 – Wavelength sensitivity for rods (dashed black line) as well as for the S- (blue), M- (green) and L-Cones (red). [16]

Rods and cones do not only differ in their position on the retina and their ability to absorb light of different wavelengths but also in their absolute sensitivity under different brightness levels. When the illumination of the environment is changed from bright (photopic) to dark (scotopic), the human eye will adapts to the illumination. This process is shown in figure 2.4, where the sensitivity curve for cones (green), rods (blue) and the combination of both (red) is shown over the time spent in a dark environment.

The terms photopic and scotopic are defined by the sensitivity of rods and cones. If only cones are active due to the light situation, this is called a photopic scene. This is valid for a luminance range of $5\,\mathrm{cd\,m^{-2}}$ and above. From $0.005\,\mathrm{cd\,m^{-2}}$ and lower only rods are active and this luminance range is called scotopic. The range in which both are active is called the mesopic range. [17]

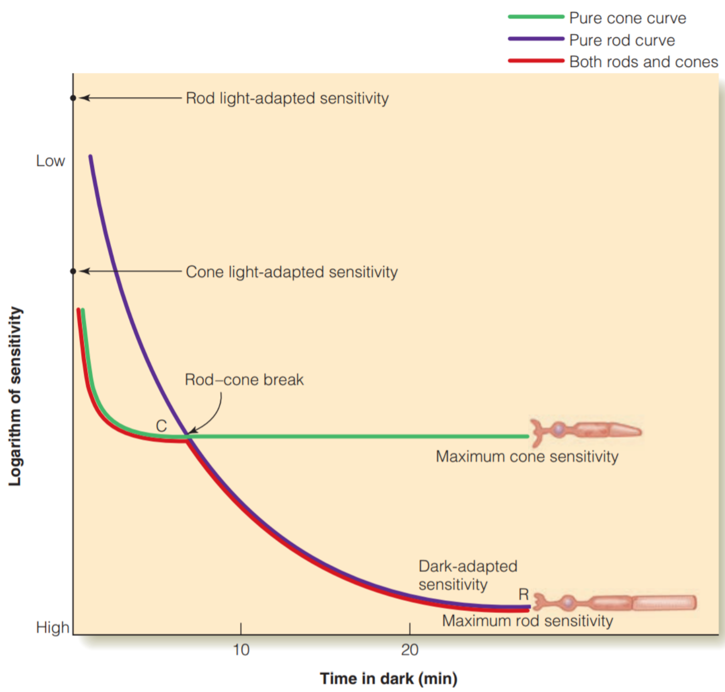

Figure 2.4 – The red line shows the two-stage dark adaptation curve, with an initial cone branch and a later rod branch. The green line is the cone adaptation curve. The purple curve is the rod adaptation curve. Note that the downward movement of these curves represents an increase in sensitivity. The curves actually begin at the points indicating "light-adapted sensitivity," but there is a slight delay between the time the lights are turned off and when measurement of the curves begins. [13]

This complex sensitivity of the photoreceptor cells results in the unique way humans perceive light under different situations, leading to the V(λ)- and the V'(λ)-curve which define the overall sensitivity of the human eye in the photopic and the scotopic range. This will be explained in detail in section 2.3. Furthermore, the *Weber-Fechner-Law* can be derived from the adaptation curve shown in figure 2.4. This law states, that an exponential increase in the stimulating intensity only leads to a linear increase in the perceived sensual stimulus.

After discussing the basic structure of the human eye and how colour perception works on a very basic level, eye movement will be discussed next.

2.1.2 EYE MOVEMENT

The observation and measurement of the above mentioned eye movements goes back to 1879 where the eye's movement during reading tasks were observed and the terms **saccade** and

fixation were mentioned for the first time [18]. The following subsections however will focus on modern methods of recording and analysis of eye movement. To fully perceive a complex environment, after looking at one object we have to shift our gaze from one object to another. This, at first glance rather simple pattern does not only involve the fastest muscular movement human bodies can perform - a **saccade**, one of only two voluntary eye movements - with up to $1000\,^\circ\,s^{-1}$ [19] but is also a highly complex task that involves more than just a single precise movement. In this section general eye movement and gaze behaviour will be discussed and the relevant points for gaze tracking will be highlighted.
The most simple task for the human eye one can think of, is looking at a stationary target. The task of maintaining the visual gaze on a single target is called a **fixation**. "Fixations are defined as a spatially stable gaze lasting for approximately 200 ms to 300 ms, during which visual attention is directed to a specific area of the visual display." [20].

When recording the eye movement during fixations, at least three different movement patterns are recognizable: [21–23]

- **the drift:** is a slow unintentional single angular movement of the gaze direction to actively move the gaze object out of the fovea,
- **the tremor:** is an uncontrolled tremble of the eye that, on average, does not move the gaze target away from the fovea.
- **micro saccades:** are short, unintentional and relatively slow eye movements to counter the effect of the drift and bring the gaze object back into the fovea.

Depending on the size of the object, the **saccade** can be induced as well.

If the gaze object starts to move slowly and as fast as the natural drift (above $0.1\,^\circ\,s^{-1}$, below $30\,^\circ\,s^{-1}$) the so-called **smooth pursuit** - the second intentional eye movement - is used to follow the objects path and fixate it in the fovea [24]. This smooth pursuit is still interrupted or distorted by the movements mentioned above. If the object speed moves beyond $30\,^\circ\,s^{-1}$ micro saccades are used to catch up with the object again up to a speed of $100\,^\circ\,s^{-1}$ [25].

If the object velocity goes above $100\,^\circ\,s^{-1}$, or multiple objects of interest appear inside the field of view, **saccades** can be triggered again [26]. During this movement or if the object speed is at least three times larger than the eye movement, all information processing by the eye will be suppressed [27].

2.2 EYE AND GAZE TRACKING

The first time external hardware was used to monitor the described eye movements was reported by DELABARRE in 1898, who proposed to use a contact lens formed from plaster to transfer the eye movement to a leaver [28]. While the eye had to be numbed using cocain, this enabled DELABARRE to record eye movements for the first time. Further improvements to this method were made in the consecutive years. Until the work of JUDD in 1905, others were able to use similar means to extract eye movements but were limited by their experimental setup to either one dimension (DODGE) or not being able to measure timing (STRATTON) [28]. In 1905 the first non-invasive eye tracking methodology was introduced by placing a white particle on the eye [29] and tracking its movement. While other methods were developed to monitor eye movement, like Electro-OculoGraphy (EOG), Photo-Oculo Graphy (POG), Video-Oculo

Graphy (VOG) and further improvements of the above mentioned Scleral Contact Lens methods were made, those methods are not applicable to this work. For example,EOG measures the difference in skin potential due to the muscular movements needed for eye movement and is applicable for detection of eye movement in a more general case. [23, 30] Since EOG does not record what a subject is looking at, it cannot be used to measure the gaze behaviour of drivers in automotive use cases to an extend as needed in this thesis. While Scleral Contact Lenses or Search Coils attached to the subjects eye deliver by far, the most accurate results of less than 5″ to 10″ [23, 31], its usable range of about 5° is too narrow for the use case at hand. POG and VOG describe different techniques to record eye movement. They often do not include the measurement of the absolute angle but focus on measuring the eye movement relative to the test subject's head [23]. Only the measurement of both, eye movement combined with a head tracker allows for a detailed identification of points of regard [23].

2.2.1 VIDEO-BASED GAZE TRACKING

Video-based gaze tracking has come to increased popularity over the last couple of years [32, 33]. New camera and computer technology enabled smaller, faster and more accurate gaze tracking [23, 34, 35]. This development leads to a broad application spectrum for gaze tracking, as collected by Duchowski which ranges from medical applications over aviation or driving tasks to marketing and advertisement analysis [36], or since as early as 1989, as a computer input interface [32, 34, 37–39].
To do this, the relative motion of a light reflection on the cornea, the so-called Purkinje Reflection (PR) of an external (infrared) light source to the movement of the pupil is recorded [40]. Due to the setup of the eye as described in 2.1, four Purkinje images are visible when using one external light source. Figure 2.5 shows the four different reflections PR 1-4.

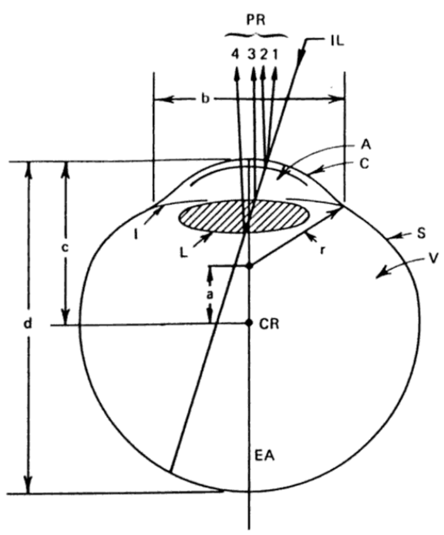

Figure 2.5 – Schematic eye setup with the four Purkinje reflections PR 1-4, the incoming light (IL), the aqueous (A), the cornea (C), the sclera (S), the lens (L) and the iris (I) [40]

The different reflections occur due to multiple transitions between layers with different refractive indices. PR 1 originates at the front surface of the cornea, PR 2 at the back surface of the cornea, PR 3 at the front of the lens and PR 4 at the back surface of the lens. Due

to the change in refraction index the PR 2 is almost exactly coincident with PR 1. PR 3 is a virtual image and much larger and more diffuse than the other reflections. PR 4 is a real image again, and is formed at almost the same plane as PR 1 and 2. However, due to the much lower difference in refractive index here, only at about 1 % of the intensity of PR 1. In case, the eye undergoes a rotation, PR 1 and 4 separate and from this physical splitting of the images, it is possible to calculate the angular orientation of the eye. [40]
New approaches to video-based gaze tracking propose conventional image processing paired with special neural networks to estimate the gaze direction from stable eye images without any additional light sources [41]. While Stiefelhagen achieves an accuracy of about 2° with the whole system being relatively inexpensive, this approach is not feasible for this thesis, since accurate gaze tracking is required for different lighting situations without disturbing the test subjects. For this reason, the use of an eye tracker paired with infrared light sources is chosen as the most suitable method.
After the angular movement of the eye is extracted from the image using the PR images, the next step is to transfer the angular motion into a gaze direction. For this, an eye ball model is fitted to each test subject. This model is based on the PR, and the known position of the light sources, as well as the known distance from the test subject to the camera. Finding the centre of the pupil enables the possibility to calculate a vector from the middle of the eyeball to the centre of the pupil thus defining the gaze vector. To estimate the absolute gaze direction, the test subject's head needs to be fixed in position, or head tracking is used to calculate the eye's linear movement. Since camera technology has advanced in recent years, the high resolution of eye tracking cameras, enables the tracker to not only focus on the subject's eyes, but to monitor the whole head and thereby track the head movement using points of interest. These points of interest are significant points on human heads, where typically ears, nose, mouth corners and the eyes themselves are used. Further detail about the functionality and the different approaches to video-based gaze tracking goes beyond the scope of this thesis but can be found, for example, in the work by Duchowski [23].

2.2.2 VIDEO-BASED PUPIL TRACKING

As mentioned above, tracking the pupil and estimating its center point is crucial for gaze tracking. Additionally, this leads to the benefit of being able to read out, and explore the pupil behaviour for the investigated situations. Furthermore, pupil dilation can be used as a measure for attention, focus and more, and blinking can be used to measure fatigue [42, 43]. For automotive use, those metrics are highly relevant since different emotions, attention and fatigue is known to influence driving and gaze behaviour. This has already been reported by Charles Darwin as early as 1872 who monitored muscular movement in animal and human faces and thereby also recorded the pupillary movement [44].

Monitoring the pupil size on film has been done over the last couple of decades. In 1960 for example, Hess recorded videos of human eyes on 16 mm film and then measured the pupil diameter as a response to different images that are used to inflict different emotions in his participants [42]. To estimate the pupil size from the recorded video data, the region around the test subject's eye is extracted and enlarged. In this area, an algorithm is used to find, depending on the use case, up to two bright/dark transitions. This has already been proposed and used successfully applied by Ebisawa in 1970 who used his approach for a human machine interface using a video-based gaze tracker to monitor the pupil diameter as well [45]. The first dark/bright transition is the border between the pupil and the iris, the second transition marks the boarder between the iris and the sclera. To track the pupil size, the first border, between pupil and iris, is sufficient. The size of the pupil can either be estimated by using a stereo camera system, that due to the calibration of the cameras to each other can also measure the distance to the subject, or a marker of known size which is attached to the eye, as shown in figure 2.6.

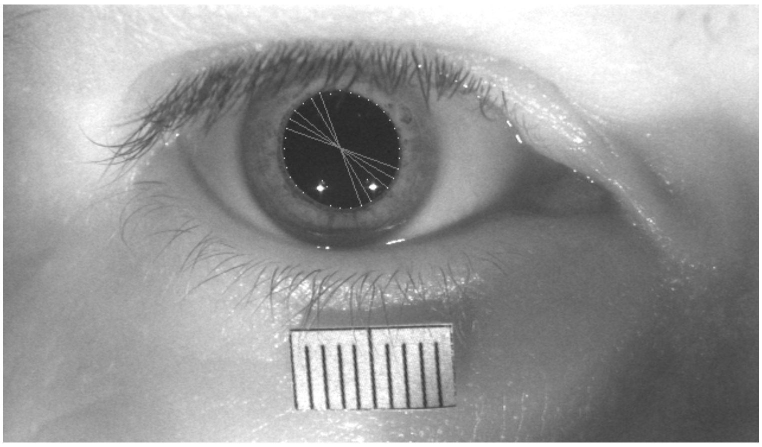

Figure 2.6 – Measurement of the pupil size with an additional measuring strip added to below the eye for accuracy calibration [46].

Adding the second transition, increases stability and robustness of the algorithm and is therefore considered a useful feature. In particular, the alogorithm performs better, when using infrared light sources and test subjects with different iris colours since the contrast between the pupil and very bright eyes will be reduced. This is due to the fact, that the reflectance of the human iris under infrared light is directly anti proportional to the reflectance under visible light and a very light iris appears dark under infrared light.
Another way, to change the contrast between the iris and the pupil is given by the position of the infrared light sources. When setting up the infrared light source, close to the optical axis of the camera, the light will be reflected back to the camera by the retina and the pupil will appear white (bright). When setting the light source further apart from the optical axis, the light is reflected away from the camera by the cornea due to the inverted geometry of the cornea compared to the retina and the pupil will therefore appear black (dark). MORIMOTO used both setups to get a clearer image of the pupil for all subjects. [47]
Tracking the pupil and calculating its size is not a difficult task, when the eye is directly in front of the camera and the pupil plane is parallel to the camera sensor. One of the challenges of tracking the pupil accurately is the distortion of the pupil under different angles towards the video cameras. This effect, the so-called pupil foreshortening error, is a technical error that can easily be avoided or re-mapped. However, many factors that cannot be recorded or controlled without a great amount of effort include fatigue, certain food and emotions. On the other hand, physiological factors can easily be recorded and limited to a certain degree. WINN investigated different physiological parameters and their influence on the pupil diameter under differnet, constant light conditions ranging from $9\,\mathrm{cd\,m^{-2}}$ up to $4400\,\mathrm{cd\,m^{-2}}$. He found, that the pupil diameter under different light conditions is independent on sex, refraction errors in the subjects lenses or iris colour, but declines linearly with age [43]. FOTIOU found similar results for the dependence on age, when investigating the pupil diameter under dark adaptation [48]. While no difference in latency was recorded between the two age groups, he measured a significantly lower pupil diameter as well as a lower pupil velocity.

2.3 LIGHTING PARAMETERS

When talking about visual perception, light and its properties as electromagnetic waves in the small range between 380 nm to 780 nm as shown in figure 2.7 and the way humans perceive different wavelengths of it needs to be discussed as well.

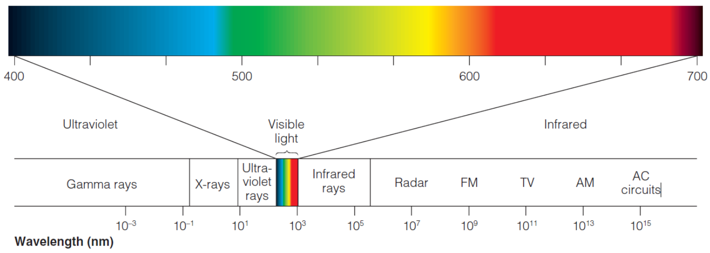

Figure 2.7 – The electromagnetic spectrum, displaying the wide wavelength range with the small portion of visible light. [13]

Light itself is defined as "any radiation capable of causing a visual sensation directly" [49], but since humans do not perceive all light in the mentioned range equal, it is crucial for further discussion, to address the way, humans perceive different wavelengths of light. Therefore, the next sections will discuss the basic lighting parameters that are necessary for a full understanding of this thesis, starting with the fundamental sensitivity curve for human eye on electromagnetic waves - the V(λ) function.

In the next part, the use of the V(λ) function to calibrate all photometric measurement equipment and scale them spectrally according to the sensitivity of the human eye is discussed. Strictly speaking, illuminance is the only photometric value, that one can measure. Every other photometric value is derived by a mathematical correlation to illuminance. Nevertheless, measurement equipment for all other relevant photometric values exist. This equipment then uses internal processing and a highly accurate geometry in the setup of the measurement instruments to calculate the corresponding values. In this section, the basic understanding for illuminance (-measurement) and the geometrical relations to the other relevant metrics will be explained and derived.

2.3.1 SPECTRAL SENSITIVITY V(λ)

Humans do not perceive light of all wavelengths equally. The sensitivity curve for human eyes is a combination of the sensitivity curves of the rods and the cones respectively, depending on the current lighting situation and adaptation levels. During photopic situations, when only cones are active, the spectral sensitivity curve is given by the V(λ) function as shown by the blue curve in figure 2.8. In photopic environments, humans have their highest sensitivity at around 555 nm. The sensitivity decreases for both, shorter and longer wavelengths [50].
This sensitivity shifts to lower wavelengths as the environment shifts to darker illumination. During scotopic (dark) adaptation, the V(λ) function becomes invalid and the so-called V′(λ)-function was defined to describe the human vision during those situations. The V′(λ) is shown in figure 2.8 as the red curve.

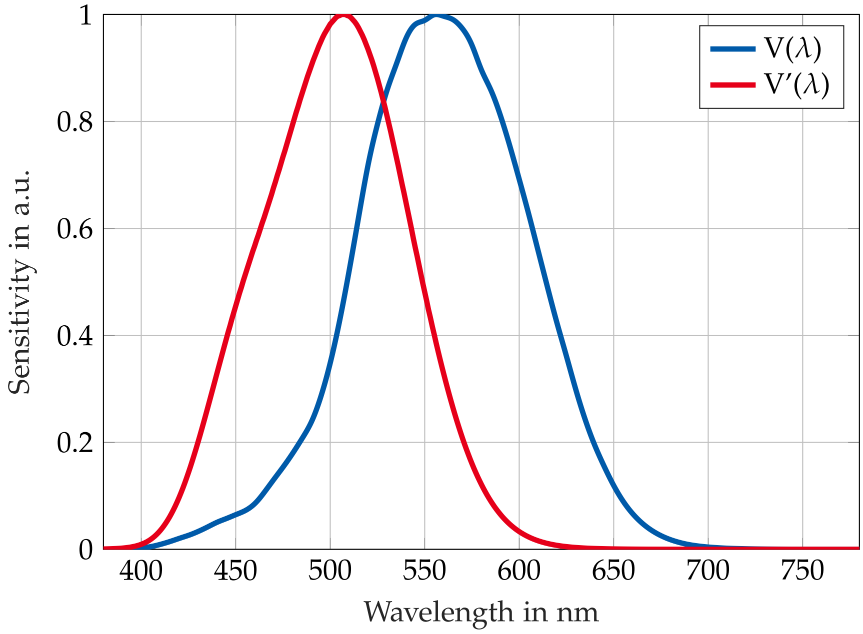

Figure 2.8 – Spectral sensitivity curves, V(λ) and V'(λ) for human vision during photopic illumination (red) and scotopic illumination (blue).

For scotopic vision, the maximum of the spectral sensitivity is at around 510 nm and it is obvious, that the vision in the lower wavelength range is significantly better while the vision in the higher wavelength range is significantly worse. For the mesopic range, the sensitivity curve shifts between the V(λ) and the V'(λ) functions [17, 51].

Despite knowing, that for different brightness levels, different sensitivity curves are valid, all photometric measurements are done using the V(λ) function. This is either done by measuring the spectral distribution and then multiplying it by the V(λ) function or the measurement equipment is already filtered with the V(λ) function. Most often this is the case, since it is much faster, requires less space and does not include any further calculations. However, this is a highly complicated and very sensitive procedure and is, up to now, often done by hand. The most accurate results are achieved by using partial filtering as shown in figure 2.9.

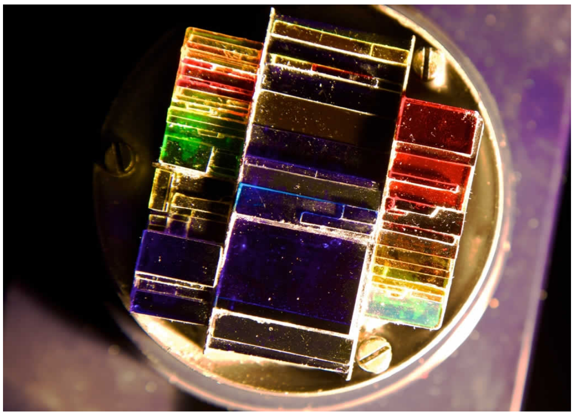

Figure 2.9 – Image of a partial V(λ) filter. Each individual filter part is selected in size and thickness to, in total, and togeather with the spectral responsivity of the silicon detectot, to a transmission curve similar to the sensitivity of the human eye. (*Image source:* [52])

In a partial filter setup, each individual filter part is selected in thickness, size and spectral transmittance in a way, that the integrated transmission of all filter parts and the sensitivity curve of the measurement sensor lead to a total sensitivity of the equipment, similar to the $V(\lambda)$ curve. Final deviations are then compensated by an individual calibration file for every measurement head.

Since this method requires a large area, sensors with a small measurement area, cannot be equipped with partial filtering. Here a selected filter-glass is used to get the total sensitivity as similar to the human sensitivity as possible. Since the spectral responsivity of every photo diode is different, and the possibility to create different transmission spectra in glass is limited, the results of this method are significantly worse compared to partial filtering.

2.3.2 LUMINOUS FLUX

Luminous flux is probably the most intuitive of all photometric values. It describes the total amount of light (weighted by the $V(\lambda)$ curve) emitted by a light source. The SI-unit for luminous flux is lm and luminous flux is indicated by ϕ.

Luminous flux is often used to objectively evaluate light sources by measuring the total light, that is emitted by a light source and is one of the photometric values often found on general lamps or headlamp lamps. In general public, luminous flux is often used to compare the brightness of different light sources. Per se, this is correct: a light bulb with 2000 lm is, overall brighter than one with only 500 lm. But since the luminous flux measures the total emitted light, any angular dependency is neglected. Therefore, a light source with a highly directed light distribution may lead to a brighter illuminated area, for example on a work desk, than a potentially higher rated light source, that distributes its light evenly into all directions.

There exist several possibilities to measure luminous flux. Small light sources, without any refracting optics, can be measured in a so called integrating (ULBRICHT) sphere as shown in figure 2.10a. An integrating sphere is a spherical optical component with its interior coated with a highly reflective ($\rho > 0.8$) and diffuse paint. In general, the principle is, that by scattering nearly all the light over and over, on average, light from all angles will be directed from the light source onto the light detector. By measuring with a standard light source with known luminous flux, one can now calculate the luminous flux of the new light source.

Light sources that are either too big to be placed into an Ulbricht sphere, or use any kind of optic, thus leading to a directed light distribution, need to be measured differently. The most common approach here is, to use a photo goniometer. Here either the light source is turned around 360° over all axis, or the sensor is turned around the light source. Which case is used, usually depends on the light source, since, for example, some fluorescent tube should not be operated under certain angles or burning positions.

(a) (b)

Figure 2.10 – Measurement equipment to measure luminous flux. (a) shows an integrating sphere to for measuring small and unidirectional light sources (*Image source:* [53]), (b) shows an automotive goniophotometer to measure headlamps and other directed light sources (*Image source:* [52])

Therefore, turning the light source around its own axis is impossible, and the sensor will be used to cover all angles. On the other hand, light sources with a highly directed light distribution, such as automotive headlamps, require a large measurement distance of 25 m and therefore moving the sensor around the light source is unreasonable. Figure 2.10b shows an automotive goniophotometer, where the light source will be turned around a defined axis.

2.3.3 LUMINOUS INTENSITY

While the luminous flux gives the complete light emitted by a light source, the parameter used to describe the light emitted by luminaires under a given angle is the luminous intensity. With the illuminance I, given by

$$I = \frac{d\phi}{d\Omega_1} \tag{2.1}$$

where Ω_1 is the solid angle under which the light is emitted. Again as with all other photometric values, an illuminance measurement head is used. The angular opening of this head is limited by a tubus so that no stray light can affect the measurement head and the distance to the light source is set to a known value. Then the luminous intensity is calculated by

$$I = E \cdot r^2 \tag{2.2}$$

with E being the illuminance. The measurement of single luminous intensity values can typically be done manually with a simple setup as described above. However, the luminous intensity of a light source, like street lights or an automotive headlamp, needs to be measured angle dependent. Therefore, automated measurement equipment was developed, that moves either the measurement arm around the light source and measures the luminous intensity with a set resolution, or, in cases the measurement distance needs to be much larger, the light source is turned as seen in figure 2.10b. For automotive headlamps, this angular measurement is necessary due to the different photometric requirements under different angles like, for example, to ensure detection in the right-hand side and avoid glare for oncoming traffic at the same time.

2.3.4 ILLUMINANCE

Illuminance, E, describes the amount of luminous flux incident on a specific area:

$$E = \frac{d\phi}{dA} \tag{2.3}$$

where A is the area at which the light is measured. Illuminance was often referred to as brightness, but since this often lead to confusion with other photometric terms like luminance, it was defined that "*brightness*" should not be used in a quantitative manner. In SI-units, illuminance is given in lux (lx).

To measure the illuminance, typically a silicon-based photo-diode with an added V(λ) filter is used. The need for the additional filter arises in the significant difference in sensitivity per wavelength between the human eye and a silicon based semiconductor. While the human eye follows the described V(λ) function, a typical silicon chip will have an absorption curve starting at about 350 nm and reaching over 1100 nm. Both sensitivity curves are shown in figure 2.11. The spectral sensitivity of silicon is shown in blue, while the V(λ) function is shown in black. Both functions are normalized.

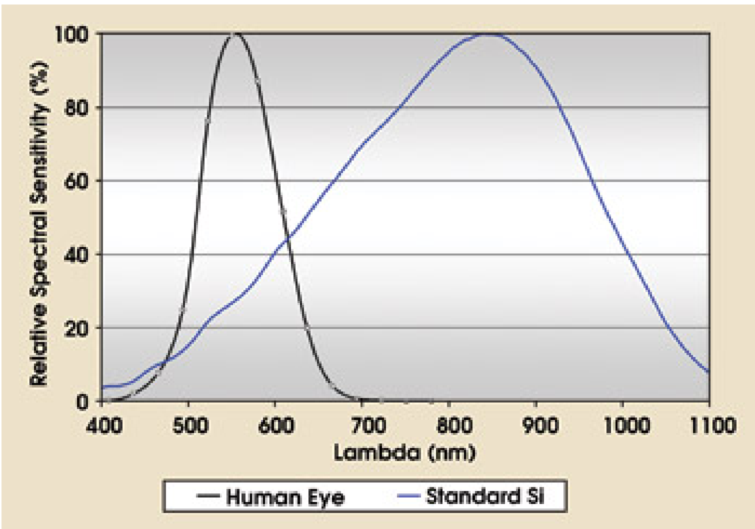

Figure 2.11 – Spectral sensitivity curves of a silicon-based semiconductor (blue) and the V(λ) curve (black) (*image source:* [54]).

On top of the filter, a LAMBERT diffuser is added to ensure a homogeneous mixing of the incoming light over the whole sensor area, as well as defining the measurement area. The so-called cosine-adaptation is a geometric appliance added to the semiconductor to ensure that any angle between the light source and the system, actually leads to a cosine behaviour on the measured illuminance. This adaptation is often done as one part including the diffuser. In many automotive studies, the measurement of the illuminance is the only feasible method of characterizing the photometric properties for dynamic situations [55–60]. This leads to the current state, where most evaluations on automotive headlamps are based upon illuminance measurements and Adrian, Flannagan, Holladay,Lehnert, Locher, Stiles, Völker, Vos and Zydek all derived similar correlations between the illuminance and the glare perception of subjects. Nevertheless, illuminance does not take any properties of the illuminated surface into account but only describes the incident light. However, since most of all materials in nature do not reflect all wavelengths equally, different materials may appear differently when illuminated with similar illuminance values. The photometric value taking this into account is the luminance.

2.3.5 Luminance

While illuminance measures the light coming onto a specific area, luminance measures the light leaving a specific area. This is described by the following equation

$$L = \frac{d\phi}{dA_1 \cdot d\Omega_1} \tag{2.4}$$

with L being the luminance.

It therefore does not describe the amount of light shining onto a surface but rather the emitted or reflected light of a given area under a solid angle. Luminance is measured in SI units as $\mathrm{cd\,m^{-2}}$ or in non SI units in *nit*. Since luminance is a photometric value, the amount of light measured is, once again, weighted by the $V(\lambda)$ function. The luminance is the photometric value associated with the brightness perception of humans. This brightness perception, however, is not a linear function but rather follows a logarithmic behaviour.

As mentioned above, the only photometric value, that is actually measurable is illuminance. But since the geometric relations between illuminance *(E)* and luminance *(L)* are known, the luminance can be calculated by

$$L = \frac{I}{A_1} \tag{2.5}$$

$$= \frac{E \cdot r^2}{A_1} \tag{2.6}$$

$$= \frac{E}{A_1/r^2} \tag{2.7}$$

$$= \frac{E}{\Omega} \quad \text{with} \quad \Omega = \frac{A_1}{r^2} \tag{2.8}$$

where Ω describes the solid angle and is given by dividing the visible area *(A)* by the distance to the measurement area *(r)* squared. Therefore, a conventional luminance meter, is a illuminance head, which is equipped with a specific geometry, to limit the solid angle under which light can be measured.
If a diffusely reflecting (lambertian) surface is measured, the luminance L can be directly calculated from the illuminance E at the surface according to

$$L = \frac{\rho}{\pi} \cdot E \tag{2.9}$$

where a ρ is the reflectance of the object.

While conventional luminance measurements are still widely used, state-of-the-art luminance cameras do not only measure under one specific angle, but are modern cameras with multiple thousands of measurement points. This leads to a much wider area of use since a single luminance picture, captures much more information. An example is shown in figure 2.12.

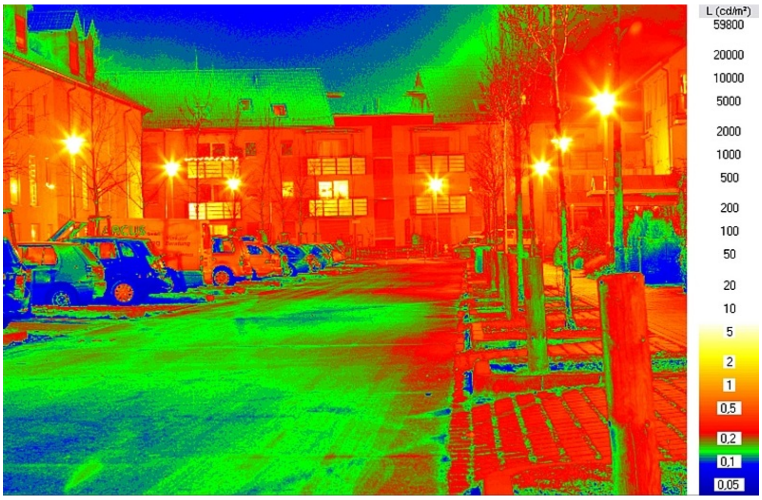

Figure 2.12 – Luminance picture as recorded using a luminance camera. The data is represented using the logarithmic colour bar on the right side.

These recordings not only enable the user to identify the luminance at a given angle very precisely, but enable the possibility to measure homogeneity, maxima, minima, surrounding light conditions like adaptation luminance, luminance contrast ratio and more. Since this is done with a single measurement, that is, all values origin from the same measurement time, the advantages are a more time effective measurement, and more consistent results.
For those cameras, each pixel is calibrated for their specific angle. For the V(λ) calibration, partial filtering is impossible, since each pixel would require its own filter combination. Hence, the use of a large full filter to achieve the $V(\lambda)$ calibration of all pixels is necessary. Due to the high integration time needed, since the area of each pixel is very low and thereby the amount of incident light per pixel is very small, this measurement needs to be done stationary [11].
Only recently dynamic luminance measurements were proposed [61] and are used under certain conditions to evaluate the lighting conditions in tunnels [62].

2.4 DETECTION

The previous sections explained the basic ways of human perception in an abstract way, describing the cells and their basic functions as well as the necessary knowledge of human vision and the required equipment for accurate photometric measurements of what humans perceive. However, all this describes the most basic function of our visual apparatus: the possibility perceive light and most importantly, differences in light. During the day, when cones are active, this difference in light might be due to the colour differences of objects. At night, when only rods are sensitive to light, this colour sensitivity is lost and only differences in brightness or more precisely luminance is perceivable. In its simplest form, this perception of luminance differences is called detection, and the point at which an object is just visible against the background is the detection threshold. This section will now focus on the physiological task of the detection of objects in complex visual environments, in general and further explain the variation of the detection threshold under varying circumstances. Since detection of objects in our environment is one of the most essential tasks in general but for driving a vehicle especially, a lot of work in the last couple of years has been focused on research on detection to describe possible correlations between perception and photometric values. The next paragraphs will introduce the most import and relevant processes.

One of the first investigation on detection thresholds was performed by Blackwell in 1946 [63]. In a large, white coated laboratory, the detection probability of visual targets under different adaptation luminance settings from 0 cd m^{-2} to 3400 cd m^{-2} is investigated with female test subjects at the age between 19 to 26 years. Additionally to the adaptation luminance, the detection target size was varied from 12.1′ to 3.6′. The contrast sensitivity was calculated by equation 2.10 where C_+ describers the contrast if the detection target is brighter than the surrounding luminance and C_- the contrast if the adaptation luminance is brighter than the target. L_a is the adaptation luminance and L_o is the luminance of the object, the detection target. [63]

$$\begin{aligned} C_+ &= \frac{L_a - L_o}{L_o} \\ C_- &= \frac{L_o - L_a}{L_o} \end{aligned} \tag{2.10}$$

This calculated contrast is known as the *Weber-Kontrast* and the objects are visualized in figure 2.13 where figure 2.13a shows positive contrast with a higher object luminance (L_O) than the adaptation luminance (L_a) and 2.13b shows negative contrast with the object being darker than the adaptation luminance.

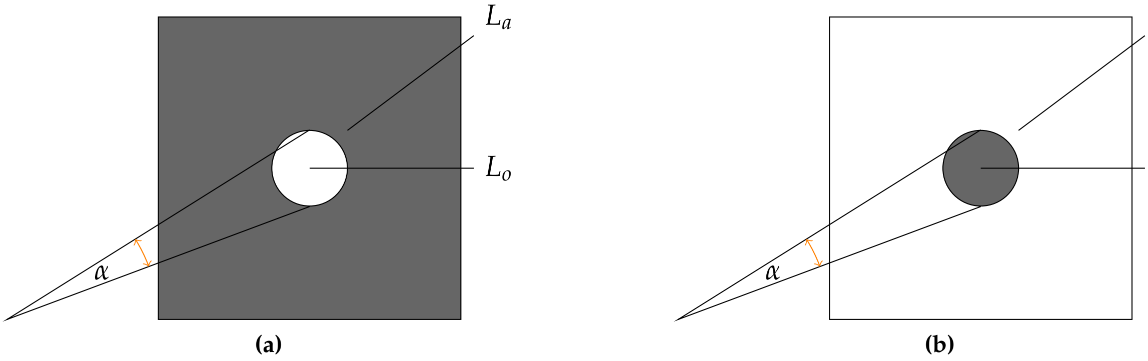

Figure 2.13 – Figure (a) shows the contrast for an object brighter than the surroundings ($L_o > L_a$, C_+) and Figure (b) shows the same image an object darker than the surroundings ($L_o < L_a$, C_-). α gives the object size or the viewing angle in degree.

Blackwell's findings show, that for both, rising adaptation luminance and increased detection target size, the required 50 % threshold contrast decreases. The 50 % threshold used, describes the luminance contrast, at which half of all participants are able to detect the presented target, this is a widely used method to describe the general process of detection, however this leaves a large margin of error, since this also means, that 50 % of the test subjects did not yet detect the object under these circumstances.

Adrian investigated target detection further and using the 90 % threshold, found that depending on the target size, two sections in the threshold luminance arise. For large targets, with a viewing angle above a certain threshold, the threshold luminance is constant for a given background and only depends on the background luminance (Weber's Law) $\Delta L/L_0 = const.$ where $\Delta L = L_a - L_0$ is the threshold luminance and L_0 the background luminance. For smaller detection targets however, the threshold is dependent on target size and follows the logarithmic function $\log \Delta_L = -2\alpha + k$ where α gives the target size and k is a constant. He further investigated the influence of exposure time of the target, resulting in the finding, that a shorter exposure time leads to a higher threshold contrast. Since all detection studies in this thesis offer "infinite" exposure time, this will not be discussed further. [64]

Another strong influence on the detection of objects is the location of objects relative to the visual axis of the test subject. This is already hinted at in section 2.1 where the distribution of photosensitive receptors on the human retina is shown. The large differences in receptor density over the different angles indicate, that not due on the active receptors, the detection threshold will vary with different detection angles, but also within one receptor type the detection will decrease for larger angles. This displacement of the detection target to the visual axis is called the detection angle and was investigated recently by Mayeur [65] and Schneider [66]. Mayeur performed a reference test on a uniform background with varying detection angles before additionally switching to more complex backgrounds simulating road geometries.

Schneider used a similar setup to the one shown by Mayeur but chose five different viewing angles (0.0°, 2.7°, 5.0°, 10° and 20°) for the laboratory study and tried to reproduce the same setup in a real life driving test. Since both studies are focused directly on detection in automotive use cases, they will be discussed in more detail in later chapters.

The most important influence on detection between the presented research in this chapter and the conducted studies for this thesis is, that all studies mentioned above are performed in a laboratory setting. Different works investigated the difference between a laboratory study and a so called field study, in the context of automotive lighting. This results in the definition of a *field factor* that converts the results from laboratory studies to results found in real life field tests. This factor is defined by the Commission Internationale de l'Éclairage (CIE) (engl. International Commission on Illumination) [67] but different studies show, that this factor varies greatly between 4.6 and 32 [65]. For the influence factors on the complex task of detection and the large differences recorded between laboratory studies and field tests, it is necessary, to perform different investigations for each individual problem. This thesis will therefore present four different field tests regarding human perception in traffic to isolate these influence factors as much as possible.

2.5 GLARE

While detection describes the possibility of drivers to see and perceive objects, the second large influence on the driver's perception is glare. Other light sources located in the field of view of a subject might either impair the vision of the driver or make the driver feel uncomfortable [68]. Both situations are associated with glare. If the vision is impaired by a light source, this is called physiological glare since a physiological influence is measurable. If however, the subject feels a discomfort, this is called psychological or discomfort glare as defined by the CIE [68]. In general, both types of glare correlate, an impairment of vision can also lead to a perceived discomfort by the subjects, however this is not necessarily the case.

[69, 70].
Both aspects are important for nighttime driving, since impairing the vision of the driver is a serious safety concern, and feeling dazzled by a light source might lead to a higher amount of blinking, gaze diversion or even increased tiredness [71] and therefore impact road safety as well, starting with physiological glare, both types of glare will be discussed in the following section.

2.5.1 PHYSIOLOGICAL GLARE

The physiological glare is a direct impairment of the vision of a person due to an additional light source in the person's field of view. This impairment of vision is manifested by a higher threshold contrast required in order to detect an object under given circumstances. This increase in the required threshold contrast can have two different causes [70].

- The additional light source increases the brightness that much, that the eye requires time to re-adapt to the new light conditions.
- The light of the additional light source is dispersed in the eye and this light is added on the retina as a veil over the light from the detection object therefore adding light to both, the object and the surroundings, effectively lowering the perceived contrast.

Since adaptation and re-adaptation due to light sources in improbable in automotive scenarios due to the short encounter times, with a few exceptions like exiting a tunnel, the focus will be set on the second case.

Refraction at the different layers of the eye, dispersion in the vitreous chamber, and opacity of the human eye cause light coming onto the eye to not only produce a single light spot on the retina but rather a Gaussian light distribution. This leads to additional light, depending on the angle between the glare source and the gaze direction, added just about anywhere on the retina with decreasing intensity the further away the point on the retina is from the glare source. This is illustrated in figure 2.14 by MILLER [72].

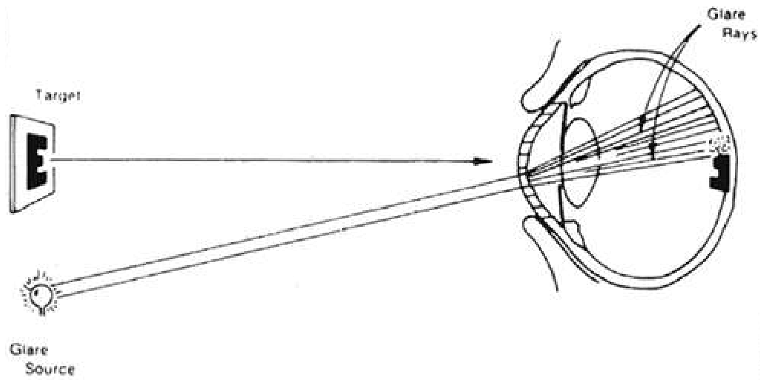

Figure 2.14 – Light scattering from the peripheral glare light source onto the retina, thereby decreasing the contrast of the image [72]

Combining this with equation 2.10 this leads to L_{gl} added to both, the surrounding luminance and the object luminance as shown in equation 2.11 as an example for a brighter object.

$$
\begin{aligned}
C_{+} &= \frac{(L_a + L_{gl}) - (L_0 + L_{gl})}{(L_0 + L_{gl})} \\
C_{+} &= \frac{L_a - L_0}{L_0 + L_{gl}}
\end{aligned}
\tag{2.11}
$$

This shows, that the perceived contrast is now lower and if the contrast was just at the threshold without the glare source, this reduction of the perceived contrast will now lead to a contrast below the threshold. The object must therefore now be illuminated more to raise the contrast to a visible level again. For automotive use cases, this means, that if an object is detectable at a certain distance with a given light function, glare sources like oncoming traffic or even traffic signs, will decrease this detection distance until the vehicle is close enough to the object, that the contrast is raised above the detection threshold again.

To measure physiological glare in a certain situation, the contrast threshold is measured with and without the additional glare source. By comparing the different thresholds, the physiological glare can be estimated. The test setup for this is similar to the ones described in the section about detection, with the difference, that a stationary glare source is added under a certain angle in laboratory studies [73] or even moving glare sources such as oncoming vehicles are used in case of field tests as shown by Zydek [55].

2.5.2 PSYCHOLOGICAL GLARE

While the physiological glare is measurable by recording the difference in the contrast sensitivity, the measurement of the psychological glare is more complex. Since psychological glare does not necessarily lead to an impairment of vision, other methods have to be used. The most straight forward method is, to ask the test subjects, if they feel dazzled [74]. The most common used method for this was developed by de Boer in 1967. The so called de Boer scale asks the test subjects to rate their glare perception on a scale from 9 - unnoticeable to 1 - unbearable. On this scale, only every second entry is described and the subjects have to rate their glare perception in whole numbers. The complete de Boer scale is shown in table 2.1 where all entries are listed. [75]
A summary of different versions of the de Boer scale is found in the work of Gellatly [76] where different use cases of the same scale with the different descriptions at the individual scale points are listed.

Table 2.1 – Numeric values and the correlating glare perception for the DE BOER scale [75]

NUMERIC VALUE	GLARE PERCEPTION
1	Unbearable
2	-
3	Disturbing
4	-
5	Just Admissible
6	-
7	Satisfactory
8	-
9	Unnoticeable

The second popular method to quantify the psychological glare is to measure the Borderline between Comfort and Discomfort (BCD), describing the average luminance of a light source that just produces the sensation of discomforting glare [77]. For this method, the test subjects are usually presented a glare light source that is adjusted until this threshold is just achieved. This is usually measured by letting the test subject adjust the glare source themselves as used by FRY [78], LUCKIESH [79] and IRIKURA [80] the adjustment method.
The different influence factors to the psychological glare perception is summarized by VÖLKER [70] and will only be listed here further summarized accordingly.

- Increasing the illuminance by a decade decreases the DE BOER rating by 2 points.
- Multiple glare sources add to the glare perception
- The larger the light source, the less glare is perceived for the same glare illuminance
- The spectrum of the light source influences the discomfort glare with a minimum at 577 nm
- Higher colour temperature increases the glare perception
- Glare is rated higher if the gaze is fixed
- Different rating methods lead to different results - using the DE BOER SCALE leads to more comparable results
- Glare is rated more severely in laboratory experiments compared to field studies
- Higher demanding tasks or multiple tasks for the test subjects lead to lower glare rating
- Older test subjects feel (slightly) more glared compared to younger test subjects
- Subjects wearing glasses or other optical aids rate glare sources about 0.5 more severely on the DE BOER scale than subjects without aids

This shows, that the influence on the psychological glare is vast and comparing different studies with different setups is difficult if not impossible.

2.5.3 THE COMBINATION OF PSYCHOLOGICAL GLARE AND OBJECTIVE MEASUREMENTS

Since asking the test subjects for their glare perception often leads to large deviations in the rating and in some cases is impossible due to the situation the test subject is in, a lot of research has been conducted in order to correlate the psychological glare rating, mostly the DE BOER rating, with objective measurements. For example, SIVAK, BULLOUGH, LEHNERT and ZYDEK all correlated the glare perception with either the illuminance or the exposure measured in their corresponding experiments [55, 56, 60, 81, 82]. However, the findings always deviate from another depending on the exact circumstances.

Newer and more complex methods to evaluate the discomfort glare of test subjects is the measurement of their unintentional physiological body functions such as heart rate and brain waves via Electroencephalography (EEG) [83]. However, this requires a lot of processing power and highly controlled environments since these values can be easily influenced by other stimuli. Therefore, this is not further discussed here.

However, as already mentioned, it is possible to deduct the glare perception by measuring the gaze behaviour of the subjects. Increased psychological glare leads to a higher blink rate and/or an averting of the gaze [72]. However, no fixed values can be given here either, since a lot of factors have to be considered, when doing this. Therefore, the relation between the values before a glare source appears and right after the glare source appears have to be compared. Furthermore, LIN also shows a correlation between light pulses, pupil size and glare perception. [84, 85]

This will be investigated further in chapter 4 where this study will be analysed and in chapter 5.3 where a similar study is conducted in order to find optimal correlation factors for the studies shown in this thesis.

Part III

BASICS OF AUTOMOTIVE LIGHTING

The interest in and the importance of exterior lighting in the automotive market has, for the past couple of years, steadily been growing. We have seen more and more advertisement arise, that focuses on the capability of current vehicles to safely illuminate our roads just as much as on the design features provided by the current generation of headlamps.

3 BASICS OF AUTOMOTIVE LIGHTING

The main goal set by this thesis is to propose new and optimized light distributions for automotive headlamps. These distributions are set to work in general nighttime driving situations and optimize the detection probability of different objects. While chapter 2 focuses completely on the human side of perception and the physical and photometric parameters needed to describe human perception in real life situations, this chapter will now introduce the automotive part for this thesis. Therefore, a brief history of the development of automotive lighting is given before current technological advancements and future possibilities for front lighting are discussed in greater detail. This chapter will close with an overview over current, European, regulations that limit the design of current headlamps at the current time.

3.1 AUTOMOTIVE HEADLAMPS - TECHNOLOGY AND EVOLUTION

The main goal of automotive headlamps is to enable the driver to see any kind of obstacles at night. This is necessary since, according to different sources, at least 90 % of all information needed when driving a vehicle is taken in via the eyes [86], [87]. While during the day, this might lead to an over-abundance of information, at night drivers are in desperate need of better sight and more visual information. This is indicated by the significantly increased accident probability during night, as described in chapter 1 as as shown on figure 1.1. While the total number of accidents at night is lower when compared to the accident rate during the day, the traffic volume at night is much lower and thereby the accident per driven kilometre is higher during the day. To increase the viewing distance at night, according to Khanh, headlamp development can be divided in three major groups [86]:

- **New Light Source Development:** Using light sources, that either increase the raw luminous flux, the luminance of the light source or that are more energy efficient. This includes for example HID light sources, improving the general luminous flux over tungsten halogen headlamps, LEDs keeping the luminous flux about the same while being much more energy efficient and Laser diodes, shrinking the size of the light source and by that increasing the luminance of the light source.

- **Adaptive Light Distributions:** Creating light distributions, that change according to the general current driving situation. This includes City Light, that widens and lowers the low beam area or motorway/autobahn light, that lifts the cut off line by 0.27°.

- **Assisting Light Distributions** Adding special functionality to the light distributions to assist during special situations or encounters. The marking light for example illuminates objects on or besides the road, that might enter the driven path.

Since this thesis will discuss all three categories, the main advances in all three categories are discussed in the paragraphs below.

The major restriction when developing a new headlamp, is to avoid any negative influence on other traffic participants without decreasing the visibility distances for the driver. To show the development achieved in these two aspects over the last couple of years, the next paragraph will briefly show the major steps over the last decades to minimize glare while maximizing viewing distances as well.

3.1.1 HISTORICAL EVOLUTION OF AUTOMOTIVE HEADLAMPS AND LIGHT SOURCE DEVELOPMENT

While the first electrical automotive front lighting introduced by *GM* as early as 1912 the classic low and high beam separation was only introduced in 1940 as mandatory in the USA. This basic tungsten halogen headlamp was the norm, until *Philips* presented the first HID headlamp in 1989 that was available from 1991 in the *BMW* 7-Series as an upgrade. The latest innovation in terms of general light sources for headlamps came in 2006 when *Lexus* introduced the *LS 600h/LS 600 L* with the first LED low beam in series production. This was followed quickly in 2007 when *Audi* started shipping the R8 with full LED headlamp which utilized LEDs for all headlamp functions. The latest step in light source technology came in 2014 when both, *Audi* and *BMW* started adding Laser as a light source to their existing LED headlamps. The main difference here is, that the Laser diode is used additionally to the LED light distribution and only adds light on top of that while all previous light sources are used as standalone setups.
While explaining the differences of these light source types in depth goes beyond the scope of this thesis, since tungsten halogen is the entry level light source that will either not be used in intelligent headlamps or be replaced by LED headlamps in the near future, HID headlamps as high end solutions are already vanishing from the automotive marked and are replaced by LED. However, the main difference between the light sources should be pointed out shortly. Tungsten halogen delivers a very warm colour temperature at around 3000 K with a limited amount of luminous flux of under 2000 lm. HID headlamps are capable of producing around 3000 lm with a much higher colour temperature of 4500 K to 5000 K. Due to their high flexibility, the general light output of LED headlamps is difficult to summarize, but it is possible to reach the same values as HID headlamps with an even higher colour temperature of 6500 K. This is showcased from the driver's view in figure 3.1 where the road illumination produced by a tungsten halogen headlamp is displayed on the left side, by an HID headlamp in the middle and the right side shows the same scene as illuminated by an LED headlamp.

Figure 3.1 – Driver's view of the road with the three different light sources: tungsten halogen (left), HID middle, and LED right [88].

Laser diodes use the same technology as LED, converting blue light from the diode into white light using a yellow fluorescent phosphor, and therefore create similar colour temperatures. The luminous flux of these Light Amplification by Stimulated Emission of Radiation (LASER) based light sources is still limited to around 250 lm per diode. However, the luminance of these LASER based light sources is about 2.5 times higher than those of HID headlamps and this high luminance is why LASER diodes are used to create additional boost functions for high beam systems. The differences between the LED high beam and the added LASER booster is illustrated by *BMW* in figure 3.2 where the left image shows the driver's view with LED low beam, the middle shows the view with LED high beam and the right side shows the view with the added LASER booster.

Figure 3.2 – Driver's view of the road with the LED low beam left, LED high beam in the middle and LED high beam and added LASER booster right [89].

3.1.2 STATE OF THE ART AUTOMOTIVE HEADLAMPS

After covering the evaluation of light sources in automotive headlamps, at least with the introduction of the HID headlamps, so called intelligent headlamps or Advanced Frontlighting System (AFS) have been developed and are now widely available to customers. AFS is a very wide and unspecific concept, that describes a large variety of headlamps, the definition of AFS is, that the headlamp needs to contain at least one additional light distribution on top of the two mandatory distributions, low and high beam. This additional light distribution needs to be loaded and activated automatically depending on the current situation, the car is in. The current form of the European norm, that is described further in the next sections, covers four major classes (C, E, V, W). Class C covers the basic low beam, class E covers different road categories like country roads or motorways, class V contains light distributions for illuminated areas like cities, and class W covers different weather situations like rain or fog. [90]

Technically speaking, the first addition to the standard headlamp systems was already introduced in the *Citroen DS21* in 1967 where a mechanical system swivelled the low beam into corners depending on the steering angle. However, this system did not distribute widely due to technical issues. [91]
In 2002 *Audi* and *Hella* introduced a similar system - the static bending light. This system utilizes an additional spot, that is activated at low velocities and illuminates large angles in very steep corners or intersections to increase detection of cyclists and pedestrians that are not being illuminated by the standard low beam [92].

Only one year later, *Hella* and *Daimler* reintroduced the dynamic bending light. Similar to the system from 1967, using an electric motor to turn the low beam into corner without using an additional module. This system is used to improve the illumination of larger curves since the standard low beam only illuminates the road tangential to the actual curve. The system is able to turn up to 15° into the corner, corresponding to a bend with a 200 m radius. For bends with even smaller radii the static bending light is utilized. The difference to the system used by *Citroen* is, that only the headlamp located on the inside of the curve is swivelled and the outer headlamp is left static to improve visibility on the side [93].

Chronologically, the next adaptive lighting function was introduced in 2005 with the high beam assistant by *Gentex*. This system tackles the issue of general under-usage of high beam as shown by Sprute [94]. The system uses a camera to constantly check, if the driven vehicle is in a situation, in which high beam can be activated, motorway or country road and no other traffic participants that could potentially be glared, and then activates or deactivates the high beam in the given situations.

As the next step, the companies *Daimler* and *Hella* presented adaptive low beam distributions in 2006. This system uses different low beam distributions that can be activated in different situations. As an example it is possible to increase the luminous flux in the low beam and lift the distribution by 0.3° thereby filling in the gap between low beam and high beam when driving at above $90\,\mathrm{km\,h^{-1}}$ on motorways, the **motorway light**. Further light distributions include **country road light**, which illuminates the sides of the road to increase detection of wild game, **city light**, a symmetrical, wider light distribution that allows for better pedestrian detection at low speeds, **living street light** for velocities between $5\,\mathrm{km\,h^{-1}}$ to $30\,\mathrm{km\,h^{-1}}$ which swivels the light outwards by up to 8° to allow for even better detection of objects and pedestrians in very close proximity to the vehicle and **bad weather light** that activates during rain and lowers the intensity on the inside of the road to minimize the reflected light to oncoming traffic and increasing the light output of the outer headlamp to increase road lane detection for the driver.

2009 it was once again *Hella* and *Daimler* who introduced the next step in automotive lighting evolution with the variable headlight range control, where the low beam dip is controlled and the pitch angle is changed according to the distance of oncoming or preceding traffic thereby allowing a fluent transition between low beam and high beam.

The current state-of-the-art in terms of merging the minimal glare of low beam and the maximum detection distance of high beam, is gfHB. This system, that cuts out parts of the high beam distribution, where other traffic participants are registered, was introduced in the *VW Touareg* in 2010. These first systems used HID headlamps and a mechanically activated shutter, that casts a shadow in the high beam distribution exactly where other traffic participants are located. Current systems use individually addressable LED that can be dimmed or switched off electrically and do not rely on mechanical setups any more. These systems use up to 82 LED per headlamp but manufacturers are already working on high resolution systems using different display technologies.

The latest addition to the AFS is the marking light by *BMW*, where an infrared camera detects game, cyclists and pedestrians and then uses an additional, 2D-rotatable light spot, that directly illuminates them thereby increasing the possible detection distances and reaction times [95].

3.1.3 Future possibilities for automotive headlamps

All the AFS functions described above, are based on the conventional split of the light distributions in low beam and high beam. gfHB systems are already rather close to merging the two light distributions for country roads. Especially the current 82 top tier system uses a single module for the base of the low beam but then uses some portion of the single segments to create the asymmetric low beam layout required by European traffic law. With the new evolving technologies in the headlamp segment, like Digital Light Processing (DLP) or Thin-Film Transistor (TFT), that allow high resolution with millions of individually addressable pixels, this transition between low beam and high beam might vanish all together.
The main benefit from this is, that until now, the changes possible to light distributions are very limited. Only the gfHB using single addressable LED actually allows for a fully customizable (high beam-) light distribution, where intensity and form of the light distribution can be changed radically. Expanding this over to the low beam and increasing the number of addressable segments or pixels would then also allow for a much greater variety of light distributions in the low beam area as well that could be loaded during the necessary situations. This could also include symbols or markers inside the light distribution to further steer the driver's attention in certain situations.
All in all, the mentioned number of different light distributions shown in the section above would increase exponentially and could even be completely dynamic in terms of where the hot spot is, where how wide the distribution should be and what kind of elements on the road should be illuminated in a special manner. *Hella* and the *L-Lab* presented one of many use cases of such high resolution systems, when two high power projectors were used to create a light distribution, that allows for exactly the same luminance on the road in any given distance. Coupling this with new developments of light sources for the automotive market, the light output as well as the efficency of LED are still increasing and LASER based lighting systems have just been introduced to the market, this will offer a near infinite amount of different light distributions to choose from [96, 97].

3.2 European regulations on automotive headlamps

While the previous section describes the currently available technology, these current headlamps are limited by two things: the technology currently available and financially viable and the current international regulations regarding automotive headlamps. Since all studies conducted in this thesis are set in Europe, more specifically in Germany, this section will only focus on European regulations - the so called United Nations Economic Commission (UNECE) regulations. These regulations contain all regulations regarding motorized vehicles from R1 (Headlamps) to R143 (Regulation on uniform provisions concerning the approval of Heavy Duty Dual-Fuel Engine Retrofit Systems (HDDF-ERS) to be installed on heavy-duty diesel engines and vehicles). These regulations are valid in Europe and a number of non European countries like Argentina and Australia. Notable exception to this list are the USA and China who use their own independent regulations. A general overview over which country belongs to which set of regulations is shown in figure 3.3.

The largest and therefore most important regulations are the Economic Commission for Europe (ECE) regulations, with the participating countries shown in red, and the Federal Motor Vehicle Safety Standards (FMVSS) with the participating regulations shown in light green.

The UNECE regulations regarding the headlights for vehicles can be divided into three major groups:

- general regulations regarding headlamps
- light source based
- light distribution based

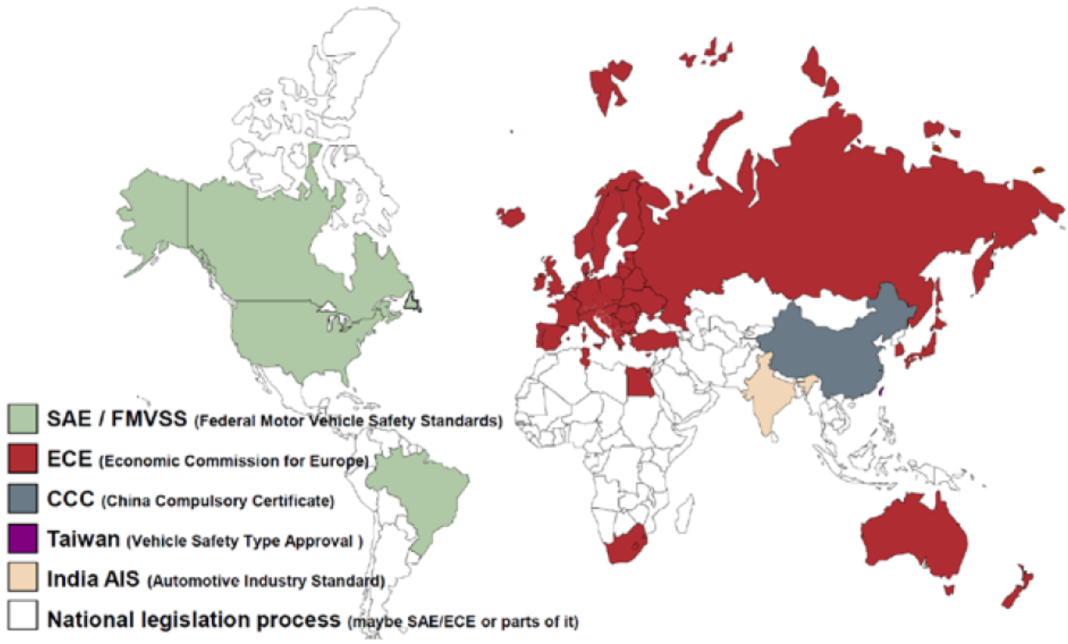

Figure 3.3 – World overview of the different headlamp regulations in different countries. The two widest distributed regulations are the UNECE, marked in red, and the SAE/FMVSS, marked in green.

As a detailed overview, these regulations are summarized in appendix A.1 starting with the first regulation R1 going all the way to R119. R123 is summarized in the next couple of paragraphs. As an overall summary, the regulations state, that a minimal illuminance or luminous intensity needs to be delivered below the horizon to ensure save object detection while at the same time, maximum values are not to be overcome above the horizon to avoid any kind of glare. For this reason, several marking points are introduced at which the minimal or maximal values are recorded. Furthermore, zones are defined that need to reach a certain threshold value of illumination. Due to the historical evolution of light sources, the different regulations for each light source, contain different values. In general, halogen light sources need to produce less light in the detection area compared to HID light sources. On the other hand, HID headlamps are also allowed a slightly higher glare illuminance.

The latest and for this thesis most important regulation is the R123 for AFSs. This regulation, as already indicated by the name, covers adaptive headlamp technology, meaning, that, as explained above, not only two static light distributions for low and high beam are available, but that depending on the current situation a certain light distribution is loaded and projected onto the road. A short outline on what kind of light distributions are available on the market right now, is already given in the section above. Figure 3.4 shows the measurement screen with the introduced measurement points for headlamp certification. The red lines and polygons show the mentioned areas, red triangles show measurement points, in which a certain maximum value may not be exceeded and blue dots show measurement points, in which a minimal value is required.

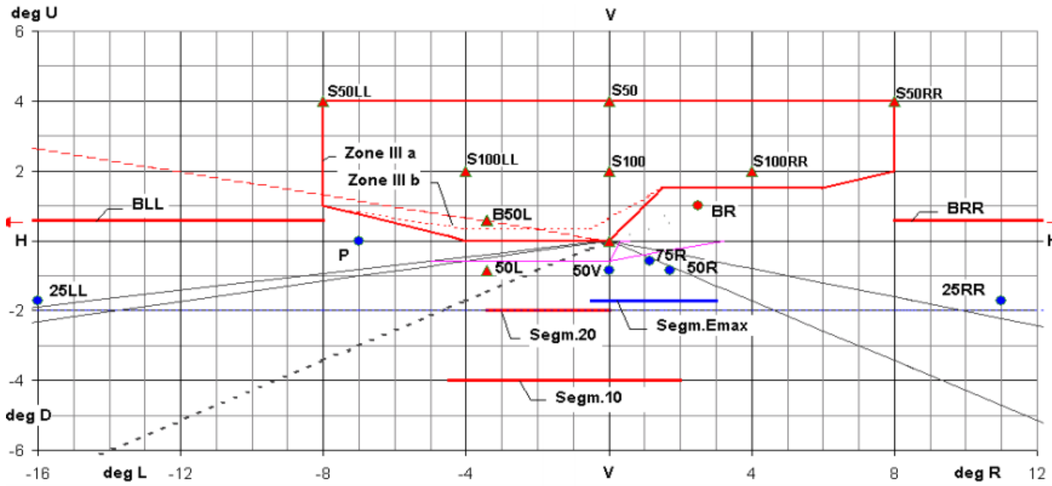

Figure 3.4 – Measurement screen for headlamp certification according to ECE R123 with all required measurement points and zones.

The most significant points on this screen are the **B50L**, **75R** and **50R**. **B50L** is the point, at which the head of an oncoming driver are located at a distance of 50 m and **75R** and **50R** mark the points of the right road side in 75 m and 50 m distance. **B50L** is the most commonly used point of reference for glare rating and the other two points are good indicators for viewing distances with the respective light distribution. Furthermore, the centre of the measuring screen at 0° horizontally and vertically is noteworthy since this is usually the point with the highest luminous intensity.

While R48 (see appendix A.1) introduces triggering events for the different AFS classes, R123 introduces the required luminous intensity values at all points for all of those classes. However, since this involves numerous different values and different points, these photometric requirements are listed in the appendix in table A.8.

While these regulations apply to the current state-of-the-art, they are ever-changing with the development and the introduction of new technology and functions for headlamps. Usually, the regulations are slower than the development of new technology and the newest introduction to the market, therefore get special single type approval before the general system or function are included in the regulations. This is the reason, why it is important to know the general required illumination numbers, but the light distributions introduced and proposed later in this thesis will only take the regulations as guidelines on what kind of values are required but will allow for slight deviations.

Part IV

RELATED WORK

No matter what you do - someone has either already done something similar or at least someone has done work that enables you to perform the next step in research or development. This applies to this thesis just as much as to any other. Therefore this part is dedicated to discussing all the relevant research that has lead up to this project.

4 RELATED WORK

As described in the introduction, the goal for this thesis is to create new light distributions that are optimized for different traffic situations, leading to an optimized use of glare free high beam and allow for the best possible detection of objects in the traffic space without causing glare for other road users. For this, using simulation and recorded real life traffic data, the segment distribution is optimized, before several laboratory and field studies regarding the detection and glare in real life situations are conducted.

This chapter will focus on highlighting the most important publications and studies relevant to this thesis and put the presented studies in an historical and intellectual context. The first part will discuss work regarding object detection and identification in automotive use cases. Following this, the assessment of glare, both physiological and psychological and especially the measurement of both during automotive research will be reviewed in detail.

In the next section the most important studies regarding Eye Tracking will be discussed. This will briefly start with basic Eye Tracking studies in general to introduce the most important findings that are needed for understanding and setting all parameters used for this thesis into context. The main part however will focus on Eye Tracking in automotive use, including work in simulations as well as real life driving studies. The penultimate section will focus on work on pupil behaviour during different lighting situations. Pupil dilation due to other factors, like stress or other emotions will not be discussed. In the final section work regarding traffic space analysis and the optimization of light distributions is discussed.

4.1 DETECTION IN AUTOMOTIVE LIGHTING

The basic principle of detection in a more general context is explained in section 2.4. This part will focus on more recent studies regarding the detection in automotive cases. This does include more or less abstract laboratory studies that aim at finding detection correlations with use for automotive lighting, studies performed in driving simulators as well as real life driving tests that include some kind of detection tests.

LABORATORY STUDIES

Since the visual context for nighttime driving is very complex, the first approach has to be, to simplify the perceived field of view in order to minimize the number of influencing factors. By doing so, the possibility is given, to isolate the task of identifying an object in a nighttime driving situation, and investigate correlations between object and photometric parameters in laboratory studies.

Adrian for example chose an object with the size of 0.6°, corresponding to an 20 cmx20 cm object in the distance of 85 m and measured the detection probability for contrast levels ranging from 0.2 to 0.4 for different background luminances. For this study, the object was shown for only 0.2 s and the participants only indicated, whether the object was detected or not. The findings here follow the findings already described before by Blackwell with one major addition being, that the relation between the 50 % threshold to the 99.96 % threshold detection is found by a field factor of 2.6 for the required contrast. [98]

Similar tests were performed by SCHILLER who presented monochromatic targets on a mesopic, homogeneous background with a luminance of $0.1\,\mathrm{cd\,m^{-2}}$ and $1.0\,\mathrm{cd\,m^{-2}}$. The monochromatic targets are set to a size of 3.0° with 21 different colours ranging from 421.9 nm to 651.9 nm and are placed at eccentricities of 0.0°, 2.7° and 10.0°. The background spectrum is varied as well between a tungsten halogen spectrum, a D65 spectrum and an isoenergetic spectrum. The goal of SCHILLER was to find the best possible wavelength/background spectrum combination to optimize headlamp spectra for detection during nighttime driving. His findings show no significant influences of the adaptation spectrum for most of the parameter combinations. Only at a viewing angle of 10.0°, the adaptation luminance of $0.1\,\mathrm{cd\,m^{-2}}$ and object wavelength of 461 nm, 502 nm and 532 nm a significant difference is found for the different adaptation spectra. The obvious significant influence of the object spectra is not discussed further by SCHILLER, since the influence of the object spectrum is sufficiently well-known as shown in chapter 2 and as indicated by the $V(\lambda)$-function. While these findings show a lot of interesting features, the direct correlation to the findings of ADRIAN and BLACKWELL is not possible due to the different approaches.
DAMASKY performed similar tests in the laboratory, but divided the background into asymmetric fields representing the road (higher luminance) and the background/sky (lower luminance). On this asymmetric adaptation background, different objects are presented to the participants at different positions. This is illustrated in figure 4.1 where the road is shown in light blue, the background is shown in a darker blue and the objects are shown as red, an object on the road, yellow simulating pedestrians besides the road, and orange, an object (traffic sign) above the road. [1]

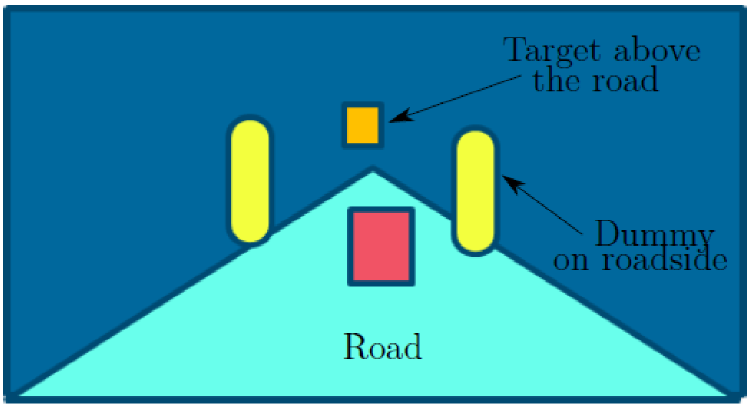

Figure 4.1 – Laboratory setup by DAMASKY where the light blue background represents the road surface, the dark blue area marks the general background, the red square shows an object on the road, the yellow objects simulate pedestrians besides the road and the orange square represents traffic signs above the road [1].

In this study, the object luminance is varied between $0.0\,\mathrm{cd\,m^{-2}}$ to $75.0\,\mathrm{cd\,m^{-2}}$ with the darker part of the background being $<10\times10^{-5}\,\mathrm{cd\,m^{-2}}$ and the simulated road surface being variable and thereby simulating different headlamp intensities. In general his findings show a correlation between the threshold luminance of the detection objects to the road luminance. In the second part of his study, DAMASKY constructed a setup to project the exact same objects with variable luminance in the driver's field of view. This field test will be further explained in the correlating section.

While the studies from ADRIAN, BLACKWELL and DAMASKY do supply information on what contrast levels are visible under different conditions like adaptation luminance, age, target

size and more, and the work from Schiller offers further insight into the influence of different spectral combinations of object and background, they don't consider the additional stress on participants through the task of safely driving a vehicle [99]. Mayeur amd Bremond therefore devised a series of studies regarding the effect of different tasks and background situations on the detection task that include laboratory studies, simulator studies and field tests.
The laboratory studies are split into three sets, where the first setup is a basic detection test of a uniform square object on a homogeneous background of under different detection angles ranging from 1.5° to 7.0°. The contrast between the object and the near background is varied between 0.0, 0.3, 1.2 and 4.8 and the stimulus is presented for 230 ms The second test setup includes an additional task for the participants, that are now asked to use controllers to steer a black square in a circular, given way while at the same time, detecting the same target as in the previous test. This is done to simulate the cognitive stress that a driving situation would have on the detection of objects in a real life situation. This part of the study was firstly done on the same homogeneous background, but was also repeated on an photograph of a street in Paris, as shown in figure 4.2. Here the detection object, the grey square, is located on the lower right side.

Figure 4.2 – Detection background used in the second part of the study by Bremond where the detection object (grey square) is inserted in a photograph of a street in paris [99].

The same experiment was conducted a third time, with the background now being a video recording from the same street in Paris as used before. In both these conditions, the detection target for each test subject is set to the individual threshold contrast of 99 %. Using the static image as a background, decreases the detection probability down to 81 % and using the video decreases this further down to 37 % showing the drastic influence of inhomogeneous backgrounds on target detection. A similar decrease in detection performance is measured between the standard test and the same test with the added tracking task, where for the same contrast, a decrease in the detection probability from 84.2 % down to 67.5 % is measured. To further investigate the influence of the driving task, the same experiment is transferred to a real driving test, that shall be discussed in the following paragraphs. [65, 99, 100]

As mentioned before, Schneider performed a combination of field and laboratory experiments in order to find the influence of object shape, position and contrast on detection. In the laboratory study, a LASER marked the fixation target for the participants, and a circle (1° and 2° in diameter) and a deer were chosen as detection targets. The background luminance is set two different levels of $0.1\,\mathrm{cd\,m^{-2}}$ and $1.0\,\mathrm{cd\,m^{-2}}$ to investigate the influence of adaptation luminance. In the driving test, a second vehicle was set up as the fixation target and the detection objects were a human dressed in black and a deer, both with a reflectance of $\rho \approx 5\,\%$. The main difference between this study and the study presented by Mayeur is, that no eye tracking system was used to verify the detection angles. Furthermore, Schneider only shows the required contrast for a 99 % detection instead of the detection probability under different detection angles for a fixed contrast ratio. The findings here are in general, that for larger detection angles, the threshold contrast is raised. However, this increase is only marginal and changes for different setups. Other findings including the influence of the participants age, the background luminance and the target size are similar to the findings of Blackwell shown above. The more relevant part of the work by Schneider is the field study. Since this test is performed dynamically, with the participants driving at $80\,\mathrm{km\,h^{-1}}$, and the targets are set to a stationary position, the real detection angle changes depending on the detection distance to the target. However, the results are only listed dependent on the target position relative to the road and not on their angular position to the driver. Therefore, the results will not be discussed here, but further investigated in chapter 5.1.3.

studies based on driving simulators

With the recent development of new and better display technology as well as the emerging technology of virtual reality, a lot of automotive research has been focused on setting up suitable driving simulators to test driving performance in different situations and to test new features for vehicles without the need of setting up a highly expensive real life driving prototype. However, the limitations of the display technology regarding possible dark levels as well as peak brightness and as a result the limited contrast level, lead to difficulties regarding the use of driving simulators in automotive lighting use. While these simulators offer great possibilities in terms of understanding and showcasing new technologies and functions, it is very difficult to generate detection or glare tests, that are transferable to the real road.

Nevertheless, Bremond performed a study in a driving simulator where the influence of different target forms are investigated [101]. Starting with the uniform square, the target is changed to the shape of a human and to the shape of a car. In total seven different targets are tested with the background being a four lane road and all targets sitting to the furthest right of the lanes. Figure 4.3 shows six of these seven targets. Only the uniform square detection target is not repeated here. On the left side, the targets are shown with a uniform, grey texture and on the right side, the same targets are shown, now using a more realistic texture. At the top, a warning triangle is presented as the detection target, the middle shows a human figure and at the bottom a vehicle parked besides the road is chosen as the target.

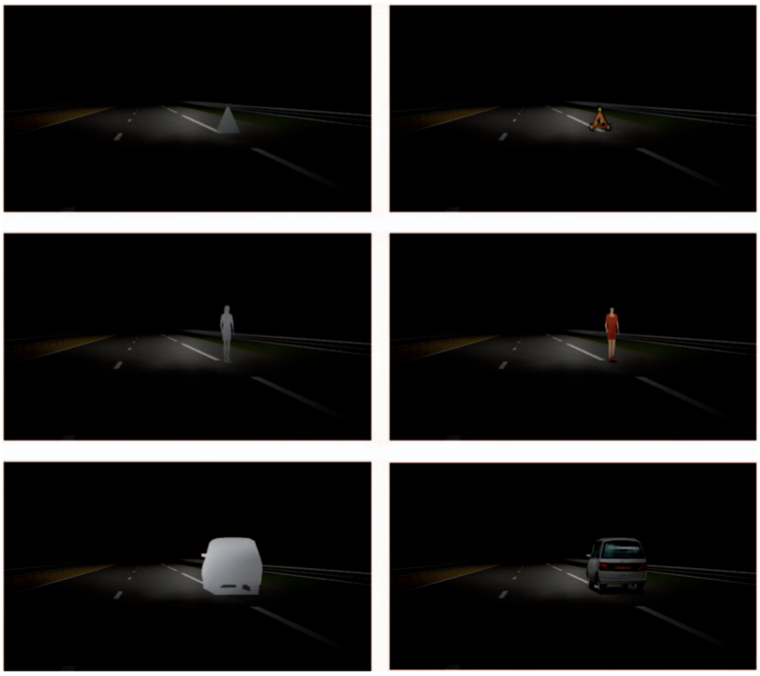

Figure 4.3 – Six of the seven different detection targets used by BREMOND in the driving simulator test. Only the uniform square target is not shown. On the left side, the target shape is shown with a uniform grey surface and on the right, a more realistic texture is chosen. The top pictures show a warining sign, the middle a human figure and at the bottom a car is selcted as the detection target. All targets are shown for a simulated distance of 20 m. [101].

The results of the detection distance measured in this study are summarized in table 4.1 where the calculated visibility level according to ADRIAN and the relative visibility to the standard square target are listed as well. Additionally, the table also shows theoretical detection distances calculated with the model by ADRIAN assuming a 35 year old test subject with a field factor of 7 and the difference between the calculated distance and the measured distance in percent. The mentioned field factor is usually used to compensate the difference between laboratory measurements and real life driving tests.

Table 4.1 – Measured detection distances and visibility levels in the driving simulator by Bremond as well as the calculated detection distances according to Adrian [101]

TARGET	REF. (SQUARE)	ROAD SIGN		PEDESTRIAN		CAR	
TEXTURE	UNI.	REAL.	UNI.	REAL.	UNI.	REAL.	UNI.
MEAS. DISTANCE	106 m	100 m	120 m	124 m	128 m	122 m	149 m
VIS. LEVEL	9	18	13	6	9	14	26
REL. VIS.	1.00	0.95	1.20	1.17	1.22	1.15	1.41
DIST. ADRIAN	115 m	112 m	131 m	124 m	129 m	126 m	146 m
DIFF. ADRIAN	8 %	9 %	12 %	1 %	0 %	−2 %	3 %

The first important detail shown by this data is, that the homogeneous targets always lead to a higher visibility level and therefore to a higher detection distance ranging from an additional 27 m for the parked vehicle to only 4 m for the pedestrian. Furthermore, it can be seen, that the difference between the calculated difference in detection distance is, for most cases, neglectable with errors below 10 % and the largest error occurring at the road sign with 12 %. However, it needs to be addressed, that this test is not viable to relate to real detection distances as distances with 100 m and more are unrealistic for driving with a dipped low beam. What this study shows how ever, is, that not only the model proposed by Adrian is viable to calculate visibility levels and that the visibility level translates to measurable detection distances, but also that this model predicts the correct detection distances within a certain margin of error. The main point of this thesis how ever is, that it emphasises the differences in the different object sizes and forms as well as the difference the object texture makes. Especially the widely used homogeneous grey coating leads to an increased detection distance when compared to a more realistic coating. [101]

Obviously, this study is not the only simulation based detection or visibility study performed. Bullough, Horberry, Sharar, Cavallo and Broughton, [102–108], all performed similar studies with similar overall results. However, since the presented thesis does not focus on simulator based results, going into depth with all these publications is not going to help the overall outcome of this work. The work of Bremond deserved special mention, since this work fits into a series of experiments that is performed in the lab, the simulator and real world driving as well.

FIELD STUDIES

While laboratory studies, and in an extend, experiments conducted in driving simulators, deliver useful insight into the mechanism of human perception and offer a very good overview over different influencing factors while being able to minimize influences from other sources, there is always the major difference, of the test participants not actually sitting in a real car and not steering the vehicle. In real life tests. three major factors appear. First of all, the traffic space changes, the car shows a dynamic behaviour in terms of acceleration and noise level and the adaptation level and the illumination changes and thereby influences the contrast dynamically. This difference in cognitive stress is often compensated by using the field factor mentioned before. However, depending on the type of the study and the chosen parameters this value can vary largely between 4.6 as suggested by LOSSAGK and 32 as measured by SCHNEIDER [66]. This means, that depending on the lighting function that needs to be investigated and the situation this is used for, a separate study needs to be conducted in order to determine the field factor for this situation. Therefore, it is highly important to perform field tests nevertheless for each introduction of new lighting functions or technology.

The first important study, that was conducted under real driving situations, was performed by DE BOER who investigated the detection distances in correlation to the luminous intensity of two different headlamp systems [75]. For this test, the participants were asked to drive the test vehicle with 60 km h^{-1} on a straight road with stationary glare sources placed on the left-hand side, simulating oncoming traffic. Besides the road, on both left and right with a distance of 60 m to each other, five detection objects, homogeneous grey squares, mounted at a height of 40 cm with a size of 28 cm x 28 cm and a reflection coefficient $\rho = 0.08$ were placed. For these detection objects, DE BOER measured the distance, at which the test participants were able to detect the objects. His findings show a significant influence of the glare source intensity, a higher intensity leads to lower detection distances, the position of the objects relative to the glare source, larger distances between object and glare source leads to larger detection distances, and an increased detection distance for an increased headlamp intensity.

As mentioned above, DAMASKY performed a second part to his laboratory study, in which he translated his setup into a real life driving test [1]. For this, he devised a method, that allowed him to project the exact same objects at different intensity and thereby varying contrast into the driver's field of view under the same angles that were used in his laboratory experiment described above and shown in figure 4.1. This field test was performed under two different situations. The first part was performed at the AUGUST EULER airstrip in Darmstadt, which represents a closed off road with no external influences regarding traffic or street lighting. For the second part, this setup was switched to real roads in real life traffic. Since the same objects were presented as in the laboratory study, DAMASKY was able to analyse the following factors: object shape, object position, test vehicle speed, object colour, visual task and participants knowledge. Examining the contrast at the 95 % threshold, his findings show, that due to the asymmetric low beam, objects on the left side receive a lower background luminance and the measured contrast is thereby significantly increased. An additional result found by DAMASKY is, that when comparing the luminance results from the closed off area at the air field with the real life traffic data. The luminance required for the 95 % detection probability is significantly increased for the real life data with the highest recorded luminance in urban environments of over 1.0 cd m^{-2} compared to $<$0.1 cd m^{-2} on the air field and about 0.2 cd m^{-2} on country roads and motorways.

While the studies mentioned so far, varied different parameters, all of them are performed mainly on unlit country road like road segments, with the real life study of DAMASKY being an exemption. GIBBONS perfomed a real life driving test with different street lighting systems in order to evaluate the influence of the colour temperature repectivily the spectrum of street lighting (colour temperatures of 2100 K, 3500 K and 6500 K) on the visual performance of the driver. Furthermore, the applicability of mesopic detection models and the field factor is investigated. This experiment is conducted on a separated road segment under controlled circumstances with adjustable overhead lighting to adapt the road luminance to the required needs. Over the test road, the luminous intensity of the overhead lighting is variied in order to find the influence of the adaptation luminance on the detection distance as well. The mean adaptation luminance is varried between $0.1\,\mathrm{cd\,m^{-2}}$ to $0.5\,\mathrm{cd\,m^{-2}}$. Detection objects (dummies) are placed at different positions to the left and the right side of the road as illustrated in figure 4.4.[109]

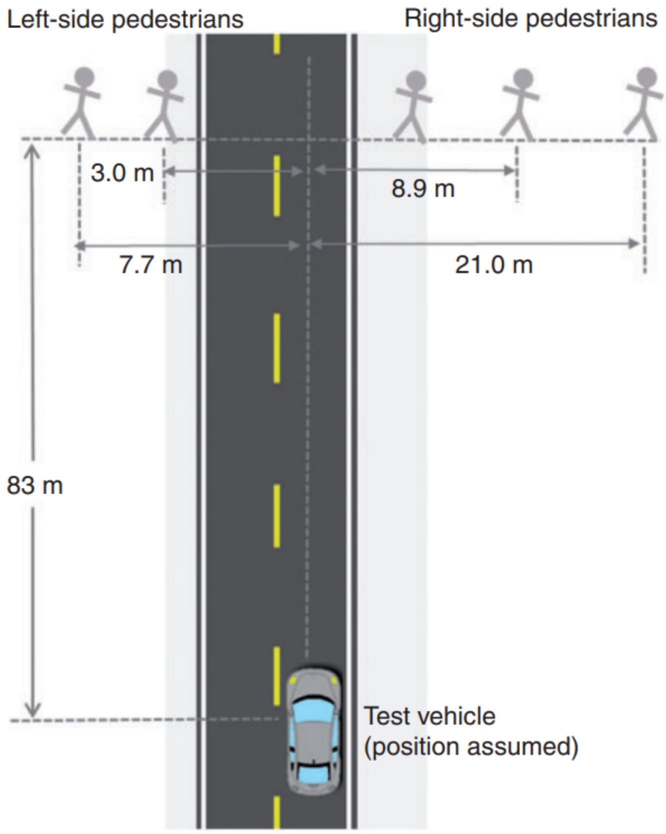

Figure 4.4 – Detection test setup with 5 dummies, two on the left road side and three on the right road side, by Gibbons [109].

Each of the participants performed the test three times, once for each overhead lighting situation. The results show an increase in the detection distance with an increased adaptation luminance. Furthermore, significant differences in the offset of the dummies to the detection distances are measured for objects located furthest to the side. The results show detection distances of around 120 m for the objects up to 8.9 m to the side and just below 100 m for the object at 21.0 m. An interesting result is, that for low offsets (eccentricities), no significant influence of the overhead spectrum is measurable, whereas for large offsets, higher Correlated Colour Temperatures (CCTs) lead to a significantly increased detection distance. However, the authors mention, that the measured effect is minimal and since the gaze of the driver is neither measured nor controlled, the off axis detection test cannot be converted to viewing angles and this might influence the findings of this paper. The recorded detection distances of over 100 m with low beam is difficult to compare to the results, that this thesis will present, due to two major reasons. First of all, the added overhead lighting in this study leads to a much higher adaptation luminance and will influence the perceived contrast. Furthermore, this test was designed and carried out in the United States of America, which leads to the use of Society of Automotive Engineers (SAE) conform headlamps that differ significantly in their light distribution to the ECE headlamps used in this thesis.

To find the effect of differently coated detection targets, as well as to examine the effect of adaptive headlamp systems, REAGAN conducted a field test, similar to the tests shown above [110]. On an unlit, closed off, rural road, that includes both, straight parts as well as curves. For this study, a total of 60 detection dummies, 30 of them with a high reflectance ($\rho = 0.4$) and 30 with a low reflectance ($\rho = 0.1$), were distributed besides the road. As lighting systems, an HID system with adaptive cornering light and a standard tungsten halogen headlamp were used. To compare the results between both systems, the test performed with the HID system was performed once with the cornering light activated and once with the cornering light deactivated. The results show, that for detection targets located on a straight roads, or on the outside of curves, the adaptive function of the HID system does not lead to any advantage. However, a general benefit in the detection distance of the HID system over the tungsten halogen system is found and that for the most difficult targets, coated with low reflectivity paint and located in steep curves, the AFS leads to significant benefits over the other two systems.

While more tests with similar setups but varying parameters were performed over the last years, the latest research, investigating the benefit of AFSs and gfHB especially, was performed by ZYDEK at the same air field in Griesheim [55]. This study investigated one of the first gfHB setups in the *VW Touareg*. When investigating the benefit of gfHB systems, both glare and detection need to be considered at the same time. The study performed by ZYDEK is therefore divided in these two parts. The complete test setup will be described here, but the glare results are shown in the following section, where current glare experiments are summarized. Since the main benefit of the gfHB system is, that driving with high beam during nearly any given moment is possible, the test setup involves oncoming traffic, that the gfHB system needs to cut out of the high beam distribution. While this oncoming traffic is located on the left-hand side, three detection dummies are located on the right side of the road. This test setup and the testing process for the detection and the glare part of this study is shown in figure 4.5.

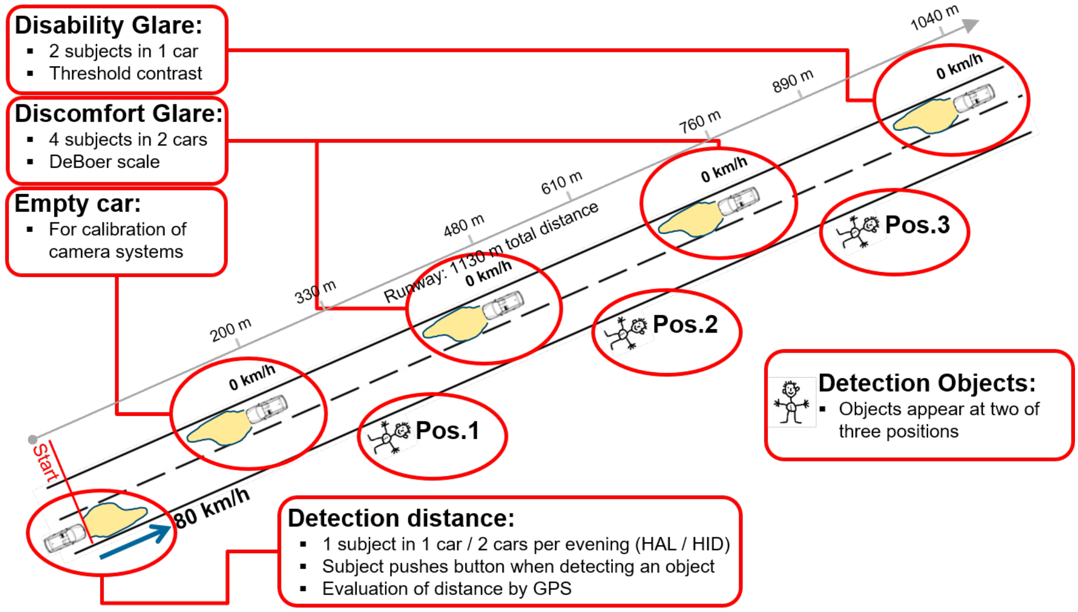

Figure 4.5 – Test setup and procedure for testing the detection benefit and glare rating of gfHB systems. Translated from [55].

Out of these dummies, two were randomly chosen to be standing up while the third one is set flat on the road. The detection distances are then measured in dependence of the light distribution. Since the system used was an HID setup, the test was performed with the gfHB activated, only the standard HID high beam activated, only the HID low beam and with an additional tungsten halogen headlamp as a base line (both high and low beam). The detection results show, that the lowest mean detection distance, equivalent to the 50 % threshold by Adrian, is measured for the tungsten halogen low beam at just below 60.0 m. With the standard HID low beam a mean detection distance of about 90.0 m is measured. The halogen high beam leads to a significant improvement with a mean detection distance of around 130.0 m that is only beaten by the HID high beam with over 140.0 m. The gfHB system leads to detection distances just under the usual high beam systems with 120.0 m, therefore leading to a significant improvement over the standard low beam, and just barely, and not statistically significantly, worse than any of high beam systems. [55]

Since the study presented by Zydek solely focuses on the aspect of oncoming traffic in a controlled, isolated environment, the THM Giessen performed a test in association with the Light Sight Safety initiative [111]. The goal is, to investigate the real life benefits of these AFS and gfHB systems and validate the findings of Zydek under more complicated situations. This test was set up on a real strech of road, with a length of 11.0 km. On this test track, 20 detection objects in three different forms are placed. Human, deer and boar shapes are used to provide real life data. Figure 4.6 shows the setup for four of those signs. Since the test track is used in both ways for this study, each of the detection objects is used twice, depending on the driven direction. Therefore, on the left side, the human dummy is marked with sign no. 6 and 15 and the boar is marked with no. 5 and 16.

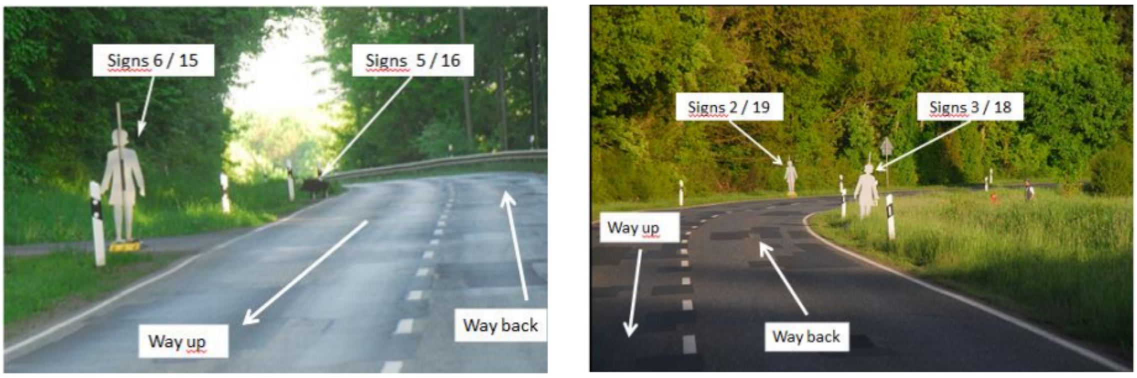

Figure 4.6 – Detection objects used by the THM GIESSEN with a human figure used for object 6, 2 and 3 and a brown boar as object 5 (left side). Two numbers are assigned for all objects since the test road is driven in both directions, indicating that all objects are used twice [111].

This figure also illustrates, that in this experiment a great number of different locations was chosen for the objects - on the inside and on the outside of a bend, on a straight line on the left and the right, and as shown on the right side of figure 4.6 with object no. 2/19, straight ahead when entering a corner. The test was then performed and evaluated for the visibility improvement in straight line driving, driving through a bend, oncoming and preceding traffic. The test was performed for driving with low beam only and driving with low beam and the additional gfHB. On average, over all different situations, the measured detection distance with only low beam activated is measured at only 56 m while the gfHB leads to a distance of 88 m thereby improving the visibility distance by 32 m or 57 % leading to an increased reaction time of 1.4 s when driving at 80 km h^{-1}. While the absolute distances differ from the findings by ZYDEK, this can be explained by the different driving situation in a much more complex environment. [111]
This review of different detection tests, including laboratory studies and real life tests on both, closed off roads as well as on real roads, show, that there are numerous different influencing factors to the presumably simple task of detecting a target besides the road. These factors include the object itself: size, shape, colour and reflectance, the position of the object, left or right side of the road and how far away from the driving lane the object is positioned, other objects in the field of view like glare sources, given fixation points, instructions given to the drivers, surrounding luminance and spectrum and of course the headlamps used for the test as well. This is not limited to the light distribution but includes any adaptive function and the light sources used as well. This is crucial when designing a new experiment to ensure comparability to other work and the influencing factors need to be known to transfer any results from the laboratory or closed off roads to real roads.

4.2 GLARE IN AUTOMOTIVE LIGHTING

Similar to the detection part of this chapter, the more general approach on glare investigations has been presented in 2.5 and this section will present more specific studies regarding glare in automotive use cases. While this is also split up into laboratory and real life driving studies, no section regarding driving simulation is presented, since the possibility of glare by a simulator is not yet given. However, with the development of new display technology, this might change in the near future.

LABORATORY STUDIES

The investigation of glare in general and in automotive use has been one of the major research areas over the last couple of years since headlamp glare has become an issue of public intereset [112]. Especially with the introduction of each new light source type (all the way back to the introduction of the tungsten halogen lamp [113], HID, LED, Laser) and the development of the gfHB systems the interest of possible glare issues with the correlating technology has increased over the last years.
Starting with the introduction of the tungsten halogen lamp for automotive headlamps, SCHMIDT-CLAUSEN performed a series of experiments to quantify the psychological and the physiological glare induced by these headlamps as well as a possible correlation between the two types of glare. The experimental setup is kept the same for all experiments. A glare source is placed under a variable angle (between 1° to 30°). The glare illuminance is varied between 2.5×10^{-3} lx to 2.5×10^{1} lx while the adaptation luminance is kept variable between 3.0×10^{-3} cd m^{-2} to 2.0×10^{1} cd m^{-2}. The adaptation luminance is kept to a triangle shaped area below the horizon, simulating a road surface. The psychological glare is rated in accordance to the DE BOER scale (table 2.1). For the physiological glare assesment, a detection object is placed in the field of view of the participants. The findings of SCHMIDT-CLAUSEN are manyfold and this short paragraph cannot do this extensive work justice. However, the main remarks are generalized formulas to calculate both, physiological and psychological glare with regard to the glare illuminance, the adaptation luminance and the glare angle. Since these formulas are not used any further in this thesis, the interested reader is refered to the original publications [113, 114].

SIVAK adressed the issue of different sizes of headlamps since new technology leads to the possibility to create smaller and smaller headlamps while still fullfilling all the photometric requirements. While this was already a topic in 1989, this is even more relevant today with the introduction of LED and LASER based headlamps. Since this topic itself is not directly relevant to this thesis, the main remarks taken from this work are the test setup and process. The test subjects were sitting in a mock-up of a real car inside of the laboratory. The glare source was placed directly in front of the subjects in a distance of 15.3 m. The glare source size could be varied between 7.6 cm and 15.2 cm (0.3° and 0.6°) and five illuminance values at the test subjects eyes are chosen: 0.0 lx, 0.1 lx, 0.3 lx, 1.0 lx and 3.1 lx. The selected illuminance values are chosen in a manner, that each values tripples the illuminance of the lesser glare pulse. The glare source was presented 2.0 s and while rating the glare perception, the subject was given a secondary task, in which the subjects were asked to use the steering wheel to keep a simulated digital road, in the centre of a monitor located directly right of the glare source (3.6° between centre of glare source and centre of the monitor). The background luminance for the laboratory was set to 0.0 cd m^{-2}. The rating of the glare perception was done on the DE BOER scale (table 2.1) and the scale is presented during the complete test procedure. The test subjects were asked to continuesly focus on the driving task and not look into the glare source. The findings show, that for same illuminance values, the smaller glare source leads to a higher glare rating (lower DE BOER rating). [81]

BULLOUGH set up two laboratory experiments to determine, whether HID headlamps lead to either an increase in physiological or psychological glare compared to tungsten halogen headlamps. His setup is devised in a way, in which he mimics the geometric conditions that are found on rural roads. The glare source is offset to a variable angle to the left side to simulate an oncoming vehicle in about 50 m distance which BULLOUGH estimates to 5° and

10° offset. With an adaptation luminance of 0.1 cd m^{-2} an adaptation phase of 3 min to 5 min was given to each subject before the test was started. For the discomfort glare, the already introduced DE BOER rating was used. To measure the disability glare, an additional Liquid Cristal Display (LCD) screen was added to the setup to project a uniform, square detection target in the field of view. The brightness of this target was varied and the participants were given to buttons to indicate, if the target was detected or not. Three different light sources were used as glare sources, a tungsten halogen light source as a base level, an HID light source and a halogen light source with a blue filter as a compromise between both situations. The results regarding the psychological glare show significant influence of the illuminance at the eye, the lamp type and the viewing angle. Increased illuminance leads to a higher glare rating, with an illuminance of about 1.0 lx required at the eye to reach the DE BOER rating of 5 and thereby crossing the threshold to glaring light sources. In general, the HID headlamp was perceived as the most glaring light source with the halogen light source being the least glaring. In terms of viewing angle, the light source located further away from the optical axis is perceived as less glaring than the one closer to the visual axis. For the investigation regarding the disability glare, no significant influence is found regarding the light source. However, strong correlation is found regarding both, the illuminance and the viewing angle. Higher illuminance and lower glare angles leading to the highest increase in threshold contrast. [56] A more recent study on glare with a slightly different purpose than those presented so far, was done by ENGLISCH. He investigated the spectral influence on physiological glare with a monochromatic light source. For this, the monochromatic glare source and the detection target appear simultaneously for 360 ms (the glare source is active 40 ms before the target is presented). The background luminance is set to 0.1 cd m^{-2} and 1.0 cd m^{-2} and the detection object is presented under 0.0°, 2.7°, 10.0° and 20.0°. The goal of this research was to find any major deviations between the spectral glare sensitivity and the spectral detection sensitivity as shown by SCHILLER [115]. While a major difference in glare sensitivity to detection sensitivity in the foveal region is found this experiment and the conclusions go beyond the scope of this work and the intereted reader is refered to the original publications [73, 116, 117].

A completely different research goal was attempted by LOCHER [118]. With the new LED ans LASER technology emerging in automotive lighting, it is possible to create headlamps and rear lamps, that are capable of delivering the requirements of the ECE regulations in terms of illuminance while having a much smaller surface area. Since this increases the luminance of the headlamps while maintaining the same luminous intensity, a laboratory study was designed, in which either the luminance or the illuminance are kept constant while the other is varied. In this experiment, both discomfort glare as well as disability glare are evaluated for both situations. While the psychological glare was rated on the DE BOER scale, the disability glare was evaluated by measuring the threshold contrast required to successfully identify the opening of a LANDOLT C. The glare source was set to either 50 000 cd m^{-2}, 100 000 cd m^{-2} and 250 000 cd m^{-2} or 0.4 lx, 0.8 lx and 1.6 lx depending on the testing scenario. The luminance values are chosen from previous luminance measurements on headlamps and the illuminance values are selected to mimic the ECE regulations for headlamp glare in **B50L**. The glare source was set at an offset to the viewing axis to simulate oncoming traffic. The results clearly show, that increasing the luminance while keeping a constant illuminance at the test subjects eyes does not effect disability or discomfort glare. Increasing the illuminance while keeping a constant luminous intensity on the other hand, influences both types of glare significantly. However, while 250 000 cd m^{-2} is "is indeed a pretty high value" [118], this is a limiting factor of this study and even higher luminance values might change the results.

While these laboratory studies are well suited to isolate different factors, similar to the detection tests, like adaptation luminance, adaptation time, contrast and more, they rarely cover the complexity of a real life traffic encounter where the overall situation is more or less identical to the ones shown for the detection tests. An inhomogeneous adaptation field, a moving glare source, a variing glare illuminance and more different factors are possible. For this reason, the next paragraph will summarize some of the vast amount of field studies regarding automotive glare.

FIELD STUDIES

While studies on glare in automotive use cases have been conducted for at least the same amount of time as the laboratory studies shown above, (see [119, 120]), this section will only showcase some of the newest entries to this topic.

Shortly summarized, LEHNERT investigated the influence of vertical vehicle movement on the perception of glare for oncoming traffic. He extracted 1605 individual glare pulses and found a correlation between these pulses and the perceived glare, by assuming a rectangular glare pulse between 0.3 s to 10 s.

$$w(E_{p,Max}, t_{pulse}) \quad = \quad 10.6 - 1.7 \cdot (\log_{10}(\frac{E_{p,Max}}{C_{E_0}})(\log_{10}(\frac{t_{pulse}}{C_{t_0}}) \tag{4.1}$$

With w describing the psychological glare, $E_{p,Max}$ the maximum pulse illuminance, t_{pulse} being the pulse duration and C_{E_0} and C_{t_0} two constants. [60]

Since this setup is the closest to some of the conducted studies presented in this thesis, the data is shown and compared later in combination with the data generated in the studies shown in section 5.3.

While the discussion about the avoidance of glare and the actual influence of disability glare on traffic safety is obvious, if a driver is, due to a glare source, unable to detect objects on or next to the road, traffic safety is at risk. The influence of discomfort glare, where a decrease in visual performance is not necessary but the driver "feels" dazzled and uncomfortable, is not that imminent. For this reason, THEEUWES designed an experiment, where an artificial glare source was mounted on a test vehicle. This is shown in figure 4.7 where the used glare source is shown next to an actual oncoming vehicle. This glare source is varied in intensity by different neutral density filters of 0.0 cd, 350 cd, 690 cd and 1380 cd correlating to 0.0 lx, 0.3 lx, 0.6 lx and 1.1 lx at the driver's eye.

Figure 4.7 – Test setup designed by THEEUWES with the artificial glare source right of an actual oncoming vehicle. The two separated glare sources are used to simulate two individual headlamps [121].

The participants were then asked to drive on a real road that is divided in nine experimental sections that can be grouped into three major groups, urban roads, rural roads and interstate. During the rural roads, plywood detection dummies ($\rho = 0.125$) were placed on both, left and right side of the road and the driver is asked to "hit the horn" as soon as he detects these dummies. Since each participant repeated the test four times (once with each glare intensity), twelve positions for the detection dummies are set, out of which randomly four to six dummies are chosen to be setup. Besides the expected results like a correlation between the glare intensity and the DE BOER rating, a reduction in speed was found in dependence of the illuminance. Additionally, a strong decrease in detection distance is measured with an increased glare illuminance. Furthermore, the difference in detection distance and glare rating is investigated for European vs. American participants and for two age groups, young (18 to 32 years) and old (57 to 69 years). No differences between the participants origin is found. In terms of the measured detection distance, a reduction in distance is measured between young and old, however the data is not significantly different. However, this might be due to the small group of older participants (8 test subjects). While the lesser detection distance can be associated with disability glare, the reduced driven speed however is assigned with the psychological glare since the driver feels uneasy.[121]

A stationary field test was developed by BULLOUGH in 2004 in order to evaluate the influence of the headlamp size, spectrum and intensity on glare rating and target detection. To investigate these factors, a combination of HID and halogen headlamps with filters are used, similar to the detection test performed by REAGAN where also the size of the headlamp area was set variable. The general schematic test set up is shown in figure 4.8 where the test subjects are set all the way to the left and the tracking target is set directly in front of the participants. The detection targets are set at different viewing angles.

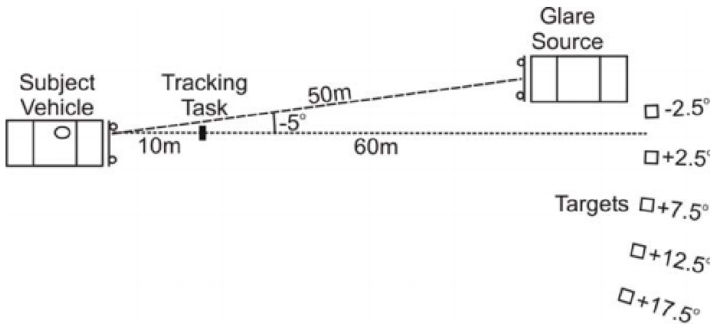

Figure 4.8 – Basic testset up by Bullough where the test participants perform a tracking task while being glared [112].

The selected glare illuminance values are set at 0.2 lx, 1.0 lx and 5.0 lx, according to Bullough corresponding to very low glare, usual glare experienced during nighttime driving, and the highest glare achievable by misaligned low beam headlamps. The influence of the spectrum is analysed with only 1.0 lx of glare illuminance and the different spectra are produced by tungsten halogen headlamps, blue filtered tungsten halogen headlamps and HID headlamps. At the same illuminance, using the HID headlamps, the size of the glare source is varied between 9 cm, 26 cm and 77 cm. The findings of this research show several correlations. First of all, the detection of the targets is angle dependent. The target closest to the glare source as well as the targets the furthest away from the line of sight are the hardest to detect. Again his findings confirm, that the higher illuminance values decreases the detection rate, but this research could also show, that the reaction times are decreased with increased illuminance. No influence of the spectrum is found, in either missed targets or reaction time and the same result is found for different glare source sizes.
With the introduction of LED headlamps, the same discussion arose as with the introduction of the HID headlamps. Therefore, Sivak conducted a field test, in which test subjects rated the discomfort glare on the de Boer scale for different headlamps simulating oncoming traffic. Five different headlamps were chosen, tungsten headlamps, HID headlamps and three different LED headlamps (4000 K, 4800 K and 6800 K). The presented glare sources were always placed at a glare angle of 0.5° above a given fixation point. The illuminance of the glare sources are varied between 0.3 lx, 0.5 lx and 1.0 lx. The correlating de Boer rating for all different glare sources is shown in figure 4.9.

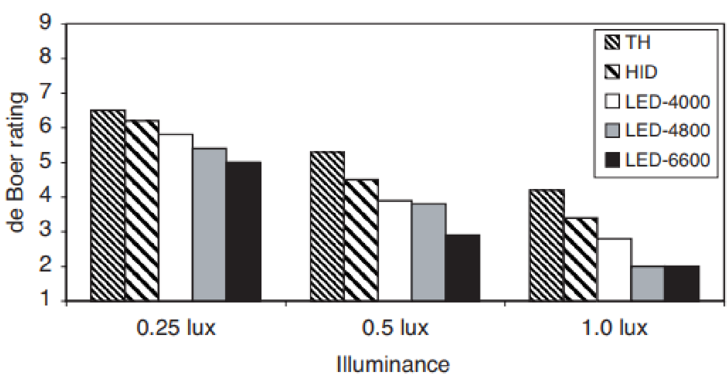

Figure 4.9 – de Boer rating for the different glare sources and different glare illuminances recorded by Sivak [122].

While the influence of the illuminance is clear and well known, the influence by the colour temperature is remarkable. The higher the colour temperature the lower the de Boer rating (higher glare rating). This even leads to the fact, that LED glare sources with 0.5 lx at the driver's eye are rated worse than a halogen headlamp with double the illuminance. This is explained by SIVAK with the stronger influence of the blue cone sensitivity at night. [122]

A similar test, just confined to halogen and HID headlamps but with regard to the adaptation spectrum (headlamps of the vehicle the test subject is sitting in) was conducted by SCHILLER in 2009. For this setup, two test vehicles are placed at a distance of 50 m on opposites sites of the road and the headlamps for both vehicles were changed between halogen (both projection and reflection systems) and HID (only projection system). Between all sets, no significant difference was measured, how ever a slight trend was perceivable in terms of the lighting system of the vehicle, the test subject is sitting in with a mean of 0.25 DE BOER ratings higher (lower glare) than for adaptation on halogen headlamps. [123]

With the introduction of gfHB in Europe, it was obviously needed to test these system on actual glare reduction. The test by ZYDEK as described in previous section, was therefore also used to estimate the glare ratings of the system used in the *Touareg*. As described above and shown in figure 4.5, on the oncoming lane, four measurement vehicles are placed to simulate oncoming traffic. In the first of these vehicles, measurement equipment is placed to measure the actual glare illuminance. In the three vehicles behind this, test subjectes are placed in order to rate the psychological glare on the DE BOER scale and to measure the physiological glare using a contrast box. This contrast box contains an LED with adjustable brightness. The test subjects are then asked to adjust the brightness of the LED, so that it is just perceivable - at the contrast threshold. With approaching oncoming traffic, the veil luminance for the test subjects should increase therefore leading to an increased threshold contrast which means that the LED needs to be set brighter the closer oncoming traffic comes. As already described previously, this test is repeated for halogen low beam, halogen high beam, HID low beam, HID high beam and HID gfHB. The glare results are easily summarized. For the psychological glare rating, no statistically significant difference between any of the low beam settings and the gfHB system is found (halogen low beam is rated the lowest) while the driving beam settings lead to a signficantly increased glare rating with HID high beam getting the highest glare rating of 1.7 on the DE BOER scale. Regarding the measured threshold contrast, the results are split into different distances to the oncoming traffic. When focusing on a distance from 400 m to 0 m, the measured threshold contrast for low beam and gfHB is again nearly identical and statistically not significant different. The high beam section on the other hand registeres nearly double the threshold contrast for the HID system compared to the halogen headlamp. However, the variance of the threshold contrast is at ±50 %. [55]
In a second study, ZYDEK investigated the influence of added load to the trunk of a vehicle and the resulting change in pitch angle and vehicle dynamics. For this, a total of 25 test vehicles, with different load (0 %, 50 % and 100 %) where driven along the same test setup as shown in figure 4.5. Again, the test subjects rated the glare according to the DE BOER scale. ZYDEK then analysed the exposure over the 400 m prior to the passing of the measurement vehicles. The exposure, H, is the integration of the illuminance measured at the driver's eye over time $H = \int_{t_0}^{t_1} E dt$ This exposure is then correlated to the glare perception of the subjects. This correlation is shown in figure 4.10.

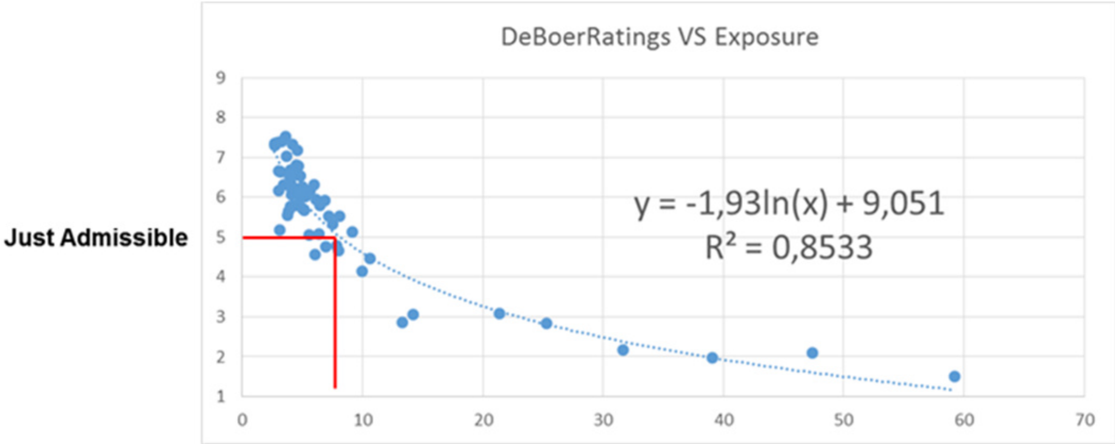

Figure 4.10 – Correlation between exposure and glare perception accoring to ZYDEK [124].

The correlation found by ZYDEK is given by equation 4.2

$$w = -1.93 ln(H) + 9.051 \tag{4.2}$$

The relation found, is of logarithmic behaviour and therefore mirrors the brightness perception of the human eye. The fit describes the data well, as indicated by $R^2 = 0.85$ as seen inside of the plot. The conclusion of this study is, that to achieve a glare rating of *just admissable* or better, the exposure over the last 400 m should not exceed 8.2 lx s.

A similar test, just utilizing LED based gfHB systems and investigating the illuminance caused at the driver's eye in more different traffic situations, is done by KOSMAS for oncoming traffic on straight roads, in bends, intersections and overtaking on straight roads. These situations are visualized in figure 4.11 where on the left side, the oncoming traffic on a straight road is shown, the next image shows the situation at an intersection, the third image shows the overtaking situation on a straight road and the last image shows the oncoming traffic in a right-hand side corner.

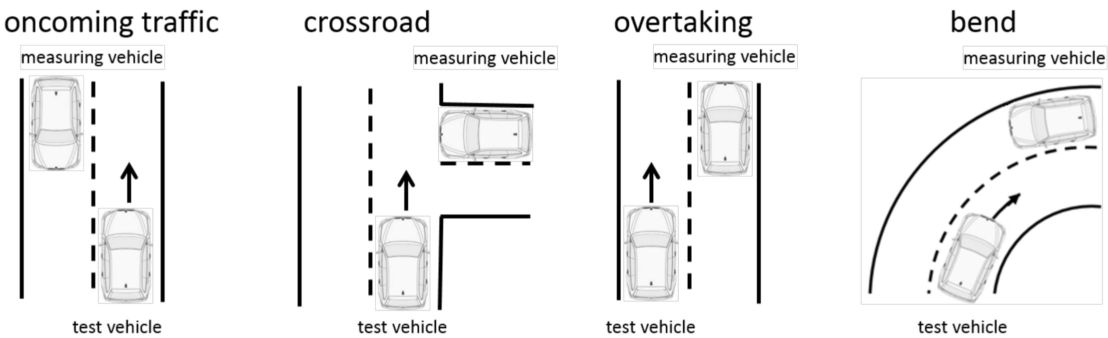

Figure 4.11 – Investigated traffic situations for the gfHB performance by KOSMAS from left to right: oncoming traffic on a straight road, an intersection, overtaking on a straight road and oncoming traffic in a right-hand side corner [58].

For all situations, the testing vehicle was driven with 80 km h^{-1} while the second vehicle (the so called measurement vehicle) was left static. Each encounter is recorded for low beam, high beam and gfHB and for each lighting function, seven test runs are performed for all seven situations. The illuminance curves are shown in figures 4.12a to 4.12d respectively. The solid red line shows the illuminance produced by the gfHB marked as Advanced Driving Beam (ADB) in the figure's legends, the dashed green line shows the illuminance created by the low beam and the blue, dotted line shows the data from high beam. The situations overtaking and oncoming traffic on straight roads show that the used gfHB system performs as expected with only a slight increase in the measured illuminance for larger distances between the two vehicles and nearly identical illuminance values for distances closer than 200 m to the low beam, while the high beam exceeds the recorded illuminance values by far. At the intersection, the gfHB system does not activate at all leading to identical values between high beam and gfHB - which is expected and wanted by some car manufacturers in order to warn other traffic participants, that a vehicle is approaching the intersection. An odd example in this setup is the corner, where no consistent behaviour could be measured. The maximum recorded illuminance changes between 1.5 lx to 11.4 lx. Figure 4.12d shows the data of all seven test runs, since the data varies greatly between all runs. Since the most interesting data happens at around 40 m, the data for this is only shown until 100 m instead of the 700 m like for the other encounters. This is either due to unpredictable behaviour of the gfHB or due to inconsistent driving through the bend.

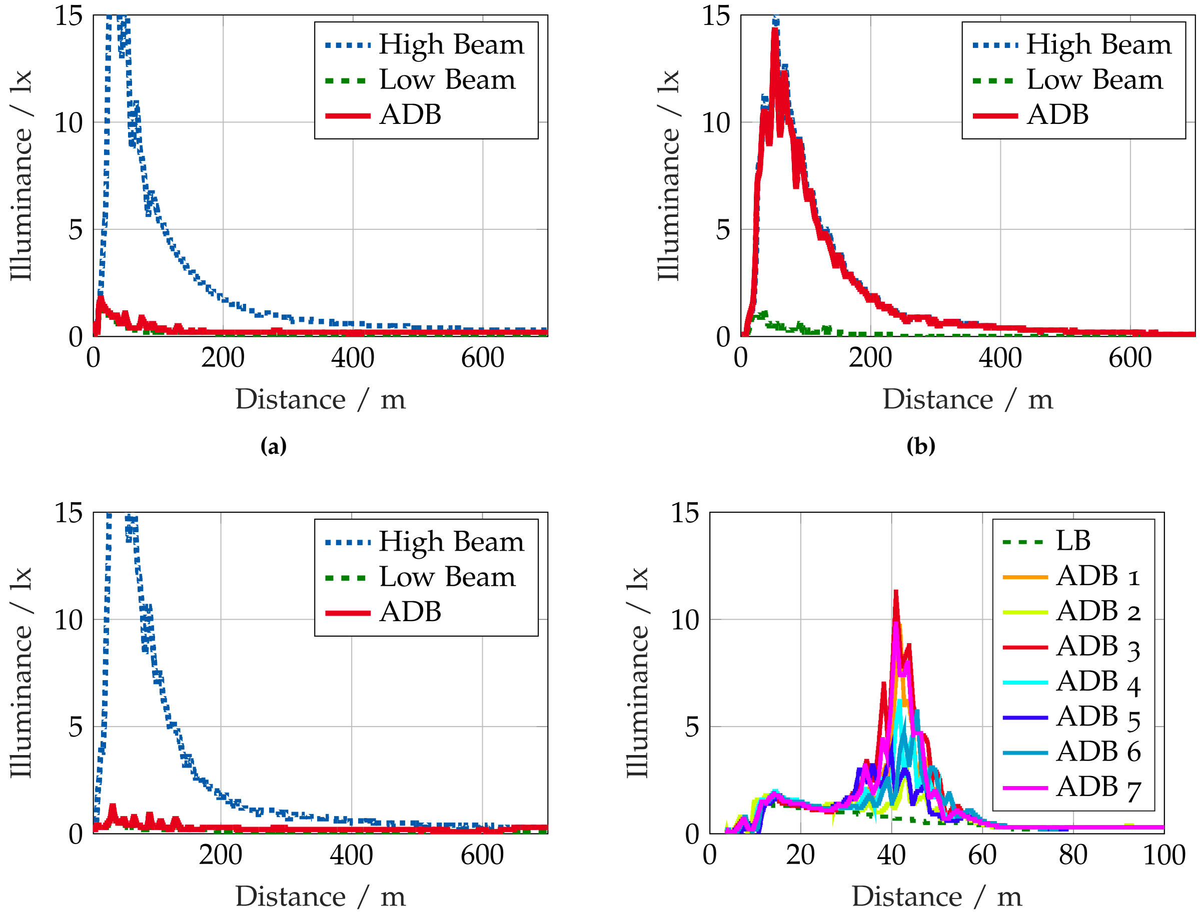

(a) (b) (c) (d)

Figure 4.12 – Comparison of the illuminance recorded at the driver's eye for the four investigated traffic encounters. Figure (a) shows the illuminance for oncoming traffic, (b) shows the illuminance for an intersection, (c) shows the recorded illuminance for overtaking, and (d) shows the illuminance recorded in a right-hand side bend. While figures (a) to (c) show low beam (green dashed line), high beam (dotted blue line) and gfHB (solid red line), (d) shows all seven test runs with the gfHB for the curve encounter since these test runs vary greatly and no high beam data is presented for this situation. [58]

In summary, Kosmas deduces, that the gfHB system in test, works fine with the same level of glare induced for oncoming or overtaken traffic as low beam. For crossroads, this gfHB system produces much more glare, identical to a normal high beam system and for traffic encounters in corners, no reproducible data is achieved and therefore no definite conclusion can be set. [58]

The conclusion from these glare studies, both laboratory based as well as field tests, is, that the main influence on glare is given by the absolute illuminance at the driver's eye. This is valid for both, physiological and psychological glare. For physiological glare, the angle between a possible detection target and the glare source is another strong influence factor, as already explained by the veil luminance in section 2.5. The restrictions known from detection tests in real life field tests apply as well to the measurement of glare. One of the major remarks that has to be given here is, that due to imperfections, unevenness in the road surface, the illuminance measured at the driver's eye does not show a smooth behaviour, but contains small peaks, as seen in the work by Kosmas. The issue that arises here is, that if the psychological glare is to be evaluated, the standard method of using the de Boer scale is very slow and only focuses on the overall illuminance measured at the driver's eye. For this reason, a correlation between the measured illuminance curve and the psychological glare is needed.

4.3 EYE TRACKING

The main section of this thesis is subject to analysing the gaze and fixation behaviour of drivers in different traffic situations. For this reason, this section is dedicated to previous findings of Eye Tracking studies starting with a very short summary of general Eye Tracking studies then focusing mainly on studies in automotive use. Since Eye Tracking systems usually utilize pupil data for the gaze tracking, the pupil diameter is recorded during all situations anyway. Therefore, the pupil diameter is evaluated for the different situations available in this thesis as well. For this reason, the last paragraph of this section summarizes studies regarding the pupil diameter under different lighting situations.

4.3.1 EYE TRACKING GENERAL

The main use of eye tracking technology at the moment is either in customer studies regarding their visual orientation in different situation, or in combination with computer usage. In this case, the eye tracker can either be used to monitor the users gaze behaviour when performing certain tasks like website browsing or text analysis, or the eye tracking system can be used as a human machine interface and the eye tracker is used as an input device meaning that the user is able (to some extend) to control the computer using the eye tracking system. Since this is not related to the topic of this thesis, the interested reader is referred to the original publications like Granka [20], Jacob [39], Goldberg [125] or Corcoran [126].
A study more related to the context of this thesis, focusing on the influence of overhead street lighting on pedestrian behaviour is conducted by Fotios. To evaluate street lighting, pedestrian fixation behaviour was recorded during day and nighttime while a secondary task was given to the pedestrian. The performance during this secondary task was used to identify critical situations with the assumption, that during those critical situations, the performance in the secondary task is reduced. In this secondary task, the test participants are asked to press a single button as soon as a certain audio stimulus was given. The reaction time be-

tween the stimulus and the press of the button is then recorded and analysed. To identify what the pedestrians were looking at, a scene camera was fixed to the head of the test subjects along with the eye tracking system. The findings show no difference of critical fixations except for the fixation of other pedestrians, where less other pedestrians are fixed at night, due to two major factors. Firstly less pedestrians are recorded overall at night, and secondly the test subjects prefer not to fixate other pedestrians at night. [127, 128]

4.3.2 EYE TRACKING IN AUTOMOTIVE USE CASES

While the general use of eye tracking systems is definitely interesting and leads to new and highly important insight, the main focus here is the automotive use. As mentioned in the introduction already, at least 90 % of the information a driver uses to safely steer and control the driven vehicle is obtained through the visual apparatus. Therefore, understanding what drivers look at and what they can perceive when driving is an obvious choice when investigating driver behaviour. Additionally, this enables researchers and engineers to investigate or verify possible benefits with different driver assistance systems. Since headlamps are the main light source and are developed to help the driver to orientate himself and detect obstacles at night, using eye tracking systems in order to evaluate headlamp systems has been common in the community over the last couple of years.

The first remarkable study, in which eye tracking is used to identify driver's performance is found in 1972, when MOURANT used an eye tracker to identify the differences in orientation behaviour of drivers with different driving experiences. For this study, two cameras are used. One camera is set up in a way, that through filming a mirror, the driver's eyes are recorded. The described cornea reflection method to calculate the gaze direction is used. The secondary camera was equipped with a wide angle objective in order to record the road scene. Both cameras are synchronized and the gaze direction is marked on the road scene as a dot. The complete test setup is shown in figure 4.13.

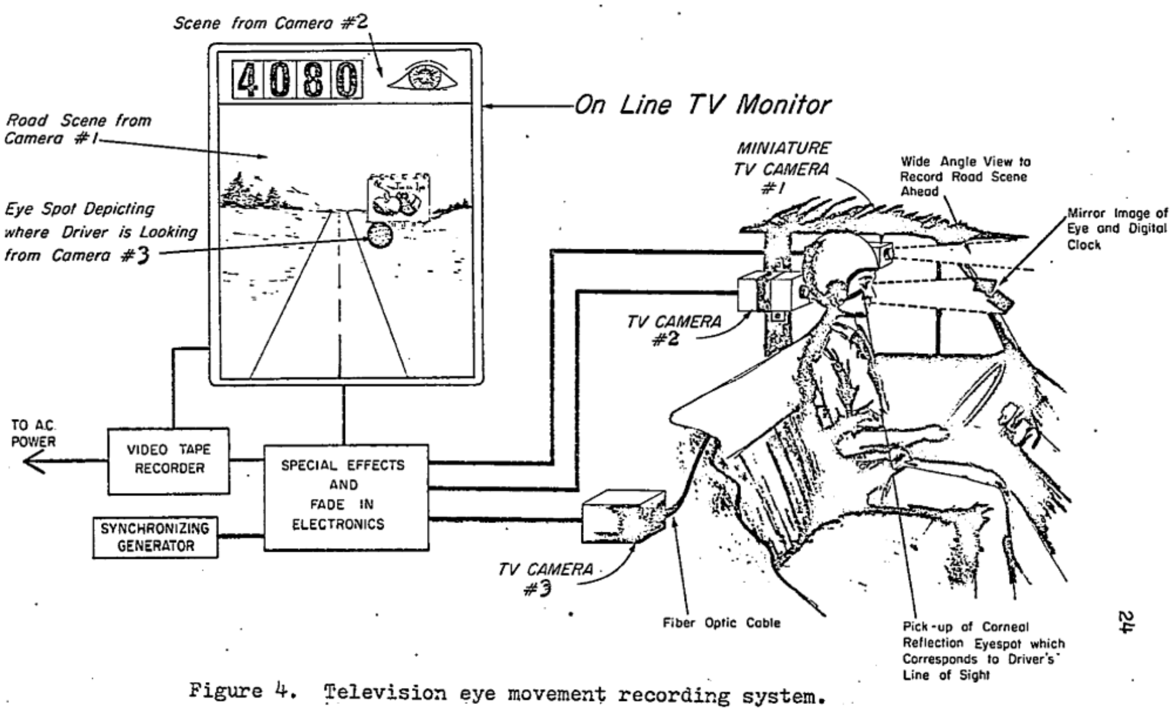

Figure 4.13 – Test setup in order to monitor the driver's gaze while recording the road scene (1972) to find differences in orientation behaviour between experienced and unexperienced drivers [129].

To reach the highest possible gap in driving experience between the test groups, the inexperienced drivers were test subjects who were actually doing their driver's licence at the time and performed some of their practice drives during the study. The main differences were found in terms of the scanning patterns. More experienced drivers tend to use a wider area in which they search for possible hazards (±13° vs ±6° for novice drivers). Furthermore, they orientate themselves further away (1.5° further up) - closer to the horizon - and about 4° further to the left than less experienced drivers. [129]
To further investigate the orientation behaviour of drivers, especially in cornering situations, Land simultaneously recorded the horizontal gaze angle as well as the steering angle. Similar to the work of Mourant, a video based eye tracking system was used to measure both, the driver's gaze as well as the road in front of the vehicle. Again, the calculated gaze direction is transferred onto the recorded video using a computer based eye model to calculate the gaze direction depending on the pupillary direction. While this study only involved three test subjects, the findings indicate, that drivers use the tangent point of corners for their main orientation. However, it is also recorded, that the drivers tend to search besides the road and only frequently return back to the tangent point for orientation - the frequency in which this is done is dependent on the driver. [130]

The first study, that is directly on the same topic as this presented thesis is from 1998 by Damasky and focuses on the influence of the light distribution of headlamps on driver's fixation behaviour at nighttime [131]. The work is divided in two parts. In the first part, different types of headlamps and the driver's fixation behaviour with these headlamps were analysed. The second part focused on the influence of the headlamps on the driving behaviour and the safety feeling of the drivers. For this, different headlamp systems were mounted on the testing vehicle using a metal rack. Different headlamps, including the tungsten halogen(H4, H7) and HID (D2R) headlamps with different reflector types were used and the testing vehicle was set up with a commercial remote eye tracking system. The tests were performed on real roads with low levels of street illumination and each test drive (per headlamp) lasted about 4 h leading over different types of roads including country roads, motorways and federal highways. To identify differences in gaze-/orientation behaviour, areas of identical attention and duration are calculated. As an example, figure 4.14a shows the presented data for a halogen headlamp of the type H4 and figure 4.14b shows the same calculation for the H7 headlamp. The iso-areas of attention are shown by yellow lines and theoretical cut-off of the used headlamps is marked by the red line.

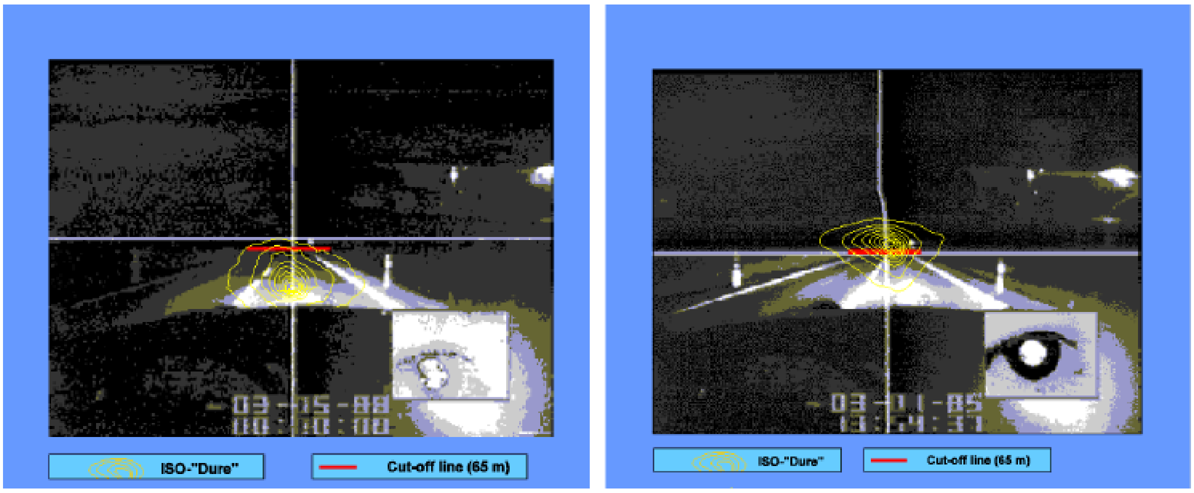

(a) (b)

Figure 4.14 – (a) Shows the iso areas of duration and attention (yellow) for driving with an H4 headlamp for one test person and theoretical cut off (red line). (b) shows the same data recorded for an H7 headlamp.[131]

The influence of the headlamp can clearly be seen in this example. For the H4 headlamp, which has a higher emphasis on close-range illumination, the vision of the driver shifts closer to the vehicle. For the HID headlamps, the opposite is found. Since the used HID headlamps deliver a lot of light close to the cut-off line, the 90 % iso-area of all gazes is lifted towards the cut-off and widened significantly. However, no significant influence of the headlamps on the driving performance is found with the recorded data. [131]

Brückmann investigated a similar case as Damasky where the influence from different headlamp systems on gaze behaviour is tested [87]. While his findings in general reveal the same results as Damasky, he added new headlamp types and most importantly, determined the difference between the gaze behaviour at night compared to the gaze behaviour during the day. In order to investigate the orientation behaviour and the information gathering by the drivers, no instructions such as directions, but only the final destination, were given to the subjects. His findings regarding the differences between day and night show, that during the night the gaze distribution is significantly narrower than the distribution recorded during the day. He associates this with the limited information that is available during the night and concludes, that the driver only looks, where light is projected to by the headlamps. These results are coherent with the findings regarding the different headlamp types he investigated and are similar to what Damasky presented.
A completely different use case for remote eye tracking was developed by Ji who used different characteristics of human facial features, including gaze orientation, eye lid opening and blinking, or rather eye lid moving in general, to identify and objectively measure driver's

vigilance. For this, a setup including two remote cameras was developed and tested in a simulator. His test setup is shown in figure 4.15a and 4.15b.

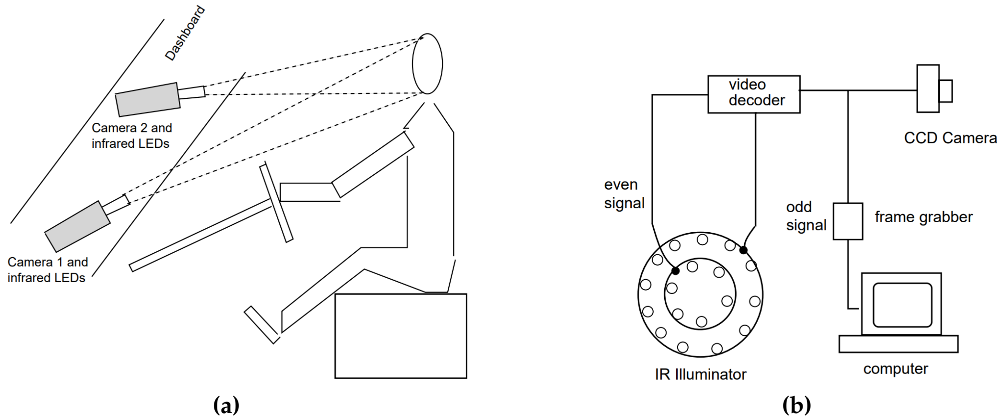

Figure 4.15 – (a) shows the camera placement in the vehicle simulator with two cameras set left and right of the optical axis of a potential driver. (b) Shows the camera setup for each of the two used cameras including the infra-red light source and the computer used to store and evaluate the data. [132]

To supply the cameras with an adequate amount of light during all simulated situations, day and night, infrared lighting is added to the system and the cameras are set up with an infrared bandpass filter. The infrared light sources are placed around the cameras to allow for bright pupil tracking. The main part of this work focuses on the used algorithm and the tracking performances of the setup, which will not be discussed here, since in the presented thesis, a state-of-the-art commercial eye tracking system is used and no new algorithms regarding the eye tracking are developed. However, JI also simulated drowsy driving and measured the gaze angles resulting in a significantly lowered gaze direction for tired drivers. [132]

DIEM tackles a more general approach on the topic of gaze behaviour during night. In a larger scale than the previously described studies, he recorded gaze behaviour during automotive driving in real life situations during the day and the night. He then split the data sets according to different road types like urban, country road and motorway driving. These data sets were then split into further groups like single lane country roads vs. multi-lane country roads. To be able to measure this enormous data set, DIEM did not only develop his own eye tracking system that suited his needs for automotive use, but similar to the other publications presented here, recorded the road ahead of the vehicle as well. He then manually evaluated the data. His findings are vast but the most important findings are shortly summarized here. The main difference between daytime driving and nighttime driving is, that during the day, DIEM finds a much narrower field in which the driver orientates himself as shown by figure 4.16

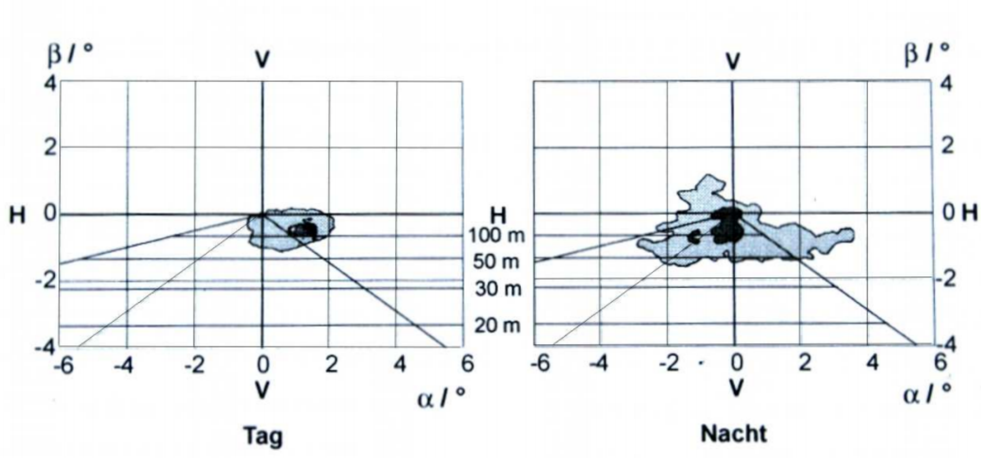

Figure 4.16 – Gaze behaviour recorded by DIEM on country roads for daytime driving (left) and nighttime driving (right) [4].

Differences between country roads and motorways are small but noticeable, however driving in urban areas leads to a (compared to the other sets) very wide orientation behaviour. Furthermore, influence by the number of available lanes is found, where different accumulation points are formed accoding to the number of available lanes, the quality of road markings and for the brightness of the road surface, where darker roads lead to a wider, more searching gaze distribution. [4]

With the introduction of adaptive bending light, the research of the fixation distribution when driving through bends needed to be renewed. To investigate the benefit, respectively the influence of dynamic bending light on the gaze distribution, SHIBATA used an HID projection system, that allows swivelling of $\pm 19°$ in both directions for both headlamps. The car was equipped with a remote eye tracking system and the gaze behaviour was recorded for driving through three different bends with radii of 65 m, 130 m and 210 m on country roads. To investigate the effect of the bending light in larger detail, the headlamp was modified, so that four different modes were available: Both headlamps swivel, only the inner headlamp swivels, both headlamps swivel but the outer headlamp swivels only 50 % of the angle of the inner headlamp and both headlamps swivel with the outer headlamp swivelling 75 % of the inner headlamp. The results for the four extreme settings are shown in the figures 4.17a to 4.17d.

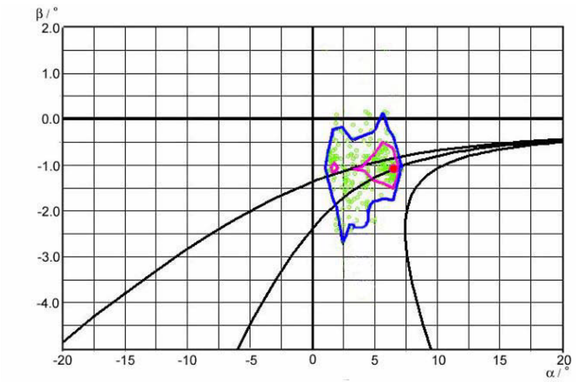

(a)

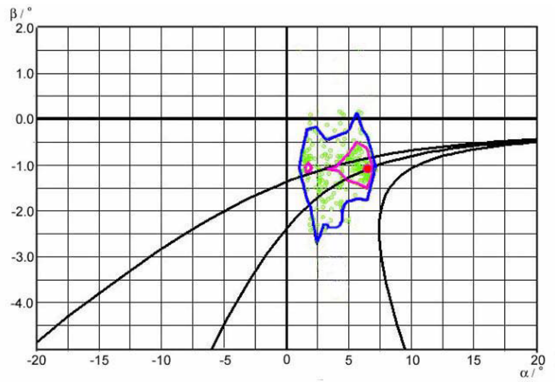

(b)

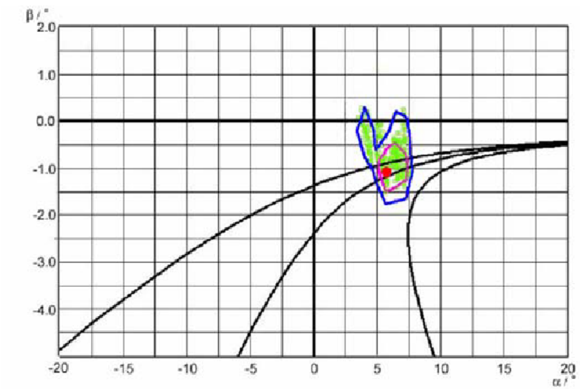

(c)

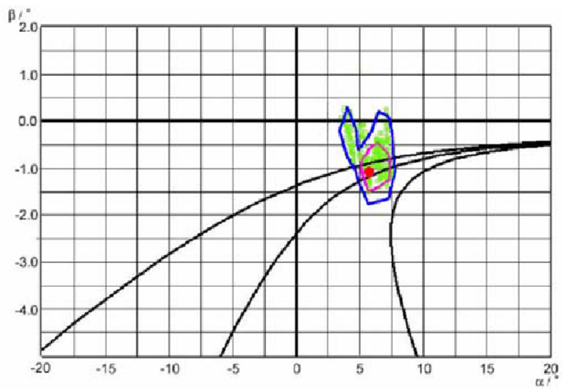

(d)

Figure 4.17 – Fixation areas (50 % area marked in blue, 90 % area marked in pink), and point of most gazes (red dot) as recorded (a) during the day and at night with (b) both headlamps fixed, (c) one headlamp swivelling, (d) both headlamps swivelling parallel [133].

Here the fixation areas are shown for 4.17a during the day, 4.17b with both headlamps fixed, 4.17c one headlamp swivelling, 4.17d both headlamps swivelling parallel. The red dots marks the point with the highest amount of fixations, the blue line marks the 90 % iso-line and the pink line marks the 50 % area of fixations and all registered fixation points are shown in green circles. The findings show, that with the AFS, the fixations are more concentrated than during the day, which is explained by Shibata by the limited and more concentrated amount of light that is available in the areas where it is most needed. Furthermore, the data shows, that curves can be divided into three sections: entering a curve, the curve itself and exiting the curve and all three of the curve segments can be correlated with the gaze behaviour. [133]

Schulz uses a commercially available eye tracking system in combination with a scene camera to measure driver's gaze behaviour and their orientation points when driving on country roads. While this research does not involve nighttime driving, the goal was to measure the gaze distribution in dependence of the available viewing distance to optimize street renewal and to allow drivers a comfortable driving experience with a high safety impression. The experiment was divided in three sections. In the first section, the participants were only asked to follow a given circuit in real life traffic with no further instructions. The gaze behaviour was measured to estimate the required information for the drivers to navigate the test vehicle. For the second part of the study, a secondary task was introduced to the vehicle to verify, if the driver feels the need to focus more on the road in situations, where the viewing distance is limited. The third part was set in a driving simulator in which the same road geometry as for the first two test parts was remodelled. In different situations, with different the viewing distance was limited, different objects (potential hazards) were added at random. The findings of Schulz show, that for viewing distances under 200 m an increased concentration and attention onto the road is needed. This increases with decreasing viewing distance and cannot be explained by any other type of road geometry. With viewing distances of below 150 m the driver's gaze is focused nearly completely onto the road and for viewing distances even lower, an increase in breaking manoeuvres (even on straight roads) is recorded. The conclusion therefore is, that limited viewing distances lead to unsure driving behaviour and require a higher level of concentration and attention. [134]

A completely different goal for using eye tracking in a real life driving scenario is presented by Winter who uses the gaze cumulation of drivers in complex situations in combination with static luminance recordings to calculate the adaptation luminance in inner city driving therefore taking the approach presented by Heynderickx and applying it in a real driving situation [135]. Similar to the work presented by Mourant, the data is also analysed for differences in the experience of the drivers. The evaluated data was recorded in a different study with a head mounted eye tracking system in which 24 subjects drove on road in Berlin, Germany. The difference in experienced drivers and inexperienced drivers is set at 10 000 km of total driving experience. The luminance recordings are taken in the same roads as the driving test was performed from the inside of a car to ensure the effect of the windscreen is taken into account. The results in terms of orientation behaviour match the results previously found, in a way, that experienced drivers tend to use a significantly wider area that is located further up to orientate themselves in given road situations. This is visualized in figure 4.18 where on the left side, the cumulative gaze for and inexperienced driver is shown, the middle shows the much wider gaze distribution for an experienced driver and the image on the right shows the gaze distribution over all test subjects.

Figure 4.18 – Differences in cummulative gaze vectors between an experienced driver (left) and inexperienced driver (middle) and cummalitve over all participants (right) [136].

The data presented shows, that the most primitive shape to describe the gaze is an 2°/10° ellipse. No further assesment regarding the adaptation luminance is made due to the large scattering of the eye tracking data. [136]
In a similar work, Winter analyses the difference in gaze behaviour for main roads and residential areas in Berlin. His findings show, that for the main road, the gaze behaviour can be described by a circular shape while for residential areas, an ellipsoid is more accurate. This also shows, that between these two road types, the vertical orientation does not differ significantly, while the horizontal orientation does. [137]

Obviously, this does not include all the research that has been done in terms of eye tracking or gaze behaviour in while driving. However, listing all available publications and shortly summarizing them would easily be enough to fill another complete book. Therefore, the interested reader is referred to the original publications on the topics general eye tracking in automotive use: [138, 139], gaze distribution on motorways [140], orientation in curve driving [141–144], adaptation luminance in dependence of gaze behaviour [145] but the presented selection of research on eye tracking should showcase the different topics that can be tackled using eye tracking.

One very important fact that arises when comparing the different findings from previous research is, that there are areas where all previous studies come to the same conclusion. This is for example the case for the dependence of the orientation behaviour between experienced and inexperienced drivers or the general orientation behaviour when driving through curves. Other very basic findings, the difference between day- and night-time driving however, lead to different results depending on which research one reads. While Brückmann and Damasky found a wider gaze distribution during the day, Diem recorded the exact opposite.

Another remark is, that many of the presented studies were performed by a very limited amount of test subjects ranging from 3 subjects (Stahl), 4 subjects (Cengiz), 6 subjects (Shibata), 12 subjects (Winter), 20 subjects Schulz, to a maximum of 23 subjects (Winter), since eye tracking studies involve a time consuming calibration and (at least used to) include an even more time consuming evaluation of the generated data. However, due to the large variance shown in all data sets, it is inevitable, that a large number of subjects participates in eye tracking studies for statistical relevance.

The conclusion from the presented available data is, that due to the new and improved technology available for todays eye tracking systems, new data sets should be recorded and evaluated to today's standards to compare them to the findings presented here. This is not only necessary due to the new technology in terms of eye tracking but new and improved headlamp technology as well. Furthermore, the traffic space in general has changed over the last couple of years with a much higher traffic density a lot more traffic happening in urban areas.

4.3.3 Pupil dilation under different lighting conditions

As mentioned in chapter 5.4, one of the metrics required for calculating the gaze direction is the pupil diameter. While the pupil diameter itself correlates to the light at the eye as already described by Darwin in 1872, the pupil regulates the amount of light on the retina to avoid overexposure, the exact pupil diameter is dependent on many factors. A general overview of different studies regarding the pupil size under different lighting conditions is collected by Watson, comparing the data found by Holladay [146], Crawford [147], Moon and Spencer [148], De Groot and Gebhard [149], Stanley and Davies [150], Barten [151], Blackie and Howland [152] and Winn, Whitaker, Elliott and Phillips [43] combining all mentioned data sets and formulas to deliver one overall pupil size calulation. This review shows, that large differences between the measurements, the reviewed factors, such as age, adapting field, monocular vs. binocular viewing are apparent. In general, the pupil diameter is measured to be between 2.0 mm to 8.0 mm. The different calculated pupil diameters are shown in figure 4.19a for binocular viewing with a 60° adaptation field and in 4.19b for monocular viewing with a 10° adaptation field. The data has been modified to fit to the given parameters.

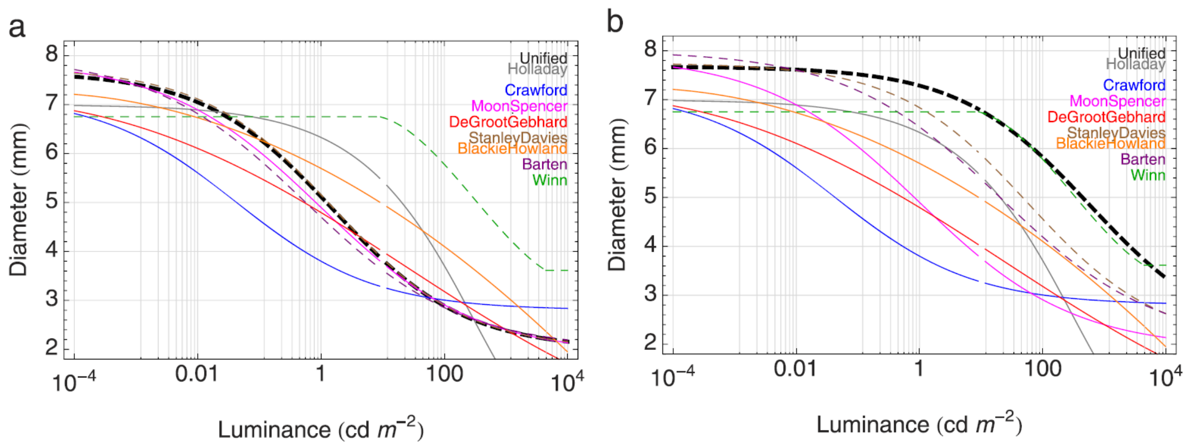

(a) (b)

Figure 4.19 – Summarized pupil diameter over the adaptation luminance for (a) binocular viewing with a 60° adaptation field and (b) monocular viewing with a 10° adaptation field for the unified pupil diameter by WATSON [153].

The data shows large differences in all regions starting from the highest pupil diameter ranging from 6.8 mm (WINN, CRAWFORD and DE GROOT AND GEBHARD) to 7.8 mm (WATSON, BARTEN and MOON AND SPENCER) over the general behaviour in the intermediate range to the smallest calculated pupil size that ranges from 3.6 mm by WINN down to less than 2.0 mm (HOLLADAY, DE GROOT AND GEBHARD, BACKIE AND HOWLAND). The interested reader can refer to either to the summary of WATSON ([153]) or to the original publications as mentioned previously.

While the presented thesis analyses the measured pupil diameter during real life driving tests and correlates the pupil diameter with the recorded photometric value, the illuminance, a significant portion of this work is dedicated to the estimatimation of the discomfort glare by measuring the pupil contraction as a result of short illuminance pulses. However, first studies regarding the correlation between the psychological glare and the measured pupil diameter show, that the pupil diameter does not correlate with the psychological glare, but that the main correlating value is indeed the illumination and the size of the glare source [154].

However, newer research indicates, that due to the correlation between the illuminance of a glare source and the discomfort glare as well as the obvious relation between the illuminance and the pupil diameter, a correlation between the pupil diameter and the discomfort glare exists.

FRY found a correlation between the BCD values and pupillary movement for different photometric values [78]. However, since the research of FRY requires very controlled environment parameters with no other light intereference to measure the exact pupil movement in correlation with the light source.
Similar results are found by OHBA who investigated the pupil adaptation to light flashes [155]. In this study, a 50 W HID light source was used to produce glare pulses. His findings show a very good correlation for the change in pupil diameter in relation to the flash intensity in dependence of the background luminance. It can also be shown, that for intermediate flashes, the pupil diameter contraction is nearly linear to the flash intensity and only for very low

and very high intensities, this behaviour changes. The results for one investigated participant are shown in figure 4.20 where the change in pupil diameter is shown over the relative flash intensity, as the fraction of the brightest available flash, for different background luminances.

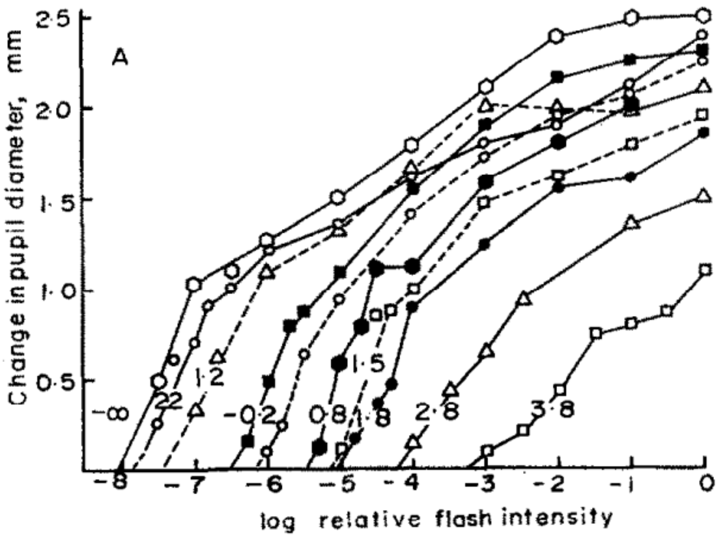

Figure 4.20 – Relative pupil size correlated with the relative flash intensity over different background luminances as measured by OHBA [155].

This shows, that depending on the background, and therefore the adaptation of the pupil, the absolute contraction of the pupil diameter decreases as well. The highest adaptation luminance, indicated by squares, show the least pupil movement, while the lowest background luminance, indicated by circles, show the largest movement in the pupil diameter. Furthermore, the data shows, that for an increase in flash intensity, the change in the pupil size always increases. However, no information is provided on the absolute flash intensity or the flash duration.

LIN took the approach one step further and measured both, the eye movement and the pupil diameter in correlation to glare pulses [85]. The setup for this test consists of a dimmable ambient light source (8000 K) at the ceiling and the glare source (3300 K and 5700 K) located 10° above the fixation angle. The ambient light was set to values of 0.0 lx, 10 lx and 200 lx vertically and the glare source was set to 20 lx, 50 lx, 125 lx and 300 lx at the test subjects eye. The horizontal viewing angle was additionally varied between 2°, 4°, 8° and 16°. The glare source was switched on for a duration of 3.0 s and during this time, both eye movement and pupillary reaction were recorded. The results show correlations for both variables but since the eye movement was only tracked using EOG and thereby mainly delivers if there is movement. Therefore, no definitive answer about the movement is given by LIN and only the findings for the pupil diameter are discussed. Findings regarding the DE BOER rating correlating with the illuminance or the background luminance are consistent to the findings presented before and will also not be discussed further here. While LIN does not provide any data on the measured pupil diameter over the given illuminance, the findings regarding the correlation between the relative pupil diameter and the glare rating on the DE BOER scale is shown in figure 4.21.

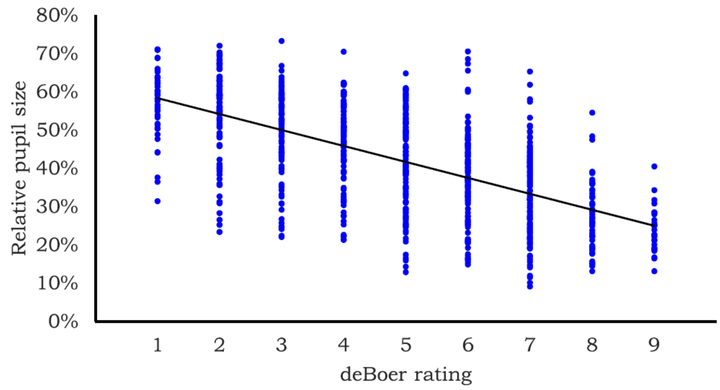

Figure 4.21 – Relative pupil size correlated with the discomfort glare for 3 s glare pulses according to LIN. 9 on the DE BOER scale indicates a rating of *unnoticable*, therefore no glare, and a rating of 1 indicates an *unbearable* glare rating. [85].

A rating of 9 on the DE BOER scale indicates, that the glare pulse is rated as *unnoticable*, and the pupil diamater stayes at around 60 %. A rating of 1 indicates an *unbearable* glare rating and the pupil contracts fown to an average of 30 % of the original diameter. While the data shows, that a general trend is visibile and a statistical correlation is found ($R^2 = 0.37$) the data also shows, that there is a significant amount of scattering and uncertainty involved when measuring the pupil diameter. [85]

However, the pupil diameter is not only influenced by the incoming light but different psychological factors further influence the diameter as well. PALINKO for example uses the pupil diameter during a driving simulator test, to estimate the cognitive load [156]. To do this however, the lighting conditions need to be kept constant. Since this is not possible for real life driving tests, calculating the stress of the driver is not done in the presented thesis and the emphasis is put on the pupillary reaction to a change in lighting conditions.

4.4 ANALYSIS OF MODERN TRAFFIC SPACE

As mentioned before, the main goal of this thesis is to propose new light distributions for different traffic situations, which means, different traffic situations have to be identified. For this reason, the German traffic space is analysed in this thesis in two ways. The general traffic distribution is simulated using available statistical data of German traffic and using image recognition and a stereo camera system, the real traffic space is analysed. This section shows similar work regarding the analysis of traffic and traffic space. A complete analysis of different traffic spaces is scarcely found. Only the work of DAMASKY provides a complete overview over a more complex amount of parameters.

The only major work regarding the analysis of real life traffic is found by DAMASKY and DIEM [157, 158]. For a route of over 5500 km video data was analysed regarding the position of different objects such as traffic lights or street signs, as well as road geometry like lane width, curve radii and the position of oncoming and preceding traffic. This analysis generated a database containing more than 20 000 objects out of which distributions were generated for different road types. Since the results of this work contain an enormous amount of data, only selected results can be presented here and the interested reader is referred to the original publications. A summary of this findings is shown in figure 4.22 where the areas, in which 90 % of all objects are located in at a distance of 100 m on country roads are depicted. The white area shows the position of the eyes of oncoming drivers, the light grey area shows traffic signs on the right-hand side and the darker grey areas indicate the delineators on both sides. Black areas show the overlap of two or more object distributions.

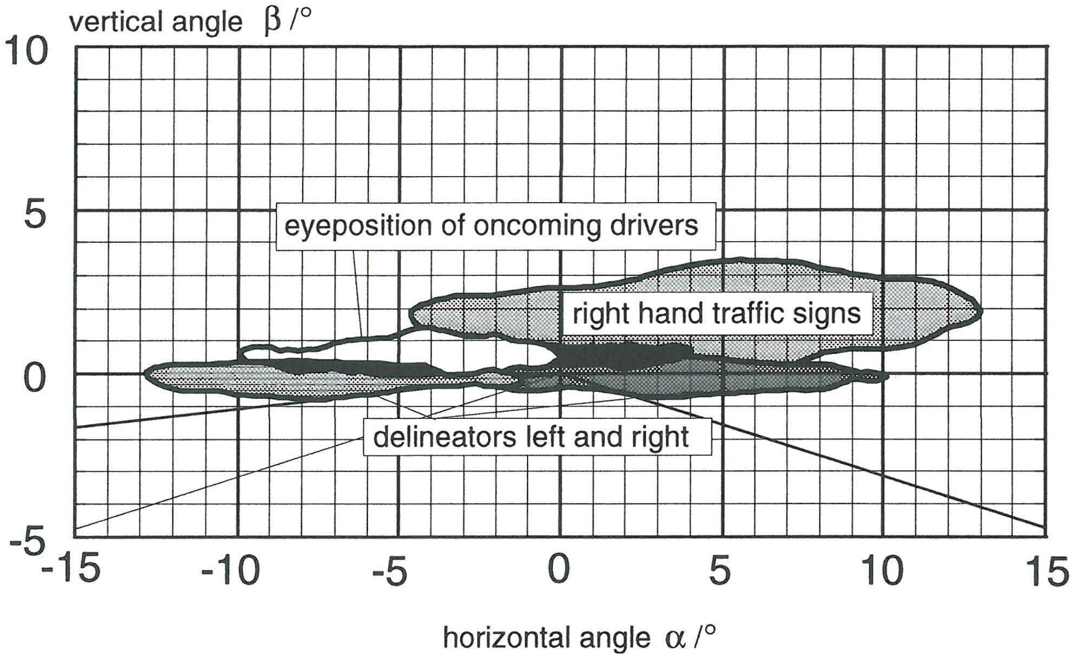

Figure 4.22 – 90 % object areas on country roads in a distance of 100 m for oncoming traffic (white), traffic signs on the right-hand side (light grey) and delineators on both road sides (dark grey) [157].

Similar evaluation of the data is shown for road geometry like curves and road width and his findings are not confined to country roads but are listed for motorways and urban roads as well. From this object distribution data, different headlamp distributions for different traffic situations are derived. These are discussed in the following section, where light distribution optimizations are summarized. [1, 157, 158]
Additionally, to this work, the work of Schwab and Kuhl are of interest, since they investigated the frequency of different geometries on German roads [159, 160]. Kuhl investigated the optimization of dynamic low beam pitch angles for roads with vertical curvature (domes and valleys). To do this, a total of 6500 km where driven through Germany and a small percentage through Austria. Figure 4.23 shows the driven route through Germany and the Austrian Alps. The parts driven on motorways are marked in black and the parts driven on country roads are shown in dark grey. Cities that are on the path are used for the data acquisition as well.

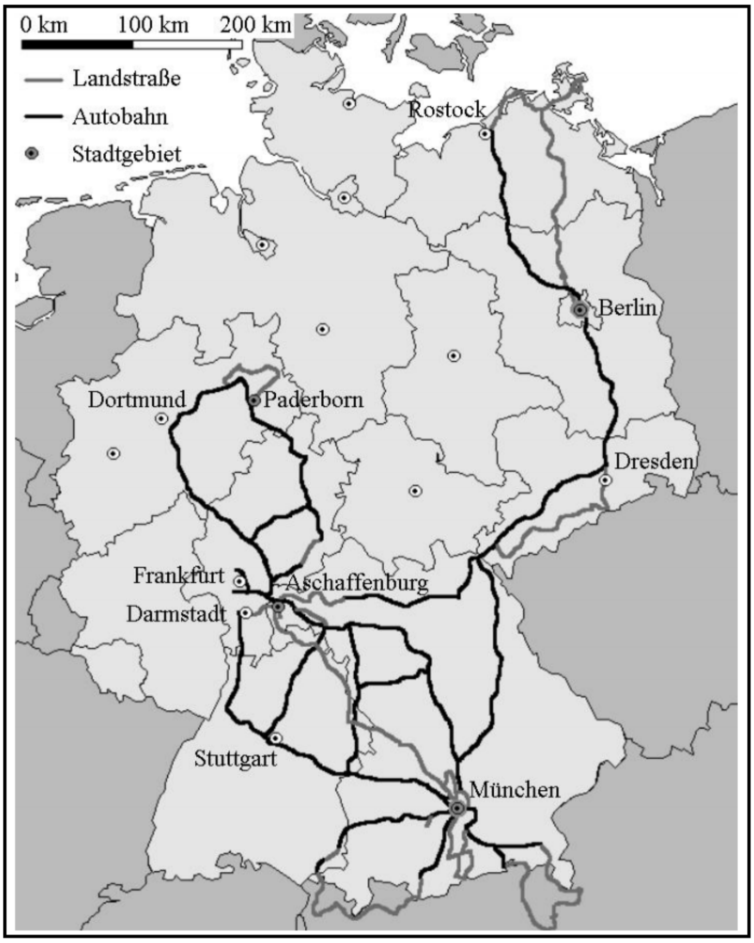

Figure 4.23 – Driven route by Kuhl to analyse the vertical curvature for different road geometries [160].

Figure 4.24a shows, that the vertical curvature is different for the three major road types, urban roads (black), country roads (grey) and motorways (light grey). Figure 4.24b now shows, the data for country roads split up in more detail for sub-country road road types, showing that even in one of these major road types (country roads) different road categories show different behaviour in terms of vertical road geometry. The data presented by Kuhl additionally shows, that there even significant differences between single cities. Obvious differences arise between flat sections of Germany and hillier or even alpine sections. Since this data is directly used for the simulation of the traffic space in chapter 5.2 the data is described in further detail in later chapter.

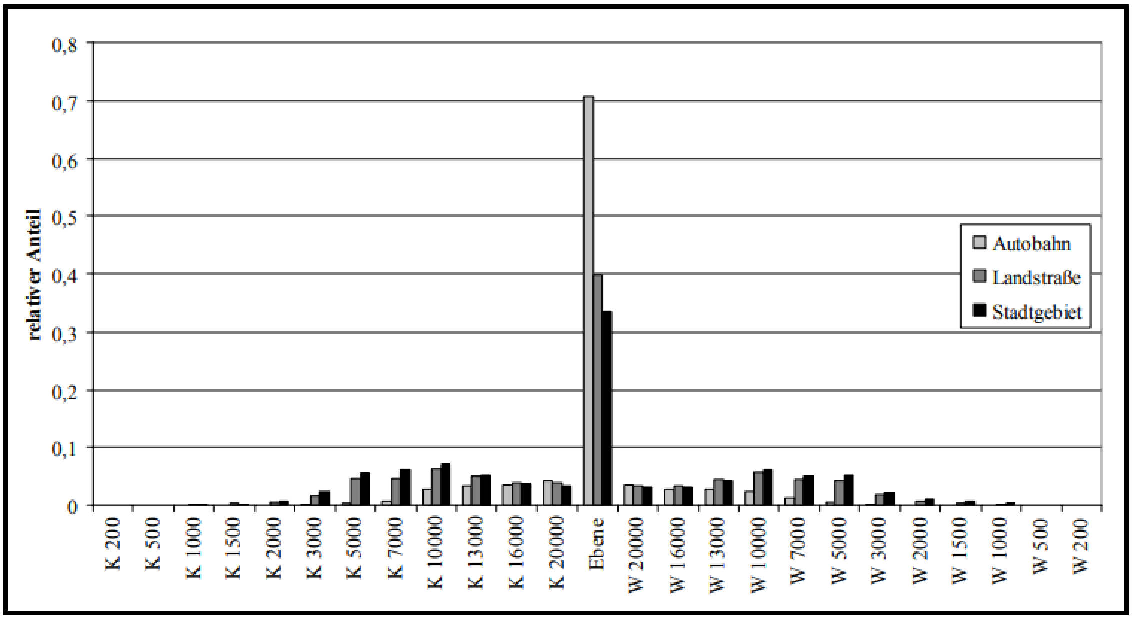

(a)

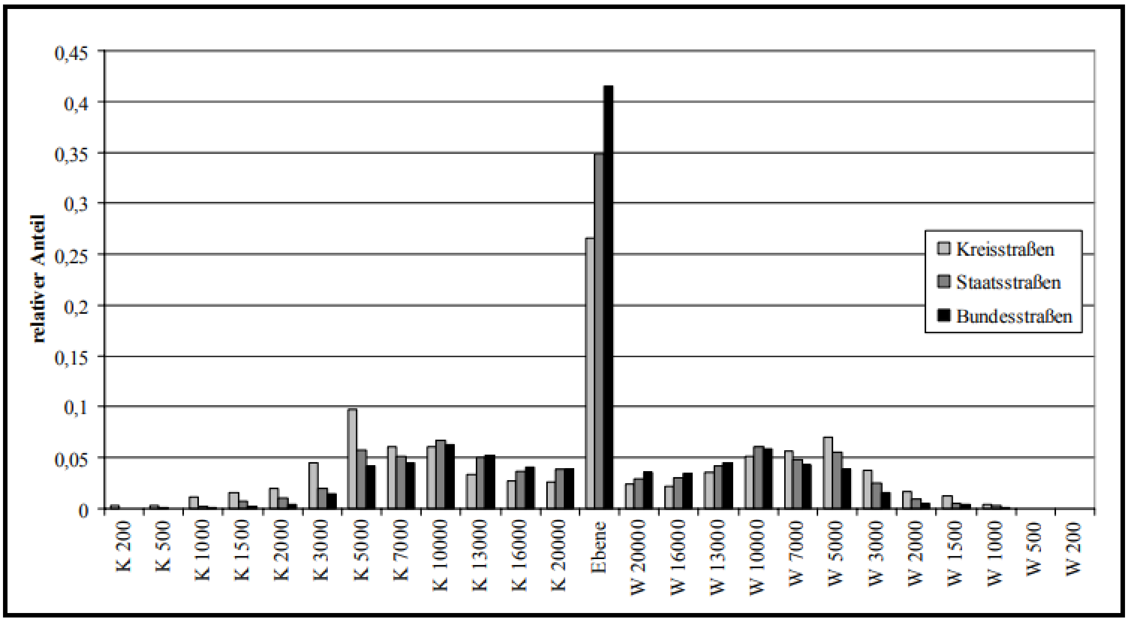

(b)

Figure 4.24 – (a) shows different curvature distributions over urban roads (black), country roads (grey) and motorways (light grey). (b) visualizes the differences on country roads by different sub-country road types. [160]

Another very important work regarding traffic space analysis is the work done by Totzauer, who, based on suggestions by Moisel [161], set up a simulation, with the goal to optimize segments for gfHB systems based on traffic densities on country roads. While the segment optimization will be discussed in the next section, the traffic space simulation and analysis is reviewed here in great detail since the simulation part in this thesis is based on similar assumptions and follows a similar goal. The basics of this thesis includes data from Damasky, Schwab and Kuhl as described above. Using this data, a random stretch of 50 km length is randomly stitched together to form a statistically relevant road segment. The simulated road segment was limited to the 50 km to limit the amount of required computing power. Based on traffic density data by the German government, random vehicles with a length of 20 m, a height of 3 m and an average density of 444 vehicles per hour are placed on this stretch of road. Then the measurement vehicle is moved with a velocity of $100\,\mathrm{km\,h^{-1}}$ in steps of 1 m. Objects within a distance of 500 m are detected. Then all object locations are summed up and a traffic density is calculated over the complete segment. This is shown in figure 4.25a where the absolute amount of vehicles under each angle is shown for the high beam area of $\pm 20°$ horizontally and from $-0.6°$ to $5°$ vertically. The asymmetric distribution is achieved due to the right-hand traffic on a single lane country road. Since the goal of his work is to calculate optimized segment distributions, the traffic density is additively mirrored as shown in figure 4.25b.

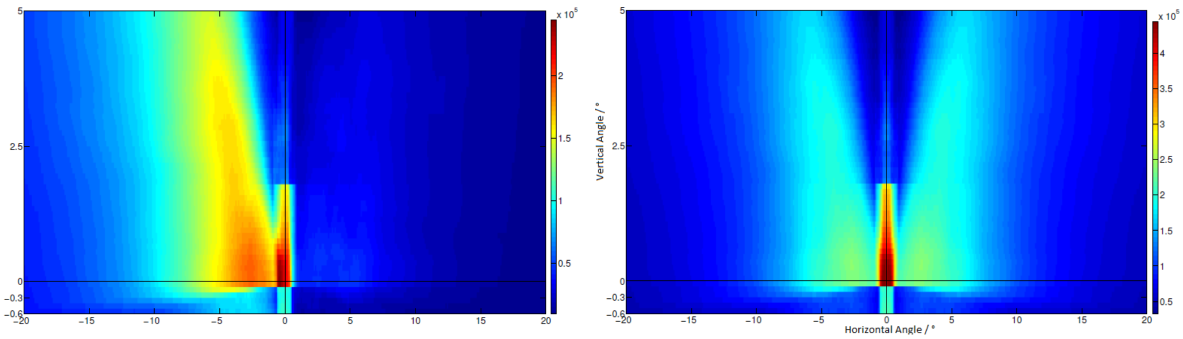

(a) (b)

Figure 4.25 – (a) shows the simulated traffic density with the absolute amount of vehicles detected under each angle. To achieve a symmetric traffic distribution, the original density is additively mirrored as shown in (b). [162]

As expected, the data shows the highest traffic density right in the centre and decreasing to the outside. This is due to the lowest relative angle velocity for traffic further away. Traffic that passes the simulated vehicle has a very high angular velocity and is thereby passed within a few frames. Thereby the recorded traffic density is low under large horizontal angles. The further proceedings with this traffic distribution is described in the next section. [162]

4.5 OPTIMIZATION OF LIGHT DISTRIBUTIONS

The optimization of light distributions for automotive use is not a new topic. Since the first headlamps were used, research was performed to deliver the best possible light distribution for drivers. This section is dedicated to the latest research on the optimization of headlamp light distributions to show, where further improvement might be needed or is possible due to the newly introduced technologies available for headlamp manufacturers.

As already shown in the previous section, Damasky acquired different object distributions by driving and analysing 5500 km throughout Germany. The data, shown in figure 4.22 for country roads, is then used in combination with other measurements to optimized low beam light distributions for given situations. Exemplary, his proposed distributions for country road driving are shown in figure 4.26a and for "bad weather conditions", including rain and fog, in figure 4.26b. HDG marks the cut off line of the low beam. Table 4.2 summarizes all areas and the proposed illuminance values on the standard ECE measurement screen for the country road lighting and table 4.3 summarizes the proposed values for wet road surfaces.

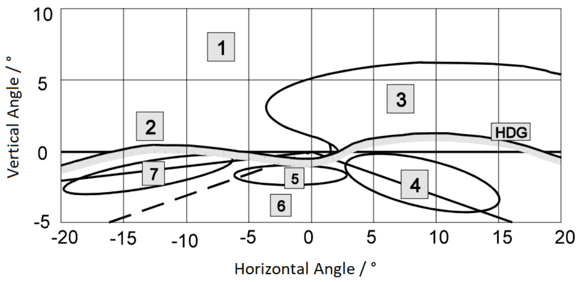

(a)

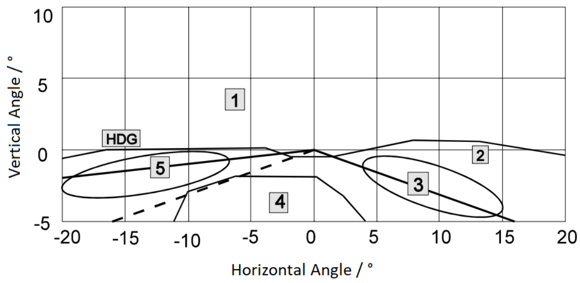

(b)

Figure 4.26 – (a) optimized country road light distribution with ECE conformidity based on the object loactions shown in figure 4.22 and (b) a light distribution for "bad weather conditions" based on asphalt reflectivity and object loacation by Damasky [163].

Table 4.2 – Suggested illuminance values for the light distribution on country roads as shown in figure 4.26a by Damasky [163].

AREA NUMBER	DESCRIPTION	PROPOSED ILLUMINANCE VALUE	
		Min.	Max
1	Overhead Road Signs	-	1.5 lx
2	Glare	0.5 lx	1.0 lx
3	Road Signs	-	2.5 lx
4	Apron Right Side	15 lx	-
5	Fixation Area	25 lx	50 lx
6	Apron Lighting	5 lx	15 lx
7	Apron Left Side	10 lx	-

Table 4.3 – Suggested illuminance values for the light distribution for "bad weather conditions" as shown in figure 4.26b byDamasky [163].

AREA NUMBER	DESCRIPTION	PROPOSED ILLUMINANCE VALUE	
		Min.	Max
1	Glare and Self-Glare	-	0.3 lx
2	Apron Lighting	5 lx	25 lx
3	Guidance Right	30 lx	-
4	Reflex Area	-	5 lx
5	Guidance Left	10 lx	-

The main guidelines given by Damasky are, that sufficient light is needed at the edges of the road, therefore leading to a rise in the cut-off line on the left side again. The main hotspot is located in the dead centre and there is a sufficient amount of light required to allow for optimal traffic sign illumination.
For "bad weather conditions" the emphasis is shifted towards not dazzling the oncoming traffic and the amount of light directly upfront of the vehicle is therefore significantly reduced. While none of the proposed distributions complied to the ECE regulations, his findings are incorporated in the newer regulations. [163]

A major part in the optimization of headlamp light distributions was contributed by Huhn, who analysed current issues regarding the current setup of HID headlamps in real life driving situations and developed an experimental setup, in which the low beam light distribution can be varied. In several driving tests, the safety impression of the drivers were evaluated for the different generated light distributions. The recommendations that come from this research can be divided into three major categories - 1) Adaptive apron lighting, 2) adaptive side illumination and 3) adaptive motorway lighting.
The influence of the intensity of the apron lighting is summarized as follows: For wet conditions, an increased intensity in the apron lighting increases glare for oncoming vehicles without benefit for the driver. For wet roads, the luminous intensity should therefore be reduced in case of an oncoming vehicle. In dry conditions an increase in this area increases the adaptation level of the driver and thereby decreases the glare sensitivity and Huhn therefore proposes an increase in the luminous intensity in the case of an oncoming vehicle for dry roads. Regarding the side illumination provided by low beam headlamps, good illumination of road guidance systems is regarded beneficial and reduces stress while single, high luminance objects such as delineators increase unnecessary gaze avertion and thereby increases stress for the driver. His suggestions therefore are to give a necessary illumination range to the sides that can be varied depending on the driven velocity with a decrease in illuminated width for higher velocities and for dry conditions. His proposition for this system is, that the width of the 1.0 lx iso-line is reduced linearly from 60° down to 20° in dry conditions when increasing the velocity from $0\,\mathrm{km\,h^{-1}}$ up to $100\,\mathrm{km\,h^{-1}}$. In wet conditions, the opening angle should be kept at 80° until a velocity of $50\,\mathrm{km\,h^{-1}}$ is reached. For higher velocities the angle should be reduced nearly linearly to 30° at $150\,\mathrm{km\,h^{-1}}$. For higher velocities, as driven on motorways, a dynamic increase in theoretical headlamp reach by increasing the pitch angle from $-1\,\%$ to $-0.5\,\%$ is recommended. The change in pitch angle should, according to Huhn be changed in dependence of positive or negative acceleration. Due to the increased need for luminous intensity, this is only recommended for HID based headlamps. [2]

As already described in the section above, Kuhl investigated the posibilities to optimize low beam light distributions on vertical changes in the road geometry on country roads and motorways. However, no change in the light distribution itself is proposed, but instead the current standard light distribution is used and the motor, that is already used for the headlamp leveling system in HID and now LED headlamps, is used to allow for a constant viewing distance on both, domes and valleys.[160]
This work will therefore not be discussed further.

As already shown in the section above, Totzauer used a traffic simulation to determine an average traffic distribution as seen from a headlamps position. This distribution is then used, to optimize high beam segments for a gfHB system. While this is not a direct optimization of the light distribution, the segment size for a gfHB does limit the possibilities of modifying the light distribution since each segment is (usually) set up by a single LED or at least by a certain number of LEDs that are controlled as a single unit. The hypothesis for this is, that areas with high traffic density need a higher resolution in order to maximize the usage of the high beam system and to be able to follow the low angular velocities recorded in the centre areas. This segment optimization is done with several concepts and degrees of freedom. These approaches can be divided into semi-flexible segment distribution and fully flexible segment distribution. The general approach is the same for both setting - the goal is to achieve high efficiency of the gfHB system and therefore use the smallest segments possible in the areas with the highest traffic density. This is done by starting with a minimal segment size (defined as 0.3°x0.3°), that is set at the point of the highest traffic density. From this starting sector, a new sector is set to the side with the highest traffic density. Its area is set to the minimal segment size and then enlarged until the traffic density of the new sector is at the same size as the average traffic density of the existing sectors minus a given tolerance. Using this approach, segments at areas with low traffic densities are automatically larger than the areas in the centre. This is shown in figure 4.27 for a gfHB with 111 segments.

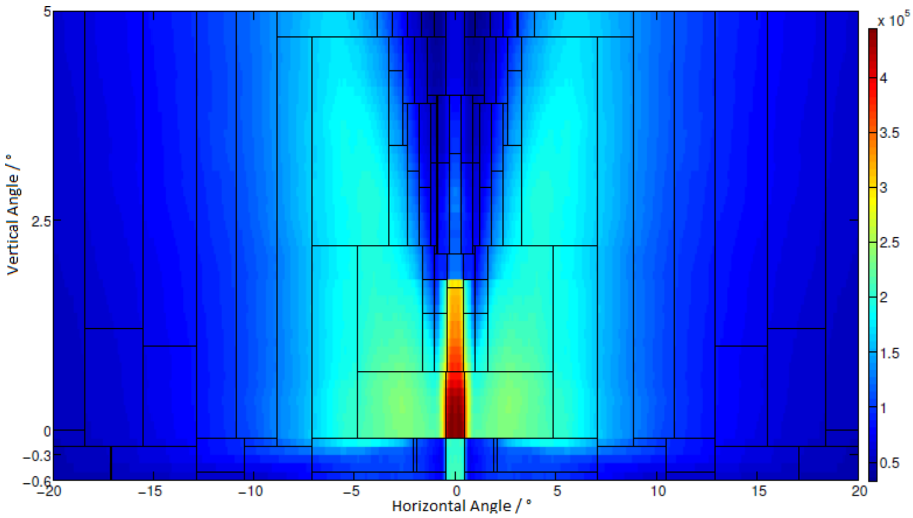

Figure 4.27 – Fully flexible optimization of the gfHB segments with 111 segements based on traffic simulations of country roads by Totzauer [162].

The second approach sets row heights for the given number of rows and then allows for flexible segment widths as shown in figure 4.28 for the same 111 segments. Here the area below and the area above the horizon are both divided in two rows each.

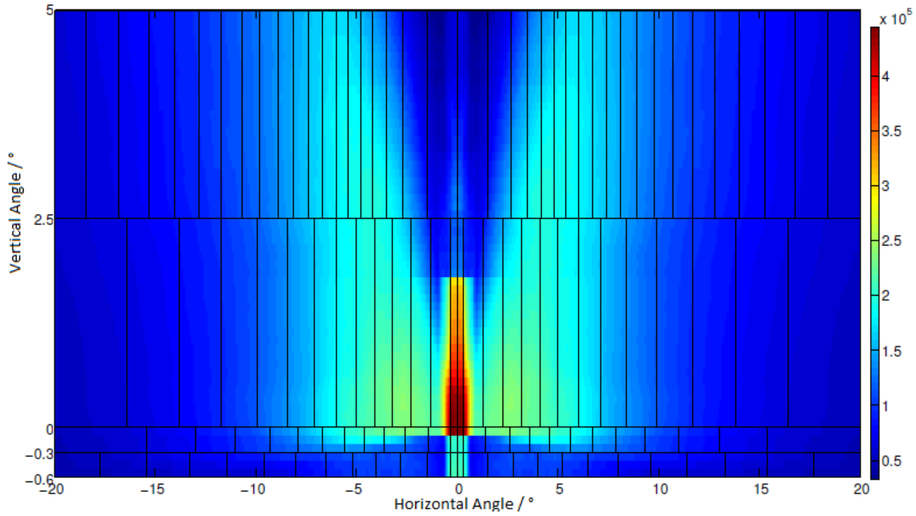

Figure 4.28 – Partially flexible optimization of the gfHB segments with 111 segements based on traffic simulations of country roads by Totzauer [162].

To evaluate the new segment distributions, their efficiency is tested by calculating the luminous flux of the activated areas divided by the total luminous flux of the complete headlamp. This needs to be done since the optimization was performed on the mirrored density distribution and therefore, the optimized distribution might not necessarily lead to better results than the conventional distribution. This calculation is done for a large set of possible combinations, both fully flexible and partially fixed. The findings show a clear increase in efficiency with an increased amount of segments, however the increase is smaller than expected with the lowest efficiency calculated for a total of 30 segments being 87.7 % and the highest efficiency being 92.0 % for 117 segments. Furthermore, nearly no difference is found between fully fixed and partially fixed distributions. [162]

4.6 RESEARCH HYPOTHESES

The overview over the previous research shows, that while a lot of research has been done in numerous single aspects of headlamps, the research has always been focused on single or at least a low number of influencing factors. Furthermore, a lot of the work focused on tungsten halogen or HID headlamps and bases on outdated technology. With the recent development in camera and computing technology as well as the introduction of gfHB-LED headlamps, and the changing traffic space with significantly higher traffic density, it is concluded, that several studies have to be conducted in order to receive up to date data. The main research in this field, conducted by Damasky, has been done in 1992 and 1994, directly after the reunion of the Federal Republic of Germany. Since then, the road network and the overall infrastructure, espeacially in the former DDR have been expanded and renewed. To summarize the issues arising from the research presented, several research questions arise.

- What influence can be found on detection by varying the light in the low beam area?
- What influence can be found on detection by varying the light in the high beam area?
- Are the current ECE regulations sufficient for night time driving?
- What luminous intensity is to be recommended for night time driving in general?
- Where do objects appear in nighttime traffic?
- Where do drivers look at when nighttime driving?
- How can headlamps be optimized in order to illuminate objects in night time driving?
- How can gfHB headlamps be optimized in order to maximize road illumination?

The following chapters will describe laboratory and field studies that aim at answering those questions.

Part V

ANALYSIS AND OPTIMIZATION OF LIGHT DISTRIBUTIONS

5

ANALYSIS AND OPTIMIZATION OF LIGHT DISTRIBUTIONS

When designing automotive headlamps, the main goal is, to ensure safe driving at night. The easiest way to do so, would be to get as much light as possible and illuminate the streets as bright and as homogeneous as possible. But since drivers are rarely alone on European roads and energy management and efficency play significant roles today, auxillary conditions have to be fulfilled. Other traffic participants, like oncoming or preceding traffic should not be dazzled at all and the headlamps should not exceed a certain amount of power draw to minimize CO_2 Emissions. As explained in Chapter 3, the lighting industry has moved forward in improving the driver's vision at night by implementing new light sources, developing and designing new headlamps, new light distributions and especially new lighting functions. However, these new lighting functions and light distributions are always based on single traffic situations or limited by governmental regulations. But since the traffic space and thereby the lighting conditions during night have changed since these regulations were set in place, and night drives consist of much more than a number of discrete traffic situations, the main goal of this thesis is to analyse German traffic space, driver's behaviour and the influence of different light distributions in both, driving and passing beam.

The first step taken, is the analysis of the influence of different luminous intensity values in both passing and driving beam on detection distance for drivers in a controlled environment.
The second part of this chapter addresses the main study for this thesis, the analysis of German traffic space, and the driver's gaze behaviour during different situations, including different lighting conditions, traffic situations and road geometry. This part is split into several larger sections starting with a simulation of German traffic space, then stepping over to the analysis of real German traffic space with monitoring driver's gaze behaviour and the investigation of different traffic situations. The obtained data is used to derive optimized light distributions for both efficiency of the system and for driver's field of view.

As explained in the chapter 3, the current light distribution for automotive headlights is setup by two separate parts - the low beam, illuminating the immediate foreground of the car and avoiding glare for other traffic participants during encounters, and the high beam, basically ignoring other traffic participants and maximizing the visibility distance in situations with no other traffic participants. The next two sections will investigate the influence of different intensities for both parts.

5.1 INVESTIGATION OF DETECTION DISTANCES UNDER VARYING LIGHT CONDITIONS

The main goal of headlamps should always be safe nighttime driving for all situations. To achieve this goal, it is necessary for the drivers to be able to detect possible obstacles or other traffic participants as far ahead as possible in different situations. This section is dedicated to finding the influence of various parameters in current light distributions on these detection distances in real life driving tests. For this reason, this section is divided in three parts. In the first part, the influence of the low beam intensity on detection distances is investigated.

The second part focuses on finding the correlation between detection distance and high beam intensity. While these two parts focus on detection of objects straight ahead, in the third part, the influence on the angular position of the detection objects on the detection distance.

5.1.1 IMPACT OF VARIABLE LUMINOUS INTENSITY IN THE LOW BEAM SECTION

To investigate the influence of the maximum intensity for the low beam section of the light distribution, a test is performed, in which the detection distances for different low beam settings are recorded.

TEST SETUP

The test is performed at the *August Euler* airfield in Griesheim, Darmstadt. The airfield offers the opportunity to set up real life driving tests on a 1.2 km straight road in a controlled environment with similar conditions on each test day and no unwanted traffic or light sources. The testing area is shown as an OpenStreetMap (OSM) image in figure 5.1. The main straight, the southern part of the airfield, is the 1.2 km straight on which the test is performed.

Figure 5.1 – Testing Area on the *August Euler* Airstrip as an OSM image.

Since current state-of-the-art headlamps are mainly using LEDs as light sources, as described in chapter 3, this test will also be based on LED headlamps. Since the variation of the low beam intensity is only possible in a very limited way for different production cars, the headlamps in use, need to be modified. For this reason, the low beam LEDs need to be addressed manually and can not be driven using the vehicles' headlamp control. Since the test vehicle is a OPEL INSIGNIA A, from 2008 (BUICK REGAL, VAUXHALL INSIGNIA), it is equipped with HID headlamps. These are replaced with AUDI A8 D4/H4 headlamps from 2009. The light distribution is shown in appendix B.1 in figure B.1. The main reason for choosing this headlamp set is, that the LEDs are addressable via the standard input pins. This is used to limit the maximum luminous intensity in the headlamp hotspot. Both headlamps are limited to 50 % for the reduced setting. This leads to 10 000 cd in the hot spot for each headlamp under 50 % and 21 000 cd in the normal setting for each headlamp.

To measure the resulting detection distance for both settings, two human like test dummies, similar in shape and colour to the ones used in the studies shown in chapter 4, are placed at both sides of the road. These dummies are coated in a matte grey paint with a reflectance of $\rho = 5\,\%$ to simulate dark clothing and therefore a worst case scenario. Measuring their reflctance also shows, that they are nearly perfectly lambertian. x1They are motorized and can be erected automatically in a randomized order with the auxiliary condition, of at least three test runs per setting, where the dummy on the right side is erect. The randomized order for both sides is used to avoid, accustoming of the participants and thereby increasing the detection distance for each run. Both test vehicle and detection dummies are equipped with General Positioning System (GPS). This setup allows for synchronization between the vehicle and the dummies positions through the time stamps. The time of detection is then recorded, by the press of a *detection button* and the resulting detection distance can be measured.

TEST PROCESS

The detection dummies are located around 500 m behind the starting point of the run way and 1 m besides the road markings. The setup is schematically shown in figure 5.2 where the starting position is shown as a red circle on the bottom left, the end position is marked by the red circle at the right side, the test dummies are shown the middle and test area is marked in red. The drivers are asked to drive the straight line with a velocity of $50\,\mathrm{km\,h^{-1}}$ using cruise control. The cruise control is pre-set by the test coordinator and the test subjects only accelerate to about $45\,\mathrm{km\,h^{-1}}$ and then reactivate the cruise control which will accelerate up to the pre-set of $50\,\mathrm{km\,h^{-1}}$. The rest of the course, marked by the grey arrows, the participants are allowed to drive according to their personal preferences since no data is recorded at those positions.

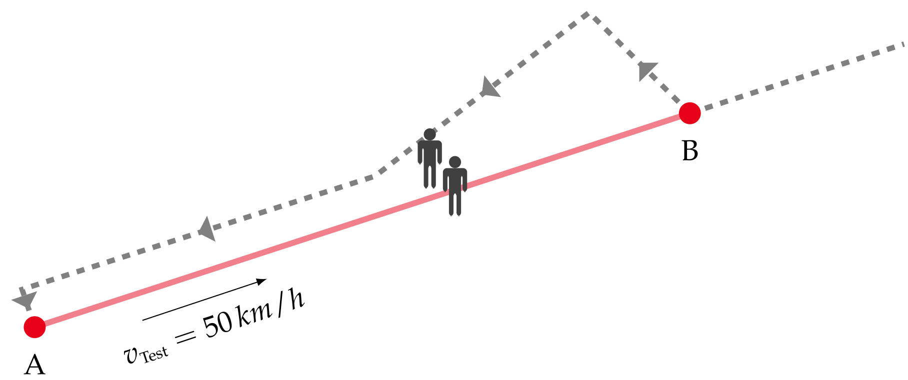

Figure 5.2 – Schematic setup for the test on the influence of luminous intensity in the low beam area. The grey human like figures indicate the possible positions of the detection dummies. The red circles mark the start end the end of the test section.

To enable a proper adaptation time for each setting, the light distribution is changed at the end point. This leads to about 2 min time for adaptation to the new brightness setting, depending on the driven speed of the participant in this area, but is never below 1.5 min. During the complete test, the test coordinator is seated on the co-drivers seat to instruct the participant and control the electronic recording of the GPS data and the correct recording of the detection times. Before the actual test runs start, each participant takes 5 runs to get accustomed to the vehicle and the course. This test set-up is also chosen to further investigate the influence of oncoming traffic and wet road surfaces on glare. Therefore, an additional vehicle

is placed on the testing area. For both vehicles the intensity in the low beam is then varied. However, since this thesis only focuses on the influence of different light distributions for the driver, all test drives done with the additional glare vehicle and the wet road surface are not discussed here. Furthermore, the data with dummies on the left side (from the driver's view) are not evaluated since the recorded data for this setting is not sufficient since the main emphasis is set upon the detection of objects closest to the driven vehicle.
19 test subjects participated at the test, all participants are either students or follow an office job. The subjects were asked to imagine a night drive on country roads, but not further introduced to the goal of the study. The mean age of the test subjects is 28 years and the complete information on all participants can be found in figure B.2 and in table B.1 in appendix B.1.
To determine the exact influence of the low beam intensity on the detection distances, luminance pictures are recorded for all light distributions in 10 m intervals starting at 100 m. As already described in chapter 2.3 these luminance recordings need to be done stationary since integration times of up to 10 s are needed due to the low surrounding luminance at the *August Euler* Airstrip. Therefore, it is important, that the lighting functions and settings are available during complete still stand. The results of these luminance recordings are summarized with the results from the following two studies in section 5.1.4.

DETECTION DISTANCES WITH VARIABLE LOW BEAM INTENSITY

The raw detection distances for both, the 50 % and the 100 % low beam settings are set into 5 m bins and the histogram data for the detection frequency is calculated for both data sets. This is shown in figure 5.3. Since the distance is calculated from the press of the button, the reaction time is already deducted from the data. With a reaction time of 500 ms, the raw detection distance would be increased by $\Delta d = 7\,\mathrm{m}$ when driving at $50\,\mathrm{km\,h^{-1}}$. This detection data shows, that the data sets are highly overlapping and a normal distribution is not necessarily given.

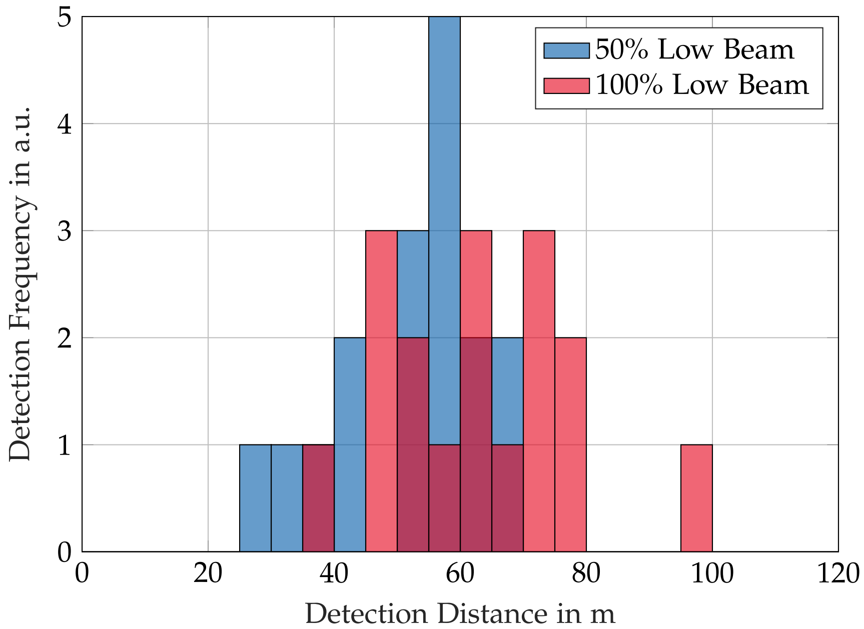

Figure 5.3 – Detection distances grouped into 5 m bins for the two low beam set ups. The dimmed 50 % low beam detection data is shown in blue, and the standard low beam (100 % is shown in red. The mean detection distances are calculated to be 52.6 m for the 50 % low beam and 62.8 m for the standard low beam.

However, normalizing the data according to equation 5.1, where x is the normalized data, d is the measured data set of the detection distances, μ is the mean detection distance for the light distribution and σ is the standard deviation for this data, this data can be tested for normal distribution using a ONE SAMPLE KOLMOGOROV-SMIRNOV.

$$x = (d - \mu)/\sigma \tag{5.1}$$

This test shows, that both data sets are indeed normal distributed, however while the 100 % low beam leads to a very good representation of a normal distribution with a $p = 0.98$, the 50 % low beam only leads to a distribution similar to a normal distribution with $p = 0.3$. The distribution form is visualized with Cumulated Distribution Function (CDF) plots in appendix B.1 figure B.3. With both data sets originating from normal distributions, the significance between the two data sets can be tested using the TWO SAMPLE KOLMOGOROV-SMIRNOV. This test shows, that the data sets from 50 % and the 100 % detection are indeed not from the same distribution. However, with $p = 0.08$, the 0.05 threshold for significant differences in data sets is only slightly crossed. This overlap of the data sets is visualized in figure 5.4 as box plots.

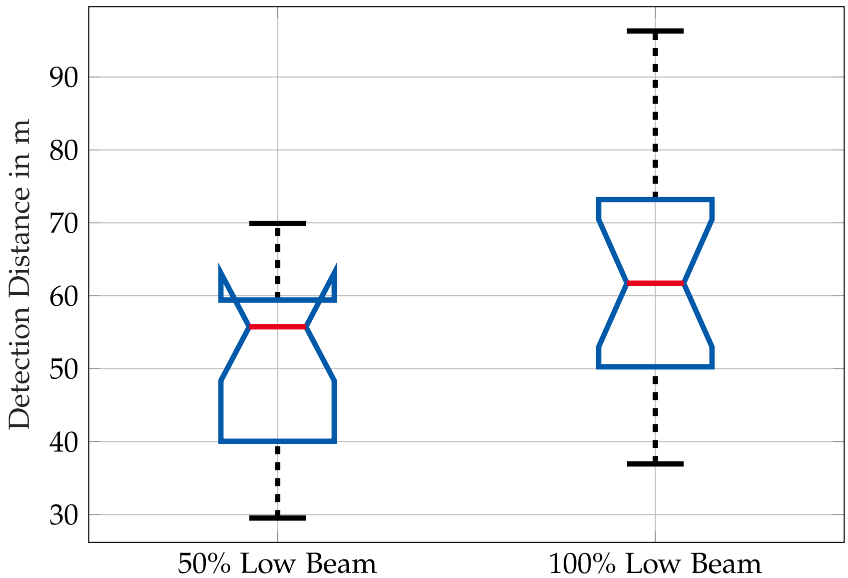

Figure 5.4 – Box Plots for 50 % low beam (left) and 100 % low beam intensity (right). The overlap of both data sets show, that $p = 0.08$ only slightly crosses the threshold for significant differences.

The mean detection distances for both distribution are measured at 52.6 m for the 50 % low beam and at 62.8 m for the standard low beam with 100 % of luminous intensity. This leads to a difference of 10.1 m or a reduction in detection distances by only 16.2 %, when decreasing the luminous intensity by half. The detection probability over the distance is shown in figure 5.5, where the probability to detect an object with 50 % low beam is shown by the blue line and the detection probability with fully activated low beam is indicated by the red line.

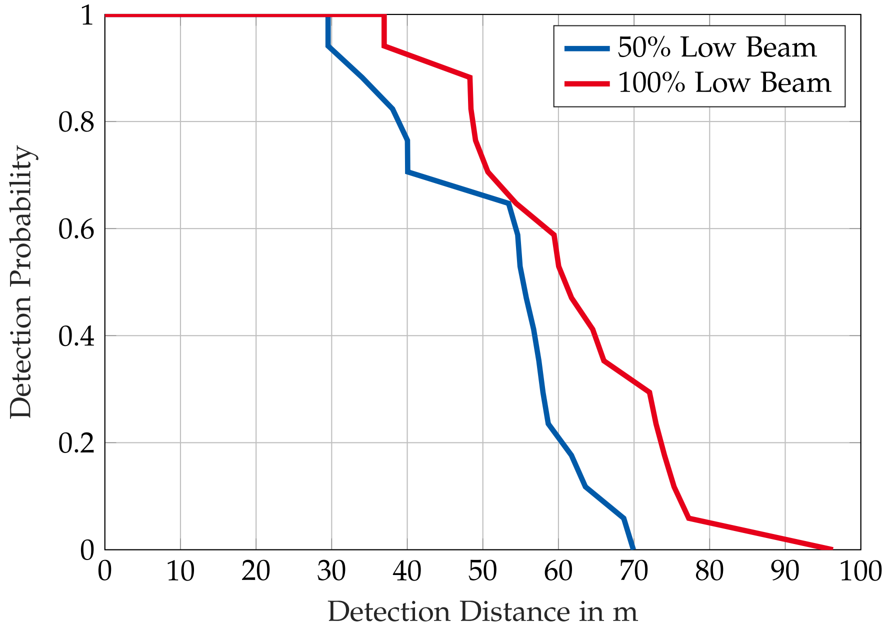

Figure 5.5 – Detection probability for 50 % low beam intensity (blue) and 100 % low beam intensity (red). The 50 % thresholds are recorded at 52.6 m for 50 % and at 62.8 m for 100 %. The 95 % threshold is measured at 29.5 m and 36.9 m respectively

.

In this figure, the 50 % probability marks the mean detection distance. Since 50 % detection probability means, that only half of the test subjects are able to detect an object at this distance, and half of the participants did not, the mean detection distance is not a good indicator for traffic safety. For this reason, additionally the 95 % probability distances are calculated, analogous to Adrian. This results in distances of 29.5 m for 50 % low beam and 36.9 m for the standard low beam, a difference of 7.4 m. The effect on traffic safety for this will be discussed later.

5.1.2 IMPACT OF VARIABLE LUMINOUS INTENSITY IN THE HIGH BEAM SECTION

In the next part, the influence of different high beam intensities on detection distances is investigated. Since modern headlamp development offers the opportunity of utilizing LASER diodes as light sources as mentioned in chapter 3, this enabled headlamp manufactures to increase the luminous intensity even more. This system is therefore used in this part to increase the luminous intensity in the centre hot spot of the high beam distribution.

TEST SETUP

For the same reasons as described in section 5.1.1, this study is located at the *August Euler* Airstrip as shown in figure 5.1. The test setup itself is a modification from the one shown before. The schematic setup is shown in figure 5.6. Again, starting and ending positions of the test run are marked with red circles and the test straight is marked in orange. The main differences in the setup is the use of 5 detection dummies instead of only two. Two are set up on the left and three on the right side. Between the dummies, on each side, a distance of 100 m is kept and the dummies on the left side are placed with an offset of 50 m to the ones on the right side leading to an alternating dummy sequence. This is done since the use of high beam and especially high intensity high beam should lead to much higher detection distances and the goal here is, to decrease the learning effect even further. Again, only one dummy is being erect for each run. Furthermore the driving speed is increased to 60 $\mathrm{km\,h^{-1}}$ since, in the series production car, the LASER hot spot is only activated at velocities above this speed. The car in use for this investigation is the BMW i8 with LED low and high beam and the additional LASER module in the high beam. The LED high beam leads to a maximum luminous intensity of 75 000 cd adding the LASER booster to that, leads to a maximum of around 215 000 cd [164]. Compared to this, the low beam has only stray light in the same spot and is only considered as a base line to compare the results to the study shown in section 5.1.1. The point with the highest luminous intensity for this passing beam was measured at 20 000 cd and BMW kindly supplied an i8 with modified lighting functions in order to activate the LASER module at any velocity.

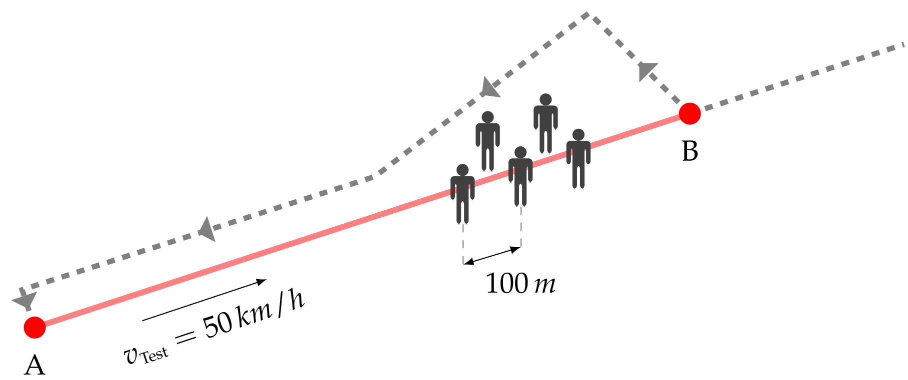

Figure 5.6 – Schematic setup for the test on the influence of luminous intensity in the high beam. The grey human like figures indicate the possible positions of the detection dummies. The red circles mark the start end the end of the test section.

Again, the dummies and the test vehicles are equipped with GPS modules to synchronize the timestamps and thereby calculating the detection distances. Since the results from the study in section 5.1.1 have shown, that light distributions can not be too bright, the brightness perception is not investigated in this study any further.
Additionally to the detection part, identification is investigated as well. Since the other studies solely focus on the detection of objects, the data and the evaluation for the identification test can be found in appendix B.2. The test is performed by a total of 30 test persons with 24 of them between 25 and 30 years of age and a smaller group of 6 participants with an age of 55 to 65 to investigate a possible influence of the driver's age. Again, detailed information on the test subjects can be found in appendix B.2 in table B.2.

TEST PROCESS

The test process is similar to the process described in the section 5.1.1. The test subjects start at the very western part of the runway, accelerate to 45 $\mathrm{km\,h^{-1}}$ and restore the cruise control so that the car keeps accelerating to the pre-set of 60 $\mathrm{km\,h^{-1}}$. Then the test subject is asked to press the detection button as soon as he is sure to detect one of the random detection dummies and the distance can be calculated. Again, the switch between the light distributions is done at the end of the runway and the way back to the staring point is used for adaptation.

As already done in the study on the detection distance as a function of the low beam intensity, additionally luminance recordings are done after the testing. Since this test investigates the detection distances for high beam, the luminance recordings are done starting at a distance at 300 m for the LASER high beam, at 200 m for the LED high beam and at 100 m for the low beam going down to 30 m for all light distributions. As already mentioned in both, chapter 2.3 and chapter 5.1.1, these recordings are done stationary due to the long integration times of up to 10 s necessary for the sensors. This is the reason, why the LASER high beam needs to be available even at speeds lower than the usual 60 km h^{-1} activation speed. Again, the results are summarized in section 5.1.4 where the detection results are used to calculate the required luminous intensities for different situations.

DETECTION DISTANCES WITH VARIABLE HIGH BEAM INTENSITY

In first step, the raw detection distances for the three light distributions are set into bins of 5 m and the detection frequency is calculated for each setting. The result of this are shown in figure 5.7 with the detection frequency on the ordinate and the detection distance in bins on the abscissa. The detection distances for passing beam is shown in blue, the red bars show the detection distances for driving beam and the yellow bars indicate the measured detection distances with driving beam and added LASER.

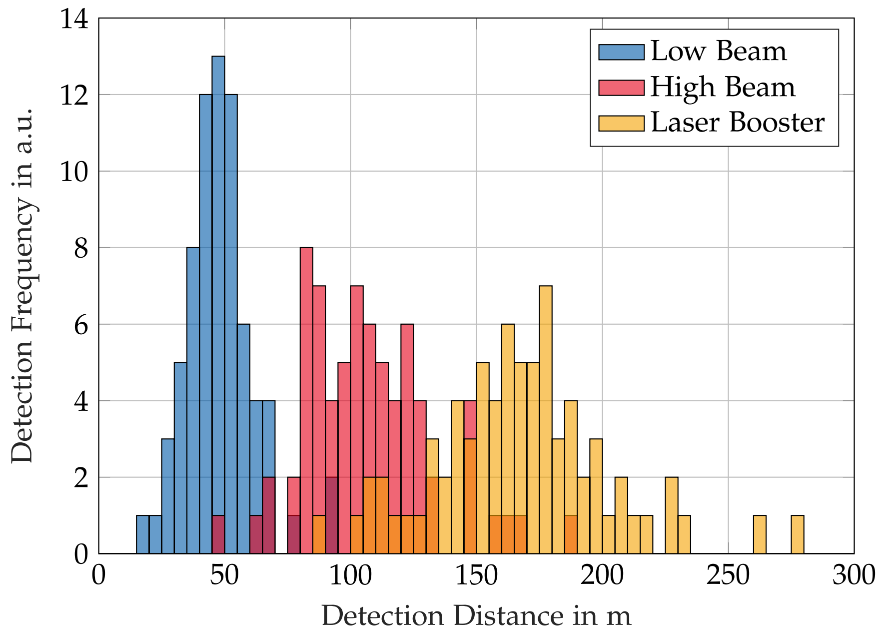

Figure 5.7 – Detection distances grouped into 5 m bins for the three light distributions. Passing beam is represented by blue bars, driving beam by red bars and driving beam with added LASER booster by yellow bars. The mean detection distances are calculated at 48.2 m for passing beam, 107.0 m for driving beam and adding the LASER booster to this, leads to 167.4 m

It is easily discernible, that the three light distributions split up by a significantly. To test if the differences are statistically significant, again all data is normalized by equation 5.1. The normalized data is then used to to calculate a ONE SAMPLE KOLMOGOROV-SMIRNOV test with a 5 % significance level on standard normal distribution.

The results show, that the null hypothesis for this test, that the data for each light distribution originate from a normal distribution, is validated for all three distributions with p values of 0.44 for passing beam, 0.86 for driving beam and 0.88 for the added LASER booster. Again, the CDF-plot to visualize the normal distribution of all data sets is shown in appendix B.2 in figure B.5.

The data is then tested by a TWO SAMPLE KOLMOGOROV-SMIRNOV tests to find, if the difference between the distributions are of statistical significance. The null hypothesis for this test is, that two tested distributions originate from the same distribution with a significance level of 5 %, meaning the test results in significant difference between datasets for p values lower than 0.05. Table 5.1 shows the resulting p values. All values are far lower than 0.05 and therefore statistically significant differences can be assumed. Obviously the p values for testing distributions with themselves lead to p values of one, therefore implying that the datasets are indeed from the same distribution.

Table 5.1 – p-values for the Two Sample Kolmogorov-Smirnov tests for the detection distance distributions between all light distributions.

	LOW BEAM	HIGH BEAM	LASER BOOSTER
LOW BEAM	1.0	4.2×10^{-27}	6.4×10^{-33}
HIGH BEAM	4.2×10^{-27}	1.0	3.7×10^{-20}
LASER BOOSTER	6.4×10^{-33}	3.7×10^{-20}	1.0

With the knowledge, that all data sets are indeed from statistically different distributions, the detection distances and probabilities can be calculated and discussed. When driving with low beam, a mean detection distance of 48.2 m is measured. This rises to 107.0 m when driving with high beam and reaches 167.4 m when activating the additional LASER module. This means, on average, driving with high beam leads to a gain of 58.5 m or 121.4 % compared to driving with low beam only. Comparing the LASER booster with low beam is a unreasonable but nevertheless the results should be discussed. This additional module would lead to a gain of 119.2 m or 247.3 % over the low beam. The more viable comparison from LASER booster to driving beam still leads to a large gain of 60.4 m or 56.4 %. This means, that in raw distance, the additional module improves the detection distance just as much as switching from low to high beam.

In order to investigate, whether the gain adding the LASER booster to the light distribution is indeed the same, as switching from low to high beam, the differences between the first runs for low and high beam and high beam and added LASER booster are calculated. The same is done for the second and third run accordingly. Again, the first step is to test both difference-distribution for normal distribution. This is done again by normalizing the data according to equation 5.1 and using the One Sample Kolmogorov-Smirnov test. This leads to a normal distribution for both difference distributions with a p value of 0.52 for the difference between the low and the high beam, and a p value of 0.99 for the difference between high beam and added LASER. The empirical CDF data for both gain distributions, gain by high beam over low beam in red and gain by LASER booster over high beam in yellow, is shown in appendix B.2 in figure B.6. This normal distribution leads to the use of the Two Sample Kolmogorov-Smirnov for the difference distributions between the different light distributions. Again, the null-hypothesis is, that both distributions originate from the same distribution. This is proven to be correct with a p value of 0.57, thereby leading to the deduction, that the gain by using the LASER module actually leads to the same improvement in detection distances switching from low to high beam.

The actual gain distributions are shown in figure 5.8 with the gain by high beam in the detection with low beam shown in red and the gain when using the LASER booster over the high beam shown in yellow. When looking at the gain distributions, it becomes apparent, that in some cases, the detection distances are actually lowered by using the light distribution with the higher maximum luminous intensity. This is the case once for high beam compared to low beam and three times for LASER booster over high beam. This is most probably the case due to lack of focus for single runs and since these are single cases that do not influence the datasets themselves, they will not be reviewed any further. Another interesting feature found in the data is the existence of gain in detection distance of over 100 m in some single cases. It has to be reported however, that all largest detection distances and largest gains for the LASER booster are measured for the same test subject. Since all three of his test runs show the characteristics, this is not treated as an analomy.

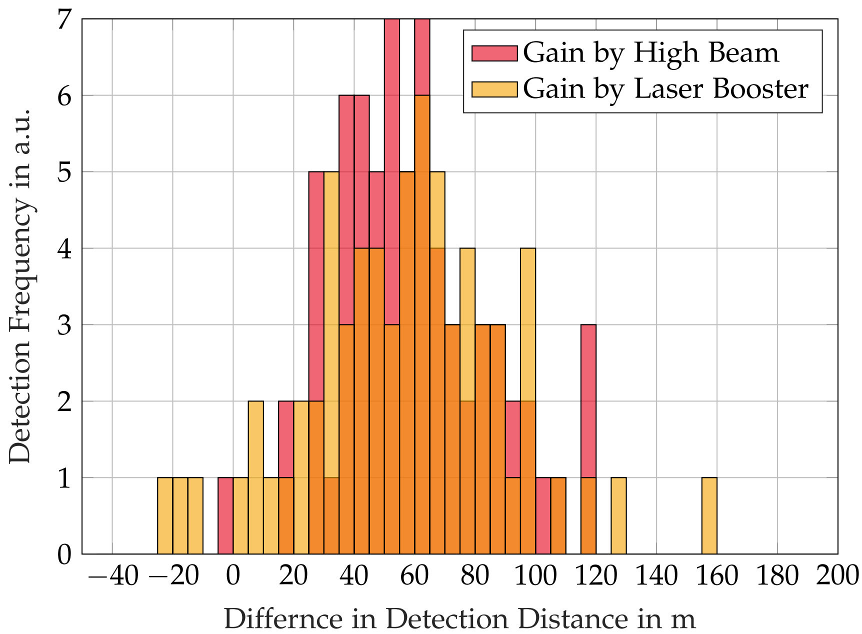

Figure 5.8 – Detection gain for by high beam over low beam (red) and the gain by LASER booster over high beam (yellow).

Up until now, only mean values for the detection distances and gains have been discussed. However, as already mentioned before, mean distances still indicate, that in half of the test cases, the test subjects did not yet detect the object besides the road side at this distance. Therefore, those test participants can not yet initiate a (necessary) braking manoeuvre. Therefore, the next step is, to calculate the detection probabilities over the distance for each light distribution. To calculate the probability over distance, the cumulated sum over the detection distances is calculated and normalized. $1 - \sum d_i$ then leads to the probability with d_i being the detection distances. The detection probability data for all tested light distributions is shown as the dots in figure 5.9. Additionally, to the data, sigmoid functions according to equation B.1, are fitted to the data sets and shown as dashed lines. x_0 is the shift on the x-axis and gives the mean detection value for the fit. c indicates the inclination for each fit. All three fits return an excellent representation of the data with R^2 values of 1.00 for low beam, 0.99 for high beam and 1.00 for the activated LASER modules. The complete statistical metrics are found in table B.3 in appendix B.2.

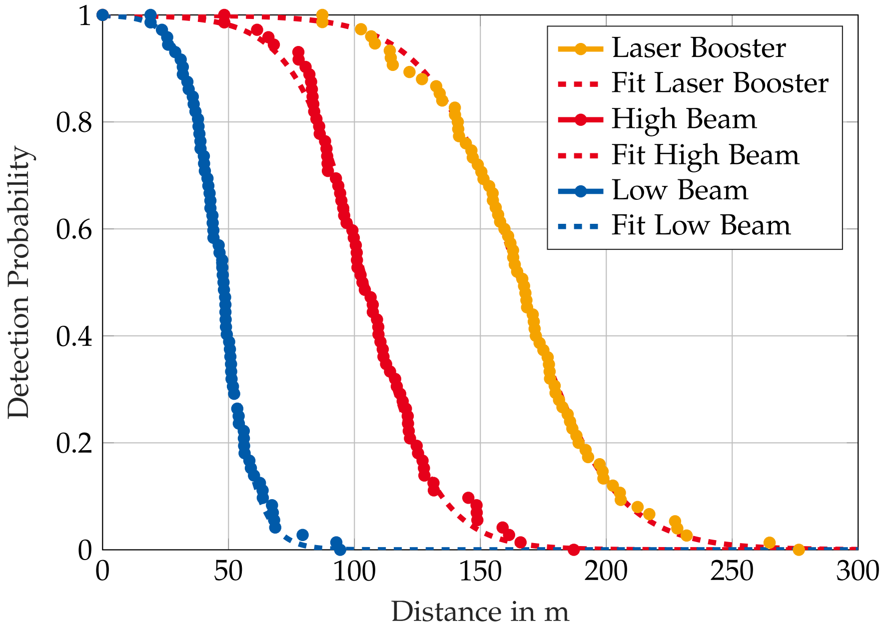

Figure 5.9 – Empiric detection probability for the three investigated lighting functions with the additional sigmoid fit functions according to equation B.1. Blue represents low beam, red high beam and blue the additional LASER booster.

The detection probability is shown in blue for low beam, in red for high beam and in yellow for the added LASER booster. Again, this data shows, that the difference between the low beam and the high beam curve is about the same as the difference between the high beam curve and the LASER curve. The 50 % probability is equivalent to the mean detection distances. This figure also illustrates again, that the difference between low beam and high beam and the difference between high beam and LASER booster are the same since the shift between the curves are very similar as well. However, the focus in this section is on the higher detection probabilities. Analogous to Schneider [165], the 95 % threshold for detection is calculated. The results for the 95 % and for the 50 % detection threshold are compared in table 5.2 for the measured data and the fit function as well. Figure 5.9 already indicates a significant gap between the fit and the real data for higher thresholds while they should be rather similar for the 50 % threshold.

Table 5.2 – 50 % and 95 % detection distance thresholds for the three different light distributions as calculated from the data shown in figure 5.9.

	low beam		high beam		laser booster	
	50 %	95 %	50 %	95 %	50 %	95 %
data	48.0 m	26.0 m	103.2 m	68.0 m	167.4 m	107.1 m
fit	47.1 m	27.0 m	104.5 m	63.9 m	165.8 m	113.1 m

Taking a look at the data, the mean difference between the fit and the actual data at the 50 % threshold is 1.3 m with the maximum difference being 1.6 m for LASER booster. For the 95 % threshold, the mean difference rises to 3.3 m with the maximum at 6 m for the detection with added LASER booster again. This again shows how accurate the fit matches the data. For further discussion, only the fit values are taken into account.

The 95 % detection distances reveal, that low beam only leads to a detection distance of 27.0 m and is thereby not to be recommended at any other situation than passing another vehicle. Switching to high beam, at least leads to a 95 % detection distance of 63.9 m thereby effectively doubling the viewing distance. Adding the LASER module to the LED high beam, again doubles the distance for the 95 % detection distance to 113.1 m.
This section shows, that increasing the luminous intensity in the high beam area can have a significant influence on the recorded detection distances. The used high beam is set up right at the edge of what is possible within the ECE regulations. The results achieved with this added luminous intensity are astonishing and much higher than expected. While the difference between driving with low beam compared to driving with high beam is pretty obvious, the benefit of added light in the high beam area is much harder to comprehend. However, this study shows, that the difference between the three lighting functions is actually pretty similar.

5.1.3 DETECTION UNDER DIFFERENT VIEWING ANGLES

The two studies described in the sections 5.1.1 and 5.1.2 respectively, focus on the detection distances of objects right besides the road. As discussed in chapters 2.1 and 2.4 however, the visual acuity changes with the detection angle. ADRIAN, DAMASKY, SCHILLER and SCHNEIDER all performed laboratory studies as explained above. To validate these findings, a field study is performed in collaboration with SCHNEIDER where parts of this study have already been published in [66, 165].

TEST SETUP

For repeatability reasons, this test is set on the *August Euler* Airstrip as well. To investigate the influence on the angular position of the detection objects on the detection distances under the test setup is modified compared to the ones shown above in the sections 5.1.1 and 5.1.2. For this study a *Mercedes E-Class* with full LED head lights is used. The detection objects are to be placed perpendicular to the test road. The selected angular positions are 2.7°, 5.0°, 6.5° and 8.0° to match the angles investigated in the laboratory study of SCHNEIDER. The angles of 0° and 20° have proven to be impractical for this test and were taken out of this study. The 0° detection test was assessed to be unsafe and objects at 20° to be undetectable. Furthermore, the 10° angle is reduced to 8° to increase the detection probability. This is also done due to the findings by SHIBATA in figure 4.17 and HUHN, as discussed in section 4.5.

Since this test is to chosen to be an investigation in real life driving situations, the test has to be conducted with a certain driving speed. Therefore, the chosen angles need to be transferred into distances perpendicular to the road. For this, the results of section 5.1.2 are taken into account. This this study shows an average detection distance with LED high beam of around 110 m. The object locations are calculated for this mean detection distance leading to positions of 5.0 m, 9.6 m, 12.5 m and 15.5 m measured from the driver. To improve variance in object positioning, two additional object positions under 5.0 m and 6.0 m on the left side of the road are added. However, these positions are only added to avoid the possibility of the test subjects learning, that objects will only appear on one side of the road, only focusing on the right side and thereby increasing the recorded detection distances. This setup is shown in figure 5.10 with the detection objects 1 to 4 corresponding to the angles 2.7°, 5.0°, 6.5° and 8.0°. Positions 5 and 6 are the two positions chosen to avoid the learning effect. To enable detection under those wider angles, and minimize the influence of the light distribution as much as possible, the test is performed with high beam only. One more major difference between this study and the two studies shown before has to be mentioned. Due to the larger angles to the right side, the detection objects have to be placed in the adjacent field. This made the use of the test dummies shown before impossible. Therefore, the detection dummies are swapped out and one of the test coordinator, dressed in dark clothing, is chosen to be the detection object leading to an even more realistic test environment.

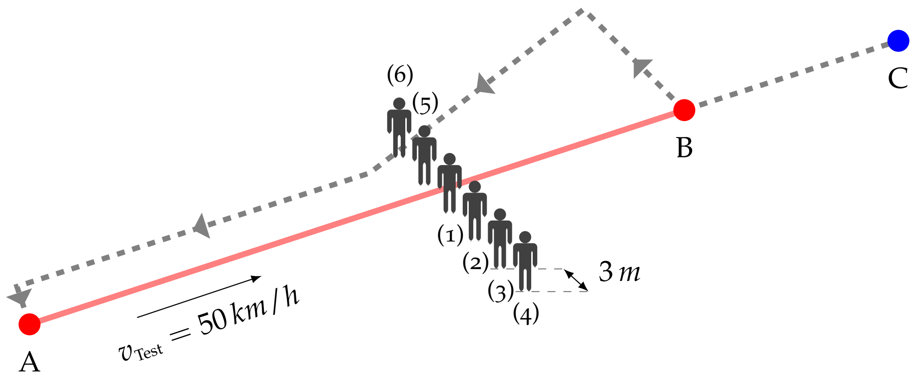

Figure 5.10 – Schematic set upfor the test on the influence of the angular position of objects on detection distances in real life driving tests. Positions 1 to 4 represent the distances 5.0 m, 9.6 m, 12.5 m and 15.5 m translating to the angles 2.7°, 5.0°, 6.5° and 8.0° for an average detection distance of 110 m. Positions 5 and 6 are added to avoid focus on one road side. The red circles mark the starting positions and the blue circle marks the orientation point given by additional, static vehicle.

The starting position and the ending point are marked as red circles, however it is not possible for this study to use the full round course and therefore the participants are asked to perform a U-turn at the ending position. This test was performed at $80\,\mathrm{km\,h^{-1}}$ to accommodate better for the average speed on country roads. Furthermore, another vehicle is positioned at the end of the runway, marked by a blue circle in figure 5.10. This vehicle is set in stand still with all lights and the engine turned off. Since the test is done with high beam, the licence plate and the rear lights still reflect a certain amount of light back to the test vehicle. This is used as an orientation point to keep the participants from searching for the detection objects. As described by Schneider, additionally to the human detection figure, a wooden deer was used to find the influence of the detection object as well. This thesis will only focus on the human detection object since investigating different object shapes would go beyond the scope of this work. For the interested reader, the results achieved with the deer are published in [66, 165].

In this study, 30 test subjects participated, and are split into two groups according to section 5.1.2 with 22 participants between 20 and 31 years of age and 8 participants with an age of 45 to 54 years of age. Again, all participants either work in an office job or are students at the moment. The complete detail on the test subjects is attached in the appendix B.1 in table B.7.

test process

The test process is again kept similar to the processes described above. The test subject accelerate to around $50\,\mathrm{km\,h^{-1}}$ and then reactivate the cruise control that will continue to accelerate the vehicle up to the preset $80\,\mathrm{km\,h^{-1}}$. The participants are again asked to press the detection button, as soon as they detect the test object at one of the given positions. During the whole driving section, they are asked to only focus on the reflections on the car at the end of the runway. The position of the detection objects is randomly switched between each test run. Each setting is repeated four times all six positions. After half of the test runs are done, the test subject is offered a break and a second participant is asked to perform his runs. Since this test process also included the deer as the detection object, this leads to 48 runs per person in total.

After the dynamic testing is done, similar to the tests described above, luminance recordings are done for all positions to evaluate the required luminance, illuminance and luminous intensity for safe detection under different angles. For the same reasons discussed above, this is done statically and after all testing is done. Again, the results are shown in section 5.1.4.

DETECTION DISTANCES UNDER DIFFERENT VIEWING ANGLES

Since the test was to some extend already published by SCHNEIDER, these results are summarized shortly [66, 165]. The data is not split into the two age groups, since the test sample of 8 elder drivers is considered to be statistically to small.
SCHNEIDER refers to the object positions only by their distance to the driving lane and uses this distance to describe the eccentricity. The general results of the dynamic detection test are shown table 5.3.

Table 5.3 – Detection distances over all test subjects regarding the object position on the right side of the driving lane expended by the standard deviation over all test subjects [66] .

OBJECT SHAPE	DETECTION DISTANCE			
OBJECT POSITION	5.0 m	9.6 m	12.5 m	15.5 m
DETECTION DISTANCE	93.2 m	95.5 m	92.9 m	84.1 m
STD.	19.3 m	22.2 m	23.7 m	21.2 m

According to SCHNEIDER, the results for the eccentricities from 5.0 m to 12.5 m show no differences. Only the object position furthest out onto the side shows an effect on the detection distance. SCHNEIDER further evaluates the influence of the age, lower detection distances for elder participants, as well as the influence of the object shape, deer vs. human, where only one significant effect for the 12.5 m position is found, as well as the influence of the test setup, static vs. dynamic with significant higher detection distances for the static test setup.

All four detection distributions are, analogue to the tests before, firstly tested for normal distribution, revealing, that all four distributions follow standard normal distributions. Testing the distributions in significant differences between them, however leads to the fact, that they all originate from one single distribution and no significant difference is found. This is already indicated by the large overlap between the different distributions, when taking the standard deviation shown in table 5.3 into account. Nevertheless, the four distributions are evaluated for any trends, that might not be visible by statistical analysis. Since the test is performed dynamically, the angle under which the objects are detected, are dependent on the distance at which the driver detects them. Therefore, the assumed angles of 2.7° to 8.0° are not the ones recorded in reality. Therefore, the first step is to calculate the actual angle at the moment of detection. This is illustrated in figure 5.11 where the newly calculated angles are shown as box plots.

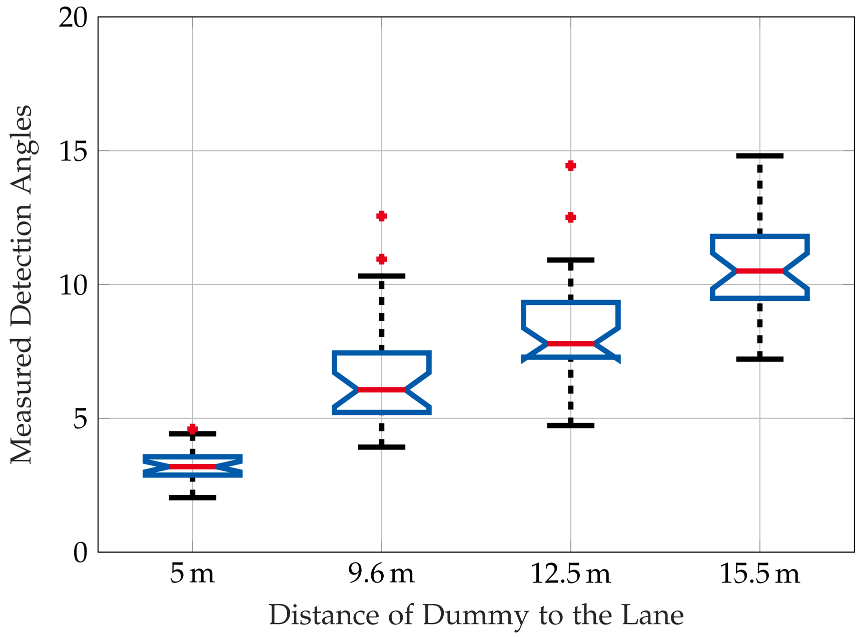

Figure 5.11 – Actual recorded detection angles for the given object positions of 5.0 m (3.2°), 9.6 m (6.1°), 12.5 m (7.8°), 15.5 m (10.5°).

The assumed values of 2.7°, 5.0°, 6.5° and 8.0° can now be corrected to the real values of 3.2°, 6.1°, 7.8° and 10.5°. From this point on, the positions of the objects are referred to by their average detection angles. A very important remark is, that some of the detection angles overlap into other groups. This means that the detection distance vary in such a way, that some participants detect the object at the closest position to the road with such short distances, that the angle to the object is larger than the angle to the second object for other participants.

Calculating the detection probabilities in correlation to the object position over the distance as shown in figure 5.12 shows, that there is no difference between the object positions for any detection distance or probability. The detection probability for the different object positions is shown in blue for the object at 3.2°, in red for the object at 6.1°, yellow for the object at 7.8° and in purple for the object at 10.5°. The data shows, that the detection probability is nearly identical for all eccentricities.

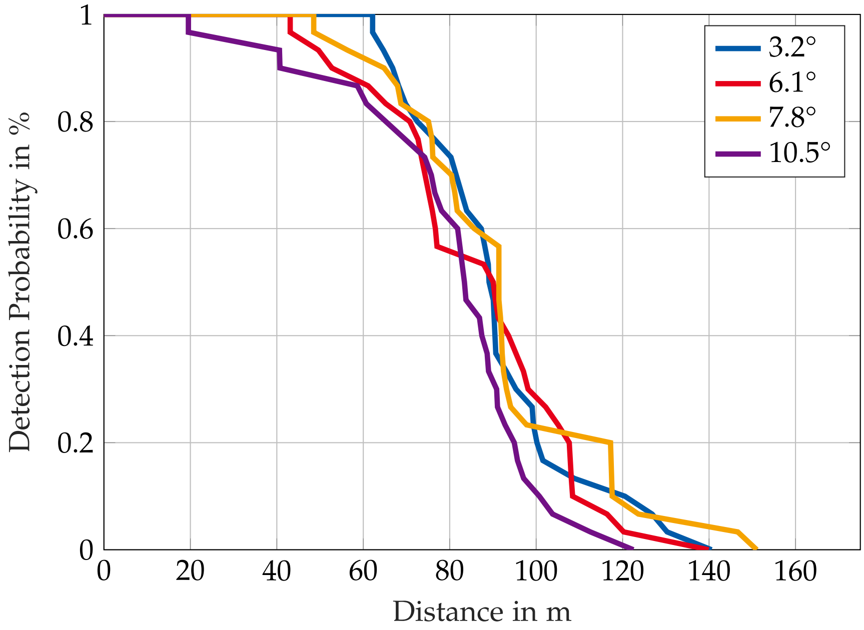

Figure 5.12 – Detection probability over the distance for the four dummy positions, 3.2° (blue), 6.1° (red), 7.8° (yellow) and 10.5° (purple).

This data shows, that for the mean detection distances only the object at 10.5° shows any difference to the other object positions. At the 95 % detection probability however a large difference between the closest object at 3.2° (detection distance of 62.2 m) and the object at 10.5° (detection distance of 19.5 m) is recorded. However, the expected result of a steadily increasing distance for increasing eccentricity is not given. The data suggests a lower detection distance for the object at 6.1° (43.1 m) compared to the object at 7.8° (48.5 m). Similar behaviour can be seen when approaching the data from the opposite direction. When looking at a certain distance, 100 m for example, the highest detection probability is found for the object located at 6.1° away from the road with about 27 %. Next up would then be the object at 7.8° with a probability of 23 % before the object right next to the road (3.2°) follows at the third position with a probability of 20 % and only the object at 10.5° follows the expected behaviour with a probability of 10 %.
As mentioned, it was expected, that the detection distance is decreased significantly by setting up the objects further to the side. The main reason for this is, that current automotive headlights direct their hot spot directly at 0.0° and the luminous intensity decreases to the outside. When looking at the 50 % detection distances, the detection angles are set to 3.3° for the closest target and go up to 10.4° for the object furthest to the side. This is a difference of over 7° between the two positions which in theory should also lead to a significant decrease in available luminous intensity of the headlamp. Additionally, to that, the point at which humans perceive information, the fovea, is located at 0.0° as well. However, this effect might be balanced out by the active rods during nighttime driving, that have their highest density at 10° to 20° as described in section 2.1.
Assuming, that the test it self was performed flawlessly as instructed by all test subjects, and that no further influencing factors are at play here, would mean that, at least for objects located to the sides, current headlamp systems are already well designed and current light distributions enable similar detection distances for objects at all positions between 0.0° to 10.0°
But, while the drivers are given the instruction to look straight ahead, onto the vehicle placed

at the other end of the run way, it was not possible to measure the gaze behaviour. Through natural search patterns, the actual difference in angles between the gaze vector and the object position might be lowered. Active suppression of the urge to look to objects that are glimpsed at out of the corner of the eye would be necessary. Several subjects reported after the test, that this was difficult and that they cannot guarantee that they followed the instructions for every test run. Furthermore, the different positions besides the road lead to different surroundings regarding grass and unevenness leading to slightly changed detection values. The luminance analysis by SCHNEIDER suggests, that due to the lesser light at outer edges provided by the headlamp, a lower contrast is needed to safely identify the regarding objects.

While the tests in the previous two sections only investigated the influence of the luminous intensity in the centre of the light distribution, and these values are known and shown above, this section investigates the detection under peripheral vision. For perfect allignment with the light distribution, a photometric measurement of the light distribution of the used headlamps would be needed. However, since the vehicle used was a rental car it was not possible to measure this. Instead, SCHNEIDER evaluated luminance recordings for all object positions under the mean, and the 95 % detection distances. These measurements are listed and explained in depth in the original work [66], and the acquired values are used for further calculations.

5.1.4 SUMMARY AND DISCUSSION

In the sections above, three detection tests in are presented, where at first, the low beam intensity is varied, then the high beam is added and the intensity is increased up to the maximum allowed in current regulations, and for the last part, the position of the detection objects is shifted from right besides the road to different viewing angles. In the following sections, the results are summarized, compared and discussed.

SUMMARY OF THE INFLUENCE OF THE LIGHT DISTRIBUTION ON DETECTION

The first remark that needs to be made when comparing the results of all three studies is, that due to availability and investigated lighting function, three different vehicles were used over the three parts. The largest difference is to be expected with the vehicle in the second part, the *BMW i8*. Here the mounting height of the headlamps is significantly lower compared to the *Opel Insignia* or the *Mercedes Benz E-Class*. This leads to decreased viewing distances with low beam. However, at that time, no other vehicle with LASER high beam was available.
The first two parts show, that an increase in luminous intensity in low and in the high beam area increases the detection distance significantly. However, the detection distances are only increased slightly for variations in the low beam intensity. The measured detection distances increase from 52.6 m to 62.8 m when switching the low beam intensity from 50 % up to 100 %, which is an increase of only 16.2 % (sections 5.1.1). Comparing these distances to the ones measured in the second part,(section 5.1.2), leads to the expected difference. The detection distances are measured at 48.0 m on average for low beam, 14.8 m lower. The main reason, for the lower distances in the second test is given by the much lower height of the headlamps and the driver in the used test vehicle. Furthermore, the velocity was increased from $50\,\mathrm{km\,h^{-1}}$ to $60\,\mathrm{km\,h^{-1}}$. A second major influence for this distance is found in the added different positions of the detection objects which makes it more difficult for the test drivers to guess, where the selected dummy is standing. Comparing the detection distances with high beam between the second and the third part leads to a difference of 12 m. The TWO SAMPLE KOLMOGOROV-

SMIRNOV reveals significant differences between the two tests. Since for this comparison, the second test leads to the higher detection distances, the reason for this cannot be found in the mounting height. The major difference between the two setups is the instruction given to the drivers. While the second test allows for free gaze roaming, the participants in the third test are asked to focus their gaze straight ahead. While the indifference between the different angular positions and the report by some subjects indicate, that this focus straight ahead was not followed through completely, this lower detection distance indicates, that at least to some degree, the visual search was limited. Additionaly diffferent detection dummies are used. While the dummy used in second part is a flat and homogeneous detection object, the dummy in the last test is a real life person with a transition in the luminance and thereby smoother edges and thereby lower contrast as shown by BREMOND and described in 4.1 [101]. Another major difference between all three tests are the used headlamps. Since it was not possible to use the same vehicle or even vehicle type in each test due to different requirements, the light distributions in both low and high beam are different for all test. All results of the mean detection distance and the distance for the more relevant 95 % detection probability are listed in table 5.4 where the low beam data is marked in blue and all data acquired with high beam or high beam and LASER booster are marked in black.

Table 5.4 – Summary of all mean detection distances as well as the distances at the 95 % detection probability over the three driving tests from sections 5.1.1. 5.1.2 and 5.1.3. The data marked in blue shows the low beam data that is not regarded for further analysis due to the low calculated distances.

Test Setup			DETECTION DISTANCE		
			50 % Det.	95 % Det.	Difference
TEST 1	50 % Low Beam		52.6 m	29.5 m	43.9 %
	100 % Low Beam		62.8 m	36.9 m	41.2 %
TEST 2	Low Beam		48.0 m	26.0 m	45.8 %
	High Beam		103.2 m	68.0 m	34.1 %
	Laser Booster		167.4 m	107.1 m	36.0 %
TEST 3	5.0 m	3.2°	93.2 m	62.2 m	33.2 %
	9.6 m	6.1°	95.5 m	43.1 m	54.9 %
	12.5 m	7.8°	92.9 m	48.5 m	47.8 %
	15.5 m	10.5°	84.1 m	19.5 m	76.8 %
AVERAGE			-	-	46.0 %
STD			-	-	12.7 %

COMPARISON TO RELATED WORK

Comparing the data to the distances achieved by BREMOND in the simulator test, shows that the values achieved in real life tests are significantly lower. BREMOND reports detection distances of 124 m compared to the 104 m. This shows, that there is a significant difference between simulator tests and real life tests even if the real life tests are under isolated circumstances.

While the test setup of GIBBONS is very similar to the setup in the second test performed here (comparing figure 4.4 to 5.10) two large differences exist. GIBBONS test setup includes overhead lighting which changes the overall luminance and contrast significantly. Furthermore, the test is performed with SAE headlamps, which provide a different light distribution with the main difference being, that the low beam is aimed at the horizon (0.0°) as compared to −0.6° as done in Europe. Therefore, the reported distances of 120 m and more are explainable. However, Gibbons also reports similar results regarding the eccentricity with only the object with the highest detection angle having significantly decreased detection distances while having an increased contrast. While the absolute position of the objects are larger (21 m) at the maximum, the increased detection distance leads to the similar detection angle of 11.9°.

Zydeck shows detection distances of 58.2 m and 88.4 m for low beam (halogen and HID headlamps) and 131.5 m and 141.3 m for high beam. These results are higher than the ones recorded in the study shown in 5.1.2. The major differences, that can lead to these increased detection distances are similar to the differences between the studies in 5.1.2 and 5.1.3, that the vehicle with HID headlamps in use was a SUV and thereby had a much higher headlamp mounting position leading to a further detection distance when compared to the "normal" station wagons used in the first and third test and even more than the low sports vehicle that was used the second test in the presented study. Additionally to that, the light distribution is different since as mentioned Zydek used an HID headlamp, while the presented thesis focuses on LED headlamps only. The second major difference was the increased reflection coefficient of $\rho = 9.7\,\%$ of the detection dummies used by Zydek compared to $\rho = 5\,\%$ in the presented studies. While any other property of the dummies and the test area is kept exactly the same, this increase in reflection coefficient will double the perceived luminance of the detection dummy and thereby also doubling the possible contrast at any given distance. It is expected, that this is the main source for the rather large difference in detection distances. Especially, since oncoming traffic was used by Zydek, leading to distracting glare sources that should lead to reduced visibility distances. Furthermore, different test subjects might behave differently since their driving experience, their concentration and even their gaze behaviour can differ.
The study performed by the THM Giessen shows low beam detection distances of about 56 m and 88 m for gfHB. While this study was performed in a more complex and less isolated environment with bends and oncoming traffic, the distances measured for low beam are identical to the values recorded in the first part of this study. This is unexpected, since the more complex driving task, the inhomogeneous background and oncoming traffic should decrease the detection distance significantly. The gfHB values are not comparable to any test performed during this thesis.

Deduction for optimal light distributions

The presented work only shows the first steps needed to create an optimal light distribution. Only the influence of the luminous flux in the hot spot of both, low and high beam, and the required luminous intensity to detect objects under different viewing angles are investigated. Using this information, the optimal luminous intensity for safe detection under given distances can be calculated. However, these values are only valid for isolated settings on straight roads with no further objects in the field of view of the driver than the detection object.

The stopping distance for different driven velocities is calculated using the emergency breaking distance as given by equation 5.2 [166].

$$s = \frac{\frac{v}{10} \cdot \frac{v}{10}}{2} \tag{5.2}$$

This equation does not include any reaction time needed by the subjects to react after detecting an object and initiating the emergency breaking. Since all presented studies used a detection button, the reaction time is already deducted in the detection distances. For driving on country roads, which the test setup is most similar to, the maximum velocity of $100\,\mathrm{km\,h^{-1}}$ is set in Germany. This leads to a breaking distance of 50 m according to equation 5.2. For motorway driving a velocity of $150\,\mathrm{km\,h^{-1}}$ can be assumed [167], leading to a breaking distance of 112.5 m.
While all the tests presented in the given studies show mean detection distances of over 50 m, with the exception of section 5.1.2, where the lowest mean detection distance was measured at 48.0 m, this does not mean, that the current headlamps with the given intensities are already perfectly suited. Three major factors have to be included in the presented approach. First of all, the 95 % should be considered. Secondly, the test was performed under very isolated conditions with the test subjects knowing, that an object will appear besides the road. Thirdly, the objects in use are plain and homogeneously coated dummies, with the exception in section 5.1.3, and therefore increase detection distance further. The effects are summarized as follows:

- 95 %**Detection Threshold:** Decrease of the detection distance by an average of 46.0 % (see table 5.4).
- **Enclosed Roads:** Damasky shows, that the required luminance on objects needs to be around two to ten times higher for real roads. Assuming double the contrast is needed, the detection distance is reduced by the factor $\sqrt{2}$.
- **Homogeneous Detection Dummies:** Bremond shows, that a real object with smooth edges (luminance) lead to a decrease in detection distance between 3.2 % and 18.1 %.

Taking these effects into account leads to minimal detection distances for low beam of 25.3 m assuming the minimal reduction in detection distance by 3.2 % for pedestrians, doubling the required contrast and using the 95 % threshold. This shows, that low beam should only be used in situations, where it is absolutely not possible to use any form of high beam. The standard high beam used in the two latest tests lead to detection distances of 42.6 m and 46.5 m in the case of objects right next to the road. This drops down to as low as 13.4 m for the object furthest out due to the drop of luminous intensity in the high beam for eccentricities of over 5°. This shows, that even the objects with the highest detection distance can not be detected safely with low beam. Increasing the speed requires more luminous intensity in the centre hot spot. Going at the average speed on motorways ($140\,\mathrm{km\,h^{-1}}$) then requires an emergency stopping distance of 98 m for which even the LASER booster does not deliver a safe detection with 73.0 m. Since these values appear significantly to low, when reviewing the accident statistics, the for further review, the factor assumed by Damasky is not regarded. This would then lead to distances of 35.8 metre, 65.8 metre and 103.7 metre for low beam, high beam and LASER booster.

Since the reflection coefficient for the objects in use is given by $\rho \leq 5\,\%$, using the luminance recordings and the equations 2.9 and 2.2 the illuminance at the objects position can be calculated. The luminance values recorded for both, the 50 % and 95 % threshold are summarized in table 5.5. The object luminance as well as the background luminance is listed and similar to before, all data measured with low beam only is marked in blue.

Table 5.5 – Recorded luminance values of the object and the surroundings at both, 50 % and 95 % thresholds. The data marked in blue shows the luminance values achieved with low beam. This data is not regarded further due to the low calculated distances as shown in table 5.4.

Test Setup			LUMINANCE AT DETECTION THRESHOLD 50 % L_O	50 % L_U	95 % L_O	95 % L_U
Test 1	50 % Low Beam		0.058 cd m^{-2}	0.015 cd m^{-2}	0.581 cd m^{-2}	0.106 cd m^{-2}
Test 1	100 % Low Beam		0.028 cd m^{-2}	0.010 cd m^{-2}	0.503 cd m^{-2}	0.082 cd m^{-2}
Test 2	Low Beam		0.110 cd m^{-2}	0.010 cd m^{-2}	0.220 cd m^{-2}	0.040 cd m^{-2}
Test 2	High Beam		0.070 cd m^{-2}	0.020 cd m^{-2}	0.110 cd m^{-2}	0.020 cd m^{-2}
Test 2	Laser Booster		0.100 cd m^{-2}	0.060 cd m^{-2}	0.150 cd m^{-2}	0.050 cd m^{-2}
Test 3	5.0m	3.2°	0.283 cd m^{-2}	0.049 cd m^{-2}	-	-
Test 3	9.6m	6.1°	0.134 cd m^{-2}	0.033 cd m^{-2}	-	-
Test 3	12.5m	7.8°	0.124 cd m^{-2}	0.026 cd m^{-2}	-	-
Test 3	15.5m	10.5°	0.089 cd m^{-2}	0.015 cd m^{-2}	-	-

The luminance recordings show, that the background luminance stays the same over all data sets, within the margin of error even though values recorded between 0.01 cd m^{-2} to 0.10 cd m^{-2} vary by a factor of 10, however these values are to be assumed noise by the luminance camera. For this reason, the contrast is not reviewed in detail since the great variability in this background luminance leads to a great variability in the contrast. This is shown in more detail in appendix B.2 in figure B.10 where the background luminance is plotted over the distance. This is due to the fact, that the background luminance includes the sky, which is not affected by the headlamps and ground far away, that is only effected slightly. The differences between the different test setups originates from overall changes in the background luminance due to different weather situations. For the 95 % detection distances for test 3 are not available. As an example of the luminance values over distance, figure B.10 in appendix B.2 shows the object luminance and the background luminance for different light distributions over the distance. However, the mean contrast calculated from this data with equation 2.10 is found at 3.3 with one major outlier. The contrast measured with the LASER-Booster is measured at only 0.7. Comparing these values to the contrast values measured in the laboratory by ADRIAN [64, 98], a factor of around 10 is found for the contrast. Compared to SCHNEIDER [66], where a contrast of 0.1 to 0.2 is found a factor of 20 is determined between the laboratory and the field tests presented here. This does include the fact, that SCHNEIDER investigated the 99 % threshold and the contrast determined here is for the 50 % threshold. Calculating the required illuminance on dark objects with a reflectance of $\rho = 0.05$ leads to a mean value of 8.4 lx on the object with the value for the dummy at porition 1 in the third test (5.0 m / 3.2°) being an outlier with a required illuminance of 17.8 lx.

As mentioned previously, low beam leads to detection distances that are too short for save driving. For this reason, the low beam is not used for further investigations. Since no data from Schneider is available for the 95 % detection threshold, the values here are calculated from the 50 % data using the factor described above. For the normal high beam at the measured 68 m for the 95 % detection probability, an illuminance of 16.0 lx is calculated. With the activated LASER, the 95 % detection distance is raised to 107 m which leads to an illuminance of 23.6 lx at the object. This increase in the required illuminance is due to the decrease in object size (angle) from 1.4° to 0.9°. As already shown in previous chapter, Blackwell and Adrian have shown, that if an object is smaller than a certain threshold, that depends on the adaptation luminance, the required contrast to detect the certain object, is increased. It can be found, that the product of object size and illuminance is constant.

With this knowledge, the required minimal luminous flux at the object position can be calculated for different velocities. While the correlation between the illuminance and the luminous intensity is exponential, the slope is additionally increased by the smaller detection objects over distance which means, that for larger velocities an even higher increase in luminous intensity is required. This is shown in figure 5.13 where the lower x-axis shows the driven velocity and the upper x-axis shows the stopping distance. The blue line therefore shows the required luminous intensity/illuminance for different velocities and the black line shows the luminous intensity/illuminance for given distances. Both y-axis are valid for both curves however, the blue graph belongs to the lower (blue) x-axis and the black graph belongs to the upper (black) x-axis.

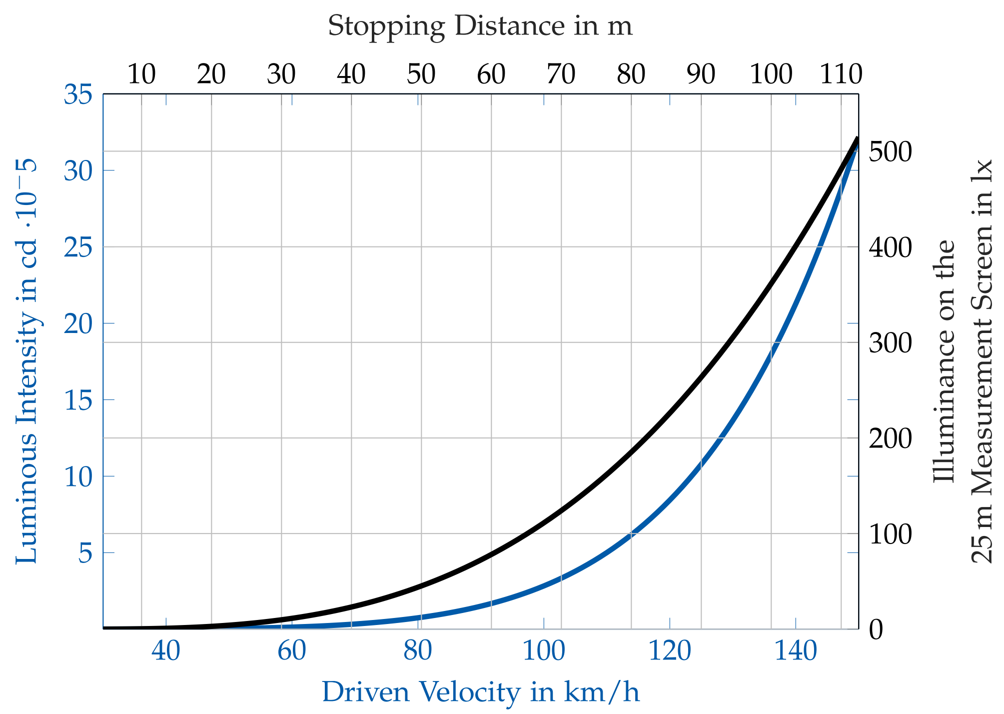

Figure 5.13 – Required luminous intensity and illuminance on the 25 m measurement screen over the driven velocity and stopping distance for safe driving at the object position. The y-axis are valid for both curves, the blue curve shows the luminous intensity for driven speed and the black curve shows the luminous intensity for a given stopping distance.

It is directly obvious, that the maximum allowed illuminance by the ECE of 344 lx or 215 000 cd per headlamp is sufficient for driving up to 150 km h^{-1} or stopping distances

of 110 m, if both hot spots of the two headlamps are indeed summed up together leading to 688 lx or 430 000 cd. However, since the brightest spot in a high beam system is actually only achieved in a very small spot with a strong decrease to both sides, this assumption will not hold true. However, even a single headlamp with a maximum of the mentioned 344 lx will be sufficient up to around 140 $\mathrm{km\,h^{-1}}$.
The second effect that should be regarded for an optimized light distribution is the illumination of the sides of the road. Since the distances measured in the field test shown here did not lead to any differences, the luminance values measured by SCHNEIDER are used to calculate the required luminous intensity values under the given detection angles. Using the luminance recordings shown in table 5.5, and the actual detection distance (line of sight) and the reflectance of the objects ($\rho \leq 5\,\%$) the required luminous intensity for the given angles can be calculated. This is already discribed in chapter 2. Using the equations 2.2 and 2.9 for lambertian objects follows:

with: (5.3)

$$I = E \cdot r^2 \quad \text{and} \quad L = \frac{\rho}{\pi} \cdot E$$

$$\text{follows} \quad E = \frac{L}{\pi} \cdot \frac{I}{r^2} \tag{5.4}$$

leading to: (5.5)

$$I = \frac{L \cdot \pi}{\rho} \cdot r^2$$

The luminance, L is measured and shown in table 5.5 and the distance, r, is the calculated and modified distance for real life driving as shown in table 5.4. This therefore allows the calculation of the required luminous intensity for all measured object angles. This is illustrated in figure 5.14 where the blue line shows the actual measurement results normalized on the required luminous intensity for the object at 3.2°. The red line shows the mirrored and extrapolated data for objects on both sides of the road with a symmetrical light distribution as a boundary condition.

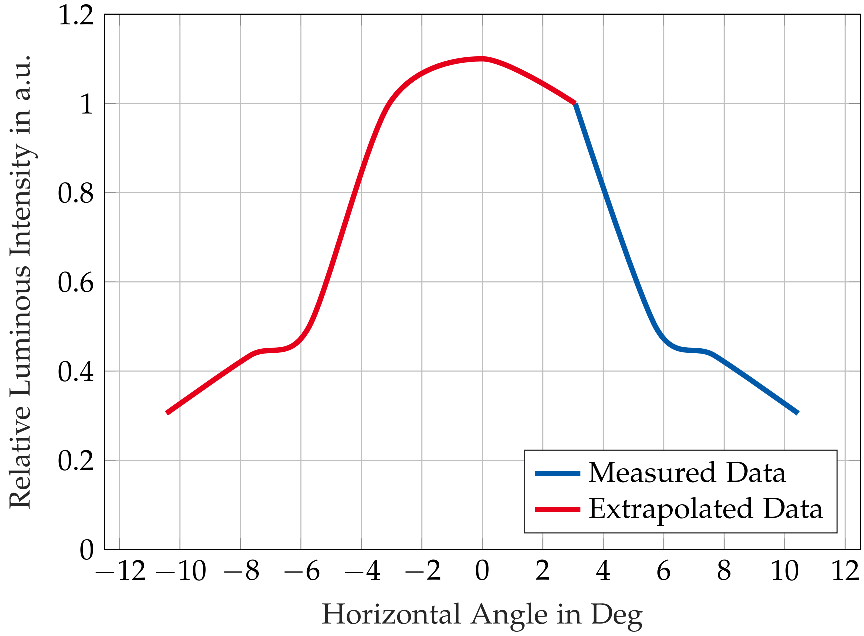

Figure 5.14 – The required relative luminous flux over different angles as calculated from data presented by Schneider. The data shown in blue corresponds to the actual, smoothed, measurement data and the data shown in red represents the mirrored data since no research was performed for objects on the left-hand side.

Combining these two findings, and the research from Huhn it can be assumed, that the best way of directing the required luminance and width for different velocities, a dynamic high beam with variable distribution is recommended. Current technologies would allow for such systems in multiple ways. They could be realized using either display technologies like DLP, TFT or much more energy efficient, scanning technology like LASER scanners where a given amount of luminous flux could be formed and directed as required. However, the proposed setup is only valid for a straight road with no other traffic participants. The next sections will focus on analysing the traffic space and objects in the traffic space to allow for a more general light distribution.

5.2 TRAFFIC SPACE ANALYSIS

The previous sections focus on the investigation of detection distances under certain conditions, with all discussed studies performed on the *August Euler* Airstrip under controlled conditions. For a valid optimization of light distributions however, it is necessary to take the real life traffic space into account. Since real traffic is composed of many different objects and may include very complex situations simulating this in a reproducible environment is nearly impossible. For this reason, in the next step, a simulation is set up, using real life traffic data. Using this simulation, a first overview over realistic traffic space is achieved and the segments for gfHBare optimization in terms of optimal illumination of the road.

In the following part, the traffic space in analysed in real life test drives. These test drives are used to collect data of curve radii, illuminance values for both day and night drives, driver's gaze behaviour and the traffic space itself. This part of thesis will only focus on the traffic space itself and the hard- and software required to record and analyse the traffic space. A more detailed discussion of the complete setup, including the test vehicle, test subject data as well as the other test equipment is given in section 5.4.

5.2.1 simulation

To get a first impression of the behaviour of gfHB systems under different traffic situations, a simulation is developed in order to test the performance of current systems and to optimize them for improved road illumination methods proposed by Moisel and Totzauer [161, 162]. This simulation is based around auxiliary conditions and presumptions. First of all, the simulation is based on real traffic data from previous work that will be described in the next sections. The simulation is based on the headlamp position to get a more precise information on where other traffic participants are located in correlation to the light sources and the whole situation is based on country road traffic. Urban traffic is too complex to get a good overview over all existing situations and on motorways, the oncoming traffic is usually separated by a centre guard rail and will therefore block most of the traffic encounters with oncoming traffic.

The gathered data on traffic volume is then further used to investigate the use of higher pixel counts and calculations for the requirements for the camera and the object recognition systems for glare free high beam systems.

simulation setup and data

The starting point for the simulation is a simulated camera with a resolution set to Full-HD (1920 by 1080 pixels) with an angular coverage of $-20°$ to $20°$ in the horizontal and $-0.6°$ to $5°$ in the vertical plane. The frame rate is kept to 10 fps. This relatively low frame rate was chosen to save calculation time and since all simulated data was done with a constant velocity interpolation between camera images is possible without any data loss. The maximum detection distance of the camera is set to 600 m and any car simulated beyond this distance is not considered for the evaluation and those frames are skipped. This distance was chosen in accordance to the data provided by Zydek and Sprute who have shown that at a distance larger than 400 m the measured illuminance at the driver's eye is negligible for low and high beam [55, 94].

The data used for the simulation is based on three major publications for the German traffic space. According to Damasky, the average lane width for a bidirectional road is 3.4 m [1]. To simulate horizontal bends, the data from Kuhl was chosen [160]. The frequency for each curve radius between ± 1000 m is shown in figure 5.15. Left hand bends are marked by negative curve radii and right-hand bends are shown with positive radii. Both sides are equally frequent since the driving direction dictates the curve direction. The curve frequency is only shown up to $\pm$ 1000 m since Kuhl considers roads with a radius above $|1000\,\text{m}|$ to be straight roads. Straight roads are assigned a probability of 67.4 %.[1, 160]

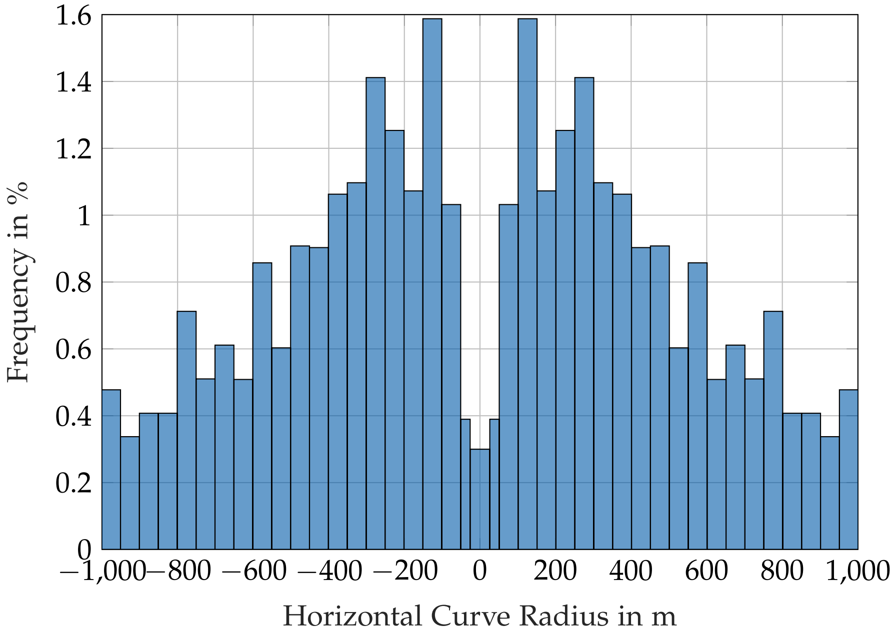

Figure 5.15 – Frequency of horizontal curves according to KUHL used for the traffic space simulation. Roads with a curve radius above 1000 m are considered straight roads. Negative curve radii represent left-hand bends, positive radii represents right-hand bends. [160]

The data for vertical curvature, domes and valleys, is taken from the work of SCHWAB and the data is shown in figure 5.16. Data with negative radii represent valleys and data with positive radii show domes. Roads with a vertical radius of over 20 000 m are considered to be flat or even roads. These even roads have are assigned a likelihood of 60 %. [159]

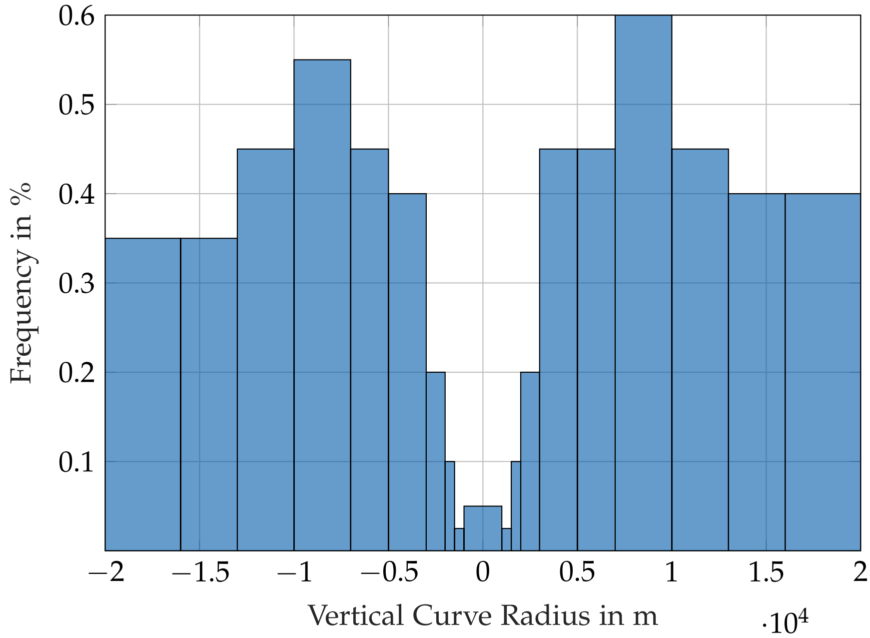

Figure 5.16 – Frequency of vertical curves, domes and valleys, according to SCHWAB [159] used for the traffic space simulation. Roads with a curve radius above 20 000 m are considered flat. Negative curve radii represent valleys, positive radii represents domes.

These geometrical traffic situations are then combined to create all possible road geometries. The resulting 903 geometrics are summarized with their frequency in table 5.6. Since no data on the actual frequency for those 903 different road geometries is available, the assumption, that the product of the probabilities for two combined situations gives the actual probability of the combined situation. As an example, a left bend with a radius between 550 m to 600 m has a probability of 0.6 % and the probability of a valley with a radius between 5000 m to 7000 m has a probability of 4.0 %. Therefore, the probability of a left-hand corner with a radius of 550 m to 600 m going into a valley with a radius of 5000 m to 7000 m is given by $0.006 \cdot 0.04 = 0.00024$ and therefore by 0.024 % .

Table 5.6 – Different traffic geometries according to KUHL and SCHWAB and their combinations.

	LEFT BENDS	RIGHT BENDS	STRAIGHT ROADS
PLANES	21	21	1
DOMES	210	210	10
VALLEYS	210	210	10
TOTAL		903	

Additionally to those 903 traffic geometries, roundabouts, with a radius of 20 m, and intersections are simulated. However, no likelihood data was acquired for these situations, therefore they are only simulated to investigate the general behaviour of cars approaching one another during those encounters but are not taken into consideration for the high beam optimization.

To simulate traffic encounters on country roads, the parameters for traffic encounters have to be set. All vehicles are simplified to cuboids with a width of 2 m, a hight of 1.3 m and a length of 5 m. The average velocity on German country roads of $80\,\mathrm{km\,h^{-1}}$ is taken for the car with the simulated camera (the *simulation car*) and oncoming traffic. In the case of a preceding car, this car is simulated with $75\,\mathrm{km\,h^{-1}}$ to ensure a change in position on the camera and the closing in on the preceding vehicle is simulated up to a distance of 20 m between both vehicles.
When approaching an intersection, both vehicles are set to drive at $80\,\mathrm{km\,h^{-1}}$ and the vehicle with the simulation car starts with a distance of 300 m to the intersection while the second car starts at 200 m before the intersection. This is done to ensure, that the vehicle fully passes the intersection right infront of the simulation car. For roundabouts, the velocity of the car in the roundabout is set to $30\,\mathrm{km\,h^{-1}}$.

SIMULATION RESULTS

In the first simulation step, each of the 903 geometric situations is simulated twice. Once for oncoming and once for preceding traffic. For each frame, the position of all 8 corners of the car are calculated. The two outer most edges are then used to simplify the vehicle to a rectangle. The position of this rectangle is then registered for all frames. As an example a left-hand bend with a radius of 1000 m up a dome with a vertical radius of 5000 m is shown in figure 5.17. The figure shows the black rectangles for oncoming and preceding vehicles as well as the road geometry. For better visualization, the vertical angles are extended to $-2°$.

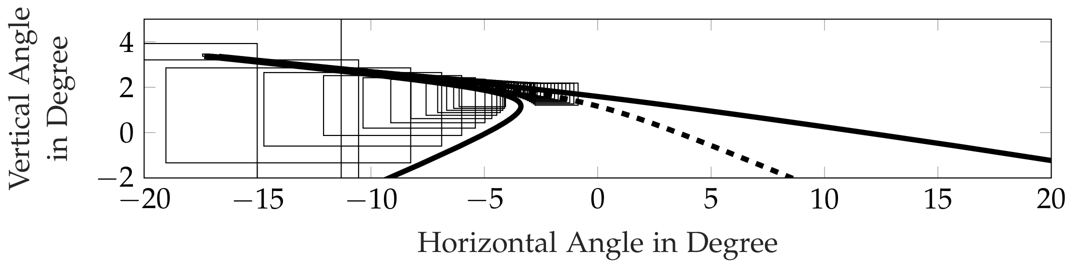

Figure 5.17 – Rectangles marking the positions for oncoming and preceding traffic for a left bend with 1000 m curve radius up a dome with 5000 m radius, simulated at 10 fps

For each pixel the frequency of vehicles registered is calculated and summed up. This is visualized in figure 5.18 for the same traffic geometry as in figure 5.17. The colour-bar indicates the amount of cars registered for each frame with the maximum count of 36 vehicles under −5.4° horizontally and 1.3° vertically. Since the goal of this simulation is to optimize the high beam segmentation, only the area relevant for high beam use is shown from here on forth.

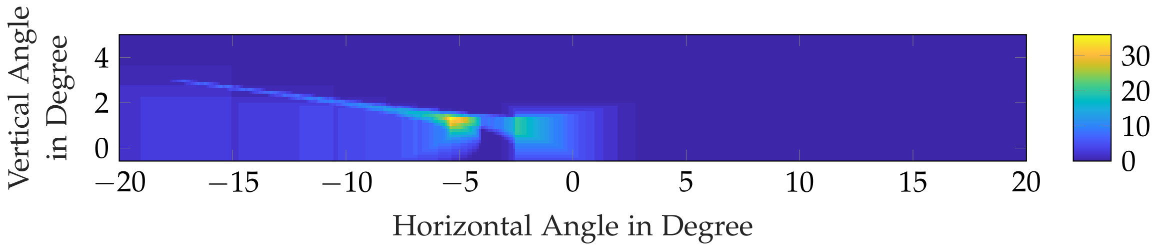

Figure 5.18 – Traffic distribution for a left bend with 1000 m curve radius up a dome with 1000 m radius. The colour bar indicates the number of cars registered for each pixel.

From this point on, the data can be regarded as a traffic density distribution, since it represents the amount of traffic for each pixel in the area of ±20° horizontally and −0.6° to 5° vertically. The data in figure 5.18 is then normalized, and multiplied by a weight factor - the statistical likelihood for each situation. All these 903 normalized traffic density distributions are then summed up to generate a mean traffic density distribution. This total density distribution is shown in figure 5.19.

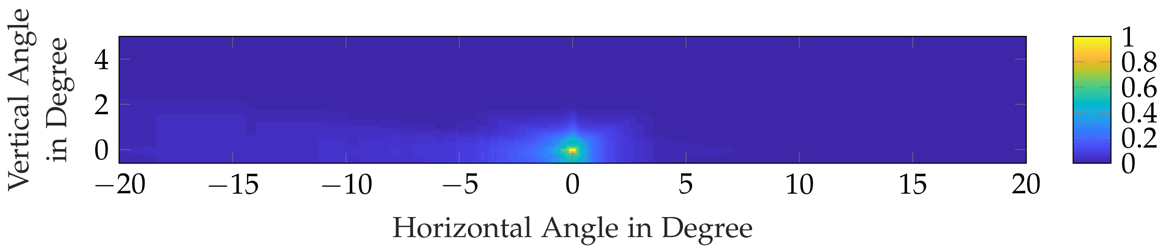

Figure 5.19 – Traffic distribution summed up for all 903 normalized and weighted geometric traffic situations. The colour bar is now showing the total percentage for each pixel normalized to the maximum probability.

In this distribution, the main accumulation point is found at directly 0° horizontally and vertically. Furthermore, it has to be mentioned, that the right side is much lower frequented than the left side. This is due multiple settings for this simulation. First of all, only single lane traffic is simulated and combining this with the right-hand side traffic that is assumed here, all oncoming traffic passes the simulation car on the left-hand side. Only a small portion of right-hand side corners leads to cars registered on the right side. Due to this asymmetric traffic density any optimization on this distribution will lead to asymmetric results. Since the main goal is to optimize the high beam distribution on this traffic space, a symmetric distribution is necessary to work well in multi lane and left-hand side traffic. Therefore, the traffic distribution is additively mirrored. This symmetrical traffic density, is now used to analyse conventional glare free high beam setups and to find possibilities to optimize them.

SEGMENT DISTRIBUTION OPTIMIZATION

Projecting the conventional, equally distributed segment distribution on this traffic distribution shows large differences of the traffic density in the individual segments. This is illustrated in figure 5.20 for a 3 by 28 segment distribution. For the shown distribution the segment with the highest traffic density reaches 168.4 % of the traffic density of the segment with the lowest traffic density. In total, this leads to a standard deviation in traffic density of 18.6 % between all segments. It needs to be mentioned, that outside of the centre hot spot, the traffic density is lower than 0.2 meaning, that only with a probability of less than 20 % compared to the centre hot spot, a segment will be disabled.

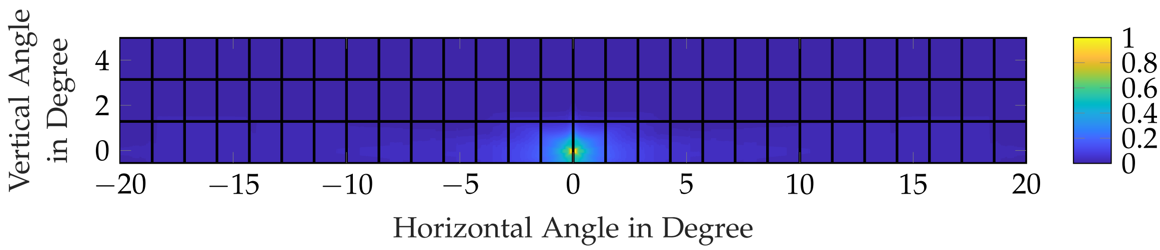

Figure 5.20 – Conventional segment distribution with equally sized segments for a 3 x 28 gfHB setup. The segment with the highest traffic density reaches 168.4 % of the traffic density of the segment with the lowest traffic density.

This standard distribution is now used as a base level for the optimization algorithm. The assumption for this optimization is, that the segment size should correlate inversely with the traffic density in the corresponding area. This leads to the optimization target, that the traffic density per segment should be equal for all segments, meaning, that all segments would be used equally often. Taking the calculated traffic density distribution into account, this leads to the result, similar to what MOISEL and TOTZAUER. The segment size will be the smallest in the centre of the high beam distribution. This would therefore enable the high beam to better mask out small vehicle movement in this area. To optimize the segment distribution in this manner, the vertical borders of all segments are set variable and only the segment width is kept constant for the rows. As an example, the 3 by 28 segment distribution is shown again with the optimized results in figure 5.21. In this example, the segment with the highest traffic density reaches only 102.2 % of the traffic density of the segment with the lowest traffic density. The standard deviation between all segments is reduced down to 0.4 %.

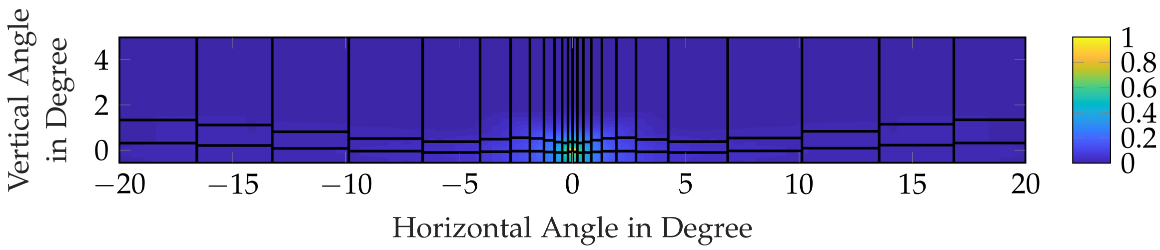

Figure 5.21 – Optimized segment distribution with flexible vertical segments. The segment with the highest traffic density reaches 102.2 % of the traffic density of the segment with the lowest traffic density.

To investigate the benefit of the proposed optimization, both, the conventional as well as the optimized segment distributions are tested against all 903 geometric traffic situations. For this test, theoretical illuminated area is calculated for every single frame. The mean illuminated area over all situations is then calculated with the statistical weighting factor discussed above.

This additional review of the segment distributions needs to be done, since due to the additive mirroring, a benefit of the optimization is not necessarily given for every situation and every segment distribution. To illustrate the possibility of a negative impact by the optimization, figures 5.22 and 5.23 show the segment switching behaviour for the 3 by 28 segment setup for the conventional and the optimized distribution. The yellow area marks segments that are switched on, the white segments mark the segments that are switched off and the black rectangle marks the position of an oncoming vehicle. The situation pictured here is a sharp right corner with a radius of 150 m, which is the reason, why the car (black rectangle) is depicted rather wide.

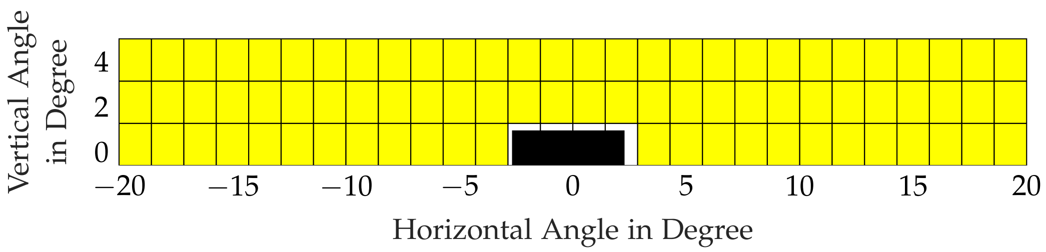

Figure 5.22 – Segment switching behaviour for the conventional segment distribution. Yellow areas mark illuminated segments, white area marks switched off segments and the black rectangle marks an oncoming vehicle.

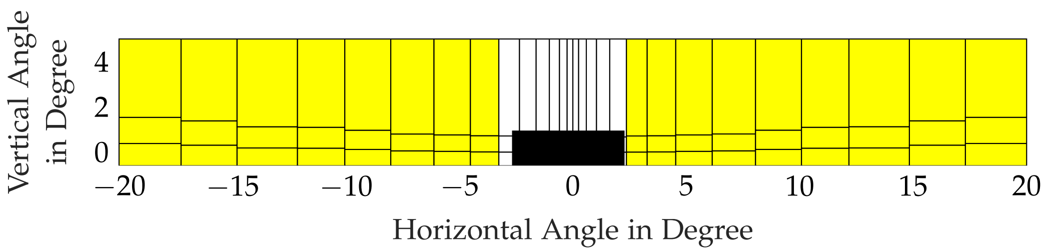

Figure 5.23 – Segment switching behaviour for the optimized segment distribution. Yellow areas mark illuminated segments, white area marks switched off segments and the black rectangle marks an oncoming vehicle.

The comparison between the illuminated area by the optimized distribution to the conventional distribution shows, for which row and column combination the proposed optimization leads to advantages. This data is visualized for some exemplary column and row combinations in figure 5.24 where the ratio between mean illuminations between both distributions is calculated.

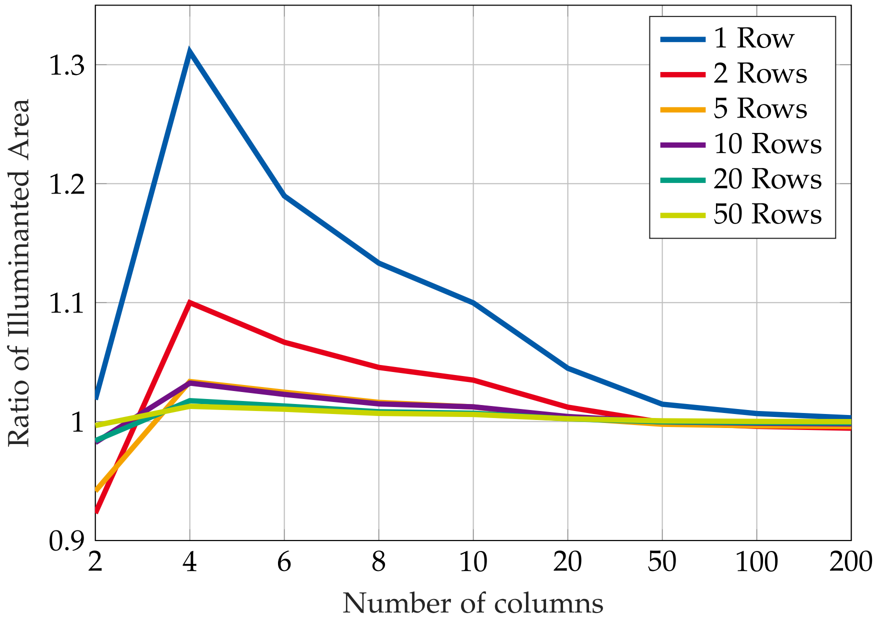

Figure 5.24 – Ratio of the illuminated surface for optimized and conventional high beam segment distributions for 1 to 50 rows and up to 200 columns.

This data shows multiple interesting points. The most obvious one is the large improvement for the illuminated area for the 1 row and 4 columns distribution. Here the mean illuminated area is increased by 31.1 %. This trend continues to the 1 by 10 segment setup, where the improvement is still at a significant 10 %. Secondly, the behaviour for 2 columns and any number of rows, where the optimization leads to less illuminated area than the conventional segment distribution. A closer investigation on this phenomenon is not performed, since setups with only 2 columns and a high row count have not been introduced to the market yet and do not seem feasible since the high beam are is, with ±20° horizontally and only about 6° vertically, much wider than high.

Further more, the fact, that the improvement diminishes for higher segment counts has to be mentioned. This is due to the diminishing size of each segment, that is optimized. The higher the segment count, the smaller the actual area that can be optimized per segment. If the range in which these segments can be optimized is lowered, the gain achievable by this optimization is lowered as well. To further investigate the benefit by the optimized segment distribution, the 1 row distributions are discussed in a more detailed level, since they offer the best improvement for road illumination. Therefore, the illuminated area is directly compared for both distributions. This data is then used to find different segment counts for both distributions that lead to the same illumination of the road. This is visualized in figure 5.25 where the average normalized illumination achievable by the conventional high beam distribution shown by the blue, solid line. The red, dashed line shows the possible illumination with the proposed optimized high beam setup.

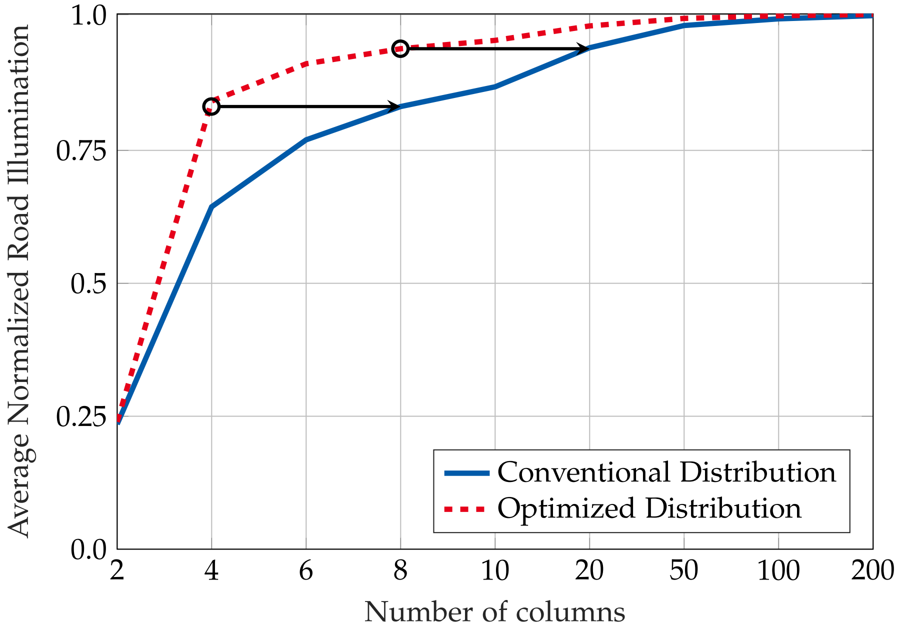

Figure 5.25 – Comparison of the average, normalized road illumination for a conventional high beam setup (blue solid line) and the optimized distribution (red dashed line) for a one-row setup.

The results show clearly, that in any 1 row configuration, the optimized distribution leads to a higher average road illumination compared to the conventional distribution. For example, a 4 column setup performs equally when optimized as a conventional 8 segment setup. The same can be found for 8 optimized segments where the corresponding conventional segment distribution is a 20 column setup. This is marked in figure 5.25 by the two arrows. Continuing this even further, an optimized 20 segment high beam can perform as well as a 50 segment conventional high beam. This shows, that at least for the different isolated situations that are investigated here, the standard gfHB does not lead to the maximum amount of road illumination and that there is room for improvement when reviewing a given segment number.

While a chip layout with different sized LEDs is unlikely and difficult to manufacture, the same result could be achieved via optics only. Since the segments at the centre of the light distribution are smaller, this would lead to a higher luminous intensity in the center of the light distribution. Due to the increasing size of the segments to the sides of the distribution, a smooth decrease in luminous intensity is achieved naturally. If further alterations to the intensity of the single segments need to done, this can be achieved using Pulse Width Modulation (PWM) since this functionality is integrated for the use as a gfHB system anyway.

Another big question that can be reviewed using the set up simulation is the influence of the pixel count on the road illumination.

SEGMENT COUNT

In this section, the focus will be shifted away from the segment distribution. For the following investigation only the conventional segment distribution is used, since this is, as shown in figure 5.25, a worst case scenario. This leads to a higher needed pixel count than the optimized distributions. For each segment distribution of the mentioned 1 to 50 rows and 2 to 200 columns, the normalized average illumination is calculated. The maximum illumination found for the 903 traffic situations is 77.2 %. However, this only includes situations with one vehicles in each frame. The illumination in real traffic will differ significantly since these situations can contain multiple objects as well as other frames containing no objects.

Since some of these column combinations will lead to the same total pixel count, the mean value for these pixel counts is calculated. Furthermore, the maximum possible illumination and the minimal possible illumination are calculated for pixel counts, where more than one distribution is possible. The results of this calculation are shown in figure 5.26, where the blue dots shows the mean illumination for a given pixel count and red line shows the minimal relative illumination achievable and the yellow line indicates the maximum illumination possible.

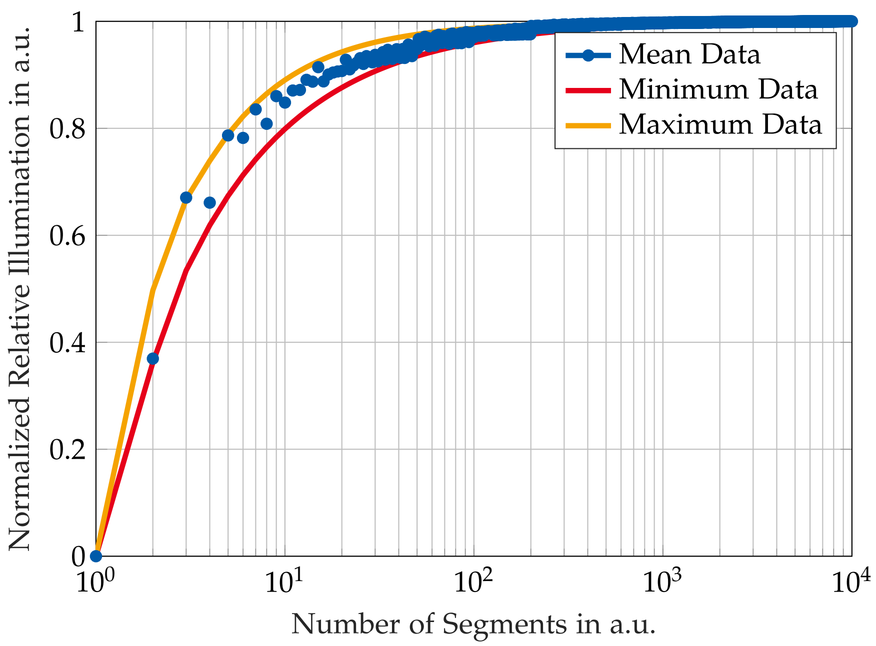

Figure 5.26 – Mean average normalized road illumination over the total pixel count per segment distribution. The whiskers indicate the standard deviation.

This data shows, that the average illumination, compared to the 1000 pixel setup, rises rapidly to around 100 pixels. After that a saturation a achieved with more than 95 % illumination. A 99 % illumination level is achieved with 201 pixels in a 3 by 67 combination. It has to be discussed how ever, that a simple increase in pixel count, does not necessarily lead to an increase of road illumination. The first example of this is found between three segments and four. If the four segment configuration is chosen as a 1 by 4 setup, an illumination of 73.9 % is calculated. If a 2 by 2 setup is chosen, the illumination decreases to 61.9 % which is lower than the illumination achieved by the 1 by 3 setup with 67.0 %. This trend is found for different nearly every configuration. The overall configuration that is found however is, that a distribution with a lower or medium amount of rows is to be preferred.

With this information, it can be concluded, that for pure illumination aspects, and pixel count higher than 201 yield no additional benefit. However, this does not include any benefit from smoothing edges, adding information for the driver into the light distribution or similar.

The next step will focus on the technical requirements for such a system to work in real life conditions.

REQUIRED SYSTEM RESPONSE TIMES

The previous section shows, that the highest necessary pixel count is around 200, and that the illumination on the road can be significantly improved by modifying the boarders for every single segment. However, this did not take into account, how fast segments need to be switched. The smaller the segments are, the faster vehicles will leave the segment and the next segment needs to be switched. Therefore, the 903 simulated geometrical situations as well as traffic encounters at roundabouts and at intersections are investigated for their angular velocities. This data is then used to calculate a maximal system response time for the headlamp systems if all traffic participants should be masked out of the high beam distribution successfully.

For this, the change in position of all four corners for each vehicle between two frames is calculated. With the constant frame time, the change in degrees per second is calculated. Analogue to the calculations for the traffic density, each situation is weighted with their statistical likelihood. While changes in angular positions arise for both vertical and horizontal movement, the horizontal movement is ten times higher than the vertical movement. Additionally, the horizontal resolution is, usually, higher than the vertical one.

The cumulative likelihood of the horizontal velocities is shown in figure 5.27. From this diagram the respective probability for each velocity is easy to extract. The median of the data is shown by the 50 % threshold with $0.2\,°\,s^{-1}$ a mean velocity of $2.8\,°\,s^{-1}$ and a 99 % velocity of $13.2\,°\,s^{-1}$. While for real data, a smooth curve would be expected, the simulated data shows a kink at about $1.1\,°\,s^{-1}$ and 66.4 %. At this angle, 95 % of all simulated velocities for the straight road simulation are recorded. Larger velocities are only recorded in single frames at the outer most edges. Due to the higher probability of straight roads, this leads to the kink in the cumulative velocity distribution.

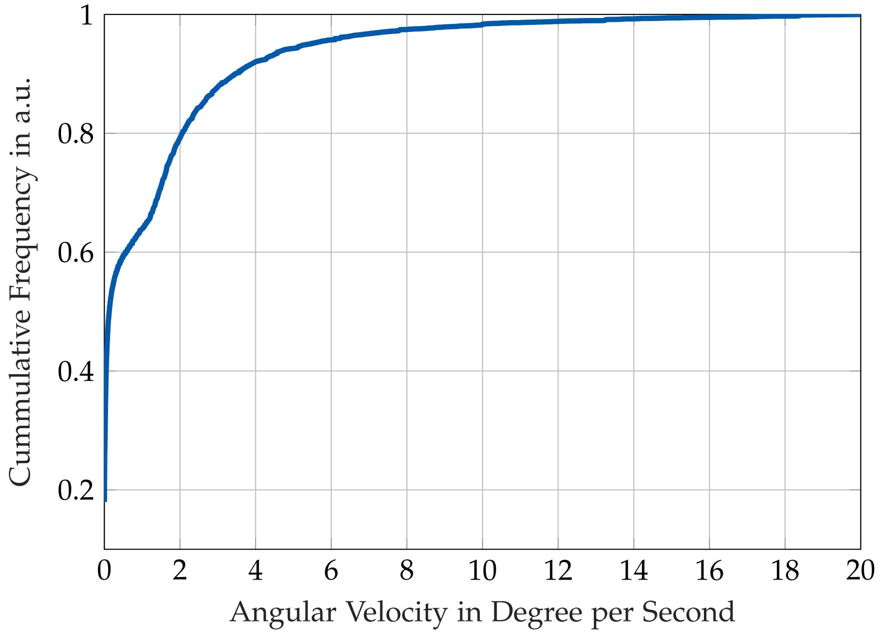

Figure 5.27 – Cumulative likelihood for the horizontal angular velocities statistically weighted for the simulated 903 geometric situations.

This data can now be expanded by the additional situations intersection and roundabout. Since for both data sets, no statistical likelihood can be found, these situations are reviewed separately. The most important results are represented in table 5.7. Here for the three parts, the mean velocity, the maximum velocity and the 99 % velocity are listed. This shows, that both the highest mean and highest 99 % velocity are recorded at intersections. One major remark has to be made to this data set. All of the highest velocities are recorded at the outer edges of the light distribution - at ±20°. This is to be expected since here the largest angular displacement between the test vehicle and an oncoming vehicle are recorded.

Table 5.7 – Simulated horizontal angular velocities for the 903 situations (normal) and the two additional traffic encounters at roundabouts and intersections.

	NORMAL	INTERCEPTION	ROUNDABOUTS
V_{mean}	$2.8\,°\,s^{-1}$	$9.1\,°\,s^{-1}$	$3.0\,°\,s^{-1}$
V_{max}	$90.0\,°\,s^{-1}$	$20.3\,°\,s^{-1}$	$5.1\,°\,s^{-1}$
$V_{99\,\%}$	$13.2\,°\,s^{-1}$	$16.7\,°\,s^{-1}$	$4.8\,°\,s^{-1}$

With these values, the necessary system response time can be calculated for different segment setups. This means, that the system needs to be able to detect on position changes of other traffic participants that exceed the angular limits of one segment and react to it. Therefore, the segment size at the position of the highest angular velocity is looked up and the time needed for a vehicle to enter and leave this segment is calculated.
As a worst case scenario, the conventional segment distribution is taken for this. Since all segments are equally large, this distribution has smaller segments at the outer edges than the optimized distributions. Since the findings above indicate, that the maximum number of segments needed for a 99 % illumination is 201 in a 3 by 67 segment distribution, this distribution is taken for this calculation. Using a distribution that is ±20° wide and has a height

of 5.6° (from −0.6° to 5.0°) leads to the segment size of 0.6° by 2.0°. If the glare free high beam should now correctly cut out 99 % of all simulated situations, the total response time of the system needs to be lower than 46 ms. If the response time and the calculation for the object recognition software are ignored, this would already lead to a required frame rate of 21 fps. If a cut out of intersections is required as well, this leads to a reaction time of 35 ms or a frame rate of 29 fps. If the optimized light distribution is used, the largest segment size is increased to 1.3° at the outer edges and thereby more than doubles the possible system latency to 100 ms or a frame rate of 10 fps for the standard situations and 80 ms or 12.5 fps for intersections as well. This means, that the optimized light distribution not only delivers a better illumination for the driver but also taxes the system much less.

5.2.2 REAL TRAFFIC SPACE

Since the optimization on the simulated traffic space leads to promising results with significantly improved road illumination and as well as giving valuable insight on possible segment setups and required system performance, a study is composed to evaluate the real traffic space in Germany. For this, a testing vehicle is equipped with a stereo camera system to record the traffic space during test drives. The recorded video data is then analysed for other traffic participants to calculate a similar traffic density distribution as shown in section 5.2 for the simulation. A stereo camera system is used for future research to estimate the distance to the recorded objects. While all data is already recorded with the stereo setup, the evaluation of the distance data is not implemented yet and will be subject for future research. The setup, the software used and the results from this study is described in the following sections.

STEREO SCENIC CAMERA

To set up a stereo camera system within the test vehicle without interfering the driver's vision is crucial for this part of thesis. Since this test vehicle is used to record the driver's gaze for different conditions such as day and nighttime (section 5.4), the camera needs to be able to record data in these lighting conditions.

MECHANICAL SET-UP AND RESTRICTIONS

The cameras selected for this purpose are GigE uEye cameras with a Sony sensor with a 2056 by 1542 resolution since this camera allows for complete control of all camera parameters via multiple programming applications. The cameras are used with an 8 mm lens from Fujifilm to allow filming of at leas ±20° horizontally and 6° vertically to record the high beam area. For these two cameras, a mounting system is designed, that fits both cameras besides the rear view mirror and thereby influencing the driver's viewing area very little.

RECORDING SOFTWARE

The software developed for the stereo system needs to record full sized stereo videos with a high frame rate (25 fps). To synchronize the recorded frames, the frame number, the system time stamp and the exposure for each frame, are written into a text file. The time stamp and the frame number are used to synchronize the frames to the GPS time stamp, which then offers the possibility to synchronise the recorded video data to the illuminance data, the GPS data to identify different road geometries and the eye tracking data.

OBJECT RECOGNITION SOFTWARE

In order to evaluate the large video data set, an automatic object recognition software is implemented. The used software is then supposed to identify the following objects out of both, day and night videos.

- **pedestrians**
- **cars**
- **buses**
- **trucks**
- **motorcycles**
- **bicycles**
- **cyclists**
- **traffic signs**

To do this, two data sets are used. As a base line, the *Cityscapes Dataset* is used [168] and to further optimize the image recognition on the used camera system training from the recorded data sets are marked by hand. One of the major challenges to overcome for this setup is the large difference in the image between daytime driving and nighttime driving. The difference in contrast and exposure for the camera makes it difficult to use the same software to identify objects during both time slots, as shown in figure 5.28a and 5.28b.

(a) **(b)**

Figure 5.28 – Example images from typical scenes during (a) daytime driving and (b) nighttime driving.

For this reason, the object recognition software is setup and trained twice, once for each time slot. For this, 250 images recorded during the day and 250 images recorded during the night are marked by hand. From these pre-marked images, 70 % are used for training the algorithm and 30 % are used for evaluation.
For the object recognition, the recorded videos are split up into single images and using the trained model, Region of Interests (ROIs) are defined using the sliding window and the Intersection of Union (IoU) method. These are then filtered and objects are recognized and their pixel coordinates are written into a text file, including all the necessary information. This contains the information generated by the image recognition but also adds the information recorded by the recording software like time stamp, exposure and frame number. A float diagram of how the software works is shown in figure 5.29.

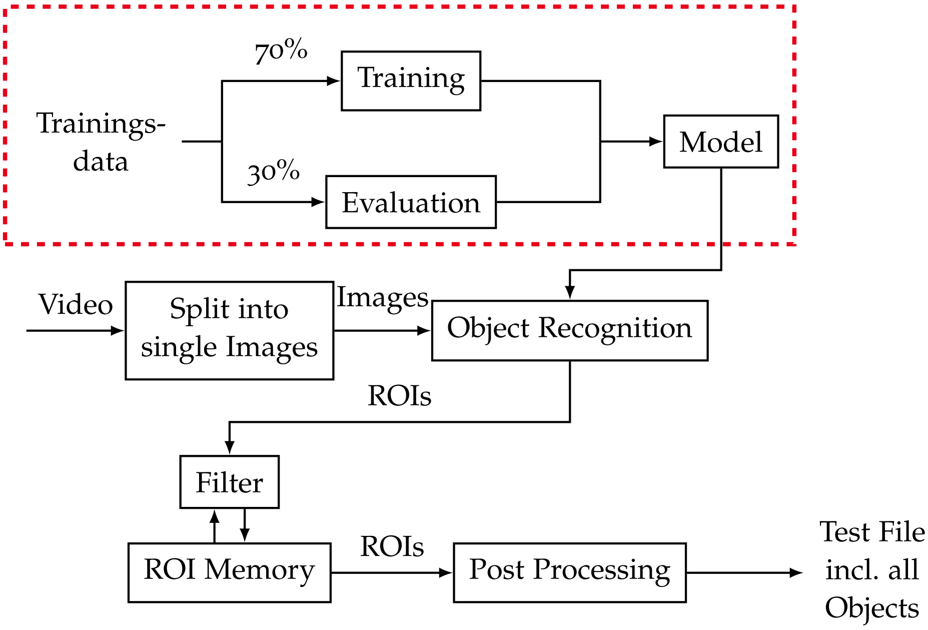

Figure 5.29 – Float diagram on how the algorithm for object recognition works starting with the training data sets to build a working model, using the video to extract single images, define ROIs and writing a text file that includes all the necessary information.

This is all done using the Tensor Flow framework with the Object Detection API. Describing the fundamental method of the object recognition in the tensor flow model would go beyond the scope of this thesis and the interested reader is referred to more subject-specific publications. [169–173]
A sample image of of the working algorithm is presented in figure 5.30, where several vehicles, traffic signs and pedestrians (persons) are marked.

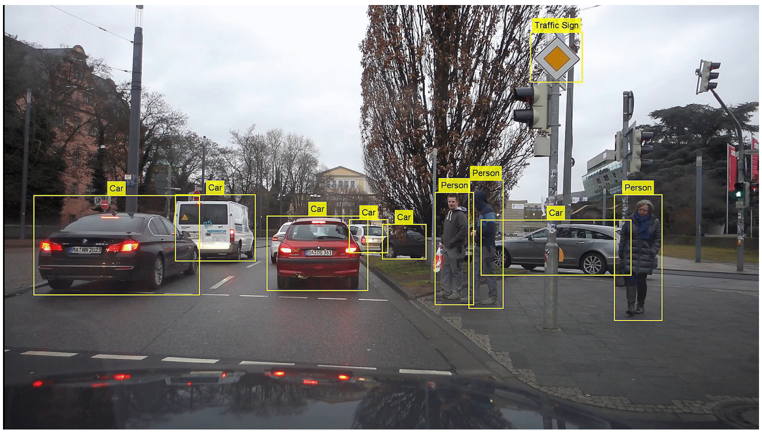

Figure 5.30 – Sample scene as recorded and evaluated with the object recognition software from an urban environment. The marked objects in yellow include traffic signs, vehicles and pedestrians (persons).

As mentioned above, the performance of the algorithm is tested with pre-marked images. The results for the overall classification rate is shown in blue in figure 5.31 where the dashed line shows the original data, and the solid line shows the same data smoothed by an moving mean filter. This is done, to avoid the high level of noise induced by the individual images and to identify solid trends to evaluate the potential performance of the system with further training.

Table 5.8 – Average performance for object recognition over all eight object classes.

OBJECT CLASS	AVERAGE PERFORMANCE
Pedestrians	39 %
Cars	64 %
Buses	47 %
Trucks	45 %
Motorcycles	38 %
Bicycles	30 %
Cyclists	41 %
Traffic Signs	24 %

The data shows, that the overall detection performance is at around 40 % and that the overall performance is not rising with more data sets. Therefore, it can be concluded, that further training with more data samples will not increase the performance significantly. While the performance of 40 % seems rather low, comparing this to state-of-the-art models with similar training data shows, that this value is to be expected [174]. This low recognition performance requires additional investigation. For this reason, the performance is analysed for each object class individually. The results for this are shown in table 5.8.

The results show vast differences between the different object categories. These difference have different origins. While cyclists, motorbikes, trucks and buses have relatively low recognition rates due to the lack of training data, the low rate for traffic signs can be explained with their large variability. Since the traffic signs can differ in size, form and colour, in urban environments at least, advertisement and billboards can be mistaken for traffic signs as well. In some cases, advertisement on trucks and buses are recognised as a traffic sign as well.

On the other hand, cars all follow the same overall form and the data set for them is the largest one available for this thesis. The recognition rate of cars is therefore by far the highest with over 64 %. The data is visualized in figure 5.31, where the general performance (blue) is compared to the individual performance for traffic signs (red) and cars (yellow) with the smoothed data shown in solid lines and the real data shown as the dashed lines.

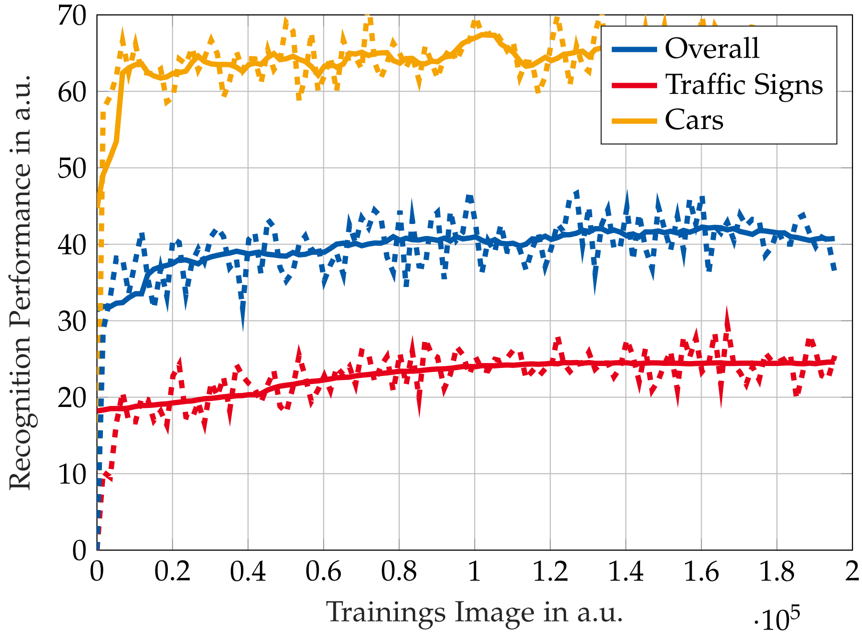

Figure 5.31 – Overall performance of the object recognition algorithm over all eight different object classes. The recognition performance shows the percentage of the correctly detected objects over the images used for training.

In order to transfer the pixel position of the recorded objects, it is essential to calibrate these coordinates to real life angles. This also included the calibration of the distortion caused by the lens. This calibration is done using a custom chessboard at the size of 2.0 m x 2.0 m and the MATLAB CAMERA CALIBRATION TOOLBOX. Two simultaneous images are recorded with both cameras and a total of 27 images per camera, 9 images at three distances, are used for the calibration routine.

This calibration method leads to a slightly different field of view as theoretically specified by the combination of camera and lens with a horizontal field of view of 46.8° horizontally compared to theoretical58.4° and 36.0° vertically compared to the estimated 44.6° which is still within the needed range of 40° x 20°.

ROAD GEOMETRY

While the exact road geometry is analysed in section 5.4, the basic route will be described here to understand the basic composition of the data shown. The route, as depicted in figure 5.32, starts in DARMSTADT (green circle), then goes over large sections of motorways (starting at point B) into the country side. At the TAUNUS (point C), the motorway is left and country roads are used to drive through the hilly and curvy region. Then a large section of pretty much straight country roads, starting shortly after point D, is followed all the way into the city centre of FRANKFURT. From FRANKFURT another stretch of straight road is followed back south to DARMSTADT. This complete route splits up into around 49 % of the time driven in urban areas, 29 % on country roads and only 22 % on motorways. The exact conditions used to assign sections into the different categories are explained in 5.4.

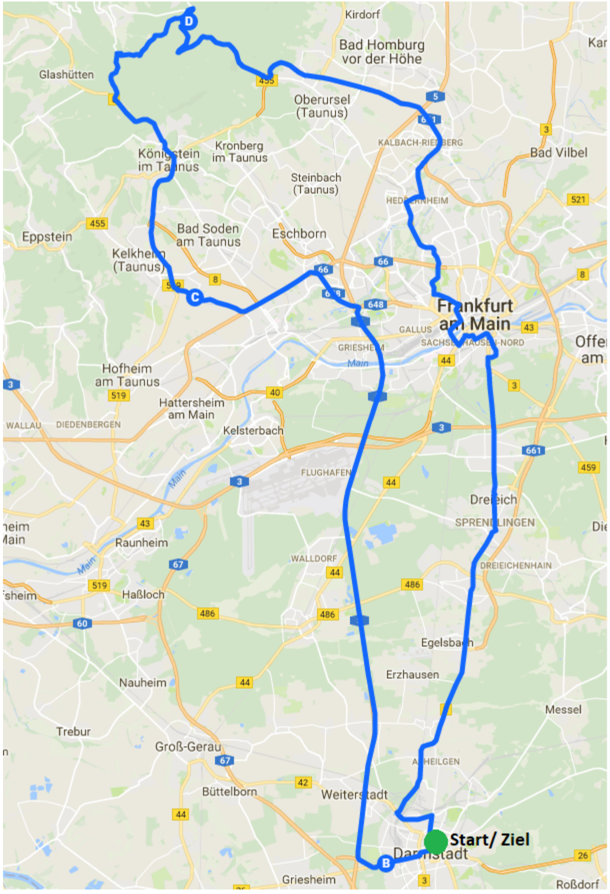

Figure 5.32 – Route selected for the test drives. Starting at Darmstadt (green dot) going to point B over the *A*5 into the Taunus and back through Frankfurt to Darmststadt.

While the simulation shown previously was only performed for single lane country roads, the real data is split into different sections, urban traffic, country roads and motorways. The first traffic analysis however is done for the overall distribution.

traffic space analysis

Before calculating and analysing object distributions in the overall traffic space, the first analysis is done regarding the relative frequency of all of the eight object classes. This is done for overall data, urban roads, country roads and motorways for day and nighttime data separately. To do this, each recorded frame is evaluated and checked if at least one object of each class is found in the frame. If more than one object of a single object class is detected in a frame, it is still only regarded as one detection. Otherwise the results could show more objects of a particular class than there are frames. The relative frequency of traffic signs and cars is shown in figure 5.33. To keep the data simple only the two major object categories are shown. The rest of the categories have overall frequencies of less than 10 % with the exception of trucks which have an overall frequency of around 20 % during the day.

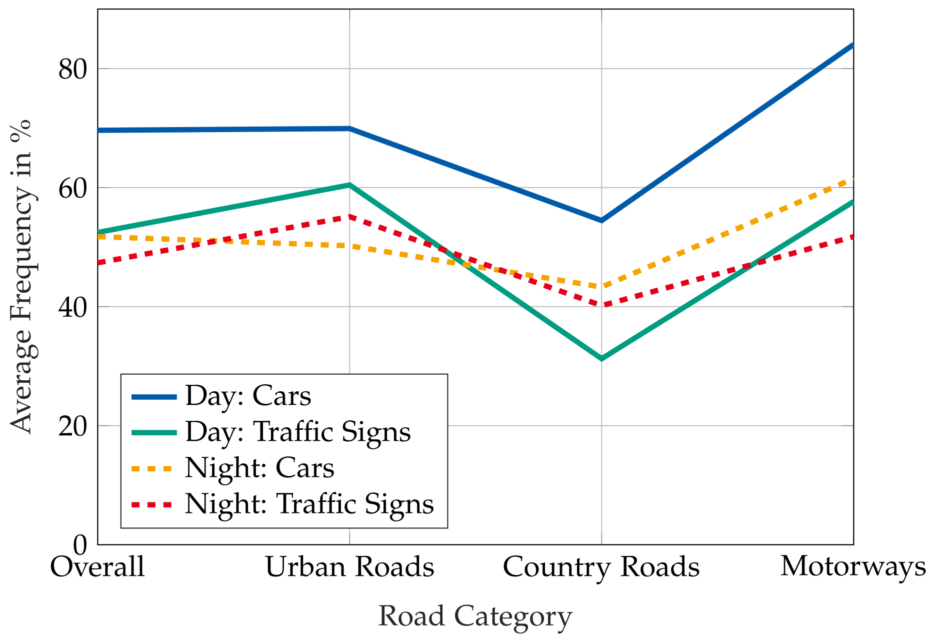

Figure 5.33 – Relative Frequency for cars (blue solid line day and orange dashed line night) and traffic signs (green solid line day and red dashed line night).

This data shows, that the frequency of objects is highest on motorways with just under 85 % off all images containing cars. The second highest object density is recorded on urban roads with around 70 %. The lowest object frequency is recorded on country roads with 60 %. The general behaviour is mirrored for nighttime drives with a reduction by 15 % to 20 % for all data sets. This behaviour of similar ratios between the road categories but lower overall frequency is seen for all object classes with an exception for traffic signs which of the same frequency during day and night. The differences between the two measurements arise through false detections or objects blocking off traffic signs.

While this frequency of images containing one or more object is relevant for the overall high beam usage, the general distribution of how many objects of a certain class are detected by the camera system relevant in terms of high beam segmentation and optimization. For this, frames with one or more objects are re-evaluated. As figure 5.33 shows, only cars and traffic signs are relevant objects for nighttime driving. For this reason, both distributions are shown as histograms in figures 5.34a and 5.34b respectively. For both figures, the data recorded during the day is shown in blue and the data recorded at night is represented by red bars.

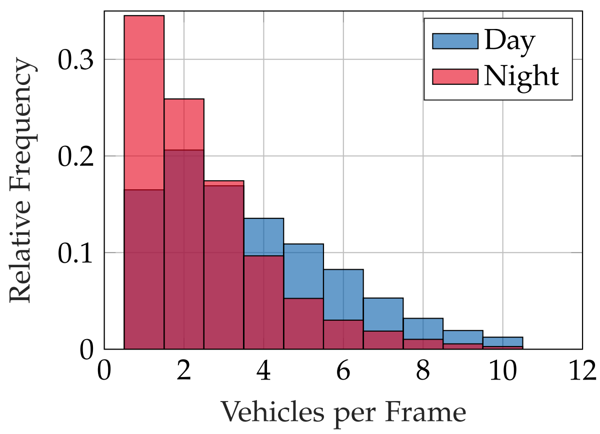

(a)

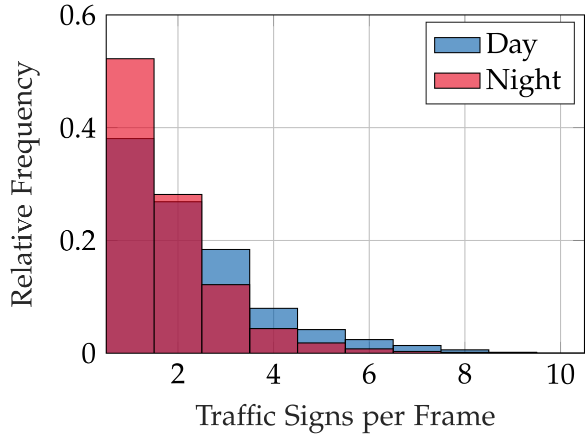

(b)

Figure 5.34 – The frequency of camera frames containing different amounts of (a) vehicles and (b) traffic signs for daytime recordings (blue) and nighttime recordings (red).

For both distributions, a clear trend of a decreasing amount of frames containing more than one object of each category is seen. The distribution for day and night data is exactly the same for traffic signs with 92 % of all images containing three or less traffic signs. The distributions are rather similar for vehicles, with a slight difference, that during the day, more images contain two vehicles than a single one. Furthermore, the 90 % threshold is only achieved at five vehicles or less per image.

While this data contains information on how often and how many certain objects appear during different situations, this does not yet contain any information on where these objects are located. Therefore, the next step is, to generate object distributions similar to the ones shown in the simulation part of this optimization. For the object distributions, all vehicle data, including cars, trucks and buses are treated equally since the headlamp behaviour when encountering one of them is the same. The object distributions are generated for nighttime recordings only since headlamp optimization is only necessary for this data set. The distributions are firstly analysed for overall data, then for the different road categories. For these distributions, only two object types are reviewed: vehicles as described, containing cars, trucks and buses, and traffic signs. For high beam segment optimization pedestrians and cyclists are irrelevant and their distribution is analysed in the gaze distribution section.

Overall traffic and object distribution

Since vehicles and traffic signs can be treated differently using gfHB systems, and doing so can lead to significant safety benefits [175], their distributions are analysed separately. Figure 5.35 shows the overall recorded distribution of vehicles for the complete route including all 54 test drives. The colour coding of all following distributions is the normalized colour coding as shown in figure 5.19. Since the test drive was set up unequally in terms of time spent in each road category, leading to different amount of data recorded in each category, this is corrected by normalizing the data on the average data length in each category. It becomes evident, that the major traffic density is not located in the centre of the viewing area but shifted to the left with the highest density recoded at $-2.5°$. Furthermore, when comparing the results to the distributions achieved by the simulation shown previously, a much higher traffic density is recorded at the outer edges of the reviewed area.

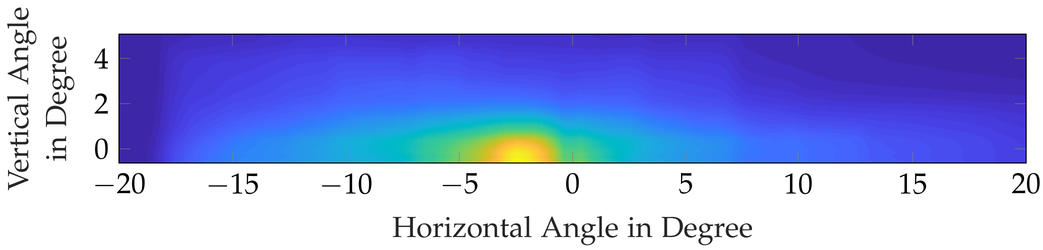

Figure 5.35 – Vehicle distribution over the complete route including urban roads, country roads and motorways and the data from all 54 drives at night.

From this point on, distributions like light distributions, object distributions and gaze or fixation distributions are all shown normalized to the maximum value with the colour coding as shown in figure 5.21 While the simulation was developed in order to simulate general vehicle distributions, no solid data was found regarding the positions of traffic signs. The data shows, that nearly all traffic signs are recorded above the horizon and only a neglectable amount of signs is found below the horizon when driving over a dome. This traffic sign distribution is shown in figure 5.36. Furthermore, the majority of traffic signs is found to the right side of the driver, as expected for right-hand side traffic. The traffic sign density on the left side only reaches about 50 % when compared to the right side.

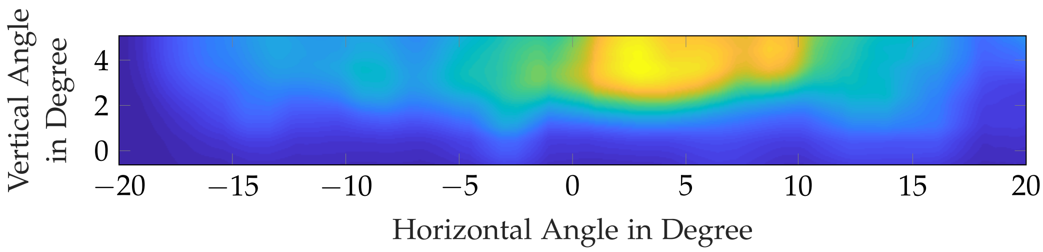

Figure 5.36 – Traffic sign distribution over the complete route including urban roads, country roads and motorways and the data from all 54 drives at night.

Comparing this data to the data shown by Damasky reveals similar distributions for both approaches, as the work by Damasky also shows a large portion of the traffic signs being located to the right-hand side. Nonetheless, it has to be mentioned, that the approaches on how to calculate the distributions are significantly different. The data presented here is achieved by checking every single image of the recorded video files for traffic signs and marks their positions. This leads to the situation, that traffic signs that are visible in successive images, are evaluated multiple times at different distances. For this approach, this is the only valid approach since drivers and headlamps will also experience traffic signs under these conditions. The data presented by Damasky however, was calculated by estimating theoretical angular position of each recorded traffic sign under for a fixed distance (50 m). Each traffic sign is therefore only evaluated once.

While this data now includes all data recorded and weighted with the same factors, it might not be a viable option to optimize the segment distribution on this overall data, since high beam or gfHB should not be used in cities. For this reason, the data is now split up into the three major road categories and evaluated for each situation separately. This then enables optimization of the gfHB on different types of road infrastructure or weighted optimization depending on the main intended use for a certain vehicle.

URBAN ROADS

Starting with urban roads, the distribution of vehicles is not significantly different from the overall distribution. Just as shown by the overall data, the major traffic is located just to the left side of the centre and just above the horizon. However, much less traffic recorded in the top corners, especially on the right side and under high vertical angles. This is due to mostly flat roads in cities as already described by KUHL. However, the distribution measured in urban areas is wider than the overall distribution. This is due to corners in cities that can include much lower radii compared to the other road categories. This traffic distribution is shown in figure 5.37.

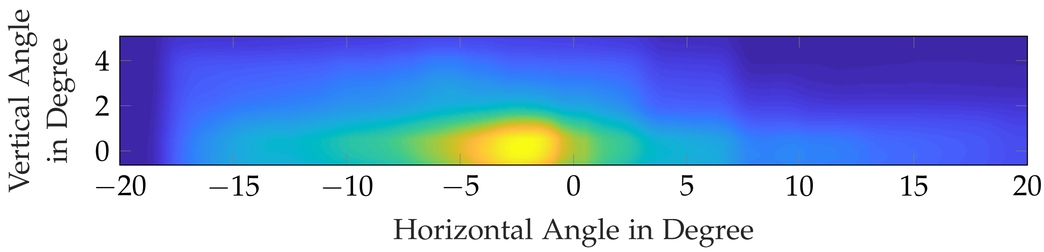

Figure 5.37 – Vehicle Distribution on urban roads for all 54 test drives.

Reviewing the traffic sign distribution reveals the largest difference between the overall distribution and a single road category. Two major factors influence the distribution of the detected traffic signs. First of all, the amount of traffic signs is the highest for urban roads. Secondly, a large portion of the urban part is driven on one way streets, resulting in traffic signs on both sides of the roads. Additionally, to this, the algorithm, as shown above, is not completely stable in terms of recognizing traffic signs and especially in urban environments, where store signs and advertisements are present in a significant amount, the correct detection rate is relatively low compared to the recognition rate of vehicles. The traffic sign distribution is shown in figure 5.38 where this effect is evident.

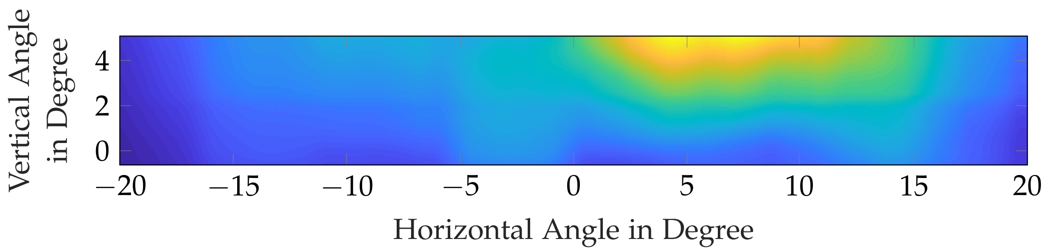

Figure 5.38 – Traffic sign distribution on urban roads.

For this distribution no major point in the distribution is found. Traffic signs are much more equally distributed and the right side only has a slightly increased object density. Furthermore, single traffic signs are visible in the distribution. This effect occurs during standing times at intersections, traffic jams and red traffic lights, that occur rather often in highly populated areas and roads as driven in Frankfurt. While this effect can easily be removed by setting an additional flag dependent on the current velocity, the choice to include these situations is made due to the fact, that drivers will experience these increased exposure times in the described situations as well.

In this section, it needs to be discussed, that the relevance of these distributions in urban areas might not be obvious at first glance. While the use of high beam in this area is currently forbidden, and road lighting should indeed lead to sufficient illumination, the analysis of different objects in urban roads is of relevance for other optimization goals as discussed in the following chapters. The major optimization target here is the optimization of the low beam part of a light distribution, and this will be discussed in later sections. However, for completeness of the data, the distribution are shown here.

COUNTRY ROADS

In terms of high beam optimization, the more relevant part of this analysis includes the data for country roads. The overall distribution of vehicles on country roads is shown in figure 5.39. This distribution shows large similarities to the overall vehicle distribution with the overall maximum being at the same position as above. However, the complete distribution is significantly smaller and nearly no vehicles are found under large angles, both horizontally and vertically.

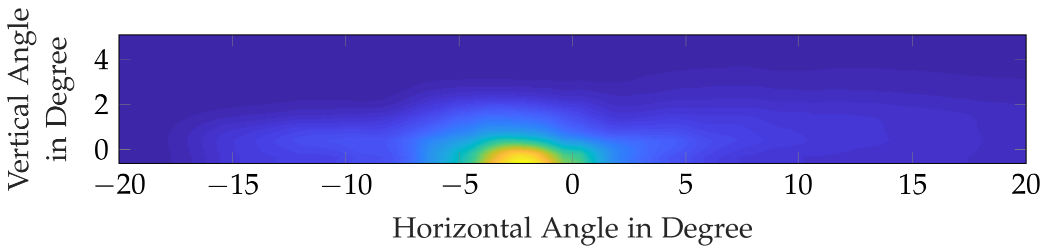

Figure 5.39 – Vehicle Distribution on country roads for the 54 nighttime drives.

Since this situation is exactly the situation as the simulated one, these two sections are need to be compared in greater detail. The distribution achieved by the simulation, shown in figure 5.19, still shows significant differences to the one recorded here. The simulated distribution shows the maximum as a very small area in the centre and rapidly decreasing density from there on outwards with a much higher distribution on the left side and close to no vehicles recorded at 5.0° or more horizontally. The traffic distribution measured in this section however, shows a much wider hot spot, shifted to the left side. Additionally, to that, the density of vehicles at larger angles, both vertically and horizontally is significantly higher. The main difference between the simulation and real life traffic can be put to several major points. First of all, only one vehicle at a time is simulated while the real traffic data can detect up to 12 vehicles. Furthermore, the simulation always assumes perfect visibility into corners, on straight roads and up domes or down valleys. On real roads, the view is often blocked by trees houses, or traffic up front therefore significantly influencing the vehicles position, that can be detected.
Reviewing the traffic sign distributions for country roads reveals a completely different distribution compared to the overall or the urban distribution. As seen in figure 5.40 a large area containing most of the traffic signs is found, starting at 2° horizontally and vertically, and going up diagonally to 4° vertically and 7° horizontally. This is explained by the German street layout. Most of the driven country roads are single lane roads with all traffic signs on the right-hand side. For straight roads, this means that traffic signs are detected around the centre, and when closing in on the traffic sign, the angular position is shifted up to the top right. The shown distribution therefore only shows the average angular movement of traffic signs.

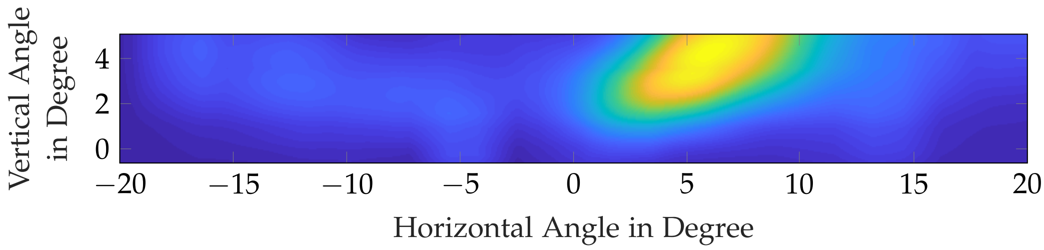

Figure 5.40 – Traffic sign distribution on country roads.

Similar to the distribution seen in urban roads, this distribution shows single, highlighted traffic signs at certain positions. The reason for this is identical to the one in urban roads. However this occurs much less frequent since traffic lights and traffic jams are less frequent as well.

MOTORWAYS

Investigating the distributions on motorways, an unexpected distribution is found. The vehicles recorded lead to a significantly wider distribution than those from urban and country roads with wing-like shapes left and right to the hot spot. It was be expected, that due to the straight nature of motorways, the distribution is much more focused to the centre and with less traffic on the sides. However, due to the multiple lanes on the motorways, with up to 5 lanes in some cases, overtaking and passing is much more frequent. Since this is true for overtaking and being overtaken with more or less equal probability, the distribution is widened up. Furthermore, the frequency of trucks is the highest on motorways and therefore increases the height of objects seen. This overall distribution can be seen in figure 5.41.

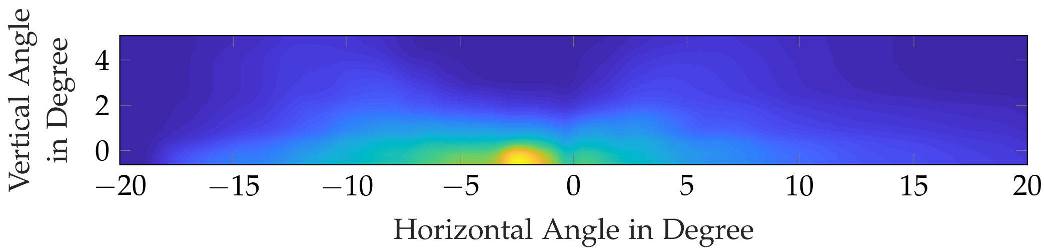

Figure 5.41 – Vehicle distribution on motorways.

When it comes to traffic signs, the variable width of motorways and the primary location of traffic signs above the road are visible. The main portion of all traffic signs is found in the centre and above of the driver. A lesser part of the traffic signs is located on the left side, but compared to city or country road drives, the main location of traffic signs is shifted significantly up.

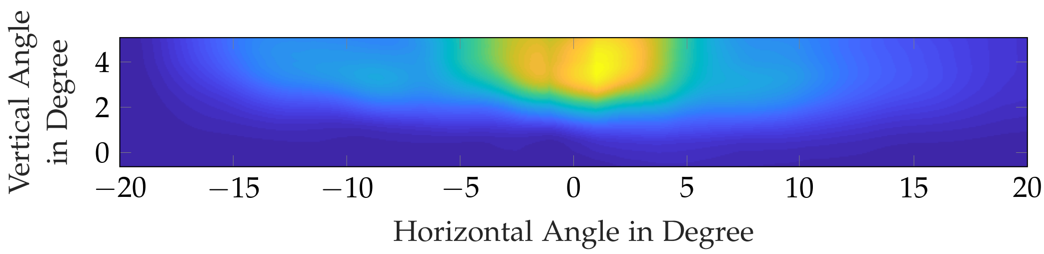

Figure 5.42 – Traffic Sign distribution on motorways.

Using the shown object locations, it is now possible to use the same algorithms to find optimized segment parameters similar to the optimization as shown above.

SEGMENT OPTIMIZATION

As the distributions in the sections above have shown, differences in the object distribution are found between real life traffic and the simulated distributions. Due to the wider centre accumulation point, and a generally more stretched distribution, wider segments are to be expected.
In the same manner as before, the distributions need to be symmetrized first in order to allow for a symmetrical headlamp set up and to allow for a simple switch between left and right hand sided traffic as well as for a more general optimization for multi lane roads. On this symmetrized object distribution, the segment optimization is performed using the equal density model. For comparing the achieved data to the data shown in the previous segments, the optimized segment distribution for a 3 x 24 setup is shown over the average object distribution in figure 5.43. The distribution in the background is the combination of the two distributions shown in figures 5.35 and 5.36, the overall distributions.

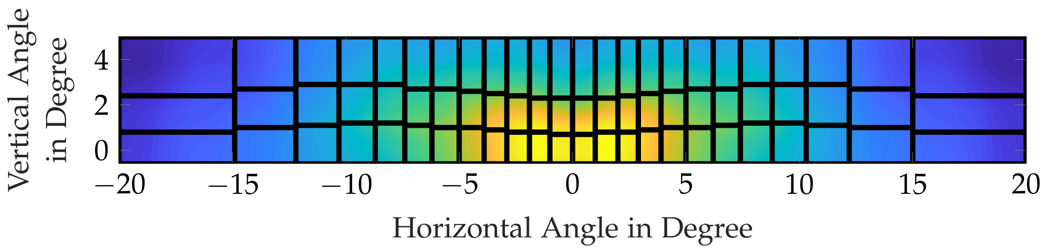

Figure 5.43 – Optimized high beam segment distribution for a 3x24 segment setup on the average object distribution as the combintation of the distributions shown in figures 5.35 and 5.36.

As expected, the difference between the distributions leads to much wider segments in the centre of and the bottom lane. While this means, that the segments are easier to realize in production, the difference to the standard distribution is reduced. For this reason, the difference in the performance is also going be reduced.
Before the performance of the proposed segment distributions is analysed, a second optimization is performed on a different object distribution. For this object distribution, the different road categories and object categories are not regarded equally important. However, it has to be understood, that this base distribution is not to be viewed as recommendation but rather as an example of what is possible with the data acquired in this thesis.
Similar to the first object distribution, this distribution also contains vehicles and traffic signs as the only objects in the traffic space. However, the weighting factors are changed since Kosmas has shown, that a 26 % high beam level on traffic signs increases the readability distance when compared to low or full high beam, as well as reducing discomfort glare compared to full high beam without a significant difference compared to low beam. While objects are weighted by 1, equalling a full shut down of the high beam segment in this area, traffic signs are weighted by 0.75 to simulate the dimming of the high beam. Furthermore, all distributions measured on urban roads are disregarded and the overall distribution is set up by weighting the country road objects with a factor of 0.6 and motorway objects by 0.4 and then summing both distributions. This is done since Zydek has shown, that most of the nighttime traffic is done on country roads [55]. The disregard of the urban roads is explained above and the different weights between the two remaining road categories is done exemplary and

could be adjusted freely. The overall distribution is shown in the background in figure 5.44. This distribution is then used to perform the same optimization for the gfHB segments as shown above.

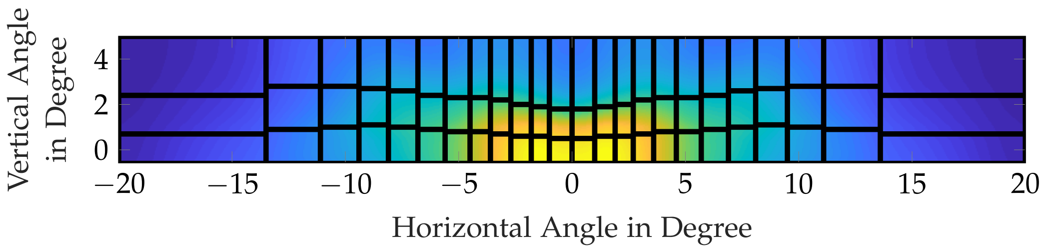

Figure 5.44 – Optimized high beam segment distribution for a 3x24 segment setup on the weighted average object distribution for country roads (60 %) and motorways (40 %).

The segment size varies slightly to the general optimization shown in figure 5.43, with wider segments at the outer edges and smaller segments in the centre. Furthermore, the lowest row is overall smaller as well.
As mentioned above, these two segment distributions are mere examples of what is possible and to visualize two distributions. Similar to the simulated study, these optimizations are not only done for one single distribution but for all possible combinations starting from 1 x 2 setups and ranging up to the 50 x 200 setup.

discussion on traffic optimization results

Analogue to the evaluation of the simulated traffic and segment distributions, the optimized distributions have to be evaluated and compared to the standard distributions in terms of overall street illumination. To evaluate both proposed example segment distributions fairly, they are both tested on the respective traffic situations. In order to do so, for the first segment proposal over the general distribution, 1000 sample images for all three road categories, urban roads, country roads and motorways are taken out of the recorded data and theoretical road illumination with the conventional segment distribution (shown in figure 5.22) as well as with the optimized distribution is calculated. The results are shown in figure 5.45. The average road illumination for the conventional segment distribution is shown by the blue graph and the optimized results are shown in red. The solid lines show the average illumination over the 3000 and the shaded area indicates the maximum (top) and minimum (bottom) illumination achievable if the same number of segments is set up by a different combination of rows and columns.

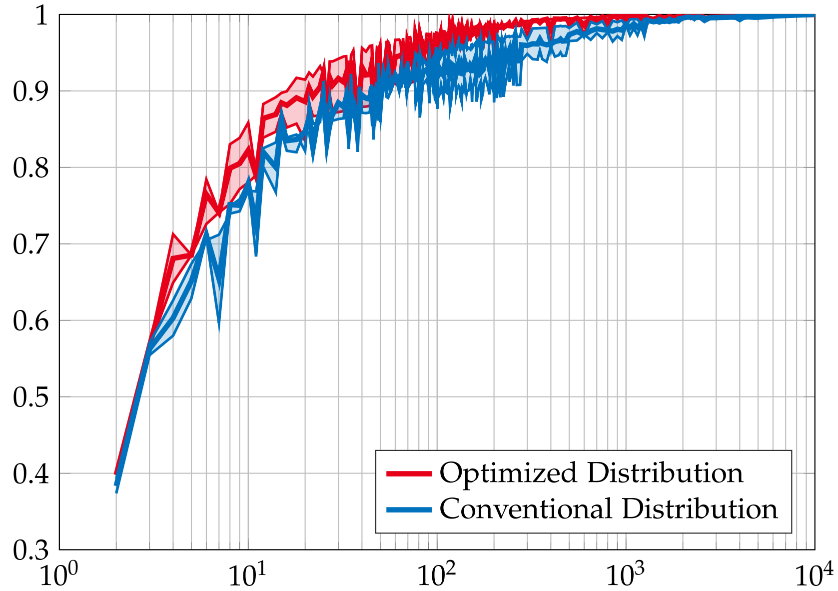

Figure 5.45 – Comparison of the average road illumination over 3000 sample images containing 1000 images of each road category. The red data shows illumination achieved with the optimized distribution and the blue data shows the illumination achieved by the conventional distribution. The top line shows the maximum illumination, the middle the mean illumination and the bottom the minimal illumination achievable with a certain amount of segments.

The data shows a clear improvement in overall illumination by the optimized setting. At a pixel count of 100 the distributions start to overlap largely but the optimized setting shows much higher mean illumination. Similar to the results shown by the simulation, the 99 % illumination compared to the 10000 pixel setup, is achieved at 280 segments for a resolution of 4 x 70 segments. For pixel counts above 1000 no difference between both distribution can be seen and a further increase in the overall segment count does not lead to an improvement of the road illumination. Again, analogue to the suggested pixel count from the simulation data, this suggestion only considers overall road illumination and does not take objective values into account. Higher resolutions for headlamps can deliver a smoother experience for different transitions between light distributions, leading to higher customer acceptance and even a more relaxed driving experience. However, this is not part of this thesis and cannot be investigated with the current setup.
For the second proposed distribution, where the traffic volume of country roads is weighted with 60 % and motorways with 40 % while urban roads are completely neglected, 18 000 images from country roads and 12 000 images from motorways are randomly selected and the corresponding mean road illumination is calculated. The results mimic the results shown in figure 5.45 and are therefore not presented again. This is to be expected, since both segment distributions are tested on the object distributions, they are optimized on.

5.2.3 SUMMARY OF THE OPTIMIZATION OF THE HIGH BEAM SEGMENTATION

In this section, a basic traffic simulation of German roads is introduced. Due to the relative simplicity of country roads compared to motorways and urban roads with a much wider bandwidth of different possible traffic situations, only country roads are simulated. Based on this simulation, traffic distributions are derived and the segmentation of gfHB is optimized. The results show, that for low resolution gfHB large improvements can be achieved in terms of overall road illumination, if the centre segments are set to smaller sizes compared to the segments at the outer edges of the high beam distribution. The data was further used to find the optimal segment count and combination, which is found at 201 segments in a 3 by 67 setup. Furthermore, the data is used to analyse angular velocities that occurs during traffic encounters and requirements for the reaction time of gfHB systems are calculated including camera, object recognition and pixel actuation times.

In the second part, a vehicle is equipped with a camera system and a large data set is recorded in 108 test drives on a route starting and ending in Darmstadt utilizing urban roads of the city centre in Frankfurt, motorways and country roads. Machine learning algorithms are used in order to detect objects in recorded video data. While the simulation only consideres other vehicles in the traffic space, the real data also finds other objects like traffic signs and adding them to the database. Using this approach, it is possible to extend the findings from the simulation of country roads to other road situations, that are too complex for simulation. The recorded data for country roads shows large similarities to the data gained by the simulation, however the calculated traffic distribution is significantly wider. This data furthermore enables the possibility to chose different road infrastructures to optimize the high beam segmentation on, depending on the planned usecase.

Two sample optimizations are proposed. The first segment setup is proposed for the overall traffic data where the data for all three major road categories is weighted equally and areas where traffic signs appear are fully switched off in the light distribution. The second proposed segment distribution is based on country roads and motorways only with a weight factor of 60 % for country roads and only 40 % for motorways. Furthermore, areas containing traffic signs are only dimmed down to 25 % of the high beam intensity based on the findings by Komas [175]. The two proposed distributions differ in their respective width, but both distributions have to be considered sample setups on what is possible and should not be taken as final due to the limitations of this study. For the real traffic data, the optimal segment count is found at 280 segments at a 4 by 70 set up. Compared to the simulation, real traffic data is rather variable and subject to a lot of change. Using different traffic situations or even test images therefore can always lead to slightly different results.

5.3 glare perception for short light pulses

While the studies presented so far, focused either on isolated situations with no other traffic participants, or in case of the segment optimization, only focuses on objective measurements, the goal of this thesis is to propose light distributions for different real world situations, that offer the best performance in any situation. One part of this needs to be the minimization of glare for other traffic participants. One step towards this is, to determine situations in real life driving, in which glare mostly occurs. Then the next steps need to be, to find a way to minimize or at least reduce the glare for other traffic participants as far as possible. For this reason, the following sections will focus on the aspect of oncoming traffic and the resulting glare.

Since glare is one of the key aspects, that arises as a distrutbing effect while driving at night [55], the first steps to performing a suitable study is, to find a feasible way to measure glare or a correlating value for glare. As described in section 2.3, Zydek, Bullough, Werner, Kosmas, Polin and Lehnert describe and correlate the glare perception during real life driving studies using the measured illuminance curves and the average exposure values. Since the main study contains a real life driving test with more than 2 h duration, this approach is unfeasible. Therefore, the idea for this thesis is to use the eye tracking system that is used to analyse the gaze behaviour, to record the pupil contraction and dilation as a result of changing light conditions similar to Lin. The first part of this chapter will therefore focus on laboratory studies to find a correlation between the pupil size, illuminance, exposure and the glare perception of test subjects.

As shown by Lehnert and Kosmas the main source for glare are short illuminance pulses [58, 60]. These illuminance pulses occur due to a pitch movement of the vehicle in different situations. This includes acceleration, added load and road unevenness. Due to this pitch of the vehicle, the cut-off-line of the low beam can be lifted above the horizon shortly, thereby glaring oncoming or preceding traffic. Two different low beam distributions are schematically shown in figure 5.46 with a sharp cut-off-line in figure 5.46a and a smooth cut-off-line in figure 5.46b.

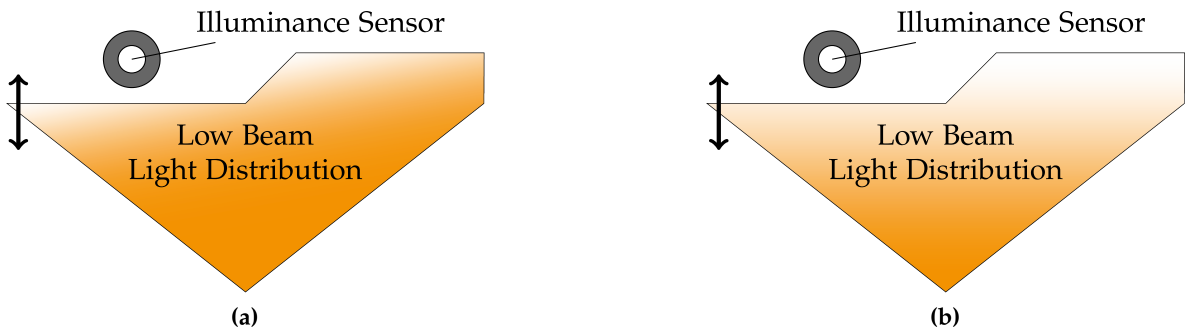

Figure 5.46 – Examples for the origin of glare pulses in real life traffic. (a) visualizes a sharp cut-off-line with very step edges of the glare pulse. (b) on the other hand shows the same situation with a very smooth low beam, thereby leading to a much smoother glare pulse. The illuminance sensor indicates, where a drivers head would be located for an oncoming vehicle. The arrows at the left side indicate the pitch movement of a vehicle

The illuminance sensor indicates a divers head for oncoming traffic and the arrows at the left side in each picture indicate the possible pitch movement of the vehicle and therefore the movement of the low beam light distribution as well. Figure 5.47 now shows the two measured illuminance curves at the drivers eye. The sharp cut-off-line leads to a much steeper pulse as indicated by the arrows showing the time between the start of the pulse and the time at which the maximum illuminance is reached.

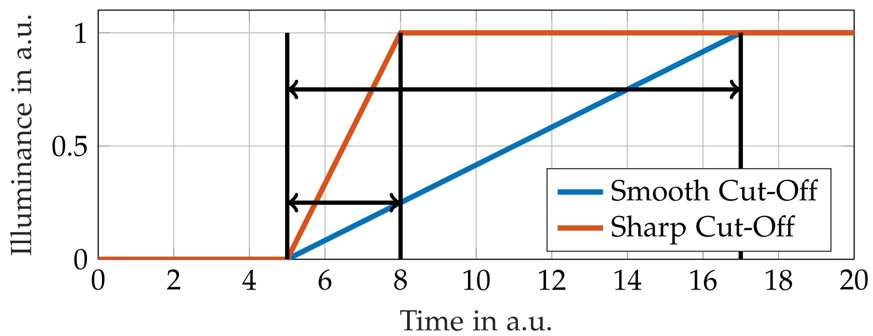

Figure 5.47 – Illuminance at the drivers eye for smooth cut-off-lines (blue) and sharp cut-off-lines (red).

Due to the different cut-off-lines, one vehicle could induce a very smooth and long glare pulse, while the other induces a short but very steep pulse.

Since reviewing the photometric values would lead to the same glare rating, an experiment is designed to identify the correlation between the photometric values of light pulses, the glare perception and the pupil diameter in order to receive an objective measurement. For this, not only the intensity and the pulse width is varied, but the pulse form is changed as well. Since this combines a psychological parameter with a physiological parameter, the results are expected to vary largely between test subjects. Furthermore, a psychological glare perception does not necessarily implicate a physiological impairment of human vision and might therefore not lead to a compulsorily physiological reaction. The results of this experiment can the be used later for the light distribution optimization, where the transition between segments that are switched off and segments that are switched on needs to be set, meaning a certain sharpness can be chosen for each segment in the glare free high beam.

5.3.1 PUPIL DIAMETER AND GLARE FOR RECTANGULAR PULSES

This proposed experiment is divided into two sub-studies. The first part investigates the influence of pulse duration and illuminance on the glare perception. This is done to find an objective way of measuring the glare load in real life traffic situations without the use of a questionnaire. The second part studies focuses on the influence of the pulse form on glare perception in order to minimize the glare perception for other traffic participants in situations, where an induced glare pulse can not be suppressed. Both studies were performed using the same experimental setup and varied only the pulses themselves. Therefore, the setup is presented up front and only the differentiating parts are described for each study individually.

EXPERIMENTAL SETUP

To measure the glare perception in correlation with the pupillary movement, the experimental setup is only consists of the eye tracking cameras and the glare source. As a glare source an automotive grade LED of the type *Lumiled Altilon AFL-M2L-0500* from PHILIPS was chosen, to reproduce a spectrum similar to the spectrum of modern automotive headlamps. For detailed information, the data sheet containing the spectrum, the temperature dependency and all other relevant data, is attached in the appendix F. Using an HID or even a halogen light source, leads to a spectrum that is more widely used in the automotive segment at the moment, and next to other problems with those light sources like size and power draw, would have caused the light pulses to be less accurate and with much more smooth edges.
Since the goal of this study is, to find a correlation between the measured illuminance peaks from real live driving situations and the glare perception as well as the pupillary movement, light pulses are chosen to range from far lower illuminance values, $E_{min} \leq 1\,\text{lx}$, to illuminance values even exceeding the values measured for high beam with $E_{max} \geq 100\,\text{lx}$ [55, 58].
Since the goal of automotive LEDs is to deliver as much light onto the roads as possible, reaching the upper limit of the illuminance values is not an issue. A neutral density filter with transmission of 4.4 %, was used to lower the illuminance range resulting in $E_{max} = 101.6\,\text{lx}$ and $E_{min} = 1.5\,\text{lx}$. Since the neutral density filter will influence the spectrum in any case, the spectrum of the LED is measured with and without the filter. Both spectra are shown in appendix D.1.1 in figures D.1 and D.2.

As introduced in section 2.1, an exponential rise in stimuli intensity, leads to a linear increase in perception. Therefore, the chosen illuminance values presented to the test subjects are exponentially spaced. All presented values are shown in table 5.9. Two control values that do not fit into the exponential spacing are shown at 38.5 % and 14.8 %. These values are the results of a malfunction in the constant current regulation of the LED driver, that were only identified during the actual test procedure.

Table 5.9 – Duty Cycle and corresponding illuminance values used in the laboratory glare experiment to find a correlation between pupil diameter and psychological glare perception.

DUTY CYCLE	ILLUMINANCE
97.7 %	101.6 lx
47.5 %	51.6 lx
38.5 %	42.3 lx
18.4 %	20.5 lx
14.8 %	16.6 lx
7.4 %	8.3 lx
3.0 %	3.4 lx
1.2 %	1.5 lx

Next to the glare source, the eye tracking system is installed. The system in use is a commercially available four camera system, Smart Eye Pro [176]. This set up allows for free camera placement at was primarily chosen for the use in the study regarding the driver's gaze behaviour in real life driving situations. Therefore, this chapter will only explain the most relevant characteristics of the system for the pupil measurement and the complete functionality is then presented in section 5.4 and the data sheet can be found in the appendix F.

The Smart Eye system offers multiple eye characteristics necessary for pupil tracking. The system tracks each eye individually and records three diameters - one for each eye and the average diameter over both eyes. Furthermore, a quality parameter is recorded for each pupil, that indicates the percentage of the pupil visible in each frame. Additionally, blinks or other eye lid movements are recorded. This leads to the possibility to only investigate data, where the pupil can measured to a certain degree of certainty. For this study the recommendation by Smart Eye is followed and only data with a quality value of over 0.5 were used. The data is recorded with an average frame rate of 120 Hz but a UNIX time stamp is included in the files for each frame to allow for higher accuracy regarding the timing of pupil diameter and glare pulse.
For the duration of this experiment, the test subjects are located under 0° opposing the glare source. The eye tracking cameras are located around the glare source with one camera to the far left, one camera close on the right side of the LED and two more cameras to the far right. The test subjects have their heads fixed in a chinrest to continuously guarantee the illuminance values shown in table 5.9 and offer a more robust pupil tracking since no head movement is possible. The complete test setup is shown schematically in figure 5.48.

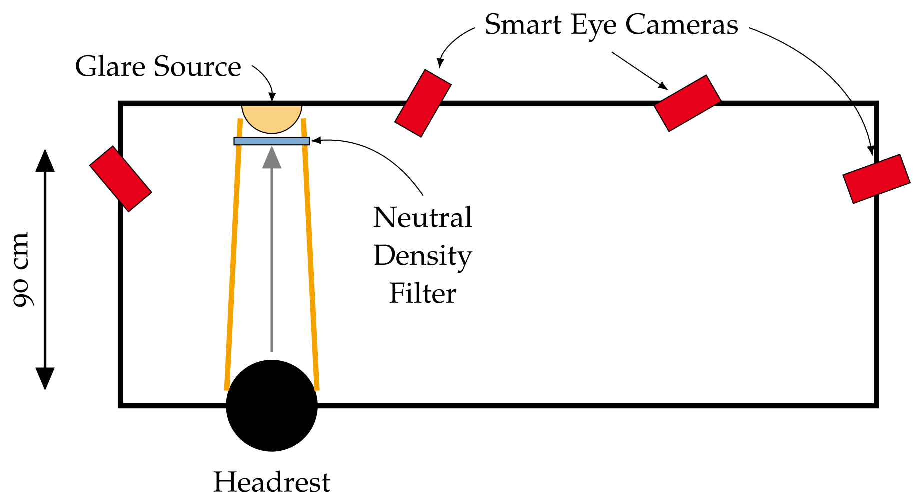

Figure 5.48 – Schematic setup of the glare source, the eye tracking system and the test subject's position.

For the test, the background luminance is chosen to be as low as possible. This is done for two major reasons. First of all, the background luminance at night in automotive scenarios is spread over a broad range from below $0.001\,\mathrm{cd\,m^{-2}}$ on unilluminated country roads and can reach up to $3\,\mathrm{cd\,m^{-2}}$ with street lighting and oncoming traffic might even lead to luminance spots of over $100\,\mathrm{cd\,m^{-2}}$ [86, 177–179]. Secondly, the influence of the background luminance should be kept to a minimum. The measured luminance for the actual experiments is recorded at below $0.010\,\mathrm{cd\,m^{-2}}$. Before each test, the test subjects are asked to adapt to the mentioned background luminance. Therefore, an adaption phase is set before each test run. This time is used to create the eye tracking profile, record the subjects personal information and introduce him to the testing procedure and the modified DE BOER scale.

To showcase the metrics used, figure 5.49 shows the pupillary reaction after a light pulse with an intensity of 100 lx and a duration of 2 s. The pulse is shown to the test subject at the 5 s mark (dashed grey line). The data extracted from the pupil diameter is the average pupil diameter before the light pulse is shown, the minimal pupil diameter, marked with a red dot and as **(a)** and the needed relaxation time until the pupil reaches 95 % **(b)**. To calculate the 95 %-point, equation 5.6 is used to fit the data from the pupil minimum to the time the next light pulse is sent. P represents the pupil size, C, is a constant, t is the time in seconds and τ is the relaxation time at which $1/e(\tau) \approx 63\,\%$ and for $3 \cdot \tau \approx 95\,\%$.

$$P = C \cdot (1 - e^{-\frac{t}{\tau}}) \tag{5.6}$$

Additionally, the relative pupil diameter is calculated using the average pupil diameter measured 2 s before the glare pulse and the measured pupil minimum.

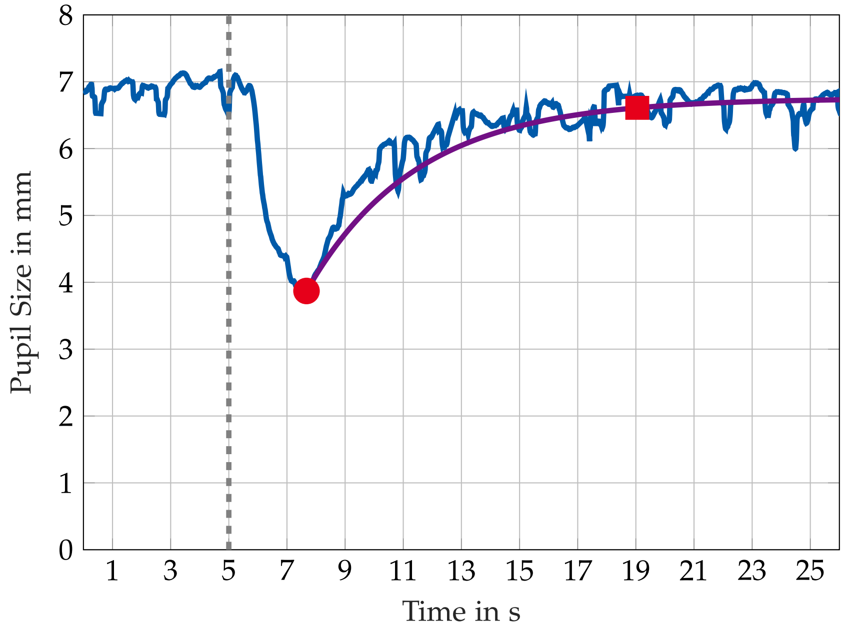

Figure 5.49 – Pupillary reaction to a light pulse send at 5 s (dashed line). The data extracted from this behaviour is the minimal pupil size (red dot), the relative minimal pupil size, and the relaxation time according to equation 5.6 with $3 \cdot \tau$ marked here by the red square

As a measure for the perceived level of glare, the DE BOER scale is modified for better intuition. Table 5.10 shows the inverted wit the description according to the original work, where only every second entry is described. In the conventional DE BOER scale, the maximum glare perception is associated with the numeric value of 1, and the least amount of glare is associated with the numeric value of 9. In pretests, this has proven to be counter-intuitive for uninitiated test subjects. Therefore, the inverted scale is used.

Table 5.10 – Numeric values for the inverted and the conventional DE BOER scale [75]

NUMERIC VALUE	INVERTED DE BOER	DE BOER
1	Unnoticeable	Unbearable
2	-	-
3	Satisfactory	Disturbing
4	-	-
5	Just Admissible	Just Admissible
6	-	-
7	Disturbing	Satisfactory
8	-	-
9	Unbearable	Unnoticeable

PHYSIOLOGICAL IMPACT OF PULSE WIDTH AND INTENSITY

The first part focuses on the correlation between psychological glare and different glare pulse parameters while keeping the pulse form to a rectangle. Rectangles are chosen as a simplified version of the light pulses seen in the studies of KOSMAS and in accordance to the work by LEHNERT [58, 60] and as visualized in figure 5.47 for the sharp cut-off. The light pulses are being varied in maximum intensity and duration. When choosing the parameters for intensity and width, special focus was set to the parameters to create bins in which pulses from different intensities and durations sustain the same exposure. This is done in accordance to the works of ZYDEK, BULLOUGH, WERNER, KOSMAS, POLIN and LEHNERT and to verify their correlations in a more controlled environment. The chosen pulse durations, intensities and the resulting exposure values are fully shown in the tables D.1 to D.4 in the appendix D.1.1. Due to the malfunction mentioned above, the exposure values shown do not match exactly but are grouped together as summarized in 5.11.

Table 5.11 – Compact summary of the shown glare pulse durations and exposures.

EXPOSURE	PULSE DURATION			
0.200 lx s	128 ms	-	-	-
0.400 lx s	128 ms	320 ms	-	-
1.100 lx s	128 ms	320 ms	800 ms	-
2.100 lx s	128 ms	-	-	-
2.600 lx s	128 ms	320 ms	800 ms	-
3.100 lx s	-	-	-	2000 ms
5.400 lx s	128 ms	320 ms	-	-
6.600 lx s	128 ms	320 ms	800 ms	2000 ms
13.000 lx s	128 ms	320 ms	800 ms	-
16.500 lx s	-	320 ms	800 ms	2000 ms
32.500 lx s	-	320 ms	800 ms	2000 ms
41.300 lx s	-	-	800 ms	2000 ms
81.300 lx s	-	-	800 ms	2000 ms
103.300 lx s	-	-	-	2000 ms
203.200 lx s	-	-	-	2000 ms

After the adaptation time of 15 min, each participant was shown the 8 pulses with a duration of 800 ms in ascending order of intensity. Further more the pulse with the lowest and the pulse with the highest exposure were shown as anchoring stimuli. The 32 different pulses are then presented to the test subject in a randomized order for each set. After the 32 pulses, a 4 min break was held for the participants in order to stretch and relax. This set of 32 pulses is repeated three times. After each pulse, the subjects is given a 20 s time slot to rate the glare perception and re-adapt to the dark. This time slot is found in a pre-test. Figure D.4 in appendix D.1.1 shows, that after those 20 s re-adaptation, the pupil dilated back to the same pupil diameter as before the glare pulse.

22 test subjects participated in this part of the study. This includes 16 male and 6 female participants in the age of 22 to 31. A small variance in age was chosen to minimize the influence of age and possible opacification of eye and the resulting influence on glare perception. The complete age distribution is shown in appendix D.1.1 in figure D.5. The participants are mainly students or carry out clerical work. Participants wearing glasses are asked to switch to contact lenses for more consistent eye tracking results. A detailed overview over all participants is shown in appendix D.1.1 in table D.5. All participants are asked not to consume any alcohol or coffee at the day of the experiment since both substances are reported to influence pupillary reaction and glare perception and recovery if ever only so slighty [180, 181].

CORRELATION BETWEEN PUPIL DIAMETER AND PHOTOMETRIC VALUES

In order to find a correlating metric between the pupil data and the photometric values, all datasets are tested against each other. All data is presented in appendix D.1.1 in figure D.6 for the normalized pupil diameter, in D.7 for the absolute pupil diameter and in D.8 for the relaxation time. The best correlation is found for the relative pupil diameter. The fit for this data is shown in equation 5.7 where $R^2 = 0.7$ is achieved. H abbreviates exposure, and P is the relative pupil diameter and P_0 is th standard pupil diameter with $P_0 = 1.000$ mm needed in order to make the equation unitless.

$$H(P/P_0) = \log\left(-0.32 \cdot P/P_0 + 2.59\right) \tag{5.7}$$

Describing the exposure as dependent on the pupil diameter is only done here in order to find correlating values. From here on forth, the pupil diameter will be treated as dependent on the exposure.
Figure 5.50 shows the box plots regarding the pupil data of all subjects. For the purpose of this figure, similar exposure values have been grouped together. The red line in each box indicates the median of each data set, and the boxes show 50 % of all recorded data. The lower edge of the rectangle shows the 25 %-quantile and the upper edge the 75 %-quantile. The antennas indicate the outliers by multiplying the inter-quantile distance with the factor 1.5 and extreme outliers are marked as red asterisks. The figure shows, that the data is widely spread between all participants. The data for the lowest exposure set ranges from 87 % down to 47 % with a median value of 69 % leading to a spread of 40 % for the extreme values. This spread stays similar for all other pulse sets. Nevertheless, a Wilcoxon-Mann-Whitney-Test leads to significant differences between all data sets, except the data between 2.100 lx s to 6.700 lx s and the data sets above 33.200 lx s.

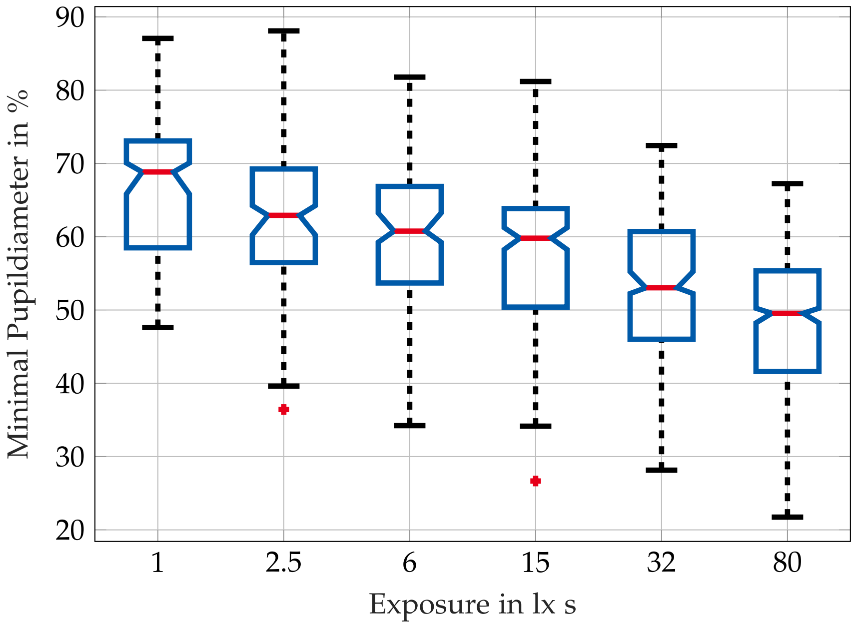

Figure 5.50 – Box Plots for all normalized minimal pupil diameters measured. Exposure values have been grouped together for a better visualization of the data. The red line indicates the median value, the blue rectangles mark the 25 %-quantile (lower border) and the 75 %-quantile (upper border).

To further understand the pupil behaviour during those light pulses, the data is split up into the different durations again. Figure 5.51a shows the relative pupil minimum over the exposure. The data for each set of specific durations is plotted individually. The blue squares mark glare pulses with a duration of 128 ms, red diamonds mark pulse durations of 320 ms, green asterisks mark durations of 800 ms and purple circles mark the pulses with a duration of 2000 ms. For all data the general trend that a higher the exposure leads to a stronger contraction of the pupil, is found.

This representation also shows, when comparing two glare pulses with the same exposure, the pulse with the lower intensity but the longer duration will inflict a stronger pupil contraction. As an example, values with an exposure of 2.740 lx s lead to pupil contractions starting at around 65 % for pulses with 128 ms or 320 ms and ranging up to nearly 50 % for a 2000 ms pulse. Since the data shows no significant difference in the pupillary reaction for pulses shorter than 320 ms, those two data sets are combined. Figure 5.51b shows the fitted data with the fit functions listed in the equations 5.8a to 5.8c where $H_0 = 1.000\,\mathrm{lx\,s}$ is similar to equation 5.7 used in order to get the equations unitless.

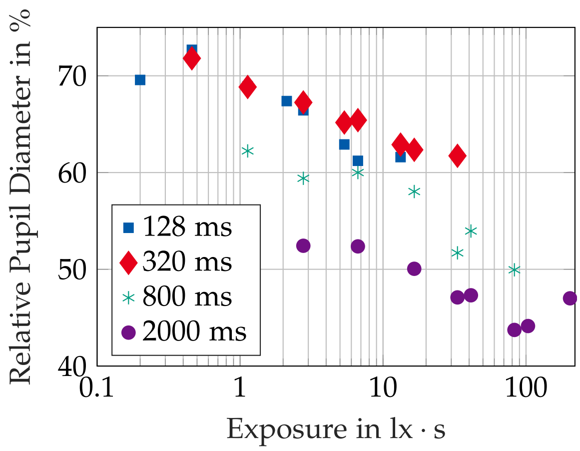

(a)

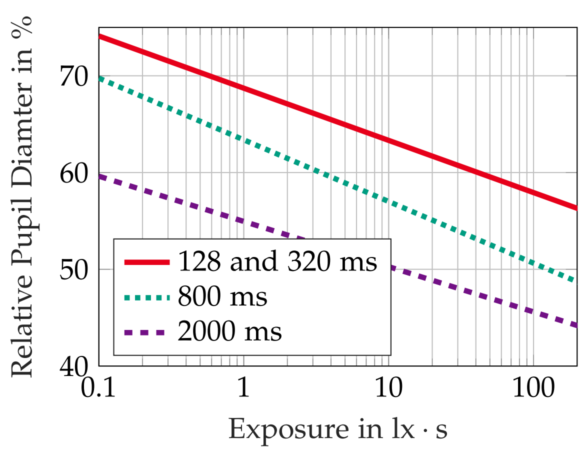

(b)

Figure 5.51 – Data for the correlation between the pupil diameter and exposure. (a) shows the average normalized pupil diameter for all participants over the exposure. (b) shows the fit functions for the datasets presented in (a) for the datasets $t_{pulse} \leq 320\,\text{ms}$ (red), $t_{pulse} \approx 800\,\text{ms}$ (green and dotted) and $t_{pulse} \approx 2000\,\text{ms}$ (purple and dashed)

$$P(H/H_0)_{t\leq 320} = -5.4 \cdot \log_{10}(H/H_0) + 68.7 \tag{5.8a}$$

$$P(H/H_0)_{t=800} = -6.4 \cdot \log_{10}(H/H_0) + 63.4 \tag{5.8b}$$

$$P(H/H_0)_{t=2000} = -4.7 \cdot \log_{10}(H/H_0) + 54.9 \tag{5.8c}$$

The statistical data for these three fit functions is listed in D.6, the R^2 values are 0.84 for the duration of 320 ms or less, 0.86 for the 800 ms pulses and 0.87 for 2000 ms pulses.

The resulting R^2 values of at least 0.7 indicate a very good correlation between the logarithmic exposure and the average pupil diameter. However, the significantly better R^2 values for each of the individual fits, for glare pulses with a duration of 320 ms and above, compared to the fit over all datasets combined, shows, that the exposure is not the correlating value. It has to be mentioned however, that for the data of 128 ms and 320 ms, exposure is the correlating value since those datasets do not split up. For the data with pulse durations of 320 ms and above, a new scaling of the correlating value is found by minimizing the Mean Square Error (MSE) for all data points by varying p in equation 5.9.

$$P = E \cdot T^p \tag{5.9}$$

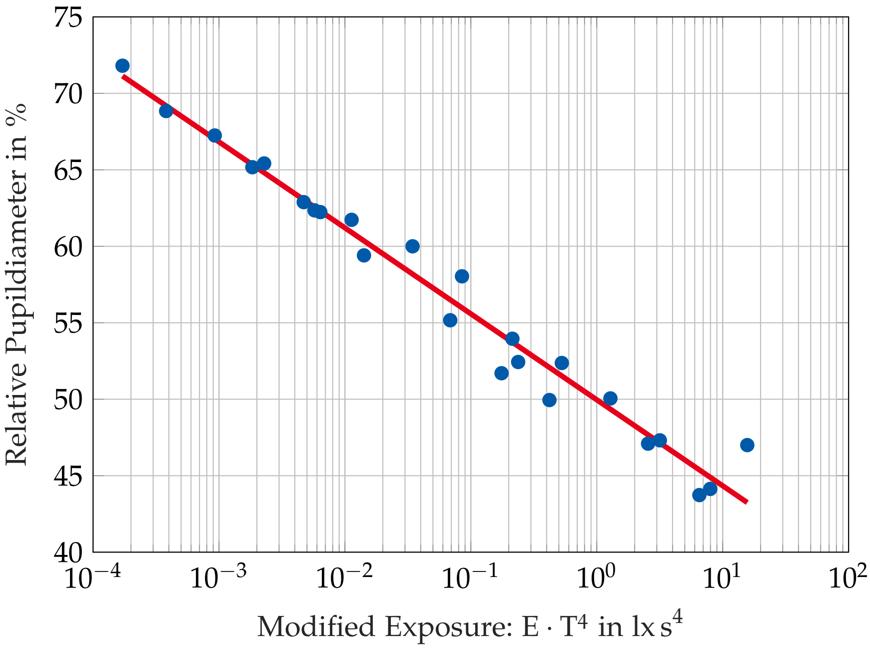

Figure 5.52 – Normalized minimum pupil diameter averaged over all test subjects for glare pulses with a duration of $t_{Pulse} \leq 320\,\mathrm{ms}$ over the scaled exposure according to equation 5.9 with $p = 4$

The resulting equation for the regression fit is given by equation 5.10 where $P(H_{optimized})$ stands for minimal normalized pupil diameter as a function of the optimized exposure $H_{optimized} = E \cdot T^4$. Similar to the previous fit equations the parameters $E_0 = 1.000\,\mathrm{lx}$ and $T_0 = 1.000\,\mathrm{s}$ are used.

$$P(H_{optimized}/(E_0 \cdot T_0^4)) \quad = \quad -5.62 \cdot \log_{10}\left((E \cdot T^4)/(E_0 \cdot T_0^4)\right) + 49.96 \tag{5.10}$$

With the new scaling factor $p = 4$, the correlation coefficient is increased to $R^2 = 0.97$. This leads to the conclusion, that, for the pupillary reaction, the duration of pulses has a stronger influence on than the illuminance. This has already been seen in the data shown in figure 5.51a and 5.52 where the pupil size is shown to decrease more for pulses with higher durations and lower intensities.

CORRELATION BETWEEN PSYCHOLOGICAL GLARE AND PHOTOMETRIC VALUES

Since the correlation between the photometric values and the pupillary reaction is found, the next step is, to evaluate the data for correlation between psychological glare and photometric values. If this is the case, the last step is, to investigate the correlation between the pupillary reaction and the psychological glare perception.

Analogue to the procedure in the section before, the first step is, to find the main correlating value between the glare perception and the photometric values. Compared to the pupil contraction, possible correlations arise between the glare perception and illuminance values as well as with the exposure of the glare pulses. This is indicated by the data in the figures D.9c and D.9d in appendix D.1.1. A regression fit is done for the inverted DE BOER rating over both data sets. The regression equations and coefficients for both are shown in 5.11a and

5.11b with E for illuminance, H for exposure and w represents the inverted DE BOER glare rating.

$$E(w) = log_{10}(-0.41 \cdot w + 2.71) \quad (5.11a)$$
$$R^2 = 0.86$$

$$H(w) = log_{10}(-0.32 \cdot w + 2.59) \quad (5.11b)$$
$$R^2 = 0.91$$

While illuminance or exposure dependent on the glare rating is contra-intuitive, this is only done here in order to find the correlating values, similar to the way, the correlation between the pupil diameter and the exposure is found in equation 5.7. From here on forth, the correlation will be turned to the intuitive way, the glare rating dependent on the exposure or the illuminance.

Aside from the fact, that the illuminance also leads to a good correlation, another major difference to the data obtained with the pupil diameter, is that the data does not seem to split up into different durations at first glance. Since the R^2 value is higher for exposure, and exposure, leads to a correlation between photometric values and pupil diameter, the exposure will be investigated to further extend. However it should be noted, that due to the correlation shown in figure D.9c illuminance values may be used in this particular case as well, to deduct the average glare perception of test subjects.

Again, it needs to be mentioned, that, while the correlation is valid for the average glare rating and the high R^2 values show a very high grade of correlation, similarly to the pupil diameter, the data is widely spread between the different test subjects. Figure 5.53 shows this spread over all test subjects. Here it is visibile, that even for pulses with the lowest exposure, ratings between 1.3, *just noticible* and 4.7, *just admissible* are recorded. This spread increases for higher exposures. The highest data set receives a span in ratings from 4 (between *satisfactory* and *just admissible* to 9, *unbearable*. Despite this wide data spread, the WILCOXON-MANN-WHITNEY-TEST leads to significant differences between all exposure sets and thereby again validating the very high R^2 from equation 5.11b.

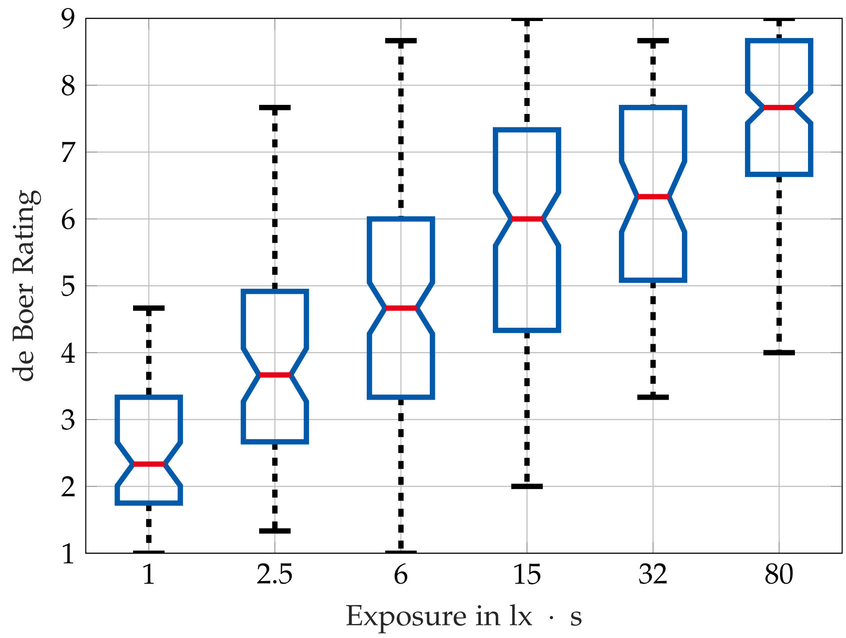

Figure 5.53 – Box Plots for the glare perception. Exposure values have been grouped together for a better visualization of the data. The red line indicates the median value, the blue rectangles mark the 25 %-quantile (lower border) and the 75 %-quantile (upper border).

As done for the average pupil diameter, the data is split up again for the different durations. This is shown in 5.54a where the glare pulses with 128 ms durations are shown as blue squares, 320 ms pulses are shown as red diamonds, pulses with a width of 800 ms are marked by green asterisks and the longest pulses with a duration of 2000 ms are shown as purple circles.

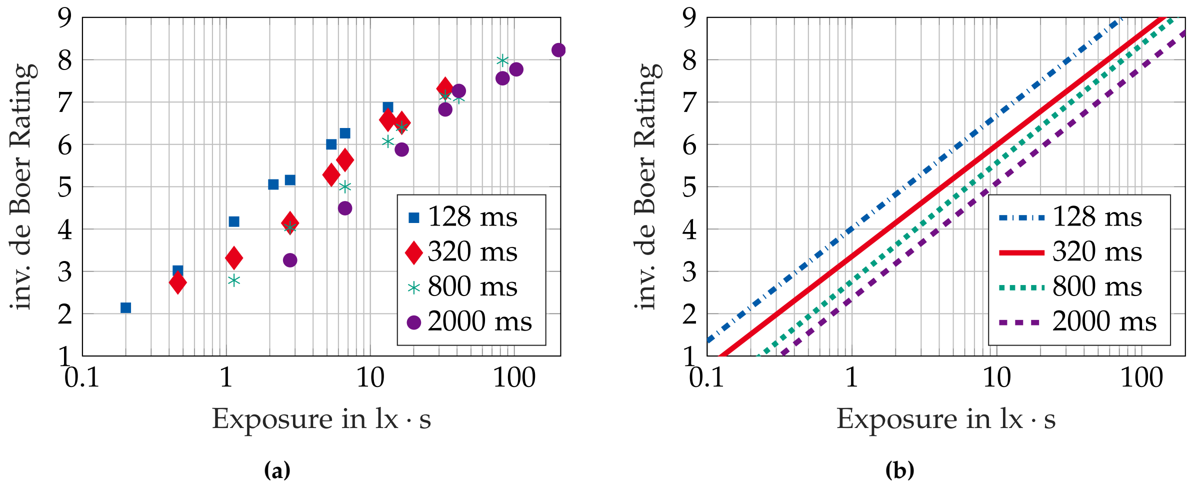

Figure 5.54 – Data for the correltaion between the glare perception and the exposure. (a) shows the average inverted DE BOER rating for all participants over the exposure. (b) shows the fit functions for the datasets presented in (a) for the datasets $t_{pulse} = 128\,\mathrm{ms}$ (blue squares), $t_{pulse} = 320\,\mathrm{ms}$ (red diamonds), $t_{pulse} \approx 800\,\mathrm{ms}$ (green asteriks) and $t_{pulse} \approx 2000\,\mathrm{ms}$ (purple circles)

Since the glare rating does split up for all four durations, the regression fit is done for all data sets individually. The fit functions are shown in the equations 5.12a to 5.12d and visualized in figure 5.54b with the staistcal quantities shown in the appendix D.1.1 in table

D.7. The regression fit equations are shown in the equations 5.12a to 5.12d. With R^2 values ranging from 0.96 for pulses with a duration of 2000 ms up to perfect representation of the recorded data for pulses with a duration of 128 ms ($R^2 = 1$). Compared to the results from the correlation between the average pupil diameter and the exposure, this indicates a much higher correlation.

$$w(H/H_0)_{t=128} = 1.2 \cdot \log_{10}(H/H_0) - 4.0 \tag{5.12a}$$

$$w(H/H_0)_{t=320} = 1.2 \cdot \log_{10}(H/H_0) - 4.7 \tag{5.12b}$$

$$w(H/H_0)_{t=800} = 1.3 \cdot \log_{10}(H/H_0) - 5.8 \tag{5.12c}$$

$$w(H/H_0)_{t=2000} = 1.2 \cdot \log_{10}(H/H_0) - 6.1 \tag{5.12d}$$

While the slope coefficient for all four equations falls within the margin of error, the offset differs significantly for all sets. This leads to a similar conclusion as already found for the correlation of pupil size and exposure. While for pupil size, a stronger influence of the duration was found, the figures 5.54a leads to the conclusion, that for the glare perception, the maximum illuminance is the stronger factor. Pulses with the same exposure tend to be perceived less disturbing, when the pulse has a longer duration and a lower intensity. This is shown especially well in figure 5.54a for the pulses with an exposure of 6.700 lx s where pulses with all durations are available. Following the method from above, a least square optimization is done for all recorded data to optimize the equation 5.9 with regard to p. The resulting data is visualized as blue circles, and the regression fit is shown as a red solid line in figure 5.55.

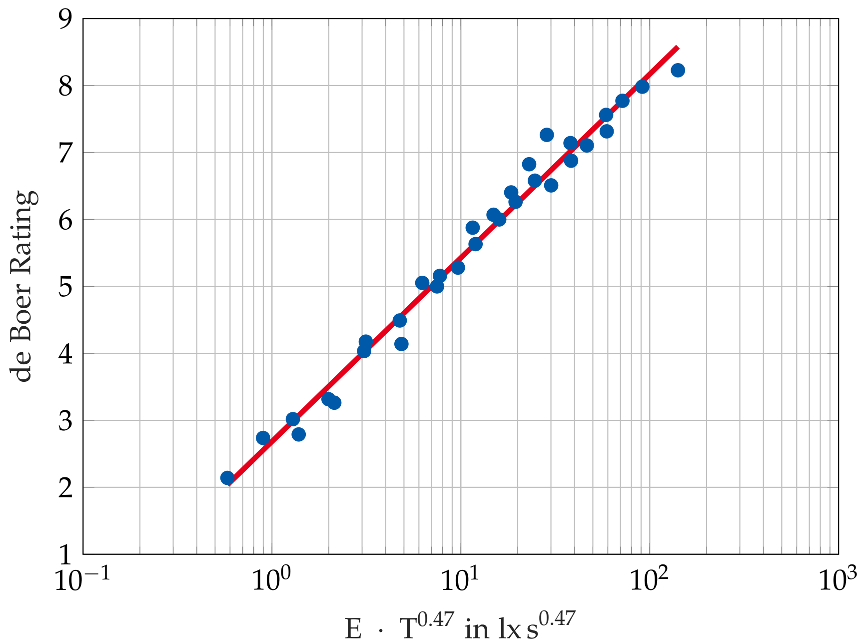

Figure 5.55 – Glare perception on the inverted DE BOER scale for all pulses over the scaled exposure according to equation 5.9 with $p = 0.47$

The resulting equation for the regression fit is given by equation 5.13 where $w(H_{opt})$ stands for glare as a function of the optimized exposure $H_{opt} = E \cdot T^{0.47}$. Similar to the correlation found between the pupil diameter and the modified exposure, p indicates the influence of the pulse duration on the glare perception.

$$w\left(H_{optimized}/(E_0 \cdot T_0^{0.47})\right) \quad = \quad -2.74 \cdot \log_{10}\left((E \cdot T^{0.47})/(E_0 \cdot T_0^{0.47} \right) + 7.32 \qquad (5.13)$$

This new equation leads to an $R^2 = 0.98$ showing a near perfect regression of the data. Even so, this is not an actual improvement over the individual fits with R^2 values ranging from 0.97 to a near perfect fit of 1.0. Comparing this result to the findings from the correlation between pupil diameter and exposure shows, that the results lead to opposite findings. For glare perception, the pulse duration shows a weaker influence than the illuminance and for pupil reaction the duration has a higher influence than the maximum illuminance.

However, both results are to be expected. If the eye has more time to adapt to a given light situation, for example due to a longer glare pulse, the pupil will have more time to react and thereby contract more. At the same time, the photoreceptor cells will get more time to accomodate to the new lighting condition. Therefore, the perception of glare will be significantly lower.

One major observation has to be mentioned for the data shown in figure 5.55. Since the de Boer scale is limited at the lower end at 1 and at the higher end at 9, a S-Curve for the ratings is to be expected if the exposure range is set from very low to extremely high since after a certain threshold every glare pulse should be *unbearable* due to the adaptiation capabilities of the human eye is limited to a certain degree in a given time. The same should apply for very low exposure pulses since below a certain illuminance value, the eye should be able to perceive a change in brightness without inflicting any kind of glare. Therefore, going lower and higher in the exposure range, should lead to an S-curve behaviour of the de Boer rating. The same should be true for the pupil diameter. As shown in chapter 4, the pupil size is limited in both minimum and maximum.
Nevertheless, both results need to be brought together in the last step to find a correlation between a psychological value, the glare perception, and a physiological value, the pupil size.

correlation between psychological glare and pupil diameter

In the last two segments correlations between the exposure of short glare pulses and both the pupillary reaction as well as the psychological glare perception can be found, if the glare pulses are split up into different segments using their duration. For both, glare perception and pupil diameter, a more general correlation could be found using modified exposure values where the influence of the duration was changed by an exponent p using equation 5.9. Since the exponent p takes on different values for both correlation types, the next step is, to investigate the behaviour of de Boer rating as a function of pupil diameter. The data for this is shown in figure 5.56a.

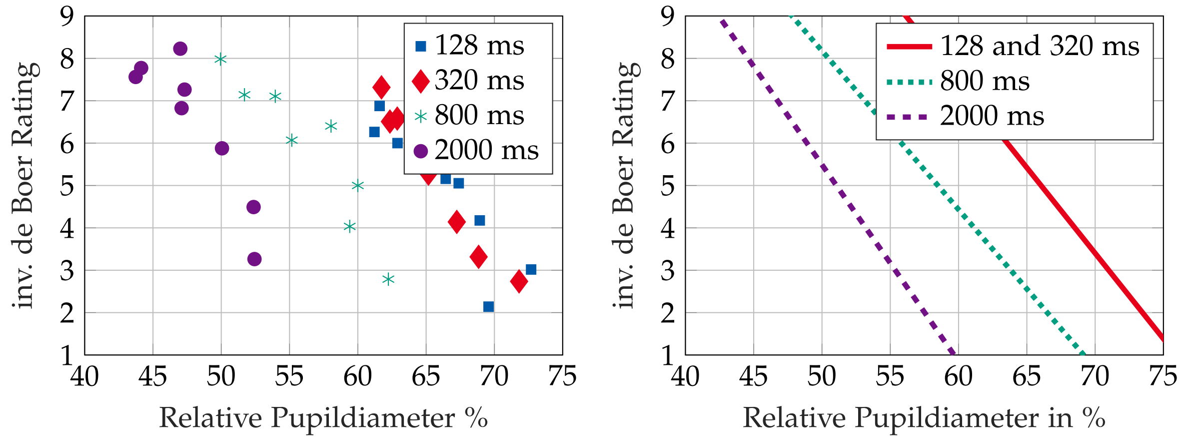

(a) **(b)**

Figure 5.56 – Data for the correlation between the glare perception and the average minimal pupil diameter. (a) shows the average inverted DE BOER rating for all participants over the average minimal pupil diameter. (b) shows the fit functions for the datasets presented in (a) for the datasets $t_{pulse} = 128$ ms (blue squares), $t_{pulse} = 320$ ms (red diamonds), $t_{pulse} \approx 800$ ms (green asteriks) and $t_{pulse} \approx 2000$ ms (purple circles)

The data shows, that for glare pulses with a duration of 128 ms and 320 ms the glare rating and the pupil diameter coincide. The general trend for all data points is, the smaller the pupil, the higher the glare perception. The data above 320 ms splits up for different durations. It can be seen, that data with the same pupil diameter does not necessarily lead to the same DE BOER rating, but the pulse duration still significantly influences the data. This is especially apparent for the critical DE BOER rating of 5, which is the threshold between glare and no glare and is therefore of special importance for automotive research. Here the pupil diameter ranges from 67 % for short pulses of 128 ms and 320 ms down to 52 % for the 2000 ms pulses. Analogue to the analysis of the pupil diameter as a function of the exposure, the data sets for the two lowest durations, 128 ms and 320 ms, will therefore be regarded as one data set. For the three data sets, least mean square fits are calculated. The resulting equations are shown in equations 5.14a to 5.14c, respectively. $w(P)$ represents the glare rating, as a function of the pupil diameter, P.

$$w(P)_{t\leq 320} = -0.40 \cdot P + 31.6 \tag{5.14a}$$

$$w(P)_{t=800} = -0.37 \cdot P + 26.9 \tag{5.14b}$$

$$w(P)_{t=2000} = -0.46 \cdot P + 28.6 \tag{5.14c}$$

The regression lines are shown in figure 5.56b. The fit function for the data from pulses with a duration of 128 ms and 320 ms is shown as solid, red line. The function for the data from pulses with a duration of 800 ms is shown in a green, dotted line and the data from the longest pulses with 2000 ms is fitted by the dashed, purple line.

The statistical quantities are shown in the appendix D.1.1 in table D.8. With the R^2 values reaching at least 0.8, a good representation of the data is achieved using the presented functions.

As expected from the data and the results shown in figures 5.52 and 5.55, the data for psychological glare perception and pupil diameter, are not, in general correlating. While it is possible to optimize certain parameters for correlations where at least one of the correlating values is compounded of two different metrics, in this case the exposure from duration and illuminance, no such optimization is possible for the direct correlation between two single metrics like pupil diameter and glare perception.

Due to these findings, a direct correlation between pupillary reaction and glare perception is not possible without knowing at least the duration and the illuminance of the glare pulse. With these known parameters, the correlation between the exposure and the glare perception is significantly better than any other measured correlation. At this point, since knowledge of the duration for each pulse is necessary, it is possible to calculate the correlation for the optimized optimization. The correlation value here is slightly lower than the correlation value achieved for the split durations when using the direct correlation. However, since the glare pulse sets were only investigated for single durations, the optimized exposure works in a more general way.

5.3.2 GLARE PERCEPTION FOR VARIABLE PULSE FORM

The section above has shown the general correlation between glare perception, photometric values and pupil metrics for solely rectangular glare pulses. Since the illuminance pulses recorded in real life encounter situations, as shown in section 4, in figure 4.11, are not rectangular, this section is dedicated to the influence of the pulse form on the glare rating. Furthermore, the findings here can be used to minimize the glare perception for possible encounters in real life traffic by setting the correct gradient in the cut-off-line of either the low beam or the switched off segments in gfHB.

To break down the influence of pulse form to a simple approach, the setup from above is kept exactly the same. As a reference, rectangle pulses are presented again. To approximate real life pulses, triangle pulses are shown, where the illuminance is linearly increased for half of the pulse duration and then linearly decreased for the rest of the duration. Rectangle and triangle pulses are presented at a random order. Due three different reasons, the values of the pulses shown are changed. Firstly, due to the second pulse form, the amount of pulses is doubled and therefore the test duration would double as well. To keep the test participants vigilant, the duration needs to be kept at the same duration as the previous test. Furthermore, the durations of the pulses need to change for two separate reasons. Firstly the duration and the illuminance values need to change to achieve sets of pulses with the same exposure, illuminance and duration between both pulse forms. Additionally, the values are changed to much lower illuminance values and much higher durations to examine the influence of these settings as well. Since the rest of the setup stayes the same, the results should still be comparable. The used pulse setup is shown in table 5.12. $T_{\square}$ stands for the pulse duration of rectangle pulses, $T_{\triangle}$ on the other hand, shows the triangle pulses. All photometric values can be grouped. The duration groups are shown by the columns, the illuminance groups are shown in the rows and the exposure groups are displayed on the diagonal sets. The exposure for the triangle pulses is calculated by $H = {}^{(E \cdot T)}/_{2}$. This means, that the durations need to be doubled for pulses to get equivalent exposures as shown in table 5.12.

Table 5.12 – Pulse parameters used for the investigation of the influence of the pulse form on the psychological glare perception. The center of the table gives the exposure calculated by the illuminance and the pulse duration. For rectangle pulses the exposure H is calculated by $E \cdot T$ and for rectangle pulses the exposure is given by $(E \cdot T)/2$.

		EXPOSURE				
	Illuminance	0.044 lx	0.176 lx	0.705 lx	2.820 lx	11.280 lx
PULSE DURATION	$T_\square = 0.300$ s $T_\triangle = 0.600$ s	0.013 lx s	0.053 lx s	0.845 lx s	0.845 lx s	3.384 lx s
	$T_\square = 1.200$ s $T_\triangle = 2.400$ s	0.053 lx s	0.845 lx s	0.845 lx s	3.384 lx s	13.536 lx s
	$T_\square = 4.800$ s $T_\triangle = 9.600$ s	0.211 lx s	0.845 lx s	3.384 lx s	13.536 lx s	54.144 lx s
	$T_\square = 19.200$ s $T_\triangle = 38.400$ s	0.845 lx s	3.384 lx s	13.536 lx s	54.144 lx s	246.576 lx s

For this test setup 17 test subjects with an age between 20 and 29 years of age, and again either students or working in an office environment, participated in the study. The complete data of the participants including the age distribution and their more detailed information on occupation and more are attached in appendix D.1.1 in table D.9 and D.10.

Analogous to the study regarding the correlation between the pupil diameter and the glare perception, the first correlation formed is the correlation between the exposure and the glare perception. This is done separately for the rectangle pulses and the triangle pulses and shown in figure 5.57a and 5.57b. All data is shown by the same symbols and colours as in the previous section with only the pulse duration changing their numeric values.

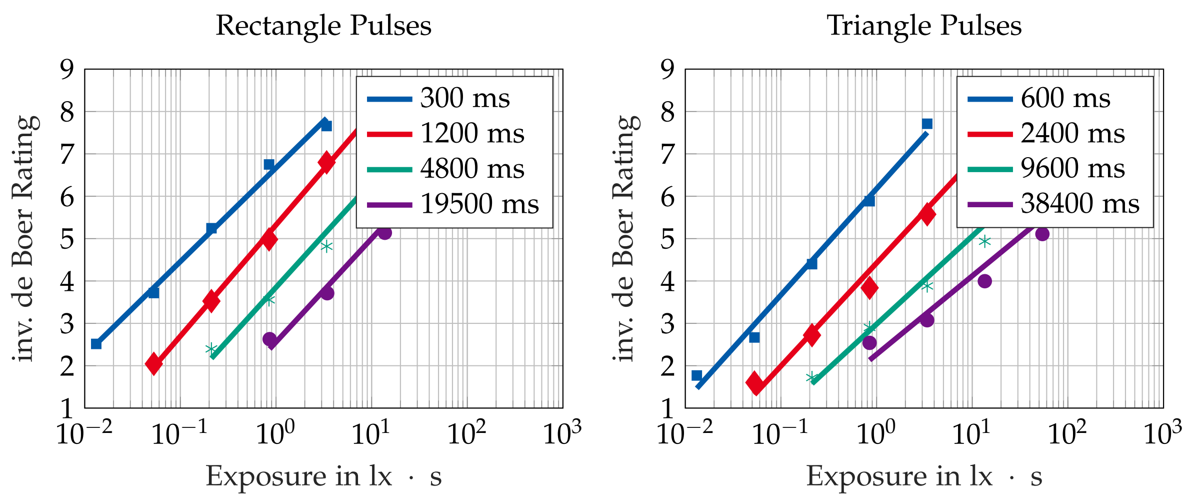

(a) (b)

Figure 5.57 – Glare perception on the inverted DE BOER scale for (a) rectangle and (b) triangle pulses for the different shown pulse durations. Blue squares show the data for 300 ms, red diamonds the data for 1200 ms, green asterisks show the data for 4800 ms and purple circles indicate the data for 19 500 ms pulses.

Similar to the data shown before, the glare perception between pulses with different durations splits up. Pulses with a shorter duration are perceived as more glaring than pulses with the same exposure, but longer pulse durations. The data for each pulse duration then follows a strictly logarithmic behaviour and the fit data, indicated by the solid lines, for each duration are nearly parallel. This is shown by the fit parameters in the equations 5.15a to 5.15d for the rectangle pulses. Again, the fit statistics are shown in table D.10 in appendix D.1.1. The shown parameters show, that all four fit equations give a very good representation of the data with R^2 values above 0.99 for all four fits and only very small fit errors in MSE, ΔW and $\sigma_{\Delta W}$. As previously, w gives the glare perception on the inverted DE BOER scale and H is the exposure in lx s.

$$w({}^{H}/{}_{H_0})_{\square t=300} = 1.0 \cdot \log_{10}({}^{H}/{}_{H_0}) + 6.7 \tag{5.15a}$$

$$w({}^{H}/{}_{H_0})_{\square t=1200} = 1.1 \cdot \log_{10}({}^{H}/{}_{H_0}) + 5.3 \tag{5.15b}$$

$$w({}^{H}/{}_{H_0})_{\square t=4800} = 1.1 \cdot \log_{10}({}^{H}/{}_{H_0}) + 3.9 \tag{5.15c}$$

$$w({}^{H}/{}_{H_0})_{\square t=19500} = 1.1 \cdot \log_{10}({}^{H}/{}_{H_0}) + 2.6 \tag{5.15d}$$

The data for the triangle pulses and the corresponding fit equations (5.16a to 5.16d) show a slightly different behaviour. While the data is again parallel for the shorter glare pulses of 600 ms and 2400 ms with the same fitted slope parameters as for the rectangle pulses, only a lower axis intercept, the slope for longer pulses decreases down from 1.1 to 0.8 for the longest pulses. Again, all fit parameters are shown in table D.11 in appendix D.1.1, showing that the fitted functions are excellent representations of the recorded data with R^2 values of over 0.94 for all fits.

$$w({}^{H}/{}_{H_0})_{\triangle t=300} = 1.1 \cdot \log_{10}({}^{H}/{}_{H_0}) + 5.4 \tag{5.16a}$$

$$w({}^{H}/{}_{H_0})_{\triangle t=1200} = 1.1 \cdot \log_{10}({}^{H}/{}_{H_0}) + 3.7 \tag{5.16b}$$

$$w({}^{H}/{}_{H_0})_{\triangle t=4800} = 0.9 \cdot \log_{10}({}^{H}/{}_{H_0}) + 2.4 \tag{5.16c}$$

$$w({}^{H}/{}_{H_0})_{\triangle t=19500} = 0.8 \cdot \log_{10}({}^{H}/{}_{H_0}) + 1.7 \tag{5.16d}$$

This data shows the first impact of the pulse form on the glare perception. Since for pulses with the same exposure, the intersection with the y-axis at $x = 0$ is always lower for the triangle pulses, the general glare perception of these pulses is lower than the perceived glare of rectangle pulses. A second observation is, that due to the decreasing slope for longer triangle pulses, it can be deducted, that for longer, triangular pulses the duration has a higher impact compared to the maximum illuminance. When looking at rectangle pulses, this behaviour can not be seen and it is thereby deducted, that the slower rise of the illuminance gives the eye the chance to adapt to the to the illuminance level. For short pulses, this adaptation time is too short and thereby no difference in the slope values of the fit data is found.

In the next step, the findings from the study regarding the correlation between the pupil diameter and photometric values are used to rescale the exposure for all data sets. For the rectangle pulses this is shown in figure 5.58a and the fit data is shown in equation 5.17a with the fit parameters shown in appendix D.1.1 in table D.12. For triangle pulses the data and the fit is shown in figure 5.58b, the fit equation in equation 5.16 and the statistical data is shown in table D.12 as well in the appendix D.1.1 .

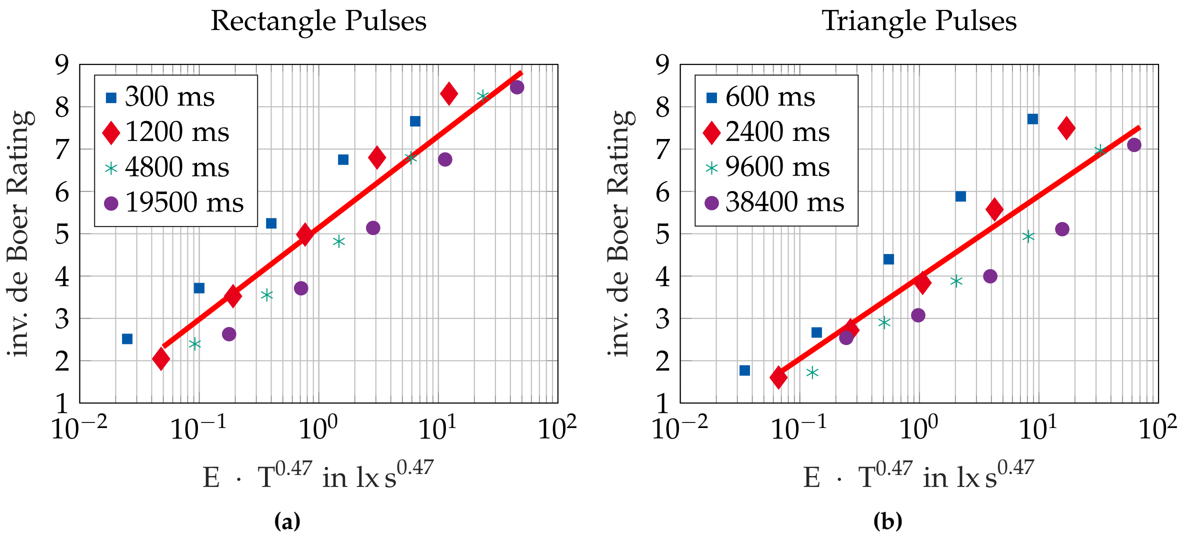

Figure 5.58 – Glare perception on the inverted DE BOER over the scaled exposure for (a) rectangle and (b) triangle pulses for the different shown pulse durations. The Exposure is scaled according to equation 5.9 with $p = 0.47$ and the fit is shown as the red solid line over all data. Blue squares show the data for 300 ms, red diamonds the data for 1200 ms, green asterisks show the data for 4800 ms and purple circles indicate the data for 19 500 ms pulses.

$$w(H/H_0)_{\square Mean} = 0.9 \cdot \log_{10}(H/H_0) + 5.1 \tag{5.17a}$$

$$w(H/H_0)_{\triangle Mean} = 1.1 \cdot \log_{10}(H/H_0) + 3.7 \tag{5.17b}$$

$$\tag{5.17c}$$

Again, the fit parameters indicate a very good data representation with R^2 values of over 0.8. However, as seen in figure 5.58a and 5.58b respectively, the data does not correlate as well as for the previous study ($R^2 > 0.98$). However, a significant improvement is made when compared to the unscaled exposure. When further investigating this behaviour, an optimized $p - value$ for this study is found at $p = 0$ leading to the best correlation with the illuminance instead of the exposure. This means, that for this study the pulse duration has no influence on the glare perception at all. This is shown for both, rectangle and triangle pulses in the figures 5.59a and 5.59b.

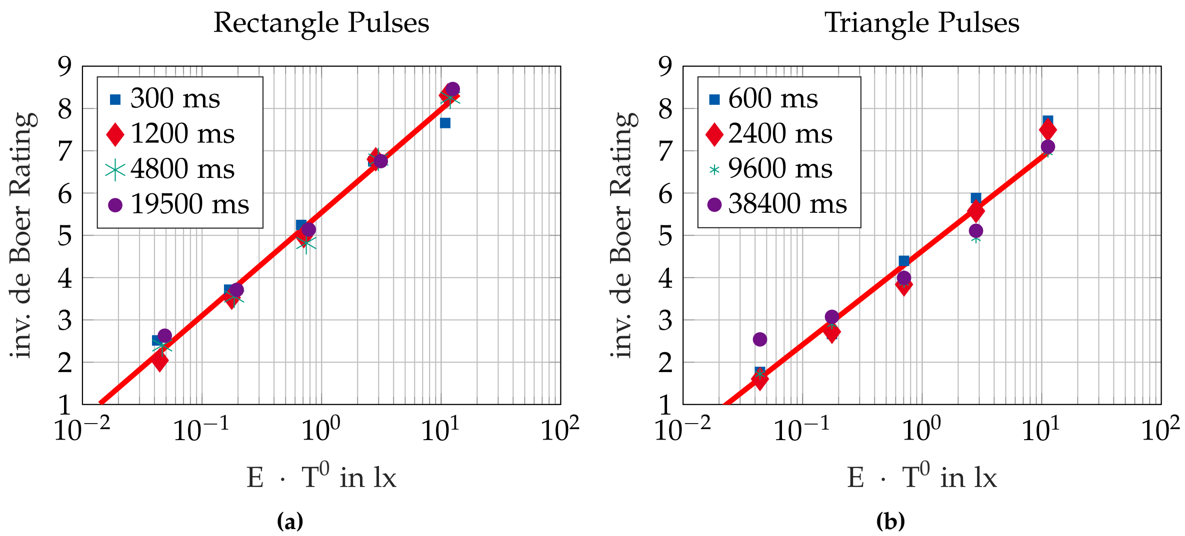

Figure 5.59 – Glare perception on the inverted DE BOER over the scaled exposure for (a) rectangle and (b) triangle pulses for the different shown pulse durations. The exposure is scaled according to equation 5.9 with an optimized $p = 0$ thereby showing the DE BOER rating over the illuminance. The fit is shown as the red solid line over all data. Blue squares show the data for 300 ms, red diamonds the data for 1200 ms, green asterix show the data for 4800 ms and purple circles indicate the data for 19 500 ms pulses.

The related fit equations are shown in 5.18a for the rectangle pulses and in 5.18b leading to the fit parameters presented in table D.13 in appendix D.1.1..

$$w(H/H_0)_{\square Mean} = 1.1 \cdot \log_{10}(H/H_0) + 5.6 \tag{5.18a}$$

$$w(H/H_0)_{\triangle Mean} = 0.9 \cdot \log_{10}(H/H_0) + 4.6 \tag{5.18b}$$

(5.18c)

This leads to much better results than the fits with $p = 0.47$. With R^2 values of over 0.95 this correlation is found to be very good. Since this is true for both pulse forms, either the way this part of the study was conducted, with two different pulse forms, influences the rating, or the $p-$value changes for different pulse durations. This might be the case, since the maximum pulse durations are changed to much longer pulses in order to investigate the influence of those. Therefore, the data from the pulses with durations higher than 2400 ms are left out of the next evaluation and for the short pulses, the fit with $p = 0.47$ is repeated for rectangle and triangle glare ratings separately. This is shown in figure 5.60. Here, the rectangle pulses are marked by the blue rectangles for 300 ms pulses and red diamonds for the 1200 ms pulses. The correlating fit is shown by the red solid line. The triangle pulses with a duration of 600 ms are represented by the orange triangles and the triangle pulses with a duration of 2400 ms are shown by the purple, upside-down triangles. The correlating fit is shown by the orange, dashed line

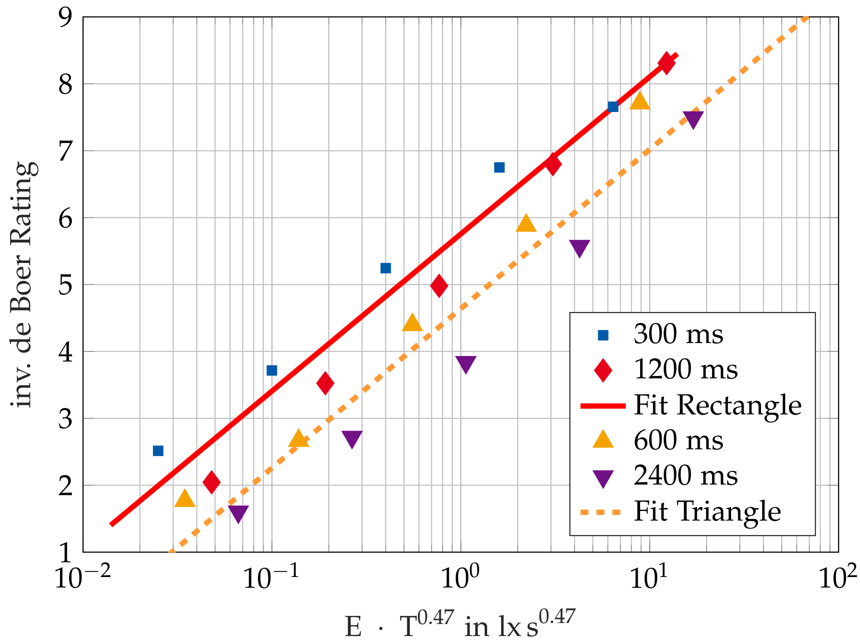

Figure 5.60 – Glare perception on the inverted DE BOER scale for all pulses under 2400 ms over the scaled exposure according to equation 5.9 with $p = 0.47$. The rectangle pulses are marked by the rectangles and the diamonds and the correlating fit is shown by the red solid line. The triangle pulses are represented by the two types of triangles and the correlating fit is shown by the orange, dashed line.

This figure again shows, that triangle pulses are, also for the shorter pulses and with the optimized exposure with $p = 0.47$, triangle pulses are regarded to be less glaring than the rectangle pulses by an average of one DE BOER rating. The fit equations for both fits are shown in the equations 5.19a and 5.19b

$$w(H/H_0)_{\square Mean} = 1.0 \cdot \log_{10}(H/H_0) + 5.8 \tag{5.19a}$$

$$w(H/H_0)_{\triangle Mean} = 1.0 \cdot \log_{10}(H/H_0) + 4.6 \tag{5.19b}$$

(5.19c)

As shown in table D.14 these fits again lead to a very good representation of the recorded data with R^2 values over 0.95 and all fit error measures much lower than shown in appendix D.1.1 in table D.12. This means, that for perfect correlation over different pulse durations, a variable $p-$value needs to be assumed. This will be addressed further in the comparison of the two glare studies.

Firstly, the focus is set to the comparison between the two chosen pulse forms. Therefore, in the next step, the comparison between the DE BOER rating for the rectangle pulses and the triangle pulses is done. In the first step, the ratings for all pulses are compared. Since the duration for each triangle pulse is doubled compared to the rectangle pulse, all pulses for each set only contain pulses with equal maximum illuminance and equal exposure. Box plots for both data sets are shown in figure 5.61a, and in more detail split up for all exposure values in 5.61b. In both figures, glare ratings for the rectangle pulses are shown by blue box plots and glare ratings for the triangle pulses are represented by the red box plots. This is also marked by the symbols at the x-axis of each plot. In figure 5.61b, the values set at the x-axix show the exposure values for the rectangle pulse (left) and the triangle pulse (right) for each data set.

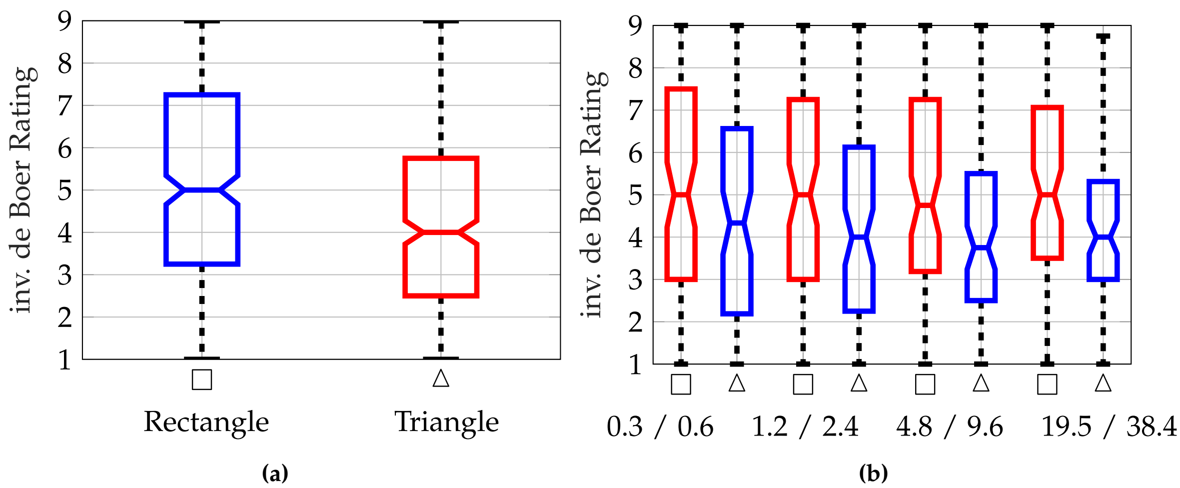

Figure 5.61 – Comparison of the glare perception on the inverted DE BOER scale between rectangle and triangle pulses. (a) shows box plots for all glare ratings over all rectangle and triangle pulses. The mean ratings are 5.2 for rectangle and 4.3 for triangle pulses. (b) shows the same data split up for the different exposure values. Red box plots indicate the rectangle pulses and blue box plots indicate triangle pulses.

Figure 5.61a clearly shows, that even so both data sets contain the same maximum illuminance and the same exposure, the triangle pulses are generally rated less glaring. Statistical analysis using the MANN-WHITNEY-TEST shows no significant difference between the rectangle and the triangle pulses ($p > 0.3$ for all data sets) due to the large deviation between the different test subjects. However, the median of the rectangle pulses is rated at 5 (*just admissible*, and thereby directly at the threshold of glaring or not glaring. The triangle pulses however are rated one step lower at 4 between *just admissible* and *satisfactory* and thereby not noticeable disturbing. Looking at the single duration sets in figure 5.61b, it is obvious, that this trend continues with every duration set of the rectangle pulses being rated one DE BOER rating lower than the correlating rectangle pulse set, even so, the pulse duration is doubled for the triangle pulses.

This leads to the conclusion, that no matter the illuminance or the duration, a light pulse, will be rated lower regarding the discomfort glare, if the edges are sufficiently smooth and the illuminance rises to its maximum value instead of setting the maximum illuminance from the very beginning. This also means, when comparing the glare load from oncoming traffic, neither illuminance nor exposure alone contain sufficient information to calculate the possible glare rating. The pulse form plays a significant role for this as well. Translating this to an automotive use case, the photometric values of two pulses could be identical and without considering the pulse form, the calculated glare perception by ZYDEK, LEHNERT or KOSMAS would lead to identical results. With the results from this study, the smoother light pulses can be rated around one inverted DE BOER rating lower than the glare perception for rectangle-like pulses. Furthermore, this part shows, that the modified exposure $E \cdot T^p$ with $p = 0.47$ is not valid over all durations. Pulses of different durations need to be evaluated differently. The exposure directly correlates to the glare perception only for very short pulses ($T < 300\,\text{ms}$) or if all pulses have the same duration. However, if all pulses have the same duration, this is equivalent to the correlation with the maximum illuminance, and to find the correlating DE BOER value, the duration needs to be known.

5.3.3 SUMMARY AND CONCLUSION OF GLARE PERCEPTION FOR SHORT LIGHT PULSES

The following sections will compare the two conducted studies regarding the glare perception of short light pulses of different properties. Then the achieved data will be compared to previous findings and a short outlook into future possibilities is given.

COMPARISON OF BOTH STUDIES

When comparing the two studies about the glare perception of light pulses, the differences in the testing procedure and the data generated need to be addressed first. The most important difference is, that no pupil data is available from the second study. The second large difference is the pulse duration. The first study consisted of pulses with the durations of 128 ms to 2000 ms and the second part used pulses of up to 19 500 ms for the rectangle pulses. Secondly, the range of the illuminance values is changed between the two setups. In the first set, the illuminance is varied between 0.2 lx and 203.2 lx. This is reduced down to illuminance values of 0.0 lx for the darkest and 11.3 lx for the brightest pulse. Since the triangle pulses cannot be compared to the data from the first test, they will be left out here.

For the rectangle pulses, the short durations between both studies can be compared. This is shown in figure 5.62 where the data from the first test is marked by V1 and the data from the second test is marked by V2.

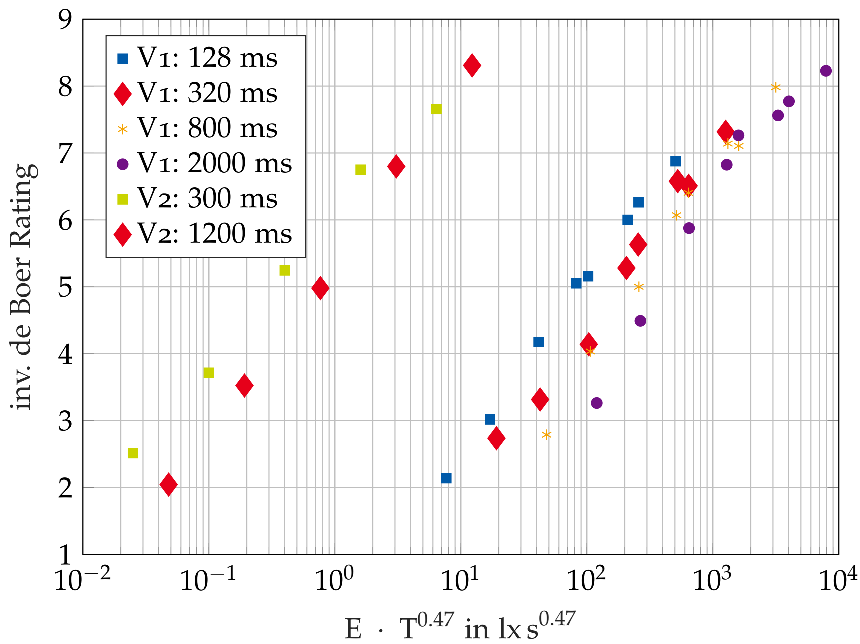

Figure 5.62 – Comparison of the glare rating for short pulses between the two performed studies. The data from the first study is marked by V1 and the data from the second test is marked with V2.

It is immediately obvious, that the two sets do not compare at all. Due to the different illuminance values, the general exposure values are much lower in the second test. However, there are exposure values that appear in both tests between 7 lx s^0.47 and 20 lx s^0.47. The important thing is, that these similar pulses are rated completely differently. The data from the first test is rated as below 3 on the inverted DE BOER scale. The data from the second test is rated between 7.6 and 8.3, meaning that the data from the first test is rated as *Satisfactory* or less and thereby not glaring while the data from the second test is rated between *disturbing* and *unbearable*. Since all surrounding parameters, like adaptation time and surrounding luminance, are kept the same, this is only explained by the way both tests are performed. In both parts, a selection of the lowest and the highest pulses are shown for the test participants as anchor stimuli. The possible explanation for this behaviour is, that due to these anchor stimuli are unconsciously used to sort all shown glare pulses onto the de Boer scale and thereby resulting in two separate data sets.

This subconscious behaviour also explains the general form found in the glare ratings. The expected results of both studies were to receive a s-curve for the glare ratings. For very very low light pulses no glare should be perceived and going even lower should not change this perception. The same is expected at the upper bounds. Beyond a certain threshold, every light pulse should be perceived as *unbearable*. However, due to the assumed subconscious sorting of all pulses according to the anchor stimuli, both maximum and minimum of the glare pulses are associated with the maximum and the minimum of the de Boer scale. All other glare pulses are then sorted linearly (on the logarithmic scale) between these anchor stimuli.

comparing the data to related work

As described in chapter 4 several studies have examined the correlation between the psychological glare perception and different photometric values. This section will now focus on comparing the results from this study with the results found by Lehnert who found a correlation between the illuminance, the pulse duration and the de Boer rating and the results from Zydek who found a correlation between the exposure and the de Boer rating in real life driving tests [55].

As explained in chapter 4 the test setup for both Lehnert and Zydek are more real life test setups and therefore the comparison between the results achieved in the laboratory study in this thesis and their results achieved under completely different setups is highly relevant since the translation from the laboratory experiments to the real life tests is one of the goals of this study. The formula provided by Lehnert is dependent of the pulse duration, his glare rating is calculated for the same experimental setup as in the first part of this study. Since this thesis used the inverted de Boer scale, the data obtained in this thesis is transformed to the original de Boer scale as well. This means, that in this case, a rating of 9 corresponds to a glare peak that is *just noticeable* and a rating of 1 means an *unbearable* glare peak is perceived. This is shown in figure 5.63 where the data obtained by the equation 4.1 is shown in the dashed lines compared to the data obtained in this study. The same is done for the glare rating obtained by Zydek in figure 5.64. However, since the work of Zydek is based on exposure calculated over a longer period of time (18 s) it is not possible to convert his data into illuminance data or to split his ratings into different pulse widths.

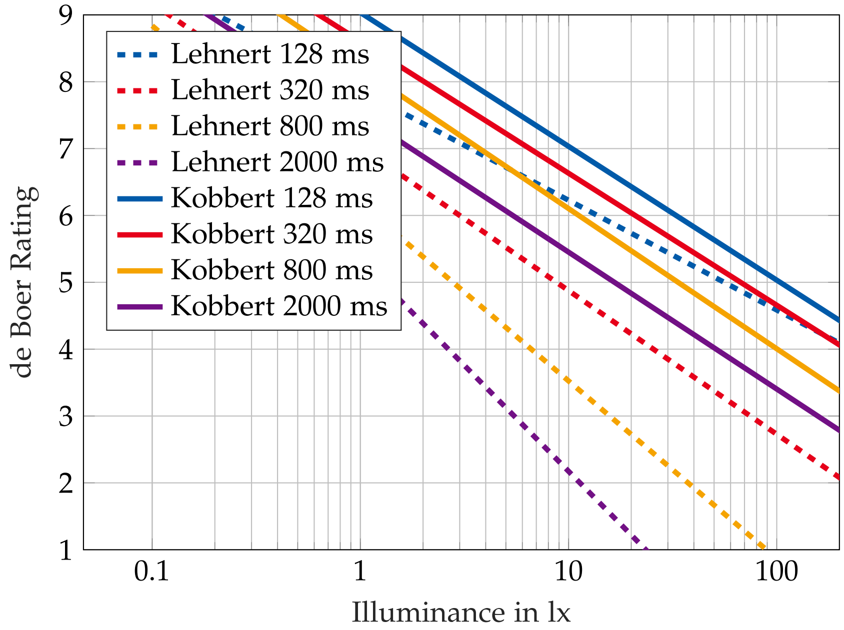

Figure 5.63 – Comparison of the glare perception on the DE BOER scale between the glare perception according to LEHNERT (dashed) over the pulse illuminance.

It can be seen, that while the range of the photometric values is similar, the resulting glare is indeed different. While the data shown by LEHNERT shows a similar slope, his illuminance pulses are in general rated more glaring than the data presented in this thesis. However, while the data obtained in this thesis is parallel over different durations, the data shown by LEHNERT widens up for higher illuminance values. The data shown by ZYDEK shows the exact opposite in terms of behaviour. The overall rating is fairly similar, however the slope is much higher in his case.

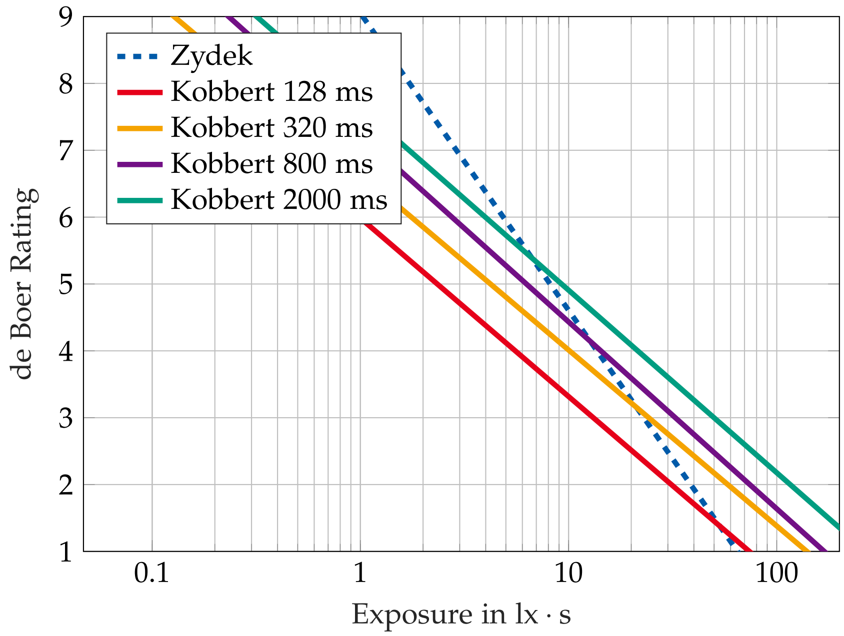

Figure 5.64 – Comparison of the glare perception on the DE BOER scale between previous work and the results from the experiments shown above, the data as found by ZYDEK (dashed) over the exposure.

Here it can be seen, that while the range of the photometric values is similar, the resulting glare is indeed different. While the data shown by Lehnert shows a similar slope, his illuminance pulses are in general rated less glaring than the data presented in this thesis. A special remark needs to be made to the dependence on the duration. The shorter the pulse duration, the smaller the deviations between the two works. This overall lesser rating is expected since the additional stress in the real life test is much higher compared to the situation in the laboratory. Additionally, it can be assumed, that the background luminance in the laboratory is much significantly lower compared to Lehnert's real life test, thereby increasing the perceived glare as well. However, while the data obtained in this thesis is parallel over different durations, the data shown by Lehnert widens up for higher illuminance values. The data shown by Zydek shows the exact opposite in terms of behaviour. The overall rating is fairly similar, however the slope is much higher in his case.
This again shows, similar to the data presented in figure 5.62, that the glare rating is very much dependent on the current situation and the other glare sources presented to the test subjects. If the overall range of the glare pulses/sources is smaller, the slope will increase. If the range is about the same, but the pulses/sources are shifted in terms of their photometric values, the overall rating will be shifted as well.

Summary, conclusion and outlook on glare and pupillometry studies

The goal of the studies is, to find a strong correlation between a physiological parameter and the glare perception of the test participants and transfer this data to real life driving tests. To achieve this, two main studies are performed. In the first part, the correlation between the photometric values illuminance and exposure, the glare rating and the pupil diameter are found with very good results for the correlation between both, de Boer rating and pupil diameter and modified exposure, respectively. In the second part, the rectangle pulses were changed to triangle pulses and the findings here, indicated a better correlation to the illuminance for longer pulse durations. Nevertheless it can be concluded that a pulse with rising edges (triangle) is always perceived less glaring than a rectangular pulse no matter what photometric value is used.

The main point, that can be taken from these two studies with regards to the correlation between photometric values and glare perception is, that neither exposure nor illuminance are correlating values over the investigated data range. The correlation found is best described by equation 5.20.

$$G = E \cdot T^{p} \tag{5.20}$$

From the data presented, it is concluded, that p is not a specific value but rather dependent on T, the pulse duration and the equation therefore needs to be modified to equation 5.21.

$$G = E \cdot T^{p(T)} \tag{5.21}$$

Taking into account all the data shown in both studies, three major regions appear. For pulse durations smaller than 300 ms the best correlation between the glare rating and the exposure is found. For medium pulse durations between 300 ms and up to around 2000 ms the correlation is optimized for $E \cdot T^{0.47}$ and for longer pulses the correlation is found to be best in line with the illuminance and the duration does not interfere at all. This leads to the following equations 5.22:

$$\text{if} \quad T < 300\,\text{ms} \quad p = 1 \tag{5.22a}$$

$$\text{if} \quad 300\,\text{ms} < T < 2000\,\text{ms} \quad p \approx 0.5 \tag{5.22b}$$

$$\text{if} \quad 2000\,\text{ms} < T \quad p = 0 \tag{5.22c}$$

Since the obtained data only covers specific points, a discrete function of p as presented is not realistic. Figure 5.65 shows an approximation of the suggested behaviour. The dotted purple line indicates the suggested behaviour of p and the three data sets indicate the findings for p at the three different pulse durations.

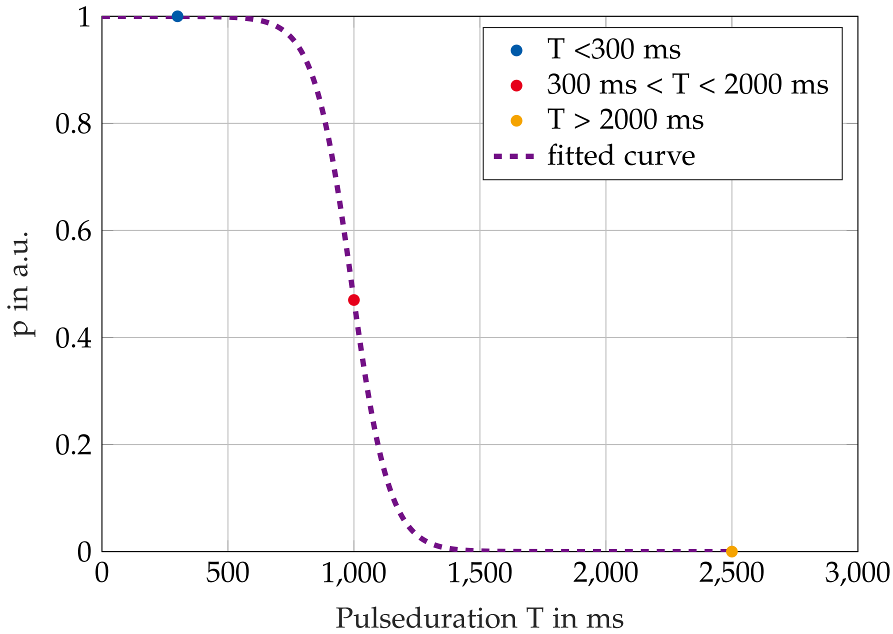

Figure 5.65 – Suggested bahaviour of p (equation 5.21. The suggested behaviour is indicated by the dashed purple line and the data points show the findings for the different pulse durations.

The proposed function in figure 5.65 is only an approximation with only three major available data points. The fit function is given in equation 5.23. With only three data points, both the x-shift (indicated by $-T + 990$) and the slope (indicated by the $x^{-0.02}$) need to be investigated further. Using this factor, it is then possible to evaluate the glare perception for different light pulses even with varying durations. The main issue here is, when comparing both studies, that due to the presented anchor stimuli, no absolute assessment can be done.

$$p(T) = \frac{1}{(1 + e^{(-T+990)})^{-0.02}} \tag{5.23}$$

However, the investigated pulses are only simplified approximations of the illuminance values recorded in real life driving tests. Additionally, to that more limitations to the performed studies have to be mentioned:

- the tests were performed with a 20 s break between all pulses. Both the pupil as well as the perception of the test subjects therefore had enough time to re-adapt to the surrounding luminance. In the real life driving tests, pulses were recorded, following nearly immediately after one another. Due to the different vehicles in real traffic situations, those pulses will additionally change in intensity, form and duration depending on the vehicle and the headlamp that is inflicting the glare pulse on other traffic participants.
- the tests were performed in the darkest setting possible to minimize the influence of adaptation. In real life tests, surrounding luminances and therefore adaptation luminance of up to $5\,\mathrm{cd\,m^{-2}}$ can be recorded.
- Between all pulses, the glare source was turned off completely. When comparing this to a real life traffic encounters, the situation would be more comparable to a situation, where the glare LED would be dimmed to a base level and the glare pulses are set to be offsets on this base level.

For further studies, each of these remarks could be investigated further for a more detailed correlation between the glare perceived in real life traffic encounters.

Concerning the correlation between a pupillary reaction as a response to a potential glare pulse it needs to be said, that while knowledge of the complete pulse properties need to be known, since correlation between pupil diameter and glare rating is highly dependent on the pulse duration, a more absolute glare rating could should be possible compared to the psychological evaluation. However, since the second part of the study did not involve any pupil data, it is impossible to predict the pupillary behaviour compared to the effect shown in figure 5.62. Therefore, it is recommended to investigate the pupillary reaction under more and different lighting conditions as well.

5.4 OPTIMIZING PARAMETERS FOR LIGHT DISTRIBUTIONS ON REAL ROADS

In the previous sections, the influence on the detection distances under ideal road conditions, with straight roads, no other traffic participants and no distracting light sources, is shown and discussed. Additionally, German traffic space is investigated with the help of a simplified traffic simulation and model that is then validated with real traffic data. Based on this data, the road illumination by gfHB systems is optimized with variable segment sizes. In the last part, the ground work for pupillary behaviour under different light pulses with the correlation to glare perception is set. With this knowledge, the setup used in the traffic space investigation is also used to monitor different data from the driver to further understand the perception of traffic and the traffic space. This section will therefore explain the test setup and the constraints that this setup is limited by, show and analyse the driven test course in detail to fully understand the auxiliary conditions of this study, introduce gaze distributions and gaze behaviour and statistically analyse this gaze behaviour for different recorded traffic situations. This data set is then used in the next sections to further optimize the light distribution for different situations for the drivers need.

5.4.1 TEST SET-UP

To fully understand the data shown in the next paragraphs, it is necessary to fully show the test setup used for this study. This paragraph will therefore focus on the test vehicle and especially the lighting systems in use, shortly introduce the measurement equipment for illuminance and GPS-data before going into further detail for the eye tracking set up. This will include the eye tracking setup it self, the calibration routine and the achievable results for accuracy. The camera system and object recognition software used for this study is already described in section 5.2.

TEST-VEHICLE AND TEST-EQUIPMENT

Since this study focuses not only on objective and independent variables like traffic density and object position, but focuses on the driver's traffic perception through gaze monitoring and the combination of this with the mentioned objective measurements, the influence of the test vehicle is not to be neglected. Therefore, the following sections will focus on the vehicle setup, the lighting parameters and the smaller measurement equipment.

VEHICLE AND LIGHTING PARAMETERS

The vehicle in use is a BMW 3-Series from 2016 equipped with a full LED headlamps. To minimize the influence of different light distributions, the headlamps are without any AFS functionality. The high beam is set to manual, so that the driver needs to decide at what point the use of high beam is necessary and useful. The measured light distribution for low beam is shown in 5.66 for a single headlamp. The light distribution for the low and the beam is found in appendix E.1 in figure E.1.

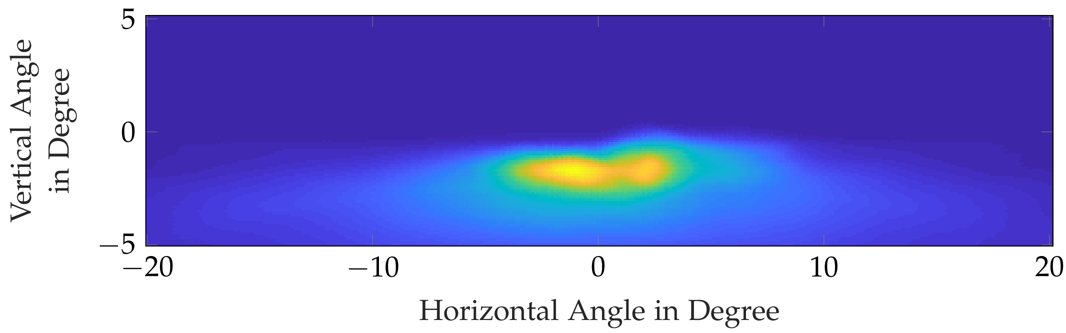

Figure 5.66 – Light distribution for low and high beam for the BMW LED headlamps used for the study. The colour map indicates the recorded luminous intensity under all angles.

The test vehicle is setup with a navigation system in the centre console and a head up display. For daytime driving, the brightness settings for all interior and armature is set to maximum to allow all participants to safely read and identify any system or navigational messages. For nighttime drives, all settings are set to minimum to minimize additional, disturbing light for the participants. An interior view of the vehicle is shown in figure 5.67.

Figure 5.67 – Interior of the test vehicle with the eye tracking cameras marked by the red circles, the infra-red light sources by green circles, the stereo (scenic) camera by yellow circles and the position of the illuminance sensor by the blue circle. The GPS sensor is located on the roof of the vehicle and therefore not present in this image.

Red circles mark the eye tracking cameras, green circles the infrared illumination, yellow circles the stero scene camera and the blue circle indicates the position of the illuminance measurement head.

GPS AND ILLUMINANCE MEASUREMENT

To measure the illuminance the driver perceives during the test drives, the illuminance is measured at all times. This is done using a X1-1 from GIGAHERTZ ELECTRONICS. The X1 allows a maximum measurement frequency of up to 20 Hz while maintaining an auto-range setting to enable measurements across a large range of illuminance. The measurement head is located right behind the rear view mirror, indicated by the blue circle in figure 5.67. Compared to the location right next to driver's head this position offers both, advantages and disadvantages. This position is located further away from the driver's head, leading to slightly different values than the driver actually perceives, and due to the position behind the mirror, it does not record light reflected by the rear view mirror. On the other hand, the driver can not cover the measurement head by moving his position. Furthermore, the position and of the sensor stays the same for all test drives and is not influenced by movement of the driver's seat. Additionally, to that, the rear view mirror in the test vehicle dims downs automatically and thereby reduces the light reflected to the driver anyways minimizing this influence.

The GPS sensor is set to 10 Hz and located on top of the test vehicle over the right passenger seat at the back.

EYE-TRACKING SYSTEM

The main measurement equipment however, the eye tracking system, is the same system as used is in chapter 5.3. This system is already pictured in figure 5.67 where the four cameras used are shown by the red circles. As explained in chapter to guarantee equal light situations for both day and night drives, the cameras are fitted with infrared passband filter and three additional light sources, marked by the green circles in figure 5.67, are installed. The cameras and the infrared light sources are placed in a manner, that allows for wide and natural head movement, while minimizing the impact on the vision of the driver.

Before each test run, the cameras need to be calibrated towards each other using integrated calibration routine of the Smart Eye software. In the next calibration step, the gaze direction for each test subject needs to be adjusted since, as explained in chapter 2, the calculated gaze direction through the eye ball centre and the actual gaze direction, are not the same and for every test subject different. The setup for this is shown in appendix E.1 in figure E.4.

5.4.2 Testing procedure

To analyse the gaze and fixation behaviour of drivers during real life driving, a course, starting in Darmstadt, following the $A5$ and leading through Frankfurt on different country roads back to Darmstadt, is selected. This route is explained in more detail in section 5.2.2. The main reasons for this course are, the large variety of road situations, so motorway, country road and urban environments can be mapped. The motorway section in the beginning is chosen to allow for an easy adaptation to the test vehicle. The route, shown in figure 5.32, is then driven twice by each participant. Once during the day and then again once after sunset. The available starting times are 9:00, 13:00 and 20:00. For this study, 54 test subjects are invited to perform the test, resulting in 108 test drives with a total recorded distance of 11 156.5 km and a duration of 285 h 38 min. Since this study, in its design already encounters a lot of variables, that can not be controlled but only recorded, the influence through the test subjects is minimized by only selecting drivers with an age above 19 and below 40 years and a minimal driving experience of 1 year and 1000 km annually. The exact data for the test subjects is found in appendix E.1 in table E.1 and visualized in figure E.5.

The complete detail about all test subjects including their starting and finishing times for both drives, and their physiological (eye-) parameter can be found in appendix E.1 in table E.1. To record and type of fatigue arising through the up to 3 h test drive, at the start of each drive an attention test is performed by each participant. For this test, a sequence of 100 single digit numbers is shown and the participant is asked to press any button on a computer keyboard, as soon as the number shown, equals the second last number. This is visualized in the following sequence, where no button press is required in the first sequence, then two consecutive presses are required in the second sequence (marked in bold) and again, no button press is required in the last sequence.

1 3 4 2 3   1 3 4 2 3 **2** **3**   1 3 4 2 3 **2** **3** 4 6

Here the amount of true-true, true-false, false-true and false-false selections are recorded. To further minimize the driver's fatigue, a short break at half time of up to 10 min is offered.

After the attention test, and the car is set up according to the driver's preferences regarding the seat position and the rear view mirror orientation, the eye tracking calibration is done. For this process, the participants are asked to look straight at P_1 to P_6 for about 1 s each. The software then records the vectors calculated from the eye model and compares them with theoretical vectors from the eye position to the calibration points. From the difference between both vectors a calibration matrix is calculated and for the calibrated gaze vectors, both accuracy and precession are calculated. This calibration routine is repeated up to 5 times or until accuracy and precession are below 2°. The limit of using 5 consecutive repetitions and recalibration is set to limit the amount of time spent for preparation. The data recorded for the accuracy, the difference between the mean gaze direction and theoretical gaze direction, is listed in appendix E.1. After the gaze calibration, the stereo camera system, the GPS and the illuminance measurements are started and the driver is asked to follow the navigation directions. During the whole preparation and testing phase, the test supervisor is positioned at the right back seat to monitor all data streams and, in case of any unexpected occurrences, intervene and help the test participant. Throughout the test drive, the test supervisor interacts in a natural, light conversation similar to normal driving. The goal is, to keep the circumstances as usual as possible and avoid any clinical atmosphere for the participants since the goal is to record normal, daily gaze behaviour under different conditions. After the course is completed, the attention test is repeated to record any differences in attention over the duration of the test drive. The results for the attention tests are shown in the figures E.6 in appendix E.1.The error made in the attention test after the test drive are in general less than the errors made before the drive. However, the difference is small and not significant. Nevertheless, the median of the errors made before the test drive is recorded at 4 errors and only 2 errors after the test. This difference should not be associated with an increase in attention during the ride but rather with a learning effect since the second run through the attention test is easier than the fist one.

5.4.3 ROAD CATEGORIZATION

Since the driver's gaze behaviour is not only of relevance in general, but for specific situations as well, the whole test drive needs to be categorized. This can be done for both, soft and hard parameters. Hard parameters are, for this thesis, defined as parameters that will stay, within a margin of error, the same for each driver. This includes road geometry, speed limits, lane numbers, traffic sign locations, motorways, country roads and rural roads. Soft parameters on the other hand are parameters that will change for each test run and of course for each test driver. Soft parameters include the illuminance measured at the driver's eye, driven speed, acceleration, individual driving manoeuvres like overtaking or lane changes, traffic volume, weather traffic lights and many more. In the next couple of section, the both parameters sets will be identified, specified and as far as possible grouped into several bins. Soft parameters that cannot be grouped into feasible bins will be listed and their influence on the test results will be discussed.

HARD PARAMETERS

Since hard parameters are constant for each run and every test person, all hard parameters can be grouped together successfully and therefore be used for analysis of the gaze distributions and behaviour. The hard parameters that were identified for this particular road are:

- **Road Location**
- **Road Curvature**
- **Speed Limits**
- **Traffic Lanes**
- **Traffic Signs**
- **Day/Night Drives**

To match each recorded GPS location to one of the mentioned hard parameters, the OSM database is chosen [182]. The OSM database is an open source and license free database, where users can submit road data to any given road. This approach leads both advantages as well as disadvantages. Compared to commercial solutions, everyone, who is interested, can submit data to road segments they have information on. This has the benefit of a large information pool and a large number of people working on the database. Additionally, there is no preference for densely inhabited areas as such. The main drawback on the other hand, is that the information passed on online, is not reviewed by anyone else than the users themselves.

However, since no other database is availabe, that provides the same amount of information, this approach is decided to be feasible. The OSM data is available for download online via the OSM overpass Application Programming Interface (API). After selecting the area, all data available is downloaded using the *Java-OpenStreetMap-Editor* [183]. This dataset is shown as a graphical visualization in figure 5.68a. It can be seen, that data is now available for the complete region. To avoid mismatching between the recorded GPS data and the OSM data, this data is now matched once by finding the closest coordinates between both datasets. Since the result still contains some data points that are outside of the specified route, the resulting data is checked manually and mismatched data is deleted from the OSM data set. The reduced dataset is visualized in figure 5.68b

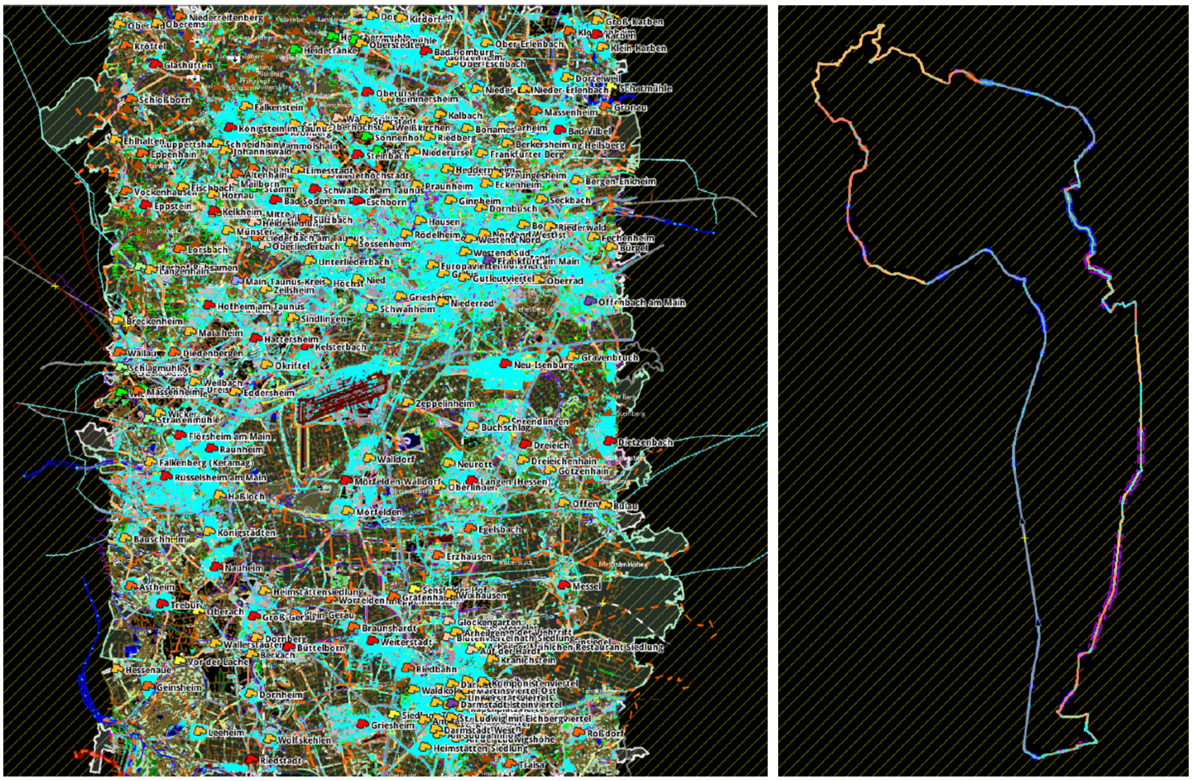

(a) **(b)**

Figure 5.68 – Visualization of the OSM data used to match the hard data to the recorded GPS data. In (a), the data for the complete area is shown, (b) shows the reduced data for the recorded course.

The data itself now consists of so called *Nodes* and *Ways*, while a *way* is the connection between two *nodes*. The GPS information is stored in the *nodes*, while the road information is stored in the *ways*. To match the data from the OSM data set to the recorded GPS data, the information stored in the *nodes* is combined with the information of the *ways* using the tool *OSM Converter* [184]. The resulting data now contains all required information - both GPS location and the hard parameters. These parameters are listed in appendix E.1 in the listing E.2.

This data is now being matched with the recorded GPS data by finding the closest possible distance between the recorded data and the position data of the OSM data.

ROAD LOCATION

To categorize the different road locations, DAMASKY, KUHL and SCHWAB used the general classification of **Motorways**, **Country Roads** and **Rural Roads**, SCHULZ and HRISTOV each only focused on one of the mentioned road locations [131, 134, 140, 159, 160]. This paper follows this suggestion to a given extend and the each data point is merged into one of these three categories.

Since the OSM database is created and filled by volunteers, not all ways are filled with all information. Therefore, it is necessary to identify the key parameters that are viable to group the GPS data into one of the three categories. To identify which parameters are suited for the categorization, a pre-selection is done. Parameters that are obviously not suited for the categorization are: OSM-ID, since no correlation between the ID and any other metric can be found, OSM-Latitude and -Longitude, since this would involve manual selection of the categories for each test subject, OSM-Speed Limit, since the Speed Limit can vary for each road segment depending on the current infrastructure, however this can be used as secondary parameter, OSM-Lanes, since again there is no correlation between the number of lanes and the road type and OSM-Surface, -Smoothness, -Construction, -Bridge and -Cycleway since these parameters are mostly arbitrary for road types. OSM-City can only distinguish between rural and non-rural roads and can therefore only be used to further improve the binning of the recorded data set but not as a key parameter.

The pre-selected parameters then only include OSM-Reference, -Motorway Type and -City. After matching the OSM data to the recorded GPS data, each of the parameters was checked for availability for the route. Table 5.13 shows the total availability for the datasets as well as the average availability in percent for the whole route.

Table 5.13 – Total and average coverage for the selected parameters, OSM-Reference, OSM-Motorway-Type and OSM-City

	COMPLETE DATA	COVERED MOTORWAY TYPE
Total Number of Data Points	83 856 357	
Number of Data Types	13	
Total Data Covered	83 856 357	66 922 154
Total Data Not Covered	0	16 934 203
Average Data Covered	100 %	79.8 %
Average Data Not Covered	0.0 %	10.2 %

Due to the low coverage of OSM-Reference with 79.8 %, the Motorway Type is the key parameter to group the data into one of the three bins. The key OSM-Motorway Type is now split into the 13 different categories with their definitions from the OSM-Database [185] as seen in the appendix E.1 in the listing E.2.

The next step is, to calculate average distance and time spent in each of those categories. Since the distance in each category should be roughly the same for each participant, with slight deviations caused by GPS issues, or blocked roads, the time spent in each section may vary largely depending on the actual speed the participants drive. Furthermore, the distance does not give a reproduction of the amount of data collected per category since the data rate is fixed to the time. The results for the time in each category are shown in appendix E.2 in table E.2. The data for the distance per category can be found in appendix E.2 for all 54 test runs as well in table E.3. This data is later used to normalize the acquired data for each category.

RURAL ROADS

A GPS datapoint is marked as a rural road, as soon as one of the following rules applies.

- The OSM-*Motorway Type* is either *Footpath*, *Path*, *Residential* or *Service*.
- The OSM-*Motorway Type* is either *Primary*, *Primary Link*, *Secondary*, *Tertiary*, *Unclassified* and the OSM-*Speed Limit* is equal to, or lower than $50\,\mathrm{km\,h^{-1}}$.
- The OSM-*Motorway Type* is *Trunk* or *Trunk Link* and the OSM-*Speed Limit* is equal to, or below $50\,\mathrm{km\,h^{-1}}$ and the OSM-*City* is either Frankfurt or Darmstadt.

COUNTRY ROADS

A GPS datapoint is marked as a country road, as soon as one of the following rule applies:

- The OSM-*Motorway Type* is either *Primary*, *Primary Link*, *Secondary*, *Tertiary* or *Unclassified* while the OSM-*Speed Limit* is higher than $50\,\mathrm{km\,h^{-1}}$ and OSM-*Lanes* is equal to two with OSM-*Oneway* yielding false.
- item The OSM-*Motorway Type* is either *Primary*, *Primary Link*, *Secondary*, *Tertiary* or *Unclassified* while the OSM-*Speed Limit* is higher than $50\,\mathrm{km\,h^{-1}}$ and below $100\,\mathrm{km\,h^{-1}}$ OSM-*Lanes* is equal to one with OSM-*Oneway* yielding true.

MOTORWAYS AND MULTI-LANE COUNTRY ROADS

A GPS datapoint is marked as a motorway, as soon as one of the following rules applies.

- The OSM-*Motorway Type* is either *Motorway* or *Motorway Link* and the OSM-*Speed Limit* is above $50\,\mathrm{km\,h^{-1}}$.
- the OSM-*Motorway Type* is either *Trunk*, *Trunk Link*, *Primary*, *Primary Link* or *Secondary* and the OSM-*Oneway* yields true, with OSM-*Lanes* being larger than one.

The matching rules are then checked for double entries in each category and then checked for entries marked in more than one category. While this is not the case, single GPS values cannot be assigned to any of the three categories. These points have their OSM-*Motorway Types* marked as *Primary* or *Secondary* but no other parameters were filled in. Since this leads to an average of 552 uncategorised data points (<0.1 %), these points are left out of the following data analysis. Table 5.14 shows the portion of the driven time for the three major road categories.

Table 5.14 – Average time driven and standard deviation between all 108 test runs in the three road categories.

	REL. TIME SPENT	ABS. TIME SPENT	STD. TIME	REL. STD.
Urban Roads	49.1 %	1 h 4 min 45 s ±	21 min 45 s ±	33.6 %
Country Roads	29.0 %	38 min 13 s ±	8 min 19 s ±	21.8 %
Motorways	21.9 %	28 min 53 s ±	5 min 34 s ±	19.3 %

This data shows a high deviation in all three categories. This is due to different traffic situations and different driven velocities for all drivers. Since all data points, that do not align with the planned route are not taken into account for the evaluation, this leads to the unexpected high variance in valid data points. Similar to the procedure above, the distance driven in each category is listed in the appendix E.2 in table E.4.

CURVATURE OF ROADS

To enable the possibility to investigate the above mentioned metrics for driving through bends, a method was developed to derive the curvature as well as the direction of the curvature from the GPS-Coordinates. This has been done before by PRATT and AI [186, 187]. Implementing and testing those methods however, did not lead to satisfying results for the presented data.

The first step of the proposed algorithm is the proper identification of a curve and its orientation. To calculate the orientation-angle Θ in degrees for each recorded GPS point, the tangent for the current path is being calculated. To do so, the latitude and longitude values have to be transformed into Universal Transverse Mercator (UTM) coordinates. In this coordinate system, distances in X and Y direction are equidistant and the distance is directly given in m. By taking the 5 prior and the 5 following GPS points of the current position, and subtracting the current position from these points, the data points are now accumulated around the axis origin. Using a least square mean fit, the a straight line, with axis intercept at (0/0) is then fitted onto those 11 points. Using the fitted value for the slope m, the angle can now be calculated by $\arctan(m)$. Since this angle does not distinguish between the quadrants I and III or II and IV, the actual direction is then calculated by the using the equations 5.24 to 5.27.

$$\begin{aligned} \text{for} \quad & X_{UTM}(i+1) > X_{UTM}(i) \quad \text{and} \quad Y_{UTM}(i+1) > Y_{UTM}(i) \\ & \Theta \quad = \quad 90 - \arctan(m) \end{aligned} \tag{5.24}$$

$$\begin{aligned} \text{for} \quad & X_{UTM}(i+1) > X_{UTM}(i) \quad \text{and} \quad Y_{UTM}(i+1) < Y_{UTM}(i) \\ & \Theta \quad = \quad 90 + \arctan(m) \end{aligned} \tag{5.25}$$

$$\begin{aligned} \text{for} \quad & X_{UTM}(i+1) < X_{UTM}(i) \quad \text{and} \quad Y_{UTM}(i+1) > Y_{UTM}(i) \\ & \Theta \quad = \quad 270 + \arctan(m) \end{aligned} \tag{5.26}$$

$$\begin{aligned} \text{for} \quad & X_{UTM}(i+1) < X_{UTM}(i) \quad \text{and} \quad Y_{UTM}(i+1) < Y_{UTM}(i) \\ & \Theta \quad = \quad 270 - \arctan(m) \end{aligned} \tag{5.27}$$

with the calculated orientation for each GPS point, the orientation change between successive data points can be calculated. A negative orientation change now indicates a left bend and a positive change in orientation, will indicate a right corner. Since the data was recorded in real traffic situations, orientation changes will occur between all successive data points, since this will still be the case for straight roads, in the next step, a threshold is defined for identifying corners. Since the possible orientation change differs for different velocities, this threshold was defined dependent on the current velocity. Equations 5.28a to 5.28c define, if a orientation change is regarded as a straight road or a left or right-hand side corner and the corner-marker C_M is defined.

$$\text{if} \quad -0.02 \cdot v^2 < \Delta\Theta < 0.02 \cdot v^2$$
$$C_M = 0 \tag{5.28a}$$

$$\text{if} \quad \Delta\Theta > 0.02 \cdot v^2$$
$$C_M = 1 \tag{5.28b}$$

$$\text{if} \quad \Delta\Theta < -0.02 \cdot v^2$$
$$C_M = -1 \tag{5.28c}$$

A $\Delta\Theta$ of 0 describes a straight road, -1 describes a left corner and $+1$ marks a right-hand side corner. The threshold of $0.02 \cdot v^2$ was defined by manually trying out several thresholds, velocity independent, dependent depending on v^2 as shown 5.28a. In the next step, the amount of consecutive corner - markers need to be defined, before a stretch of road is actually defined as a corner. For this thesis, the threshold was set to 5 consecutive GPS points, or 1 s of driving with a change in direction over the set threshold. If during a set of 5 or more points a single data point is calculated to belong to another corner type, this single point is then overwritten to ensure that small fluctuations within the GPS coordinates do not influence the definition of corners. The datasets with the same corner-marker are used to calculate the corresponding radius for each corner. Therefore, for each identified corner, the point with the largest change in orientation $\Delta\Theta_{max}$ is extracted. Then the minimal distance between $\Delta\Theta_{max}$ and either end of the corner is calculated. This distance is then used to calculate the number of data points, in both directions, that are used to calculate the actual corner radius. If the larger distance from $\Delta\Theta_{max}$ to the other end of the corner, is larger than 1.5 times the distance to the closer end and contains more than 5 GPS points, a new curve is defined here. This is done to avoid miscalculation of corner radii for situations in which a corner with a small radius directly leads into a corner of the same orientation, but with much larger corner radius, or the other way around. The defined points for a single curve $x_1, ...x_{11}$ and $y_1, ...y_{11}$ are then used to fit a circle onto the given data points by minimizing the sum of squared radial deviations. The general equation for a circle is given by the function 5.29a with the centre point of the circle $(-g, -f)$ and the radius R given by equation 5.29b.

$$0 = x^2 + y^2 + 2gx + fy + c \tag{5.29a}$$
$$R = \sqrt{g^2 + f^2 - c} \tag{5.29b}$$

The equation system for the least square minimization is shown in equation 5.30 with x and

y being the given UTM coordinates. $\vec{a}$ is the coefficient-vector for the circle equation, and the indices a_1, a_2, a_3 representing the circle function according to the equation 5.31.

$$\begin{bmatrix} x_{i-5} & y_{i-5} & 1 \\ x_{i-4} & y_{i-4} & 1 \\ \vdots & \vdots & \vdots \\ x_i & y_i & 1 \\ \vdots & \vdots & \vdots \\ x_{i+5} & y_{i+5} & 1 \end{bmatrix} * \vec{a} = \begin{bmatrix} x_{i-5}^2 + y_{i-5}^2 \\ x_{i-4}^2 + y_{i-4}^2 \\ \vdots \\ x_i^2 + y_i^2 \\ \vdots \\ x_{i+5}^2 + y_{i+5}^2 \end{bmatrix} \tag{5.30}$$

$$\begin{aligned} g &= -0.5 \cdot a_1 \\ f &= -0.5 \cdot a_2 \\ R &= \sqrt{\frac{a_1^2 + a_2^2}{4} - a_3} \end{aligned} \tag{5.31}$$

The results for this curve detection and radius fit can be seen in figure 5.69. Curves with a radius over 1000 m are treated as straight roads and radii below 50 m are declared as intersections and will therefore not be reviewed.

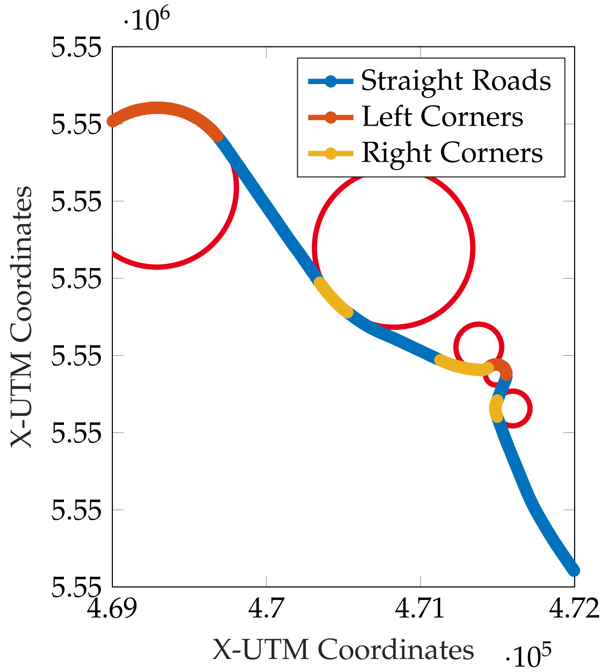

Figure 5.69 – Visualization of the curve-fitting algorithm with a zoomed in example with successive left and right bends. Blue marks straight roads, yellow marks left bends and red marks right bends.

This curve fitting algorithm is used for each test run separately since each driver might use a different driving line for each bend. The resulting bend distribution over all test drives is shown in figure 5.70. Negative curve radii describe left-hand bends and positive radii describe right-hand bends. The distribution for the different road sections, *Motorway*, *Country Roads* and *Rural Roads* are marked in the usual colours. This shows, that the smaller curve radii are much more likely for urban roads, then intermediately frequent for country roads and the least frequent for motorways. Very large curve radii on the other hand do not appear in cities at all, but are only present on motorways and country roads.

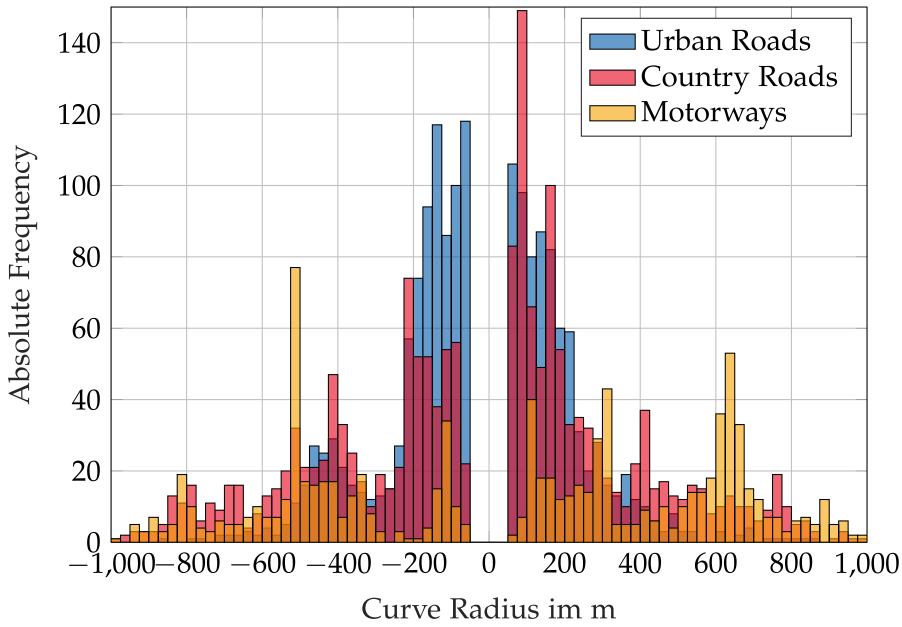

Figure 5.70 – The results of the curve fitting divided by the three road categories. Blue marks *Rural Roads*, yellow marks *Country Roads* and red marks *Motorways*. Negative radii describe left-hand bends, positive radii describe right-hand bends.

Furthermore, this data shows, that the curve distribution does not follow the distribution found by KUHL with a much more pronounced height in the small radii and a much more pronounced antisymmetry. One of the reasons here might be the more or less elliptical shape of the route, that clearly favours right-hand side curves. Furthermore, the fact that despite the large distance recorded, only the same route is repeated over and over again thus limiting the amount of different road geometries. A much broader test setup with different, or much larger, routes for each participant might therefore lead to different curvature distributions but would, on the other hand lead to other restrictions regarding repeatability or the possible number of test subjects.

On average, 30.7 curves are recorded in cities, 32.2 curves are recorded on country roads and 16.8 curves are measured on motorways. While fractions of a curve should not exist in this context, the reason for these values is, that due to GPS glitches, not all test drives are recorded completely and thereby for some participants, a lower number of curves is recorded and by averaging over all participants, fractions of curves can occur.

SPEED LIMITS

The road geometry is not the only limiting factor, that stays, with a few exceptions due to construction work, equal for all test drives. The speed limit for all driven segments stays similarly equal. For this reason, both, distance travelled and time spent within the limits of the different speed limits are evaluated. Speed limits available on the course are 30 $\mathrm{km\,h^{-1}}$, 50 $\mathrm{km\,h^{-1}}$, 60 $\mathrm{km\,h^{-1}}$, 70 $\mathrm{km\,h^{-1}}$, 80 $\mathrm{km\,h^{-1}}$, 100 $\mathrm{km\,h^{-1}}$, 120 $\mathrm{km\,h^{-1}}$ and 130 $\mathrm{km\,h^{-1}}$ and on motorways no speed limit. The average time spent and distance travelled within these speed limits for the recorded 108 test runs are shown in the appendix E.1 in table E.5.

This data however, is only the speed limit enforced by German government. This data needs to be compared and evaluated with the actual driven speed. Since the driven speed depends on many different parameters, the actual speed is set into the category of soft parameters and will be discussed in the following sections.

5.4.4 SOFT-PARAMETERS

In the sections above, parameters that do not or only in a very limited amount, change between test runs. This section on the other hand, will focus solely on parameters that change drastically between each test run due to a variety of reasons. For example the actual driven speed may deviate from the speed limit due to traffic, weather conditions, the driver's personality or other unknown factors. These variables like speed, traffic density, weather and lighting conditions are analysed and listed in accordance to their occurrence in the following paragraphs.

DRIVEN SPEED

As mentioned above, the data for the time spent/distance travelled in each of the speed limits gives a good idea on the actual velocity distribution. The speed distributions for all participants is shown in figure 5.71 separately for day and night drives. This is then split further into the driven speed for the different road types of urban roads, country roads and motorways. The blue bars mark the speed recorded in urban environments during the day, red marks urban environments during the night, yellow shows the velocity on country roads during the day, purple indicates speeds on country roads during the night, light blue marks the speed on motorways during the day and green bars show the speed driven on motorways during the night.

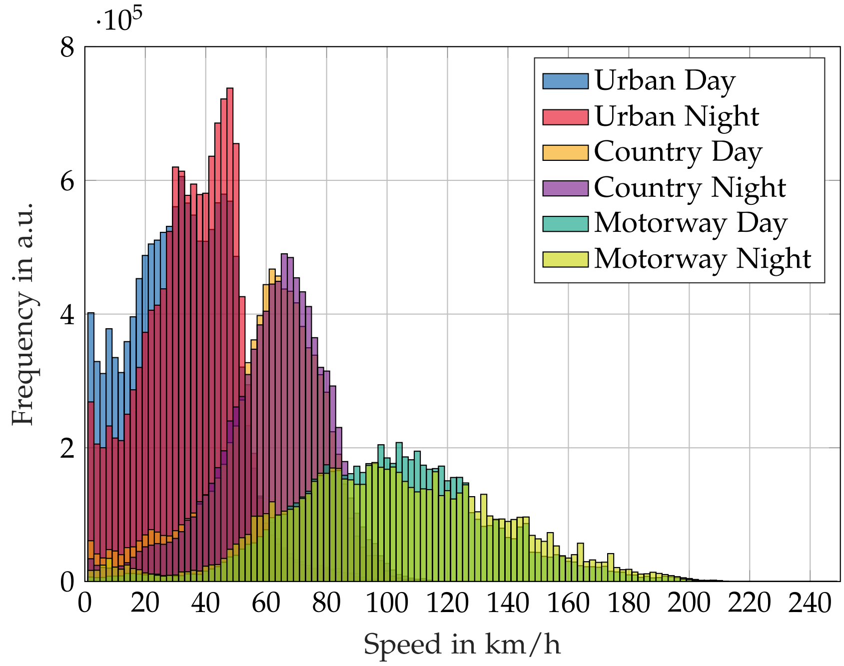

Figure 5.71 – Actual driven speed distributions over all test drives for day and night as well as the three major road categories. The blue bars mark the speed recorded in urban environments during the day, red marks urban environments during the night, yellow shows the velocity on country roads during the day, purple indicates speeds on country roads during the night, light blue marks driven speed on motorways and green bars show the speed driven on motorways during the night.

The mean velocities that are recorded during the day are 24.9 $\mathrm{km\,h^{-1}}$ in the city, 61.2 $\mathrm{km\,h^{-1}}$ on country roads and 100.3 $\mathrm{km\,h^{-1}}$ on motorways. For nighttime, the data is similar with only one deviation. The recorded velocity in the city is 31.6 $\mathrm{km\,h^{-1}}$. This figure visualizes for country and motorway driving directly, that the distributions of the driven velocities between day and night driving to not differ significantly in neither form nor absolute frequency. The data shown only includes speed data with a recorded speed above 1 km h^{-1} since data recorded while standing still will not be evaluated at all.

Remarkable features in this data are, that even for urban driving velocities of up to 100 km h^{-1} are recorded. However, these are single data points and originate from drivers entering a city from a country road and slowing down right at the city limit combined with slight GPS inaccuracies, as explained above, the speed limit in urban areas is limited to 50 km h^{-1}. For both, country roads and motorways a significant portion of the driven speed is below 50 km h^{-1} and even goes down to stand still. This is due to traffic jam, construction zones, intersections and traffic lights.

It needs to be highlighted, that dividing the recorded data by these major road categories will not do justice to the overall recorded data and that the dynamic factors need to be considered as well. A more detailed look at the driven speed in each section is given in appendix E.1 in table E.6.

TRAFFIC DENSITY

The traffic density is already evaluated in section 5.2.2 for overall data in figures 5.33 and 5.34. Therefore, the data is used from this section for further evaluation.

ILLUMINANCE

When investigating the drivers gaze behaviour and especially the pupil diameter during the rides, it is necessary to know the lighting conditions in which the rides take place. Analogue to the data shown regarding the actual driven speed, this section will show the different illuminance levels recorded at the driver's eye. Compared to the speed data however, this data here is split up in different sections for day and night drives, since the data here is expected to be significantly different for these two sets. Additionally, to the general lighting situations, the illuminance values are investigated regarding the adaptation level of the driver and therefore on possible occurring glare situations and their relative frequency. Figure 5.72 shows the general illuminance distributions for the 54 daytime test runs. Blue bars indicate the data recorded in urban environments, red shows the data recorded on country roads and yellow marks data from the motorways. The data is shown on a logarithmic x-axis to account for the brightness perception of the test participants and by that to better reflect the illuminance perceived by the drivers. Furthermore, this is a more accurate representation of the data for later correlation to the gaze behaviour and the pupil diameter.

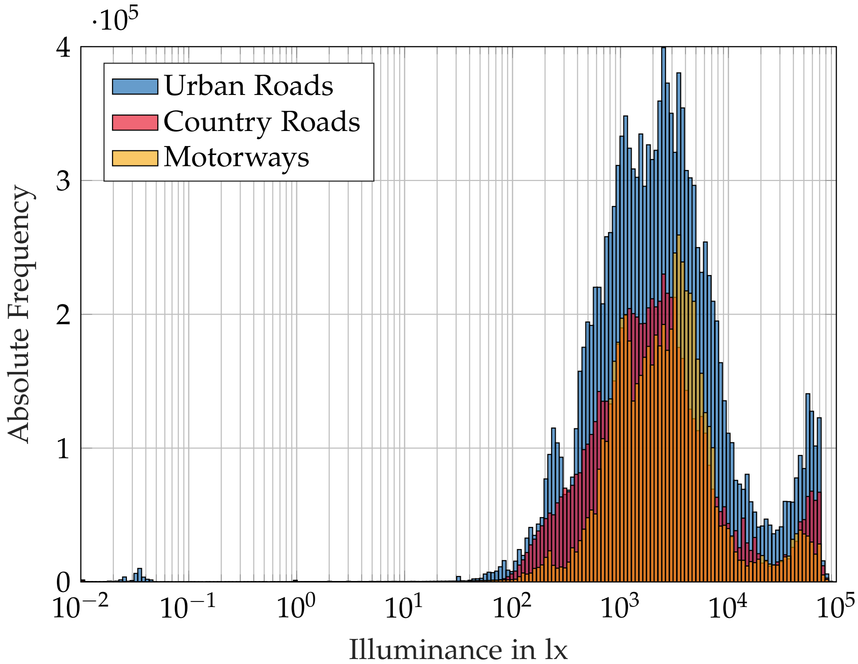

Figure 5.72 – Illuminance values recorded during the daytime drives for all 54 participants split up into the three major road categories. Blue bars indicate values recorded on urban roads, red bars show the illuminance values from country roads and yellow bars visualize the illuminance measured on motorways.

The data shows, that the recorded illuminance data between the three road categories is similar to each other. For statistical analysis the data is logarithmized and tested for normal distribution using the One Sample Kolmogorov-Smirnov test. The tests show, that none of the data sets origins from a normal distribution. Therefore, a Wilcoxon Rank Sum Test is used to calculate differences between the different road categories. While the data seems fairly similar, due to the very large sample size, the test rejects the hypothesis, that the distributions origin from the same distribution with $p = 0$.

Figure 5.73 shows the illuminance data at night analogue to figure 5.72. The x-axis is logarithmized, and the colour coding is kept the same. Again, One Sample Kolmogorov-Smirnov tests are calculated to test for normal distribution on the logarithmized data. The results show, that none of the data sets is normal distributed. Therefore, Wilcoxon Rank Sum tests are calculated to test for differences between the different distributions. Again, these tests reject the hypothesis of all distributions originating from the same distribution with $p = 0$. Here, a visible shift in the histogram peak is prominent for all three data sets.

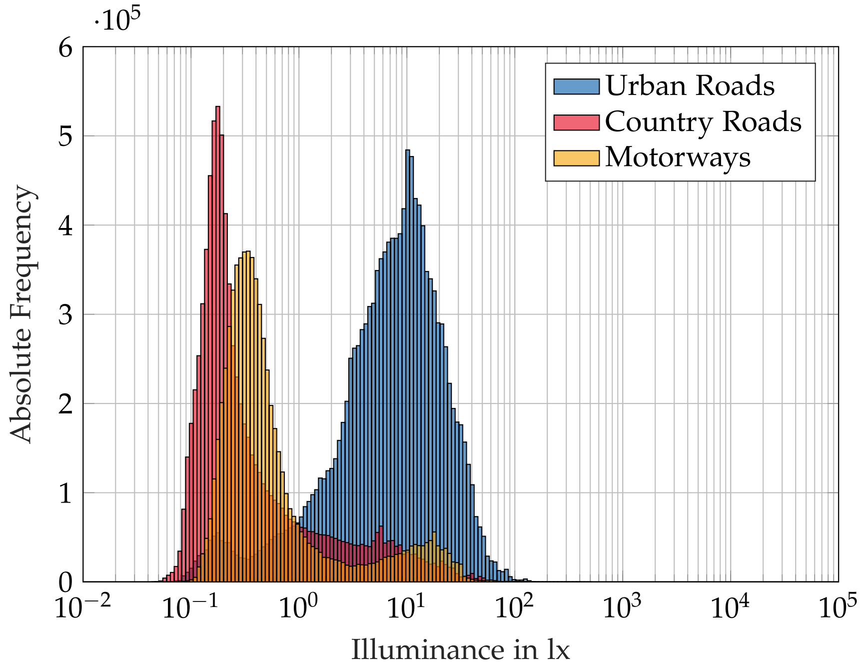

Figure 5.73 – Illuminance values recorded during night drives for all 54 participants over all three major road categories. Blue marks illuminance values recorded in urban environments, red marks the illuminance on country roads and yellow marks the illuminance on motorways.

Important is the fact, that for day and night drives, a significant difference between the illuminance data in the road categories is found. At night in urban environments, the illuminance is recorded to be about 34 times higher than on country roads and 20 times higher than on motorways. This is to be expected due to street lighting, a higher traffic density and illuminated store fronts. No significant difference is found between country roads and motorways. The complete statistical data is summarized in table 5.15 where the data for the tests between day and night drives is listed as well. The distributions shown in figure 5.73 show a clear cut off at around 10×10^2 lx and only single data points beyond that. The illuminance recorded for country roads and motorways with $E > 1.5$ lx is recorded in situations, where road lighting is added due to close passing of urban areas. This data is matched and evaluated using the GPS data presented previously. Only a small margin of this data occurs in areas, where the only probable reason is oncoming traffic.

Table 5.15 – The median, the standard deviation, the maximum as well as the minimum of the illuminance recorded at the driver's eye for the three major road categories split up by day- and night-time driving as shown in figure 5.72 and 5.73 respectively.

	URBAN ROADS		COUNTRY ROADS		MOTORWAYS	
	DAY	NIGHT	DAY	NIGHT	DAY	NIGHT
E_{Med}	2.15×10^3 lx	7.88 lx	1.81×10^3 lx	0.23 lx	2.43×10^3 lx	0.40 lx
σ	1.35×10^4 lx	1.55×10^2 lx	1.08×10^4 lx	2.06×10^1 lx	1.08×10^4 lx	3.20×10^1 lx
E_{Max}	8.81×10^4 lx	4.77×10^2 lx	8.86×10^4 lx	6.77×10^1 lx	8.51×10^4 lx	1.53×10^2 lx
E_{Min}	0.00 lx	0.06 lx	0.11 lx	0.04 lx	0.00 lx	0.17 lx

For both drives, day and night, a large overlaps in the recorded illuminance data and especially at night, a large spread of recorded illuminance values is recorded. This means, that similar to the velocity data, it is not sufficient to simply use the three road categories as dividing values for the gaze analysis, but a split due to different illuminance values should be investigated as well.

GLARE RATING DURING THE TEST DRIVES

While the general illuminance distributions give a good overview over the illuminance values experienced by the drivers on average, they do not offer any insight into the experienced glare. A high illuminance level over a longer period of time will increase the adaptation level and thereby decrease the sensitivity to glare. To derive any glare ratings comparable to section 5.3 from the recorded illuminance values and the pupil diameter, illuminance peaks have to be identified from the general illuminance curve. The data can then be compared to the laboratory studies. To achieve this, the adaptation illuminance is calculated for any given moment of the drive using a weighted moving mean function over the preceding illuminance data of 1 min. The moving mean value is weighted linearly decreasing to the data the furthest away. As an example of the adaptation luminance of a daytime drive versus the current illuminance, a short part of the data is visualized in figure 5.74. The blue curve indicates the calculated adaptation illuminance and the red curve shows the actual illuminance.

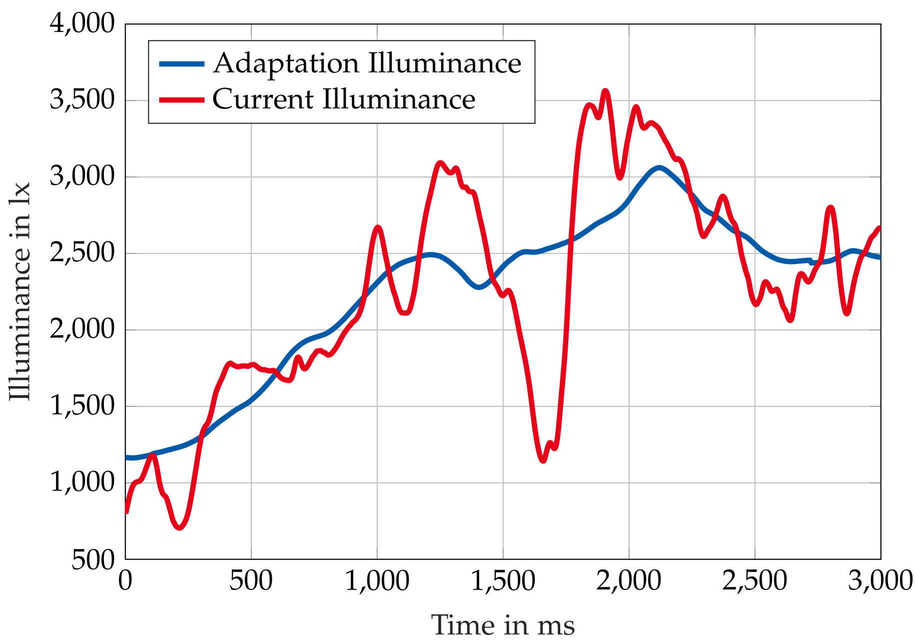

Figure 5.74 – Calculated adaptation illuminance (blue) and current illuminance (red) for a short time window of one recorded daytime test drive.

This figure already shows around 6 major peaks in the real illuminance data, that are flattened out in the adaptation illuminance curve. In the next step, the relative change in illuminance is calculated via equation 5.32, where the difference between the current illuminance to the adaptation illuminance is calculated and then divided by the current adaptation illuminance. The choice to calculate an adaptation illuminance instead of using the standard adaptation luminance is forced, the only way to properly measure the luminance is, as explained in the previous parts, a static measurement with luminance cameras. A workaround would be a calibration matrix for a normal video camera, this however, would only work satisfyingly for the used calibration spectrum.

$$E_{rel} = \frac{E - E_{ad}}{E_{ad}} \tag{5.32}$$

In this data, illuminance peaks are now identified, that are at least 10 % higher than the adaptation illuminance and are at least 100 ms away from the previous recorded peak. If different glare pulses are recorded inside the 100 ms window, the highest pulse is selected and the lower pulses are dismissed. This is illustrated for the same data sample as shown in figure 5.74. Figure 5.75 shows the relative illuminance in blue and the identified peaks are marked by blue triangles. The pulse hight is indicated by red lines and the pulse width, Full Width at Half Maximum (FWHM), is shown by orange vertical bars and if two pulses are registered overlapping, the border is marked by a purple bar as shown at 2 s. In this example 6 glare peaks are identified with a height of 14 % to 30 %. Smaller peaks next to the main peaks are ignored as evident by the last identified peak at around 1.8 s.

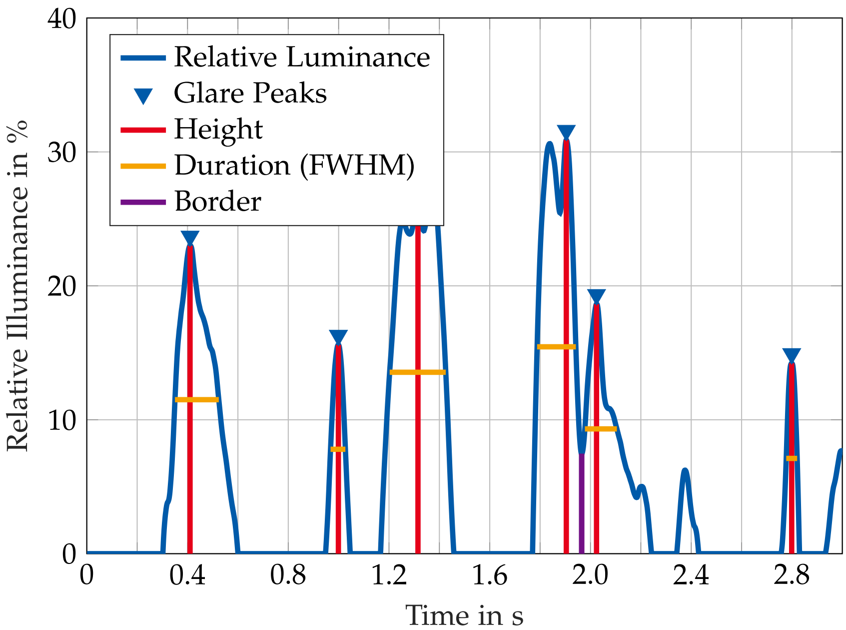

Figure 5.75 – Relative illuminance calculated according to equation 5.32 and identified peaks with a height of at least 10 % over the adaptation illuminance and a distance of at least 100 ms after the previous peak.

This is done for all test drives, day and night and the number of pulses per drive is calculated.

Figure 5.76a shows the distribution of glare peaks for day (blue) and night (red) as histograms. In total, 37 756 peaks are registered during the day and with 87 699 peaks, more than double that amount is registered during the night with both data sets consisting of about the same number of valid data points. It is evident, that during the day, the majority of test drives experienced far less illuminance peaks. In mean, 699.222 glare pulses are recorded during the day and 1624.200 glare pulses are seen during the night leading to nearly three times as much glare pulses during the nighttime drives compared to the daytime drives. Figure 5.76b shows the same distributions more compact as boxplots, indicating the difference in experienced glare pulses even further with the medians being 1912 at night and only 539.500 during the day. Both figures already imply, that the distributions seen are not normal distributed. Using the One-sample Kolmogorov-Smirnov test on both normalized distributions confirms this with $p < 0.05$ for the daytime data and $p = 0.02$ for the data at night. Using the Whitney-Mann-U-Test on the data sets then shows, that both data sets are from significantly different distributions ($p = 3.7 \cdot 10^{-10}$).

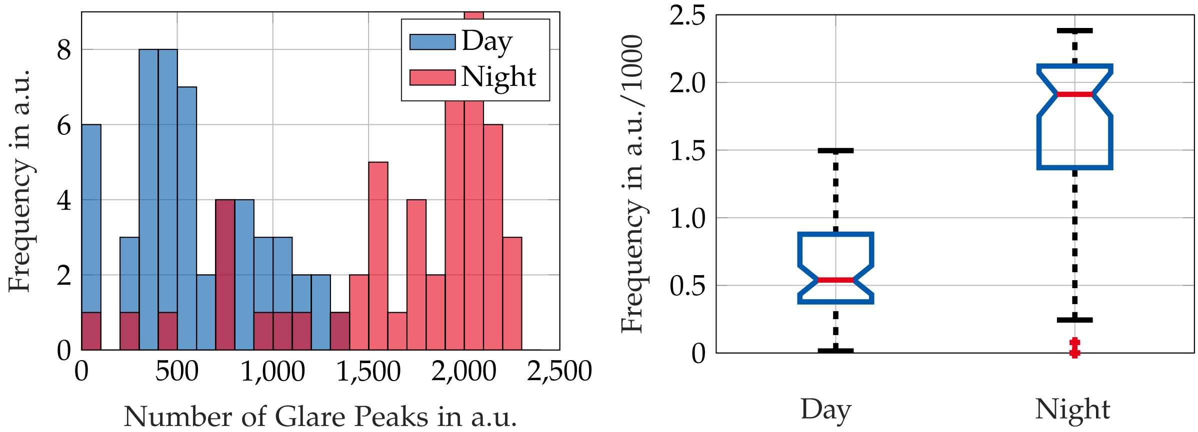

(a) **(b)**

Figure 5.76 – (a) histogram of glare pulses detected over the 54 test drives for day (blue) and night (red). (b) box plots of the same data with medians of 539.5 for the daytime data and 1912 for the data recorded at night.

Additionally, for all recorded pulses, the pulse width is measured to calculate the exposure. Figure 5.77 shows the distribution of the calculated pulse width for the day and night data. The laboratory study in section 5.3 shows, that there is a large impact of the pulse width on the glare perception, and depending on the duration, the correlation between the glare perception and the photometric value changes. However, since the information on the correct adaptation illuminance is missing from the laboratory study, no proper correlation between the measured peaks and the glare rating can be done. The main information, that can be transferred from the laboratory study to this data is, that shorter pulses with the same illuminance lead to a significant higher glare rating.

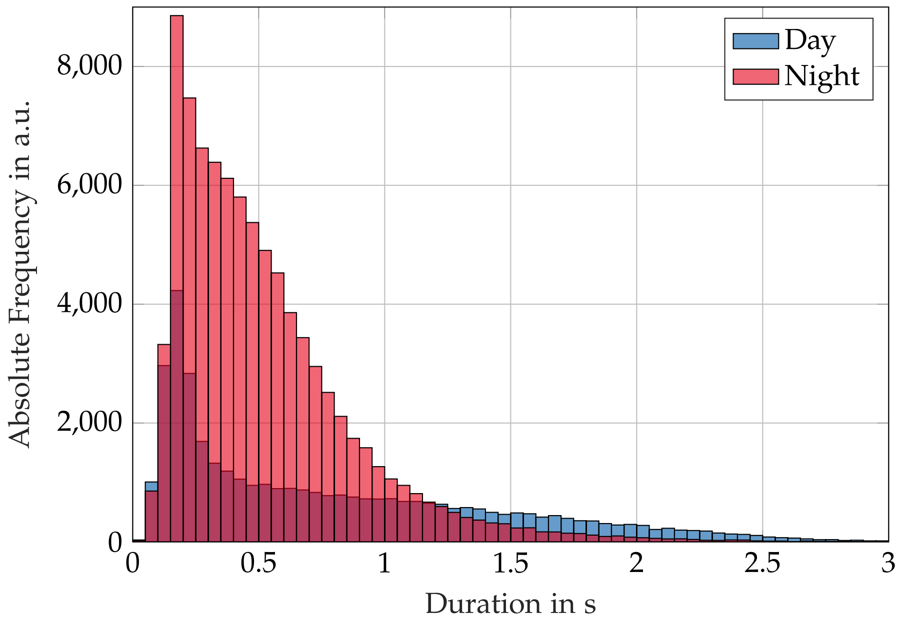

Figure 5.77 – Absolute frequency of the durations over all pulses for day (blue) and night (red) drives.

The data indicates, that there are not only more pulses registered at night, but that the median duration is much lower with a median of 435.5 ms at night and 585.2 ms for the pulses recorded at daytime. This leads to the conclusion, that in addition to the higher amount of pulses, already leading to a higher glare probability, the pulses are, at least overall, shorter and therefore lead to an even higher glare perception.

In the next step, the illuminance peaks are grouped in different bins according to their relative peak illuminance. This is done, since section 5.3 shows, that the maximum illuminance correlates with the perceived glare for similar or known durations of all glare pulses. For this reason, the glare pulses during night are analysed first and sorted by their maximum illuminance. The highest bin, that still contains a significant amount of peaks reaches over 640 % of the adaptation illuminance. From this maximum value, the lower illuminance bins are derived and set up in a way, that resembles the human perception as close as possible without sacrificing to much data. The chosen bins are set to <20 %, <40 %, <80 %, <160 %, <320 %, <640 % and >640 % of relative illuminance. The same bins are then used for the data recorded during the day. However, due to the much higher base illuminance during the day, it is not expected, that the highest bin values are reached during the day. These pulse categories are then correlated with an approximate glare rating. Since all other studies regarding glare involve either known adaptation luminance instead of illuminance or focus on completely or nearly completely dark surroundings, the direct comparison to other studies is not possible for day and night drives. However, Söllner proposed a 2 lx limit after which pulses (during night) are perceived as glaring, which matches the findings shown section 5.3. Since the mean adaptation luminance is calculated at 2.9 lx, the addition of 2 lx would be inside the 80 % to 160 % bin. Using this baseline, all bins beneath this illuminance level are regarded as *non glaring* and the bins above are regarded as *glaring*. This leads to the modified de Boer implementation shown in table 5.16

Table 5.16 – Modified DE BOER glare rating according to the bins selected due to the measured illuminance values.

RELATIVE E_{max}			INV. DE BOER RATING	INV. DE BOER VALUE
	-		Unbearable	9
640 %	$< E_{Max}$		-	8
320 %	$< E_{Max} <$	620 %	Disturbing	7
160 %	$< E_{Max} <$	320 %	-	6
80 %	$< E_{Max} <$	160 %	Just Admissible	5
40 %	$< E_{Max} <$	80 %	-	4
20 %	$< E_{Max} <$	40 %	Satisfactory	3
10 %	$< E_{Max} <$	20 %	-	2
0 %	$< E_{Max} <$	10 %	Just Noticeable	1

Pulses with a relative illuminance of below 10 % are set to be *just noticeable* and are not included in the data shown. The smallest shown pulses (10 % to 20 %) are set between *Just Noticeable* and *Satisfactory*. These are the first pulses shown in figure 5.76a and 5.76b respectively. The most important illuminance bin is the already mentioned bin with a range from 80 % to 160 % which is associated with *Just Admissible* and thereby just on the boarder between *glaring* and *not glaring*. Important is, that the DE BOER scale value 9 (*unbearable*) is not associated with any data. This is done because the assumption is, that during normal nighttime driving, no situation should occur, in which a single light situation is perceived as *unbearable*. This is done due to the results shown in section 5.3 where the highest illuminance pulse was rated below *unbearable*. The binning is done for each participant separately and the mean amount of pulses in each bin over all subjects as well as the standard deviations are visualized in figure 5.78 where the pulses recorded during the day are shown in blue and the pulses seen at night are marked in red.

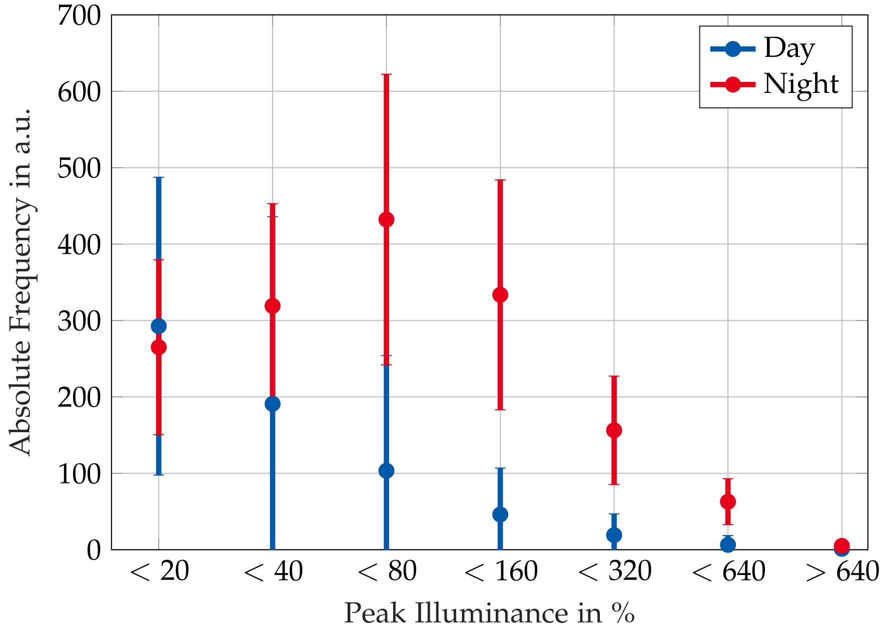

Figure 5.78 – Median number of glare pulses for all selected illuminance bins with a minimum peak illuminance of 10 % for daytime driving (blue) and nighttime driving (red). The standard deviation over all subjects is shown by the whiskers.

This data shows again, the differences in the total amount of pulses registered for both driving conditions. However, this data also shows, that the daytime drives do tend to register more lower intensity pulses, between 10 % and 20 % compared to the nighttime drives. In all other bins, more pulses are registered during the night. All pulse bins are tested on normal distribution and all except for the nighttime bins ($20\,\% < E < 40\,\%$, and $320\,\% < E < 640\,\%$) are not normal distributed and the selected One-sample Kolmogorov-Smirnov test rejects the null hypothesis with $p < 0.05$. For the two mentioned bins, the threshold for the normal distribution is just surpassed with $p = 0.11$ and $p = 0.07$. Therefore, all pulse data sets are assumed to be not normal distributed. The pulse data is then tested on significance between day and night for all bins using the Wilcoxon-Mann-Whitney-Test. Here the findings are, that for all bins, the data collected during the day and the data collected at night is significantly different except for the very first bin with the lowest illuminance values between 10 % and 20 % ($p = 0.56$). Since this data shows, that the probability of glare during daytime driving is significantly lower compared to driving at night.

For the next step, the data shown in figure 5.78 is split up into the three road categories to get an rough estimation on which kind of roads lead to the most glare and in which situation the drivers are less affected by glare. As shown, driving at daytime leads to nearly no glare peaks when compared to driving at night. Therefore, for this part, only the night data is being shown. For the daytime data, no significant difference between the three categories is found. Since the available amount of data for the three categories is largely different, the amount of glare pulses measured is weighted by the data quantity and then again normalized on the maximum pulse frequency. This is shown in figure 5.79 with data from urban roads marked by blue dots and whiskers, data from country roads shown in red and the motorway data indicated by yellow bars.

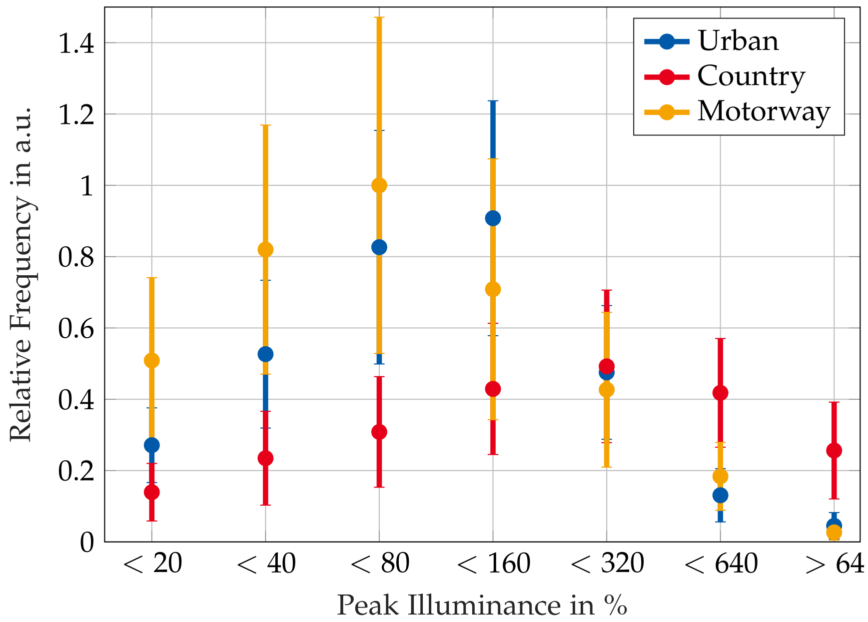

Figure 5.79 – Median number of glare pulses for all selected illuminance bins with a minimum peak illuminance of 10 % recorded at night for urban roads (blue), country roads (red) and motorways. The standard deviation over all subjects is shown by the whiskers.

This shows quite interesting results that need to be explained in detail. For low intensity peaks, up to 80 % of the adaptation illuminance, the most peaks are registered on motorways and the least peaks are recorded for country roads. The data from city roads falls right in the middle. This is probably the case due to the larger traffic volume on motorways and in cities compared to country roads and the increased amount of light sources that may lead to those peaks. In cities these light sources are traffic lights, road lighting, shop/advertisement lighting and of course other traffic participants. Since motorways are defined to be multi-lane roads, the increased number of peaks may be caused by the higher number of other vehicles on these lanes that are either passing the test driver or are being passed by him. Since the peak intensity is low and assumed to be non dazzling, this means, that the main light source here is the rear lighting. Front lighting as a light source will only play a minor role since German motorways have a lane separator between them.

Since these peaks are not assumed to be dazzling, more emphasis is put towards the higher intensity peaks. For the bin that is associated with *just admissible*, the largest overlap between the three categories is found. The most peaks are registered in this category for urban roads and while the peaks counted for motorway driving are decreasing again, urban road peaks have reached their maximum. For this bin, all data sets are non normal distributed and from significantly different distributions. This is evident since the median values of all distributions are separated quite significantly.

This means, that most of the pulses registered just at the borderline of glaring are seen in cities and on motorways leaving still room for improvement for those situations. However, the highest peaks measured (>320 %), and therefore the most important peaks since they will not only influence the glare perception of the driver the most, but also increase the contrast threshold needed to identify objects, are most prominent on country roads. For pulses between 160 % to 320 % no significance in the amount of peaks is found but the median in number of peaks is highest for country roads. For the remaining two bins the peaks on

country roads are significantly more frequent than on the other two categories, meaning that the most glare and thereby impairment of vision will most probably occur on country roads. This is explained by the lower surrounding light compared to the urban measurements and the undisturbed light from oncoming traffic therefore leading to the highest relative illuminance peaks. As shown section 5.3, this can be significantly reduced by using a smoother cut-off. While a hard cut-off will provide a larger viewing distance and a smooth cut-off might therefore reduce safety at night, this is only an issue as long as only dedicated low and high beam setups are used. Applying this knowledge to gfHB however, would not probably not reduce the visibility distance of the driver, but therefore reduce the stress inflicted on other traffic participants through glare. For the low beam section of a gfHB system this would simply mean a smoother cut-off. In the high beam area however, this would most likely lead to a higher number of segments required for optimal illumination. Since the current trend already goes beyond the proposed 280 segments, this also should not be an issue.
However, since the association from relative illuminance peak to the inverted DE BOER scale is done numerically, the results have to be reviewed with caution. This is a rough estimation of the perceived glare but should be investigated further in controlled situations, where the adaptation illuminance can be set to different levels and record the correct DE BOER ratings for different relative illuminance peaks.
With this knowledge, it is now possible to use the illuminance data and find a correlation to the pupil diameter.

PUPIL MEASUREMENT

Since the illuminance distribution is known for all of the test drives, and section 5.3 has shown a clear correlation between glare and illuminance or exposure and the pupil diameter, the next section will focus on the pupil diameter during the recorded drives. First a general look at the pupil diameter is taken similar to the illuminance values in the section above, then the illuminance is correlated in general with the pupil diameter over the recorded illuminance range and the last step is again, calculating similar glare bins to the ones shown in figure 5.79 but by using the pupil diameter.

AVERAGE PUPIL DIAMETER IN DIFFERENT ROAD SEGMENTS This first segment will focus on the raw pupil diameter as it was recorded during day and night drives. The data presented is shown only for eye tracking data, where the visible pupil border is at at least 50 % since this is the recommended threshold by SMARTEYE. This cleans the data from blink-artefacts, where the pupil diameter is recorded to be 0 mm and from larger errors, when the pupil is not completely visible.

NORMALIZED AVERAGE PUPIL DIAMETER IN DIFFERENT ROAD SEGMENTS
Since the general pupil diameter between subjects can vary greatly due to interpersonal differences, as shown in section 5.3, the raw pupil data is not discussed here. The raw data and the corresponding evaluation is shown in appendix E.3. The data for each test subject is normalized to the median of the pupil diameter during the corresponding drive and then, after the normalization split up into the three road categories. Figure 5.80 shows the data for the daytime drives with the same colour coding as before. Blue bars show the normalized pupil diameter recorded on urban roads, red bars show the normalized data from country road driving and the yellow bars indicate the data recorded on motorways. The median pupil diameter for urban roads is calculated to be at 101.2 % $\pm$ 19.4 %, 102.2 % $\pm$ 21.6 % for

the country road data and 95.4 % ± 16.2 % for the pupil diameter on motorways but the complete data is summarized in table 5.17.

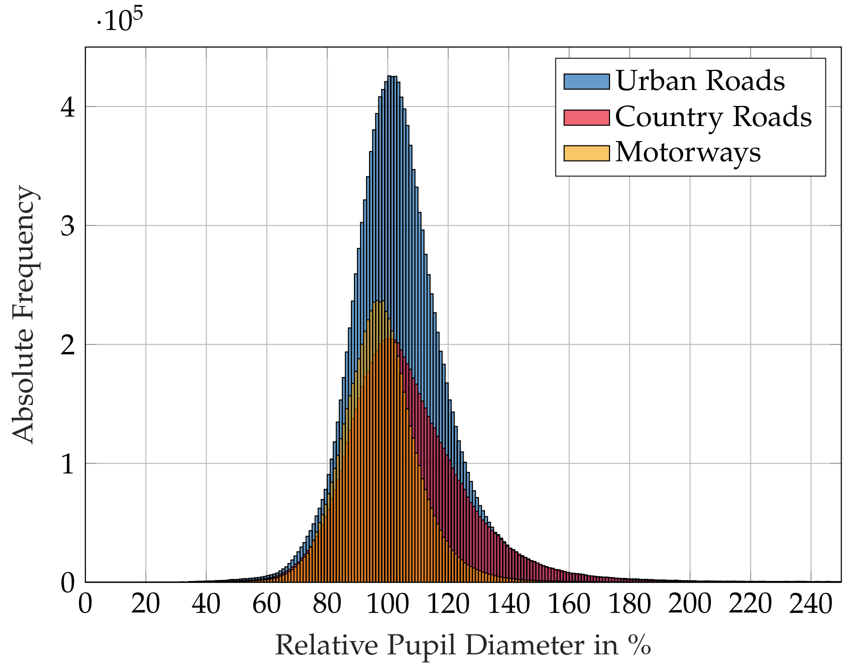

Figure 5.80 – Normalized Pupil diameter in percent for the three major road categories during the day. Pupil diameter on urban roads is marked by blue bars, data recorded on country roads is indicated by yellow bars and red bars show the data recorded on motorways.

The data *looks* very much normal distributed for all three road categories. However, testing the data on normal distribution leads to a rejection of the null hypothesis, and the data therefore does not originate from a normal distribution. Since the distributions contain up to 14×10^6 data points, the tests on normal distribution are very rigid and will find any small deviation from theoretical normal distribution. For this reason, visual tests on normal distribution and significant differences need to be done. CDF and the most common visual test on correlation given by Quantile-quantile plots (QQ-plots) are shown and discussed in appendix E.3. The analysis still shows a clear deviation from the normal distribution for high and low quantiles. The optical analysis of the correlation between pupil diameter in the different road types shows, that the data does originate from the same distribution thereby contradicting the numerical test.

The same steps are then performed for the data recorded during the nighttime drives. The data is normalized on the overall median pupil diameter and then split up for the three road types. This is shown in figure 5.81 with the same colours as before, blue indicates urban data, red shows country road data and yellow marks the data from motorways. When comparing the normalized data to the raw data, it is evident, that the normalized data looses most of the skewness. The median pupil diameter for urban roads is calculated to be at 97.8 % ± 13.1 %, 103.0 % ± 15.5 % for the country road data and 101.9 % ± 13.4 % for the pupil diameter on motorways but the complete data is summarized in table 5.17. Compared to the day data, it is noticeable, that the data set with the smallest pupil diameter is the urban data compared to the motorway pupil diameter during the day. At night, this is explainable by the additional light sources and thereby increased background luminance in the city.

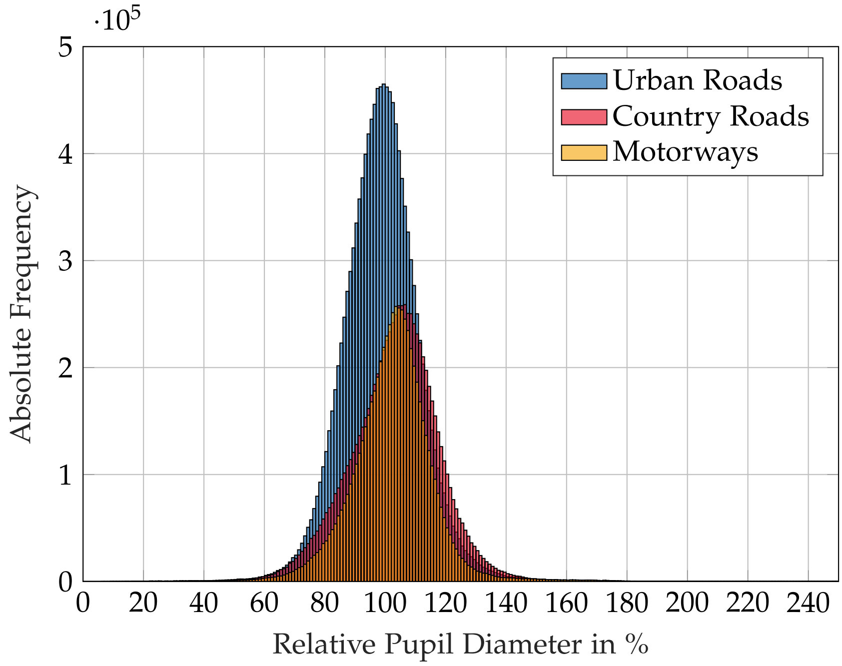

Figure 5.81 – Normalized Pupil diameter in percent for the three major road categories during the night. Pupil diameter on urban roads is marked by blue bars, data recorded on country roads is indicated by yellow bars and red bars show the data recorded on motorways.

Analogous to the daytime data, One Sample Kolmogorov-Smirnov Tests are used to find, if the data sets are normal distributed. Again, the null hypothesis is rejected and the tests lead to the conclusion, that the three sets are not normal distributed. Since the daytime data has shown, that the statistical tests do not necessarily lead to convincing results when the test data sample is very large, visual tests are perfomed again. Similar to before, the CDFs and QQ-plots are calculated for all three data sets and shown in the appendix E.3. Again, the data shows that the data is not normal distributed. The main difference between the nighttime data however is, that the data sets do not originate from the same distribution.

Table 5.17 – The median, the standard deviation, the maximum as well as the minimum of the normalized pupil diameter recorded for the three major road categories split up by day- and night-time driving as shown in figure 5.80 and 5.81 respectively.

	URBAN ROADS		COUNTRY ROADS		MOTORWAYS	
	DAY	NIGHT	DAY	NIGHT	DAY	NIGHT
P_{Med}	101.19 %	97.78 %	102.21 %	103.03 %	95.43 %	101.92 %
σ	19.38 %	13.10 %	21.64 %	15.48 %	16.24 %	13.42 %
P_{Max}	281.95 %	230.80 %	285.30 %	238.61 %	276.33 %	245.07 %
P_{Min}	32.33 %	22.37 %	33.72 %	20.81 %	35.40 %	20.97 %

With the findings above, about the general pupil diameter data and the differences during day and night as well as the differences between the three road categories, the next step is, to investigate, if the correlation between illuminance and the pupil diameter that was shown in the laboratory studies, can be identified in this field test as well.

CORRELATION BETWEEN PUPIL DIAMETER AND ILLUMINANCE

In this section, the two data sets shown above, illuminance and pupil diameter for day and night drives are correlated. Therefore, the illuminance is binned into 500 logarithmic bins ranging from 10×10^{-2} lx to 10×10^{5} lx. The median of the pupil diameter as well as the standard deviation for each of these bins is calculated. This is done for day and night as well as for the three different road categories since the data shown above indicated, that at least for the data recorded at night, significant differences between the road sets can be found for the overall distribution. The data is then normalized on the absolute median pupil diameter for each of the categories since the laboratory studies have shown, that due to the large variance between different test subjects, the normalized pupil diameter is the better correlating value. The results separated for day and night for this are shown in figure 5.82. The night time data has the same colour coding as before with urban data being marked in blue, country road data in red and motorway data in orange. The daytime data is then marked in purple for urban data, green for country roads and lime for motorways.

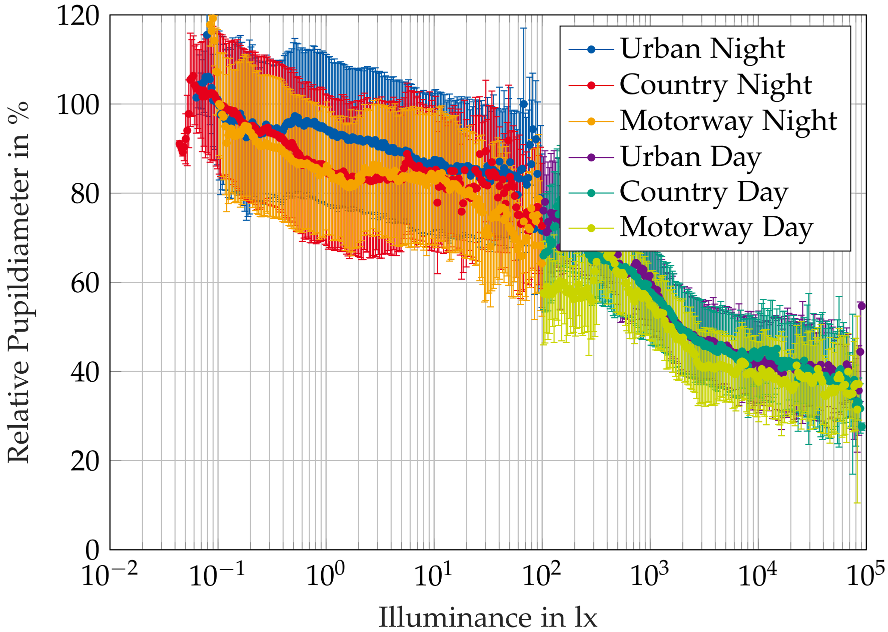

Figure 5.82 – The median pupil diameter over the recorded illuminance values for day and night drives in the three major road categories. The data recorded during the day is shown in blue (urban roads), red (country roads) and yellow (motorways). The nighttime data is indicated by purple (urban roads), green (country roads) and cyan (motorways).

The data for day and night shows a good transition at the threshold of 10×10^{2} lx except for the data recorded during the day on motorways. Here the data shows a significant step in the pupil diameter from 75 % down to 60 %. This is due to the small amount of datapoints gather in this range. The rest of the data however shows a very good transition with two plateaus at 100 % for as a upper limit and going down to 35 % as a lower limit for the relative pupil diameter.

As expected, the pupil diameter is only dependent on the current illuminance and the difference in pupil diameter between the different road sections originate from the different illuminance levels. Furthermore, the large quantity of the data allows for observations, that could not be done during the laboratory studies described in section 5.3. Here a clear minimum pupil diameter and a maximum pupil diameter can be seen. While the normalized pupil diameter is set to 100 % at its maximum and at 40 % for the minimum.

The main difference to the laboratory studies shown in chapter 5.3 is, that compared to the laboratory studies, the subjects are not exposed to a fixed illuminance level but rather to a changing adaptation level. Combined with the fact shown in figure 5.49, that the pupil reacts with a few milliseconds after an change in illuminance and reaches its minimum up to 1000 ms after the change in illuminance, this means, that the variance in pupil diameter for the same illuminance is much larger. This also leads to the fact, that the actual maximum values and minimal values are not going to be reached by the median values for the different bins. However, this data presents a the more realistic view on the pupil diameter that will be measured under real circumstances.

In order to compare the overall data to the data shown by Watson, [153], and presented in chapter 4 the absolute pupil diameter is now investigated. Due to the real life nature of this study, large differences in the absolute pupil diameter for different lighting situations are to be expected, since as with the comparison to the own laboratory studies, the dynamic change in the adaptation level should influence the absolute pupil diameter significantly. The raw data is shown in figure 5.83 with the medians for each illuminance bin shown as a dot and the standard deviation presented by the whiskers. The data recorded at night is shown in red, and the data recorded at daytime is marked in blue.

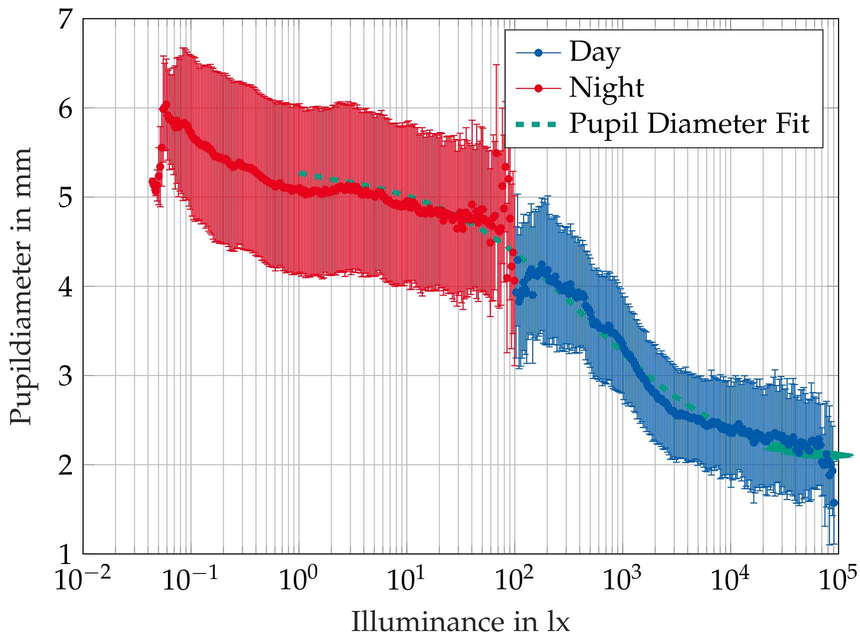

Figure 5.83 – Absolute median and standard deviation of the measured pupil diameter in mm over the measured illuminance. Blue shows data recorded recorded during the day and yellow shows the data recorded at night. The green line shows the fitted curve corresponding to the equation shown in equation 5.33.

The absolute pupil diameter P is fitted in dependence of the illuminance E with the function

$$P(E) = \frac{d}{1 + e^{(\log_{10}(E)+E_0)^c}} + a \tag{5.33}$$

E_0 shows the illuminance value, at which the slope of the fit changes and d and a are offsets for the pupil diameter with d giving the maximum pupil diameter and a the minimal pupil diameter. The fitted function according to equation 5.33 is shown by the green, dashed line.

The resulting fit reaches an R^2 of 0.99 with an MSE of 0.14 and thereby represents the shown data very well. The fitted parameters are $d = 3.31$, (3.22 and 3.39) , $a = 1.97$ (1.90) and 2.03) , $c = 1.84$ (1.74 and 1.93) and $E_0 = 2.69$ (2.65 and 2.73) with the number in brackets indicating the confidence intervals. The maximum fitted pupil diameter is given by $d + a$ and is therefore calculated to be at 5.27 mm (5.27 mm to 5.42 mm, which is significantly less than the values presented by Holladay, 7 mm, Moon and Spencer, 7.80 mm or Barton 8 mm. The reasons for this are explained above.

Corresponding glare ratings correlated to the pupil behaviour

After analysing the general pupil diameter over the different road types and the two time slots, and finding the correlation between the pupil diameter and the current illuminance, the next step is to verify the illuminance glare peak data by analysing dips in the pupil diameter. The fact, that the pupil does indeed correlate with the glare perception as well is shown in section 5.3.

To do so, firstly the dynamic base pupil diameter needs to be calculated. This is done using a moving mean filter over a 20 s frame for the data up to the current point. The 20 s frame was chosen due to the findings in the chapters above. The current pupil diameter then needs to be smoothed as well, since a lot of noise and unwanted pupil movement occurs during the measurements. The pupil diameter curve is smoothed using the Savitzky-Golay filter, applying a second order polynomial over 60 previous data points. The base level as well as the filtered pupil diameter are shown in figure 5.84

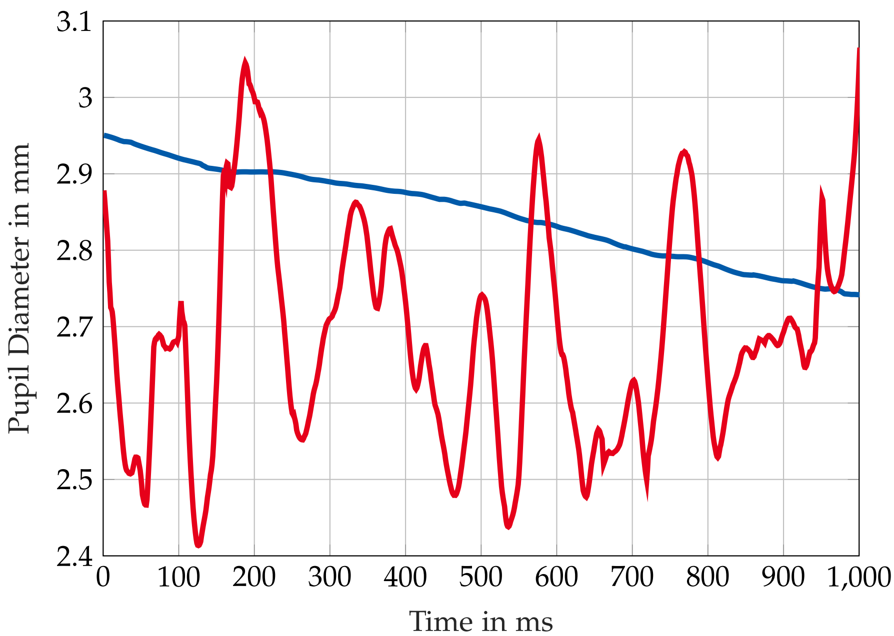

Figure 5.84 – Absolute pupil diameter for a sample data set during the day. Blue shows the base pupil diameter and red indicates the current pupil diameter smoothed with the Savitzky-Golay filter.

In the next step, the current data is subtracted from the base level the difference is normalized by the base level. This leads to a pupil diameter relative to the current, dynamic base pupil diameter. From this data, only dips in pupil diameter are interesting, since a glare pulse leads to a significant pupil contraction. Therefore, all data larger than the base pupil diameter is set to 0. The remaining data is then analysed for local minima with the restriction of a dip to at least −10 %, relative pupil size of 90 %. This is exemplified in figure 5.85

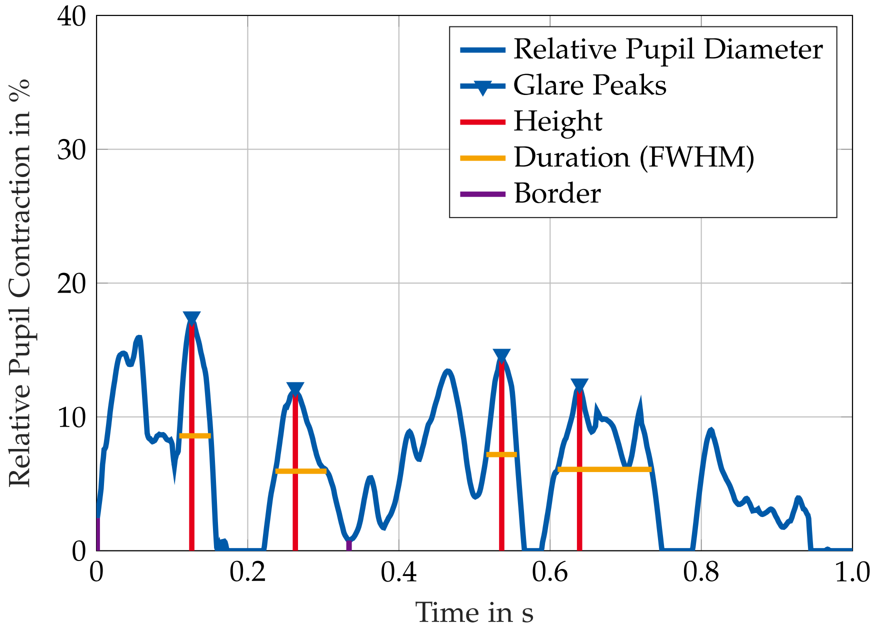

Figure 5.85 – Relative pupil diameter to the dynamic base diameter with all measured data points showing an enlarged pupil set to 0. All dips, that show a relative pupil size of <90 % are marked by blue triangles.

This is then calculated for all test subjects for both daytime data as well as for the nighttime data. The amount of pupil contractions measured for each subjects is shown in figure 5.86a as a histogram. The same data is shown as box plots in figure 5.86b to highlight the similarities between the two distributions.

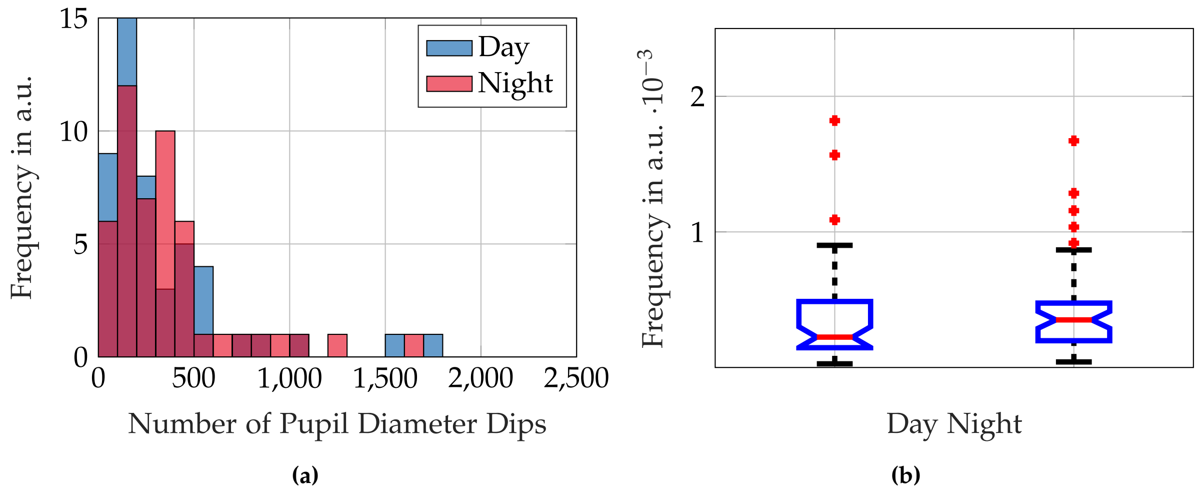

Figure 5.86 – (a) histogram of the amount of pupil contractions measured over the 54 test drives for day (blue) and night (red). (b) box plots of the same data with medians of 224 for the daytime data and 351 for the data recorded at night.

It is immediately obvious, that both distributions are rather similar. Looking at the median amount of significant dips in the pupil diameter, a small difference is found with 224 ± 364.17 dips found during the day and 351 ± 331.68 dips at night. This data shows the large overlap between the two sets. The Wilcoxon-Mann-Whitney-Tests consequently reveals, that this is indeed the case and both data sets are not significantly different. This also shows the large difference to the glare peaks extracted from the illuminance data, where a large difference is found regarding the amount of pulses between day and night. Looking further into this data, the pupil dips are divided into bins of <20 %, <30 %, <40 %, <50 % and >50 % and both the median number of pupil dips as well as the standard deviation of those are calculated for these bins. This is shown in figure 5.87. This figure illustrates again, what is already visible from figures 5.86a and 5.86b, no significant difference can be found between the daytime data and the data recorded at night.

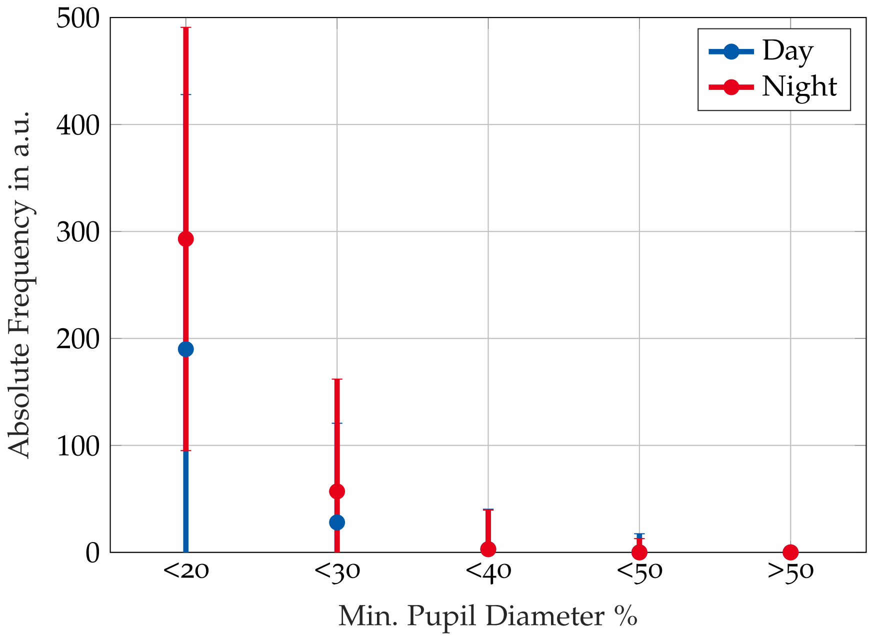

Figure 5.87 – Median amount of dips in pupil size divided by dip strength for day (blue) and night (red).

To conclude this, the general correlation between the recorded illuminance and the pupil diameter is found. While a correlation between the immediate pupil contraction to peaks in illumianance are found under laboratory conditions, no such correlation is found in real life data. The reason for this is most likely to be due to the unconscious pupil movement as well as the fact, that the pupils reaction is delayed and the pupil minimum is registered up to 1 s after the pulse. Further data analysis might lead to better correlations, since glare analysis of real driving data is only one small part of this thesis, other investigations are not performed.

Gaze behaviour in different driving situations

The previous sections, described and analysed the parameters found and recorded in real life traffic that might influence the gaze and driving behaviour of the selected test subjects. While all data so far was presented for all 54 subjects or 108 test drives (day and night), the following sections will only show the data for subjects with both, accuracy and precision in the gaze calibration, of below 2.00°. This leaves 19 subjects for the daytime and 15 subjects for nighttime driving making it immediately clear, why such a high number of test subjects needed to be invited. This section will now describe and analyse the general gaze and more in detail fixation behaviour during the test runs. To calculate the fixation behaviour, the Jacob algorithm is implemented. For each gaze vector, it is calculated, if the following gaze vectors are within a 2° range of this first gaze vector. If, for more than 200 ms, gaze vectors are located within the mentioned 2° circle, the gaze behaviour is set as a fixation until one of the following gaze points is outside of the set region. The center of the 2° circle is set to move along with the current gaze to include *smooth pursuit* gaze behaviour in the data.

This section will first go into general fixation distributions overall for night and day driving, and the three major road categories. In the next steps, the fixation behaviour is analysed for more detailed situations including the described factors from above.

GAZE BEHAVIOUR DIFFERENCES DURING DAY- AND NIGHT-TIME DRIVING

In this section, the focus is set to the differences in gaze and fixation behaviour between driving at night and driving during the day.

The amount of data, that is associated with fixations is only 17.63 % for the daytime data and 24.42 % for the night driving. This means, that most of the time, no fixation is registered and assuming all fixations are registered correctly, and only objects that are fixated by the driver are thoroughly gazed at. For at least 75 % of the time, the driver lets his eyes wander around aimlessly. This also further undermines the point discussed in the introduction, that it is close to impossible to derive, what a driver perceives and processes by only looking at the gaze behaviour. Not everything a person looks at is also perceived and on the other hand, simply because a person does not look at something directly and for a longer time, it can't be concluded, that the person actually identified and processed the object he looked at. However, up to now, the analysis of gaze and fixation behaviour is still the best option to analyse, what a driver sees while driving and what information he gets and needs to safely steer a vehicle. However, this data also shows, that there might be an over-abundance of information during the day since the fixation rate is 29.24 % lower than during the night even though more traffic and other traffic participants are recorded during the night.

To illustrate gaze and fixation behaviour graphically, the intersection between the gaze vectors and a virtual plane perpendicular to the driving direction is calculated. Then the amount of intersections between the vector and the plane is calculated. As an example of this, the gaze distribution and the fixation distribution over all test subjects during the day is shown in figure 5.88 and 5.89. Analogue to the traffic distributions shown in chapter 5.2, the distributions are normalized to their maximum value and the colour coding is identical to the one shown in figure 5.19. Here the gaze and the fixation data from all 19 test subjects is shown. The figure clearly shows, that only a single accumulation point in the distributions exist.

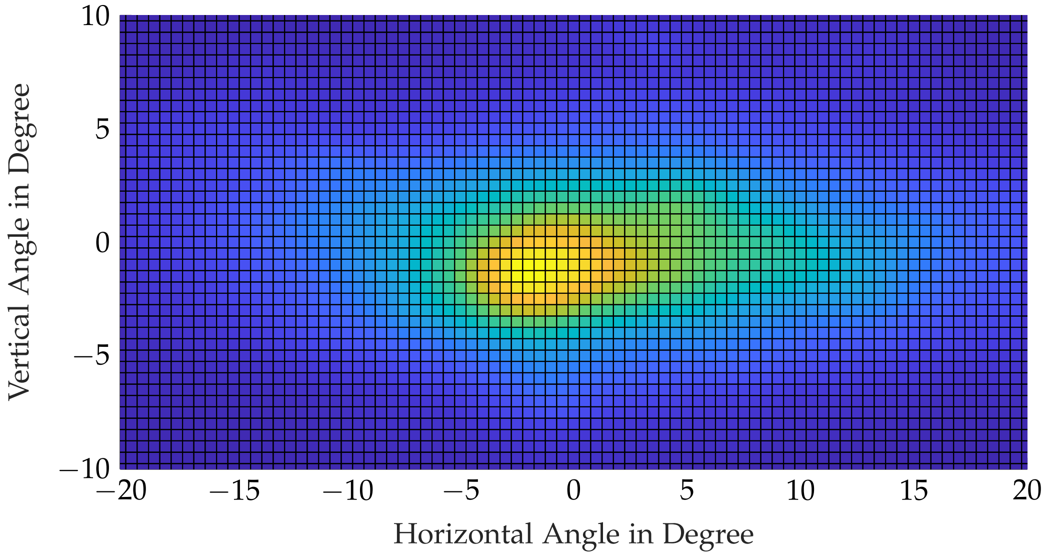

Figure 5.88 – Overall gaze distribution over all 19 test subjects for the data recorded during the day. The horizontal median is calculated to be at $-0.87° \pm 8.66°$, and the vertical median at $-0.42° \pm 3.58°$ with only one major accumulation point over all test subjects.

The vertical and the horizontal distributions of the general gaze distributions are attached in the appendix E.4 in figures E.23 and E.24 respectively.

The same calculation is done for the fixations. The results are shown in figure 5.89.

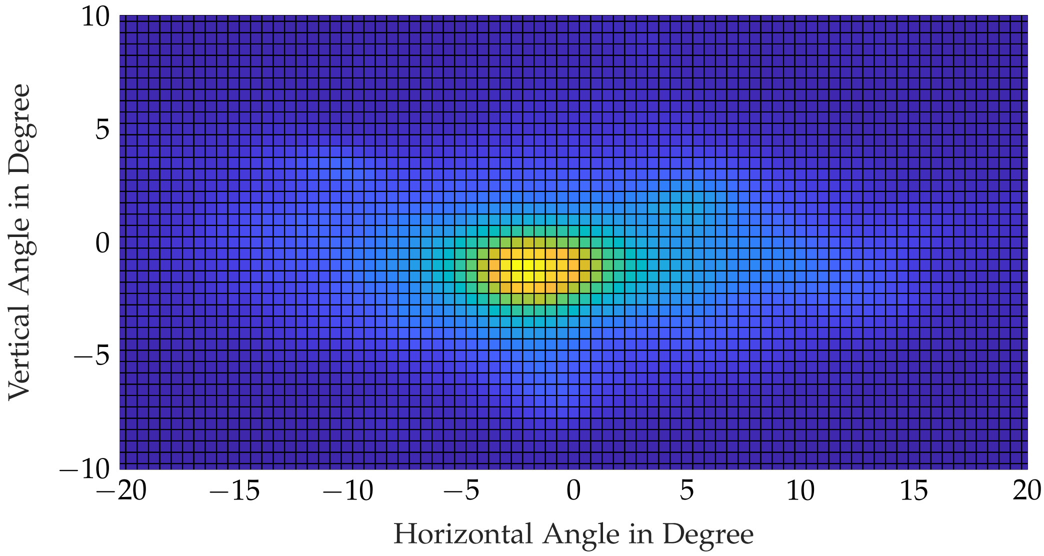

Figure 5.89 – Overall fixation distribution over all 19 test subjects for the data recorded during the day. The horizontal median is calculated to be at $-0.86° \pm 7.65°$, and the vertical median at $-0.80° \pm 3.08°$ with only one major accumulation point over all test subjects.

When comparing the gaze distribution to the fixation distribution, it is clear, that the gaze distribution contains more data points, since as already mentioned only about 17 % of the gaze data matches the fixation criteria. Furthermore, the gaze distribution is found to be wider. The standard deviation is 13 % larger for the general gaze distribution horizontally and 16 % larger vertically. Furthermore, the accumulation point, the median of both, horizontal and horizontal vectors, is about half a degree further to the right for the gaze distribution compared to the fixation distribution. Since this is the main difference recorded all further analysis will focus on the fixation distributions. The fixation data is further illustrated further in figures E.21a and E.21b in appendix E.4 where histograms are shown for the horizontal and the vertical fixation angles. Since both distributions are tested to be non-normal distributed, the median is calculated for both distributions. The horizontal fixation median is calculated to be located at $-0.86° \pm 7.65°$. The vertical fixation median is located at $-0.80° \pm 3.08°$ and thereby slightly below the horizon.

Using the main accumulation point, the distance at which the main fixation points intersect with the road can be calculated as an estimated measure of the orientation distance. Assuming a 1.20 m hight of driver's eyes, this calculates to an orientation distance of 85.94 m and subtracting the standard deviation the minimum orientation distance is calculated to be at 17.68 m. Adding the standard deviation obviously leads to an orientation distance of infinity since the gaze angle is located over the horizon then.
The complete data, including the angles horizontally and vertically as well as the orientation distances is summarized in table 5.18.

Since this is straight forward, the same is calculated for the overall nighttime gaze and fixation behaviour. The resulting fixation distribution is shown in figure 5.90. Since no significant differences in the overall distributions are found between the gaze and the fixation behaviour, only the fixation data is shown from here on out. However, the gaze data is presented in appendix E.4 in figure E.20 with the horizontal and vertical distributions shown separately in figures E.25 and E.26. Here a large difference is visible compared to the nighttime data. First of all, the fixation behaviour seems much wider, both horizontally and vertically. Furthermore, a larger second vertical and a smaller second horizontal accumulation point is visible.

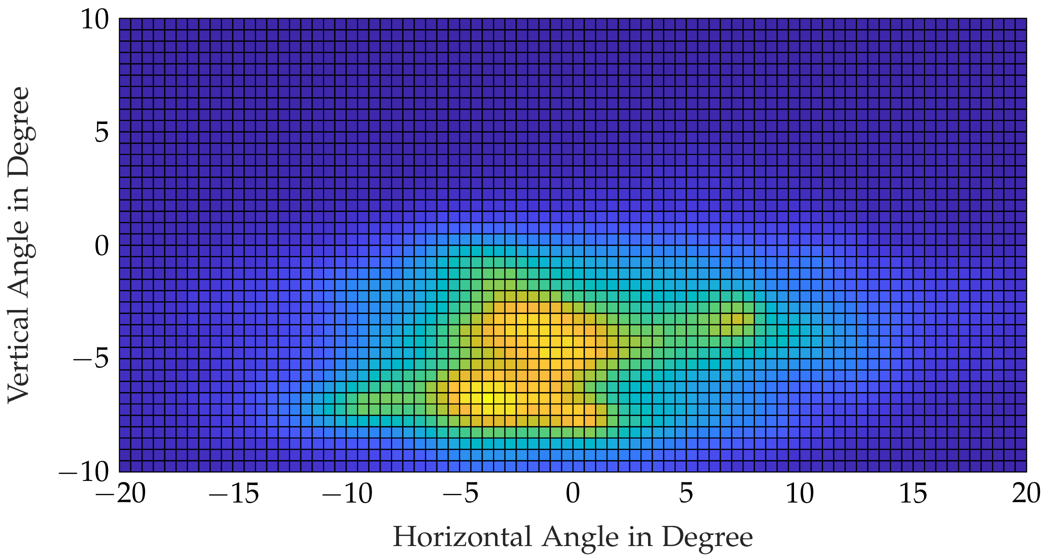

Figure 5.90 – Overall fixation distribution over all 15 test subjects for the data recorded during the nighttime drives. The horizontal median is calculated to be at $-0.82° \pm 7.34°$, and the vertical median is found at $-2.05° \pm 3.01°$

Similar to the daytime data, the vertical and the horizontal distributions are calculated independent of each other. The data is shown the appendix E.4 in the figures E.22a and E.22b respectively. This data shows, that the vertical accumulation point is far less pronounced than the larger, main peak and the horizontal accumulation point can be regarded as more of plateau in the fixation distribution than an actual second peak. The horizontal median of the fixation distribution is calculated to be at $-0.82° \pm 7.38°$, just to the left of the centre, therefore aiming mostly at the centre of the road. The median of the vertical fixation distribution is registered at $-2.05° \pm 3.01°$ therefore significantly below the horizon.

Using this data, the orientation distances are calculated to be at 33.54 m for the median and including the standard deviation of the fixation distribution the drivers orient themselves at 13.55 m for the closest part to the vehicle. The complete data is, together with the data from the daytime driving, summarized in table 5.18.

However, since the distribution shown in figure 5.90 shows two accumulation points, the distances are again calculated for those two points. The maximum of the upper accumulation point is located at $-1.07°$ resulting in an orientation distance of 64.25 m and the lower maximum is located at $-4.41°$ and therefore leading to a distance of only 15.56 m.

Table 5.18 – Fixation data for daytime and nighttime driving. The median for both vertical and horizontal gaze vectors are shown over all test drives as well as their standard deviations. For the vertical fixation distributions, the distance, at which the median vector intersects with a planar road is calculated.

	DAY	NIGHT
MEDIAN HOR.	$-0.857°$	$-0.816°$
STD (σ) HOR.	$7.647°$	$7.377°$
MEDIAN VERT.	$-0.800°$	$-2.049°$
STD (σ) VERT.	$3.083°$	$3.013°$
d_{Med}	85.938 m	33.536 m
$d_{Med-\sigma}$	17.682 m	13.547 m
$d_{Med+\sigma}$	∞	∞

To further compare the data from daytime driving and the night data, both vertical and horizontal distributions are plotted in figures 5.91 and 5.92 where in both figures, the daytime data is shown by blue bars and the nighttime data is indicated by the red bars.

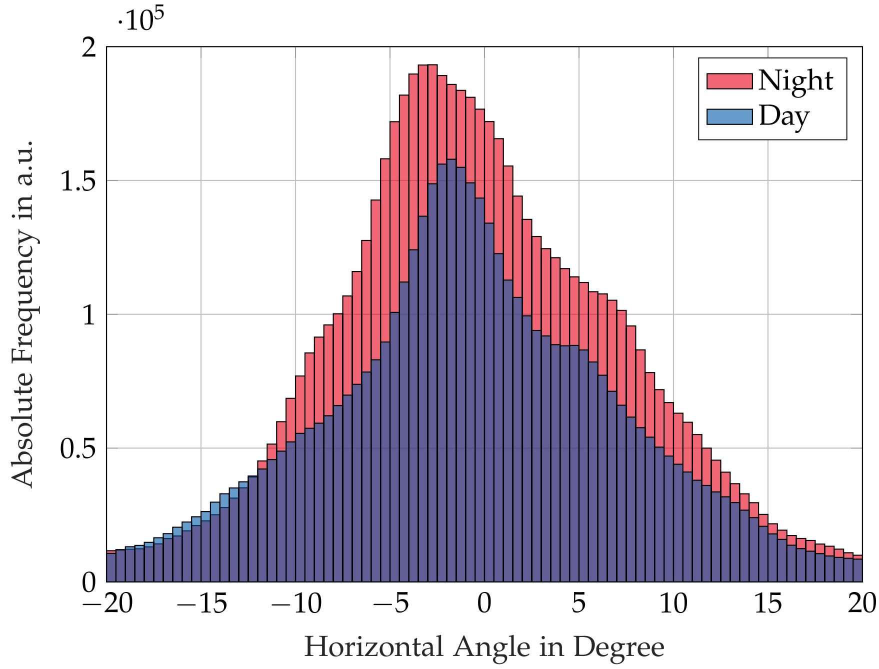

Figure 5.91 – Comparison of the horizontal fixation distribution between daytime driving (blue) and driving at night (red).

Figure 5.91 shows, that the horizontal fixation distribution is very similar between day and night. The distribution recorded at night has a slightly wider distribution but both median as well as the maximum in both distributions are within the margin of error. Thereby the conclusion for the horizontal fixation behaviour needs to be, that with the given headlight system, over all recorded parts of the driven course, the horizontal gaze behaviour is similar for day and night. No significant difference can be found between these distributions.

On the other hand, when looking at the vertical fixations, larger differences occur. As already shown in table 5.18, the mean and the median vertical fixation point differ quite substantially between daytime and nighttime data. However, as already mentioned above, the maximum of the vertical distribution is pretty similar between both situations.

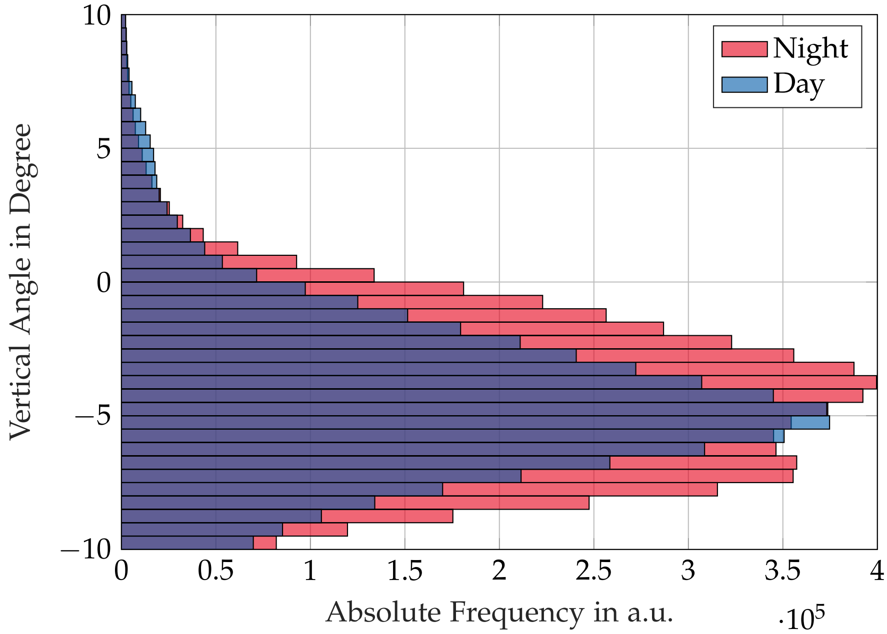

Figure 5.92 – Comparison of the vertical gaze distribution between daytime driving (blue) and driving at night (red).

The previous part describes the general gaze and fixation behaviour for day and nighttime driving. As with all other recorded data sets, this section will now split the mentioned fixation data into the three major road categories, urban roads, rural or country roads and motorways.
First of all, the frequency of fixation data in these situations will be discussed, before the fixation distributions are analysed.
As mentioned above, for daytime driving, only 17.6 % respectively 24.4 % for nighttime driving of all recorded gaze data is associated with a fixation. Splitting this data up into the mentioned road categories does not lead to a significant change, however a trend can be seen. During the day, the most fixations are recorded on country roads and the least fixations are recorded on motorways. At night, the highest fixation count is still recorded on country roads, but the city data shows the least amount of fixations now. All six data sets are presented in table 5.19.

Table 5.19 – Data associated with fixation for day- and nighttime driving divided into the three major road categories urban roads, country roads and motorways.

	DAY	NIGHT
OVERALL	18.311 %	24.425 %
URBAN ROADS	18.396 %	23.320 %
COUNTRY ROADS	19.495 %	24.473 %
HIGHWAYS	17.040 %	24.223 %

Further display of fixation distributions is not deemed feasible since they reproduce the same overall behaviour as already shown in chapter 4. The differences between the gaze behaviour in the different road categories are thereby summarized shortly and shown in table 5.20.

Table 5.20 – Fixation data for day and nighttime driving in the three major road categories, urban roads, country roads and motorways.

	DAY			NIGHT		
	URBAN	COUNTRY	MOTORW.	URBAN	COUNTRY	MOTORW.
MEDIAN HOR.	$-0.928°$	$-0.768°$	$-0.729°$	$-0.834°$	$-1.022°$	$-2.308°$
STD (σ) HOR.	$9.982°$	$8.669°$	$7.647°$	$6.906°$	$6.594°$	$5.775°$
MEDIAN VERT.	$0.604°$	$-3.288°$	$-0.311°$	$-0.811°$	$0.742°$	$-0.182°$
STD (σ) VERT.	$3.086°$	$2.733°$	$2.987°$	$2.744°$	$2.698°$	$2.896°$

Like Brückmann, Weber and Diem, the gaze distribution in the urban environment shows the largest spread. Since the mentioned publications already discuss the different gaze in these situations in great detail, only a short overview over this data is presented here. The gaze distribution on motorways on the other hand is very focused. The differences between night and day only arise in terms of vertical gaze orientation. At night the gaze is lowered in all situations by up to 4° (urban roads) and at least by 0.5° (on country roads). The horizontal gaze only shows one major outlier with the gaze registered for motorway driving, where the median is shifted to the left by 1°. The main difference in the horizontal gaze is found for the spread of the data. As expected, the gaze distribution in urban environment is the widest and the gaze on the motorways is the smallest. Similar to all data before, the large spread of the data leads to no significant deviations between the data sets therefore the data is not analysed in more detail.

GAZE BEHAVIOUR IN DIFFERENT CURVES

The previous part focuses on general and overall fixation behaviour in the main road categories. This section now will divide these section according to the calculated road curvature as described in section 5.4.3. For this, the fixation data is evaluated for the complete way through the curve. This is important, since it is to be expected, that the fixation and gaze behaviour is different when entering or leaving a curve compared to being at the apex of the curve since the orientation point for the driver will be vastly different. In general, the fixation angles for driving through curves are recorded as expected. In left bends, the fixation points are shifted to the left and in right bends, the fixation is shifted to the right. The general horizontal fixation data is presented in table 5.21. The vertical data does not differ at all from the general data presented and is therefore not discussed here but is shown in detail in appendix E.4 in table E.9 and visualized in figure 5.94.

Table 5.21 – Horizontal fixation data in left and right-hand side bends for day and nighttime driving.

	DAY			NIGHT		
LEFT BENDS	$-4.012°$	$\pm$	$8.574°$	$-3.842°$	$\pm$	$8.081°$
RIGHT BENDS	$1.943°$	$\pm$	$8.964°$	$2.107°$	$\pm$	$8.445°$

The data shows two major things, one being, that drivers tend to look further into corners when driving through left-hand side bends ($-4.0°$) compared to right-hand side bends ($1.9°$) during the day ($-3.8°$ vs $2.1°$ during the night). This is explainable with the right lane traffic in Germany. For a similar curve radius, a left bend offers a larger viewing angle into the corner due to the additional lane on the left side when compared to the right-hand side traffic. When comparing day and night data however, no differences are recorded between the different time sections. This is an artefact in the measurement from the used headlamp system, that seems to provide a wide light distribution for general curve driving. While the horizontal fixation point is different for these points, the deviation in fixation angles does not change significantly between all four data sets. While the difference between left and right-hand side corners are to be expected, it is not expected, that no differences between day and nighttime bends are recorded since the difference that is recorded for the general fixation between day and nighttime driving should also translate into corners.
To analyse the data further, the curve data presented in figure 5.70 is divided into different bins ranging from 0 m to 1000 m, separately for left and right-hand side bends as well as for driving during the day and during the night. This raw data is shown in table E.8 in the appendix E.4.

The trend shown in table 5.21 is there here again. When comparing similar fixation behaviour for the same curve radius, the gaze is located significantly further to the side in left-hand side curves compared to the right-hand side bends. When increasing the curve radius, this recorded shift to the sides is lowered step by step. This again is obvious, since a larger radius means, that the curves apex is located further away and the curve is more similar to a straight road. However, the data for very large curve radius still shows significant differences to straight roads, meaning, that for both, left and right-hand side corners, the fixation is shifted to the sides. This is again illustrated in figure 5.93 where the horizontal fixation points are plotted over the curve radius with daytime data shown in blue and nighttime data shown in red.

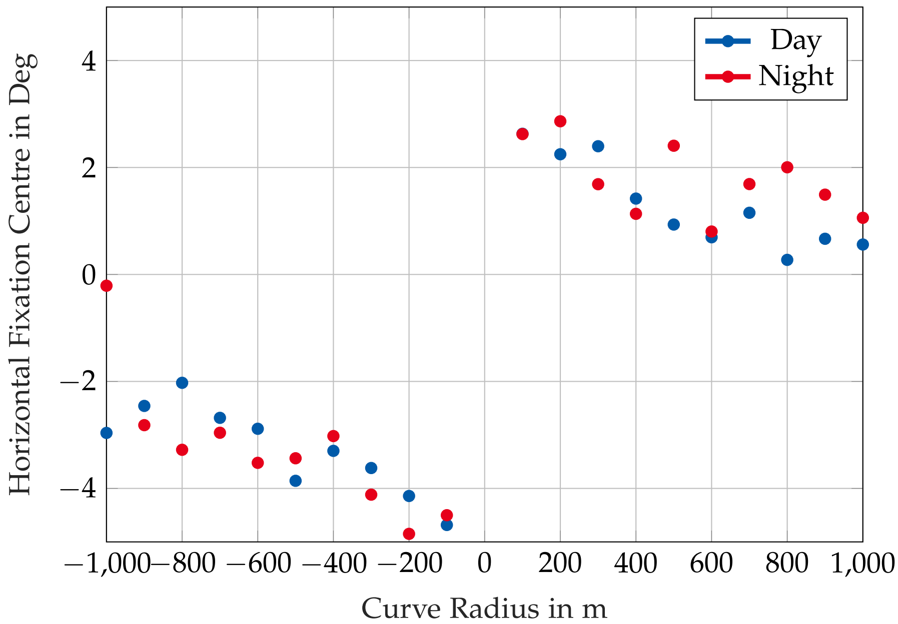

Figure 5.93 – Comparison of the horizontal fixation for different curve radii. Negative radii show left-hand side curves and positive radii show right-hand side bends. Daytime data is shown in blue, nighttime data is presented in red.

This shows that the vertical orientation changes with the curve radius as well. The raw data for this is shown in table E.9 in the appendix E.4.

For daytime driving, the data shows for both left and right-hand curves, that the smaller the curve radius is, the further down does the driver look. The larger the curve radius is, the further away the driver looks. This is evidently the case since wider curves with a larger radius allow for orientation further back. The fact, that the vertical orientation is pretty much symmetrical for left and right-hand side bends means, that despite the different horizontal angles, the orientation distance is equal for both curves. Therefore, the only recorded influence is the additional lane for left side curves. For nighttime driving, this effect is not visible, all data points are scattered just below 0° and thereby no trend is found. This is illustrated in figure 5.94 where additional to the vertical fixation data for daytime driving (blue) and nighttime driving (red) a Gaussian fit for the daytime data is shown by a red, solid line, to further illustrate the gaze behaviour at night. The fit is not used to describe the fixation behaviour any further but only to show the general behaviour for the daytime data. For the nighttime data, no fit is found, which further illustrates, that no trend is found at night at all.

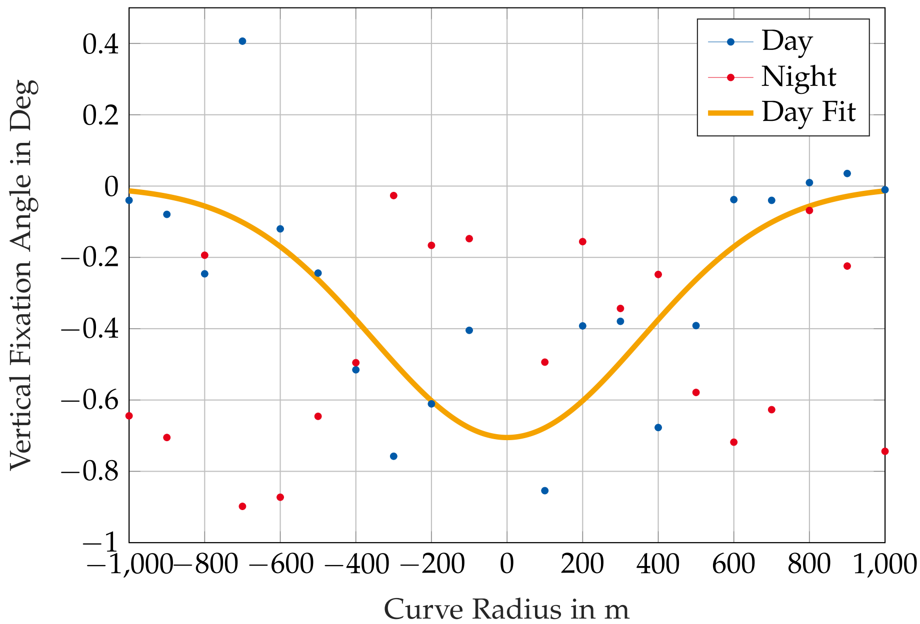

Figure 5.94 – Comparison of the vertical fixation for different curve radii. Negative radii show left-hand side curves and positive radii show right-hand side bends. Daytime data is shown in blue, nighttime data is presented in red and the Gaussian fit for the daytime data is shown as the red solid line.

The results very much comparable to the data found by SHIBATA and lead to nearly identical fixation directions for horizontal orientation. The vertical orientation is not further discussed by SHIBATA. To illustrate this, the data for similar curve radii as used by SHIBATA (150 m to 250 m) is extracted and the data recorded by SHIBATA as shown in figure 4.17b is digitalized again. This is shown in figure 5.95 where the data by SHIBATA is shown by the red crosses while the data from this thesis is shown in the background. The schematic road is transfered from figure 4.17b as well.

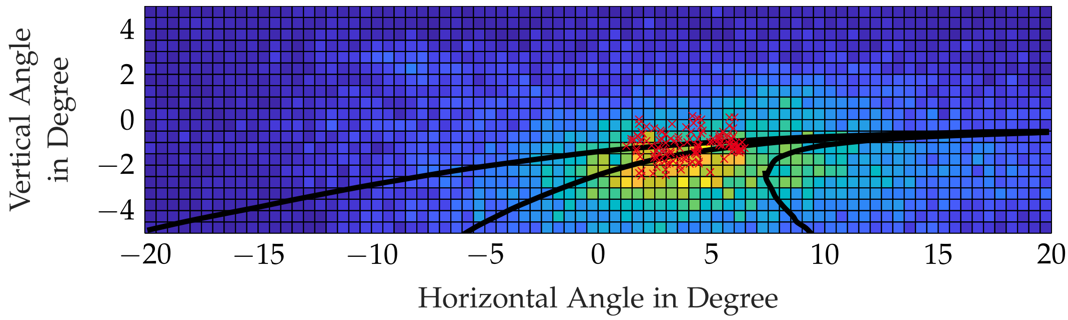

Figure 5.95 – Data for fixations recorded in curves with raddi between 150 m to 250 m compared to the data by SHIBATA as marked by the red crosses.

.

The overlap of both data sets show is clearly shown. The small individual differences, like the lower vertical angle for the data recorded during this thesis, is explainable by the possible different light distribution as well as the different roads. While SHIBATA used single bends with defined radii, this thesis shows the data for many different bends with radii in the range of what SHIBATA investigated. However, no detailed information on light distribution or vehicle in use is available.

GAZE BEHAVIOUR IN DIFFERENT ILLUMINANCE SITUATIONS

After looking at different road geometries, the next step is to investigate different lighting situations. For this, the data presented in figure 5.72 and 5.73 is divided into different bins ranging from $<10\,\mathrm{lx}$ to $10 \times 10^5\,\mathrm{lx}$. The data is not divided into daytime and nighttime driving additionally since the division is done automatically since the illuminance data shows a clear cut off at $10 \times 10^2\,\mathrm{lx}$ for both data sets. The horizontal and the vertical fixation data is shown in table 5.22 for all bins.

Table 5.22 – Fixation data for day and nighttime drives for different overall illuminance values.

ILLUMINANCE RANGE	MED. H.	MED. V.
OVERALL	$-0.8° \pm 7.5°$	$-4.0° \pm 2.9°$
$<10 \times 10^5\,\mathrm{lx}$	$-4.8° \pm 11.1°$	$-0.4° \pm 4.0°$
$<10 \times 10^4\,\mathrm{lx}$	$-1.7° \pm 9.8°$	$-0.5° \pm 3.8°$
$<10 \times 10^3\,\mathrm{lx}$	$0.6° \pm 10.1°$	$-0.5° \pm 3.9°$
$<10 \times 10^2\,\mathrm{lx}$	$-0.1° \pm 11.5°$	$-0.9° \pm 4.7°$
$<10 \times 10^1\,\mathrm{lx}$	$-0.4° \pm 10.5°$	$-0.9° \pm 4.1°$
$<10\,\mathrm{lx}$	$-0.8° \pm 9.1°$	$-0.9° \pm 3.6°$

The data shows, no clear trend for both, horizontal fixation point and the deviation in fixiation points horizontally and vertically when splitting the data by the mentioned illuminance bins. While at first thought, this might be counter intuitive, and one might expect different orientation angles for different illumination levels, most of the influence will probably come from the adaption level and changes in illuminance and not from the illuminance itself. The only trend that can be found is a slight change in the vertical median leading to a slightly lower orientation point for lower illuminance values. However, this effect is very limited with a difference of below 0.6° and thereby lower than the average accuracy of the used eye tracking system. However, since the eye tracking accuracy is indeed a systematical error, and the trend is valid over all subjects and a very large data sets, this behaviour can not be neglected.

GAZE BEHAVIOUR AFTER GLARE

Until now, the influence of different illuminance values at the driver's eye on the fixation behaviour is discussed. While this general approach is interesting in itself, the next step will go into further details. Here, the influence of the glare pulses described above and shown in figure 5.78 and 5.79 are is investigated. In the first step, the average amount of fixations registered directly after a glare pulse is recorded is calculated and compared to the average over the complete data set. As mentioned above, during the day an average fixation rate of 17.6 % is registered. To investigate the influence of the registered glare pulses on the fixation behaviour, a timeslot of 5 s after a registered pulse is chosen. This is done, since the pulse data shown in figure 5.77 indicates, that no glare pulse longer than 3 s is recorded and an additional time of 1 s is needed for the full pupillary reaction. On these 4 s an additional 1 s timeslot is added, to investigate the gaze or fixation behaviour not only directly during the glare pulse but shortly after as well. In this timeslot, during the day, the fixation rate drops down to a 16.0 % fixation rate - a reduction by 9.0 %. A similar, but much stronger, trend can be found in the nighttime data, where the fixation rate goes from an average 24.4 % down to 18.9 % - a reduction by 22.8 %. This data does not involve the amount of data, that was not evaluated, because the tracking accuracy at that moment was to low due to difficult angles between the cameras and the eye or a very low eyelid opening due to the glare pulse. This unusable data did if only slightly increase right after the registered illuminance peaks from an average 24.6 % to 26.3 % at daytime and dropped slightly from 21.3 % down to 18.4 % for nighttime drives.

The fixation distribution for the 5 s interval after an illuminance pulse during the day shows no significant difference to the general fixation distributions recorded during the day. However, the horizontal mean is recorded to be at $0.9° \pm 9.0$ and thereby one degree further to the right. The larger standard deviation in this distribution also indicates, that the drivers appear to increase their variance in where they are looking during and after the glare pulse. Most probably, this is to avoid looking directly into a glare source. The vertical median is calculated to be at $-0.3° \pm 3.5$ and therefore still slightly below the centre of the road. When looking at the fixation distribution right after the glare impulses, shown in figure 5.96, one major difference between the general gaze difference is, that a larger but narrow second accumulation point appears under $-14°$ and that the general fixation area seems a bit wider. This second accumulation point explains the slight shift in horizontal fixation angles, however the calculated values for the standard deviation do not indicate a wider distribution.

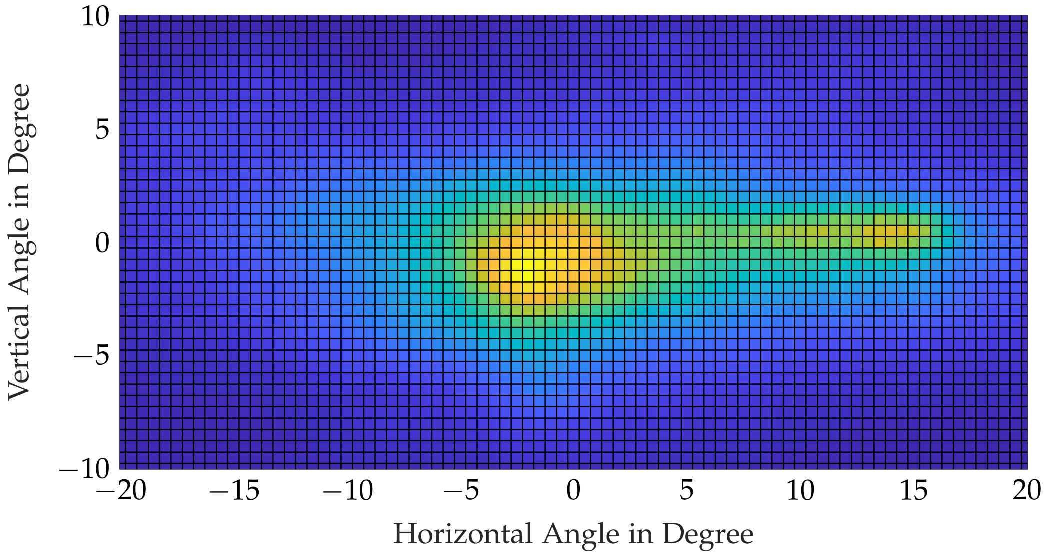

Figure 5.96 – Fixation distribution for all daytime data recorded up to 5 s after an illuminance peak is registered. The median value for the horizontal fixation is calculated at 0.9° ± 9.0 and the vertical median is at −0.3° ± 3.5°.

For completeness, the histograms for the both, the vertical and the horizontal fixation distributions after glare illuminance pulses are found in appendix E.4 in figures E.27 and E.28. However no significant or unexpected forms are found for those distributions.
The same data is evaluated for the nighttime drives. Here an even larger difference between the general fixation distribution and the fixation distribution directly after illuminance peaks is found. The horizontal median of the gaze direction is now found at 1.4° ± 8.1 thereby resulting in a shift of 2.2° compared to the general data. The vertical median also shifts significantly down by 1.8° to only −3.8° ± 3.2 thereby leading to a much lower median viewing distance of only 18.0 m. The fixation distribution of this is shown in figure 5.97 where compared to the distribution during the day, no second accumulation point is to be found.

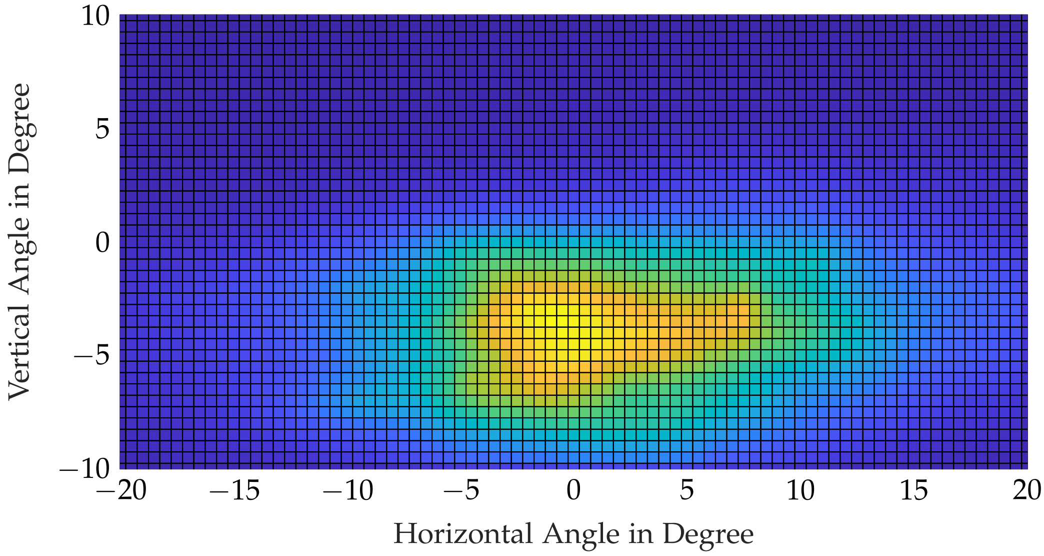

Figure 5.97 – Fixation distribution for all data recorded at night and up to 5 s after an illuminance peak is registered. The median value for the horizontal fixation is calculated at 1.4° ± 8.1 and the vertical median is at −3.8° ± 3.2°.

Since this data includes all glare pulses detected and shown in figure 5.78, and thereby also includes pulses that are rated just above noticeable, the same calculation is done for all 7 different pulse categories for day and night. Showing all gaze distributions and discussing their form will not lead to any more insight. Therefore, the important parameters, like fixation rate and median fixation angles are summarized for all datasets in table 5.23. In the fixation rate, no significant difference is found. While for daytime driving, the fixation rate is constant over all pulse categories, a trend can be seen during the night, where the fixation rate decreases with higher pulse intensities. This is to be expected since higher glare should lead to more distraction. The same behaviour was expected for the daytime data as well. However, as shown above, the data sample for higher pulse intensities is much lower during the day. This makes this data more unreliable than the nighttime data.

More interesting is the shift in the fixation distributions that is recorded for the different pulse sets. During the day, the slow shift from looking at the centre of the road and at the horizon for low intensity pulses to looking to the right side of the road and downwards is directly visible. However, due to the large standard deviations compared to the shift in vertical and horizontal fixation angles, no significant differences are found. At night, this shift is not as pronounced since the shift already occurs directly for even the lowest intensity pulses.

Table 5.23 – Fixation data for day and nighttime drives directly after a glare pulse is registered sorted by ascending pulse intensity.

MAX E.	DAY			NIGHT		
	MED. H.	MED. V.	FIX.	MED. H.	MED. V.	FIX.
OVERALL	$0.9° \pm 9.0°$	$-0.3° \pm 3.5°$	17.6 %	$1.4° \pm 8.1°$	$-3.8° \pm 3.2°$	24.4 %
>640 %	$1.6° \pm 8.9°$	$-1.4° \pm 3.2°$	13.3 %	$1.1° \pm 7.8°$	$-3.5° \pm 3.3°$	15.9 %
<620 %	$1.3° \pm 9.2°$	$-1.1° \pm 3.4°$	15.8 %	$1.3° \pm 7.9°$	$-3.0° \pm 3.3°$	18.3 %
<320 %	$0.2° \pm 9.2°$	$-1.1° \pm 3.5°$	16.0 %	$1.6° \pm 8.0°$	$-3.0° \pm 3.3°$	17.8 %
<160 %	$-1.4° \pm 8.6°$	$-0.8° \pm 3.5°$	16.2 %	$1.4° \pm 8.0°$	$-4.1° \pm 3.4°$	18.4 %
<80 %	$-1.2° \pm 8.1°$	$-0.3° \pm 3.4°$	14.2 %	$1.1° \pm 8.1°$	$-4.0° \pm 3.4°$	18.7 %
<40 %	$-1.9° \pm 7.6°$	$-0.1° \pm 3.4°$	16.2 %	$1.1° \pm 8.1°$	$-4.1° \pm 3.4°$	19.7 %
<20 %	$-1.9° \pm 10.0°$	$-0.3° \pm 3.5°$	16.9 %	$1.4° \pm 8.3°$	$-4.0° \pm 3.4°$	19.4 %

This fixation rate is again illustrated in figure 5.98 where the base level for daytime fixations is indicated by the blue line, and the base line for nighttime fixation is shown by the red line. The fixation rates for the different pulse intensities for day are then shown in yellow while the fixation rates after the different glare pulses during the night are shown in purple. Figure further illustrates a few things. Firstly, the drop in average fixation rates is much higher during the night. Secondly, even after glare pulses, the fixation rates during the night are higher than the average fixation rate during the day with the exception of the pulses with the highest intensity. Thirdly, the reduction in fixation rates after glare pulses is nearly identical for day and nighttime driving.

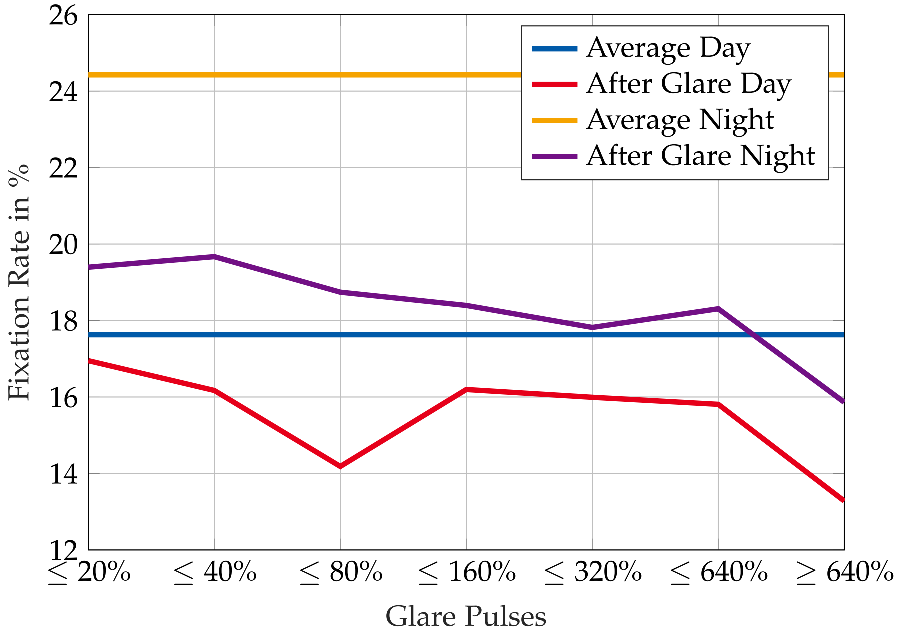

Figure 5.98 – Average fixation rates during the day (blue) and night (red) as well as the fixation rates 5 seconds after a registered glare pulse in the different pulse categories for day (yellow) and night (purple).

These findings confirm, that the chosen method of finding pulses and the way they are sorted and binned is scientifically correct and no unexpected or unexplainable effects occur. The introduced method can therefore be not only used to identify glaring pulses in large illuminance distributions, but also be used to describe the effect of glare on the fixation behaviour.

GAZE BEHAVIOUR IN DIFFERENT DRIVEN VELOCITIES

The next step in analysing the fixation behaviour of the recorded test participants is to find any influence of the driven speed on the fixation behaviour. The recorded velocities are already presented in figure 5.71. This data is now split into different bins as follows: $<30\,\mathrm{km\,h^{-1}}$, $<50\,\mathrm{km\,h^{-1}}$, $<70\,\mathrm{km\,h^{-1}}$, $<100\,\mathrm{km\,h^{-1}}$, $<130\,\mathrm{km\,h^{-1}}$ and $>130\,\mathrm{km\,h^{-1}}$. This is again done for day and night separately since the general effect between day and nighttime driving is to be expected to show here as well. All data sets are summarized in table 5.24.

Table 5.24 – Fixation data for day and nighttime drives for different driven velocities.

DRIVEN SPEED	DAY		NIGHT	
	MED. H.	MED. V.	MED. H.	MED. V.
OVERALL	$-0.9° \pm 7.6°$	$-0.8° \pm 3.1°$	$0.8° \pm 7.4°$	$-2.0° \pm 3.0°$
$>130\,\mathrm{km\,h^{-1}}$	$-0.4° \pm 8.7°$	$-0.2° \pm 2.8°$	$-0.0° \pm 8.9°$	$-1.2° \pm 3.6°$
$>100\,\mathrm{km\,h^{-1}}$	$-1.0° \pm 9.0°$	$-0.7° \pm 3.2°$	$-0.4° \pm 9.0°$	$-1.1° \pm 3.8°$
$>70\,\mathrm{km\,h^{-1}}$	$-0.6° \pm 8.8°$	$-0.8° \pm 3.2°$	$-0.9° \pm 8.5°$	$-1.1° \pm 3.8°$
$>50\,\mathrm{km\,h^{-1}}$	$-1.0° \pm 9.1°$	$-1.0° \pm 3.3°$	$-1.1° \pm 8.6°$	$-1.4° \pm 3.7°$
$>30\,\mathrm{km\,h^{-1}}$	$-1.2° \pm 9.2°$	$-1.3° \pm 3.3°$	$-1.0° \pm 9.3°$	$-1.6° \pm 3.8°$
$<30\,\mathrm{km\,h^{-1}}$	$-1.4° \pm 10.1°$	$-1.7° \pm 3.7°$	$-1.2° \pm 11.7°$	$-2.2° \pm 4.2°$

In general it can be summarized, that there is no difference in the horizontal orientation of the driver for different velocities in both day and night. However, the standard deviation in the horizontal plane shows a clear trend for both day and nighttime driving, in a way, that for higher velocities the gaze distribution gets narrower indicating, that the driver focuses more on what is straight ahead and reduces the search patterns. For the vertical gaze, trends can be seen for both, the median as well as for the standard deviation. The median of the vertical gaze is lifted upwards for higher velocities and thereby indicates, that the faster the velocity, the further away the driver looks on the road. At the same time, the standard deviation in the vertical plane is decreased similar to the horizontal gaze indicating, that the search pattern is decreased and narrower for higher velocities.

GAZE BEHAVIOUR IN DIFFERENT TRAFFIC SITUATIONS

While all gaze patterns analysed so far, are pretty similar or even identical to findings in the literature, they are necessary for several reasons. First of all, comparison with other work is always necessary to validate the new findings. Furthermore, with dynamic research like traffic analysis or headlamp distribution, renewing research with state-of-the-art technology to refine older findings is absolutely the right ways.

However, this part of thesis will focus on research not found in previous studies. For this reason, the data already presented in 5.2.2 will be evaluated in terms of gaze and fixation behaviour.

For this, the exact location of the gaze vectors are checked and compared to the objects positions. Due to the uncertainty in the gaze calibration and the fact, that the human eye is capable of consciously obtaining information within a two degree field of view from the visual axis, this is evaluated in several steps starting with the exact object coordinates and going up stepwise in 0.1° steps up to an additional area of 2.0° around the object. This additional area around the object is from here on forth referred to as *error-window*. This is done for all different object classes separately. Gaze or fixation distributions will not be shown in this section since the goal here is to compare to distributions which would get unwieldy.

The general results of this investigation are shown for the 0° error window around objects and best summarized as follows. Vehicles are fixated twice as often during the night com-

pared to during the day. Other traffic participants like trucks, buses and motorbikes are fixated around the same during day and night and only bicycles and traffic signs are fixated more often at night compared to the day with bicycles being gazed at around 50 % more often and traffic signs even twice as much. This data is consistent for all test subjects and all road categories. The absolute fixation ratio for a 0° error-window is at 18.0 % for cars, 3.9 % for trucks, 5.9 % for buses, 4.0 % for bikes and cyclists and 12.0 % for traffic signs. These numbers appear to be rather low.
However, the data shown in figure 5.34 has to be taken into account. This data shows, that in most frames, more than one object is present and the gaze vector can only imply a fixation on one of the vehicles. A more general approach would be, to find ratio of the driver looking at an object compared to the amount of time, the driver does not look at an object. The condition, that an object needs to be in the field of view needs to be considered for this. This ratio is then significantly increased to 39 % during the day and 46 % during the night. Again, no significant difference can be found between the different road types with only a slight deviation for motorways that is not significant but the trend is seen for both day and night. Here a slightly lower percentage of fixations is set upon vehicles or other objects (34 % during the day and 41 % during the night).

Expanding the error window only increases the absolute ratio in each class but does not influence the ratio between day and night and is therefore not discussed any further. After this analysis of the gaze behaviour in different situations, like different traffic situation, different road categories and different lighting conditions, the next step needs to be to deduct optimized light distributions from the presented data.
A more interesting investigation arises, when comparing the overall object distribution with the gaze behaviour. To do so, the distributions for objects and fixations in the different road categories are compared. To quickly summarize the findings all distributions are quickly summarized again. For the object distributions, the urban environment leads to the largest spread in object positions both vertically and horizontally. Country roads show the tightest distributions and motorways lead to an intermediate object distribution. For the gaze distributions a different behaviour is found. While the widest distribution is still found for the urban environment, the smallest distribution is found for motorways. Country roads lead to an intermediate gaze distribution. This leads to the assumption, that at least with the dataset and the evaluation process presented here, no correlation between the gaze distribution and object locations can be found. However, this is also not expected with the light distribution in use.

The better correlation is found when investigating the driven speed and the gaze distribution. As already shown in figure 5.71 the driven speed also correlates directly with the road category, thereby already explaining the recorded gaze distributions in each road category.
This is not to be expected, since objects in the field of view are expected to lead to a gaze appropriation. However, since this thesis only focuses on the overall object and gaze distributions, no definite answer can be given on the impact of objects to the gaze behaviour. While the presented data shows the results for the overall distributions, an interesting approach would be to select different velocity ranges and compare all data sets in there as well. It might be probable, that for higher velocities on country roads and motorways, objects tend to be less distracting. In urban environments however, the large quantity of objects in the field of view makes it difficult if not impossible to correlate overall distributions. However,

this selection of even smaller sub-samples of the presented data goes beyond the scope of this thesis and is recommended to be part of future works.

5.4.5 SUMMARY OF DIFFERENT PARAMETERS FOR LIGHT DISTRIBUTION OPTIMIZATION

The section above shows the field test conducted in order to find different parameters, that can be used to optimize existing and future light distributions for better nighttime driving performance. Within this field test, the same data as described previously in section 5.2 was evaluated and complemented by illuminance data and eye tracking data including gaze and fixation data as well as the pupil diameter. Furthermore data regarding the driven route like curve radii, speed limits and actual driven speed are evaluated for the general data as well as for the previously described major road categories like urban and country roads as well as for motorways.

The first part focuses on the pupil data and the glare estimation during these drives. While the pupil data does not lead to any viable glare estimation, a method is proposed to calculate the current glare load based on the illuminance. Knowledge gained from section 5.3 is used in order to estimate a adaptation illuminance and short glare peaks above this illuminance threshold are identified. Based on their relative intensity, these pulses are correlated to DE BOER rating and the different glare load in different situations is calculated. This shows, that the glare load is most disturbing on country roads and the least disturbing in urban environments. Furthermore, real life data on pupil diameter in correlation to the current illuminance at the drivers eye is found leading to significantly different values when compared to data achieved in laboratory environments.

The second part focuses on the calculation of the gaze and fixation behaviour. While in general, gaze behaviour previously reported in other studies is confirmed, a new approach, correlating the gaze behaviour to objects on the road, was not successful. However, the general distributions of both data sets, fixations and objects do correlate. Furthermore, the influence of glare pulses on the fixation behaviour is analysed, showing that shortly after a glare pulse, the fixation rate is dropped significantly and the gaze wanders off to the side.

5.5 LIGHT DISTRIBUTION OPTIMIZATION

While the segment optimization as shown in section 5.2 used the obtained object distributions in real traffic space to find new segment distributions, that allow for a significantly more efficient use of high beam and therefore a more illuminated road in general, this section now combines the data on object position and gaze distribution to deduct, where light needs to be set. The main constrain the distribution is limited by, is that the light distribution needs to be smooth and without sharp edges in the light distribution. Furthermore, the angular luminous intensity distribution shown in 5.1.4 needs to be fulfilled. While section 5.2 shows, that the high beam part can be set together by 280 segments, this used as a base line for the distribution since the LED setup can be modified using PWM to achieve the required distribution.

The approach chosen for this thesis is the combination of the overall fixation and object distributions. Since the section 5.1.1 shows, that the influence of the low beam is very minimal, the focus is set on the high beam area.

Since the previous chapter has shown, that the correlation between objects and gaze distribution is not necessarily given, the proposed method is to use the object distribution as base distribution. From this object distribution, the normalized fixation distribution is subtracted, leading to a difference-distribution as shown in figure 5.99. This distribution is set as an example and contains objects and gaze directions from all test drives in all situations weighted accordingly. As already shown in the previous sections, due to the deviations between the different situations, headlamps with other primary use cases can be achieved by different weighting factors for different object situations.

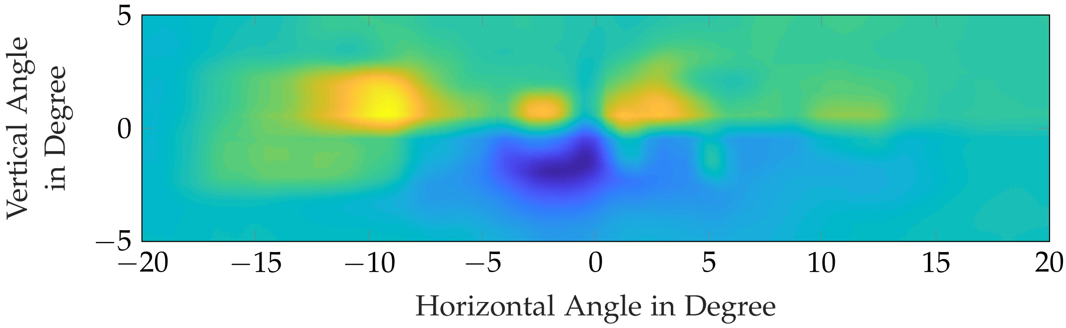

Figure 5.99 – Difference between the normalized object and gaze distribution for the overall datasets.

This distribution now shows the differences between in object position and gaze locations. Areas with positive values are areas, that contain relatively speaking, more objects than fixation vectors. Negative areas contain more fixation vectors than objects. Since the goal is, to create a light distribution that enables safer driving, the goal here is, to direct more light into areas, where objects are but the driver does not look at. At the same time, light should only be directed into areas, where objects actually appear. In order to achieve a symmetrical light distribution, this distribution is then additively mirrored. This symmetrical difference-distribution is then added to the general light distribution proposed in chapter 5.1.4 and shown in figure 5.14 where the field tests are summarized. This step leads a light distribution, that delivers more light into areas with objects, while at the same time maintaining the optimization for object detection. On the other hand, areas, where drivers tend to look at often, without any object being present, is given less light in order to minimize the distraction. In order to avoid sharp edges in the light distribution, the resulting distribution is then smoothed in both directions using a moving mean filter over 10 values. As an example, the resulting distribution, with a relative luminous flux to the standard distribution is shown in figure 5.100. Again the colour coding is identical to the colour coding as shown in figure 5.19 for all following distritbutions. This light distribution weights the influence of base light distribution, object distribution and fixation distribution all equally, since the weighting factors are not known for the different distributions in order to guide the driver's gaze. In order to find these factors, further research needs to be conducted

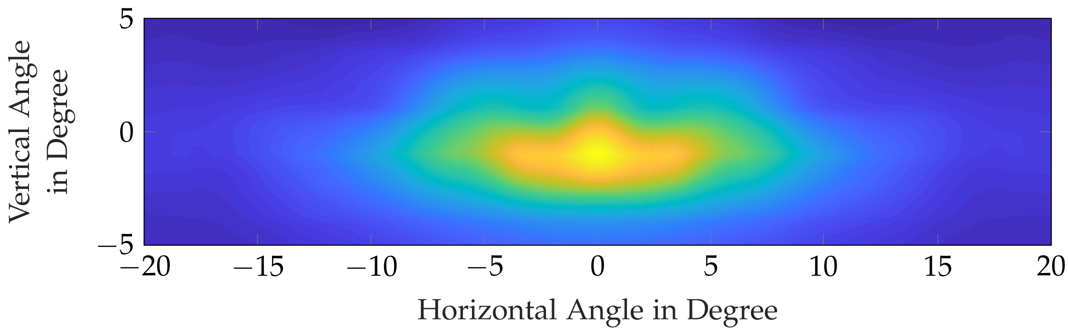

Figure 5.100 – Proposed new light distribution based on the detection tests shown in section 5.1.4, the object distributions shown in section 5.2 and the gaze distributions found in section 5.4

.

This light distribution now shows a resemblance to the standard light distribution used in this test. The part below the horizon (<0° vertically) is illuminated by a wide low beam. To compare this distribution to other light distributions, the width at 50 % intensity is compared. The high beam part of this distribution has a clear hot spot in the centre, much smaller than the hot spot in the low beam area. While the low beam part of the distribution reaches 50 % at ±9.3°, the high beam part reaches this threshold already at ±7.5° horizontally. This means, that compared to the intensity distribution shown in chapter 5.1.4, where the 50 % intensity is reached at ±5°, a much wider distribution is achieved using the proposed method.
In the next step, this distribution is split into the two conventional parts. The low beam section is selected from −0.5° to −5.0°. This distribution is cut out of the distribution without any further modification. This is shown in figure 5.101.

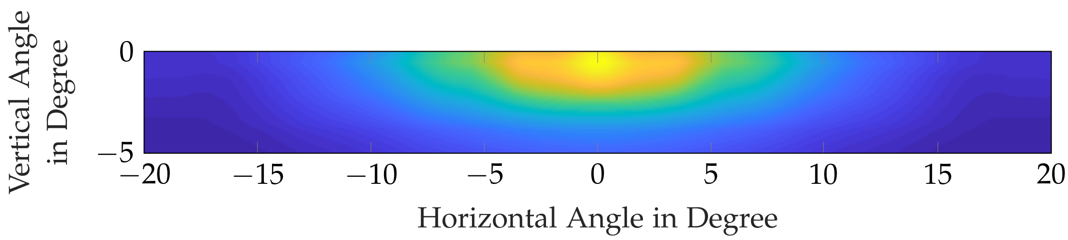

Figure 5.101 – Proposed low beam light distribution based on the detection tests shown in section 5.1.4, the object distributions shown in section 5.2 and the gaze distributions found in section 5.4

.

For the high beam section, from 5.0° to −0.6°, the 4 x 70 segment distribution, that is found to deliver 99 % of road illumination, is taken as a base distribution. The relative intensity for each of the 280 is determined by the mean intensity measured from the ideal light distribution in this area. The resulting high beam light distribution for the gfHB setup is shown in figure 5.102.

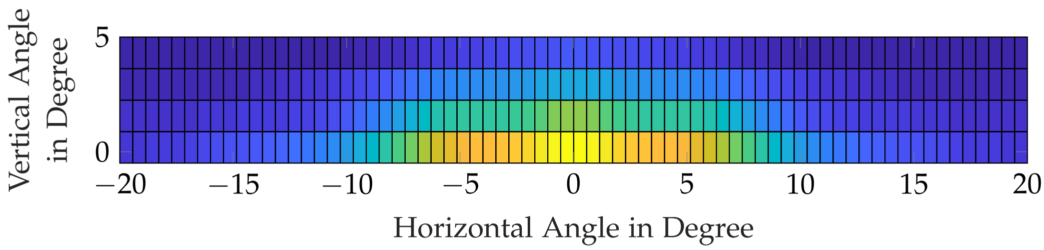

Figure 5.102 – Proposed segmented gfHB light distribution based on the optimized light distribution as seen in figure 5.100.

This shows, that due to the segmentation, the high beam distribution has significantly sharp edges compared to the ideal, smooth distribution. Since this is an ideal calculation, and a real implementation of this setup would lead to smooth edges between the different segments, this behaviour is neglectable. The major difference here is, that the 50 % illumination is now reached at a smaller angle at ± 8.5°. Due to the segmentation, this segment reaches an intensity of 53.3 % and the neighbouring segment falls down to 46.9 %. However, this still provides a significantly wider distribution than found by Schneider. While this seems rather small, the light distribution used in the test vehicle reaches the 50 % threshold already at 4° in the high beam and at around 5.5° in the low beam. This shows, that the proposed light distribution is significantly wider in both areas. The reason for this is found in the base distribution, since this base distribution is already much wider and only slightly modifies.

The results presented here only show the relative luminous intensity proposed under different viewing angles. To deduct the absolute intensity, the combination of the studies in sections 5.1.1 to 5.1.3 show the required illuminance for given stopping distances in the centre hot spot. This will not be further evaluated here since this is a simple rescaling of the proposed relative light distributions.

While this segmentation shows ideally sharp edges for all segments, section 5.3 shows, that a smooth gradient for between shut off areas and switched on segments is able to minimize glare for other traffic participants. While a perfectly sharp projection of each segment is technically possible, smoother edges would also create the benefit of a smoother light distribution without single hotspot segments. As figure 5.79 shows, the glare load during country road driving is significantly larger than the glare load in the other situations. When optimizing a light distribution with the main purpose of being used on country roads, this needs to be considered.

The obvious next step is now, to test the proposed light distributions for dynamic detection tests on isolated roads and in real life traffic. Furthermore, the acceptance by drivers needs to be tested. For this thesis, this was not possible in the given time frame. Therefore, future studies have to focus on realizing the proposed distributions and testing them.
One major remark in this approach has to be, that it was not possible within this thesis to investigate the required luminous intensity to direct and influence the gaze. Therefore, the weighting proposed here, where objects, gaze and relative luminous intensity are all regarded equal, is to be understood as an example. The next steps need to be to investigate this relation between the three distributions.

5.5.1 Summary and discussion of optimized light distribution

This section uses the data previously determined in the sections 5.1.1 to 5.1.3 and 5.2.2 to 5.4.4 in order to derive new and optimized light distributions. In order to do so, the ideal light distribution as proposed in figure 5.14 is modified depending on the recorded objects and gaze distributions. Light is added at angular positions, where objects are detected by the camera, but no gaze appropriation is registered. Areas, where a lot of attention by the driver is registered, but less objects area detected, light is reduced. The aquired light distribution is then split into a low beam part and a high beam part. Comparing this distribution to the light distribution as used in the testing vehicle shows, that a much wider distribution for both low and high beam is required when following the proposed method.

Furthermore, the segment optimization proposed in section 5.2.2 is used and a segmented light distribution is created. This section also shows, that different limitations are in place, that keep the proposed light distributions from being the perfect solutions. The presented approach should therefore only be considered as a proposal.

Part VI

SUMMARY, DISCUSSION AND OUTLOOK

6 SUMMARY, DISCUSSION AND OUTLOOK

The presented thesis is split into three major parts, over which the optimization of overall light distributions is investigated.
In the first part, three major field tests where conducted to find several factors of the light distribution on detection rates and distances while driving on country roads. These included the variation of the low beam intensity, the variation in the high beam intensity and the variation in the detection angle. The results show, that the major influence is only found in the luminous intensity of the high beam hot spot. This data is used in combination with the findings from previous studies, to deduct a minimal luminous intensity for given detection distances. The main point in this study is, that the values allowed within current regulations are sufficient in order to guarantee safe driving at night, as long as high beam is used.
The angular positioning of the detection dummies in regard to the visual axis of the driver did not lead to a significant influence on the detection distance. From the achieved data, recommendations for the luminous intensity under different angles are derived. The use of low beam can be discouraged in general and no further investigation of the low beam is done since gfHBs systems already allow for driving solely with low beam in a very limited amount of situations and the visibility level of high beam can be obtained the majority of the time. However, all tests are performed under closed off, isolated conditions without other traffic participants and test subjects, that were introduced into the detection test. For this reason, all acquired data sets therefore have to be regarded with caution since more complex situations will decrease the measured distances. While the influence of the detection object form and colour are corrected, it was not possible, correct the data for real traffic situations.

In the second part, German traffic was analysed and the segment distribution for gfHBs is optimized for maximum illumination on the road. This is done in several steps. The first proof of concept was done with the means of a traffic simulation of German country roads. The results show, that especially for low resolution systems, high performance gains are possible by allowing for smaller segments in the centre of the high beam area. For example, it was possible to show, that an optimized high beam setup with only 8 segments can achieve the same overall road illumination as a conventional 20 segment high beam. Furthermore, it was determined, that the analysed situations, a setup consisting of $3 \cdot 67$ segments already leads to 99 % of road illumination. From a technical view, this means, that according to the simulation, the maximum amount of pixels required for near perfect road illumination is found at 201 segments.
To validate this data, in the second part of this, object recognition software is used to extract average object positions in the German traffic space in different road categories like urban roads, country roads and motorways. The basis for this analysis is a video database that was recorded for this theses on over 108 drives with 128 km each, out of which half were performed at night and half are performed during the day. This data allowed to analyse more complex situations and to get real life traffic data for the segment optimization. Two exemplary optimization distributions are proposed, where the general distribution is optimized on the overall object distribution. The more specialized segment distribution only evaluates country roads and motorways with the mania factor being given by country roads. Due to the more complex situations large differences in the overall distribution are found

when compared to the simulation results. The object distributions found for all situations are significantly wider, both horizontally as well as vertically. On these object distributions, the same high beam optimization is performed as on the simulation data. The resulting segment distribution leads to wider segments compared to the results found with the previously. However, a significant improvement can still be seen and for real life traffic the maximum amount of segments needed for nearly perfect illumination at any moment is found with a 4 x 70 distribution.

In a laboratory study the effect of glare pulses by oncoming traffic was analysed. The goal of this study was to find a correlation between the pupil reaction to short light pulses in order to deduct glare perception in real life driving tests. This correlation was found for the condition, that the photometric parameters are known. A more general result however was found regarding the correlation between photometric values and the glare perception. By varying the duration of the glare pulses, it was possible to show, that both, illuminance as well as exposure are only valid correlating values in certain areas. While the exposure correlates with the glare perception for very short light pulses with a duration of 300 ms or less, the illuminance correlates to the glare perception for very long pulse durations of 2 s and above. For intermediate durations, a correlation is found for $E \cdot T^{0.47}$.

In the third part, the gaze and fixation behaviour of drivers is analysed for 54 different participants. Each participant drove a certain road consisting of urban roads, rural roads and motorways both during day and nighttime. While the gaze behaviour is analysed for all participants, the large spread in the gaze distribution leads to results, that are not statistically significant. At the same time, all trends that are described in previous works are confirmed and the average fixation behaviour is measured. It was further possible to determine the influence of short illuminance pulses on the glare perception and the general glare load in different road categories. This shows significant differences in glare for different road categories and also shows the influence of the found glare pulses on the gaze behaviour. The potential impact of these light pulses on road safety is determined, showing that right after registered glare pulses, drivers tend to show a significantly reduced amount of fixations therefore leading to a reduced amount of processed information. An unexpected result is found, when no influence of the object density or distribution in the driver's field of view on the gaze behaviour was measured. Since only general distributions are compared how ever, this does not mean, that there is no definite correlation between the two.

Combining the object data with the gaze data (and the used light distribution) enables the possibility to determine requirements for future light distributions. Several optimized light distributions depending on the preferred use-case are proposed with regard to differences in object locations and driver's fixation.
This means, that the main goal of this thesis, proposing new optimized light distributions is successfully done, it was not possible to evaluate these new distributions due to the lack of the necessary hardware. Furthermore, the limitations of this proposal have to be mentioned. While the used headlamp system was a state-of-the-art LED system, the gaze distribution is only recorded for this single light distribution. Furthermore, it was not possible to determine the differences between the low and the high beam light distribution. It is therefore not possible to determine the actual influence of the light distribution on the gaze behaviour and the proposed light distributions are based on previous recorded findings. The secondary goal of finding a correlation between a physical response of the pupil to the psychological glare per-

ception to analyse the discomfort glare in real life driving situations, was not possible since the laboratory studies have shown, that the influence of the pulse form, both in duration and maximum intensity as well as overall form is necessary to find the correlation between the pupil diameter and the glare perception. Since the correlation directly between the photometric values and the discomfort glare is more constant, this approach is to be preferred.

While the presented conclusions are valuable and present important insight in the driver's orientation and the overall traffic space, the main benefit of the shown studies is definitely the setup and the upkeep of the recorded data and the overall data base. Since all data is stored in raw format, further investigations into more detailed situations and the derivation of light distributions and functions for more individual situations is definitely possible. To do so, further development of the object recognition software using the ever evolving TENSOR FLOW machine learning algorithms is definitely recommended to improve the object detection probability.
The next main steps however have to be the evaluation of the proposed light distributions. This can be done in one of two major ways. Either a real headlamp setup is developed using a high resolution headlamp, or driving simulators could be used. In this evaluation, the two major factors for light distributions, detection distance and acceptance by the drivers, have to be evaluated. Since the light distributions are optimized for more complex situations, and as shown in this thesis, the detection distance on straight roads under closed off conditions only the maximum luminous intensity influences the detection distance, this evaluation needs to be set up in a more complex environment simulating real life traffic more closely. To evaluate the acceptance by drivers multiple possibilities arise. The most straight forward solution would be, to evaluate the driving using questionnaires after using the light distributions in real life traffic. However, questionnaires are known to lead to a large variance in responses and can only evaluate larger, more general driving tests. Therefore, using objective measurements like EEG systems and the eye tracking to evaluate the concentration and well being of the driver.

Further the proposed light distribution is based on overall and general distributions of object positions and fixation behaviour. While a short part of this thesis is dedicated to analyse the fixation behaviour for situations with objects in the current field of view, the exact gaze behaviour and what the driver perceives for different objects is not analysed. Since the data is now available and a working object recognition software was set up during this thesis, this is a possibility for further analysis. Additionally, only major situations are reviewed here. The test setup as well as the data presented in this thesis offer much more potential to analyse more detailed situations. As an example, intersections and roundabouts are not investigated. The possibility to investigate the gaze behaviour for different discrete driving manoeuvres is also given. Using the video data those situations can be identified and analysed. Regarding the overall high beam resolution needed for optimal performance, only photometric illumination of the road is reviewed. A higher number of segments can increase driver's comfort and acceptance by delivering smoother transitions between different light distributions. As an example, a cornering light, in which only the hot spot is dynamically shifted into the corner, can be displayed with much more detail delivering a much better experience without visible segment shifting when using more segments. Other features, like projecting objects onto the road can also not be realized with the proposed resolution.

Regarding the correlation between the pupil diameter, the exposure and glare perception, a lot of potential is given as well. Several points that still need investigation are already listed throughout the study. The most important point would be to further investigate the behaviour of the exposure for intermediate pulse durations to correctly define the slope and the x-shift of the proposed curve. Additionally, to that, the influence of background (il-)luminance needs to be investigated further in terms of automotive studies. Furthermore, the influence of light pulses following in shorter time frames on each other is still not understood as well.

Regarding the traffic space analysis, the presented data is only shown for the high beam section. While the data is recorded for a much wider area, this goes beyond the scope and the aim of this study. However, the analysis of the low beam area is of interest as well. Additionally, to that, the chosen route was selected with specific goals regarding the gaze behaviour and therefore does not represent the overall traffic space of Germany or even Europe. Expanding the research on a wider area and therefore not repeating the same route several times should be one of the key elements for the next part of the study. In this regard, the stereo system that was already installed and recorded data, was not yet used for the analysis. However, it can be assumed, that the additional information on the distance to certain objects is of interest as well. This information could be used to further select the collected data and find more exact correlations.

BIBLIOGRAPHY

[1] J. Damasky, "Lichttechnische Entwicklung von Anforderungen an Kraftfahrzeug - Scheinwerfer," PhD thesis, Technische Hochschule Darmstadt, 1995.

[2] W. Huhn, "Anforderungen an eine Adaptive Lichtverteilung für Kraftfahrzeugscheinwerfer im Rahmen der ECE-Regelungen," PhD thesis, Technische Universität Darmstadt, 1999.

[3] M. Kleinkes, "Objektivierte Bewertung des Gütemerkmals Homogenität für Scheinwerfer-Lichtverteilungen," PhD thesis, Universität Bielefeld, 2003.

[4] C. Diem, "Blickverhalten von Kraftfahrern im dynamischen Straßenverkehr," PhD thesis, Technische Universität Darmstadt, 2005, ISBN: 978-3-8316-0451-7.

[5] Statistisches Bundesamt. (2013). Verkehr auf einen Blick. (Accessed on 07/29/2018), [Online]. Available: `https://www.destatis.de/DE/Publikationen/Thematisch/TransportVerkehr/Querschnitt/BroschuereVerkehrBlick0080006139004.pdf?__blob=publicationFile`.

[6] ADAC und Statistisches Bundesamt. (2016). Tödlich Verunglückte bei Nachtunfällen nach Ortslage. (Accessed on 07/19/2018), [Online]. Available: `https://www.adac.de/_mmm/pdf/statistik_6_3_nachtunfaelle_z_43060.pdf`.

[7] T. Åkerstedt, G. Kecklund, and L.-G. Hörte, "Night driving, season, and the risk of highway accidents," *Sleep*, vol. 24, no. 4, pp. 401–406, 2001.

[8] B. Flemming, "New Technologies in Electric-Powered Vehicles," *IEEE Vehicular Technology Magazine*, vol. 5, no. 1, pp. 4–103, 2010.

[9] H. Ursprung and P. L. Käfer, *Sicherheit im Straßenverkehr*. Fischer-Taschenbuch-Verlag, 1974, ISBN: 3-436-01812-0.

[10] M. Green, M. J. Allen, B. S. Abrams, *et al.*, *Forensic Vision with Application to Highway Safety*, Third Edition. Lawyers & Judges Publishing Company, Inc., 2008, ISBN: 978-1-933264-54-7.

[11] H. J. Hentschel, *Licht und Beleuchtung: Grundlagen und Anwendungen der Lichttechnik. 5., neu bearb. und erw*, 5th ed. Hüthig-Verlag, Heidelberg, 2001, ISBN: 978-3-778528-17-4.

[12] "Variations in Eyeball Diameters of the Healthy Adults," *Journal of Ophthalmology*, 2014. [Online]. Available: `http://dx.doi.org/10.1155/2014/503645`.

[13] E. B. Goldstein and J. Brockmole, *Sensation and Perception*. Cengage Learning, 2016, ISBN: 978-1-133958-49-9.

[14] F. M. Toates, "Accommodation Function of the Human Eye," *Physiological Reviews*, vol. 52, no. 4, pp. 828–863, 1972.

[15] R. F. Schmidt, F. Lang, and M. Heckmann, *Physiologie des Menschen: mit Pathophysiologie*, 31st ed. Springer-Verlag, 2010, ISBN: 978-3-642016-50-9.

[16] J. K. Bowmaker and H. J. Dartnall, "Visual Pigments of Rods and Cones in a Human Retina," *The Journal of physiology*, vol. 298, no. 1, pp. 501–511, 1980.

[17] Commission Internationale de l'Éclairage, "Mesopic Photometry: History, Special Problems and Practical Solutions," Tech. Rep., 1989.

[18] N. J. Wade and B. W. Tatler, "Did Javal Measure Eye Movements During Reading?" *Journal of Eye Movement Research*, vol. 2, no. 5, pp. 1–5, 2009. [Online]. Available: `http://dx.doi.org/10.16910/jemr.2.5.5`.

[19] A. Bulling, J. A. Ward, H. Gellersen, *et al.*, "Eye Movement Analysis for Activity Recognition Using Electrooculography," *IEEE Transactions on Pattern Analysis and Machine Intelligence*, vol. 33, no. 4, pp. 741–753, 2011, ISSN: 0162-8828.

[20] L. A. Granka, T. Joachims, and G. Gay, "Eye-Tracking Analysis of User Behavior in WWW Search," in *Proceedings of the 27th Annual International ACM SIGIR Conference on Research and Development in Information Retrieval*, ACM, 2004, pp. 478–479.

[21] A. L. Yarbus, "Eye Movements During Perception of Complex Objects," in *Eye Movements and Vision*, Springer, 1967, pp. 171–211.

[22] E. Kowler, "Eye Movements: The Past 25 Years," *Vision Research*, vol. 51, no. 13, pp. 1457–1483, 2011.

[23] A. T. Duchowski, *Eye Tracking Methodology, Theory and Practice*. Springer Verlag, 2007, ISBN: 978-1-84628-609-4.

[24] D. A. Robinson, J. L. Gordon, and S. E. Gordon, "A model of the Smooth Pursuit Eye Movement System," *Biological cybernetics*, vol. 55, no. 1, pp. 43–57, 1986.

[25] R. H. S. Carpenter, *Movements of the Eyes, 2nd Rev*. London: Pion Limited, 1988, ISBN: 978-0-850861-09-9.

[26] L. A. Abel, B. T. Troost, and L. F. Dell'Osso, "The Effects of Age on Normal Saccadic Characteristics and their Variability," *Vision Research*, vol. 23, no. 1, pp. 33–37, 1983.

[27] B. Bridgeman, D. Hendry, and L. Stark, "Failure to Detect Displacement of the Visual World During Saccadic Eye Movements," *Vision research*, vol. 15, no. 6, pp. 719–722, 1975.

[28] E. B. Delabarre, "A Method of Recording Eye–Movements," *The American Journal of Psychology*, vol. 9, no. 4, pp. 572–574, 1898.

[29] C. H. Judd, C. N. McAllister, and W. M. Steele, "General Introduction to a Series of Studies of Eye Movements by Means of Kinetoscopic Photographs," *Psychological Review Monographs*, vol. 7, no. 1, pp. 1–16, 1905.

[30] A. Bulling, D. Roggen, and G. Tröster, "It's in Your Eyes: Towards Context-Awareness and Mobile HCI Using Wearable EOG Goggles," in *Proceedings of the 10th International Conference on Ubiquitous Computing*, ACM, 2008, pp. 84–93.

[31] H. Collewijn, F. Van der Mark, and T. C. Jansen, "Precise Recording of Human Eye Movements," *Vision research*, pp. 447–450, 1975.

[32] T. Ohno, N. Mukawa, and A. Yoshikawa, "FreeGaze: a Gaze Tracking System for Everyday Gaze Interaction," in *Proceedings of the 2002 Symposium on Eye Tracking Research & Applications*, ACM, 2002, pp. 125–132.

[33] D. Beymer and M. Flickner, "Eye Gaze Tracking Using an Active Stereo Head," in *2003 Proceedings of the Computer Society Conference on Computer Vision and Pattern Recognition*, IEEE, vol. 2, 2003, 451–458.

[34] C. H. Morimoto and M. R. M. Mimica, "Eye Gaze Tracking Techniques for Interactive Applications," *Computer Vision and Image Inderstanding*, vol. 98, no. 1, pp. 4–24, 2005.

[35] Z. Zhu and Q. Ji, "Novel Eye Gaze Tracking Techniques Under Natural Head Movement," *IEEE Transactions on biomedical engineering*, vol. 54, no. 12, pp. 2246–2260, 2007.

[36] A. T. Duchowski, "A Breadth–First Survey of Eye-Tracking Applications," *Behavior Research Methods, Instruments, & Computers*, vol. 34, no. 4, pp. 455–470, 2002.

[37] T. E. Hutchinson, K. P. White, W. N. Martin, *et al.*, "Human-Computer Interaction Using Eye–Gaze Input," *IEEE Transactions on systems, man, and cybernetics*, vol. 19, no. 6, pp. 1527–1534, 1989.

[38] R. J. K. Jacob, "The Use of Eye Movements in Human-Computer Interaction Techniques: What You Look at is What You Get," *ACM Transactions on Information Systems (TOIS)*, vol. 9, no. 2, pp. 152–169, 1991.

[39] R. J. K. Jacob and K. S. Karn, "Eye Tracking in Human-Computer Interaction and Usability Research: Ready to Deliver the Promises," in *The Mind's Eye*, Elsevier, 2003, pp. 573–605.

[40] H. D. Crane, "The Purkinje Image Eyetracker, Image Stabilization, and Related Forms of Stimulus Manipulation," *Visual science and Engineering: Models and Applications*, pp. 15–89, 1994.

[41] R. Stiefelhagen, J. Yang, and A. Waibel, "Tracking Eyes and Monitoring Eye Gaze," in *Proceedings of the Workshop on Perceptual User Interfaces*, 1997, pp. 98–100.

[42] E. H. Hess and J. M. Polt, "Pupil Size as Related to Interest Value of Visual Stimuli," *Science*, vol. 132, no. 3423, pp. 349–350, 1960.

[43] B. Winn, D. Whitaker, D. B. Elliott, *et al.*, "Factors Affecting Light-Adapted Pupil Size in Normal Human Subjects," *Investigative Ophthalmology & Visual Science*, vol. 35, no. 3, pp. 1132–1137, 1994.

[44] C. Darwin, *The Expression of the Emotions in Man and Animals*. Dover Publications, 1872. [Online]. Available: `http://pubman.mpdl.mpg.de`.

[45] Y. Ebisawa, "Unconstrained Pupil Detection Technique Using two Light Sources and the Image Difference Method," *WIT Transactions on Information and Communication Technologies*, vol. 15, 79–*89, 1970.

[46] SmartEye Inc., *Accuracy and Precision of the Pupil Size Measured with SmartEye Pro*, 2010.

[47] C. H. Morimoto, D. Koons, A. Amir, *et al.*, "Pupil Detection and Tracking Using Multiple Light Sources," *Image and Vision Computing*, vol. 18, no. 4, pp. 331–335, 2000.

[48] D. F. Fotiou, C. G. Brozou, D. J. Tsiptsios, *et al.*, "Effect of Age on Pupillary Light Reflex: Evaluation of Pupil Mobility for Clinical Practice and Research," *Electromyography and Clinical Neurophysiology*, vol. 47, no. 1, pp. 11–22, 2007.

[49] Commission Internationale de l'Éclairage, "International Lighting Vocabulary, 4th ed.," Tech. Rep., 1987.

[50] ——, "The Basis of Physical Photoemtry, 2nd Edition," Tech. Rep., 1983.

[51] P. Z. Bodrogi, C. Schiller, and T. Q. Khanh, "Testing the CIE System for Mesopic Photometry in a Threshold Detection Experiment," *Lighting Research and Technology*, vol. 48, no. 8, pp. 992–1004, 2016.

[52] Photometrik, *Phototometrik – Ihr Labor für Lichtmesstechnik-Dienstleistungen*, `https://www.photometrik.de/`, (Accessed on 07/29/2018), 2018.

[53] Opsira, *Luminous Flux Measurement: Opsira GmbH*, `https://www.opsira.de/en/products/optical-measurement-systems/integrating-sphere-uku800-luminous-flux-measurement.html`, (Accessed on 07/29/2018), 2018.

[54] Photonics. (2018). Ambient-light sensors mimic the eye. (Accessed on 07/29/2018), [Online]. Available: `https://www.photonics.com/Articles/Ambient-Light_Sensors_Mimic_the_Eye/a28345`.

[55] B. Zydek, "Blendungsbewertung von Kraftfahrzeugscheinwerfern unter dynamischen Bedingungen," PhD thesis, Technische Universität Darmstadt, 2014.

[56] J. D. Bullough, Z. Fu, and J. V. Derlofske, "Discomfort and Disability Glare from Halogen and HID Headlamp Systems," Tech. Rep., 2002. [Online]. Available: `https://doi.org/10.4271/2002-01-0010`.

[57] C. Werner, B. G. Kleinert, and S. G. Bogdanow, "Blendfreie dynamische Abblendlichtverteilung für Kfz-Scheinwerfer–Anforderungen und Validierung," in *Tagungsband Lux junior 2015*, Technische Universität Ilmenau, vol. 12, 2015, pp. 139–144.

[58] K. Kosmas, D. Polin, C. Schiller, *et al.*, "Comparing the Glare Load of Low Beam, High Beam and Glare-Free High Beam Under Different Traffic Conditions on the Road," in *Proceedings of the 11th International Symposium on Automotive Lighting (ISAL)*, Herbert Utz Verlag, München, 2015, pp. 229–238, ISBN: 978-3-8316-4481-0.

[59] D. Polin, C. Bruns, S. Klir, *et al.*, "Evaluation System of Adaptive Lighting Systems in Dynamic Situations at Night-Time," in *Proceedings of the 11th International Symposium on Automotive Lighting (ISAL)*, Herbert Utz Verlag, München, 2015, pp. 221–230, ISBN: 978-3-8316-4481-0.

[60] P. Lehnert, *Auswirkungen der Fahrzeugdynamik auf die Lichtverteilung von Scheinwerfern*. Herbert Utz Verlag, 2001, ISBN: 978-3-8316-8013-9.

[61] F. Schmidt, "Dynamische Ortsaufgelöste Leuchtdichtemessungen auf Straßen und in Tunneln," *Licht*, 2004.

[62] H. Lehmann, "Freie Fahrt für die Dynamische Tunnel-Licht-Messung," *Journal of Metrology*, pp. 4–11, 2014.

[63] H. R. Blackwell, "Contrast Thresholds of the Human Eye," *The Journal of the Optical Society of America*, vol. 36, no. 11, pp. 624–643, 1946.

[64] W. Adrian, "Visibility of Targets: Model for Calculation," *Lighting Research & Technology*, vol. 21, no. 4, pp. 181–188, 1989.

[65] A. Mayeur, R. Brémond, and J. C. Bastien, "Effects of the Viewing Context on Target Detection. Implications for Road Lighting Design," *Applied Argonomics*, vol. 41, no. 3, pp. 461–468, 2010.

[66] K. Schneider, "Kontrastbestimmung von Objekten bei Peripherer Sicht Unter Nächtlichen Fahrbedingungen," PhD thesis, Technische Universität Darmstadt, 2018.

[67] Commission Internationale de l'Éclairage, "An Analytic Model for Describing the Influence of Lighting Parameters upon Visual Performance, 2nd Ed. Vol.1," Tech. Rep., 1983.

[68] ——, "Cie international lighting vocabulary : Iec international electrotechnical vocabulary," Tech. Rep., 1987.

[69] H. Schober, *Das Sehen I u. II*. Leipzig: VEB Fachbuchverlag, 1970.

[70] S. Völker, *Blendung durch Kfz-Scheinwerfer im nächtlichen Straßenverkehr: ein Review bis 2006–Beschreibung, Maßzahlen, Bewertungsmethoden*. Universitätsverlag der Technische Universität Berlin, 2017, vol. 10, ISBN: 978-3-798329-56-0.

[71] M. A. Mainster and G. T. Timberlake, "Why HID Headlights Bother Older Drivers," *British journal of ophthalmology*, vol. 87, no. 1, pp. 113–117, 2003.

[72] D. Miller and G. Benedek, *Intraocular Light Scattering: Theory and Clinical Application*. Charles C. Thomas Publisher, 1973, ISBN: 978-0398026653.

[73] D. Englisch, "Untersuchungen zur Spektralen Empfindlichkeit des Auges für Detektion und Physiologische Blendung im Mesopischen Bereich," PhD thesis, Technische Universit Darmstadt, 2017.

[74] R. G. Hopkinson, "Evaluation of Glare," *Illuminating Engineering*, vol. 52, no. 305, pp. 329–336, 1957.

[75] J. B. De Boer, "Visual Perception in Road Traffic and the Field of Vision of the Motorist," *Public lighting*, pp. 11–96, 1967.

[76] A. W. Gellatly and D. J. Weintraub, "User Reconfigurations of the de Boer Rating Scale for Discomfort Glare," Tech. Rep., 1990.

[77] M. Luckiesh and S. K. Guth, "Brightness in Visual Field at Borderline Between Comfort and Discomfort (BCD)," *Illuminating Engineering*, vol. 44, no. 11, pp. 650–670, 1949.

[78] G. A. Fry and V. M. King, "The Pupillary Response and Discomfort Glare," *Journal of the Illuminating Engineering Society*, vol. 4, no. 4, pp. 307–324, 1975.

[79] M. Luckiesh and S. K. Guth, "Brightness in visual field at borderline between comfort and discomfort (BCD)," *Illuminating Engineering*, vol. 44, no. 11, pp. 650–670, 1949.

[80] T. Irikura, Y. Toyofuku, and Y. Aoki, "Borderline Between Comfort and Discomfort of Blinking Light," *Journal of Light & Visual Environment*, vol. 22, no. 2, pp. 212–215, 1998.

[81] M. Sivak, C. J. Simmons, and M. J. Flannagan, "Effect of Headlamp Area on Discomfort Glare," *Lighting Research & Technology*, vol. 22, no. 1, pp. 49–52, 1990.

[82] J. D. Bullough, J. Van Derlofske, C. R. Fay, *et al.*, "Discomfort Glare from Headlamps: Interactions among Spectrum, Control of Gaze and Background Light Level," Society of Automotive Engoneers, Warrendale, 2003.

[83] N. Müller, "Komplexitätswahrnehmung im Nächtlichen Straßenverkehrsraum - Einflussfaktoren und Analyse," PhD thesis, Technische Universität Darmstadt, 2017.

[84] Y. Lin, Y. Liu, Y. Sun, *et al.*, "Model Predicting Discomfort Glare Caused by LED Road Lights," *Optics Express*, vol. 22, no. 15, pp. 18 056–18 071, 2014.

[85] Y. Lin, S. Fotios, M. Wei, *et al.*, "Eye Movement and Pupil Size Constriction Under Discomfort Glare," *Investigative Ophthalmology & Visual Science*, vol. 56, no. 3, pp. 1649–1656, 2015.

[86] H. Winner, S. Hakuli, and G. Wolf, *Handbuch Fahrerassistenzsysteme: Grundlagen, Komponenten und Systeme für Aktive Sicherheit und Komfort*. Springer Verlag, 2012, ISBN: 978-3-658-05733-6.

[87] R. Brückmann, M. Chielarz, J. Churn, *et al.*, "Blickfixationen und Blickbewegungen des Fahrzeugführers sowie Hauptsichtbereiche an der Windschutzscheibe," *FAT - Schriftenreihe*, no. 151, 2000.

[88] Mein Autolexikon. (2018). Scheinwerfer. (Accessed on 06/16/2018), [Online]. Available: `https://www.mein-autolexikon.de/autolexikon/produkt/produkt/Produkt/pdf/scheinwerfer.html`.

[89] Auto–News.de. (2018). BMW-Laserlicht: Wenn das Laserschwert in die Nacht schneidet. (Accessed on 06/16/2018), [Online]. Available: `http://www.auto-news.de/auto/news/bildergalerie_Wenn-das-Laserschwert-in-die-Nacht-schneidet_id_35144&picindex=1`.

[90] E. C. for Europe, "Uniform provisions concerning the approval of adaptive front-lighting systems (AFS) for motor vehicles, Revision 2," Tech. Rep., 2013.

[91] B. Wördenweber, P. Boyce, D. D. Hoffman, *et al.*, *Automotive Lighting and Human Vision*. Springer Verlag, 2007, ISBN: 978-3-540-36697-3.

[92] W. Hendrischk, M. Grimm, *et al.*, "Adaptive Scheinwerfer. Kurvenlicht Erhöht die Verkehrssicherheit," *Automobiltechnische Zeitschrift*, vol. 104, no. 11, 968–973, 2002. DOI: `https://doi.org/10.1007/BF03223479`.

[93] J. Seuss and D. Stryschik, "Steuerungselektronik fuer Dynamisches Kurvenlicht," *Automobiltechnische Zeitschrift*, vol. 105, no. 6, 598—601, 2003.

[94] J. H. Sprute, "Development of Lighting Engineering Criteria to Minimize the Glare of Adaptive High Beam Systems," PhD thesis, Technische Universität Darmstadt, 2012.

[95] D. Schneider, "Markierungslicht: Eine Scheinwerferlichtverteilung zur Aufmerksamkeitssteuerung und Wahrnehmungssteigerung von Fahrzeugführern," PhD thesis, Technische Universität Darmstadt, 2011, ISBN: 978-3-8316-4116-1.

[96] C. Gut, "Laserbasierte Hochauflösende Pixellichtsysteme," PhD thesis, Karlruhe Institut of Technology, 2007.

[97] B. Kubitza and C. Wilks, "HD-Headlamp Technologies and Development Process: From simulation to demonstration under real traffic conditions," in *Proceedings of the 12th International Symposium on Automotive Lighting (ISAL)*, Herbert Utz Verlag, 2017, pp. 343–347.

[98] W. Adrian, "Visibility Levels Under Night-Time Driving Conditions," *Journal of the Illuminating Engineering Society*, vol. 16, no. 2, pp. 3–12, 1987.

[99] R. Bremond and A. Mayeur, "Some Drawbacks of the Visibility Level as an Index of Visual Performance While Driving," *Proc. 27th session of the CIE D*, vol. 4, 2011.

[100] A. Mayeur, R. Brémond, and J. C. Bastien, "Effect of Task and Eccentricity of the Target on Detection Thresholds in Mesopic Vision: Implications for Road Lighting," *Human Factors*, vol. 50, no. 4, pp. 712–721, 2008.

[101] R. Brémond, V. Bodard, E. Dumont, *et al.*, "Target Visibility Level and Detection Distance on a Driving Simulator," *Lighting Research & Technology*, vol. 45, no. 1, pp. 76–89, 2013.

[102] T. Horberry, J. Anderson, and M. A. Regan, "The Possible Safety Benefits of Enhanced Road Markings: a Driving Simulator Evaluation," *Transportation Research Part F: Traffic Psychology and Behaviour*, vol. 9, no. 1, pp. 77–87, 2006.

[103] A. Shahar, R. Brémond, and C. Villa, "Can Light Emitting Diode-Based Road Studs Improve Vehicle Control in Curves at Night? A Driving Simulator Study," *Lighting Research & Technology*, vol. 50, no. 2, pp. 266–281, 2018.

[104] A. Shahar and R. Brémond, "Toward Smart Active Road Studs for Lane Delineation," in *TRA2014-Transport Research Arena: Transport Solutions: from Research to Deployment-Innovate Mobility, Mobilise Innovation!*, Paris, 2014, 10p. [Online]. Available: `https://hal.archives-ouvertes.fr/hal-01217817`.

[105] J. D. Bullough and M. S. Rea, "Simulated Driving Performance and Peripheral Detection at Mesopic and Low Photopic Light Levels," *International Journal of Lighting Research and Technology*, vol. 32, no. 4, pp. 194–198, 2000.

[106] J. W.A. M. Alferdinck, "Target Detection and Driving Behaviour Measurements in a Driving Simulator at Mesopic Light Levels," *Ophthalmic and Physiological Optics*, vol. 26, no. 3, pp. 264–280, 2006.

[107] K. L. M. Broughton, F. Switzer, and D. Scott, "Car Following Decisions Under Three Visibility Conditions and two Speeds Tested with a Driving Simulator," *Accident Analysis & Prevention*, vol. 39, no. 1, pp. 106–116, 2007.

[108] V. Cavallo, M. Ranchet, M. Pinto, *et al.*, "Improving Car Drivers' Perception of Motorcyclists Through Innovative Headlight Configurations," in *Proceedings of the 10th International Symposium on Automotive Lighting (ISAL)*, 2013, 7p.

[109] R. B. Gibbons, T. Terry, R. Bhagavathula, *et al.*, "Applicability of Mesopic Factors to the Driving Task," *Lighting Research & Technology*, vol. 48, no. 1, pp. 70–82, 2016.

[110] I. J. Reagan, M. Brumbelow, and T. Frischmann, "On-Road Experiment to Assess Drivers' Detection of Roadside Targets as a Function of Headlight System, Target Placement, and Target Reflectance," *Accident Analysis & Prevention*, vol. 76, pp. 74–82, 2015.

[111] T. G. LSS, "Prove Benefit of ADB Systems Under Real Life Conditions," Tech. Rep., 2015. [Online]. Available: `https://clepa.eu/wp-content/uploads/2016/04/Benefits-of-Adaptive-Driving-Beam-systems-under-real-life-conditions-1.pdf`.

[112] J. D. Bullough, J. Van Derlofske, P. Dee, *et al.*, "An Investigation of Headlamp Glare: Intensity, Spectrum and Size," Tech. Rep., 2004.

[113] H.-J. Schmidt-Clausen and J. T. H. Bindels, "Assessment of Discomfort Glare in Motor Vehicle Lighting," *Lighting Research & Technology*, vol. 6, no. 2, pp. 79–88, 1974.

[114] J. B. de Boer and H. J. Schmidt-Clausen, "Über die Zulässige Blendung in der Kraftfahrzeugbeleuchtung," *CIE, XVII Session, Barcelone*, 1971.

[115] C. Schiller, "Untersuchungen über Spektrale Kontrastempfindlichkeitsfunktionen des Menschlichen Auges im Mesopischen Bereich und ihre Einflussparameter," PhD thesis, Technische Universität Darmstadt, 2015.

[116] D. Englisch and T. Q. Khanh, "Spectral Sensitivity of Disability Glare in the Mesopic Range for Objects in the Periphery," in *Proceedings of the 12th International Symposium on Automotive Lighting (ISAL)*, T. Q. Khanh, Ed., vol. 17, Herbert Utz Verlag GmbH, 2017, pp. 715–725, ISBN: 978-3-8316-4671-5.

[117] D. Englisch, C. Schiller, N. Haferkemper, *et al.*, "Spectral Sensitivity for Disability Glare in the Mesopic Range for Detection Objects in the Periphery: Setup and Method," in *Tagungsband der 22. Gemeinschaftstagung der lichttechnischen Gesellschaften Deutschlands, Österreichs, der Schweiz und der Niederlande*, 2016, pp. 648–654.

[118] J. Locher, L. Aldiek, and P. Stroop, "Influence of Luminance and Illuminance on Headlamp Glare," in *Proceedings of the 11th International Symposium on Automotive Lighting (ISAL)*, T. Q. Khanh, Ed., vol. 16, München, 2015, pp. 680–687, ISBN: 978-3-8316-4482-7.

[119] P. L. Olson and M. Sivak, "Discomfort Glare from Automobile Headlights," *Journal of the Illuminating Engineering Society*, vol. 13, no. 3, pp. 296–303, 1984.

[120] ——, "Glare from Automobile Rear-Vision Mirrors," *Human Factors*, vol. 26, no. 3, pp. 269–282, 1984.

[121] J. Theeuwes, J. W.A. M. Alferdinck, and M. Perel, "Relation Between Glare and Driving Performance," *Human Factors*, vol. 44, no. 1, pp. 95–107, 2002.

[122] M. Sivak, "Blue Content of LED Headlamps and Discomfort Glare," Tech. Rep., 2005.

[123] C. Schiller, J. H. Sprute, N. Haferkemper, *et al.*, "Psychologische Blendung bei Halogen- und Xenonscheinwerfern," *ATZ-Automobiltechnische Zeitschrift*, vol. 111, no. 2, pp. 132–138, 2009.

[124] B. Zydek, N. Haferkemper, and T. Q. Khanh, "Klettwitz Levelling Test: Analysis of Photometric Data and Comprehension," in *Proceedings of the 11th International Symposium on Automotive Lighting (ISAL)*, 2013.

[125] J. H. Goldberg, M. J. Stimson, M. Lewenstein, *et al.*, "Eye Tracking in Web Search Tasks: Design Implications," in *Proceedings of the 2002 Symposium on Eye Tracking Research & Applications*, ACM, 2002, pp. 51–58.

[126] P. M. Corcoran, F. Nanu, S. Petrescu, *et al.*, "Real-Time Eye Gaze Tracking for Gaming Design and Consumer Electronics Systems," *IEEE Transactions on Consumer Electronics*, vol. 58, no. 2, pp. 347–355, 2012.

[127] S. Fotios, J. Uttley, C. Cheal, *et al.*, "Using Eye-Tracking to Identify Pedestrians' Critical Visual Tasks, Part 1. Dual Task Approach," *Lighting Research & Technology*, vol. 47, no. 2, pp. 133–148, 2015.

[128] S. Fotios, J. Uttley, and B. Yang, "Using Eye-Tracking to Identify Pedestrians' Critical Visual Tasks, Part 2. Fixation on Pedestrians," *Lighting Research & Technology*, vol. 47, no. 2, pp. 149–160, 2015.

[129] R. R. Mourant and T. H. Rockwell, "Strategies of Visual Search by Novice and Experienced Drivers," *Human Factors*, vol. 14, no. 4, pp. 325–335, 1972.

[130] M. F. Land and D. N. Lee, "Where We Look When We Steer," *Nature*, vol. 369, no. 6483, pp. 742–744, 1994.

[131] J. Damasky and A. Hosemann, "The Influence of the Light Distribution of Headlamps on Drivers Fixation Behaviour at Nighttime," in *SAE Technical Paper*, SAE International, Feb. 1998. [Online]. Available: `https://doi.org/10.4271/980319`.

[132] Q. Ji and X. Yang, "Real-Time Eye, Gaze, and Face Pose Tracking For Monitoring Driver Vigilance," *Real-Time Imaging*, vol. 8, no. 5, pp. 357–377, 2002.

[133] Y. Shibata, H.-J. Schmidt-Clausen, and C. Diem, "The Evaluation of AFS Beam Pattern using the Movement of the Driver's Eye-Fixation Points," in *SAE Technical Paper*, SAE International, Apr. 2006. [Online]. Available: `https://doi.org/10.4271/2006-01-0944`.

[134] R. Schulz, "Blickverhalten und Orientierung von Kraftfahrern auf Landstraßen," PhD thesis, Technische Universität Dresden, 2012, ISBN: 9783867803236.

[135] I. Heynderickx, J. Ciocoiu, and X. Zhu, "Estimating Eye Adaptation for Typical Luminance Values in the Field of View while Driving in Urban Streets," *Light & Engineering*, vol. 21, no. 4, pp. 32–38, 2013.

[136] J. Winter and S. Völker, "Typical Eye Fixation Areas of Car Drivers in Inner-city Environments at Night," *Proceedings of the 12th Lux Europa*, 2013.

[137] J. Winter, S. Fotios, and S. Völker, “Gaze Direction When Driving After Dark on Main and Residential Roads: Where is the Dominant Location?” *Lighting Research & Technology*, vol. 49, no. 5, pp. 574–585, 2016.

[138] P. Green, “Where do Drivers Look while Driving (and for How Long),” *Human Factors in Traffic Safety*, pp. 77–110, 2002.

[139] F. Stahl and M. Kleinkes, “Eye-Tracking as a Method for Determing the Quality of Headlamp Light Distributions,” in *Proceedings of the 6th International Symposium on Automotive Lighting (ISAL)*, vol. 11, Herbert Utz Verlag, 2005, pp. 912–920.

[140] B. Hristov, “Untersuchung des Blickverhaltens von Kraftfahrern auf Autobahnen,” PhD thesis, Technische Universität Dresden, 2009.

[141] M. Sodhi, B. Reimer, J. Cohen, *et al.*, “On-road Driver Eye Movement Tracking Using Head-Mounted Devices,” in *Proceedings of the 2002 Symposium on Eye Tracking Research & Applications*, ACM, 2002, pp. 61–68.

[142] F. I. Kandil, A. Rotter, and M. Lappe, “Car Drivers Attend to Different Gaze Targets when Negotiating Closed vs. Open Bends,” *Journal of Vision*, vol. 10, no. 4, pp. 24–24, 2010.

[143] O. Lappi, E. Lehtonen, J. Pekkanen, *et al.*, “Beyond the Tangent Point: Gaze Targets in Naturalistic Driving,” *Journal of Vision*, vol. 13, no. 13, pp. 11–11, 2013.

[144] O. Lappi, J. Pekkanen, and T. H. Itkonen, “Pursuit Eye-Movements in Curve Driving: Differentiate Between Future Path and Tangent Point Models,” *PloS one: e68326*, vol. 8, no. 7, 2013. DOI: `https://doi.org/10.1371/journal.pone.0068326`.

[145] C. Cengiz, H. Kotkanen, M. Puolakka, *et al.*, “Combined Eye-Tracking and Luminance Measurements While Driving on a Rural Road: Towards Determining Mesopic Adaptation Luminance,” *Lighting Research & Technology*, vol. 46, no. 6, pp. 676–694, 2014.

[146] L. L. Holladay, “The Dundamentals of Glare and Visibility,” *Journal of the Optical Society of America*, vol. 12, no. 4, pp. 271–319, 1926.

[147] B. H. Crawford *et al.*, “The Dependence of Pupil Size Upon External Light Stimulus Under Static and Variable Conditions,” *Proceedings of the Royal Society of London B: Biological Sciences*, vol. 121, no. 823, pp. 376–395, 1936.

[148] P. Moon and D. E. Spencer, “On the Stiles-Crawford Effect,” *Journal of the Optical Society of America*, vol. 34, no. 6, pp. 319–329, 1944.

[149] S. G. De Groot and J. W. Gebhard, “Pupil Size as Determined by Adapting Luminance,” *Journal of the Optical Society of America*, vol. 42, no. 7, pp. 492–495, 1952.

[150] P. A. Stanley and A. K. Davies, “The Effect of Field of View Size on Steady-State Pupil Diameter,” *Ophthalmic and Physiological Optics*, vol. 15, no. 6, pp. 601–603, 1995.

[151] P. G. J. Barten, *Contrast Sensitivity of the Human Eye and its Effects on Image Quality*. Spie Optical Engineering Press Bellingham, WA, 1999, vol. 19, ISBN: 9-780-8194-349-68.

[152] C. A. Blackie and H. C. Howland, “An Extension of an Accommodation and Convergence Model of Emmetropization to Include the Effects of Illumination Intensity,” *Ophthalmic and Physiological Optics*, vol. 19, no. 2, pp. 112–125, 1999.

[153] A. B. Watson, “A Formula for the Mean Human Optical Modulation Transfer Function as a Function of Pupil Size,” *Journal of Vision*, vol. 13, no. 6, pp. 1–11, 2013. DOI: `10.1167/13.6.18`.

[154] R. G. Hopkinson, "Glare Discomfort and Pupil Diameter," *Journal of the Optical Society of America*, vol. 46, no. 8, pp. 649–656, 1956.

[155] N. Ohba and M. Alpern, "Adaptation of the Pupil Light Reflex," *Vision research*, vol. 12, no. 5, pp. 953–967, 1972.

[156] O. Palinko, A. L. Kun, A. Shyrokov, *et al.*, "Estimating cognitive load using remote eye tracking in a driving simulator," in *Proceedings of the 2010 Symposium on Eye-Tracking Research & Applications*, ACM, 2010, pp. 141–144.

[157] J. Damasky, "Geometry of the Road Area and Effects on Motor Vehicle Lighting," in *Symposium Progress in Automobile Lighting, PAL*, vol. 7, 1995.

[158] C. Diem and H.-J. Schmidt-Clausen, "Headlamp Performance in Traffic Situations," in *Symposium Progress in Automobile Lighting, PAL*, vol. 8.

[159] G. Schwab, "Untersuchungen zur Ansteuerung adaptiver Kraftfahrzeugscheinwerfer," PhD thesis, Technische Universität Ilmenau, Osnabrück, 2003, ISBN: 978-3-89959-047-0.

[160] P. Kuhl, "Anpassung der Lichtverteilung an den Vertikalen Straßenverlauf," PhD thesis, Universität Paderborn, 2006.

[161] J. Moisel, "Adaptive Headlights Utilizing LED-Arrays," in *Proceedings of the 8th International Symposium on Automotive Lighting (ISAL)*, vol. 13, Herbert Utz Verlag, 2009, pp. 287–296, ISBN: 978-3831-60904-8.

[162] A. Totzauer, "Erarbeitung einer Effizienten Fernlichtunterteilung Abgeleitet aus einem Stochastischen Modell der Bedingungen des Deutschen Straßenverkehrs," *Studienarbeit*, 2008.

[163] J. Damasky and W. Huhn, "Variable Headlamp Beam Pattern - Lighting Requirements for Different Driving Situations," in *SAE Technical Paper*, SAE International, Feb. 1997. [Online]. Available: `https://doi.org/10.4271/970647`.

[164] C. Amann, S. Weber, and A. Buck, "Laser Light in the BMW i8—Design und Vehicle Integration," *ATZ worldwide*, vol. 119, 2014. DOI: `https://doi.org/10.1007/s35148-014-0475-2`.

[165] K. Schneider, J. Kobbert, and T. Q. Khanh, "Age-related Field Study for Determination of the 95%-Detectability of Objects Under Peripheral Vision Conditions," in *Intelligent Vehicles Symposium (IV), 2017 IEEE*, IEEE, 2017, pp. 1552–1557.

[166] ADAC e.V., München. (2012). ADAC Verkehrssicherheitsprogramme. (Accessed on 01/15/2017), [Online]. Available: `https://www.adac.de/_mmm/pdf/Verkehr_und_Mathe_Anhalteweg_45164.pdf`.

[167] EARSandEYES Marktforschung. (2008). Autobahn - Geschwindigkeit ohne Tempolimit | Umfrage. (Accessed on 07/09/2018), [Online]. Available: `https://de.statista.com/statistik/daten/studie/1359/umfrage/normale-geschwindigkeit-auf-autobahn-ohne-tempolimit/`.

[168] M. Cordts, M. Omran, S. Ramos, *et al.*, "The Cityscapes Dataset for Semantic Urban Scene Understanding," in *Proceedings of the IEEE Conference on Computer Vision and Pattern Recognition*, 2016, pp. 3213–3223.

[169] A. Martín, A. Agarwal, P. Barham, *et al.* (2015). TensorFlow: Large-scale Machine Learning on Heterogeneous Systems. (Accessed on 02/12/2018), [Online]. Available: `http://tensorflow.org/`.

[170] J. Adamy, *Fuzzy Logik, Neuronale Netze und Evolutionäre Algorithmen*. Shaker Verlag, 2011, ISBN: 978-3844003970.

[171] R. Girshick, J. Donahue, T. Darrell, *et al.*, "Rich Feature Hierarchies for Accurate Object Detection and Semantic Segmentation," *CoRR*, pp. 580–587, 2013. [Online]. Available: `http://arxiv.org/abs/1311.2524`.

[172] A. Krizhevsky, I. Sutskever, and G. E. Hinton, "Imagenet Classification with Deep Convolutional Neural Networks," in *Advances in neural information processing systems*, 2012, pp. 1097–1105.

[173] J. Huang, V. Rathod, C. Sun, *et al.*, "Speed/Accuracy Trade-Offs for Modern Convolutional Object Detectors," *CoRR*, vol. 4, 2016. [Online]. Available: `http://arxiv.org/abs/1611.10012`.

[174] Pkulzc. (2017). Tensorflow detection model zoo. (Accessed on 07/18/2018), [Online]. Available: `https://github.com/tensorflow/models/blob/master/research/object_detection/g3doc/detection_model_zoo.md`.

[175] K. Kosmas, J. Kobbert, and T. Q. Khanh, "Field-Test to Determine the Optimal Traffic Sign Illumination Based on Glare-Free High Beam," in *Proceedings of the 12th International Symposium on Automotive Lighting (ISAL)*, T. Q. Khanh, Ed., vol. 17, München, 2017, pp. 185–190, ISBN: 978-3-8316-4671-5.

[176] SmartEye Inc., *Smart Eye Pro Homepage*, (Accessed on 03.17.2018). [Online]. Available: `http://smarteye.se/`.

[177] B. L. Hills, "Visibility Under Night Driving Conditions: Part 2. Field Measurements Using Disc Obstacles and a Pedestrian Dummy," *Lighting Research & Technology*, vol. 7, no. 4, pp. 251–258, 1975.

[178] D. Armstrong, M. F. Marmor, and J. M. Ordy, *The Effects of Aging and Environment on Vision*. Springer Verlag, 1991, ISBN: 978-0-306-43920-9.

[179] A. Ekrias, M. Eloholma, L. Halonen, *et al.*, "Road Lighting and Headlights: Luminance Measurements and Automobile Lighting Simulations," *Building and Environment*, vol. 43, no. 4, pp. 530–536, 2008.

[180] A. J. Adams, B. Brown, G. Haegerstrom-Portnoy, *et al.*, "Marijuana, Alcohol, and Combined Drug Effects on the Time Course of Glare Recovery," *Psychopharmacology*, vol. 56, no. 1, pp. 81–86, 1978.

[181] H. Bardak, M. Gunay, U. Mumcu, *et al.*, "Effect of Single Administration of Coffee on Pupil Size and Ocular Wavefront Aberration Measurements in Healthy Subjects," *BioMed Research International*, vol. 2016, 2016.

[182] Open Street Map. (2018). Open Street Map – Die freie Wiki-Weltkarte. (Accessed on 03/15/2018), [Online]. Available: `\url{https://www.openstreetmap.org/export#map}`.

[183] ——, (2018). Java – Open Street Map – Editor. (Accessed on 03/15/2018), [Online]. Available: `https://josm.openstreetmap.de/`.

[184] ——, (2018). OSMConvert – OpenStreetMap Wiki. (Accessed on 03/15/2018), [Online]. Available: `https://wiki.openstreetmap.org/wiki/DE:Osmconvert`.

[185] ——, (2018). Key:highway – OpenStreetMap Wiki. (Accessed on 03/15/2018), [Online]. Available: `https://wiki.openstreetmap.org/wiki/Key:highway`.

[186] M. P. Pratt, J. A. Bonneson, and J. D. Miles, “Measuring the Non–Circular Portions of Horizontal Curves: An Automated Data Collection Method Using GPS,” in *Proceedings of the Transportation Research Board 90th Annual Meeting*, 2011.

[187] C. Ai and Y. Tsai, “Automatic Horizontal Curve Identification and Measurement Method Using GPS Data,” *Journal of Transportation Engineering*, vol. 141, no. 2, pp. 401–408, 2014.

[188] S. Michenfelder, *Konzeption, Realisierung und Verifikation eines Automobilen Forschungsscheinwerfers auf Basis von Digitalprojektoren*. KIT Scientific Publishing, 2015, vol. 9, ISBN: 978-3-731503-01-9.

[189] L. Thaler, A. C. Schütz, M. A. Goodale, *et al.*, “What is the Best Fixation Target? The Effect of Target Shape on Stability of Fixational Eye Movements,” *Vision Research*, vol. 76, pp. 31–42, 2013.

Part A

APPENDIX A, HEADLAMP REGULATIONS

A HEADLAMP REGULATIONS

A.1 DETAILED LOOK INTO EUROPEAN HEADLAMP REGULATIONS

The following sections will describe these regulations and analyse the restraints that are put onto the current state-of-the-art headlamps. All regulations include basic definition, and formal requirements for the technical approval and the way, the approval should be marked on the headlamps before technical requirements are set. Here, only the technical requirements for the headlamps are listed.

GENERAL REGULATIONS REGARDING HEADLAMPS

- **R1: Headlamps (including R2 and/or HS1 lamps):** Passing (low) beam filaments require a minimal luminous flux of 450 lm ± 5 % with a power consumption of 40 W ± 5 %. The high beam (driving beam) filament requires at least 700 lm with a power consumption of 45 W − 10 %. This regulation also states, that the cut-off of the low beam is "sufficiently" sharp for aiming. Also the general form of the cut-off line is set to be horizontal on the side of oncoming traffic with a rising slope of 15° on the driving side above the horizon. Aiming for low beam is set to be −1 % while the maximum illumination of driving beam is set to be in the centre point. Furthermore, detailed requirements for the light distribution are made with regards to the standard measuring screen shown in figure A.1 as listed in table A.1.

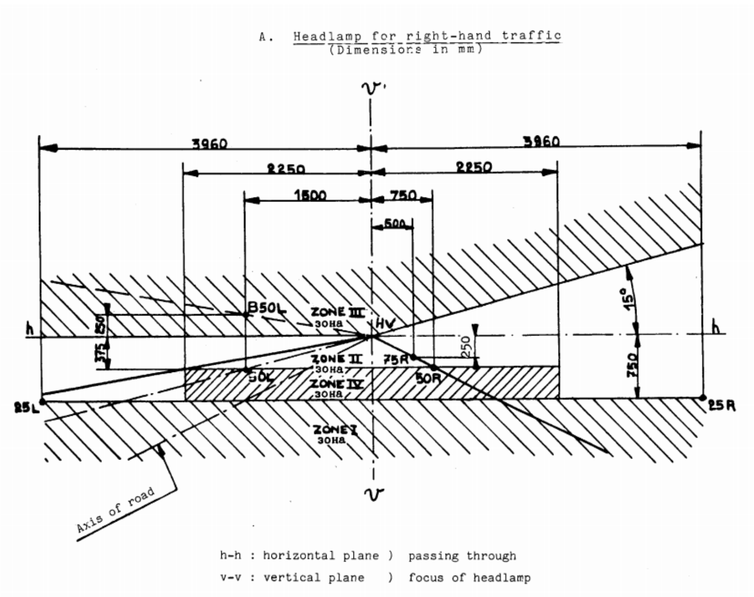

Figure A.1 – Standard ECE measuring screen for halogen headlamps.

Table A.1 – Required minimal and maximal illumination on the ECE standard measuring screen for halogen low beam headlamps.

Point on measuring screen: Headlamps for right-hand traffic	Point on measuring screen: Headlamps for left-hand traffic	Required illuminance
Point B 50 L	Point B 50 R	$\leq 0.40\,\mathrm{lx}$
〃 75 R	〃 75 L	$\geq 6.00\,\mathrm{lx}$
〃 50 R	〃 50 L	$\geq 6.00\,\mathrm{lx}$
〃 25 L	〃 25 R	$\geq 1.50\,\mathrm{lx}$
〃 25 R	〃 25 L	$\geq 1.50\,\mathrm{lx}$
Any Point in Zone III		$\leq 0.70\,\mathrm{lx}$
〃 〃 〃 〃 IV		$\geq 2\,\mathrm{lx}$
〃 〃 〃 〃 I		$\leq 20\,\mathrm{lx}$

For high beam requirements, it is stated, that, if high and low beam are produced by the same headlamp, the hh-vv point should be within the 90 % isolux line, and the maximum illuminance measured should be at least 32 lx.

- **R5: Sealed Beam Headlamps:** This regulation describes the requirements for headlamps that are sealed within one confinement during the production process. Here, both power rating as well as illumination ratings differ slightly from those required by **R1**. The power ratings are summarized in table A.2. For the illumination ratings, only the point B50L is changed to 0.3 lx.

Table A.2 – Required power limits for different halogen headlamps divided by size and type.

		Circular units of 180 mm		Circular units of 145 mm	
Rated Voltage		6 V	12 V	6 V	12 V
Tested Voltage		6 V	12 V	6 V	12 V
		Rated wattage and permitted tolerance			
Double Filaments	Driving Beam	37.5 W ± 0 %		37.5 W ± 0 %	
	Passing Beam	50 W ± 0 %		50 W ± 0 %	
Driving Beam Filaments Only		75 W ± 0 %		50 W ± 0 %	
Passing Beam Filaments Only		50 W ± 0 %		50 W ± 0 %	

Here the power requirements are divided into multiple groups depending on their size, driving/passing beam and the used voltage.

- **R8: Headlamps (H1, H2, H3, HB3, HB4, H7, H8, H9, HIR1, HIR2 and/or H11):** As already obvious from the title, this regulation splits the requirement into different filament types with minimal luminous flux requirements for all different halogen headlamps ranging from 825 lm for the HB4 filament to 1840 lm for H1R1. Furthermore, the required illuminance values were changed. Table A.3 shows these deviations marked in bold. All changes made, increase minimal amount of light required at the measurement points. The most remarkable change however is, that zone I has a dynamic maximum value depending on the illuminance measured at the point B 50 L/R.

Table A.3 –]
Required illuminance values according to the ECE R8. Values that deviate from R1 are marked in bold. The location of all points is found in figure A.1.

POINT ON MEASURING SCREEN		REQUIRED ILLUMNANCE	
HEADLAMPS FOR RIGHT-HAND TRAFFIC	HEADLAMPS FOR LEFT-HAND TRAFFIC	MINIMUM	MAXIMUM
Point B 50 L	Point B 50 R	-	$\leq$0.40 lx
" 75 R	" 75 L	$\geq$ **12 lx**	-
" 50 R	" 50 L	$\geq$ **12 lx**	-
" 25 L	" 25 R	$\geq$ **2 lx**	-
" 25 R	" 25 L	$\geq$ **2 lx**	-
Any Point in Zone III		-	$\leq$ 0.70 lx
" " " " IV		$\geq$ **3 lx**	-
" " " " I		-	$\leq$ **2· B 50 L/R**

- **R20: Headlamps (H4):** For this type of light source, the H4 lamp, the light power consumption is set to "about 55 W" leading to a luminous flux of at least 750 lm and "about 60 W" with a luminous flux of 1250 lm. The required values for the different testing points are kept the same as in table A.3. Furthermore an additional 8 measurement points on and above the horizon are added, that further limit the maximum amount of light, that could potentially dazzle oncoming traffic. In terms of the cut-off line, the slope is changed from 15° to 45°.

- **R31: Headlamps (halogen sealed beam (HSB)):** While this regulation stays similar to R5, the test voltage is raised to 13.2 V. While the power consumption is stays at 75 W for the driving beam, it is raised to allow up to 68 W for the passing beam. Compared to R1, the centre of the testing area is now only required to be within the 80 % isolux line with a minimum of 48 lx (16 lx more than in R1).

- **R48: Installation of lighting and light-signalling devices:** This regulation states the colour limitations of headlamps, rear lighting and other light installations on motorized vehicles. Furthermore, the working boundaries of automated headlamp (de-)activation sensors are set. Since a lot of the following work covers some kind of automated headlamp switching, this is a very important aspect for the main part of thesis: The sensors need to be able to identify other vehivles in ± 15° horizontally and, depending on the sensor mounting hight, up to ± 5° vertically. Oncoming vehicles need to be detected in a distance of at least 400 m and preceding vehicles at a distance of at least 100 m. Additionally, the mounting positions in regard to the vehicle are set and the possible headlamp aiming range is set. More definitions regarding headlamp levelling devices and other technical and electrical requirements are set.

- **R98: Headlamps with gas-discharge light sources:** This Regulation primarily focuses on the aiming of HID headlamps and fail save protection in case of malfunctioning electronics or mechanics. Furthermore, limits and minimal values for the illuminance values recorded on the measuring screen are set for these types of headlamps. Since the HID light sources can produce a much higher light output, additionally to changing the values, further measurement points are introduced. All measurement points are shown in figure A.4.

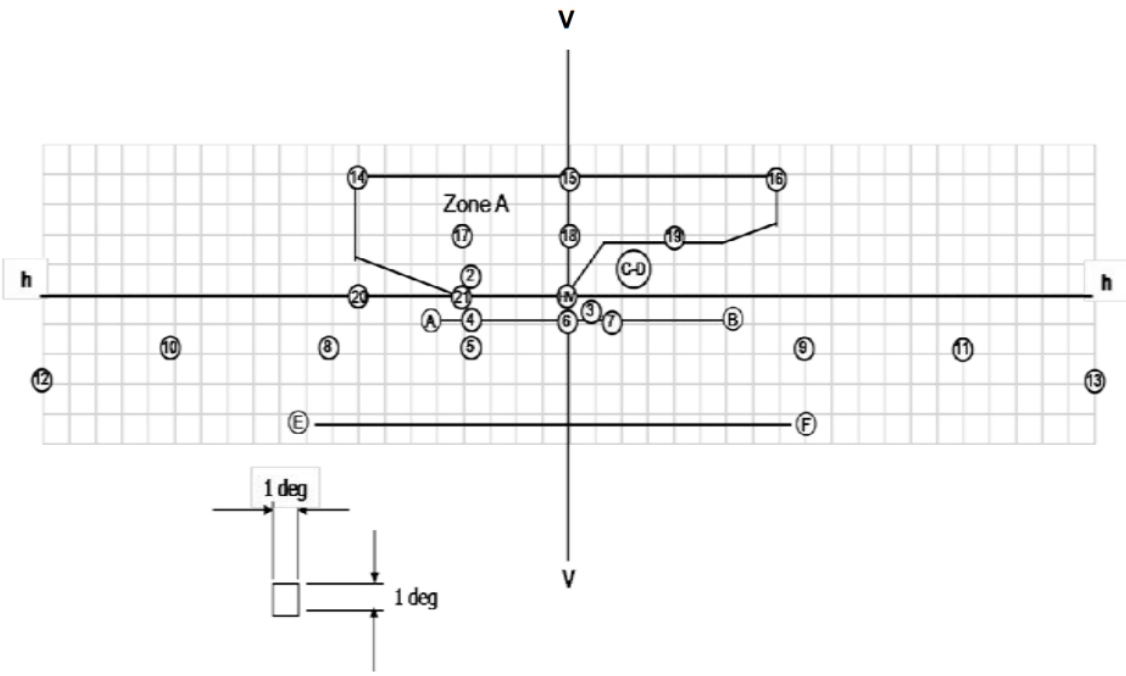

Figure A.2 – Standard ECE measuring screen for HID headlamps.

The main difference between the values shown here for the HID headlamps and the values shown before for the halogen headlamps is, that these values are now given as the luminous intensity instead of the illuminance. The values can easily be converted between each other by 2.2 with the given distance of 25 m to the measuring screen. Table A.4 therefore shows the illuminance values calculated from the luminous intensity values given in ECE R98. Values that changed in regards to the R1 are marked as bold. New measurement points are marked italic.

Table A.4 – Required illuminance values for HID headlamps at the different measuring points for right-hand traffic. For left-hand traffic L and R are changed in the column designation.

POINTS OR SEGMENTS	DESIGN.	LUMINOUS INTENSITY MAX	LUMINOUS INTENSITY MIN	HOR. ANGLE	VERT. ANGLE
Any Point in Zone A		$\leq$ **1.0 lx**			
1	HV	$\leq$ **1.0 lx**		0°	0°
2	B 50 L	$\leq$ **0.6 lx**		−3.3°	0.6°
3	75 R		$\geq$ **20 lx**	1.2°	−0.6°
4	50 L	$\leq$ 29.6 lx		−3.3°	−0.9°
5	25 L1	$\leq$ 30.1 lx		−3.3°	−1.7°
6	50 V		$\geq$ 12 lx	0°	−0.9°
7	50 R		$\geq$ **20 lx**	1.7°	−0.9°
8	25 L2		$\geq$ 4 lx	−9.0°	−1.7°
9	25 R1		$\geq$ 4 lx	0°	−1.7°
10	25 L3		$\geq$ 2 lx	0°	−1.7°
11	25 R2		$\geq$ 2 lx	0°	−1.7°
12	15 L		$\geq$ 1 lx	0°	2.9°
13	15 R		$\geq$ 1 lx	0°	2.9°
14			*	0°	4.0°
15			*	0°	4.0°
16			*	0°	4.0°
17			*	0°	2.0°
18			*	0°	2.0°
19			*	0°	2.0°
20			$\geq$ 0.1 lx	0°	0.0°
21			$\geq$ 0.2 lx	0°	0.0°
A to B	Segment I		$\geq$ 6 lx	0°	−0.9°
C - D		$\leq$ 2.8 lx		0°	1.0°
E to F	Segment III and Under	$\leq$ 20 lx		0°	−4.3°
	E_{max} Right	$\leq$ 70.1 lx		$\leq$ 0°	$\geq$ −1.7°

E_{max} Left	$\leq 50.1\,\text{lx}$	$\leq 0°$

LIGHT SOURCE BASED

- **R37: Filament lamps:** While the regulations mentioned above introduce different requirements for the light source and correlating electric setup like power consumption and overall luminous flux, as well as different measurement points in the light distribution that need to be full-filled, this regulation gives specific requirements on the light source it self. This is mainly focused on the geometric setup of the halogen light sources. As an example, the geometric requirements for an H7 lamp is shown in figure A.3.

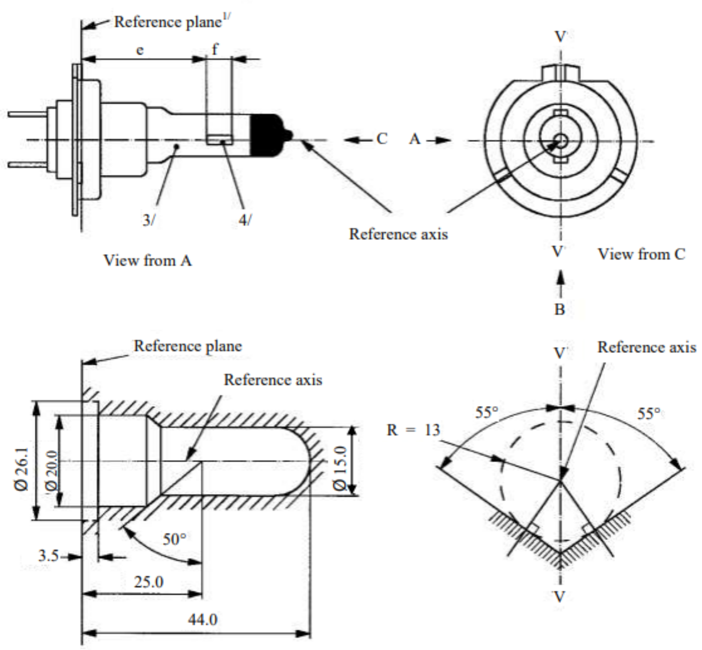

Figure A.3 – Geometric requirements for the H7 halogen light sources according to ECE R37.

Additionally, to the geometric requirements, the colour temperature and the colour coordinates are limited by this regulation.

- **R99: Gas-discharge light sources:** This regulation is kept analogous to R37, simply swapping out the halogen light sources and their technical requirements for the HID light sources. Since this thesis will not go into light source development, this is not being discussed further.

LIGHT DISTRIBUTION BASED

- **R112: Headlamps emitting an asymmetrical passing-beam:** With the release of LED headlamps, the regulations released are more general and R112 requires either a filament as a light source OR LED. Besides limits for using headlamps that are designed for right-hand traffic in left-hand traffic or vice versa, the general aiming regulations from R98 is repeated. For the photometric values, the headlamps are now divided into classes A and B depending on their photometric properties. While most of the requirements at the measuring points are the same for both classes and identical to R98, some values are changed. B 50 L is kept the same as for HID headlamps, but 75 R is lowered to a minimum of 16.2 lx (Class B) or 8.2 lx (Class A) compared to 20 lx in R98 to mention one of the most important changes. Since class B hast the higher minimal requirements, and the maximum values are equal for class A and B, only class B is listed here. Table A.5 shows all mentioned points with the required values converted to illuminance values for better comparison to the values shown above.

Table A.5 – Measuring points and required illuminance values calculated from R112.

Designation	HOR. ANGLE	VERT. ANGLE	REQUIRED ILLUMINANCE	
			MAX.	MIN.
B 50 L	0.6°	−3.4°	0.6 lx	
BR	1.0°	2.5°	2.8 lx	
75 R	−0.6°	1.2°		16.2 lx
75 L	−0.6°	−3.4°	17.0 lx	
50 L	−0.9°	−3.4°	21.1 lx	
50 R	−0.9°	1.7°		16.2 lx
50 V	−0.9°	0.0°		8.2 lx
25 L	−1.7°	−9.0°		2.7 lx
25 R	−1.7°	9°		2.7 lx
Any Point in Zone III			1.0 lx	
Any Point in Zone IV				4.0 lx
Any Point in Zone I			$\leq 2\cdot$ B 50 L	

Aside from these changes, the alignment process is repeated from before without changes.

- **R113: Headlamps emitting a symmetrical passing-beam:** This regulation gives the requirements for headlamps, that produce a symmetrical low beam and add the "shoulder" with use of the high beam system. Here headlamps are further divided into classes A to E with the photometric properties listed in table A.6. Class A to D may use halogen or LED light sources and class E headlamps uses an HID or an LED light source.

Table A.6 – Minimal and maximal luminous flux of the passing beam for headlamps in the different Classes A to E according to ECE R113

	CLASS A	CLASS B	CLASS C	CLASS D	CLASS E
PASSING BEAM MINIMUM	150 lm	350 lm	500 lm	1000 lm	2000 lm
PASSING BEAM MAXIMUM	900 lm	1000 lm	2000 lm	2000 lm	-

Table A.7 – Measurement points and photometric requirements for symmetrical low beam headlamps according to ECE R113

NO.	ANGULAR COORDINATES		REQUIRED ILLUMANCE					
			CLASS B		CLASS C		CLASS D, E	
	HOR. ANGLE	VERT. ANGLE	MIN.	MAX.	MIN.	MAX.	MIN.	MAX.
1	0.0°	± 0.0°	25.6 lx	-	32.0 lx	-	48.0 lx	-
2	0.0°	± 2.5°	14.4 lx	-	16.0 lx	-	32.0 lx	-
3	0.0°	± 5.0°	4.0 lx	-	5.6 lx	-	8.0 lx	-
4	0.0°	± 9.0°	-	-	3.2 lx	-	5.4 lx	-
5	0.0°	± 12.0°	-	-	1.0 lx	-	1.6 lx	-
6	−2.0°	0.0°	-	-	1.6 lx	-	2.7 lx	-
E_{max}			32.0 lx	344.0 lx	40.0 lx	344.0 lx	64.0 lx	344.0 lx

Since the symmetrical low beam requires different measurement points, new points are listed. The graphical illustration of these points is shown in figure A.4

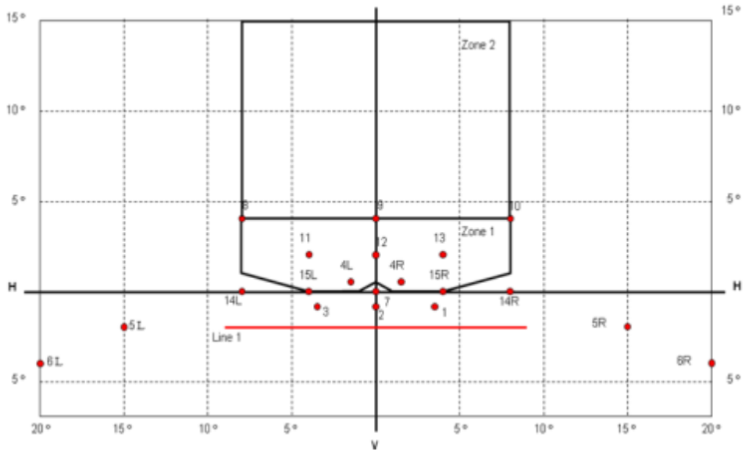

Figure A.4 – Measurement points and zones for Class C,D and E headlamps according to ECE R113.

The minimal and maximal required values as well as the angular positions of all points and zones are listed in table A.7 split up for the different classes.

- **R123: Adaptive Front-Lighting Systems** Since this regulation is already summarized in chapter 3 only the required values of the measurement points according to figure 3.4 are presented here in table A.8.

Table A.8 – Measurement points and required illuminance values for the different classes defined in R48 for AFS Headlamps.

TABLE REQUIREMENTS			POSITION			PASSING BEAM							
			HOR.		VERT.	CLASS C		CLASS V		CLASS E		CLASS W	
	NO.	ELEMTENT	AT./FROM	TO	AT	MIN.	MAX.	MIN.	MAX.	MIN.	MAX.	MIN.	MAX
PART A	1	B 50 L	−3.4°		0.6°	0.1 lx	0.6 lx	0.1 lx	0.6 lx	0.1 lx	1.0 lx	0.1 lx	1.0 lx
	2	HV	0.0°		0.0°	0.1 lx	1.0 lx	0.1 lx	1.0 lx	0.1 lx		0.1 lx	
	3	BR	2.5°		1.0°	0.1 lx	2.8 lx	0.1 lx	1.4 lx	0.1 lx	2.8 lx	0.1 lx	4.2 lx
	4	Segment BRR	8.0°	20.0°	0.6°	0.1 lx	5.7 lx		1.4 lx		5.7 lx		8.5 lx
	5	Segment BLL	−8.0°	−20.0°	0.6°	0.1 lx	1.0 lx		1.4 lx		1.4 lx		1.4 lx
	6	P	−7.0°		0.0°	0.1 lx						0.1 lx	
	7	Zone III					1.0 lx		1.0 lx		1.4 lx		1.4 lx
	8	S 50 + S 50 LL + S 50 RR			4.0°	0.3 lx				0.3 lx		0.3 lx	
	9	S 100 + S 100 LL + S 100 RR			2.0°	0.6 lx				0.6 lx		0.6 lx	
	10	50 R	1.7°		−0.9°			8.2 lx					
	11	75 R	1.2°		−0.6°	16.2 lx				24.3 lx		32.5 lx	
	12	50 V	0.0°		−0.9°	8.2 lx		8.2 lx		16.2 lx		16.2 lx	
	13	50 L	−3.4°		−0.9°	5.7 lx	21.1 lx	5.7 lx	21.1 lx	10.9 lx		10.9 lx	42.2 lx
	14	25 LL	−16.0°		−1.7°	1.9 lx		1.4 lx		1.9 lx		5.4 lx	
	15	25 RR	11.0°		−1.7°	1.9 lx		1.4 lx		1.9 lx		5.4 lx	
	16	Segment 20 and below	−3.5°	0.0°	−2.0°								28.2 lx
	17	Segment 10and below	−4.5°	2.0°	−4.0°		19.7 lx		19.7 lx		19.7 lx		11.4 lx
	18	E_{max}				27.0 lx	70.6 lx	13.4 lx	70.6 lx	27.0 lx	126.9 lx	47.2 lx	112.8 lx
PART B	1	B 50 L	−3.4°		0.6°	0.1 lx	0.8 lx		0.8 lx				1.3 lx
	2	HV				0.1 lx	1.4 lx		1.4 lx				

7	Zone III				1.4 lx		1.4 lx		1.4 lx		1.4 lx
13	50 L	−3.4°	−0.9°	2.7 lx		2.7 lx		5.4 lx		5.4 lx	
18	E_{max}			16.2 lx	70.6 lx	8.2 lx	70.6 lx	16.2 lx	126.9 lx	32.5 lx	112.8 lx

Part B

APPENDIX B, INVESTIGATION OF DETECTION DISTANCES UNDER VARYING LIGHT CONDITIONS

B

APPENDIX B, INVESTIGATION OF DETECTION DISTANCES UNDER VARYING LIGHT CONDITIONS

This section contains detailed information on the participants of the studies on the impact of intensity in low and high beam as well as object positioning on detection and identification distances. Furthermore, statistical data is discussed and for the study regarding the high beam intensity, the identification tests are presented and discussed.

B.1 IMPACT OF VARIABLE LUMINOUS INTENSITY IN THE LOW BEAM SECTION

This part shows the data for the investigation of the influence of the low beam intensity on the detection distances as shown in section 5.1.1. The normalized light distribution used in the test to investigate the influence of the luminous flux in the low beam on the detection distance is shown in figure B.1.

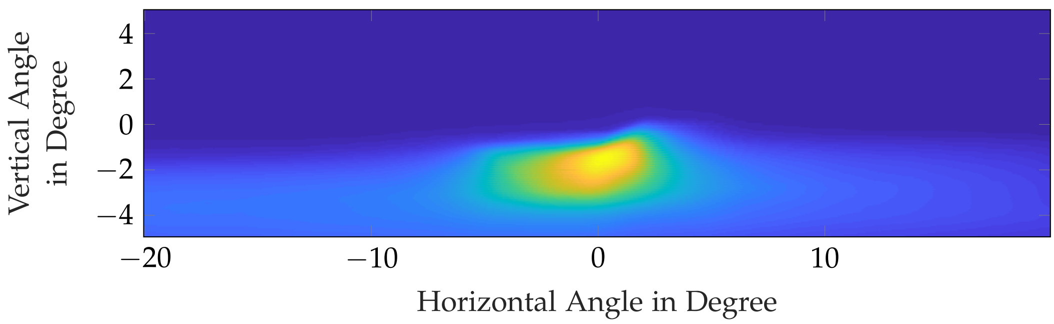

Figure B.1 – Low beam light distribution as used to investigate the influence of low beam intensity on detection distances. The distribution is normalized to the maximum luminous intensity.

The age distribution for these subjects is visualized in figure B.2.

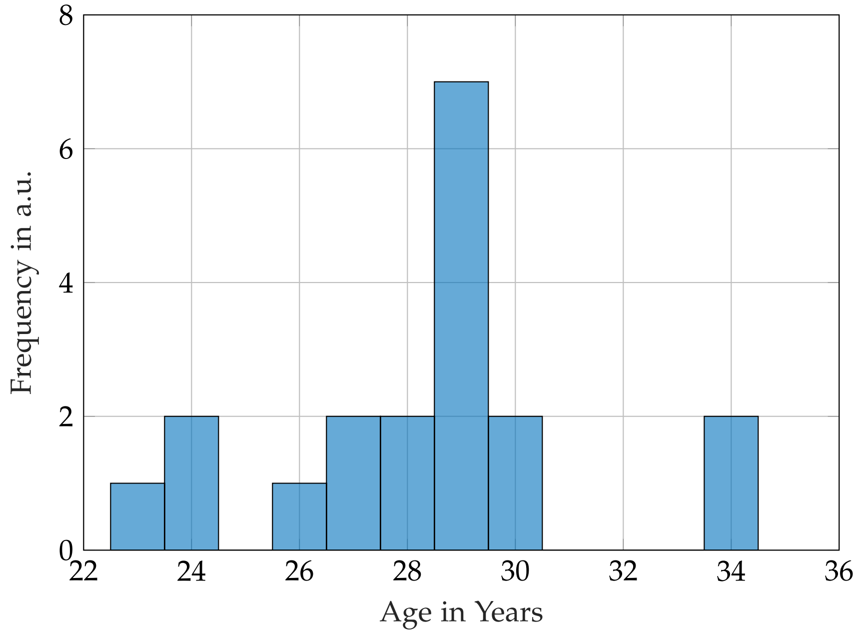

Figure B.2 – Subject age distribution for the investigation on detection distance with variable low beam intensity

Table B.1 shows the detailed data for the participants in this study, including their age and occupation.

Table B.1 – Overview over the participants in the study on the impact of low beam intensity on detection distances as described in chapter 5.1.1.

NR	AGE	WORK
1	24	Student
2	34	Clerk
3	34	Clerk
4	29	Clerk
5	27	Student
6	29	Student
7	26	Student
8	24	Student
9	30	Student
10	29	Student
11	29	Student
12	29	Student
13	23	Student
14	28	Student
15	29	Student
16	30	Clerk
17	27	Student
18	29	Student
19	28	Student

Figure B.3 shows, that the cumulative data for the 100 % low beam (red) is much closer to the standard distribution (green, dashed line) than the distribution recorded with the 50 % low beam.

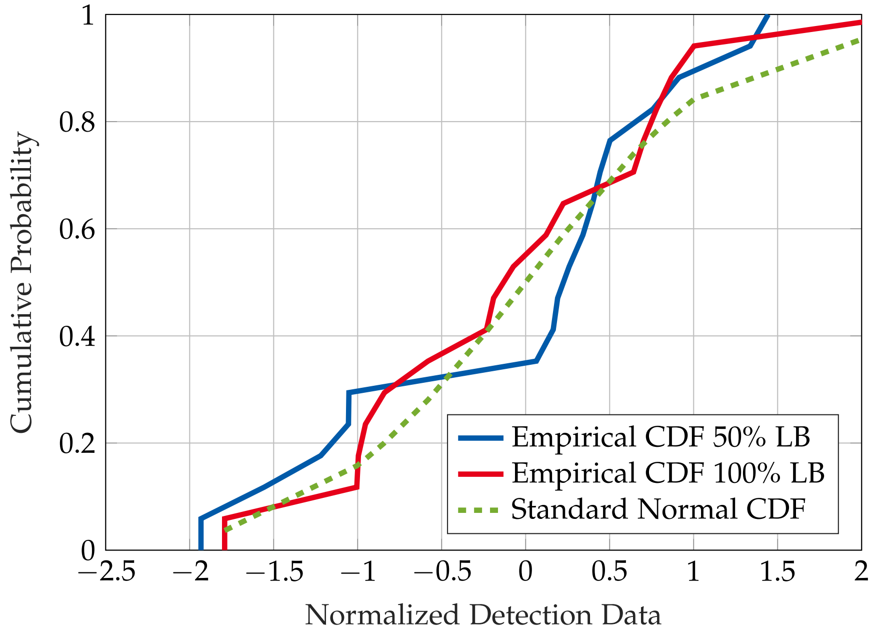

Figure B.3 – Empiric CDF for the two low beam setups. Blue representing 50 % low beam and red 100 % low beam. The normal CDF is shown in the green, dashed line.

B.2 IMPACT OF VARIABLE LUMINOUS INTENSITY IN THE LOW BEAM SECTION

This section first shows the data for the participants in the study regarding the influence of high beam intensity on detection and identification distances as shown in section 5.1.2. The second part is dedicated to describing the identification test, including the results achieved in this test.

B.2.1 SUBJECT DATA

The age distribution of the subjects in both study parts is shown in figure B.4 where the two age groups are marked by blue for the younger participants and red for the older participants.

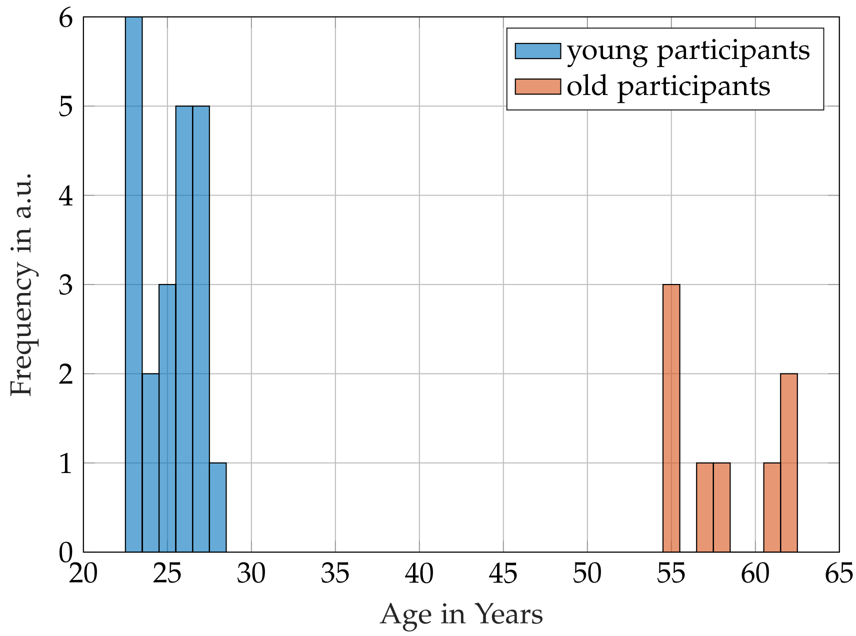

Figure B.4 – Subject age distribution for the investigation on detection distance with variable high beam intensity. Young subjects are shown in blue and the older age group is shown in red.

Table B.2 shows the detailed subject data for both, detection and identification tests.

TEST PROCEDURE IDENTIFICATION

For the identification tests, the human like dummies in the setup shown in figure 5.6 are replaced with identification sign, set together from two squares with the size of 40 cm x 40 cm and 20 cm x 20 cm where the smaller square is attached to either the top, the bottom, the left or the right side of the larger square. The identification signs are coated with matt grey paint to achieve a reflection coefficient of 10 %. For the identification test, the participants are asked to identify the orientation of the smaller square in regard to the larger square. This setup is done analogue to the test by Michenfelder as described in chapter 4 [188].
The test procedure is similar to the procedure described for the detection test in section 5.1.2. For the identification test, the simple one-button detection button, is switched for a four-way button with the directions that correlate to the four possible positions of the smaller square in regard to the larger square. The test is repeated for each of the mentioned three light distributions three times thereby leading to 9 runs per test and 18 runs per person. To keep the participants vigilant, after the detection test, a short break is inserted for each subject during which a second test subject will perform the detection test. The same procedure is redone after the identification runs. The data for the participating test subjects is shown in table B.2.

RESULTS AND STATISTICAL DATA

The detection data for the three lighting distributions is visualized in figure B.5 where the empirical cumulated data is shown for all three light distributions with respect to the standard normal CDF. The light distributions are represented by the same colours as in 5.7, meaning passing beam is shown in blue, driving beam in red and driving beam with additional LASER

Table B.2 – Overview over the participants in the study on the impact of high beam intensity on detection distances with the LASER high beam system as described in chapter 5.1.2.

NR	AGE	GLASSES	WORK
1	23	-	Student
2	23	-	Student
3	25	-	Student
4	26	x	Student
5	23	x	Student
6	27	-	Student
7	24	x	Student
8	25	-	Student
9	23	-	Student
10	27	-	Clerk
11	28	-	Clerk
12	23	-	Clerk
13	26	-	Student
14	27	-	Student
15	23	-	Student
16	24	-	Clerk
17	26	x	Student
18	27	x	Student
19	25	x	Student
20	26	-	Student
21	26	-	Student
22	27	-	Student
23	55	-	Clerk
24	58	x	Clerk
25	57	x	Clerk
26	61	x	Clerk
27	62	x	Clerk
28	62	x	Clerk
29	55	x	Clerk
30	55	-	Clerk

booster in yellow. The standard normal CDF is shown as the green, dashed line. The close match of all four curves indicates the normal distribution shown by the p values above.

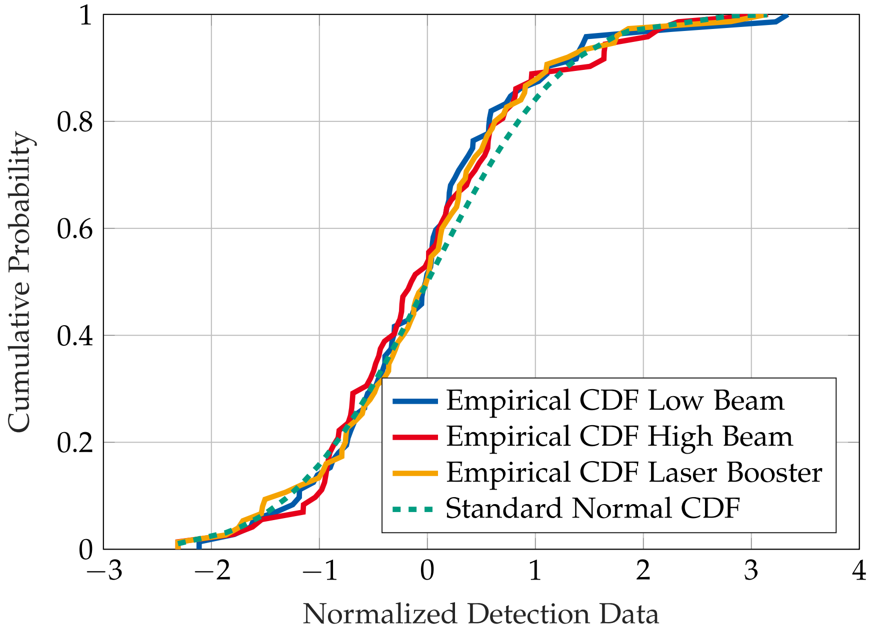

Figure B.5 – Empiric CDF for the three light distributions with blue representing low beam, red representing high beam and yellow the additional LASER booster. The normal CDF is shown in the green, dashed line.

The empirical CDF data for both gain distributions, gain by high beam over low beam in red and gain by LASER booster over high beam in yellow, is shown in figure B.6 with the standard normal CDF as the dashed green line. Again the CDF data shows, that the data is very close to a normal distribution and it is visualized, that the gain distribution for the LASER booster is very close to the normal distribution.

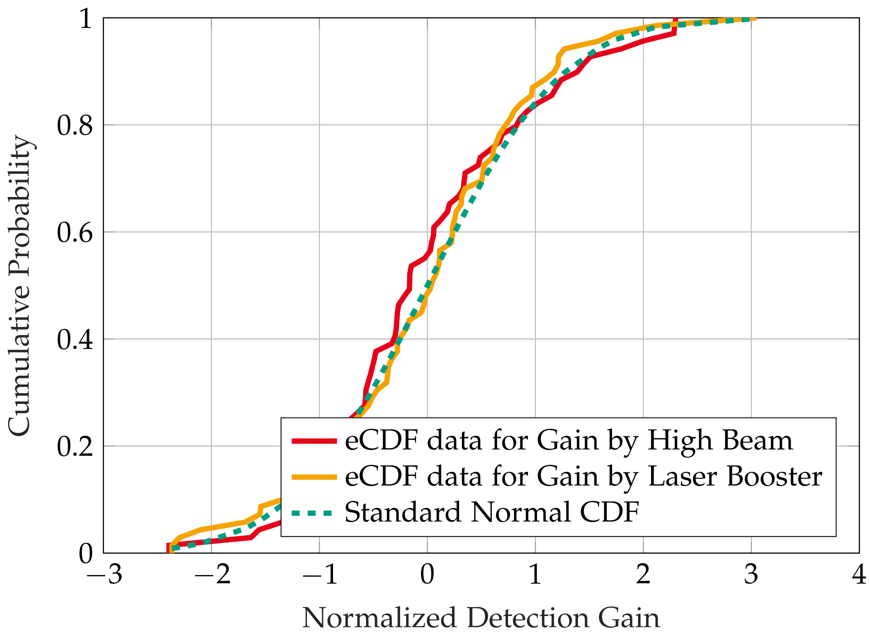

Figure B.6 – Empirical CDF data for the distributions of difference in detection between low beam and high beam in red, and the difference between high beam and LASER booster in yellow as well as the standard normalized CDF as the green dashed line

The statistical metrics for the detection probabilities shown in figure 5.9 are shown in table B.3 with ΔW representing the mean difference between the fit and the data, the MSE, the standard deviation of ΔW and the statistical determination coefficient R^2

$$f(x) = \frac{1}{1 + e^{(-x+x_0)^c}} \tag{B.1}$$

Table B.3 – Statistical metrics for the fits for the detection probabilities shown in figure 5.9.

	LOW BEAM	HIGH BEAM	LASER BOOSTER
ΔW	0.762	1.184	1.020
MSE	0.010	0.016	0.014
$\sigma_{\Delta W}$	0.008	0.014	0.012
R^2	0.996	0.995	0.998

IDENTIFICATION DISTANCES WITH VARIABLE HIGH BEAM INTENSITY

The section above describes the detection of objects besides the road. During the described study, the participants knew, to a certain degree, where the detection objects are located and are aware, that only the detection dummies are located besides the road. This might increase the measured distances by a significant margin. To accommodate for this effect, in the second part of this study, the identification distance is measured.
Similar to the detection, the first step is to investigate the raw identification distances. This is shown in figure B.7.

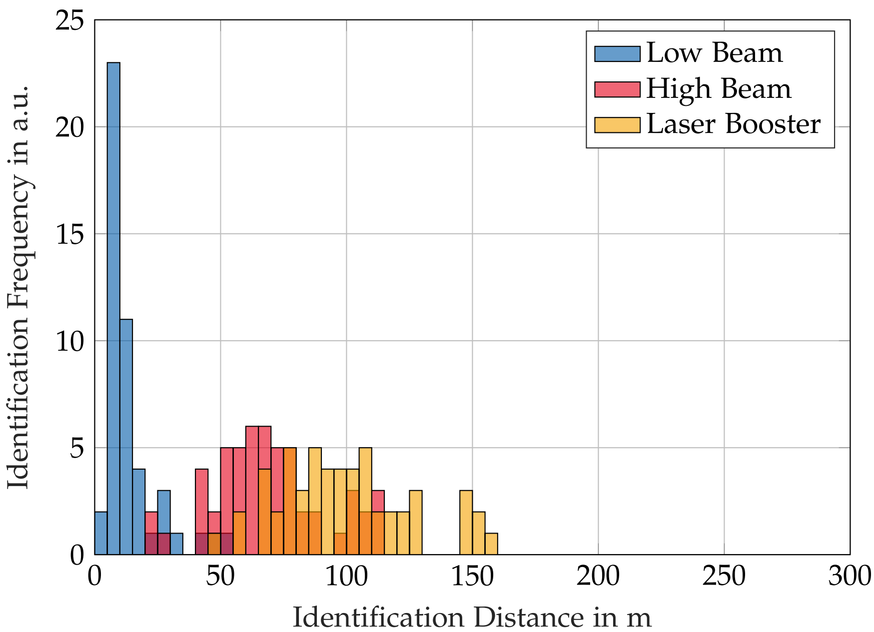

Figure B.7 – Identification distances grouped into 5 m bins for the three light distributions. Passing beam is represented by the blue bars, driving beam by red bars and driving beam with additional LASER booster by orange bars. The median detection distance is calculated at 13.9 m for passing beam, and the mean distances are 68.4 m for driving beam and adding the LASER booster to this, leads to 98.9 m

The shown identification distributions are then normalized according to equation 5.1 and tested for normal distribution. This leads to normal distribution for high beam ($p = 0.79$) and added LASER booster ($p = 0.89$). For low beam the null hypothesis has to be neglected with $p = 0.01$. The normalized CDF data is shown in figure B.8. As above, the low beam data is represented by the blue line, the high beam data is represented by the red line, the LASER booster data is represented by the yellow line and the standard normalized CDF is shown as the green dashed line. This again exemplifies the fact, that the low beam identification distances are not normal distributed since the CDF data for low beam, does not represent the standard normal CDF.

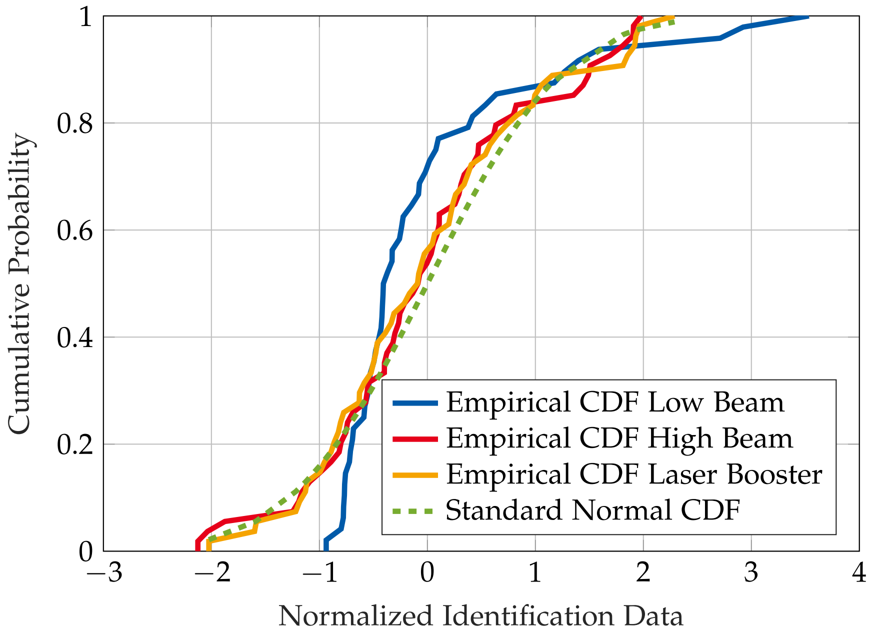

Figure B.8 – Empiric CDF for the three light distributions with blue representing low beam, red representing high beam and yellow the additional LASER booster. The normal CDF is shown in the green, dashed line.

This non normal distribution is the result of the configuration of the identification sign. The sign is placed at a height of 1.2 m. Since low beam is dipped under a given angle of 0.6° for the light distribution left of the centre, and at 0° for the part on the right side of the centre, the maximum height of the low beam is the height of the headlamps which in this case, is under 70 cm. This means, that the identification sign can never be illuminated completely and thereby making an early identification near impossible. Therefore, for the identification distances, only high beam and high beam with additional LASER booster will be discussed analogue to the detection distances. To find if there the low beam identification distance distribution, is statistical significant different from the high beam and LASER booster identification distribution, a Wilcoxon-Mann-Whitney-Test is performed. This is a non parametric test for the null hypothesis that the two tested distributions origin from one continuous distribution. Unlike the Kolmogorov-Smirnov-Test used before, this test does not require normal distributions. For the significance test between the high beam identification distance and the LASER booster however, the Kolmogorov-Smirnov-Test is used again since those distributions are normal distributions and this test leads to more stable results in this case.

The two tests reveal, that all three identification distances are indeed significantly different to each other by dismissing the null hypothesis. The p-values indicating the strength of the significance are listed in table B.4. Similar to the values shown in table B.3, all tests reveal significant differences between all identification distance distributions. Again, all p values are far lower than the set theshold of 5 %. However, it has to be noted, that the distributions for high beam identification and LASER booster identification moving much closer together with the highest p-values recorded so far. This is already evident in figure B.7 where both distributions overlap to a given extend at around 80 m. Again, testing the identification distance distributions of a light distibution with itself, leads to p-values of one and thereby stating that both distributions origin from the same continuous distribution.

Table B.4 – p-values for the Wilcoxon-Mann-Whitney-Test between the identification distances of low and high beam and between low beam and LASER booster as well as the p-values for the Two Sample Kolmogorov-Smirnov tests between the identification distances of high beam and added LASER booster.

	LOW BEAM	HIGH BEAM	LASER BOOSTER
LOW BEAM	1.0	4.1×10^{-17}	4.2×10^{-18}
HIGH BEAM	4.1×10^{-17}	1.0	4.5×10^{-7}
LASER BOOSTER	4.2×10^{-18}	4.5×10^{-7}	1.0

After testing for significant differences between all distributions, the median/mean identification distances for all light distributions can be calculated according to the detection section of this study. Since the low beam identification distance distribution is not normal distributed, for this setting the median distance is calculated. The median for low beam is calculated at 9.5 m, the mean for high beam is at 68.4 m and for the LASER booster the mean is calculated to be at 98.9 m, resulting in a gain of identification distance of 59.0 m (623.1 %) from low to high beam and 30.5 m (44.6 %) from high beam to LASER booster. While the 623.1 % increase when switching from low to high beam seems impressive, the fact, that early identification with low beam is near impossible with the chosen identification setup needs to be kept in mind. The far lower increase of only 44.6 % however is much more comparable to the gain recorded in the detection tests with 56.4 %. The increase when switching from low beam directly to the LASER module is calculated at 89.5 m or 945.3 % but as already mentioned above, this comparison is not viable.

While for the detection part of this study, the gain between the light distributions is statistically identical, this is not the case for the identification test. This is already obvious, since the identification distribution with the low beam is not a normal distribution. Therefore, this part of the calculation is skipped and identification probabilities including the 95 % thresholds are calculated directly. Again the probability is calculated according to $1 - \sum d_i$ and equation B.1 is fitted to the data points. Both data, as well as the fit functions are shown in figure B.9 where the low beam data is represented by the blue dots (data) and line (fit). High beam is represented in red and the LASER data is shown in yellow.

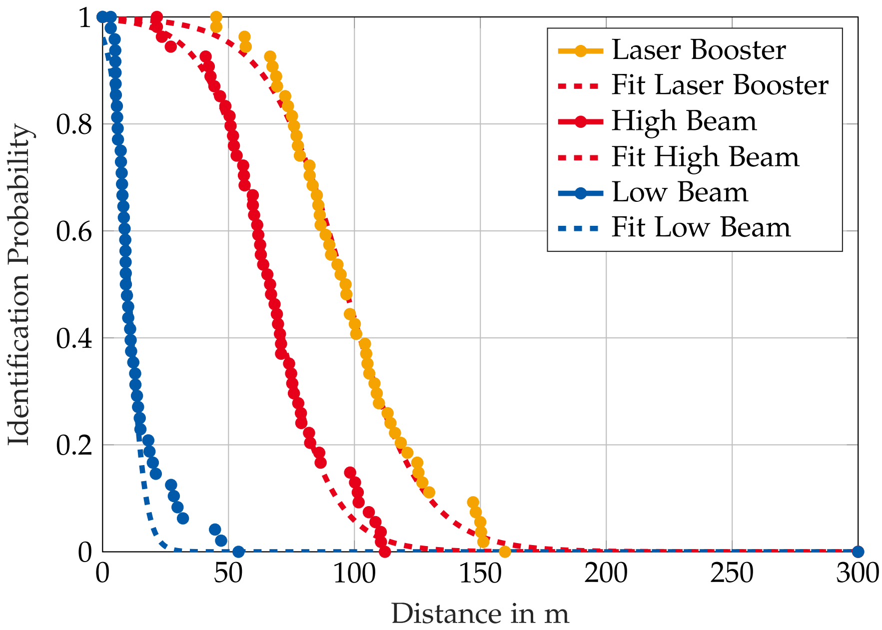

Figure B.9 – Empiric identification probability for the three investigated lighting functions with the additional sigmoid fit functions according to equation B.1. Blue represents low beam, red high beam and blue the additional LASER booster.

The fit coefficients are shown in table B.5 analogue to the ones presented above. Again, the R^2 values show a very good fit representation with the lowest $R^2 = 0.960$ for the low beam data. This is also apparent in figure B.9 where the low beam fit does not represent the data well for identification probabilities below 20.0 %. The figure also shows similar, but less pronounced behaviour for both high beam as well as for LASER beam.

Table B.5 – Statistical metrics for the fits for the identification probabilities shown in figure B.9, low beam, high beam and high beam with added LASER booster.

	LOW BEAM	HIGH BEAM	LASER BOOSTER
ΔW	2.454	0.914	0.986
MSE	0.048	0.016	0.018
$\sigma_{\Delta W}$	0.038	0.017	0.013
R^2	0.960	0.994	0.995

However, since the R^2 values show a very good data representation, all further discussion will focus on the fit data. Analogous to the detection probability, the 50 % and the 95 % thresholds are calculated. This is shown for both, fit data and recorded data in table B.6. For the 50 % threshold, a mean difference between the fit and the recorded data of 2.4 m is calculated with the maximum difference being 5.5 m for high beam. For the 95 % threshold a mean difference of 4.6 m with the maximum being 6.0 m for identification with the added LASER module, is calculated. It is noteworthy, that for identification, the 95 % detection distances are calculated to be at 0.9 m, 31.0 m and 50.8 m respectively. These values are far lower than the values calculated for detection. However this was to be expected due to the different nature of the task the participants had to full fill.

Table B.6 – 50 % and 95 % identification distance thresholds for the three different light distributions as calculated from the data shown in figure B.9.

	LOW BEAM		HIGH BEAM		LASER BOOSTER	
	50 %	95 %	50 %	95 %	50 %	95 %
DATA	9.250 m	4.810 m	66.510 m	27.080 m	96.500 m	56.840 m
FIT	10.304 m	0.874 m	66.496 m	30.967 m	96.019 m	50.808 m

Figure B.10 shows the luminance recordings on the detection object for all three light functions with blue marking the low beam, red marking the high beam and yellow marking high beam with added LASER-Booster. While all object luminance recordings decrease continuously over the distance, the background luminance, shown in purple, stays constant over all distances with some level of noise added. This means, when calculating the contrast according to equation 2.10 the resulting value will not decrease continuously. For this reason, the contrast is not reviewed any further.

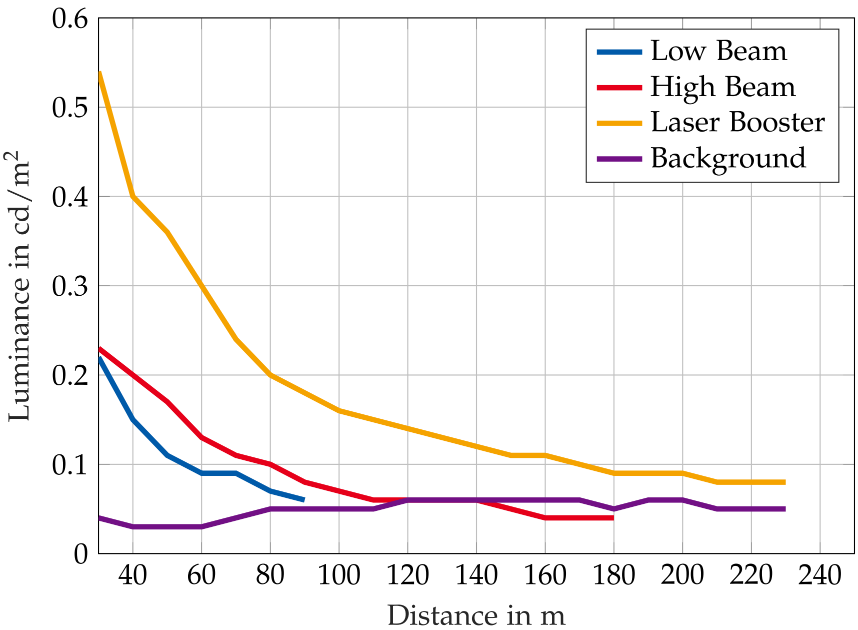

Figure B.10 – Object luminance dependent on distance and light distribution. Blue shows the luminance at the object with low beam, red shows the luminance at the object with high beam, yellow shows the luminance at the object with added LASER booster and purple shows the luminance of the background.

B.3 DETECTION UNDER DIFFERENT VIEWING ANGLES

Listing the test subjects that participated in the field test regarding the influence of the object position with regard to the driver on the detection distance as described in section 5.1.3.

B.7 shows the detailed overview of the participants in the mentioned test.

Figure B.11 shows the age distribution for young participants (blue) and old participants (red). While the data shown in this thesis does not focus on the two age groups, the original work by Schneider shows the differences in detection distances in great detail [66, 165].

Table B.7 – Overview over the participants in the study on the impact of angular position of objects on detection distances as described in 5.1.3.

NR	AGE	GLASSES	WORK
1	20	-	Student
2	20	x	Clerk
3	20	-	Student
4	23	x	Clerk
5	23	-	Student
6	23	-	Student
7	25	-	Student
8	25	-	Student
9	25	-	Student
10	26	-	Student
11	27	-	Student
12	27	-	Student
13	27	x	Student
14	27	x	Student
15	27	x	Student
16	28	-	Student
17	29	x	Student
18	29	x	Student
19	30	-	Student
20	30	-	Student
21	30	-	Student
22	31	-	Student
23	45	-	Clerk
24	45	x	Clerk
25	47	x	Clerk
26	52	x	Clerk
27	52	x	Clerk
28	53	x	Clerk
29	54	x	Clerk
30	54	-	Clerk

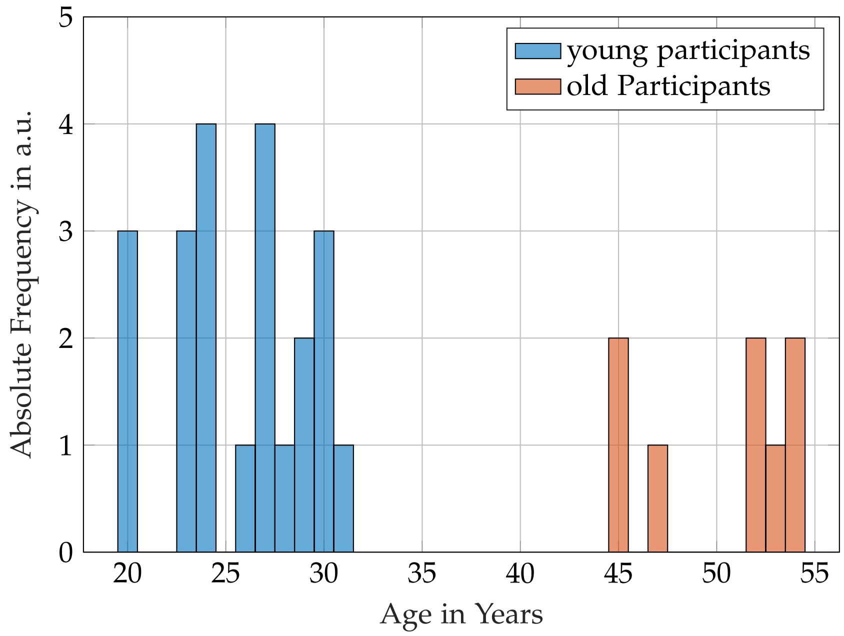

Figure B.11 – Age distribution for the participants of the study on the detection distance under vaying object positions.

Part C

APPENDIX C, TRAFFIC SPACE ANALYSIS

APPENDIX C, TRAFFIC SPACE ANALYSIS

C.1 TRAFFIC SPACE ANALYSIS

Figure E.9 shows box plots of the individual OSM *Highway Types* to visualize the variance in distance travelled in each section.

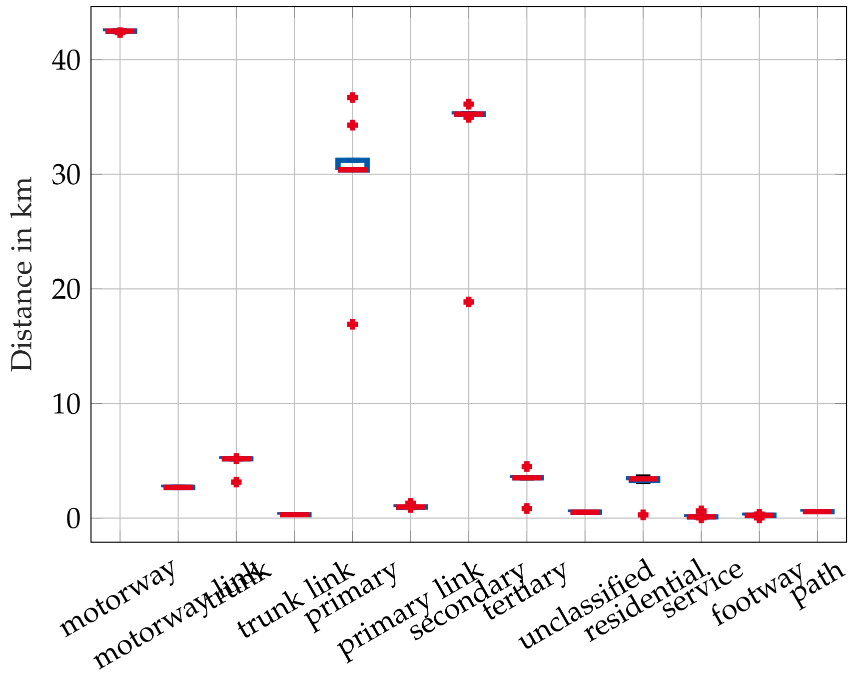

Figure C.1 – Boxplot for the OSM-*Highway Type* Parameters and their distribution for driven distance

Figure E.9 shows box plots of the individual OSM *Highway Types* to visualize the variance in time spent in each section.

Table C.1 – Average distance driven and standard deviation between all 108 test runs in total as well as in each of the thirteen highway categories.

	REL. DISTANCE	ABS. DISTANCE		STD. IN DISTANCE		RELATIVE STD.
total	100.0 %	103.3 km	±	3.4 km	±	3.6 %
motorway	35.6 %	36.8 km	±	0.9 km	±	2.5 %
motorway l.	2.2 %	2.3 km	±	0.1 km	±	4.0 %
trunk	4.1 %	4.2 km	±	0.1 km	±	1.9 %
trunk l.	0.2 %	0.2 km	±	0.0 km	±	1.7 %
primary	23.4 %	24.2 km	±	0.1 km	±	0.3 %
primary l.	0.8 %	0.9 km	±	0.2 km	±	16.6 %
secondary	27.3 %	28.2 km	±	0.2 km	±	0.6 %
tertiary	2.5 %	2.6 km	±	0.0 km	±	0.0 %
unclassified	0.4 %	0.4 km	±	0.0 km	±	1.9 %
residential	2.5 %	2.5 km	±	0.0 km	±	1.6 %
service	0.1 %	0.1 km	±	0.0 km	±	0.2 %
footway	0.2 %	0.2 km	±	0.0 km	±	4.4 %
path	0.5 %	0.5 km	±	0.0 km	±	2.4 %

Part D

APPENDIX D, GLARE PERCEPTION FOR SHORT LIGHT PULSES

D APENNDIX D, GLARE PERCEPTION FOR SHORT LIGHT PULSES

D.1 GLARE PERCEPTION FOR SHORT LIGHT PULSES

Similar to section 5.3 this section is split into two parts, where the data for the influence of duration and intensity on the pupil diameter and the glare perception is listed. The second part shows the data for the influence of the pulse form on the glare perception.

D.1.1 INFLUENCE OF PULSE DURATION AND INTENSITY ON GLARE PERCEPTION AND PUPIL DIAMETER

This section includes all data exceeding the scope of the main part regarding the study to glare perception of short illuminance pulses as described in section 5.3. This includes data for the glare source, the electronic, further information on the glare pulses and the participants. Figure D.1 shows the spectrum of the glare source as measured in an integrating sphere without any filtering. The peak produced by the blue LED and the wide range of illumination procured by the phosphor are clearly visible.

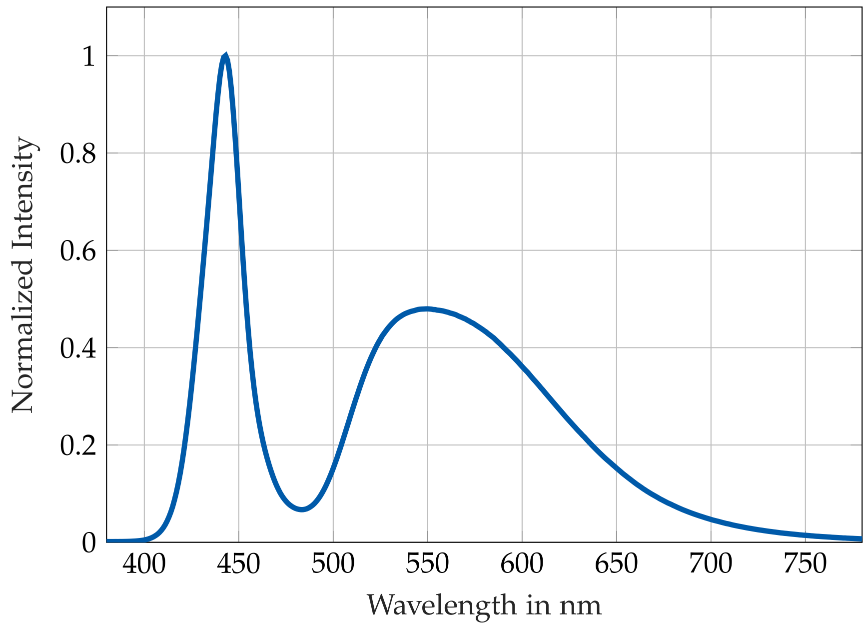

Figure D.1 – Spectrum of the glare LED used in chapter 5.3 without neutral density filter.

As mentioned above, the LED needs to be dimmed down in order to reach the required illuminance values. Since neither constant current regulation, PWM nor a combination of both achieved the desired results, neutral density filters are used to further dim the LED. The spectrum of the glare source after this neutral density filter is shown in figure D.2.

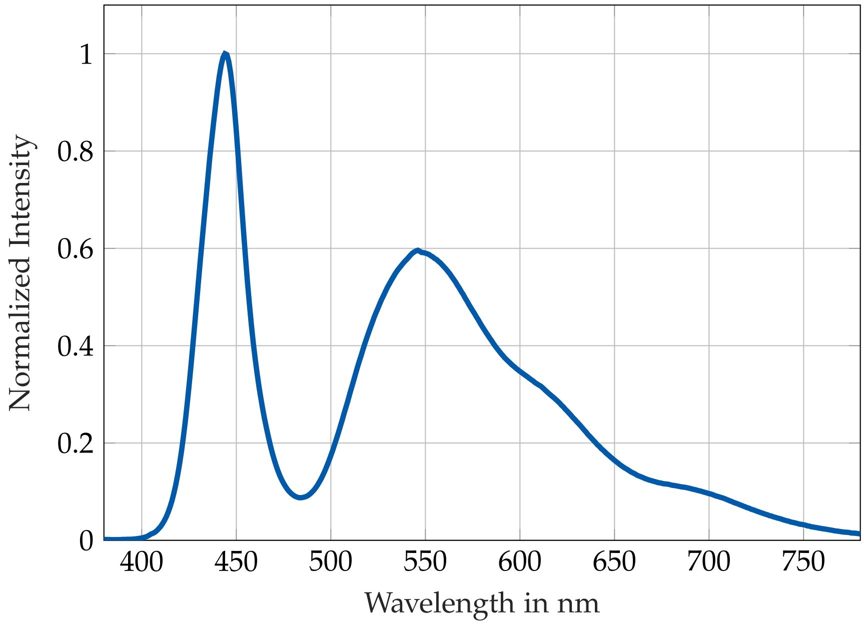

Figure D.2 – Spectrum of the glare LED used in chapter 5.3 with neutral density filter.

Knowing the original spectrum (figure D.1) and the spectrum after the neutral density filter (figure D.2) the transmission spectrum of the filter is calculated. The result is shown in figure D.3. While the transmission is mostly linear and constant between 450 nm to 650 nm, due to the relative low intensities at the outer edges of the spectrum, the measurement produces larger relative errors and thereby sets noise on top of the measurement thereby producing the results seen here. The large maximum at around 720 nm is unexpected, but the absolute effect is minimal as seen when comparing figure D.1 and D.2.

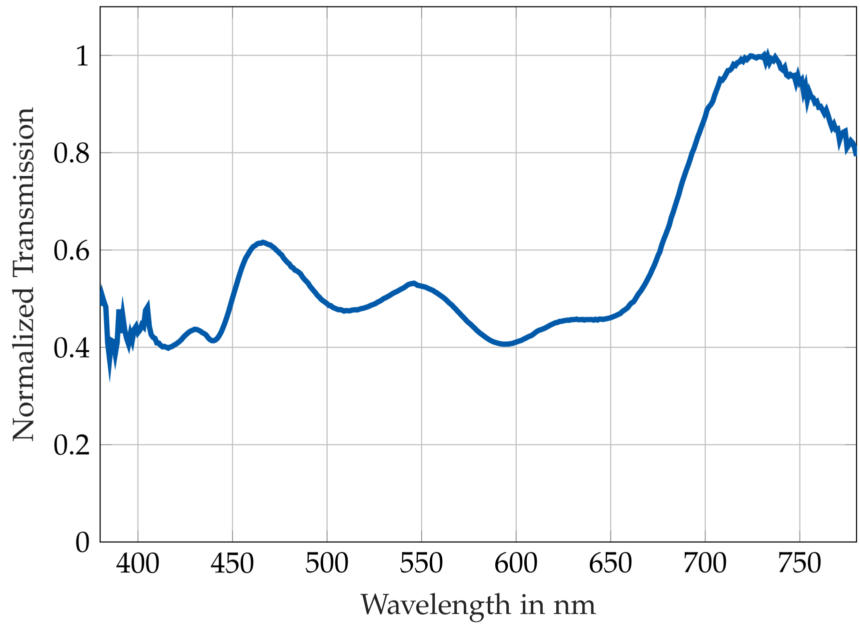

Figure D.3 – Relative transmission of the neutral density filter with an average transmission of 4.4 %

Figure D.4 shows the pupil average pupil size after readapting 20 s after all glare pulses. The fact that, on average all measured pupil diameters are the same shows, that 20 s intervals between the pulses are long enough for the pupil to re-adapt to the dark condition.

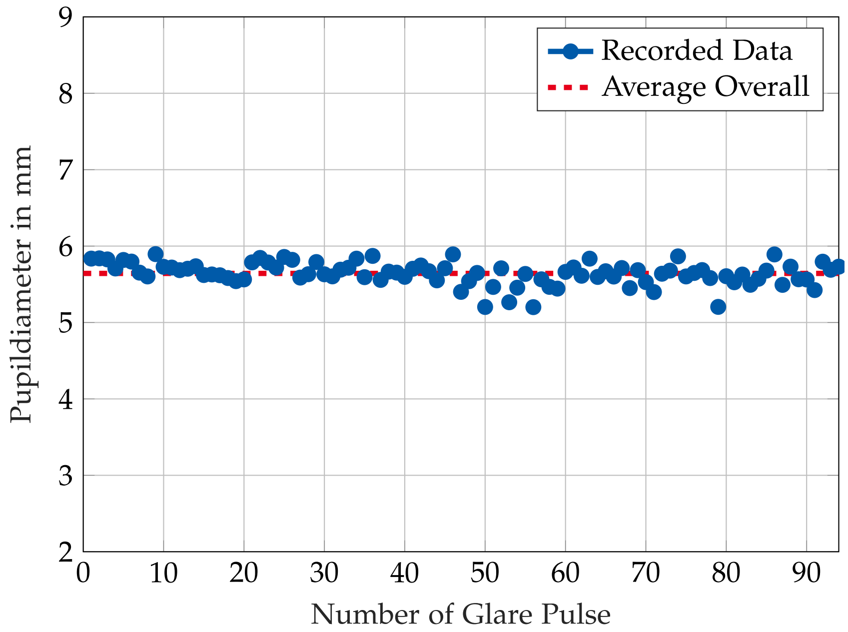

Figure D.4 – Average Pupil Size in mm after 20 s for 94 different light pulses. The solid blue line shows the actual data and the dashed red line shows the mean values over all measurements. The mean pupil diameter is measured at 5.8 mm, standard deviation is 0.2 mm

Table D.1 to D.4 show the detailed pulse data for the first set of pulses for the different pulse durations of 128 ms, 320 ms, 800 ms and 2000 ms.

Table D.1 – The parameters used for the 128 ms glare pulses in order to determine the correlating value between physiological glare, pupil size and photometric values.

DURATION	ILLUMINANNCE	EXPOSURE
128 ms	1.5 lx	0.2 lx s
128 ms	3.4 lx	0.4 lx s
128 ms	8.3 lx	1.1 lx s
128 ms	16.6 lx	2.1 lx s
128 ms	20.5 lx	2.6 lx s
128 ms	42.3 lx	5.4 lx s
128 ms	51.6 lx	6.6 lx s
128 ms	101.6 lx	13.0 lx s

Table D.2 – The parameters used for the 320 ms glare pulses in order to determine the correlating value between physiological glare, pupil size and photometric variables.

DURATION	ILLUMINANNCE	EXPOSURE
320 ms	1.5 lx	0.5 lx s
320 ms	3.4 lx	1.1 lx s
320 ms	8.3 lx	2.7 lx s
320 ms	16.6 lx	5.3 lx s
320 ms	20.5 lx	6.6 lx s
320 ms	42.3 lx	13.5 lx s
320 ms	51.6 lx	16.5 lx s
320 ms	101.6 lx	32.5 lx s

Table D.3 – The parameters used for the 800 ms glare pulses in order to determine the correlating value between physiological glare, pupil size and photometrics.

DURATION	ILLUMINANNCE	EXPOSURE
800 ms	1.5 lx	1.2 lx s
800 ms	3.4 lx	2.7 lx s
800 ms	8.3 lx	6.7 lx s
800 ms	16.6 lx	13.3 lx s
800 ms	20.5 lx	16.4 lx s
800 ms	42.3 lx	33.9 lx s
800 ms	51.6 lx	41.3 lx s
800 ms	101.6 lx	81.3 lx s

Table D.4 – The parameters used for the 2000 ms glare pulses in order to determine the correlating value between physiological glare, pupil size and photometrics.

DURATION	ILLUMINANNCE	EXPOSURE
2000 ms	1.5 lx	3.1 lx s
2000 ms	3.4 lx	6.8 lx s
2000 ms	8.3 lx	16.6 lx s
2000 ms	16.6 lx	33.1 lx s
2000 ms	20.5 lx	4.1 lx s
2000 ms	42.3 lx	84.6 lx s
2000 ms	51.6 lx	103.3 lx s
2000 ms	101.6 lx	203.2 lx s

Figure D.5 visualizes the age distribution of the participants in this study.

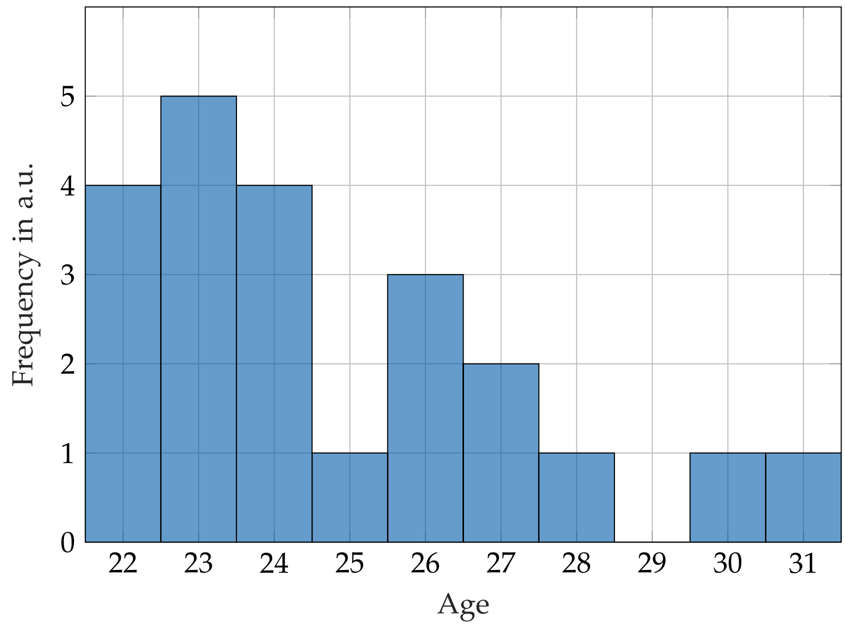

Figure D.5 – Age distribution of the participants for the studies on the correlation between the pupil size and the psychological glare perception.

Table D.5 shows the information of the participants in greater detail.

Table D.5 – Overview over the participants in the glare perception study presented in chapter 5.3 regarding the pulse duration and intensity.

NR	AGE	TIME	IRIS	SHORT SIGHTED	FAR SIGHTED	COLOUR BLIND	GLASSES	WORK
1	23	08:00	blue	-	-	-	-	Student
2	22	16:00	blue	x	-	-	x	Clerk
3	26	17:00	blue	-	-	-	-	Student
4	28	18:00	blue	x	-	-	x	Clerk
5	24	08:50	green	x	-	-	-	Student
6	22	17:00	brown	-	-	-	-	Student
7	23	18:00	green	x	-	-	-	Student
8	24	08:00	green	x	-	-	-	Student
9	22	09:00	brown	-	-	-	-	Student
10	26	16:00	brown	-	-	-	-	Student
11	27	08:15	blue	-	-	-	-	Student
12	24	19:00	blue	-	-	-	-	Student
13	23	08:15	blue	x	-	-	x	Student
14	22	16:00	brown	x	-	-	x	Student
15	22	17:00	brown	x	-	-	x	Student
16	22	08:15	blue	x	-	x	x	Student
17	31	16:00	blue	x	-	-	x	Student
18	23	08:30	blue	x	-	-	x	Student
19	22	16:30	brown	-	-	-	-	Student
20	23	13:15	brown	-	-	-	-	Student
21	24	15:00	blue	-	-	-	-	Student
22	30	16:15	blue	x	-	-	-	Clerk

Figure D.6 shows the ascending absolute pupil diameter for the different recorded photometric values. This data indicates, that only for the exposure a valid correlation is to be expected. This is further investigated in chapter 5.3.

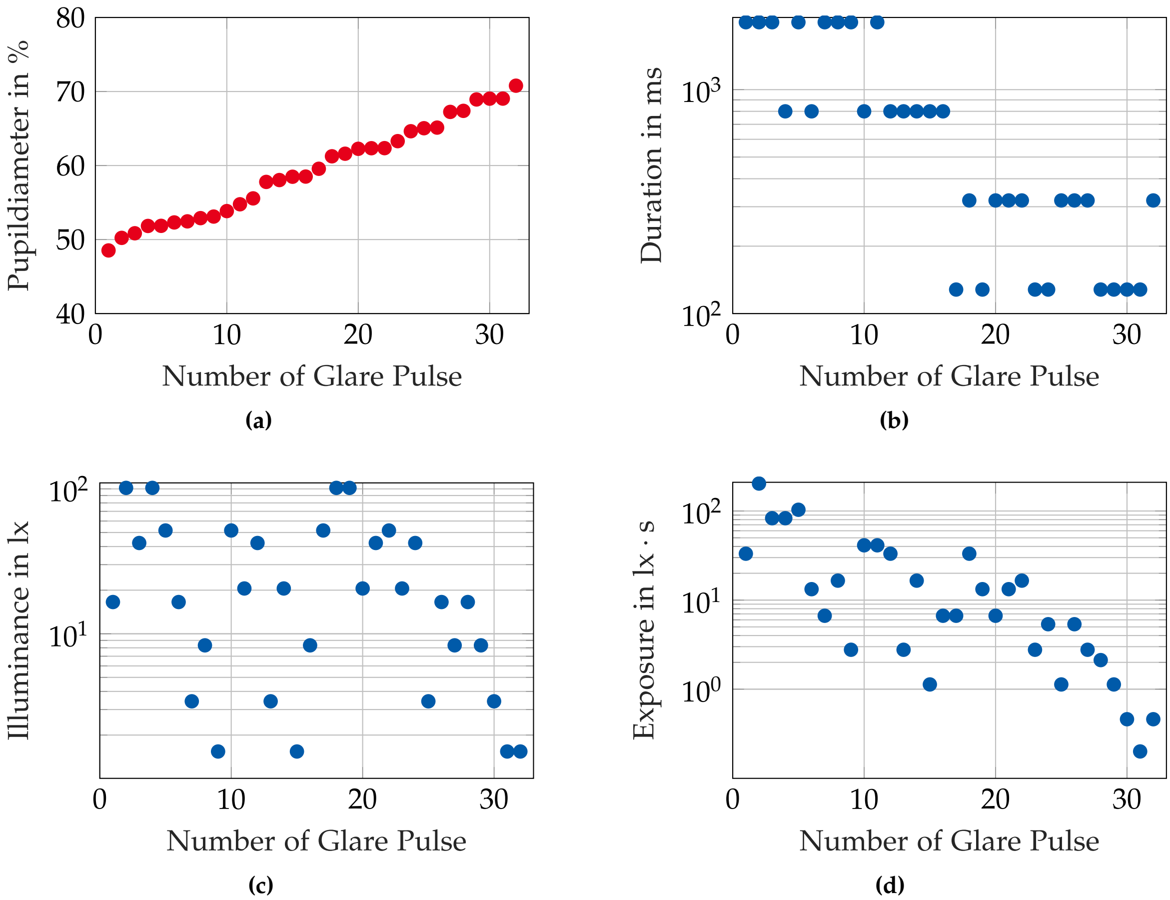

Figure D.6 – Photometric values sorted by ascending normalized minimal pupil diameter as shown in (a). (b) shows the duration, (c) the illuminance, (d) shows the exposure sorted by the pupil Diameter.

Figure D.6a shows the sorted glare pulses for ascending normalized minimal pupil diameter. In figure D.6b the exposure is plotted according to the ascending pupil diameter as seen in figure D.6a and figure D.6c presents the illuminance values for the sorted pupil diameter. While neither of the figures D.6b and D.6c suggest a direct correlation, Figure D.6d shows a possible correlation between relative minimal pupil diameter and the exposure.

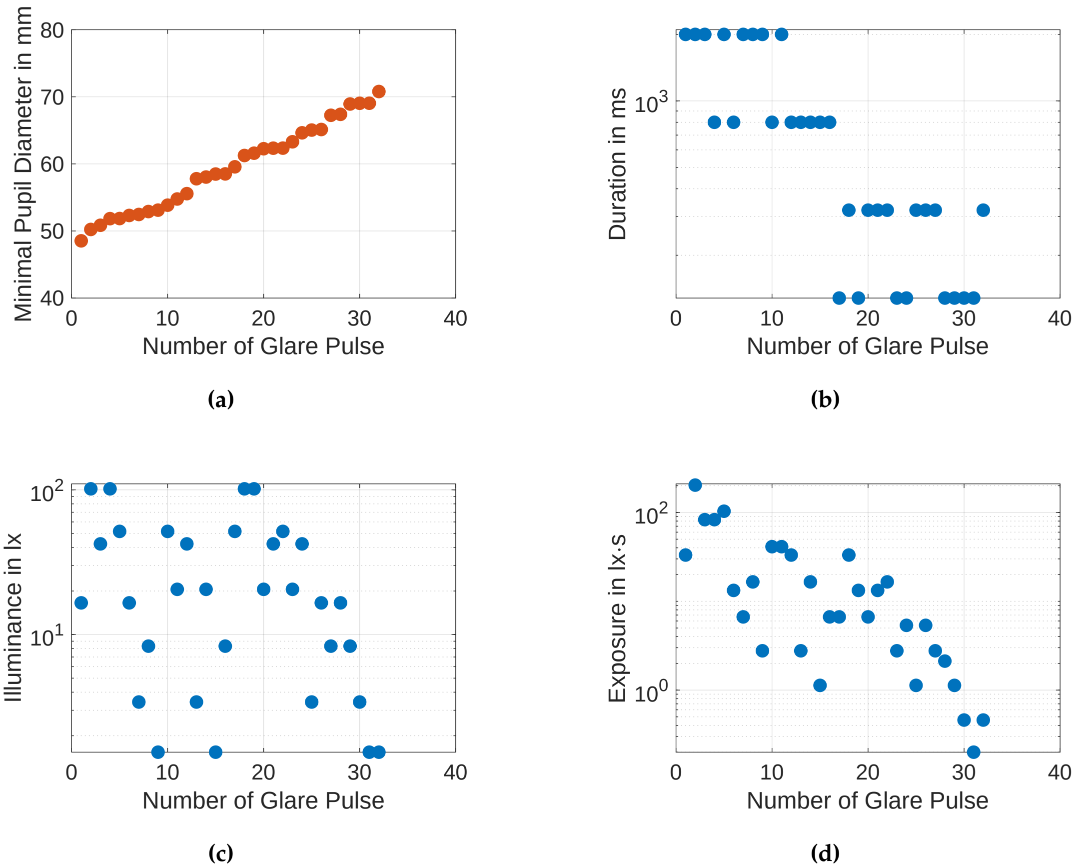

Figure D.7 – Photometric values sorted by ascending absolute minimal pupil diameter as shown in (a). (b) shows the duration, (c) shows the exposure, (d) the illuminance sorted by the pupil Diameter.

Figure D.8 shows the same data, just sorted for the time needed by the pupil to re-adapt to the relaxed pupil diameter. Again, the only possible correlation arises for the exposure. However, the data is much more scattered compared to the absolute or normalized pupil diameter.

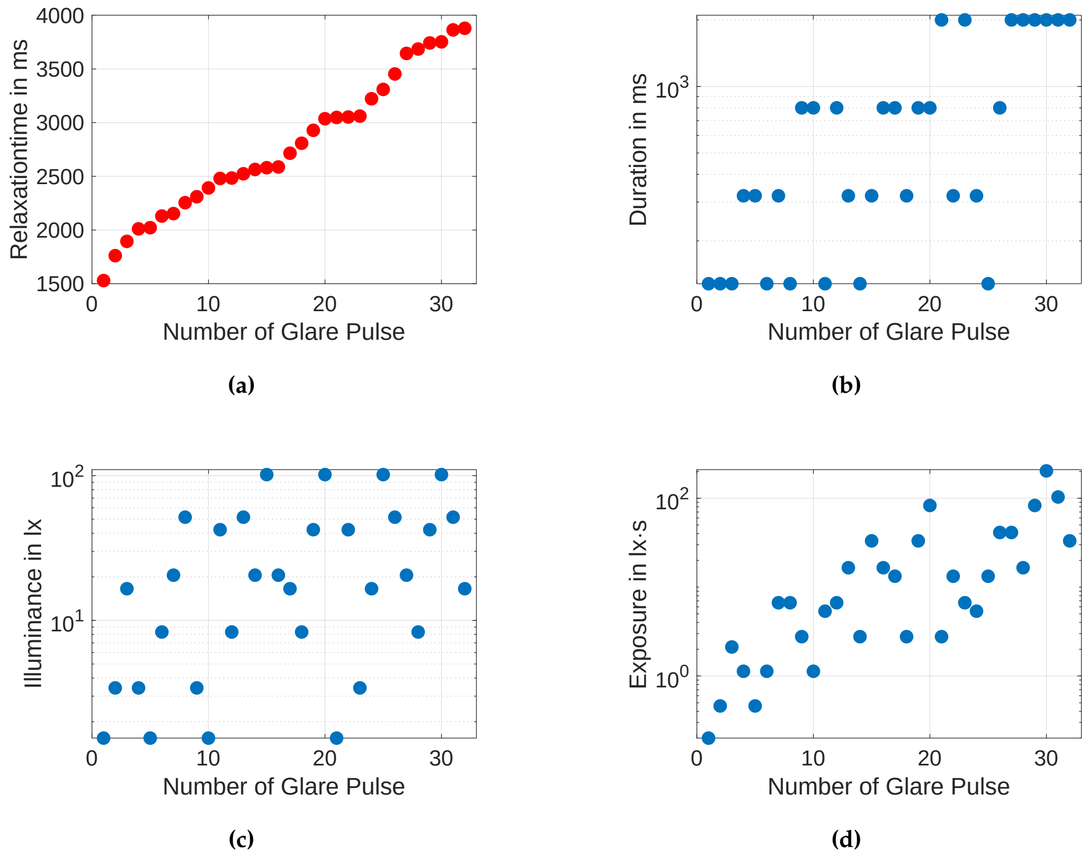

Figure D.8 – Photometric values sorted by ascending relaxation time needed by the pupil to reach 95% of its diameter as shown in (a). (b) shows the duration, (c) shows the exposure, (d) the illuminance sorted by the pupil Diameter.

From the data shown above, the normalized pupil diamter is chosen for further investigation over exposure. The data is fitted for the different durations. Table D.6 shows the statistical quantities for these fits.

Table D.6 – Statistical quantities for the fit functions shown in the equations 5.8a to 5.8c and figure 5.51b and the data visualized in the figures 5.51a.

	$\leq$ 320 ms	800 ms	2000 ms
ΔW	1.12	2.18	3.18
MSE	2.08	15.12	40.96
$\sigma_{\Delta W}$	1.44	3.89	6.40
R^2	0.84	0.86	0.87

The statistical data for the three fit functions shown in equation 5.8 is listed in D.6. The metrics are the same as shown in section 5.1.2 where ΔW is the mean difference between the data and the fit function, the MSE, the standard deviation of ΔW, $\sigma_{\Delta W}$ and the determinition coeffitient R^2.

Since the main metric in this part, is the DE BOER rating, the glare pulses are sorted ascending by glare perception and possible correlation is investigated again for duration, illuminance and exposure. These datasets are shown in figure D.9a to D.9d respectively. It is important to keep in mind, that the inverted DE BOER scale is used and a higher rating represents a higher glare perception.

[t!]

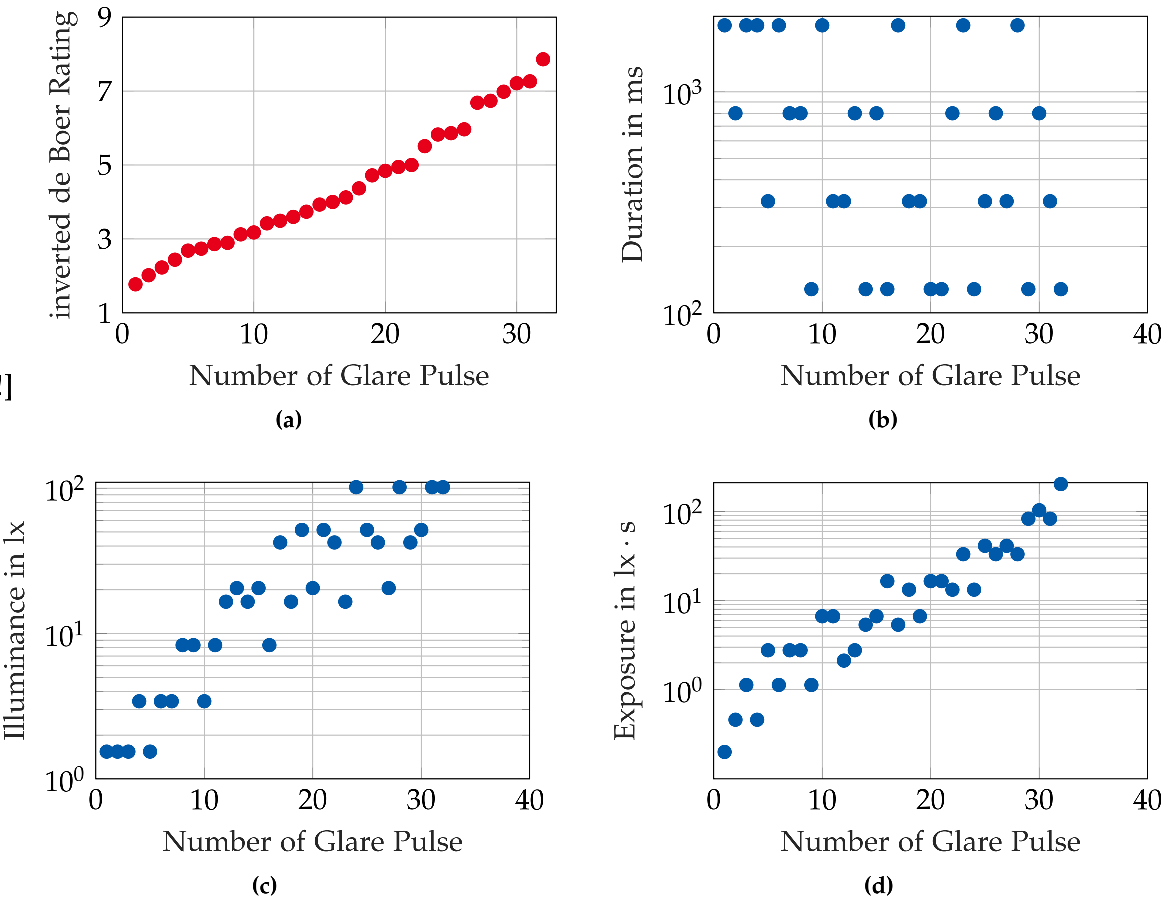

Figure D.9 – Photometric values sorted by ascending glare perception as shown in (a). (b) shows the duration, (c) the illuminance, (d) shows the exposure all sorted by the inverted DE BOER glare rating.

Similar to the data shown above, the data is fitted for the complete data set as well as for the different durations in the main part of this thesis. The statistical quantities are shown in table D.7 and D.8.

Table D.7 – Statistical quantities for the fit functions shown in the equations 5.12a to 5.12d and figure 5.54b and the data visualized in the figures 5.54a.

	128 ms	320 ms	800 ms	2000 ms
ΔW	0.0456	0.1582	0.1566	0.2741
MSE	0.0036	0.0374	0.0307	0.1079
σ_{DeltaW}	0.0415	0.1189	0.0839	0.1935
R^2	0.9985	0.9849	0.9890	0.9604

Table D.9 – Overview over the participants in the glare perception study presented in chapter 5.3 regarding the pulse form

NR	AGE	TIME	IRIS	SHORT SIGHTED	FAR SIGHTED	COLOUR BLIND	GLASSES	WORK
1	22	09:00	blue	-	-	-	-	Student
2	24	13:00	blue	x	-	-	x	Clerk
3	25	07:00	green	-	-	-	-	Student
4	23	10:00	blue	-	-	-	x	Student
5	25	11:00	green	x	-	-	-	Student
6	27	12:00	brown	-	-	x	-	Student
7	24	15:00	green	-	-	-	-	Student
8	27	18:00	green	x	-	-	-	Student
9	23	14:00	brown	-	-	-	-	Clerk
10	25	15:00	brown	-	-	-	-	Student
11	26	15:00	blue	-	-	-	-	Student
12	27	12:00	blue	-	-	-	-	Student
13	28	10:00	brown	x	-	-	x	Student
14	23	11:00	brown	x	-	-	x	Student
15	21	12:00	brown	x	-	-	x	Student
16	23	13:00	brown	x	-	x	x	Student
17	24	13:00	blue	x	-	-	x	Student

Table D.8 – Statistical quantities for the fit functions shown in the equations 5.14a to 5.14c and figure 5.56b and the data visualized in the figures 5.56a.

	$\leq$320 ms	800 ms	2000 ms
ΔW	0.42	0.55	0.60
MSE	0.29	0.41	0.55
$\sigma_{\Delta W}$	0.54	0.64	0.74
R^2	0.88	0.85	0.80

D.1.2 influence of the pulse form on the glare perception

Table D.9 shows the data for the participants in the study.

This data is visualized again in figure D.10.

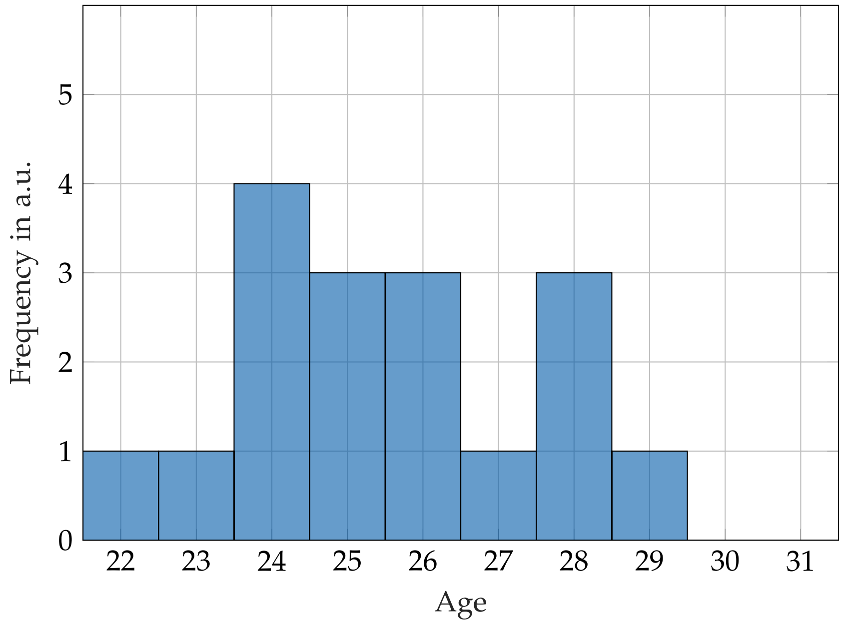

Figure D.10 – Age distribution of the participants for the studies on the correlation between the pulse form and the psychological glare perception.

Table D.10 shows the statistical quantities for the fits for the rectangle pulses in this second study shown in the equations 5.15a to 5.15d and in figure 5.57a.

Table D.10 – Statistical quantities for the fit functions shown in the equations 5.15a to 5.15d and the data visualized in the figure 5.57a.

	300 ms	1200 ms	4800 ms	19 500 ms
ΔW	0.1246	0.0710	0.1838	0.1648
MSE	0.0226	0.0074	0.0422	0.0308
$\sigma_{\Delta W}$	0.0940	0.0541	0.1027	0.0676
R^2	0.9937	0.9985	0.9907	0.9929

The data for the triangle pulses, fitted with the equations 5.16a to 5.16d and shown in figure 5.57b are listed in table D.11.

Table D.11 – Statistical quantities for the fit functions shown in the equations 5.16a to 5.16d and the data visualized in the figure 5.57b.

	600 ms	2400 ms	9600 ms	38 400 ms
ΔW	0.2040	0.2425	0.2389	0.3648
MSE	0.0501	0.0747	0.0737	0.1447
$\sigma_{\Delta W}$	0.1030	0.1440	0.1027	0.1204
R^2	0.9891	0.9829	0.9771	0.9450

After fitting all pulse durations individually, table D.12 shows the data for the fits for the overall data for both pulse sets, rectangle and triangle over the exposure.

Table D.12 – Statistical quantities for the fit functions shown in the equations 5.17a to 5.17b and the data visualized in the figures 5.58a and 5.58b.

	RECTANGLE PULSES	TRIANGLE PULSES
ΔW	0.6107	0.6671
MSE	0.4957	0.6644
$\sigma_{\Delta W}$	0.3595	0.4806
R^2	0.8865	0.8216

Table D.13 shows the data for the fits for the overall data for both pulse sets, rectangle and triangle over the illuminance.

Table D.13 – Statistical quantities for the fit functions shown in the equations 5.18a to 5.18b and the data visualized in the figures 5.59a and 5.59b.

	RECTANGLE PULSES	TRIANGLE PULSES
ΔW	0.180069048505437	0.304350138718858
MSE	0.0481308688357315	0.159134222078472
$\sigma_{\Delta W}$	0.128579307112594	0.264585505312275
R^2	0.988981859927663	0.957280133059497

Table D.14 shows the data for the fits for the overall data for both pulse sets, rectangle and triangle over the optimized exposure for the short pulses.

Table D.14 – Statistical quantities for the fit functions shown in the equations 5.18a to 5.18b and the data visualized in the figures 5.59a and 5.59b.

	RECTANGLE PULSES	TRIANGLE PULSES
ΔW	0.354842762832589	0.304350138990971
MSE	0.175261960194439	0.159134222078473
$\sigma_{\Delta W}$	0.234161800328496	0.264585504982793
R^2	0.959118001597615	0.957280133059497

Part E

APPENDIX E, GAZE BEHAVIOUR IN REAL LIFE DRIVING SITUATIONS

E

Appendix D, Gaze Behaviour in Real Life Driving Situations

This section contains additional data for the test described in the section 5.4. This includes data for the driven course with time spent and distance travelled in each of the categories, participant data and additional gaze and fixation distributions.

E.1 Eye Tracking Setup

This section describes the basic setup for the eye tracking test, including the used light distribution, mechanical mounting, the calibration routine and details on the test participants.

Figure E.1 shows thelight distribution with low and high beam of the test vehicle.

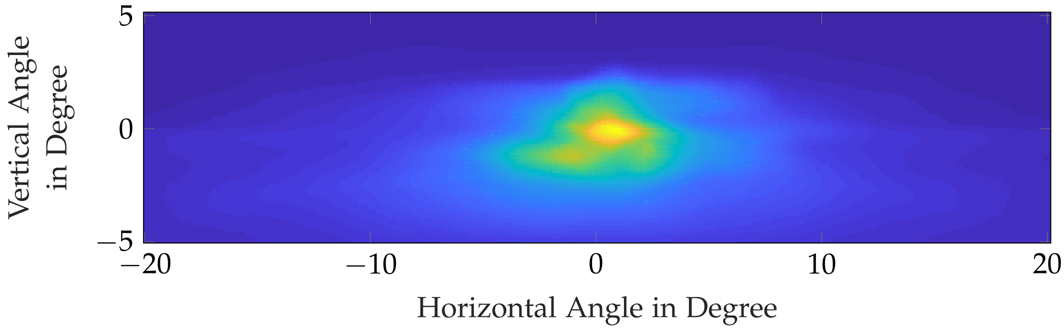

Figure E.1 – Light distribution for low and high beam for the BMW LED headlamps used for the study presented in 5.4. The colour map indicates the recorded luminous intensity under all angles.

For this test, different measurement equipment is used. All equipment is fastened directly to the chassis of the testing vehicle with custom camera mounts. The mounts for the eye tracking camera are shown in figure E.2 and made from solid aluminium to minimize camera movement. A ball bearing is used to allow for angular adjustments for all cameras to fit the cameras to each test subjects needs.

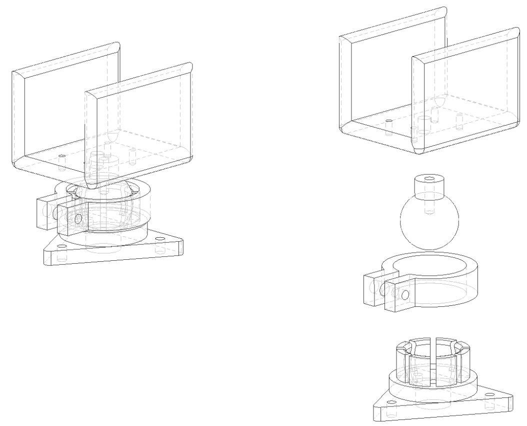

Figure E.2 – Schematic 3D drawing of the custom full aluminium camera mount for the eye tracking cameras. The triangle shaped plate at the bottom is mounted directly to the vehicle chassis. The ball bearing is used to adjust the camera towards each test participant.

The stereo cameras are mounted using the set up shown in figure E.3. The cameras are placed all the way to the sides and the illuminance measurement head is mounted right in the centre.

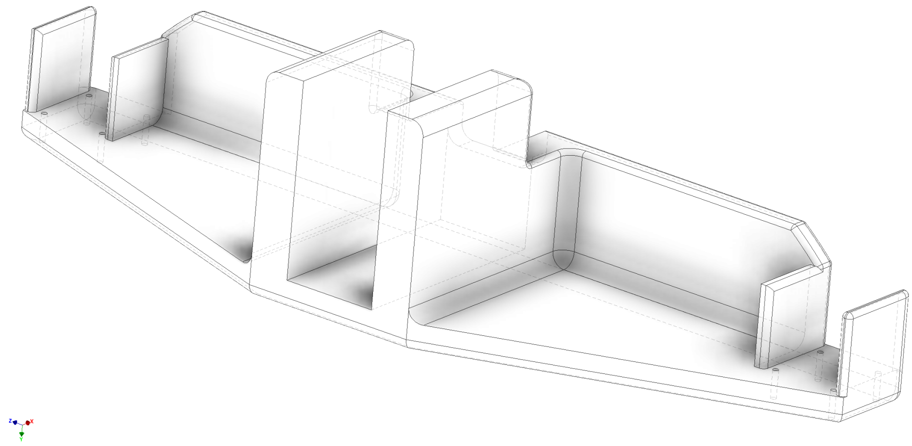

Figure E.3 – Schematic 3D drawing of the custom full aluminium camera mount for the stereo cameras.

For the camera calibration according to SMART EYE, a chessboard with a given square size, is placed in front of all cameras. With the known square size and the recorded distortion of the squares in the camera images, both camera position and orientation can be calculated. This camera calibration is very sensitive to any movement or rotation of the cameras. Therefore, the camera mounts respectively the camera's positions are tested for movement or vibration by measuring the pixel projection between the four cameras using the integrated test software from SMART EYE. This software measures the position of the same chessboard used for the calibration for each camera and then estimates theoretical position of the chessboard on the other camera images, if no movement happened. The theoretical position of the chessboard is then compared to the measured position and the displacement between the two is calculated. SMART EYE recommends a mean pixel displacement error of less than 0.3 for accurate use. Using the constructed mounts, the average pixel displacements measured are 0.17 directly after calibration and after three hours of driving at 0.24.

Since this shows only very limited camera displacement even after a longer test drive, the next step is to set up a global coordinate system, from which all calculated vectors, like head position or gaze direction originate from. This is, again, done using the beforehand measured chessboard. A mounting mechanism positions this chessboard at the exact same position in front of the driver's seat. The centre of the chessboard is then used as the coordinate origin with the x-axis in plane with the road, but perpendicular to the driving direction, showing to the right of the test vehicle, the y-axis showing up, through the roof, and the z-axis showing in driving direction.

Gaze calibration setup for the eye tracking test: A calibration matrix consisting of 6 calibration points is installed at a distance of 6 m from the coordinate origin. This 2 by 3 matrix is shown in figure E.4 where the used calibration points are marked by green circles. Insted of using simple points, a combination of cross-hair and a bullseye in the middle is used to focus the visual attention point to the centre of the dot, this is done in accordance to the work of THALER who shows, that this target generates the most stable fixations for gaze calibrations [189]. 6 calibration points were used after pretests have shown, that 9 or even 18 calibration points lead to worse results and need more repetitions for proper calibration.

Figure E.4 – 2 by 3 calibration matrix with the points P_1 to P_6 in a distance of 6.0 m from the coordinate origin marked by the green circles. Markers are placed on the ground to ensure proper positioning of the testing vehicle before each round.

The exact coordinates in metres for the 6 calibration points are as follows:

$$\vec{P}_1 = \begin{pmatrix} +1.944 \\ +1.034 \\ +6.035 \end{pmatrix} \quad \vec{P}_2 = \begin{pmatrix} -0.185 \\ +1.018 \\ +6.035 \end{pmatrix} \quad \vec{P}_3 = \begin{pmatrix} -2.093 \\ +0.986 \\ +6.325 \end{pmatrix}$$

$$\vec{P}_4 = \begin{pmatrix} +1.915 \\ +0.150 \\ +5.985 \end{pmatrix} \quad \vec{P}_5 = \begin{pmatrix} -0.100 \\ +0.150 \\ +5.985 \end{pmatrix} \quad \vec{P}_6 = \begin{pmatrix} -2.083 \\ +0.150 \\ +5.985 \end{pmatrix}$$

Where the z-vector shows the distance to the wall, the y-axis shows the distance up, perpendicular to the road, and the x-axis represents the directions left and right to the viewing direction. The coordinates are measured using a LASER range finder with an accuracy of 0.1 mm that can be placed onto the mounting mechanism of the chessboard and is thereby places directly into the coordinate origin. The coordinates for the 6 calibration points are transferred to a 3D world model along with the positions of the cameras, the coordinate origin and the positions of the infra red light sources. With this world model, the gaze calibration is performed.

The data for the participants in the test described in section 5.4 is given in E.1. No. gives the anonymous identification number for the subjects, LICENCE shows the year, in which the driver gained his licence. KM/Y indicates the average driven distance per year, GLS shows, if the test subject is wearing any glasses or contact lenses, Acc_L gives the measured accuracy for the left eye in degree, Std_L gives the precision of the left eye in degree, Acc_R gives the accuracy for the right eye in degree, Std_R the precision for the right eye in degree. FT indicates the false-true answers and TF the true-false answers for the attention tests with the indices S indicating the start of each test and E the end of each test.

Table E.1 – Data for the participants in the test described in section 5.4. No. gives the anonymous identification number for each participant, licence indicates the year, the driver's licence was gained, km/y indicates the average driven distance per year, Gls shows, if the test subject is wearing any glasses or contact lenses, Acc_L gives the measured accuracy for the left eye in degree, Std_L gives the precision of the left eye in degree, Acc_R gives the accuracy for the right eye in degree, Std_R the precision for the right eye in degree. FT indicates the false-true answers and TF the true-false answers for the attention tests with the indices S indicating the start of each test and E the end of each test.

1	27	male	2008	2000	x	Day	11.19.17	10:25	13:10	0.60	0.70	6.3	8.9	0	8	2	0
						Night	11.09.17	20:10	22:30	1.6	3.5	1.9	3	1	1	4	4
2	27	male	2008	3000	x	Day	12.09.17	09:05	12:05	3.2	2	1.8	2.2	3	10	4	17
						Night	28.09.17	20:00	22:20	1.9	3.7	2.7	8.7	6	14	5	5
3	30	male	2005	60000	-	Day	12.09.17	13:15	16:00	3.9	3	1.5	0.80	3	12	5	6
						Night	12.09.17	20:15	22:35	2.1	3.5	1.2	2.8	0	6	0	0
4	22	male	2013	10000	x	Day	21.09.17	09:15	11:50	2	3	1.9	3.8	7	6	3	6
						Night	13.09.17	20:25	22:30	3.4	0.40	1.3	1.8	5	11	7	7
5	28	male	2007	1000	-	Day	14.09.17	09:20	12:20	1.8	4.9	3.6	4.7	4	6	4	7
						Night	29.09.17	19:50	22:15	1.5	3.9	1.6	9	6	5	4	4
6	24	male	2009	3000	-	Day	14.09.17	13:15	16:00	1.7	3.4	1.9	4.7	8	8	1	18
						Night	18.09.17	20:15	22:35	0.70	2.7	3.6	3	1	11	1	1
7	27	male	2007	1000	-	Day	18.10.17	12:15	14:45	0.80	1.2	5	5.6	1	6	1	7
						Night	14.09.17	20:10	22:40	1.5	1.6	1.1	1.7	4	16	1	1
8	26	male	2008	12500	-	Day	18.09.17	09:15	12:00	0.90	2.3	1.9	1.4	5	13	7	10
						Night	19.09.17	20:00	22:25	1	0.90	2.5	1.7	6	6	5	5
9	26	male	2008	1000	-	Day	20.09.17	13:10	15:50	1.2	0.80	2.3	5	6	10	3	10
						Night	20.09.17	20:00	22:15	2.4	1.8	2.3	2.2	8	8	3	3
10	28	male	2012	5000	-	Day	02.10.17	09:15	11:45	0.60	0.60	3.2	0.80	1	12	2	10

NO.	AGE	SEX	LICENCE	KM/Y	GLS	DRIVE	DATE	START	END	Acc_L	Std_L	Acc_R	Std_R	FT_S	TF_S	FT_E	TF_E
						Night	21.09.17	20:00	22:35	1.8	1.4	5.8	3.8	2	17	1	1
11	26	male	2008	10000	-	Day	03.10.17	09:20	11:30	1.7	3.6	3.3	8.7	1	4	2	7
						Night	22.09.17	20:15	22:15	0.90	1.8	1.4	1.8	0	6	0	0
12	33	male	2002	1000	x	Day	03.10.17	12:15	14:40	0.10	0.20	1.7	1.1	1	17	4	9
						Night	06.10.17	19:25	21:50	2.2	1.4	2.4	1.2	1	11	0	0
13	26	male	2009	10000	-	Day	09.10.17	12:05	14:35	0.90	1.1	1.3	1	1	7	0	5
						Night	09.10.17	19:30	21:35	0.80	1	1.2	1.8	2	8	2	2
14	30	female	2005	10000	-	Day	12.10.17	09:10	11:40	3.5	2.8	0.90	5.6	3	2	4	3
						Night	10.10.17	20:10	22:30	0.70	1	2	5.2	2	7	3	3
15	26	male	2009	15000	-	Day	12.10.17	13:15	16:55	1	0.80	1.2	2	2	11	4	12
						Night	12.10.17	19:05	21:20	1.7	1.2	1.6	0.90	1	9	2	2
16	29	male	2006	20000	x	Day	16.10.17	09:05	11:50	4.4	6.1	4	4.1	7	7	8	2
						Night	11.12.17	19:05	21:30	1.4	2.5	2.5	1.5	0	24	3	3
17	38	male	1998	6000	-	Day	17.10.17	09:05	11:45	0.70	1.4	7	10.4	2	17	7	13
						Night	24.11.17	19:20	22:10	2.8	4.1	3.1	2.4	1	22	2	2
18	23	male	2011	5000	-	Day	19.10.17	09:10	12:00	1.5	4.4	3.8	7.5	6	6	1	9
						Night	14.11.17	19:30	22:15	2.5	3.1	4.8	3.7	0	17	0	0
19	25	male	2009	19000	-	Day	26.10.17	13:10	16:00	2.4	1.2	5.4	3.3	12	2	11	8
						Night	06.11.17	19:25	22:15	9.4	6.6	7.8	3.2	11	8	10	10
20	21	male	2013	15000	-	Day	27.10.17	13:20	16:20	0.40	1.4	4	7.1	4	7	5	3

NO.	AGE	SEX	LICENCE	KM/Y	GLS	DRIVE	DATE	START	END	ACC_L	STD_L	ACC_R	STD_R	FT_S	TF_S	FT_E	TF_E
						Night	27.10.17	19:00	21:35	1.1	1.1	3	3.3	1	3	2	2
21	29	male	2006	2000	-	Day	06.11.17	13:30	16:20	0.70	1.9	1.2	2.4	9	10	5	7
						Night	08.11.17	19:00	21:30	1.5	0.90	1.7	1.1	4	11	4	4
22	26	male	2011	7000	-	Day	08.11.17	09:10	12:05	2.1	2.1	2.5	6.1	2	7	1	3
						Night	10.11.17	18:30	21:30	7.6	3.8	11.9	6	0	0	0	0
23	31	male	2004	5000	-	Day	09.11.17	08:45	11:45	1.7	1.4	3	5.7	2	15	4	6
						Night	16.11.17	19:00	21:50	2.1	3.7	3.4	5.6	0	18	1	1
24	22	male	2013	1000	-	Day	15.11.17	13:05	15:40	1.8	1.6	2.1	3.4	3	25	0	27
						Night	22.11.17	19:30	21:45	2.6	2.5	2.6	3.9	0	27	2	2
25	21	female	2013	1000	x	Day	20.11.17	13:05	16_00	1.1	0.70	2.2	2.4	3	27	0	27
						Night	15.11.17	19:40	21:25	3.2	3.7	2.2	1.3	0	18	1	1
26	24	male	2011	1000	-	Day	16.11.17	09:00	11:35	1.8	2.3	3.6	6.5	2	24	0	27
						Night	27.11.17	19:40	22:05	2.1	1.8	2.5	3.5	0	11	0	0
27	24	male	2011	1000	-	Day	30.11.17	13:10	16:20	3.4	2	6.1	6.8	3	22	NaN	NaN
						Night	20.11.17	19:50	22:10	2.8	1.5	6.8	10.5	1	23	2	2
28	21	male	2014	1000	-	Day	22.11.17	13:25	16:10	4.7	4.3	2.4	2.6	0	10	0	15
						Night	25.01.18	19:30	21:50	3.9	4.2	8.1	6	0	0	0	0
29	22	female	2009	5000	-	Day	24.11.17	09:15	11:45	2.8	4.5	2.1	3.3	4	26	0	23
						Night	28.11.17	19:10	21:30	5	6.3	4.6	2.4	0	26	0	0
30	19	male	2015	6000	-	Day	06.12.17	09:15	11:50	2.6	3.4	3.1	2.3	1	21	0	22

NO.	AGE	SEX	LICENCE	KM/Y	GLS	DRIVE	DATE	START	END	Acc_L	Std_L	Acc_R	Std_R	FT_S	TF_S	FT_E	TF_E
						Night	13.12.17	19:35	22:00	4.7	5.1	13.6	9.5	1	26	1	1
31	26	female	2008	1200	-	Day	04.12.17	13:30	16:20	4.1	2.4	2.9	3.6	0	23	0	26
						Night	06.12.17	19:55	22:15	3.3	1.5	2.6	0.30	0	19	0	0
32	23	male	2012	10000	-	Day	28.11.17	09:10	12:10	2.6	2.9	1.6	2.4	0	25	0	17
						Night	29.11.17	19:00	22:15	2.7	3.7	3.6	3	0	26	1	1
33	21	female	2013	5000	x	Day	29.11.17	09:15	12:10	4.7	4.7	5.4	3.2	0	26	2	13
						Night	30.11.17	19:20	21:55	7.1	5.8	4.4	3.6	0	6	1	1
34	19	male	2015	10000	-	Day	12.12.17	09:10	11:35	6.8	0.40	6.3	10.2	0	26	2	9
						Night	01.12.17	19:15	22:05	2.3	3.4	3.3	2.6	1	26	0	0
35	26	male	2009	6000	x	Day	08.12.17	13:00	16:00	5.6	4.7	2.9	4	1	16	0	26
						Night	04.12.17	19:35	22:05	1.8	1.5	3.1	5.3	1	21	1	1
36	25	male	2011	5000	-	Day	11.12.17	13:15	16:35	1.1	4.1	2.6	5.1	2	26	4	22
						Night	12.12.17	19:35	22:00	1.6	1.6	2.5	4.8	1	23		
37	26	male	2009	1000	x	Day	13.12.17	09:10	11:50	5.3	5.9	3.2	1.6	1	26	2	20
						Night	14.12.17	19:25	22:05	4.7	1.6	7.2	5.6	0	8	2	2
38	19	male	2015	2000	-	Day	14.12.17	09:00	12:00	5.9	3.2	6.1	6.9	2	14	1	14
						Night	26.01.18	19:30	21:50	6.2	5.9	5.5	11.6	2	0	1	1
39	21	male	2013	12000	-	Day	29.01.18	09:10	11:55	1.6	1.5	3.2	4.1	4	2	5	0
						Night	18.12.17	19:44	22:12	2.2	1.3	4.2	4.2	5	4	1	1
40	26	male	2008	1000	x	Day	19.12.17	09:35	12:25	15	1.4	4.6	4.5	1	4	2	5

NO.	AGE	SEX	LICENCE	KM/Y	GLS	DRIVE	DATE	START	END	Acc_L	Std_L	Acc_R	Std_R	FT_S	TF_S	FT_E	TF_E
						Night	21.12.17	19:05	21:30	9.6	3.3	10.4	5.7	2	3	1	1
41	19	male	2015	1000	-	Day	21.12.17	12:55	15:40	3.1	3.8	2.8	4.2	0	3	1	7
						Night	19.12.17	19:45	22:10	6.4	5.6	7.7	2.7	1	3	1	1
42	23	male	2011	1000	-	Day	20.12.17	13:15	16:00	1.5	2.7	4.2	9.1	3	6	2	7
						Night	19.01.18	19:45	22:05	1.7	1.1	3.2	2.4	3	3	2	2
43	24	male	2010	1200	x	Day	19.01.18	08:45	11:10	4.7	6	6.3	3.9	4	5	3	2
						Night	18.01.18	19:40	21:50	7.4	5.8	3.2	4	7	5	7	7
44	27	male	2007	10000	x	Day	30.01.18	09:00	11:35	1.4	1.9	2.2	3.4	4	4	0	1
						Night	29.01.18	19:45	22:00	2.4	3.2	1.8	3.2	7	5	8	8
45	27	female	2009	2500	-	Day	22.01.18	09:20	12:05	6.8	10.6	1.5	2.6	6	11	3	6
						Night	22.02.18	19:45	22:15	7.9	3.4	5.6	8.9	7	5	6	6
46	23	female	2011	30000	-	Day	23.02.18	12:55	15:30	4.9	5.3	6.9	6.9	4	2	3	7
						Night	02.02.18	19:45	22:15	1.3	1.1	8.1	8.4	4	2	8	8
47	25	male	2008	1000	-	Day	07.02.18	13:15	15:50	3.7	3.7	4	5.1	2	4	0	4
						Night	16.02.18	19:40	21:50	2.7	0.60	3	1.8	1	1	3	3
48	20	male	2014	5000	-	Day	25.01.18	13:10	15:55	2.8	4.4	2.8	7.3	5	3	4	2
						Night	05.02.18	19:45	22:00	0.90	2.1	3	10.2	0	0	0	0
49	19	female	2014	1500	-	Day	16.02.18	09:05	11:35	2.2	2.4	1.4	2.4	2	2	NaN	NaN
						Night	07.02.18	19:40	22:05	1.8	2.9	5.9	3.3	4	7	2	2
50	25	female	2009	8000	x	Day	24.01.18	09:15	11:40	5.8	7	5	2.4	2	6	0	5

NO.	AGE	SEX	LICENCE	KM/Y	GLS	DRIVE	DATE	START	END	Acc_L	Std_L	Acc_R	Std_R	FT_S	TF_S	FT_E	TF_E
						Night	30.01.18	19:10	21:25	1.8	3.5	7.2	5.4	1	0	1	1
51	20	male	2014	1000	-	Day	02.02.18	09:10	11:45	2.2	6	2.1	4.1	1	1	1	2
						Night	01.02.18	19:35	21:55	2.9	3.2	2	3.9	0	2	0	0
52	20	male	2015	5000	x	Day	19.02.18	09:15	11:45	1.2	0.50	6.7	8	2	0	1	0
						Night	26.02.18	19:50	22:10	2	4.2	1.3	2.8	0	1	0	0
53	22	male	2013	20000	-	Day	09.02.18	09:20	11:50	1.6	2	1.6	6.1	2	1	1	1
						Night	13.02.18	19:45	21:55	3.3	5.1	1.8	7.6	3	1	0	0
54	21	male	2014	10000	-	Day	21.02.18	09:05	11:45	2.8	4	4.9	6.6	1	2	3	1
						Night	19.02.18	19:30	21:45	1	2.8	0.90	2.7	2	1	1	1

E.5a shows the age distribution as a histogram. The driving experience is visualized in figure E.5b where the histogram of the average distance driven per year for all participants is shown.

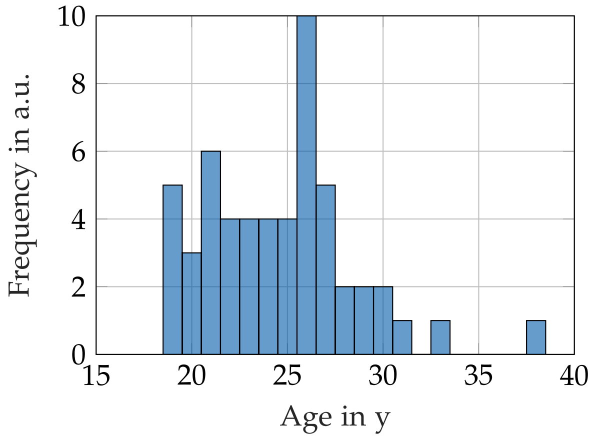

(a)

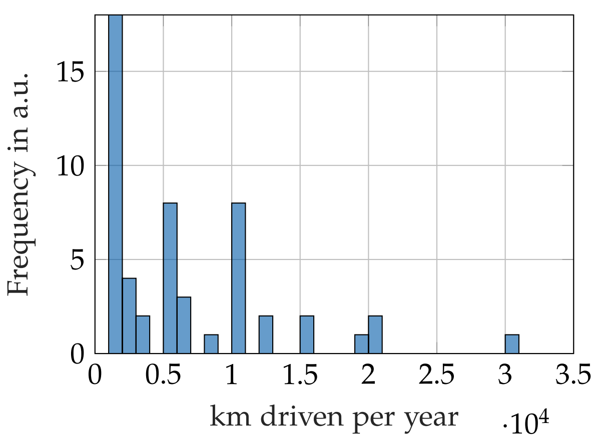

(b)

Figure E.5 – Overview over the driver's data with the age distribution shown in (a) and the average distance driven for all participants shown in (b).

The absolute distribution of all errors in the attention test before (blue) and after the drive (red) are shown in figure E.6a, and E.6b where the same data is visualized in box plots.

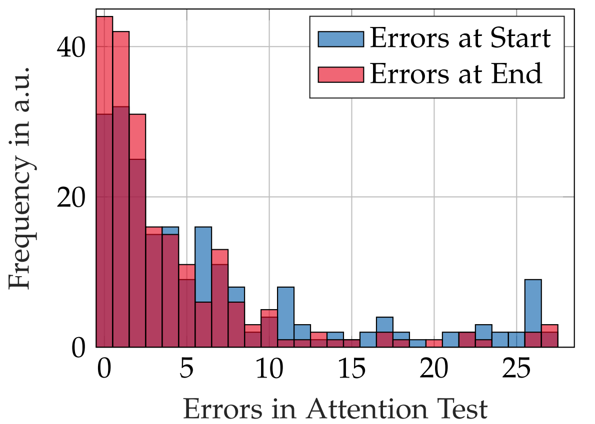

(a)

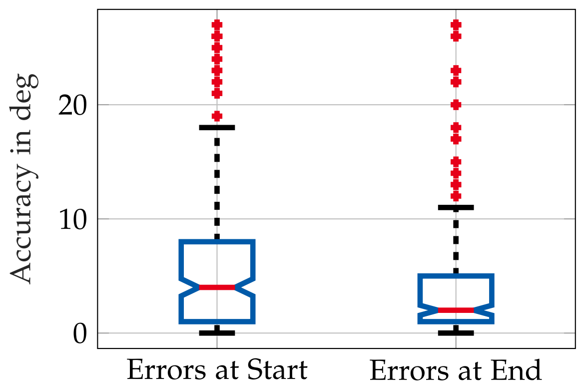

(b)

Figure E.6 – Error data before and after the test drives. (a) shows the absolute error distribution, where the errors made before the test drive is shown in blue and the errors made after the drive are shown in red. (b) shows the same data in form of box plots. The median for the errors before the test drives is 4 errors and only 2 errors after the drive.

The histogram for the accuracy is shown in figure E.7a for both, left and right eye. The left eye is marked in blue and the right eye is marked in red. The same data is visualized in box plots in figure E.7b. The median for the left eye is recorded to be 1.1° and the median for the right eye is recorded to be 1.5°. The smallest accuracy recorded is at 0.1° for the left eye and the maximum accuracy is recorded at 7.5° for the left eye as well. The distributions of both left and right eye are not significantly different. It needs to be mentioned, that the data from left and right eye do not necessary correlate, meaning that high accuracy values for one eye does not necessarily relate to similar values on the other eye.

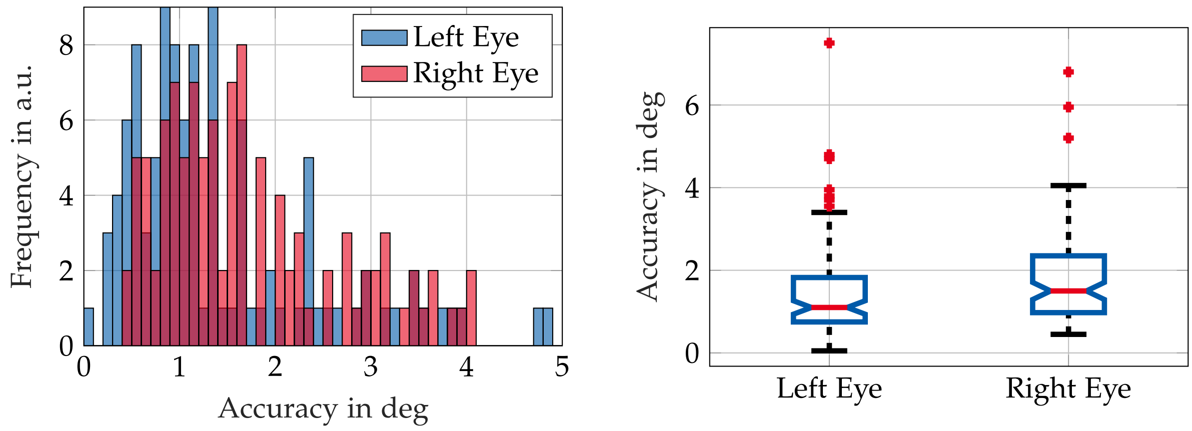

(a) (b)

Figure E.7 – The accuracy distribution over all 104 test drives is shown as a histogram in (a) for the left (blue) and the right eye (red) separately and as box plots in (b).

The data for the precession - calculated as the standard deviation of the recorded gaze directions - is shown in figures E.8a as a histogram with blue bars showing the data for the left eye and the red bars showing the data for the right eye, and as a box plot in E.8b. Again both datasets are not significantly different even though the data for the right eye is in general worse when compared to the left eye. The median values read out to 1.4° for left and 1.9° for the right eye data. The minimal precission is measured at 0.1° for the left eye and the maximum precission is recorded at 5.8° for the right eye.

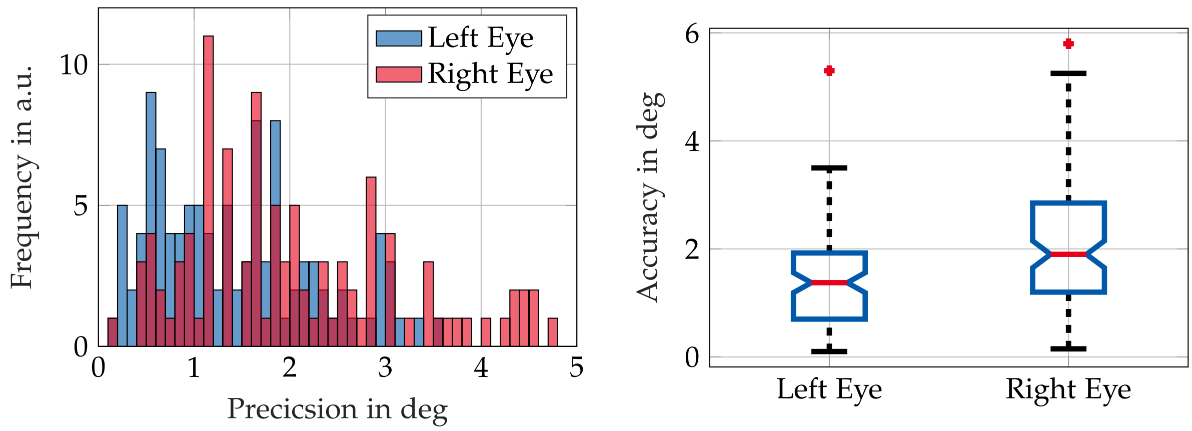

(a) (b)

Figure E.8 – The precision distribution over all 104 test drives is shown as a histogram in (a) separately for the left (blue) and the right eye (red) and as a box plot in (b).

E.2 EYE TRACKING ROUTE

The difference between the times spent in each category for the individual runs, as explained above, originates from the different driven velocities due to different traffic volume, weather and driver experience and personality. The distance per category and their deviations, found in the appendix E.2 in table E.3.

Table E.2 – Average time driven and standard deviation between all 108 test runs in total as well as in each of the thirteen road categories calculated for all 54 participants test-runs.

	REL. TIME SPENT	ABS. TIME SPENT				STD. IN TIME			RELATIVE STD.
total	100.0 %	2 h	38 min	41 s	±	33 min	22 s	±	21.0 %
motorway	12.2 %		20 min	18 s	±		40 s	±	3.4 %
motorway l.	1.5 %		2 min	26 s	±		4 s	±	2.7 %
trunk	2.2 %		3 min	41 s	±		4 s	±	2.0 %
trunk l.	0.1 %			13 s	±		0 s	±	7.4 %
primary	22.5 %		35 min	30 s	±	4 min	15 s	±	12.0 %
primary l.	0.8 %		1 min	6 s	±		3 s	±	5.6 %
secondary	25.8 %		41 min	1 s	±	4 min	39 s	±	11.4 %
tertiary	3.6 %		5 min	57 s	±		56 s	±	15.8 %
unclassified	0.6 %			51 s	±		5 s	±	10.6 %
residential	4.7 %		7 min	,16 s	±		34 s	±	7.8 %
service	0.2 %			12 s	±		2 s	±	18.2 %
footway	1.4 %		2 min	0 s	±		2 s	±	2.3 %
path	0.4 %			33 s	±		4 s	±	12.1 %

The parameters available through OSM are:

- **OSM-ID:** Contains the ID *ways*
- **OSM-Latitude:** Latitude coordinate of the centre point of the *way*
- **OSM-Longitude:** Longitude coordinate of the centre point of the *way*
- **OSM-Reference:** Gives the Combination of the street identifiers and numbers for larger roads in Germany. E.g. A5 (Autobahn 5), B26 (Bundesstraße 26),K818 (Kreisstraße 818) or L3004 (Landstraße 3004)
- **OSM-Highway Type:** Categorizes the road in 14 different road types, ranging from service residential roads, to motorways
- **OSM-Speed Limit:** Gives the known speed limit in $\mathrm{km\,h^{-1}}$
- **OSM-Lanes:** Gives the number of lanes available in total. Exception: Motorways with separated lanes in each direction - here both lanes are represented as and the lane number is given for each direction individually
- **OSM-Surface:** Gives the type of surface for this particular stretch of road. E.g. asphalt, concrete or paved

- **OSM-Smoothness:** Describes the level of smoothness for the given stretch of road in a describing manner
- **OSM-City:** If the *way* is located inside the city limits of a larger city, this gives the city name
- **OSM-Oneway:** Describes, if the road is a one-way street
- **OSM-Construction:** Indicates if the road is under construction at the time of database request
- **OSM-Bridge:** Indicates if the *way* is located on a bridge
- **OSM-Cycleway:** Indicates if a cycleway is available, and if at which position the cycleway is located

The key **OSM-Highway Type** split into the 13 different highway sub-categories.

- **motorway:** A restricted access major divided motorway, normally with 2 or more running lanes plus emergency hard shoulder. Equivalent to the Freeway, Autobahn, etc..
- **motorway link:** The link roads (sliproads/ramps) leading to/from a motorway from/to a motorway or lower class motorway. Normally with the same motorway restrictions.
- **trunk:** The most important roads in a country's system that aren't motorways. (Need not necessarily be a divided motorway.)
- **trunk link:** The link roads (sliproads/ramps) leading to/from a trunk road from/to a trunk road or lower class motorway.
- **primary:** The next most important roads in a country's system. (Often link larger towns.)
- **primary link:** The link roads (sliproads/ramps) leading to/from a primary road from/to a primary road or lower class motorway.
- **secondary:** The next most important roads in a country's system. (Often link towns.)
- **tertiary:** The next most important roads in a country's system. (Often link smaller towns and villages)
- **unclassified:** The least most important through roads in a country's system – i.e. minor roads of a lower classification than tertiary, but which serve a purpose other than access to properties. Often link villages and hamlets. (The word 'unclassified' is a historical artefact of the UK road system and does not mean that the classification is unknown [...])
- **residential:** Roads which serve as an access to housing, without function of connecting settlements. Often lined with housing.
- **service:** For access roads to, or within an industrial estate, camp site, business park, car park etc. Can be used in conjunction with service=* to indicate the type of usage and with access=* to indicate who can use it and in what circumstances.

- **footway:** For designated footpaths; i.e., mainly/exclusively for pedestrians. This includes walking tracks and gravel paths. If bicycles are allowed as well, you can indicate this by adding a bicycle=yes tag. Should not be used for paths where the primary or intended usage is unknown. Use motorway=pedestrian for pedestrianised roads in shopping or residential areas and motorway=track if it is usable by agricultural or similar vehicles.

- **path:** A non-specific path. Use motorway=footway for paths mainly for walkers, motorway=cycleway for one also usable by cyclists, motorway=bridleway for ones available to horses as well as walkers and motorway=track for ones which is passable by agriculture or similar vehicles.

Table E.2 shows, that the main road categories are motorways, primary roads and secondary roads with total time of 61.0 %. However, these categories alone are not enough to merge the data into the selected bins since in larger cities, it is possible for a primary or secondary road, to be inside the city limits. Therefore, more of the named parameters have to be accessed for a complete grouping of the data. However the main parameter will, for all categories be the road type but further auxiliary conditions are used to define the complete set of matching rules. For each of the three main categories, multiple matching rules were selected.

Table E.3 – Average distance driven and standard deviation between all 108 test runs in total as well as in each of the thirteen road categories.

	REL. DISTANCE	ABS. DISTANCE		STD. IN DISTANCE		RELATIVE STD.
total	100.0 %	103.3 km	±	3.4 km	±	3.6 %
motorway	35.6 %	36.8 km	±	0.9 km	±	2.5 %
motorway l.	2.2 %	2.3 km	±	0.1 km	±	4.0 %
trunk	4.1 %	4.2 km	±	0.1 km	±	1.9 %
trunk l.	0.2 %	0.2 km	±	0.0 km	±	1.7 %
primary	23.4 %	24.2 km	±	0.1 km	±	0.3 %
primary l.	0.8 %	0.9 km	±	0.2 km	±	16.6 %
secondary	27.3 %	28.2 km	±	0.2 km	±	0.6 %
tertiary	2.5 %	2.6 km	±	0.0 km	±	0.0 %
unclassified	0.4 %	0.4 km	±	0.0 km	±	1.9 %
residential	2.5 %	2.5 km	±	0.0 km	±	1.6 %
service	0.1 %	0.1 km	±	0.0 km	±	0.2 %
footway	0.2 %	0.2 km	±	0.0 km	±	4.4 %
path	0.5 %	0.5 km	±	0.0 km	±	2.4 %

This is visualized in figure E.9 again as box plots for all different road categories.

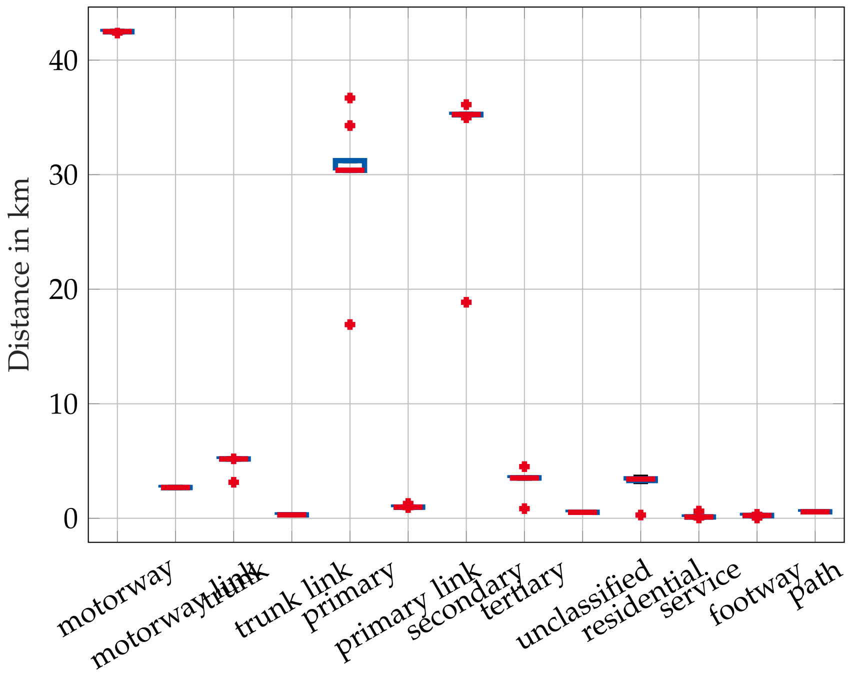

Figure E.9 – Boxplot for the OSM-*Highway Type* Parameters and their distribution for driven distance

Figure E.9 shows box plots of the individual OSM *Highway Types* to visualize the variance in time spent in each section.

Using the schema explained in the main part in section 5.4, the data is grouped into three main road categories. Urban roads, country roads and motorways. The distance driven in each category is listed in table E.4.

Table E.4 – Average distance driven and standard deviation between all 108 test runs for the three major road categories.

	REL. DISTANCE	ABS. DISTANCE		STD. IN DISTANCE		RELATIVE STD.
Urban Roads	25.9 %	26.6 km	±	11.4 km	±	42.8 %
Country Roads	34.4 %	33.4 km	±	13.4 km	±	40.0 %
Motorways	41.7 %	42.8 km	±	15.1 km	±	35.4 %

For the analysis of the different speed limits available on the course, the data is split into the different groups as shown in table E.5.

Table E.5 – Average time spent and distance travelled within the given speed limits over all test subjects over the 108 test runs.

SPEED LIMIT	TIME SPENT					DISTANCE TRAVELLED		
$30\,\mathrm{km\,h^{-1}}$	6 min	45 s	±	3 min	27 s	3.6 km	±	1.4 km
$50\,\mathrm{km\,h^{-1}}$	51 min	19 s	±	19 min	54 s	28.1 km	±	9.9 km
$60\,\mathrm{km\,h^{-1}}$	8 min	5 s	±	2 min	24 s	8.6 km	±	2.8 km
$70\,\mathrm{km\,h^{-1}}$	5 min	44 s	±	3 min	1 s	5.6 km	±	2.4 km
$80\,\mathrm{km\,h^{-1}}$	9 min	27 s	±	1 min	49 s	11.5 km	±	4.1 km
$100\,\mathrm{km\,h^{-1}}$	9 min	32 s	±	2 min	43 s	14.5 km	±	5.3 km
$120\,\mathrm{km\,h^{-1}}$	0 min	33 s	±	0 min	29 s	<1 km	±	0.3 km
$130\,\mathrm{km\,h^{-1}}$	3 min	58 s	±	3 min	37 s	1.6 km	±	0.6 km
none	18 min	12 s	±	5 min	4 s	36.3 km	±	12.6 km

Since the speed limit does not necessary account for the actual driven speed, the average speed driven in the different road categories is listed in table E.6.

Table E.6 – Median as well as the standard deviation of the actual driven speed for the three major road categories split up by day- and night-time driving as shown in figure 5.71.

	URBAN ROADS		COUNTRY ROADS		HIGHWAYS	
	DAY	NIGHT	DAY	NIGHT	DAY	NIGHT
MEDIAN	$24.9\,\mathrm{km\,h^{-1}}$	$31.6\,\mathrm{km\,h^{-1}}$	$61.2\,\mathrm{km\,h^{-1}}$	$63.8\,\mathrm{km\,h^{-1}}$	$100.3\,\mathrm{km\,h^{-1}}$	$99.5\,\mathrm{km\,h^{-1}}$
STD	$19.8\,\mathrm{km\,h^{-1}}$	$19.3\,\mathrm{km\,h^{-1}}$	$23.8\,\mathrm{km\,h^{-1}}$	$21.3\,\mathrm{km\,h^{-1}}$	$33.4\,\mathrm{km\,h^{-1}}$	$38.1\,\mathrm{km\,h^{-1}}$

E.3 REAL LIFE PUPIL ANALYSIS

Figure E.10 shows this raw data for the test drives during the day. The colour coding is kept identical to the colour coding before. Blue bars represent the data from urban roads, red bars show the data from country road driving and yellow bars indicate the data from motorways. Since figure 5.72 already shows very similar illuminance values for the three categories, very similar values for the pupil diameter are to be expected. All data sets are normalized and tested for normal distribution using the One Sample Kolmogorov-Smirnov test and the results are similar to the results for the illuminance data. For all data sets, the null hypothesis, that the data originates from normal distributions, is rejected. This is directly visible from the histograms shown. All three distributions are skewed to the right and motorway and country road data even has small ditches in the distribution.

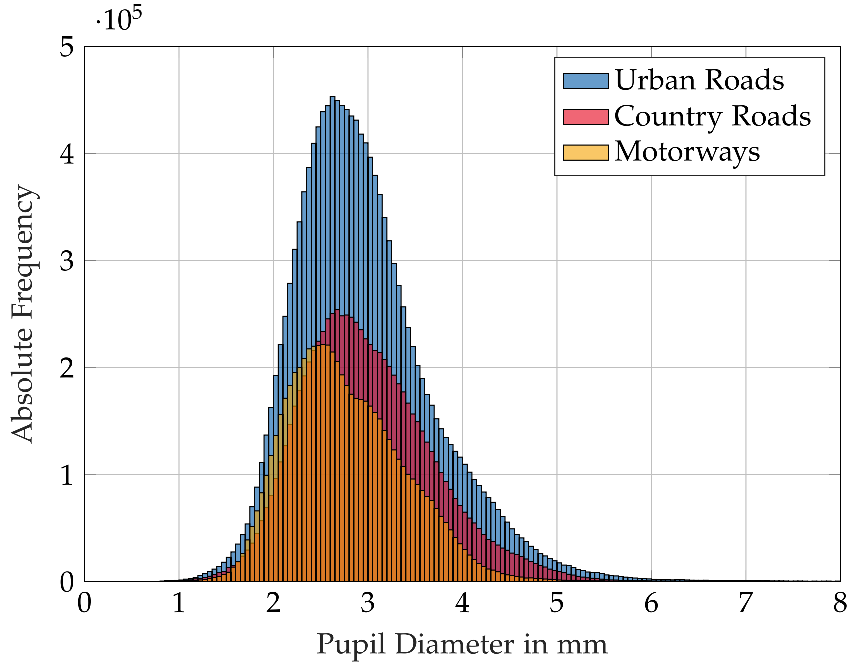

Figure E.10 – Pupil diameter in mm for the three major road categories during the day. Pupil diameter on urban roads is marked by blue bars, data recorded on country roads is indicated by yellow bars and red bars show the data recorded on motorways.

The data from figure E.10 leads to a median pupil diameter of (2.80 ± 1.23) mm during the day. The data from the three road categories is summarized in table E.7. Using a Whitney-Mann-U-Test on all distributions, reveals, that the three data sets are significantly different and originate from different distributions. However, since all median values, as well as the standard deviations and the distributions shown in figure E.10 show a large overlap, a qq-plot is calculated between all data sets. This is shown for every 10000th data point, to keep the figure as uncluttered as possible, in figure E.11. While the qq-plot in figure E.11 tested the data sets on normal distributions, the qq-plot here shows the quantiles of two different data sets over each other. If the data is set on a straight line, it can be assumed, that the two data sets originate from the same distribution. In figure E.11 all data sets are tested if they originate from the same distributions. Blue shows the data collected on urban roads versus the data from country roads, red shows the data from urban roads versus data from motorways and yellow data indicates the samples from country roads versus the samples from motorways. The green dashed lines indicate theoretical values for perfectly identical distributions.

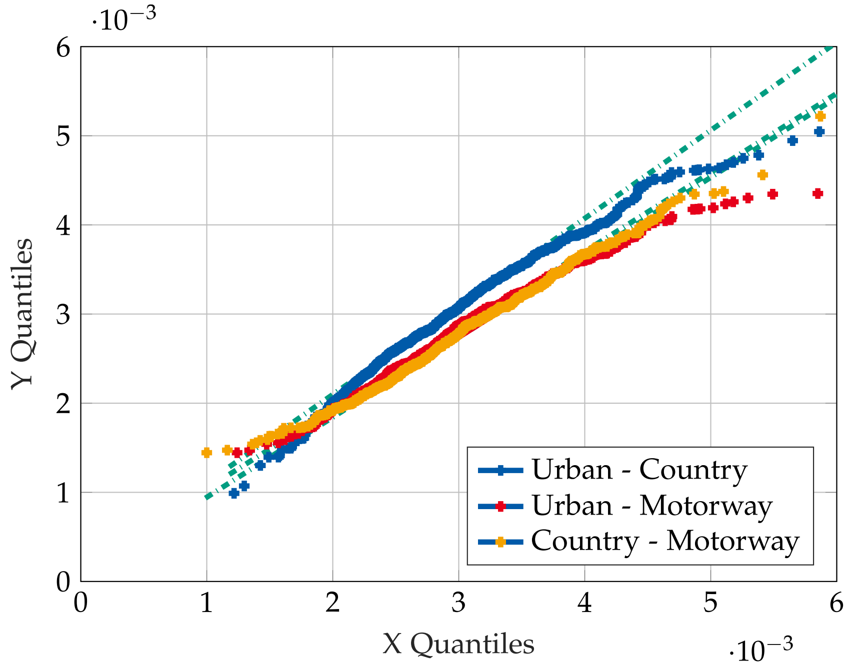

Figure E.11 – qq-plot of the three pupil diameter distributions recorded during the day tested on originating from the same distributions (only every 10000th data point is shown). In blue, the qq-plot for data recorded on urban roads is plotted versus the data on country roads. Red indicates the data recorded on urban roads versus the data from motorways and yellow shows the data from country roads over the data recorded on motorways. The green dashed lines indicate theoretical values, if both distributions are exactly the same.

For all three plots, a clear trend is visible. For the majority of the data, a straight line is well represented. Only at the upper edges of the data, the measured data deviates from theoretical data. Despite the tests showing, that all three data sets origin from different distributions, these qq-plots show, that for the raw data, this is indeed not the case and all three pupil diameter distributions originate from the same main distribution. The difference in the statistical test results versus the graphical analysis are explainable with the large test samples. The data that is tested here contains up to 10×10^7 data points. With this many data points, it is difficult to assume only a *data sample* therefore all tests on both normal distribution and if two or more *data samples* originate from the same distribution are strict and will find any deviation from a perfect normal distribution. Since real data is subject to noise and other influences however, the visual identification of normal distributions and correlations is recommended.

The same data is recorded for the drives during the night. The complete distributions are shown in figure E.12 with the same colours set for the different road types as before, blue indicates data recorded in cities, red shows the data from country roads and yellow represents motorway data. The data shows large similarities to the data shown for the day. The general distributions look like skewed normal distributions. The main difference here is, that the orientation of the skewness is oriented in the opposite direction. This is easily explainable by the boundary conditions of both data sets. While during the day, the pupil will reach a lower boundary in size, somewhere under 2 mm depending on the test subject, but is not really limited by the upper boundary at around 8 mm, the slope towards the upper limit can be much more pronounced. During the night, the median pupil diameter shifts due to the general shift in lighting towards darker illumination. Therefore, the upper boundary is a much higher constraint and the slope towards smaller pupil diameters can be much flatter. Again, testing the data sets on normal distribution, the tests result in a rejection of the null hypothesis, that the data is normal distributed. The general median is found at (5.0730 ± 1.6622) mm. The data for all three road categories is summarized in table E.7 where the median, the standard deviation as well as the maximum and the minimum recorded diameters are listed.

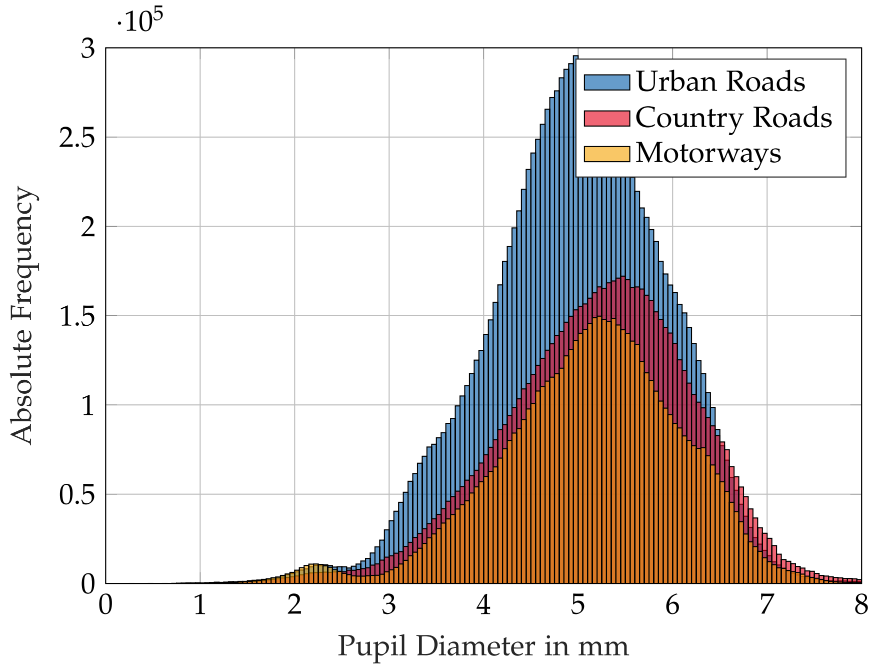

Figure E.12 – Pupil diameter in mm for the three major road categories during the night. Pupil diameter on urban roads is marked by blue bars, data recorded on country roads is indicated by red bars and yellow bars show the data recorded on motorways.

Testing if the data sets originate from one single distribution using the Whitney-Mann-U-Test, leads to the same results, as above, that all distributions are significantly different. Since the median values as well as the standard deviation shown in table E.7 as well as figure E.12 show a clear overlap, similar to the data shown above, a qq-plot is calculated for the three data sets using every 10000th data point, regarding the pupil diameter during night. This is shown in figure E.13, where analogous to the data for daytime driving, the correlation between data from urban and country roads is shown in blue, data from urban roads and motorways is shown in red and data from country roads and motorways is visualized in yellow. Again, theoretical data is represented by green dashed lines. This plot is shows an even stronger correlation between all three data sets. Not only do they all follow a straight line nearly perfectly, all the diagrams follow the same slope and the same ideal function. Only at the outer edges, where the data size is not as large as in the centre, deviations from theoretical function can be found. Therefore, it is assumed, similar to the data recorded during the day, that all data sets originate from one continuous distribution.

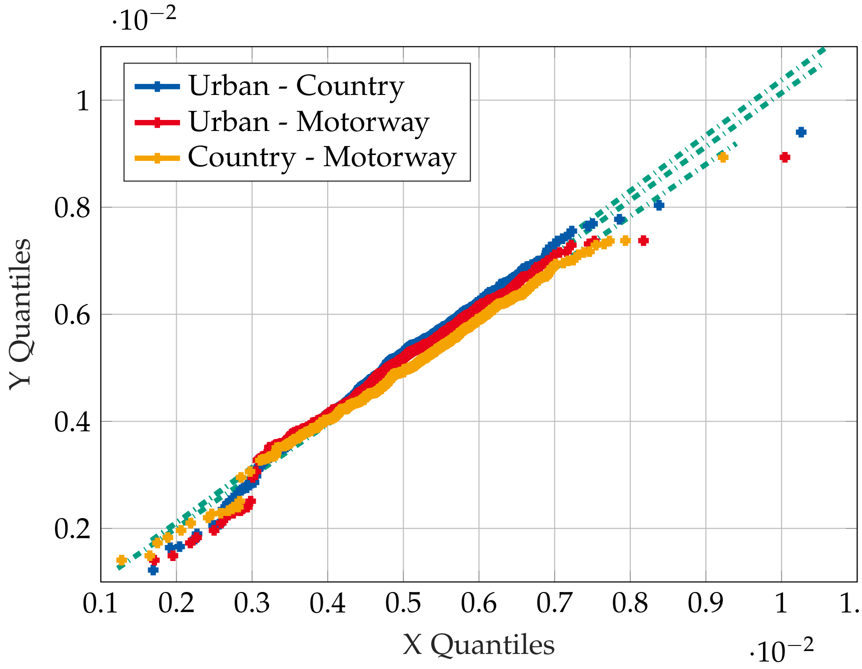

Figure E.13 – qq-plot of the three pupil diameter distributions recorded during the night tested on originating from the same distributions (only every 10000th data point is shown). In blue, the qq-plot for data recorded on urban roads is plotted versus the data on country roads. Red indicates the data recorded on urban roads versus the data from motorways and yellow shows the data from country roads over the data recorded on motorways. The green dashed lines indicate theoretical values, if both distributions are exactly the same.

Table E.7 – The median, the standard deviation, the maximum as well as the minimum of the raw pupil diameter recorded for the three major road categories split up by day- and night-time driving as shown in figure E.10 and E.12 respectively.

	URBAN ROADS		COUNTRY ROADS		MOTORWAYS	
	DAY	NIGHT	DAY	NIGHT	DAY	NIGHT
P_{Med}	2.86 mm	5.01 mm	2.91 mm	5.27 mm	2.69 mm 5.19 mm	
σ	0.77 mm	0.95 mm	0.74 mm	1.01 mm	0.66 mm	0.99 mm
P_{Max}	15.67 mm	14.14 mm	17.64 mm	15.66 mm	19.02 mm	14.60 mm
P_{Min}	0.29 mm	0.29 mm	0.42 mm	0.46 mm	0.34 mm	0.48 mm

Firstly the already used CDF is calculated for all three distributions and shown in figure E.14. The cumulative probability for the urban data (blue), country road data (red) and motorways (yellow) is shown with theoretical standard cumulative distribution function as the green, dashed line. This data shows, that the normalized probability functions for all three data sets follow theoretical probability of a normal distribution very well, especially when comparing this to the CDFs shown in section 5.1.1 and 5.1.2 in figures B.3 and B.5 where the tests lead to normal distribution, but the calculated CDF plots show a significantly worse behaviour. However, since the CDF does not allow for any assumption regarding the correlation between different data sets, further tests need to be done.

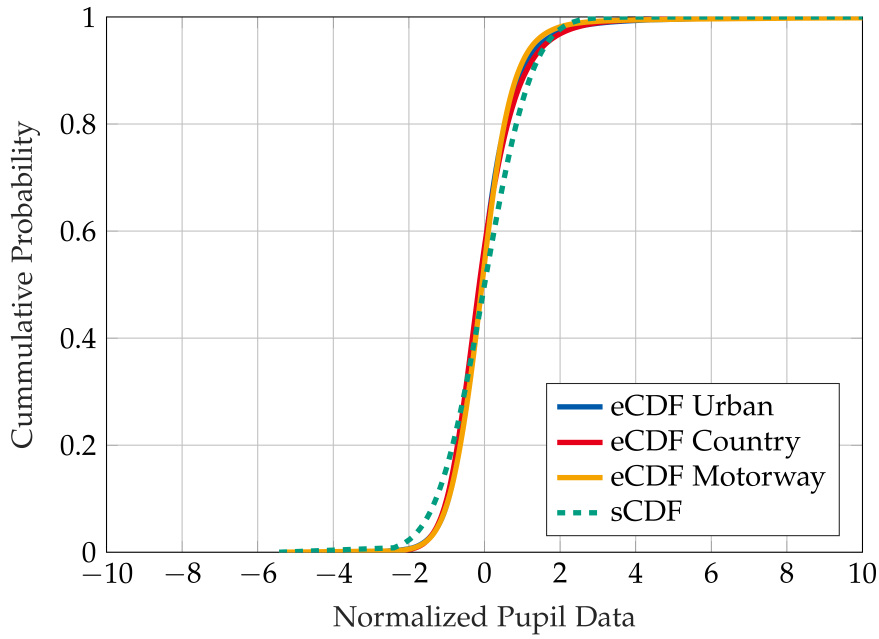

Figure E.14 – Empirical cumulative normal distribution for the normalized pupil diameters for the three road categories during the day shown in blue (urban roads), red (country roads) and yellow (motorways) as well as theoretical cumulative distribution (green dashed line).

The most common visual test on correlation is given by QUANTILE-QUANTILE PLOTS, (qq-plots). In this plot, the quantile of two distributions that are to be compared are plotted against each other. If both data sets originate from the same distribution, the plot reveals a (more or less) straight line. This visual test can be used to test data on normal distribution, by plotting the quantiles of a measured distribution over theoretical quantiles of a standard normal distribution. This is shown in figure E.15 for all three data sets. To increase the overview, only every 10000th data point is shown. Again, the data from urban roads is shown in blue, country roads in red and motorway data is indicated by yellow. The theoretical, ideal data is shown in the green dashed line. It is visible, that most of the quantiles can are indeed on theoretical straight line. Only for larger quantiles, the measured data deviates significantly from theoretical distribution showing, that the data is indeed skewed to the right side.

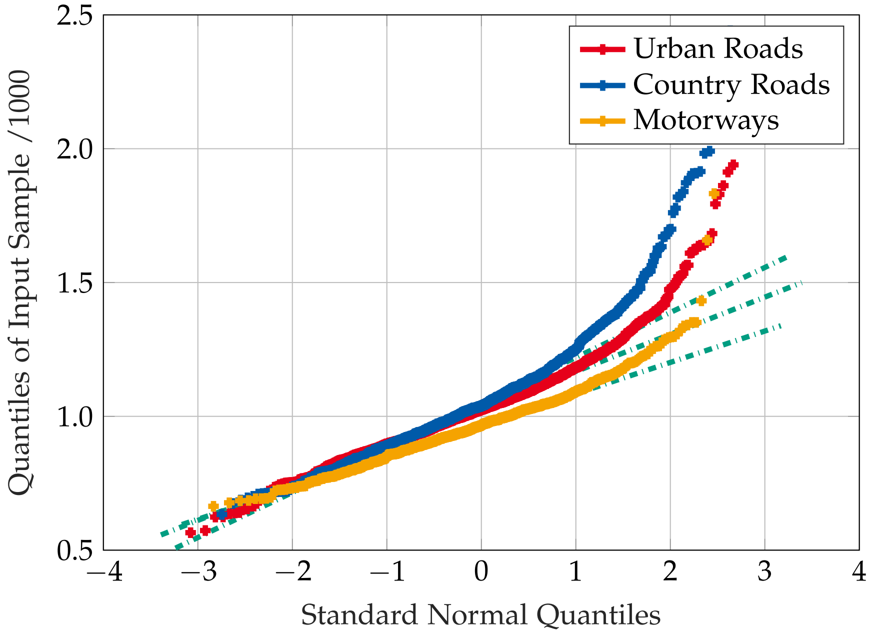

Figure E.15 – QUANTILE-QUANTILE PLOT for the pupil data recorded during the day over the standard normal distribution, reduced to every 10000th data point for better overview. The colour coding is kept identical.

This deviation from the standard normal distribution leads to the conclusion, that the calculated tests do indeed lead to the correct assumption, that the data is not normal distributed even though the CDFs show a nearly perfect behaviour for a normal distribution.

The next question is, if the distributions shown originate from the same distribution or if they are significantly different from each other. This is done using the WILCOXON-MANN-WHITNEY-TESTS since the data is not normal distributed. For all three distribution, the tests reject the null hypothesis, that the data sets originate from the same distribution and finds significant differences. However, as shown in table 5.17 all median values are close to each other with large overlaps when looking at the calculated standard deviations. This is also visible in figure 5.80 where the distributions for country roads and motorways are completely inside the data set from urban roads. For this reason, the qq-plot is used to verify these findings. In figure E.16 the quantiles of all data sets are plotted over the quantiles of the other data sets. Blue marks the quantiles of the urban data set over the quantiles of the country road data, red illustrates the quantiles of the urban data versus the quantiles from the motorway data and yellow shows the country road quantiles over the motorway quantiles.

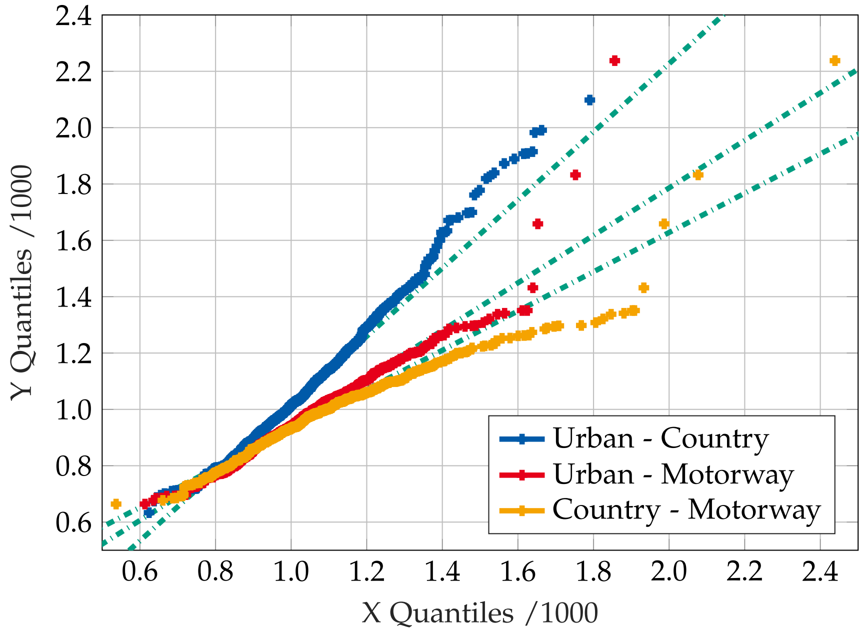

Figure E.16 – qq-plots to test the daytime pupil data of all three data sets on differences between each other. Blue shows the urban over the country data, red shows the urban over the motorway data and yellow shows the country over the motorway data.

Despite the Wilcoxon-Mann-Whitney-Tests, this shows, that the data does indeed seem to originate from the same distribution. All three qq-plots are nearly perfectly linear and thereby show, that the quantile distribution of all three data sets are nearly identical. This then leads to the assumption, that all data sets are indeed from one single main distribution. This is to be expected, as the illuminance data has already shown, that the data for all three situations are very similar in mean and standard deviation. Since the main influence factor for the pupil diameter should be the illuminance, the three distributions should be very similar as well. This means, that during the day, for pure pupil diameter investigation, similar to the illuminance distributions, no differences need to be done between the three road categories.

Figure E.17 shows the CDF plots for the urban data shown in blue, the country data shown in red, the motorway data shown in yellow and the ideal normal data is shown by the green dashed line.

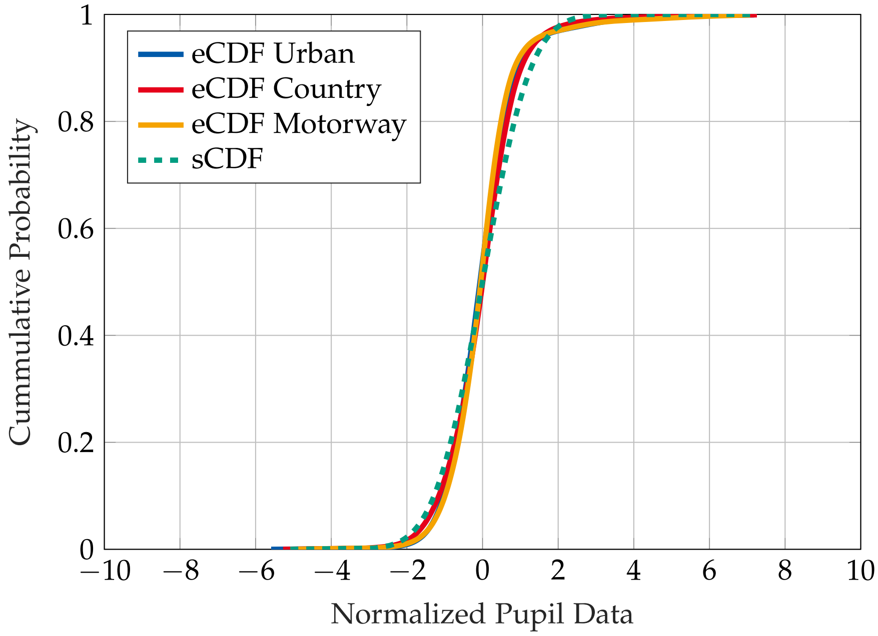

Figure E.17 – Empirical cumulative normal distribution for the normalized pupil diameters for the three road categories during the night shown in blue (urban roads), red (country roads) and yellow (motorways) as well as theoretical cumulative distribution (green dashed line)

The CDFs plots show, that the data follows the ideal normal CDF nearly perfectly with only small deviations at the beginning and the end. The smoothness of the graph is due to the, again, large number of data points.

However, the daytime data has already shown, that the CDF plot does not contain all of the information regarding the normal distribution. Therefore, qq-plots over the standard normal distribution are calculated for the three data sets. This is shown in figure E.18 with the urban data shown in blue, the country data in red and the motorway data in red. Similar to the data recorded during the day, the quantile data between -2 and 2 is pretty linear but beyond this, the data deviates quite drastically from the normal distribution. The main difference to the daytime data is, that all three sets are nearly identical with similar slopes and overlap significantly in the linear region.

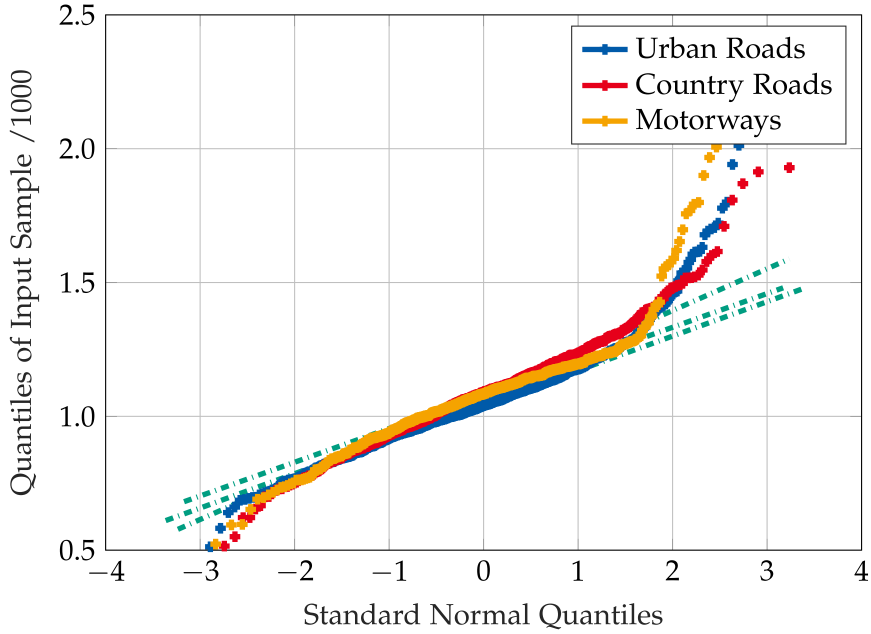

Figure E.18 – qq-plot for the pupil diameter datasets recorded at night shown in figure 5.81, reduced to every 10000th data point for better overview. The colour coding is kept identical to before.

This overlap already indicates, that the three distributions are fairly similar if not identical. To further test this, firstly, the Wilcoxon-Mann-Whitney-Tests are performed between all data sets, which again leads to the result, that all three sets are significantly different. Since the daytime data as well as the illuminance analysis have already shown, a visual test is necessary to test this result further. Similar to the daytime pupil data, a qq-plot between all three data sets is calculated and the result is shown in figure E.19. The data combination of urban and country road pupil diameter is shown in blue, the urban data versus the motorway data is shown in red and the country data versus the motorway data is marked yellow. The three ideal qq-plots are shown was green, dashed lines. The results presented here are very similar to the results shown for the daytime data. All three datasets follow a linear behaviour most of the time. However, after a certain threshold, the data deviates greatly from the ideal line with a bend downwards for the urban vs. country road data and a bend upwards for the other two test sets and before a certain quantile, all datasets are bend downwards therefore indicating, that indeed none of the three data sets share the same main data distribution.

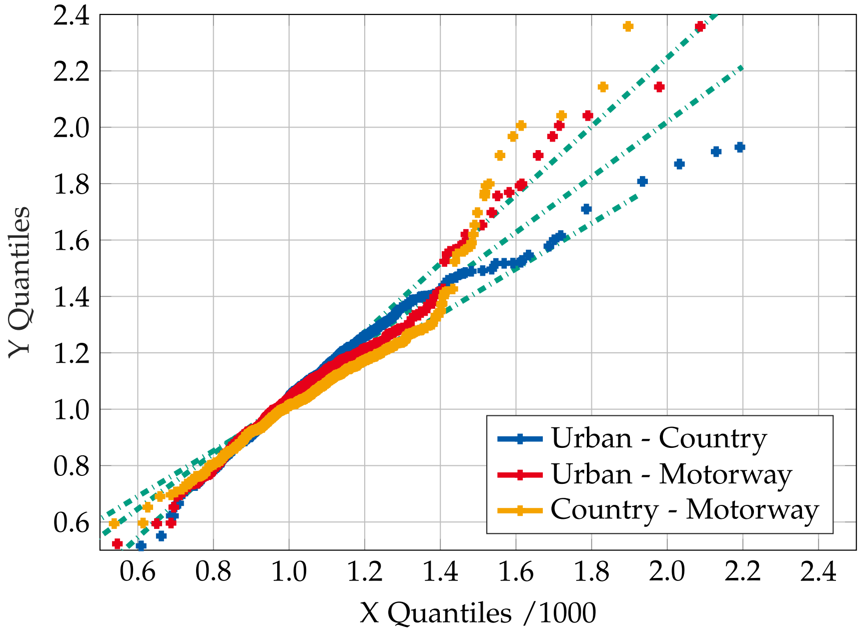

Figure E.19 – qq-plots to test the pupil data from the night drives of all three data sets on differences between each other. Blue shows the urban over the country data, red shows the urban over the motorway data and yellow shows the country over the motorway data.

E.4 EYE TRACKING DATA

In this part of the appendix, data is presented, that adds to the data and the figures shown in chapter 5 including gaze and fixation distributions for different situations, that go beyond the chapters in the main part of this thesis.

E.4.1 GENERAL GAZE AND FIXATION DATA

Figure E.20 shows the general gaze distribution during the night for all test subjects. The horizontal median is found at $0.5° \pm 14.3°$, and the vertical median at $-1.7° \pm 6.6°$. Only one accumulation point is visible.

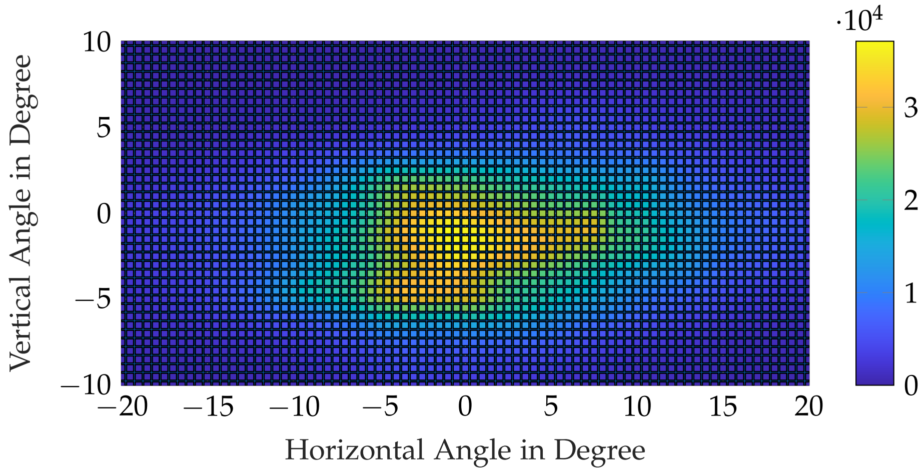

Figure E.20 – Overall gaze distribution over all 54 test subjects for the data recorded during the night. The horizontal median is calculated to be at 0.5° ± 14.3°, and the vertical median at −1.7° ± 6.6° with only one major accumulation point over all test subjects.

The data shown in figure E.21 shows the vertical and the horizontal fixation data during the day in more detail. The overall distribution and the corresponding values are found in chapter 5.4.

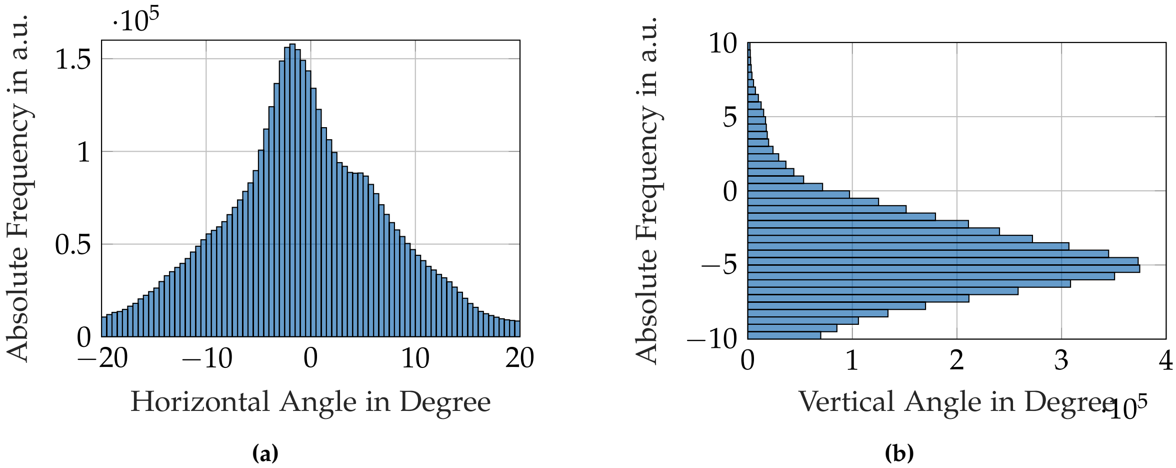

Figure E.21 – (a) shows the histogram of the horizontal fixation angles over all daytime data and all test subjects. (b) shows the vertical fixation distribution over all daytime data.

The data shown in figure E.22 shows the vertical and the horizontal fixation data during the night in more detail. The overall distribution and the corresponding values are found in chapter 5.4.

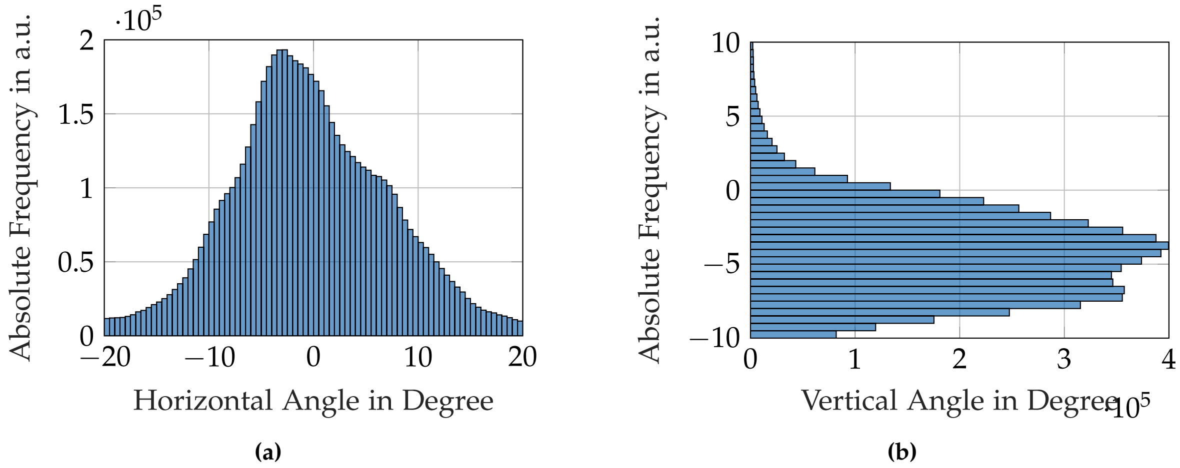

Figure E.22 – (a) shows the histogram of the horizontal fixation angles over all nighttime data and all test subjects. (b) shows the vertical fixation distribution over all data recorded at night.

E.4.2 Fixation and gaze data after glare

Figures E.23 and E.24 show the horizontal and the vertical gaze distributions right after a glare pulse is registered during the day. The horizontal median is found at $0.9° \pm 9.0°$ and the vertical median is found at $-0.3° \pm 3.5°$

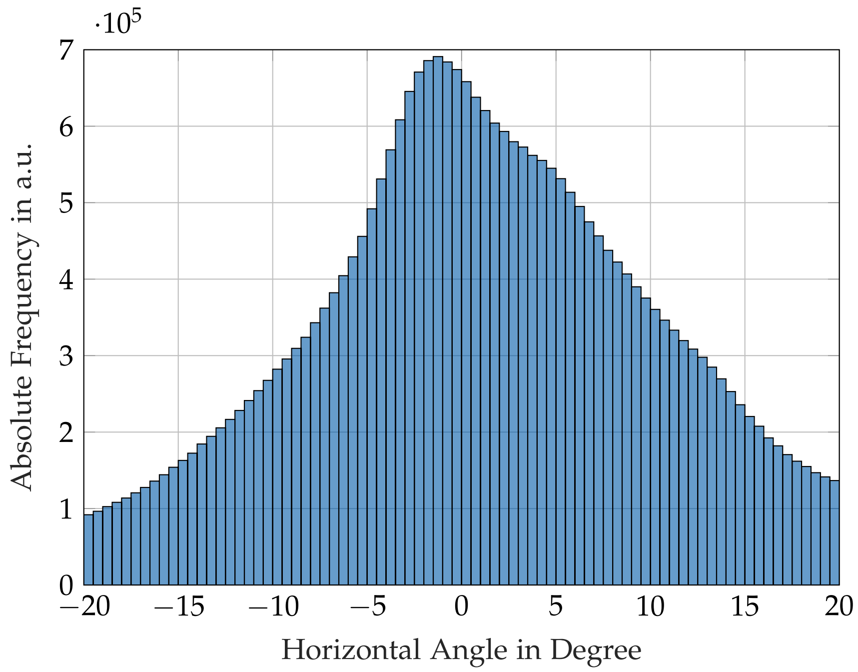

Figure E.23 – General horizontal gaze distribution over all 54 participants during the day after a registered glare pulse. The horizontal median is found at $0.9° \pm 9.0°$.

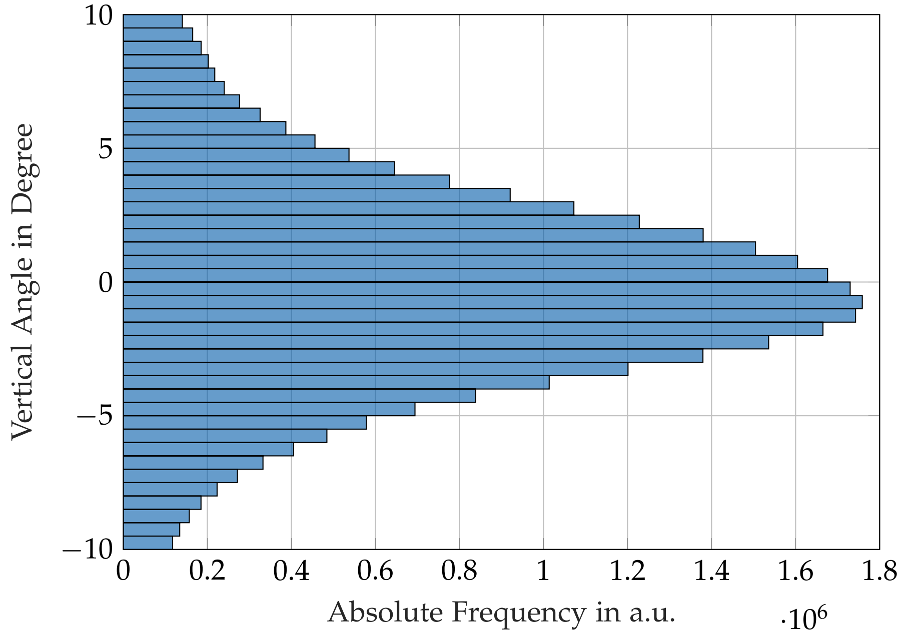

Figure E.24 – General vertical gaze distribution over all 54 participants during the day after a glare pulse. The vertical median is found at $-0.3° \pm 3.5°$

Figures E.25 and E.26 show the horizontal and the vertical gaze distributions right after a glare pulse is registered during the night. The horizontal median is found at $1.4° \pm 8.1°$ with the vertical median at $-3.8° \pm 3.1°$.

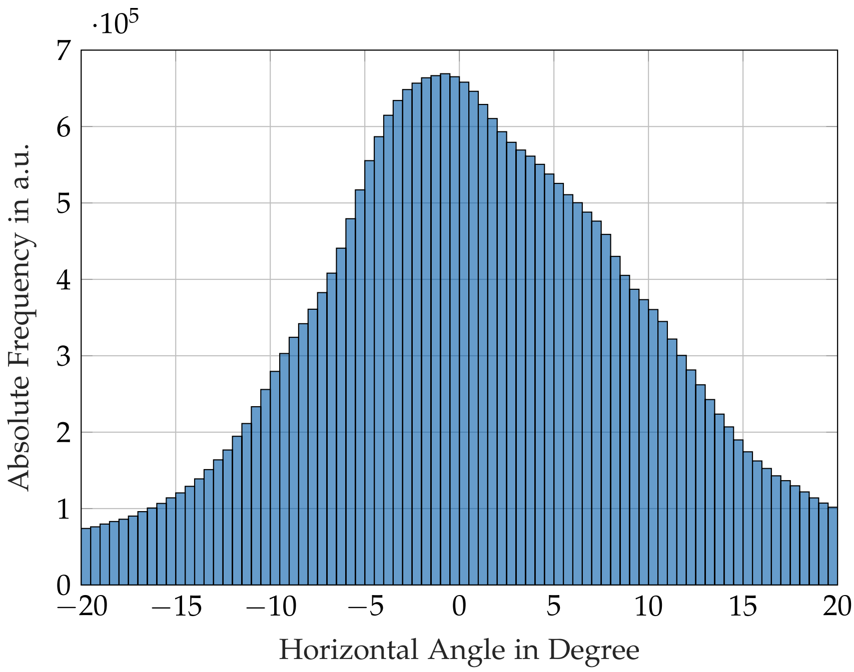

Figure E.25 – General horizontal gaze distribution over all 54 participants during the night after a registered glare pulse. The horizontal median is found at $1.4° \pm 8.1°$

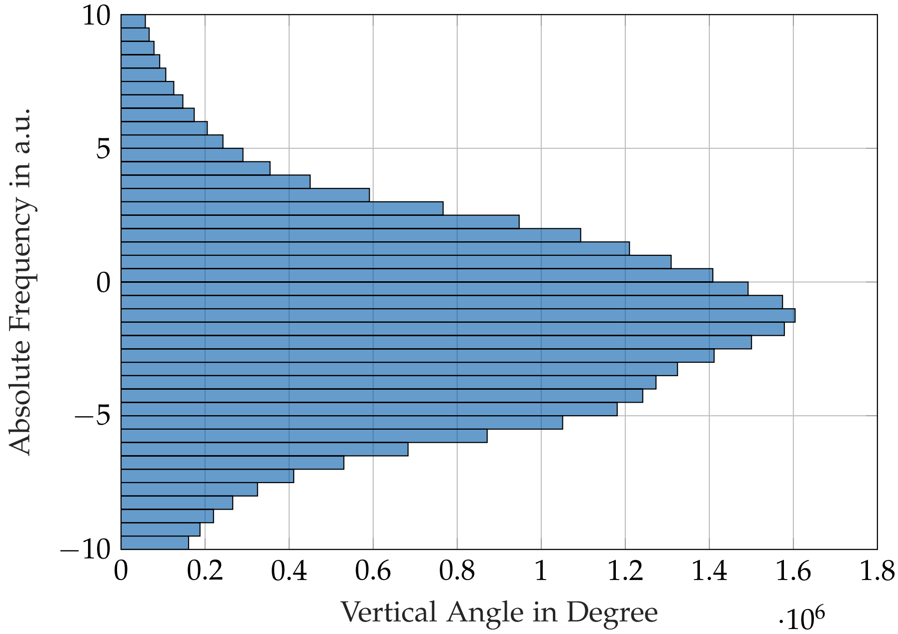

Figure E.26 – General vertical gaze distribution over all 54 participants during the night after a registered glare pulse. The vertical median is found at $-3.8° \pm 3.1°$

Figures E.27 to E.30 show the fixation distributions split up into horizontal distributions for day- and nighttime driving 5 s after a glare pulse is registered. Compared to the data without glare, the gaze direction is shifted towards the right side. For both, day and night a second plateau is found at the right side of the distribution. Compared to the normal gaze distribution no significant difference is found.

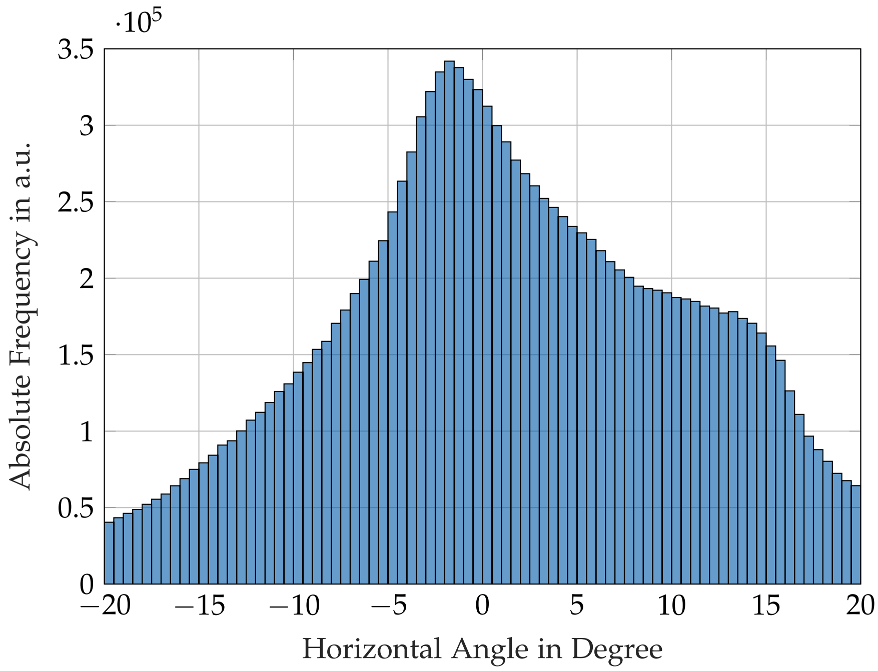

Figure E.27 – Horizontal fixation distribution recorded 5 s after the detection of a glare illuminance pulse during the day.

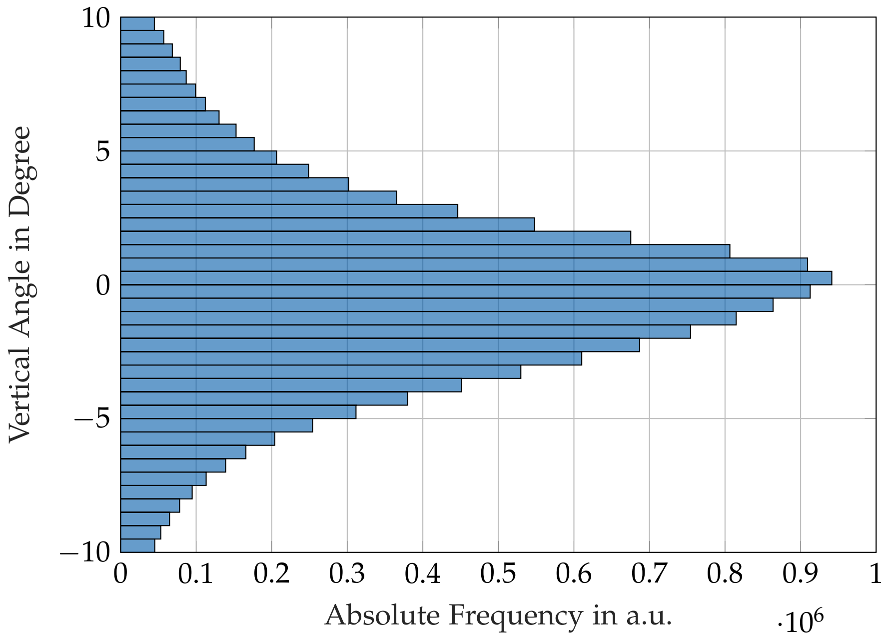

Figure E.28 – Vertical fixation distribution recorded 5 s after the detection of a glare illuminance pulse during the day.

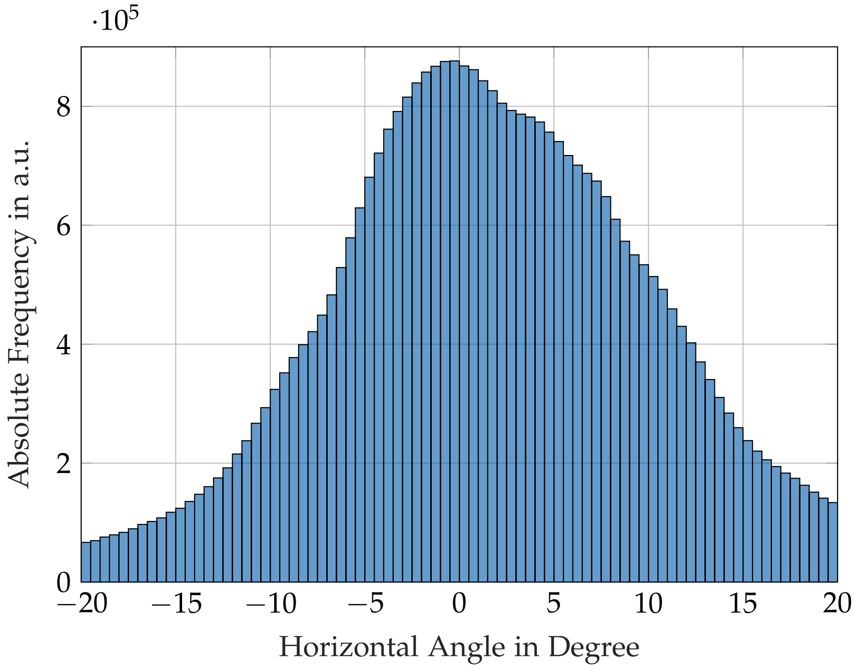

Figure E.29 – Horizontal fixation distribution recorded 5 s after the detection of a glare illuminance pulse during the night.

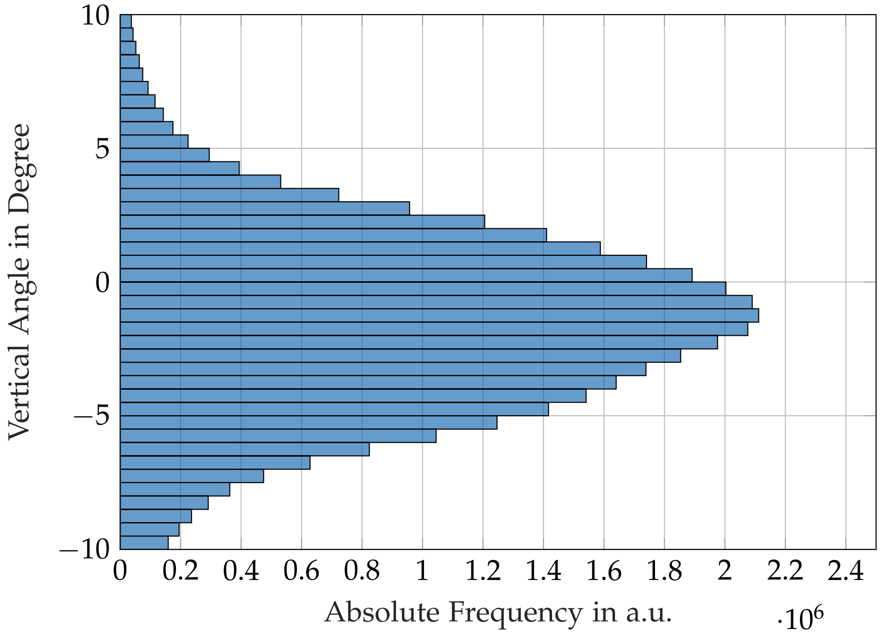

Figure E.30 – Vertical fixation distribution recorded 5 s after the detection of a glare illuminance pulse during the night.

E.4.3 FIXATION AND GLARE DATA IN BENDS

Table E.8 and E.9 show the horizontal and vertical fixation data for day and night time driving for left and right hand-side bends. Negative curve radii indicate left hand-side bends and positive curve radii indicate right hand side bends. The data clearly shows, that for lower curve radii, and therefore stronger bends, the gaze is shifted to the sides and for lower curve radii the gaze goes back to the same values as for general gaze behaviour. For the vertical gaze behaviour the data shows, that the gaze is lowered for stronger bends indicating an orientation point closer to the vehicle.

Table E.8 – Horizontal fixation data in left and right-hand side bends split up into bins from −1000 m to 1000 m with negative radii showing left bends and positive radii right bends, for day and nighttime driving.

CURVE RADIUS	DAY			NIGHT		
−1000 m	−2.962°	±	9.163°	−0.210°	±	7.781°
−900 m	−2.458°	±	7.524°	−2.817°	±	6.823°
−800 m	−2.026°	±	8.498°	−3.278°	±	6.617°
−700 m	−2.681°	±	8.795°	−2.959°	±	7.113°
−600 m	−2.885°	±	8.146°	−3.522°	±	7.386°
−500 m	−3.858°	±	8.193°	−3.436°	±	7.550°
−400 m	−3.298°	±	8.360°	−3.021°	±	7.974°
−300 m	−3.619°	±	8.322°	−4.117°	±	8.051°
−200 m	−4.141°	±	8.588°	−4.850°	±	8.252°
−100 m	−4.683°	±	9.440°	−4.501°	±	8.990°
100 m	2.630°	±	9.458°	2.624°	±	9.142°
200 m	2.248°	±	8.892°	2.864°	±	8.403°
300 m	2.397°	±	9.018°	1.688°	±	8.534°
400 m	1.419°	±	9.133°	1.134°	±	8.530°
500 m	0.933°	±	8.434°	1.407°	±	8.015°
600 m	0.695°	±	8.758°	1.803°	±	8.645°
700 m	1.153°	±	8.603°	1.690°	±	7.528°
800 m	0.273°	±	8.173°	2.004°	±	7.413°
900 m	0.667°	±	8.909°	1.492°	±	7.243°
1000 m	0.560°	±	8.646°	1.060°	±	8.207°

Table E.9 – Vertical fixation data in left and right-hand side bends split up into bins from $-1000\,\mathrm{m}$ to $1000\,\mathrm{m}$ with negative radii showing left bends and positive radii right bends, for day and nighttime driving.

CURVE RADIUS	DAY			NIGHT		
-1000 m	$-0.040°$	$\pm$	$3.834°$	$-0.644°$	$\pm$	$2.867°$
-900 m	$-0.079°$	$\pm$	$3.261°$	$-0.705°$	$\pm$	$3.513°$
-800 m	$-0.246°$	$\pm$	$3.384°$	$-0.194°$	$\pm$	$3.255°$
-700 m	$0.406°$	$\pm$	$3.371°$	$-0.898°$	$\pm$	$3.236°$
-600 m	$-0.120°$	$\pm$	$3.466°$	$-0.873°$	$\pm$	$3.435°$
-500 m	$-0.244°$	$\pm$	$3.262°$	$-0.646°$	$\pm$	$3.423°$
-400 m	$-0.515°$	$\pm$	$3.410°$	$-0.495°$	$\pm$	$3.301°$
-300 m	$-0.758°$	$\pm$	$3.305°$	$-0.227°$	$\pm$	$3.402°$
-200 m	$-0.611°$	$\pm$	$3.381°$	$-0.166°$	$\pm$	$3.402°$
-100 m	$-0.405°$	$\pm$	$3.516°$	$-0.147°$	$\pm$	$3.438°$
100 m	$-0.854°$	$\pm$	$3.196°$	$-0.494°$	$\pm$	$3.257°$
200 m	$-0.392°$	$\pm$	$3.255°$	$-0.156°$	$\pm$	$3.278°$
300 m	$-0.379°$	$\pm$	$3.258°$	$-0.343°$	$\pm$	$3.232°$
400 m	$-0.677°$	$\pm$	$3.214°$	$-0.248°$	$\pm$	$3.245°$
500 m	$-0.391°$	$\pm$	$3.018°$	$-0.579°$	$\pm$	$3.175°$
600 m	$-0.038°$	$\pm$	$3.396°$	$-0.718°$	$\pm$	$3.250°$
700 m	$-0.400°$	$\pm$	$3.358°$	$-0.627°$	$\pm$	$3.393°$
800 m	$0.010°$	$\pm$	$3.307°$	$-0.068°$	$\pm$	$3.035°$
900 m	$0.035°$	$\pm$	$3.257°$	$-0.224°$	$\pm$	$3.159°$
1000 m	$-0.010°$	$\pm$	$2.879°$	$-0.744°$	$\pm$	$3.105°$

Part F

APPENDIX F, DATA SHEETS

F

APPENDIX E, DATA SHEETS

This part of the appendix contains all relevant data sheets for the presented thesis, beginning with the glare source for section 5.3, the circuit wiring diagram for the LED driver, the eye tracking system SmartEye Pro used in both 5.3 as well as in 5.4.

- First, an excerpt of the data sheet for the *Lumiled Altilon* AFL-M2L-0500 from Philips used in section 5.3, listing the original spectrum, the current and temperature dependancy of the total luminous flux and the angular distribution.

- The schematic circuit diagram for the LED driver used in 5.3

- The data sheet for the SmartEye Pro eye tracking system. The system in use is a 120 Hz using four different cameras leading to a coverage of 180°

LUMILEDS

AUTOMOTIVE

LUXEON Altilon

Functional solution for forward lighting systems

LUXEON Altilon delivers distinctive brilliant white light for your automotive forward lighting designs. LUXEON Altilon is designed and tested to withstand extreme temperatures and engineered to simplify optical design and ease of manufacturing and assembly. With advanced phosphor technology, LUXEON Altilon meets both SAE and ECE color specifications and provides finer granularity than existing systems.

FEATURES AND BENEFITS

- 1A drive current enables high light output per package for reduced LED count
- 150°C maximum case temperature, T_c, ensures application performance at extreme conditions
- Industry's lowest thermal resistance enables smaller heatsinks for smaller designs
- 1x2 and 1x4 configuration options with or without spade lugs for design flexibility
- AEC-Q101C qualified and PPAP documentation available

PRIMARY APPLICATIONS

- Adaptive Lighting
- Daytime Running Lights
  - Front Position
- Front Fog
- Headlight
  - Cornering Light
  - High Beam
  - Low Beam

Table of Contents

General Product Information

Product Test Conditions

LUXEON Altilon LEDs are tested and binned using a 20ms monopulse (MP) at 1000mA drive current, junction temperature, T_j, of 25°C.

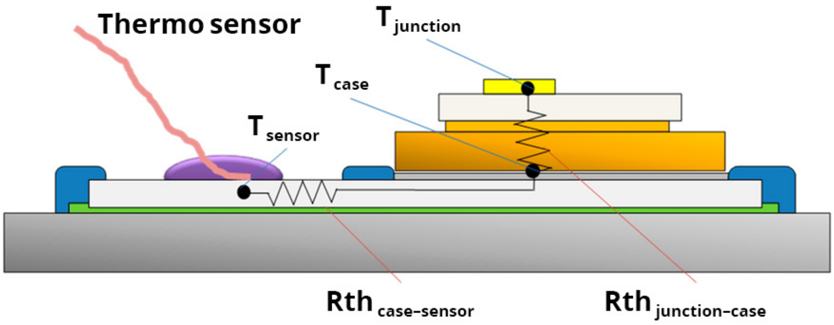

Figure 1. Case temperature location on sample board for LUXEON Altilon.

Part Number Nomenclature

Part numbers for LUXEON Altilon follow the convention below:

L A F L – M **D E** – **F F F F**

Where:

D – designates number of die (2=2 die and 4=4 die)

E – designates connector type (L=spade lugs and S=solder)

F F F F – designates minimum luminous flux bin (see luminous flux bin definitions)

Therefore, a LUXEON Altilon with 4 die, solder connector and 500 minimum luminous flux will have the following part number:

L A F L – M **2 S** – **0 5 0 0**

Environmental Compliance

Lumileds LLC is committed to providing environmentally friendly products to the solid-state lighting market. LUXEON Altilon is compliant to the European Union directives on the restriction of hazardous substances in electronic equipment, namely the RoHS Directive 2011/65/EU and REACH Regulation (EC) 1907/2006. Lumileds LLC will not intentionally add the following restricted materials to its products: lead, mercury, cadmium, hexavalent chromium, polybrominated biphenyls (PBB) or polybrominated diphenyl ethers (PBDE).

Performance Characteristics

Product Selection Guide

Table 1. Product selection for LUXEON Altilon at 1000mA, 20ms MP, T_c=25°C.

CONFIGURATION	MINIMUM LUMINOUS FLUX [1, 2] (lm)	PART NUMBER
1x2	500	LAFL-M2x-0500
1x4	925	LAFL-M4x-0925
	1000	LAFL-M4x-1000
	1050	LAFL-M4x-1050
	1100	LAFL-M4x-1100
	1150	LAFL-M4x-1150

Notes for Table 1:
1. Lumileds maintains a tolerance of ±10% for luminous flux measurements.
2. Flux levels are tested via a pulsed measurement at a case temperature, T_c, of 25°C.

Optical Characteristics

Table 2. Typical optical characteristics for LUXEON Altilon at 1000mA, 20ms MP, T_c=25°C.

PART NUMBER	CORRELATED COLOR TEMPERATURE (K) or DOMINANT WAVELENGTH (nm)		TOTAL INCLUDED ANGLE [2] $\theta_{0.90V}$	VIEWING ANGLE [3] $2\theta_{1/2}$
	MINIMUM	MAXIMUM		
LAFL-M2x-xxxx	5000K	6150K	142°	120°
LAFL-M4x-xxxx	5000K	6150K	142°	120°

Notes for Table 2:
1. Spectral width at ½ of the peak intensity.
2. Total angle at which 90% of total luminous flux is captured.
3. Viewing angle is the off axis angle from lamp centerline where the luminous intensity is ½ of the peak value.

Electrical and Thermal Characteristics

Table 3a. Typical electrical and thermal characteristics for LUXEON Altilon at 1000mA, 20ms MP, T_c=25°C.

PART NUMBER	FORWARD VOLTAGE [1] (V_f)		DYNAMIC RESISTANCE [2] (Ω) R_D	THERMAL RESISTANCE—JUNCTION TO CASE (°C/W)			
				$R\theta_{J\text{-}C\ EL}$ [4]		$R\theta_{J\text{-}C\ REAL}$ [5]	
	MINIMUM	MAXIMUM		TYPICAL	MAXIMUM	TYPICAL	MAXIMUM
LAFL-M2x-xxxx	5.6	7.5	0.53	2.1	2.5	3.0	3.6
LAFL-M4x-xxxx	11.2	15.0	1.07	1.4	1.8	2.0	2.6

Notes for Table 3a:
1. Lumileds maintains a tolerance of ±0.06V on forward voltage measurements.
2. Dynamic resistance is the inverse of the slope in linear forward voltage model for LEDs.
3. Measured between 80°C and 90°C at binning current, I_f.
4. Electrical thermal resistance.
5. Thermal resistance with wall plug efficiency included. Reference JESD51-51, JESD51-14, 4.1.3.

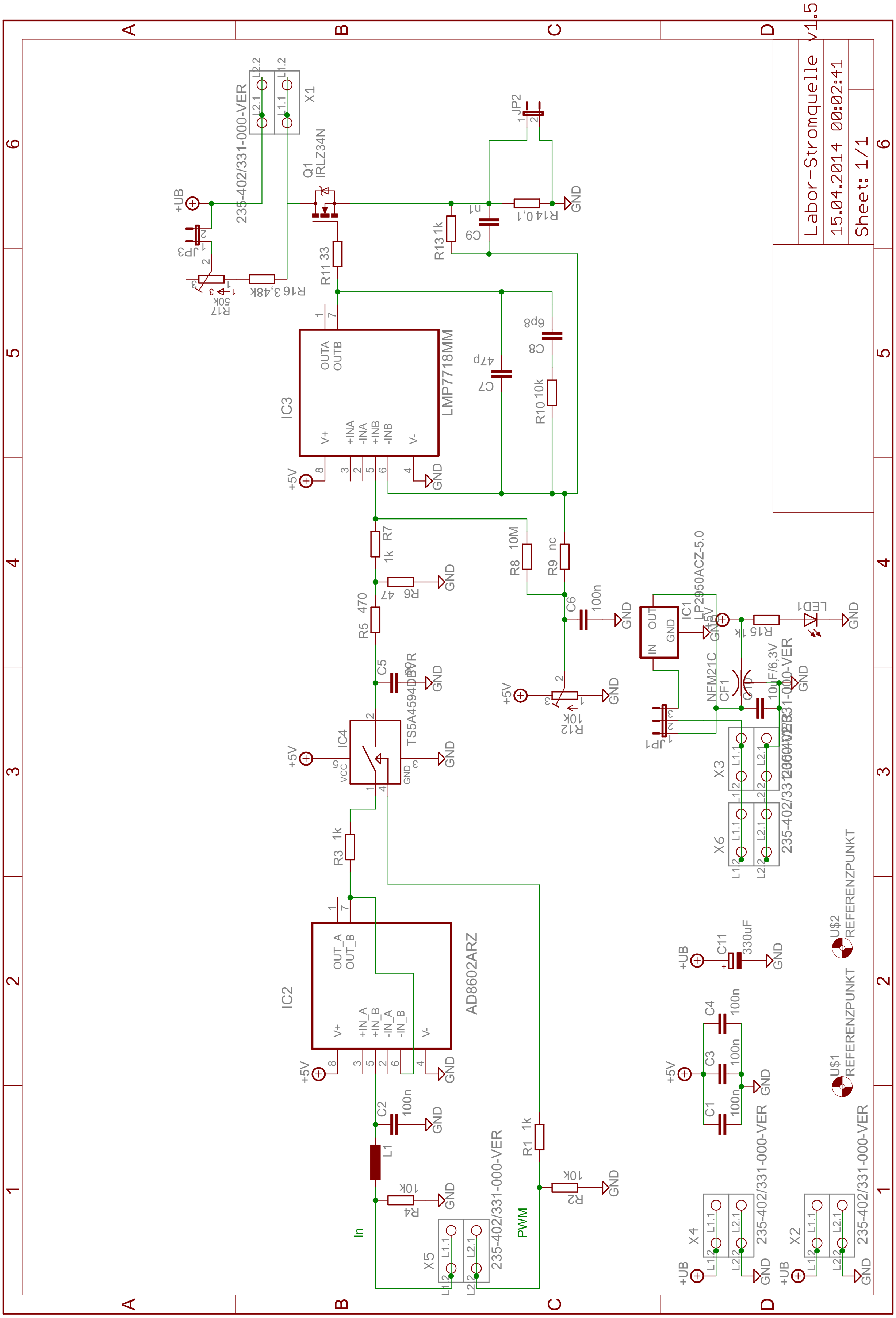
Labor-Stromquelle v1.5
15.04.2014 00:02:41
Sheet: 1/1
IC3
LMP7718MM
IC2
AD8602ARZ
IC4
TS5A4594DBVR
IC1
LP2950ACZ-5.0
Q1
IRLZ34N
X1
235-402/331-000-VER
X5
235-402/331-000-VER
X4
235-402/331-000-VER
X2
235-402/331-000-VER
In
PWM
U$1
REFERENZPUNKT
U$2
REFERENZPUNKT
C11
330uF
NFM21C
CF1
R14 0,1
R13 1k
R11 33
R16 3,48k
R17
50k
R10 10k
R8 10M
R9 nc
R7
1k
R5 470
R3 1k
R1 1k
R2
10k
R4
10k
R12
10k
JP2
C9
n1
C7
47p
C8
6p8
C2
100n
C3
100n
C4
100n
C1
100n
C6
100n
L1
LED1
+UB
+5V
GND

SMART EYE PRO

3D Eye Tracking for Research

NEW FEATURES OF SMART EYE PRO 6

Significantly increased ease of use and reduced start-up time
- Fully automatic head tracking initialization.
- Increased rotations and translations

Enhanced freedom for natural head movements
- Algorithms have been improved scaling and rotation for forwards/backwards and sideways head tilt movements.
- Auto Exposure of the cameras improves tracking for movements towards or away from the system (z direction). This especially simplifies setups where subjects are sitting at varying distances from the system.

Increased gaze tracking area and availability
- Improved algorithms reduce tracking restrictions. One eye visible in one camera is sufficient for tracking.
- Intelligent selection of the best eye clips in multi-camera set-ups, for achieving the best-possible tracking results.

Robustness and stability of the tracking enhanced notably
- The automatic head profiles are self-learning and improving over time.
- The gaze tracking algorithms take advantage of the information from of all available cameras in a more intelligent way.

STANDARD FEATURES OF SMART EYE PRO

- 60hz or 120hz sampling rate
- Gaze accuracy of 0.5 degrees (in ideal conditions)
- Fully time-stamped output data
- Multiple data output streams via TCP, UDP, CAN Output or as a simple text log file that can be exported in to excel, Mat lab etc.
- Easy to use API for Integration requirements. Existing application interfaces: PST e-Prime, EGI Net Station, EyesDx MAPPS, Eyetellect Gaze Tracker, Noldus The Observer, MathWorks MATLAB
- Data output for both the head, left and right eye with over 145 data output values covering Gaze tracking, Head tracking (6DOF), Eyelid tracking, Pupilometry tracking, raw and filtered gaze, Blinks, Fixations, Saccades and more
- 'Real World' 3D Tracking. The Smart Eye World Model Module allows you to build real 3D models of the experiment environment to detect gaze intersections with objects in that environment.
- WCS, "World Coordinate System" feature which makes it simple to transform output data to other coordinate systems.
- Camera Calibration in less than 15 seconds and Gaze calibration in less than 30 seconds
- Changeable camera lenses (4,5mm – 25mm) depending on participant distance from the cameras

SMART EYE®
Contact Information:
SMART EYE AB | sales@smarteye.se | www.smarteye.se | Gothenburg, Sweden
Phone: +46 (0) 31 60 61 60

SMART EYE®

SUITABLE APPLICATIONS:

Instrumented vehicle
Take advantage of the largest continuous field of view on the market and track human gaze during natural head movements. Due to Smart Eye's big head box tracking data will not be lost. The system is configurable with the numbers of cameras required in your project and works in bright sunlight as well as during total darkness.

Simulators
Smart Eye Pro allows totally free head movements and fast participant set-up time. Easily add, subtract or reposition cameras to create the desired head box or visual field needed in your project. Smart Eye Pro is used in all kinds of simulators and integrated with many of the leading simulator manufacturers.

Single Screen
Easy to use, yet flexible enough to meet special customer needs. Smart Eye Pro can be equipped with 2-3 cameras for screens up to 42". Create heat maps, dynamic ROI's, gaze trails etc. with our partner's analysis software.

Multi-Screen and Control Room
Smart Eye Pro allows you to measure on up to 7-8 screens and a large projection surface in front of the screens. Information about the time period spent on each screen, ROIs, heat maps etc. can be gathered.

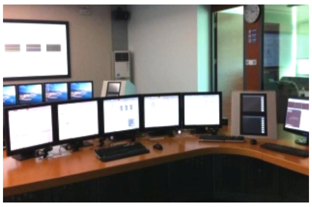

Long Range
To ensure a natural environments for example when sitting in front of big screens, video games, displays walls, movies etc. it is possible to place the system up to 2,5m from the subject.

TECHNICAL SPECIFICATIONS

Sampling Rate	60 Hz (with up to 8 cameras)	120 Hz (with up to 4 cameras)
Field of View	90° - 360° (depending on number of cameras)	
Head Box (freedom of head movement)	For a typical 2-camera screen measurement set-up (8mm lenses): 40 x 40 x 50 (typ). Adjustable with lenses and positioning of cameras	
Tracking Accuracy	Head: Rotation 0.5 degrees (typ.)	Gaze: 0.5 degrees (typ.)
Output	TCP / UDP / CAN (optional)	
Delivered data	Head tracking (6DOF), eye position, eye gaze, pupil diameter, Saccades, fixations, blinks, eyelid opening and many more.	
Recovery Time (Blink / Tracking Lost)	Immediate	
Optimal Camera – Eye Distance	30 – 300 cm - adjustable with lenses and positioning of cameras	
Eyewear Compatibility	Glasses, contact lenses and sunglasses of non IR-type	
Calibration Mode	Any number of calibration points	
Eye Tracking Principle	Pupil and Iris / Corneal Reflection and Head Model	

SMART EYE®

Contact Information:
SMART EYE AB | sales@smarteye.se | www.smarteye.se | Gothenburg, Sweden
Phone: +46 (0) 31 60 61 60

OWN PUBLICATIONS

As this thesis is part of an evolving study over a larger time period, some of the parts, ideas and figures included in this thesis may have been published in one of the following publications:

Publications:

[1] K. Kosmas, J. Kobbert and T. Q. Khanh, "Optimal Traffic Sign Luminance with Glare-free High Beam," *ATZ - Automobiltechnische Zeitschrift*, (9/2018) pp. 84–87, 2018.

[2] K. Kosmas, J. Kobbert and T. Q. Khanh, "Influence of Dirt on Glare-free High Beam Systems ," *ATZ - Automobiltechnische Zeitschrift*, (6/2018) pp. 68–71 , 2018.

[3] J. Kobbert, K. Kosmas, D. Englisch and T. Q. Khanh, "Comparison between LED and Laser Headlamp Systems," *ATZ - Automobiltechnische Zeitschrift*, (2/2018) pp. 68-71, 2018.

[4] K. Kosmas, J. Kobbert and T. Q. Khanh, "Field-test to determine the optimal traffic sign illumination based on glare-free high beam," *International Symposium on Automotive Lighting*, Darmstadt, 2017.

[5] C. Schiller, K. Kosmas, J. Kobbert and T. Q. Khanh, "Dirty Headlamps – Efficiency of Headlamp Cleaning Devices and the Impact on Stray Light: Method and first results," *International Symposium on Automotive Lighting*, Darmstadt, 2017.

[6] K. Schneider, J. Kobbert and T. Q. Khanh, "Contrast determination based on object detection distances under peripheral vision conditions and conclusions for future lighting distribution concepts," *International Symposium on Automotive Lighting*, Darmstadt, 2017.

[7] W. Löffler, J. Kobbert, K. Kosmas and T. Q. Khanh, "Determining the effects of sharp cut-off lines vs. smooth cut-off lines on glare rating," *International Forum on Automotive Lighting*, Shanghai 2017.

[8] J. Kobbert, D. Englisch, K. Kosmas, M. Szarafanowicz and T. Q. Khanh, "Contrast measurements for detection and recognition with Laser High Beam Systems in real life driving tests," *International Forum on Automotive Lighting*, Shanghai 2017.

[9] K. Schneider, J. Kobbert and T. Q. Khanh, "Age-related field study for determination of the 95 %-detectability of objects under peripheral vision conditions," *IEEE Intelligent Vehicles Symposium*, Los Angeles, 2017.

[10] K. Kosmas, J. Kobbert and T. Q. Khanh, "Glare-free High Beam: Optimal Traffic Sign Illumination," *International Forum on Automotive Lighting*, Shanghai, 2017.

[11] J. Kobbert, W. Löffler, K. Kosmas and T. Q. Khanh, "Estimation of glare load from small illuminance peaks in real life driving situations.," *Société des Ingénieurs de l'Automobil, VISION*, Paris, 2016.

[12] J. Kobbert, K. Kosmas, D. Polin, D. Englisch, K. Schneider and T. Q. Khanh, "Field test of visibility distances and recognition rates - comparison of LED and Laser Systems," *Society of Automotive Engineers, World Congress*, Detroit, 2015.

[13] C. Schiller, K. Kosmas, J. Kobbert and T. Q. Khanh, "Influence of dirty headlamps on straylight and glare - A test series under real driving conditions," *International Forum on Automotive Lighting*, Shanghai, 2015.

[14] J. Kobbert, K. Kosmas, D. Polin, D. Englisch, K. Schneider and T. Q. Khanh, "Field Test of Visibility distances and recognition rates – comparison of LED and Laser systems," *International Symposium on Automotive Lighting*, Darmstadt, 2015.

[15] K. Kosmas, D. Polin, C. Schiller, J. Kobbert and T. Q. Khanh, "Comparing the glare load of low beam, high beam andglare-free high beam under different traffic conditionson the road," *International Symposium on Automotive Lighting*, Darmstadt, 2015.

[16] K. Kosmas, D. Polin, J. Kobbert, C. Schiller and T. Q. Khanh, "Dynamic illuminance measurements – Glare-free high beam (ECE) vs. SAE headlamps," *International Symposium on Automotive Lighting*, Darmstadt, 2015.

Furthermore, one large part as a doctoral student at the TECHNISCHE UNIVERSITÄT DARMSTADT is to supervise students during their graduation theses. Some of the presented work thereby originates to some extend in one of the theses listed below. This includes some graphics, data and even complete test setups. While some of this work originates from these theses, the segments are not quoted as such in the thesis since the advancements were all done with this thesis as a goal.

- **Master Theses:**

[1] M. Bartenschlager, "*Analysis of Gaze Behaviour in Different Real Life Traffic Conditions and Situations*", Darmstadt, Germany: Technische Universität Darmstadt, 2017.

[2] D. Bopp, "*Development and Validation of a Scanning Headlamp System Used to Generate High-Definition Headlamps*", Darmstadt, Germany: Technische Universit at Darmstadt, 2018.

[3] D. Bursasiu, "*Optimization of Pixel Headlights Limits Based on Current Traffic and Infrastructure Data*", Darmstadt, Germany: Technische Universität Darmstadt, 2016.

[4] A. Erkan, "*Glare and Acceptance Potential of Retrofit LED Headlamp Lightsources*", Darmstadt, Germany: Technische Universität Darmstadt, 2018.

[5] S. Namyslo, "*Optimal Evaluation of Light Guides for the Ambient Interior Lighting in Automotive Use*", Darmstadt, Germany: Technische Universität Darmstadt, 2017.

[6] T.Singer, "*Implementation and Setup of a Gaze-Controlled Light Distribution*", Darmstadt, Germany: Technische Universität Darmstadt, 2016.

[7] C. Tang, "*Optical Method for Automatic Aiming of Automotive Headlamps*", Darmstadt, Germany: Technische Universität Darmstadt, 2017.

[8] Z. Wei, "*Development of an LED Glare Source for the Investigation of Spectral Glare Sensitivity*", Darmstadt, Germany: Technische Universität Darmstadt, 2015.

[9] K. Yalcin, "*Development and Validation of Lighting Functions in Urban Environments for Autonomous Level 5 Vehicles*", Darmstadt, Germany: Technische Universität Darmstadt, 2018.

[10] A. Yamazaki, "*Preparation of the Development of a Photometric Model for the Characterization of Side-Emitting Glass Fibre*", Darmstadt, Germany: Technische Universität Darmstadt, 2017.

Bachelor Theses:

[11] K. Degen, "*Development of a Fast and Mobile Illuminance Measurement Device*", Darmstadt, Germany: Technische Universität Darmstadt, 2017.

[12] J. El-Moussaoui, "*Glare-Free High Beam: Dynamic Research of Traffic Sign Self-Glare*", Darmstadt, Germany: Technische Universität Darmstadt, 2017.

[13] A. Erkan, "*Field Study and Validation of the Headlamp Aiming Process*", Darmstadt, Germany: Technische Universität Darmstadt, 2016.

[14] A. Frank, "*Collection and Evaluation of CAN-Bus Data*", Darmstadt, Germany: Technische Universität Darmstadt, 2015.

[15] D. Hoffmann, "*Development and Validation of a System to Measure Vehicle Dynamics*", Darmstadt, Germany: Technische Universität Darmstadt, 2016.

[16] M. Klingenstein, "*Simulation and Software-Based Pixellight Driving and Measurement of Relevant Photometric Variables*", Darmstadt, Germany: Technische Universität Darmstadt, 2016.

[17] A. Kramer, "*Validation and Setup of a Poratble Eye Tracker for Automotive Use and Research in Lighting Technology*", Darmstadt, Germany: Technische Universität Darmstadt, 2016.

[18] W. Löffler, "*Development and Validation of a Measurement System to Characterize the Glare Effect of Illuminance Peaks With Varying Intensity and Width*", Darmstadt, Germany: Technische Universität Darmstadt, 2016.

[19] D. Roth, "*Simulation and Software-Based Pixellight Driving and Measurement of Relevant Photometric Variables*", Darmstadt, Germany: Technische Universität Darmstadt, 2016.

[20] O. Schön, "*Development of a System to Controll and Read Data From the Automatic Headlamp Levelling Motor*", Darmstadt, Germany: Technische Universität Darmstadt, 2016.

[21] K. Yalcin, "*Influence of Realistic Levels of Dirt on the Light Distribution of ADB Vehicles*", Darmstadt, Germany: Technische Universität Darmstadt, 2016.

Furthermore, the presented thesis includes the work of student assistants on multiple occasions. While this work includes several areas and did not lead to any publications, much of the presented thesis would not have been possible without their contributions. The students are therefore listed below.

C. Becker, M. Borger, C. Bruns, D. Bursasiu, A. Erkan, D. Hoffmann, S. Klir, A. Kramer, W. Löffler, J. Simon, D. Witon.

CURRICULUM VITAE

Persönliche Daten

Jonas Kobbert
Friedrichstr. 34
64293 Darmstadt

Tel.: (+49) 172 / 25 34 314
E-Mail: kobbert@lichttechnik.tu-darmstadt.de

Geb. am 23.06.1988 in Heidelberg
ledig, deutsch

Berufserfahrung

11/2014–heute **TU Darmstadt, Fachgebiet Lichttechnik**
Hochschulstr. 4a, 64289 Darmstadt

11/2014–aktuell Wissenschaftlicher Mitarbeiter

- Leitung diverser Forschungsprojekte zu den Automobile Frontscheinwerfer, Innenraumbeleuchtung sowie Heckleuchten
- Betreuung von Lehrveranstaltungen und studentischen Arbeiten
- Organsiation von Tagungen und Seminaren der Lichttechnik sowie fachgebietsinterne Organisation
- Förder- und Drittmitteleinwerbung
- Lichttechnische Dienstleistungen sowie Durchführung von Auftragsmessungen und Begutachtungen

03/2014–11/2014 HiWi an der Technischen Universität Darmstadt: Vorlesungsbetreuung Lichttechnik I und II

10/2010–09/2011 Werksstudent, SakostaCAU, Bau-Immobilien und Umwelt - Gesundheit Frankfurt

04/2009–03/2014 HiWi an der Technischen Universität Darmstadt: Übungsgruppenleiter für diverse Veranstaltungen experimenteller Physik (u.a. Betreuung Grundpraktikum, Physik für Maschinenbauer, Vertiefungsvorlesung Optik)

Schulbildung

09/2001–07/2008 Allgemeines Gymnasium | Michelstadt
Leistungskurse: Physik, Biologie
Abschluss: Abitur (Note 1,8)

Studium

10/2009–09/2012 **TU Darmstadt:** Bachelor-Studium der Physik
Thema der Abschlussarbeit: *NMR-Untersuchungen zur molekularen Dynamik in hexagonalem Eis nahe des Schmelzpunktes.*
Abschluss: Bachelor (Note 2,8)

03/2012–06/2012	**TU Darmstadt:** Studentische Miniforschung Thema: *Herstellung und NMR-Spektroskopie der Eis-Phase IX*
10/2011–03/2014	**TU Darmstadt:** Master-Studium der Physik Schwerpunkt Festkörperphysik Thema der Abschlussarbeit: *Kalibrierung, Optimierung und Charakterisierung eines Eye-Tracking-Systems für den KFZ-Einsatz* Abschluss: Master (Note 1,8)

Darmstadt, 23. August 2018

Jonas Kobbert

DECLARATION

§ 8 Abs. 1 lit. c PromO

Ich versichere hiermit, dass die elektronische Version meiner Dissertation mit der schriftlichen Version übereinstimmt.

§ 8 Abs. 1 lit. d PromO

Ich versichere hiermit, dass zu einem vorherigen Zeitpunkt noch keine Promotion versucht wurde. In diesem Fall sind nähere Angaben über Zeitpunkt, Hochschule, Disserationsthema und Ergebnis dieses Versuchs mitzuteilen.

§ 9 Abs. 1 PromO

Ich versichere hiermit, dass die vorliegende Dissertation selbstständig und nur unter Verwendung der angegebenen Quellen verfasst wurde.

§ 9 Abs. 2 PromO

Die Arbeit hat bisher noch nicht zu Prüfungszwecken gedient.

Darmstadt, 23. August 2018

Jonas Kobbert

COLOPHON

This document was typeset using the typographical look-and-feel `classicthesis` developed by André Miede. The style was inspired by Robert Bringhurst's seminal book on typography "*The Elements of Typographic Style*". `classicthesis` is available for both LaTeX and LyX:

`https://bitbucket.org/amiede/classicthesis/`

Happy users of `classicthesis` usually send a real postcard to the author, a collection of postcards received so far is featured here:

`http://postcards.miede.de/`

Final Version as of January 21, 2019 (`classicthesis` version 0.1).